Shadow-wall lithography as a novel approach to Majorana devices

van Loo, N.

DOI
10.4233/uuid:34bcaaa6-ec2b-44fd-ad25-387236568911

Publication date
2023

Document Version
Final published version

Citation (APA)
van Loo, N. (2023). *Shadow-wall lithography as a novel approach to Majorana devices*. [Dissertation (TU Delft), Delft University of Technology]. https://doi.org/10.4233/uuid:34bcaaa6-ec2b-44fd-ad25-387236568911

Important note
To cite this publication, please use the final published version (if applicable).
Please check the document version above.

Shadow-wall lithography as a novel approach to Majorana devices

Shadow-wall lithography as a novel approach to Majorana devices

Proefschrift

ter verkrijging van de graad van doctor
aan de Technische Universiteit Delft,
op gezag van de Rector Magnificus prof. dr. ir. T.H.J.J. van der Hagen,
voorzitter van het College voor Promoties,
in het openbaar te verdedigen op
vrijdag 29 september 2023 om 12:30 uur

door

Nick VAN LOO

Master of Science in Applied Physics,
Technische Universiteit Delft, Nederland,
geboren te Velsen, Nederland.

Dit proefschrift is goedgekeurd door de promotoren.

Samenstelling promotiecommissie:

Rector Magnificus,	voorzitter
Prof. dr. ir. L.P. Kouwenhoven,	Technische Universiteit Delft, promotor
Dr. M.T. Wimmer,	Technische Universiteit Delft, promotor
Onafhankelijke leden:	
Prof. dr. C.J. Palmstrøm,	University of California, Santa Barbara
Prof. dr. G. Katsaros,	Institute of Science and Technology, Austria
Prof. dr. J. Klinovaja,	University of Basel, Switzerland
Prof. dr. G.A. Steele,	Technische Universiteit Delft
Prof. dr. J.M. Thijssen,	Technische Universiteit Delft, reservelid
Overige leden:	
Dr. G.P. Mazur,	Technische Universiteit Delft

Keywords:	Majorana zero mode, Kitaev chain, semiconductor-superconductor hybrid, proximity effect, superconductivity, quantum dot, superconducting diode, nanofabrication, lithography
Printed by:	Ipskamp Printing, Enschede
Cover:	Diversity and complexity of shadow-wall evaporation, by N. van Loo
Style:	TU Delft House Style, with modifications by Moritz Beller `https://github.com/Inventitech/phd-thesis-template`

Casimir PhD Series, Delft-Leiden 2023-24

ISBN 978-90-8593-572-8

An electronic version of this dissertation is available at `http://repository.tudelft.nl/`.

To my wonderful parents
Ria, Gerrit and Marjon

Contents

Summary

The development of quantum computers is perhaps one of the most exciting innovations of our time. The most investigated quantum computers, however, suffer from the fact that quantum information is lost due to interaction between the quantum bits and their environment. As a radically different approach, it has been proposed that one can instead use topological phases of matter to create quantum bits that are immune to environmental noise. The most prominent example of such a topological state of matter is the topological superconductor, which hosts Majorana zero modes. These quasiparticles can be used to store information non-locally, and their non-abelian exchange statistics allow for the implementation of protected quantum gates. Their postulated appearance at the edges of a one-dimensional semiconductor coupled to a superconductor has been a hot research topic over the last decade. Yet, their claimed observation in condensed-matter experiments has not been unequivocal. While the experiments produce some of the signatures of Majorana zero modes, they often exhibit significant deviations from the theory. The main obstacle here is that one of the fundamental properties of Majorana zero modes, namely their non-locality, has not yet been accessible due to the design of these experiments.

In this thesis, we have developed shadow-wall lithography as a novel approach to Majorana devices. One of the key concepts of this technique is to move the majority of the required nanofabrication steps prior to the formation of a semiconductor-superconductor hybrid, which significantly improves the performance of the device. Moreover, the shallow-angle deposition of a thin superconducting film allows the hybrid section to be grounded. This facilitates the simultaneous investigation of both ends of the device, enabling the search for the predicted end-to-end correlation of the Majorana zero modes. We extend the fabrication improvements by also considering the material used in these devices. For their operation, a magnetic field is required, which quenches the superconductivity in the superconducting film due to both orbital and paramagnetic effects. The paramagnetic effects are suppressed through the use of Pt impurities, which provide spin-orbit scattering centers in the film. For the thinnest films, we are able to extend the critical magnetic field up to $B_{\parallel} \sim 7\,\mathrm{T}$. We further demonstrate that the inclusion of Pt does not prevent the quantum states in the semiconductor from obtaining a Zeeman splitting. We combine the improved nanofabrication technique and material developments with novel measurement schemes, such as the use of radio-frequency reflectometry and non-local conductance spectroscopy. The former allows us to map out large regions of the available experimental parameters while looking for the predicted end-to-end correlation of zero energy states. We demonstrate that such correlations are lacking in these devices, indicating that they do not exhibit an extended topological superconducting phase with Majorana zero modes at their ends. With non-local measurements, we instead focus on the induced superconducting gap in the bulk of such a hybrid. We demonstrate a significant tunability through electrostatic

gating and show a closing and reopening of the induced gap, though the absence of zero-bias peaks also indicates that this is not due to an extended topological phase transition. These experiments strongly suggest that the realization of a topological superconductor in semiconductor-superconductor hybrids requires monumental efforts in the development of better materials.

While the bulk of this thesis is devoted to the creation of a topological superconductivity, the final chapters take an alternative approach. We demonstrate that these hybrids possess all the necessary ingredients to form a topological superconductor by using the shadow-wall lithography technique to realize an artificial Kitaev chain. By coupling two quantum dots via a gate-tunable proximitized quantum state in the hybrid segment, we show that the system can be brought to a sweet spot that hosts unpaired Majorana zero modes. To demonstrate the versatility of the developed platform, we finally move away from the study of Majorana zero modes and instead focus on the superconducting diode effect. We show that the tunability of the superconducting properties in a hybrid segment can be used to control the presence and magnitude of the superconducting diode effect in short nanowire Josephson junctions. These two chapters offer an inspiring perspective on the future of semiconductor-superconductor hybrid devices.

Samenvatting

De ontwikkeling van quantumcomputers is misschien wel een van de meest opwindende innovaties van onze tijd. De meest onderzochte quantumcomputers hebben echter last van het feit dat quantuminformatie verloren gaat door interactie tussen de quantumbits en hun omgeving. Als een radicaal andere benadering is voorgesteld dat men topologische fasen van materie kan gebruiken om quantumbits te creëren die immuun zijn voor omgevingsruis. Het meest prominente voorbeeld van zo'n topologische toestand van materie is de topologische supergeleider, die Majorana-nultoestanden bevat. Deze kwasideeltjes kunnen worden gebruikt om informatie niet-lokaal op te slaan, en hun niet-Abelse uitwisselingsstatistieken maken de implementatie van beschermde quantum gates mogelijk. Hun veronderstelde verschijning aan de randen van een ééndimensionale halfgeleider gekoppeld aan een supergeleider is de afgelopen tien jaar een hot topic geweest in het onderzoek. Hun beweerde waarneming in gecondenseerde-materie-experimenten is echter niet ondubbelzinnig geweest. Hoewel de experimenten enkele van de handtekeningen van Majorana-nultoestanden produceren, vertonen ze aanzienlijke afwijkingen van de theorie. Het belangrijkste obstakel hierbij is dat één van de fundamentele eigenschappen van Majorana-nultoestanden, namelijk hun niet-lokaalheid, nog niet toegankelijk is vanwege het ontwerp van deze experimenten.

In deze scriptie hebben we schaduwmuur-lithografie ontwikkeld als een nieuwe benadering voor Majorana-apparaten. Een van de belangrijkste concepten van deze techniek is om het grootste deel van de benodigde nanofabricagestappen vóór de vorming van een halfgeleider-supergeleiderhybride uit te voeren, wat de prestaties van het apparaat aanzienlijk verbetert. Bovendien maakt de ondiepe-hoekdepositie van een dunne supergeleidende film het mogelijk om het hybride gedeelte te aarden. Dit zorgt er voor dat beide uiteinden van het apparaat tegelijkertijd onderzocht kunnen worden, waardoor de zoektocht naar de voorspelde end-to-end correlatie van de Majorana-nultoestanden mogelijk wordt gemaakt. We breiden de fabricageverbeteringen uit door ook het materiaal dat in deze apparaten wordt gebruikt te overwegen. Voor hun werking is een magnetisch veld vereist, terwijl dat ook de supergeleiding in de supergeleidende film dooft als gevolg van zowel orbitale als paramagnetische effecten. De paramagnetische effecten worden onderdrukt door het gebruik van Pt-verontreinigingen, die spin-baanscatteringcentra in de film bieden. Voor de dunste films zijn we in staat om het kritische magnetische veld uit te breiden tot $B_{\parallel} \sim 7\,\mathrm{T}$. We tonen verder aan dat de inclusie van Pt niet voorkomt dat de kwantumtoestanden in de halfgeleider een Zeeman-splitting verkrijgen. We combineren de verbeterde nanofabricagetechniek en materiaalontwikkelingen met nieuwe meetmethoden, zoals het gebruik van radiofrequentie-reflectometrie en niet-lokale geleidbaarheidsspectroscopie. De eerste maakt het mogelijk om grote gebieden van de beschikbare experimentele parameters in kaart te brengen terwijl we op zoek zijn naar de voorspelde end-to-end correlatie van nultoestanden. We tonen aan dat dergelijke correlaties ontbre-

ken in deze apparaten, wat aangeeft dat ze geen ondoorbroken topologische supergeleidingsfase vertonen met Majorana-nultoestanden aan hun uiteinden. Met niet-lokale metingen richten we ons in plaats daarvan op de geïnduceerde supergeleidende kloof in het bulkmateriaal van dergelijke hybriden. We tonen een aanzienlijke afstembaarheid door elektrostatische velden en laten een sluiting en heropening van de geïnduceerde kloof zien, hoewel de afwezigheid van nulspanningspieken ook aangeeft dat dit niet te danken is aan een ondoorbroken topologische fasovergang. Deze experimenten suggereren sterk dat de realisatie van een topologische supergeleider in halfgeleider-supergeleiderhybriden monumentale inspanningen vereist bij de ontwikkeling van betere materialen.

Hoewel het grootste deel van deze thesis gewijd is aan de creatie van topologische supergeleiding, nemen de laatste hoofdstukken een alternatieve aanpak. We tonen aan dat deze hybriden alle noodzakelijke ingrediënten bezitten om een topologische supergeleider te vormen door gebruik te maken van de shadow-wall lithography-techniek om een kunstmatige Kitaev-keten te realiseren. Door twee kwantumdots te koppelen via een afstembare proximiteitsgeïnduceerde kwantumtoestand in het hybride segment, tonen we aan dat het systeem naar een sweet spot kan worden gebracht die ongepaarde Majorana-nultoestanden herbergt. Om de veelzijdigheid van het ontwikkelde platform te demonstreren, stappen we ten slotte weg van de studie van Majorana-nultoestanden en richten we ons in plaats daarvan op het supergeleidende diode-effect. We laten zien dat de regelbaarheid van de supergeleidende eigenschappen in een hybride segment kan worden gebruikt om de aanwezigheid en omvang van het supergeleidende diode-effect te controleren in korte nanodraad Josephson-juncties. Deze twee hoofdstukken bieden een inspirerend perspectief op de toekomst van halfgeleider-supergeleider hybride apparaten.

1

Introduction

Isn't it a noble, an enlightened way of spending our brief time in the sun, to work at understanding the universe and how we have come to wake up in it?

Richard Dawkins

1.1 Understanding our universe

From the very beginning of our existence, humans have strongly desired to understand everything around us. This innate curiosity has driven us to explore, observe, and learn about the world we live in. Science, with its focus on empirical observation and the systematic use of the scientific method, has revolutionized our understanding of the universe. With each scientific revolution, we have gained new insights into the nature of reality, and the boundaries of what we thought we knew have been pushed further and further. The pursuit of knowledge and the quest for understanding have been driving forces behind the evolution of our species.

Perhaps one of the most important revolutions in science has been the invention of the computer, which continues to have a profound impact on our ability to understand the universe. Through advanced computational models, we have been able to analyze large sets of data and perform complex calculations that would have been impossible by hand. The computer has enabled us to discover patterns, make predictions, and test hypotheses in ways that were never before possible. From the smallest subatomic particles to the largest structures in the universe, it has opened up new avenues for exploration and understanding.

Nevertheless, there exist scientific problems that ordinary computers are fundamentally unable to solve. One hope is that instead, we can build computers that operate according to the laws of quantum mechanics. By exploiting some of the strange and counterintuitive properties of quantum mechanics like superposition and entanglement, these quantum computers should potentially be able to solve some of the most complex problems. Just like the inventors of the classical computer could have never imagined what a transformative effect these machines would have, so too do we not yet grasp how quantum computers one day may revolutionize our lives.

However, one of the biggest challenges in building practical quantum computers is the problem of decoherence. Decoherence occurs when quantum systems interact with their environment and lose their quantum properties, leading to errors in calculations. While such errors could in principle be corrected if the decoherence is weak enough, another approach would be to try to make the system immune to the sources that cause decoherence in the first place. This is the concept of topological quantum computation [1]. Topological quantum computers could play a crucial role in solving some of the most challenging scientific problems of our time.

1.2 The Majorana paradox

The most prominent building block for realizing a topological quantum computer is the Majorana quasiparticle. Such quasiparticles can arise at the boundaries of topological superconductors. Without dwelling on what topology means in this context, these particles possess unique properties which make them well-suited to utilize in quantum bits. One

can think of these Majorana zero modes as being half an ordinary fermion, which can be expressed by splitting a fermionic quantum field operator into two Majorana operators: $c = (\gamma_1 + i\gamma_2)/2$. This seemingly mathematical trick has interesting consequences if one can spatially separate the two Majoranas. Due to the particle-hole symmetry of the superconductor, the separated Majoranas can only have zero energy. Indeed, this is why they are commonly referred to as Majorana zero modes. Moreover, inverting the mathematical expression for the Majorana operators shows that they can be described as an equal superposition of electrons and holes. Thus, the Majorana zero modes possess no electrical charge and no spin. As such, these properties evidence that the Majoranas are, in fact, their own antiparticles[1] [2].

These special properties are also the fundamental reason Majorana zero modes are interesting for quantum computation. Indeed, if the two Majorana modes are well-separated, any local fluctuations in the environment can not couple to the individual Majorana mode. Hence, any quantum information that is stored in them should be immune to decoherence. What is more is that they obey a special kind of exchange statistics, which is referred to as non-abelian. This means that exchanging two Majoranas in space results in a non-trivial transformation of the ground state - so that such braiding operations can be used as topologically protected gates in the sense of quantum information processing.

It is thus with good reason that these particles are intensely sought after. Historically, non-abelian quasiparticles were first predicted to appear in the fractional quantum Hall effect [3] and later shown to occur in superconductors with an exotic type of pairing [4]. This preceded the inception of the Kitaev chain toy model [5], which first described the existence of unpaired Majorana zero modes at the ends of a one-dimensional topological superconductor. Various works predicted how to emulate this toy model physically, first based on topological insulators [6] and later culminating in the seminal works by Lutchin [7] and Oreg [8]. The latter is the so-called Lutchyn-Oreg model, which describes how to create a topological superconductor through the combination of a semiconducting wire with spin-orbit coupling, standard *s*-wave superconductivity, and a magnetic field[2]. It formed the basis for over a decade of experimental research into the creation of Majorana zero modes in hybrid semiconductor-superconductor nanowires.

In experiments, the non-abelian nature of the Majorana zero modes can be demonstrated through complex braiding experiments. However, they also manifest a collection of other experimental signatures. For example, the most common experimental signature is a robust conductance peak at zero bias in tunneling experiments. The observation of such a zero-bias peak should further exhibit specific features: notably, the formation should be accompanied by the closing and reopening of the superconducting gap, demonstrate a quantization of the conductance value, and possess end-to-end correlation between two

[1] The fact that these operators are their own antiparticles is the reason why they are referred to as *Majorana* quasiparticles, for these are the condensed-matter analog to the Majorana fermions described by Ettore Majorana in 1937.

[2] This model is described extensively in chapter 2.

sides of a hybrid device. The observation of zero-bias peaks quickly followed the first predictions, and though none of the specific features were observed, they were indeed attributed to the presence of Majorana zero modes [9].

A decade of research followed, with more and more reports on the observation of zero-bias peaks. There exists an abundance of experimental work that claims to have observed Majorana zero modes, where over the years, the observation of any enhanced conductance at zero bias has become synonymous to having a topological superconductor [9–30]. Yet, quantum bits based on Majorana zero modes have not yet been demonstrated, or any experiment more advanced than the demonstration of zero-bias peaks. This is the Majorana paradox[3]: *Where are the Majorana qubits?*

1.3 Developments in the fabrication of semiconductor-superconductor heterostructures

As experimental research progressed, the simultaneous theoretical developments helped to elucidate the shortcomings of the first generation of devices. This has led to the extensive development of the materials and fabrication of semiconductor-superconductor hybrids. As the first generation of hybrids based on InSb and NbTiN used aggressive argon milling as the surface treatment, the induced superconducting gap exhibited a finite sub-gap density of states often referred to as a *soft gap*. The realization that the surface treatment and interface properties between the materials played a crucial role was made, as the first samples with a significantly suppressed sub-gap conductance were realized [31].

Further improvements in the fabrication came with the development of in situ deposition of the superconductor onto the semiconductor, thereby circumventing the need to remove the native oxide from the semiconductor [32]. This method was extended to InSb, where native-oxide removal was achieved through hydrogen-radical cleaning [33]. In both cases, the resulting semiconductor-Al hybrid exhibited a suppressed sub-gap conductance referred to as a *hard gap*. Such hybrids were state-of-the-art around the start of this Ph.D. endeavor.

The main downside of the semiconductor-Al hybrids is that the superconducting shell is deposited onto the nanowire growth chip. Since the superconducting films are on the order of 10 nm thick, the film can, in such cases, not be grounded. Thus, it was impossible to fabricate three-terminal devices for which the end-to-end correlation of the hybrid could be investigated. To see whether the observation of zero-bias peaks can be attributed to Majorana zero modes, one indeed needs to demonstrate such correlations.

[3] Which is somewhat reminiscent of Enrico Fermi's famous paradox (*Where is everybody?*) about the lack of evidence for extraterrestrial life, despite the massive amount of observable stars in the universe.

1

1.4 Outline of this thesis

In this thesis, we have developed a new paradigm for creating hybrid semiconductor-superconductor nanowires. A conceptual overview of the relevant theoretical concepts behind such devices is given in **chapter 2**. We touch upon the basics of superconductivity and its limitations when subjected to a magnetic field. We then move to the concept of topological superconductivity and Majorana zero modes in the Lutchyn-Oreg model. Finally, we will see that one can emulate a Kitaev chain using the very same ingredients, which provides an attractive alternative to the continuous-nanowire approach investigated over the last decade.

The novel nanofabrication technique we have dubbed *shadow-wall lithography* relies on first creating the necessary surrounding elements of a hybrid device while postponing the superconductor deposition as one of the final steps. Grounding the superconducting shell grown on top of a semiconducting nanowire and performing three-terminal measurements requires the film to be grown at shallow angles from the substrate after the nanowire is deposited. In order to selectively deposit the superconducting film, we use dielectric wall structures on the chip, which cast a shadow on predefined locations. In **chapter 3**, an in-depth description of the technique is provided while **chapter 4** demonstrates the design principles and characterization of basic quantum transport devices based on this technique.

While the shadow-wall lithography technique has allowed us to create three-terminal devices, the realization that Majorana zero modes might be hard to find in the vast parameter space of these devices requires the implementation of faster measurement techniques. Radio-frequency reflectometry is well-suited for this, which we use in **chapter 5** to look for end-to-end correlation of zero-energy states and map out the parameter space of such hybrids.

The realization that Al has poor magnetic-field compatibility has led us to consider how to improve this. On the one hand, orbital effects of the magnetic field can be suppressed by growing thinner films. However, superconductors like Al with a low elemental weight also suffer from paramagnetic effects. These can effectively be suppressed through spin-orbit scattering centers, such as heavy-elemental impurities. We implement this by incorporating a sub-monolayer of Pt in our superconducting films. In **chapter 6**, we investigate the basic properties of such films and the enhanced field compatibility it offers to hybrid devices. In **chapter 7**, we add the measurement technique of non-local spectroscopy to characterize the gate-tunable bulk properties of InSb/Al/Pt hybrids in a three-terminal geometry.

In contrast, **chapter 8** turns to the physical implementation of a minimal Kitaev chain. Shadow-wall lithography enables the creation of hybrid devices with gate-defined quantum dots, which possess all the necessary ingredients. We demonstrate that these dots can be coupled via a short superconducting segment, which enables the creation of Majorana

zero modes at a fine-tuned device configuration.

In **chapter 9**, we turn away from the subject of topological superconductivity and instead investigate the superconducting diode effect. The chapter is intimately linked to chapter 7, as we demonstrate that the tunability of the proximity effect can also be used to affect the superconducting diode effect in a nanowire Josephson junction.

Finally, in **chapter 10**, we draw conclusions from the studies presented in this work and look forward to what the future of semiconductor-superconductor hybrid devices has to offer.

References

[1] A. Y. Kitaev, *Fault-tolerant quantum computation by anyons,* Annals of physics **303**, 2 (2003).

[2] E. Majorana, *Teoria simmetrica dell'elettrone e del positrone,* Il Nuovo Cimento (1924-1942) **14**, 171 (1937).

[3] G. Moore and N. Read, *Nonabelions in the fractional quantum hall effect,* Nuclear Physics B **360**, 362 (1991).

[4] N. Read and D. Green, *Paired states of fermions in two dimensions with breaking of parity and time-reversal symmetries and the fractional quantum hall effect,* Physical Review B **61**, 10267 (2000).

[5] A. Y. Kitaev, *Unpaired majorana fermions in quantum wires,* Physics-uspekhi **44**, 131 (2001).

[6] L. Fu and C. L. Kane, *Superconducting proximity effect and majorana fermions at the surface of a topological insulator,* Physical review letters **100**, 096407 (2008).

[7] R. M. Lutchyn, J. D. Sau, and S. D. Sarma, *Majorana fermions and a topological phase transition in semiconductor-superconductor heterostructures,* Physical review letters **105**, 077001 (2010).

[8] Y. Oreg, G. Refael, and F. Von Oppen, *Helical liquids and majorana bound states in quantum wires,* Physical review letters **105**, 177002 (2010).

[9] V. Mourik, K. Zuo, S. M. Frolov, S. Plissard, E. P. Bakkers, and L. P. Kouwenhoven, *Signatures of majorana fermions in hybrid superconductor-semiconductor nanowire devices,* Science **336**, 1003 (2012).

[10] M. Deng, C. Yu, G. Huang, M. Larsson, P. Caroff, and H. Xu, *Anomalous zero-bias conductance peak in a nb–insb nanowire–nb hybrid device,* Nano letters **12**, 6414 (2012).

[11] A. Das, Y. Ronen, Y. Most, Y. Oreg, M. Heiblum, and H. Shtrikman, *Zero-bias peaks and splitting in an al–inas nanowire topological superconductor as a signature of majorana fermions,* Nature Physics **8**, 887 (2012).

[12] H. Churchill, V. Fatemi, K. Grove-Rasmussen, M. Deng, P. Caroff, H. Xu, and C. M. Marcus, *Superconductor-nanowire devices from tunneling to the multichannel regime: Zero-bias oscillations and magnetoconductance crossover,* Physical Review B **87**, 241401 (2013).

[13] A. Finck, D. Van Harlingen, P. Mohseni, K. Jung, and X. Li, *Anomalous modulation of a zero-bias peak in a hybrid nanowire-superconductor device,* Physical review letters **110**, 126406 (2013).

[14] M. Deng, C. Yu, G. Huang, M. Larsson, P. Caroff, and H. Xu, *Parity independence of the zero-bias conductance peak in a nanowire based topological superconductor-quantum dot hybrid device,* Scientific reports **4**, 7261 (2014).

[15] S. Nadj-Perge, I. K. Drozdov, J. Li, H. Chen, S. Jeon, J. Seo, A. H. MacDonald, B. A. Bernevig, and A. Yazdani, *Observation of majorana fermions in ferromagnetic atomic chains on a superconductor,* Science **346**, 602 (2014).

[16] M. Deng, S. Vaitiekėnas, E. B. Hansen, J. Danon, M. Leijnse, K. Flensberg, J. Nygård, P. Krogstrup, and C. M. Marcus, *Majorana bound state in a coupled quantum-dot hybrid-nanowire system,* Science **354**, 1557 (2016).

[17] H. J. Suominen, M. Kjaergaard, A. R. Hamilton, J. Shabani, C. J. Palmstrøm, C. M. Marcus, and F. Nichele, *Zero-energy modes from coalescing andreev states in a two-dimensional semiconductor-superconductor hybrid platform,* Physical review letters **119**, 176805 (2017).

[18] F. Nichele, A. C. Drachmann, A. M. Whiticar, E. C. O'Farrell, H. J. Suominen, A. Fornieri, T. Wang, G. C. Gardner, C. Thomas, A. T. Hatke, *et al.*, *Scaling of majorana zero-bias conductance peaks,* Physical review letters **119**, 136803 (2017).

[19] J. Chen, P. Yu, J. Stenger, M. Hocevar, D. Car, S. R. Plissard, E. P. Bakkers, T. D. Stanescu, and S. M. Frolov, *Experimental phase diagram of zero-bias conductance peaks in superconductor/semiconductor nanowire devices,* Science advances **3**, e1701476 (2017).

[20] Ö. Gül, H. Zhang, J. D. Bommer, M. W. de Moor, D. Car, S. R. Plissard, E. P. Bakkers, A. Geresdi, K. Watanabe, T. Taniguchi, *et al.*, *Ballistic majorana nanowire devices,* Nature nanotechnology **13**, 192 (2018).

[21] M.-T. Deng, S. Vaitiekėnas, E. Prada, P. San-Jose, J. Nygård, P. Krogstrup, R. Aguado, and C. Marcus, *Nonlocality of majorana modes in hybrid nanowires,* Physical Review B **98**, 085125 (2018).

[22] H. Zhang, C.-X. Liu, S. Gazibegovic, D. Xu, J. A. Logan, G. Wang, N. Van Loo, J. D. Bommer, M. W. De Moor, D. Car, *et al.*, *Retracted article: Quantized majorana conductance,* Nature **556**, 74 (2018).

[23] A. Fornieri, A. M. Whiticar, F. Setiawan, E. Portolés, A. C. Drachmann, A. Keselman, S. Gronin, C. Thomas, T. Wang, R. Kallaher, *et al.*, *Evidence of topological superconductivity in planar josephson junctions,* Nature **569**, 89 (2019).

[24] H. Ren, F. Pientka, S. Hart, A. T. Pierce, M. Kosowsky, L. Lunczer, R. Schlereth, B. Scharf, E. M. Hankiewicz, L. W. Molenkamp, *et al.*, *Topological superconductivity in a phase-controlled josephson junction,* Nature **569**, 93 (2019).

[25] A. Grivnin, E. Bor, M. Heiblum, Y. Oreg, and H. Shtrikman, *Concomitant opening of a bulk-gap with an emerging possible majorana zero mode,* Nature communications **10**, 1940 (2019).

[26] M. Desjardins, L. Contamin, M. Delbecq, M. Dartiailh, L. Bruhat, T. Cubaynes, J. Viennot, F. Mallet, S. Rohart, A. Thiaville, *et al.*, *Synthetic spin–orbit interaction for majorana devices,* Nature materials **18**, 1060 (2019).

[27] S. Vaitiekėnas, G. Winkler, B. Van Heck, T. Karzig, M.-T. Deng, K. Flensberg, L. Glazman, C. Nayak, P. Krogstrup, R. Lutchyn, *et al.*, *Flux-induced topological superconductivity in full-shell nanowires,* Science **367**, eaav3392 (2020).

[28] S. Vaitiekėnas, Y. Liu, P. Krogstrup, and C. Marcus, *Zero-bias peaks at zero magnetic field in ferromagnetic hybrid nanowires,* Nature Physics **17**, 43 (2021).

[29] D. M. van Zanten, D. Sabonis, J. Suter, J. I. Väyrynen, T. Karzig, D. I. Pikulin, E. C. O'Farrell, D. Razmadze, K. D. Petersson, P. Krogstrup, *et al.*, *Photon-assisted tunnelling of zero modes in a majorana wire,* Nature Physics **16**, 663 (2020).

[30] M. Aghaee, A. Akkala, Z. Alam, R. Ali, A. A. Ramirez, M. Andrzejczuk, A. E. Antipov, M. Astafev, B. Bauer, J. Becker, *et al.*, *Inas-al hybrid devices passing the topological gap protocol,* arXiv preprint arXiv:2207.02472 (2022).

[31] O. Gül, H. Zhang, F. K. de Vries, J. van Veen, K. Zuo, V. Mourik, S. Conesa-Boj, M. P. Nowak, D. J. van Woerkom, M. Quintero-Pérez, *et al.*, *Hard superconducting gap in insb nanowires,* Nano letters **17**, 2690 (2017).

[32] P. Krogstrup, N. Ziino, W. Chang, S. Albrecht, M. Madsen, E. Johnson, J. Nygård, C. M. Marcus, and T. Jespersen, *Epitaxy of semiconductor–superconductor nanowires,* Nature materials **14**, 400 (2015).

[33] S. Gazibegovic, D. Car, H. Zhang, S. C. Balk, J. A. Logan, M. W. De Moor, M. C. Cassidy, R. Schmits, D. Xu, G. Wang, *et al.*, *Retracted article: Epitaxy of advanced nanowire quantum devices,* Nature **548**, 434 (2017).

2

Theory

With four parameters I can fit an elephant, and with five I can make him wiggle his trunk.

John von Neumann

This chapter introduces the theory behind various topics, providing a background for understanding the experiments presented in this thesis. The description will be predominantly on a conceptual level while omitting many of the details, in order to give the reader an intuitive understanding. We start with superconductivity, which is fundamental to all the following topics. The focus is on the microscopic description in the form of BCS theory. In addition, we use some results from Ginzburg-Landau theory to look at the properties of superconductors in a magnetic field. We then look at topological superconductivity, an exotic form of superconductivity that is accompanied by the emergence of Majorana zero modes. It will first be described in the Kitaev chain model, which gives a good intuition on the subject. We then turn to the Lutchyn-Oreg model, which describes how we can realize a topological superconductor by combining a regular superconductor with a semiconductor, spin-orbit coupling, and a magnetic field. More realistic extensions of this model are briefly mentioned, and we will see what signatures of Majorana zero modes one can expect in experiments. Finally, we revisit the Kitaev chain and see how one can physically realize one using the same ingredients as the Lutchyn-Oreg model.

2.1 Superconductivity

If the temperature of some materials is lowered below a critical temperature, they undergo a special phase transition. Upon this transition, the material suddenly exhibits zero electrical resistance and starts to expel magnetic fields. The perfect conductivity associated with the absence of electrical resistance gave this phenomena its name: superconductivity. Its initial discovery by Heike Kamerlingh Onnes [1] in 1911 was a complete surprise, as no classical physics could have predicted it. It gave rise to decades of development in theoretical physics, which culminated in two paramount theoretical frameworks: The Ginzburg-Landau theory [2] and Bardeen-Cooper-Schrieffer (or BCS) theory [3]. The former is a phenomenological description that predicts the electrodynamics of superconductors remarkably well. Since we are especially interested in the critical magnetic field upon which superconductors transition into the normal state, we will present some of its primary results. More important to us, however, is the microscopic description given by BCS theory and solutions found using the Bogoliubov-de Gennes formalism [4, 5] - as this framework can be extended to investigate even more exotic systems, such as proximitized semiconductors.

2.1.1 BCS theory and the Bogoliubov-de Gennes formalism

The core idea of BCS theory is that it is energetically favorable for electrons to form pairs, known as Cooper pairs, if there is some attractive interaction between them. The most common form of superconductivity is known as *s*-wave superconductivity. For such superconductors, the interaction is described in the form of a potential $V_{kk'}$ which scatters a pair of electrons with opposite spin and opposite momenta from $(k', -k')$ to $(k, -k)$. With creation and annihilation operators as $c^\dagger_{k\sigma}$ and $c_{k\sigma}$ for electrons with momentum k and spin σ, the system can be described [6] using the pairing Hamiltonian:

$$\mathscr{H} = \sum_{k\sigma} \xi_k c^\dagger_{k\sigma} c_{k\sigma} + \sum_{kk'} V_{kk'} c^\dagger_{k\uparrow} c^\dagger_{-k\downarrow} c_{-k'\downarrow} c_{k'\uparrow} \tag{2.1}$$

Here, $\xi_k = \hbar^2 k^2 / 2m^* - \mu$ represents the single-particle energies relative to the Fermi level μ, with $\hbar$ the reduced Planck constant and m^* the effective mass. Upon realizing that the pairing term needs to scatter electrons from occupied to unoccupied states, it follows that the attractive interaction only applies to electrons close to the Fermi level. One can then use the BCS approximation to replace $V_{kk'} \longrightarrow -V$ where the attractive potential $-V$ is constant over the relevant energy range.

Subsequently, the mean-field approximation can be used to simplify the Hamiltonian 2.1 further. The basic idea behind the mean-field approximation is to assume that the behavior of each particle in the system is determined by the average effect of all the other particles rather than by the individual interactions between each pair of particles. In our case, this means we can expand a pair of operators like $c_{-k'\downarrow} c_{k'\uparrow}$ into a sum of their expectation value $\langle c_{-k'\downarrow} c_{k'\uparrow} \rangle$ plus some fluctuations, and assume that the fluctuations are negligible. We then write $\Delta = V \sum_{k'} \langle c_{-k'\downarrow} c_{k'\uparrow} \rangle$ which represents the superconducting pairing, so that we arrive at the BCS Hamiltonian in the mean-field approximation:

$$\mathscr{H}_M = \sum_{k\sigma} \xi_k c^\dagger_{k\sigma} c_{k\sigma} - \sum_k (\Delta c^\dagger_{k\uparrow} c^\dagger_{-k\downarrow} + \Delta^* c_{-k\downarrow} c_{k\uparrow}) \tag{2.2}$$

This form of the Hamiltonian can be solved by diagonalizing it, which is most conveniently done using the Bogoliubov transformation. However, it is more instructive to introduce at this stage the Bogoliubov-de Gennes formalism, which is a generalization of the Bogoliubov transformation that can also be applied to systems with broken spin degeneracy.

In the Bogoliubov-de Gennes formalism, one defines a new basis known as a Nambu spinor Ψ. This spinor explicitly includes both electron and hole operators, as well as both spin species. The Hamiltonian can then be written in this basis as

$$\mathscr{H}_M = \frac{1}{2} \sum_k \Psi^\dagger H_{\mathrm{BdG}} \Psi, \qquad \Psi^\dagger = (c^\dagger_{k\uparrow}, c^\dagger_{k\downarrow}, c_{k\downarrow}, -c_{k\uparrow}) \tag{2.3}$$

with the Bogoliubov-de Gennes Hamiltonian H_{BdG} given by

$$H_{\mathrm{BdG}} = \xi_k \tau_z + \Delta \tau_x \tag{2.4}$$

Here, τ_i represent Pauli matrices acting on the particle-hole subspace of the Hamiltonian. Solutions of this Hamiltonian can be found by solving the characteristic equation $det(H_{\mathrm{BdG}} - E_k) = 0$, which gives us the excitation spectrum

$$E_k = \pm \sqrt{\xi_k^2 + \Delta^2} \tag{2.5}$$

This spectrum actually contains four bands, two resulting from spin degeneracy and the other two are symmetric copies of these bands around the Fermi level. These copies result from particle-hole symmetry $E_{k\sigma} = -E_{-k-\sigma}$, which is revealed by explicitly treating holes and electrons in the Nambu spinor. If we think of the system without superconducting pairing, we can describe the electronic excitations with dispersion ξ_k (as shown in figure 2.1a(i)) and hole excitations with dispersion $-\xi_{-k}$. The superconducting pairing then hybridizes these bands, opening up a gap of 2Δ in the energy spectrum where the bands initially crossed - that is, around the Fermi level. The resulting spectrum is shown in figure 2.1a(ii), where we see that the lowest-energy excitation at $\xi_k = 0$ still requires an energy of Δ. For this reason, it is commonly referred to as the superconducting gap. A zoom-in near the Fermi level is shown in figure 2.1a(iii). We emphasize that in the case of metallic systems, the Fermi level is typically much larger than the superconducting pairing. The energies differ about five orders of magnitude in the particular case of aluminum [7], with $\mu = 11.27\,\mathrm{eV}$ and $\Delta \approx 150 - 350\,\mu\mathrm{eV}$.

The hybridization of the bands also means that electrons and holes are no longer the elementary excitations of a superconductor. Instead, the excitations are now quasiparticles described by a superposition of electrons and holes. To find the appropriate operators for these quasiparticles, we look to solve the Bogoliubov-de Gennes equations

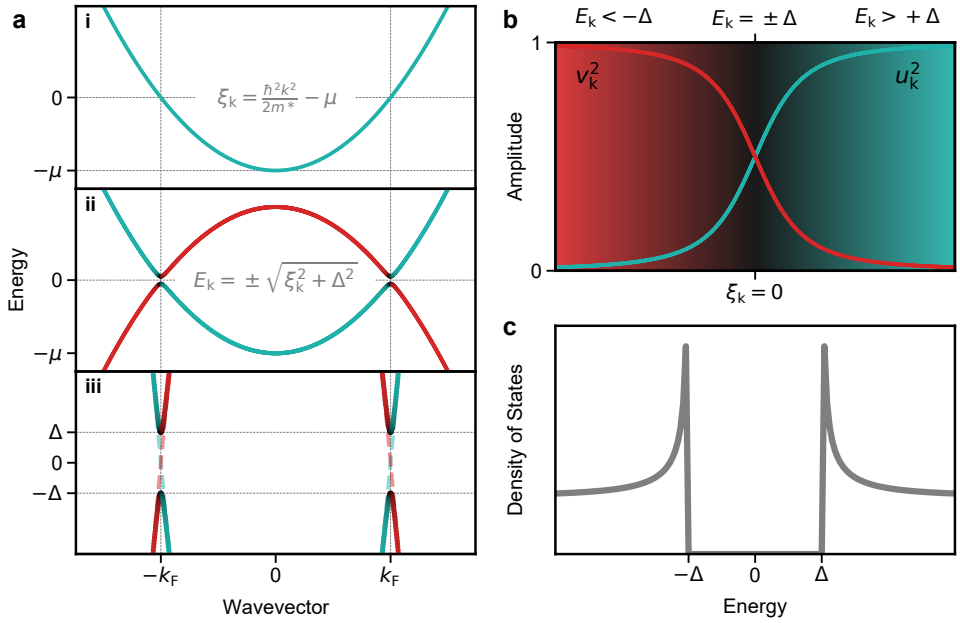

Figure 2.1: **Excitation spectrum, coherence factors, and density of states of a superconductor. a.** (i) Excitation spectrum in the absence of superconductivity. (ii) Upon using the Bogoliubov-de Gennes formalism, we explicitly obtain electron (turquoise) and hole (red) solutions. The bands are hybridized via the superconducting pairing Δ. (iii) Close to the Fermi level, the hybridization opens up a gap of 2Δ in the spectrum. Dashed lines correspond to the dispersion in the absence of superconductivity. **b.** Coherence factors u_k and v_k near the Fermi level. The background color represents the quasiparticle charge, going from e (red) via 0 (black) to $-e$ (turquoise). This color is superimposed on the band structure of **a**, visualizing that quasiparticles near the gap edge are chargeless superpositions of electrons and holes. **c.** Density of states of a superconductor, exhibiting coherence peaks at the edge of the superconducting gap.

$$H_{\mathrm{BdG}}\phi_k = E_k\phi_k, \qquad \phi_k = (u_{k\uparrow}, u_{k\downarrow}, v_{k\downarrow}, v_{k\uparrow})^\top \tag{2.6}$$

Since we are dealing with a spin-degenerate system, we have $u_{k\uparrow} = u_{k\downarrow} \equiv u_k$ and $v_{k\uparrow} = v_{k\downarrow} \equiv v_k$. These are known as the coherence factors and represent the electron- and hole components of the excitations. The solution is given by

$$|u_k|^2 = \frac{1 + \xi_k/|E_k|}{2}, \qquad |u_k|^2 + |v_k|^2 = 1 \tag{2.7}$$

and the excitations, known as Bogoliubov quasiparticles, can be written as

$$\gamma_{k\uparrow}^\dagger = u_k c_{k\uparrow}^\dagger - v_k c_{-k\downarrow}, \qquad \gamma_{k\downarrow}^\dagger = u_k c_{-k\downarrow}^\dagger + v_k c_{k\uparrow} \tag{2.8}$$

From the coherence factors, the charge of the quasiparticles can be calculated as $-e(|u_k|^2 - |v_k|^2)$. Thus we see that far below the Fermi level, the excitations are hole-like, whereas

far above the Fermi level, they are electron-like. Moreover, the lowest energy excitations at the energy of the superconducting gap feature an equal superposition of electrons and holes. The coherence factors close to the Fermi level are shown in figure 2.1b. The gradient color represents the quasiparticle charge, with electron-like excitations as turquoise, equal superpositions as black and hole-like excitations as red. The charge is also superimposed on the spectra in figure 2.1a.

Finally, we can calculate the density of states N_s of a superconductor. This is done by recognizing there is a one-to-one correspondence between the electronic operators in the normal state and the Bogoliubov quasiparticles in the superconducting state. This means that $N_s(E)dE = N_n(\xi)d\xi$, and since the relevant energy range is much smaller than the Fermi level, we can approximate the normal-state density of states $N_n(\xi)$ as constant $N_n(\xi) = N_0$. Then, as shown in figure 2.1c, we find

$$\frac{N_s}{N_0} = \left| \frac{E_k}{\sqrt{E_k^2 - \Delta^2}} \right| \tag{2.9}$$

which diverges at the edge of the superconducting gap $E_k = \Delta$. The sharp peaks are known as the coherence peaks, and far from the Fermi level, we see that the superconducting density of states approaches that of the normal state.

2.1.2 Superconductors in a magnetic field

So far, we have treated the superconductor in the absence of a magnetic field. A magnetic field generally acts on the different spin species through the Zeeman effect. This either raises or lowers their energy, resulting in a modified excitation spectrum and density of states. If we ignore the effect of the magnetic field on the orbital motion of the electrons and assume the superconductor possesses no spin-orbit scattering, the Hamiltonian in equation 2.4 can be modified [8] to read

$$H_{\mathrm{BdG}} = \xi_k \tau_z + \frac{1}{2} g \mu_{\mathrm{B}} \mathbf{B} \cdot \boldsymbol{\sigma} + \Delta \tau_x \tag{2.10}$$

Here g is the Landé g-factor, μ_{B} is the Bohr magneton, $\mathbf{B} = (B_x, B_y, B_z)$ is the magnetic field and $\boldsymbol{\sigma} = (\sigma_x, \sigma_y, \sigma_z)$ are the Pauli matrices acting on the spin subspace of the Hamiltonian. The direction of the magnetic field now defines the quantization axis for the spins. In addition, the energy of the excitations is adjusted by the Zeeman energy $E_Z = g\mu_{\mathrm{B}}B/2$ depending on the spin direction, where B is the magnitude of the magnetic field. The excitation spectrum is shown in figure 2.2a, where the color now represents the spin of each branch. The formerly-degenerate dispersion branches have evolved into four non-degenerate branches, given by

$$E_{k\uparrow} = \pm \sqrt{\xi_k^2 + \Delta^2} + \frac{1}{2} g \mu_{\mathrm{B}} B, \qquad E_{k\downarrow} = \pm \sqrt{\xi_k^2 + \Delta^2} - \frac{1}{2} g \mu_{\mathrm{B}} B \tag{2.11}$$

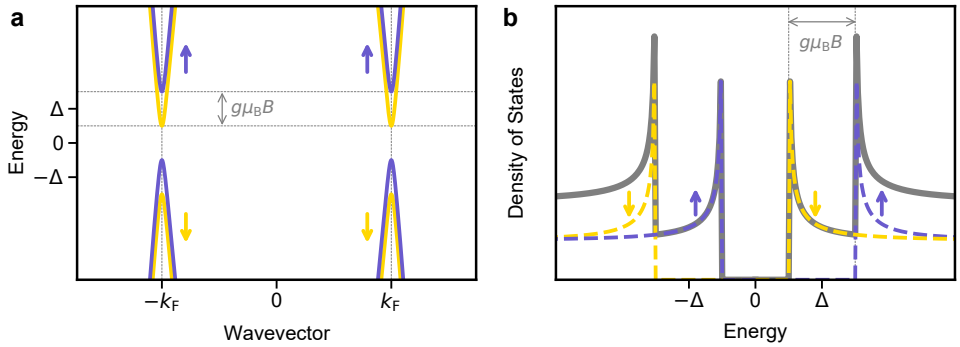

Figure 2.2: **Excitation spectrum and density of states of a superconductor in a finite magnetic field. a.** A magnetic field increases the energy of the spin-up band and lowers the energy of the spin-down band, separating the two by twice the Zeeman energy $2E_Z = g\mu_B B$. **b.** Zeeman splitting also affects the density of states. The total density of states becomes the sum of two Zeeman-split versions of the original density of states.

The Zeeman splitting also shows up in the density of states. One way to think about it is to see that the density of states at zero field contains two copies with a statistical weight of $\frac{1}{2}$, one for each spin species. The magnetic field then shifts these copies either up or down by the Zeeman energy, similar to how it acts on the excitation spectrum. The total density of states becomes the sum of the two, which is given by

$$\frac{N_s}{N_0} = \frac{1}{2}\left| \frac{E_k - \frac{1}{2}g\mu_B B}{\sqrt{(E_k - \frac{1}{2}g\mu_B B)^2 - \Delta^2}} + \frac{E_k + \frac{1}{2}g\mu_B B}{\sqrt{(E_k + \frac{1}{2}g\mu_B B)^2 - \Delta^2}} \right| \tag{2.12}$$

The density of states in a finite magnetic field is shown in figure 2.2b. One notices that the Zeeman splitting tends to close the energy gap in the system. In particular, the gap closes when the Zeeman energy equals the magnitude of the superconducting gap at zero field. That is, at a magnetic field of $B = 2\Delta/g\mu_B$. In the case of aluminum, for example, this happens at $B = 4.3\,\mathrm{T}$ assuming $\Delta = 250\,\mu\mathrm{eV}$. In practice, superconductivity in bulk aluminum is destroyed far before such magnetic fields are reached.

2.1.3 Critical magnetic field of thin films

Magnetic fields affect both the motion and spin of conduction electrons, which can hinder the formation of Cooper pairs and hence superconductivity. In most cases, the impact of a magnetic field on electron orbits is the main factor suppressing superconductivity, as it is usually more potent than its effect on spins [8]. However, there are methods to minimize the impact on the electron motion, such as utilizing thin films with a parallel magnetic field [9]. If the magnetic field's impact on electron orbits is small, its impact on electron spins may become dominant.

Let us first focus on the orbital effects of the magnetic field. Since superconductors are characterized by the absence of electrical resistance, any applied field will induce screen-

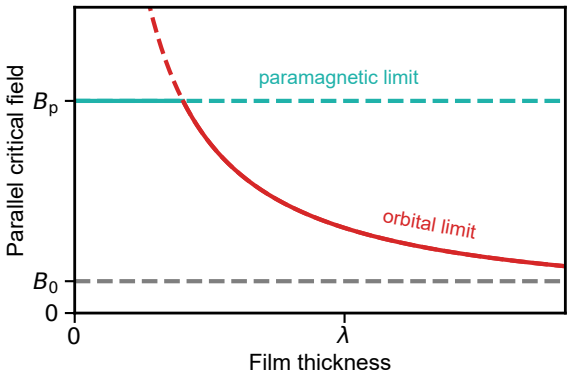

Figure 2.3: **Limitations to the critical magnetic field of thin superconducting films.** For bulk superconductors, the critical field is given by the thermodynamic critical field B_0. In films which are thin compared to the penetration depth, orbital effects of the magnetic field are suppressed, and the critical field is enhanced, as shown by the red curve. For very thin films, paramagnetic effects put an upper limit on the critical field B_p.

ing currents flowing in the material. These currents, in turn, generate their own magnetic field that opposes the external magnetic field. As a result, the magnetic field is completely expelled from the interior of the superconductor, a phenomenon known as perfect diamagnetism or the Meissner effect [10]. The screening currents induced in the superconductor, however, do contribute to the free energy of the material. The free energy density in the superconducting state f_s in the absence of a magnetic field is lower than that in the normal state f_n by an amount known as the condensation energy $f_n - f_s$. If the screening currents in the material raise f_s above f_n, the normal state becomes energetically favorable. The magnetic field for which this happens is the thermodynamic critical field B_0, given by $f_n - f_s = B_0^2/8\pi$. In our case, bulk aluminum at zero temperature typically has very poor field compatibility characterized by a thermodynamic critical field on the order of $B_0 \sim 10\,\mathrm{mT}$ [11, 12].

One way to overcome this limitation is to make the material very thin and apply the magnetic field parallel to the film. In particular, if the thickness d of a film becomes comparable to or smaller than the penetration depth λ, no sufficiently strong screening currents can arise in the material [8]. In this scenario, an applied parallel field can exceed the thermodynamic critical field. If one ignores screening currents altogether, one can rely on Ginzburg-Landau theory to find that

$$B_{c\parallel} = 2\sqrt{6}B_0\frac{\lambda}{d} \tag{2.13}$$

where $B_{c\parallel}$ is the parallel critical field. The dependence on the thickness of the film is shown in figure 2.3 as the orbital limit (red curve). One sees that in thin enough films, the parallel critical field diverges. However, as these orbital effects are more and more suppressed, the effect of the magnetic field on the electron spins can become dominant.

To see how paramagnetic effects limit the critical field of a thin film, let us again consider the free energy density while neglecting the orbital effects of the magnetic field. The free energy in the normal state can be lowered due to the magnetization of the film by an amount proportional to the paramagnetic susceptibility and the magnetic field strength. The paramagnetic susceptibility typically vanishes in the superconducting state at temperatures far below T_c [13]. Thus, paramagnetic effects can lower the free energy in the normal state below that of the superconducting state - also triggering a phase transition. The free energy difference is, in this case, given by

$$f_n - f_s = \frac{1}{2}\chi_p B_p^2 \tag{2.14}$$

where we have anticipated a paramagnetic limit to the critical field B_p. The paramagnetic susceptibility can be written in terms of the density of states as $\chi_p = g^2\mu_B^2 N_0/2$. In addition, the condensation energy can also be found from BCS theory as $f_n - f_s = N_0\Delta^2/2$. Inserting these two into equation 2.14, one finds the Pauli paramagnetic limit or Clogston-Chandrasekhar limit [14, 15]

$$B_p = \frac{\sqrt{2}}{g\mu_B}\Delta \tag{2.15}$$

This limit is also shown in figure 2.3 as the turquoise curve. For example, if we assume a thin aluminum film has a superconducting gap $\Delta = 250\,\mu$eV, we find that $B_p = 3.1\,$T - a factor $\sqrt{2}$ smaller than we found the Zeeman field to close the superconducting gap.

In practice, relevant parameters like the superconducting gap and the penetration depth may vary with the thickness of the superconductor. In the case of aluminum [16], Δ increases as the film becomes thinner - thus resulting in an elevated paramagnetic limit. Similarly, the penetration depth increases as the thickness of the film is reduced [6], which in turn raises the orbital limit of the critical field. It becomes clear that in order to reach as high critical fields as possible, one needs to grow the film thin and apply the magnetic field in parallel. Moreover, the addition of spin-orbit scattering impurities can lift the paramagnetic limit [9]. We exploit these techniques in chapters 6 and 7, where we use thin aluminum coated by platinum impurities to proximitize indium-antimonide nanowires.

2.2 Topological superconductivity: Majorana zero modes

We have seen that regular superconductors exhibit *s*-wave superconductivity, where electrons of opposite spin species form pairs. However, one can also imagine pairing up electrons with the same spin. The Pauli exclusion principle then requires the orbital part of the superconducting wavefunction to be antisymmetric, for example by using the *p*-orbital instead of the *s*-orbital. It is in systems with this type of *p*-wave pairing that the existence of topological superconductivity was predicted [17, 18]. Such superconductors host Majorana zero modes, which in a one-dimensional system are bound to its ends [19–21]. The most prominent theoretical model that realizes a topological superconductor is known as

the Kitaev chain [22], which consists of discrete sites of spinless fermions. Such a chain can be implemented physically [23–25], as we will see in section 2.3. It also formed the foundation for a continuous model, first described by Lutchyn [26] and Oreg [27]. This model is remarkable because it gives a minimalistic description of how to engineer an effective p-wave superconductor, starting from an s-wave superconductor. Majorana zero modes are indeed predicted to arise in both models, and we will see what specific experimental signatures are expected to result from their emergence.

2.2.1 The Kitaev chain

A superconducting Hamiltonian can be modified to engineer more exotic forms of superconducting pairing. In particular, one can attempt to create a topological superconductor by pairing up electrons with the same spin, otherwise known as p-wave or spin-triplet pairing. To understand how this works, we first consider a simplified model known as the Kitaev chain. The Hamiltonian for this chain is given by

$$H = -\mu \sum_{n=1}^{N} c_n^\dagger c_n - t \sum_{n=1}^{N-1} \left(c_n^\dagger c_{n+1} + c_{n+1}^\dagger c_n \right) + \Delta \sum_{n=1}^{N-1} \left(c_n c_{n+1} + c_{n+1}^\dagger c_n^\dagger \right) \tag{2.16}$$

It describes a chain of N lattice sites labeled by index n, each hosting a single fermionic excitation which is assumed to possess no spin. The excitations each have an on-site chemical potential μ, which is assumed to be equal for all sites. Moreover, they can hop between adjacent sites via a hopping parameter $t > 0$. Finally, the superconducting pairing Δ creates or destroys pairs of fermions at adjacent sites. An illustration of the model is shown in figure 2.4a.

To see under what conditions this chain hosts topological superconductivity, we rewrite all the fermionic operators in the Hamiltonian in terms of Majorana operators defined by

$$\begin{gathered} \gamma_{n,A} = c_n^\dagger + c_n, \qquad \gamma_{n,B} = i(c_n^\dagger - c_n) \\ \gamma_{n,\alpha}^\dagger = \gamma_{n,\alpha}, \quad \gamma_{n,\alpha}^2 = 1, \quad \{\gamma_{n,\alpha}, \gamma_{m,\beta}\} = 2\delta_{\alpha\beta}\delta_{nm} \end{gathered} \tag{2.17}$$

so that the fermionic operators are described by $c_n = (\gamma_{n,A} + i\gamma_{n,B})/2$. The fermions on one lattice site can be artificially split into two Majorana modes, defined on two new sublattices A and B. Plugging this definition into the Hamiltonian 2.16, we get

$$H = -\frac{\mu}{2} \sum_{n=1}^{N} (1 + i\gamma_{n,A}\gamma_{n,B}) + \frac{i}{2} \sum_{n=1}^{N-1} \left((\Delta + t)\gamma_{n,B}\gamma_{n+1,A} + (\Delta - t)\gamma_{n,A}\gamma_{n+1,B} \right) \tag{2.18}$$

We see that μ couples Majorana operators on the same site, whereas the new coupling parameters $\Delta + t$ and $\Delta - t$ now couple them between adjacent sites. The Hamiltonian in this form is illustrated in figure 2.4b.

We now consider two particular limits of the Hamiltonian. First, let us see what happens if we set $\Delta = t = 0$ and $\mu \neq 0$. It becomes evident that the second term in the Hamiltonian 2.18

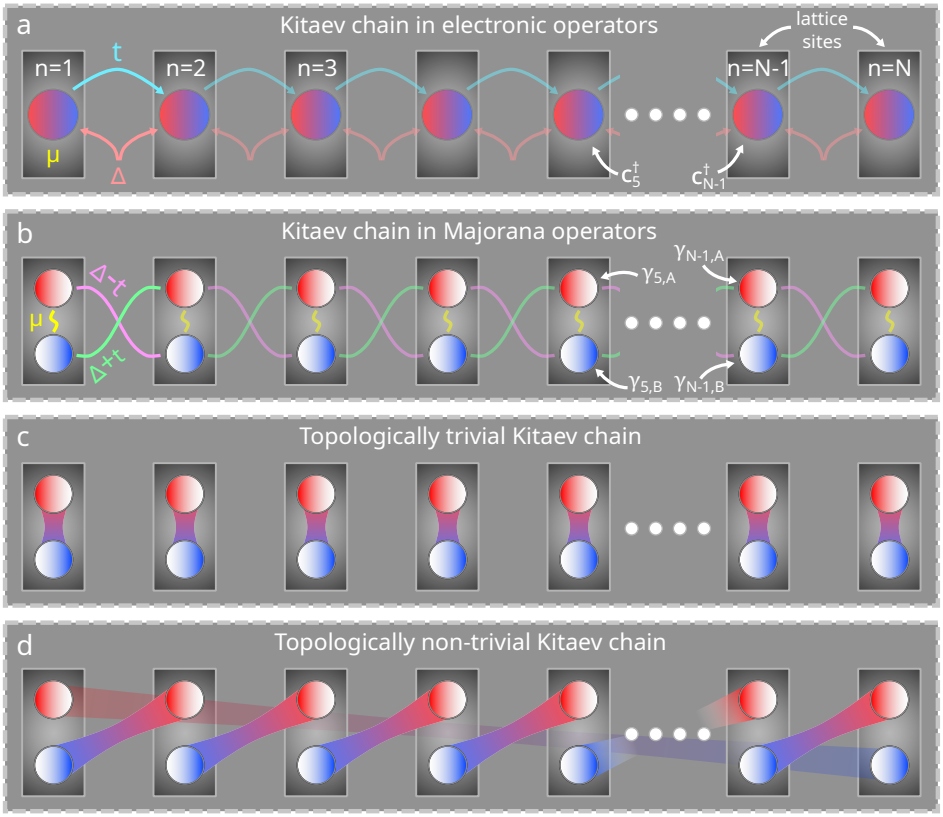

Figure 2.4: **Emergence of topological superconductivity in the Kitaev chain. a.** Kitaev chain in electronic operators. There are N lattice sites labeled by n, each hosting a single spinless excitation with on-site energy μ. Neighboring sites are coupled through regular tunneling t and a shared superconductor Δ. **b.** Kitaev chain expressed in Majorana operators. This creates two sublattices A (red) and B (blue), which are coupled on-site via μ and off-site via $\Delta - t$ and $\Delta + t$. **c.** In the absence of hopping terms ($\Delta = t = 0$ and $\mu \neq 0$), the Majorana modes hybridize to form localized fermions on each site. This describes the topologically trivial scenario. **d.** In the absence of an on-site coupling and equalizing the off-site couplings ($\Delta = t \neq 0$ and $\mu = 0$), two unpaired Majorana zero modes remain at the ends of the chain, which together form a delocalized fermion. This describes the topologically non-trivial scenario.

drops out, and we are left only with an on-site coupling. The Majorana modes hybridize and form fermionic modes, localized on the individual sites and with an excitation energy $|\mu|$ - thus leaving the bulk of the chain with an energy gap of this magnitude. This scenario is topologically trivial and is depicted in figure 2.4c.

In contrast, we can also set the on-site coupling $\mu = 0$ and pick $\Delta = t \neq 0$. In this case, the only remaining coupling term in the Hamiltonian is between adjacent sites. Again, the modes hybridize to form fermionic modes with a bulk excitation gap of 2Δ. However, unlike in the trivial case, 2 Majorana operators are now missing from the Hamiltonian: $\gamma_{1,A}$ and $\gamma_{N,B}$. Together they form a delocalized fermionic excitation which has zero energy

due to its absence from the Hamiltonian. Thus, it introduces a ground state degeneracy that differs only in the occupation of this fermionic mode. This state of the Kitaev chain is topologically non-trivial, as shown in figure 2.4d.

More generically, we can allow all parameters $\mu, \Delta, t \neq 0$. This will lead to hybridization between all Majorana modes, both on-site and between sites. It then becomes a contest to see which of the couplings dominates. One can imagine the coupling between sites to dominate as long as μ remains small. Moreover, for any finite t we will have $(\Delta + t)$ to dominate over $(\Delta - t)$. In this scenario, we still maintain two uncoupled Majorana modes at the ends of the chain - although the bulk excitation gap will start to shrink. In general, this gap will close when $|\mu| = 2t$, which marks the transition between the trivial ($|\mu| > 2t$) and non-trivial ($|\mu| < 2t$) topology of the chain.

2.2.2 The Lutchyn-Oreg model

One of the critical assumptions in the Kitaev chain model is that the chain consists of spinless fermions, which are coupled via some superconducting pairing. However, we have seen in section 2.1 that superconductivity typically pairs up electrons with opposite spin. One can, in principle, try to engineer a physical system that behaves like the Kitaev chain by combining conventional materials. This was first recognized by Lutchyn [26] and Oreg [27], and we will follow their approach to demonstrate how Majorana zero modes may arise in proximitized semiconducting nanowires.

The system under consideration combines four physical ingredients. A one-dimensional semiconductor forms the basis, in which transverse confinement splits the band structure into subbands. We then choose to look only at the lowest subband, for which the Fermi level is near the bottom of the band. Moreover, we only consider momentum along the direction of the wire and assume it is infinitely long. Second, we assume the nanowire possesses spin-orbit coupling, which generates an effective magnetic field perpendicular to the motion of the electrons. The third ingredient is a magnetic field perpendicular to the field induced by the spin-orbit coupling. Finally, we assume that there is an s-wave superconducting pairing in the system, which is characterized by the phenomenological pairing parameter Δ. We again use the Bogoliubov-de Gennes formalism in the basis of equation 2.3. The BdG Hamiltonian for this system reads

$$H_{\mathrm{BdG}} = \xi_k \tau_z + \alpha k_z \sigma_y \tau_z + \frac{1}{2}\mu_{\mathrm{B}} \mathbf{B} \cdot \boldsymbol{\sigma} + \Delta \tau_x \tag{2.19}$$

where k_z denotes the momentum along the nanowire and α is the Rashba spin-orbit parameter. The nanowire and used coordinate system are shown in figure 2.5a, where we have chosen the nanowire axis along z and the spin-orbit field B_{SO} along y. The excitation spectrum of this system is given by

$$\begin{gathered} E_k = \pm \sqrt{\xi_k^2 + \alpha^2 k_z^2 + E_{\mathrm{Z}}^2 + \Delta^2 \pm 2\sqrt{\xi_k^2(\alpha^2 k_z^2 + E_{\mathrm{Z}}^2) + \Delta^2 E_{\mathrm{Z}}^2}} \\ \xi_k = \frac{\hbar^2 k_z^2}{2m^*} - \mu, \qquad E_{\mathrm{Z}} = \frac{1}{2} g \mu_{\mathrm{B}} B \end{gathered} \tag{2.20}$$

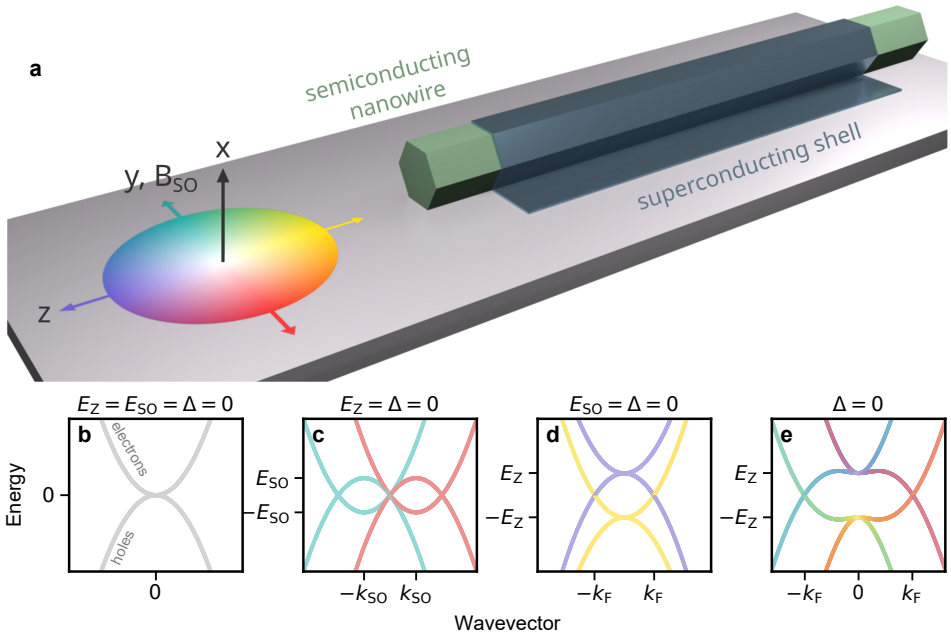

Figure 2.5: **Excitation spectrum of a semiconducting nanowire with spin-orbit coupling and a magnetic field. a.** Illustration of a nanowire coupled to a superconducting shell, together with the used coordinate system. The colored disk denotes the spin orientation of the excitation spectra presented in figure 2.5b-e and figure 2.6. **b.** Excitation spectrum of a semiconductor nanowire in the Bogoliubov-de Gennes formalism. In the absence of spin-orbit coupling, superconductivity, and a magnetic field, the bands are spin-degenerate parabolas with the Fermi level located at the band bottom. **c.** The inclusion of spin-orbit coupling shifts the bands along momentum by $k_{SO} = m^*\alpha/\hbar^2$ and in energy by $E_{SO} = \hbar^2 k_{SO}^2/2m^*$. The bands are no longer spin-degenerate, except at $k_z = 0$. **d.** Including instead only a magnetic field polarizes the bands and introduces a Zeeman splitting. Spin degeneracy is lifted, but only a single spin species is present at the Fermi level, preventing the spectrum from obtaining a superconducting pairing from an *s*-wave superconductor. **e.** When both spin-orbit coupling and a magnetic field are included, the spin orientation becomes dependent on the values of k_z and B. At large k_z, spins are predominantly aligned with the spin-orbit field, whereas near $k_z = 0$, they align with the magnetic field. The spectrum forms a helical liquid, where the direction of the spin is linked to the direction of momentum.

To get an intuitive understanding of how the system behaves, we can turn off various components of the Hamiltonian and look at the resulting spectrum.

Semiconducting nanowires

For simplicity, let us start with a nanowire without any superconducting pairing. Without spin-orbit coupling and a magnetic field, the excitation spectrum is given by $E_k = \xi_k$. The parabolic dispersion is shown in figure 2.5b. Here, we have also assumed $\mu = 0$, thus setting the bottom of the band at the Fermi level. There are again four bands, two coming from electrons and holes, since we treat the hole excitations explicitly by using the BdG formalism. In addition, both bands are spin-degenerate in the absence of a magnetic field and spin-orbit coupling. In order to resemble the Kitaev chain, we thus need to break spin degeneracy by enabling these terms in the Hamiltonian.

If we first include only the magnetic field, we split the excitation spectrum via the Zeeman splitting. Assuming the magnetic field to be oriented along the nanowire axis, the excitation spectrum is shown in figure 2.5d. The applied field now defines the spin quantization axis along the nanowire. The color of the bands indicates the expectation value and orientation of the spins, corresponding to the colored disk in figure 2.5a. At the Fermi level, only a single electronic band is present with a single spin species - effectively creating the spinless chain. However, this also forbids the band from obtaining a superconducting pairing, which requires the presence of opposite spin species near the Fermi level.

We can instead try to break spin degeneracy via the spin-orbit coupling. This is a relativistic effect for which a charged particle moving in an electric field experiences an effective magnetic field. In our case, the electric field originates from a structural inversion asymmetry. This can quite literally result from the asymmetry in the device geometry due to the presence of a nanowire-substrate interface on one of the facets and the semiconductor-superconductor interface on some of the other facets. Moreover, one can also externally apply an electric field through electrostatic gating. In the geometry presented in figure 2.5a, such gates are typically located underneath the substrate so that we can assume the electric field to point out of the plane, that is, in the x-direction. The resulting spin-orbit field points perpendicular to the motion of the electrons and the electric field, which is indeed along y as we assumed in equation 2.19. The effect on the excitation spectrum is shown in figure 2.5c: the bands split both in energy and momentum, with the spin quantization axis along the spin-orbit field. Electrons of opposite momentum near the Fermi indeed have opposite spin, as required for the superconducting pairing. However, two bands are now available with opposite spin at the Fermi level, as spin degeneracy is preserved at $k_z = 0$. In order to reach an effectively spinless regime in the nanowire that can still obtain a superconducting pairing, we thus need to combine both effects.

The effect of the spin-orbit interaction depends on the momentum and, in particular, vanishes when the momentum is close to zero. At $k_z = 0$, the spectrum experiences a Zeeman splitting just like the case without any spin-orbit interaction. At the same time, the magnetic field defines the spin quantization axis along z for low-momentum states. At finite momentum, on the contrary, the spin-orbit field competes with the magnetic field to define the quantization axis. The spin-orbit field strength increases with momentum so that the spins are increasingly tilted away from the direction of the external field. Moreover, since the direction of momentum is coupled to the spin direction, electrons with opposite momentum have their spins tilted in the opposite direction. The resulting excitation spectrum is shown in figure 2.5e. Thus the combination of a magnetic field and spin-orbit coupling has allowed us to gap out one of the spin species in the semiconductor, creating a helical liquid for which the spin direction is coupled to the direction of momentum. In addition, the spin canting allows the remaining band to maintain the ability to acquire a superconducting pairing.

Superconducting nanowires and Majorana zero modes

Having seen that a semiconducting wire with spin-orbit coupling and a magnetic field can form the basis for our one-dimensional p-wave superconductor, we will now turn on the s-wave pairing parameter. It is insightful to start without an external field, such that both bands are polarized along the spin-orbit field. Like in the case of a conventional

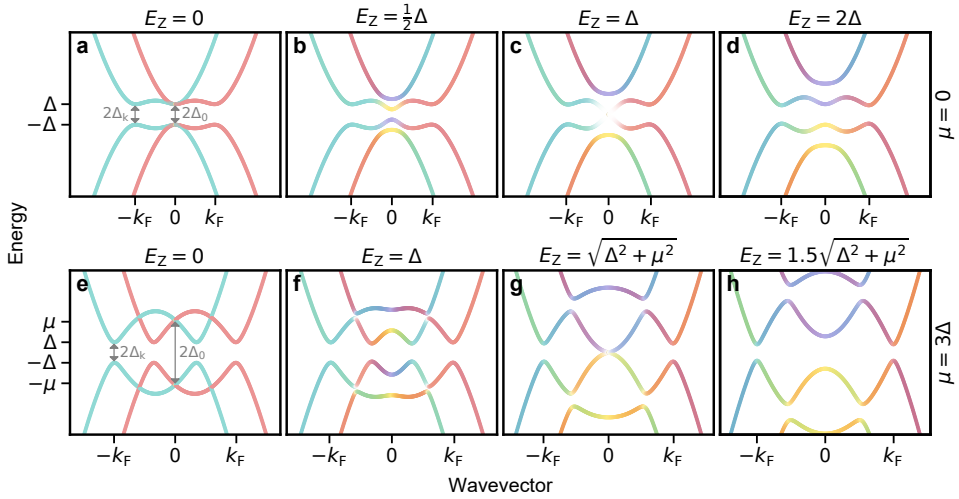

Figure 2.6: **Excitation spectrum of the Lutchyn-Oreg model, when the Fermi level is at the band bottom ($\mu = 0$, a-d) or has a finite value ($\mu = 3\Delta$, e-h). a.** Without a magnetic field, the superconducting pairing opens up an energy gap of $\Delta_k = \Delta_0 = \Delta$ in the spectrum. **b.** A small magnetic field polarizes the bands near $k_z = 0$, and starts to split them via the Zeeman splitting. **c.** When the magnetic field is sufficiently strong, the gap closes at $k_z = 0$, which signals the topological phase transition. **d.** Further increasing the magnetic field causes the gap to reopen with an inverted band structure at low momentum. **e.** The gap at low momentum $\Delta_0 = \sqrt{\Delta^2 + \mu^2}$ is increased when the Fermi level is not at the bottom of the band. **f.** The same magnetic field which causes a topological phase transition when $\mu = 0$ is now insufficient to close the gap. **g.** Instead, the gap closes when the magnetic field equals $E_Z^c = \sqrt{\Delta^2 + \mu^2}$. **h.** Further increasing the magnetic field again causes the gap to reopen with an inverted band structure.

superconductor, the pairing parameter hybridizes the electron and hole excitations of the system to open up energy gaps of 2Δ around the Fermi level. Three such crossings are present (or four if $\mu \neq 0$): 2 at a finite momentum k_F and one at zero momentum. The resulting spectrum is shown in figure 2.6a for $\mu = 0$ and figure 2.6e for $\mu = 3\Delta$.

Let us now focus on the special case of $\mu = 0$. If we turn on a small magnetic field as shown in figure 2.6b, the excitation spectrum near $k_z = 0$ starts to become polarized and obtains a Zeeman splitting. While in the absence of the superconducting pairing, this would be enough to gap out one of the spin species, the gap opened up by the superconducting pairing actually works against the Zeeman effect. Thus, the magnetic field must be sufficiently large to overcome the superconducting gap. As shown in figure 2.6c, the gap at $k_z = 0$ closes once the Zeeman energy equals the superconducting gap $E_Z = \Delta$. The closing of this gap signals the topological phase transition. Increasing the magnetic field further reopens the gap with an inverted band structure close to $k_z = 0$, indicating that the system has become a topological superconductor - accompanied by Majorana zero modes at its ends.

In the more general case, we have $\mu \neq 0$. This results in an increased energy gap $\Delta_0 = \sqrt{\Delta^2 + \mu^2}$ around $k_z = 0$, while the energy gap at finite momentum $\Delta_k \approx \Delta$ does not de-

pend strongly on μ. Upon the application of a magnetic field, the Zeeman splitting starts to shrink the zero-momentum gap according to $\Delta_0 = \sqrt{\Delta^2 + \mu^2} - E_Z$. Recognizing that we need to close this gap to trigger the topological phase transition, we can find the phase-transition field $E_Z^c = \sqrt{\Delta^2 + \mu^2}$. In figure 2.6e-f, we show that when $\mu = 3\Delta$ the zero-momentum gap is dominated by μ, has not yet closed at $E_z = \Delta$, closes at $E_Z = \sqrt{\Delta^2 + \mu^2}$ and reopens for higher Zeeman energies.

2.2.3 Beyond the Lutchyn-Oreg model

The appearance of Majorana zero modes in the Lutchyn-Oreg model is indeed quite intriguing, predominantly because the fundamental physics can be captured in such a minimalistic model. We will now see that the real world is, in fact, not so accurately described by this model. Perhaps the most obvious shortcoming is that real nanowires are three-dimensional objects of finite length. One of the consequences is that it is no longer sufficient to consider only a single subband, and that the orbital effects of the magnetic field need to be considered. What is more problematic, however, is that superconductivity is added to the model via a phenomenological parameter. It turns out that the presence of a superconducting material is very relevant, and one needs to take into account how exactly superconductivity is induced in the semiconductor. In addition, many of the parameters are assumed to be constant over space. However, all key ingredients (α, Δ, B, and μ) are likely to be spatially dependent, for example due to the presence of disorder in realistic systems. Finally, the effect of electrostatic gating is only included by affecting μ in the model. In contrast, in reality it affects almost every relevant parameter - as we will see later in this section.

The proximity effect

To see how superconductivity is properly included, we first need to understand how superconductivity is induced in the nanowire. This is known as the proximity effect, and the underlying physical mechanism is known as Andreev reflection [28]. Historically, Andreev reflection was introduced as the mechanism underlying transport between a superconductor and a metal when the voltage difference between the materials is smaller than the gap of the superconductor $eV < \Delta$ - which we here choose to be $eV = 0$. One assumes the incoming electron in the semiconductor to be a Bloch wave coming from infinity. What happens upon reaching the semiconductor-superconductor interface depends crucially on the interface transparency T [29]. There are two possibilities: electrons can Andreev reflect with probability $2T^2/(2-T)^2$, a process for which the electron can grab a second electron from below the Fermi surface and enter the superconductor as a Cooper pair. On the other hand, the electron can reflect back with probability $1 - 2T^2/(2-T)^2$. The Andreev reflection process effectively leaves a hole excitation in the semiconductor, which forms a phase-conjugated pair with the incident electron. It is this pairing that opens up an energy gap in the spectrum of the semiconductor, which decays away from the interface [30] and is diminished for lower interface transparencies.

In nanowires, however, the interface between the materials is not perpendicular to some infinite semiconductor. In fact, the dimensions of the semiconductor in this direction are required to be small, as we are looking for an effective one-dimensional system with

transverse confinement. So, instead of pure Bloch waves, the electrons participating in the Andreev reflection constitute standing waves along the cross-section whose wavefunction is defined by the geometry. These wavefunctions are precisely the subbands of the one-dimensional nanowire, and they determine the rate of Andreev reflection of the particular subband: If the wavefunction of a subband is located near the interface, the rate of Andreev reflection is high, in which case the obtained superconducting pairing can be as large as the size of the gap in the superconductor. In contrast, the superconducting pairing is reduced and can even vanish altogether if the wavefunction of a subband is located far away from the interface. The main consequence is that each subband obtains its own superconducting pairing, and they need to be considered individually. Moreover, the presence of the superconductor also strongly affects the electrostatic potential profile in the nanowire and, thus, where the subbands are formed. These effects also need to be taken into account, as we will see below.

Electrostatic effects in hybrid nanowires

For an insightful and more realistic modeling of the hybrid nanowires, we follow the work of Antipov et al[1] [31]. Let us start by considering an infinite semiconducting nanowire, but explicitly introduce a finite cross-section. Moreover, we consider the presence of the superconductor on two facets of the nanowire instead of simply assuming a phenomenological pairing parameter. We also introduce an electrostatic gate to the problem, which is operated via a gate voltage V_g and is located on the bottom of the nanowire. A schematic illustration of the cross-section is shown in the inset of figure 2.7a.

As anticipated in the previous section, we are looking for the band structure of the nanowire. In order to do so, a Hamiltonian describing the three-dimensional nanowire is used, which includes the electrostatic profile $\phi(z)$ of the nanowire. To find $\phi(z)$, one needs to self-consistently solve the Poisson equation and the Schrödinger equation for the problem. Figure 2.7a shows the setup for the Poisson equation: At the interface between the superconductor and semiconductor, the electrostatic potential is determined by the band offset W between the materials. On the other end of the wire cross-section, the potential is determined by the value of V_g.

An example of the calculated cross-sectional density profile at $V_g = 0\,\mathrm{V}$ and corresponding eigenstates are shown in figure 2.7b. Most of the electronic density is located near the semiconductor-superconductor surface. This is not surprising, as the assumed negative band offset is known to generate an accumulation layer. Consequently, the wavefunctions of the various subbands also carry a large weight near the interface. This situation also holds when the applied gate voltage is negative: the electrostatic potential creates a strong confinement of the carrier density near the interface. In contrast, a positive gate voltage causes the electrostatic potential to drop at some distance from the interface and can cause some bands to appear which are not confined there.

Each of the subbands couples differently to the superconductor. One can think of this as the result of hybridization between states in the semiconductor and states in the superconductor. Then, the coupling between the materials can be characterized by the weight

[1] The mathematical models are too cumbersome to reproduce here and on their own not very insightful, so we instead focus on the results in this section.

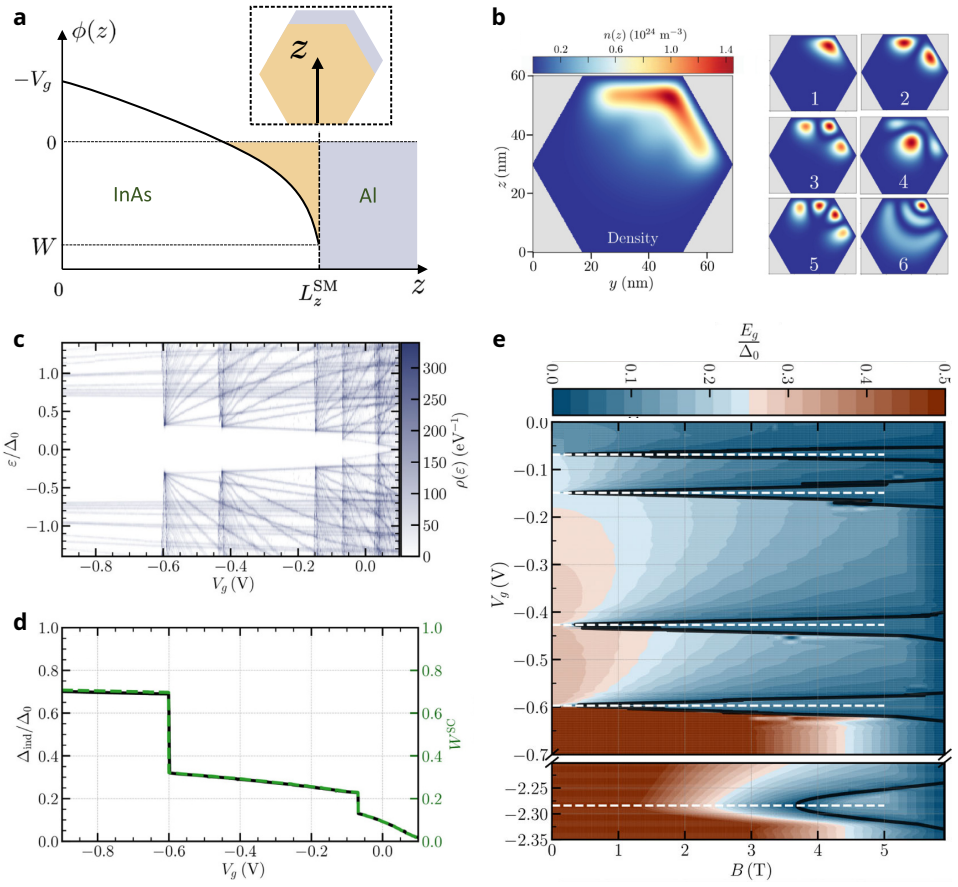

Figure 2.7: **Effects of electric fields on semiconductor-superconductor nanowires. a.** Electrostatic profile along a nanowire cross-section, depending on gate voltage V_g and band-offset W. Inset shows the wire geometry. **b.** Electron density and subbands in the normal state of the nanowire at $V_g = 0$ V. **c.** Density of states as a function of V_g. The gate voltage controls the number of subbands in the nanowire, each with their own induced gap. **d.** Induced gap in the nanowire (black) and the corresponding weight in the superconductor (green). **e.** Topological phase diagram as a function of V_g and parallel magnetic field B. Each subband can transition into a topological phase when the gate voltage is near their band bottom, with the black lines presenting the phase transition boundaries. Adapted from [31].

of the subband in the superconductor W^{SC}, which essentially describes how much of the wavefunction of each subband is located in the superconductor. In other words, subbands with a large weight in the superconductor are subject to a strong coupling to it. At this point, we need to make a distinction between the superconducting gap Δ_0 in the superconductor and the induced gap Δ_{ind} in the semiconductor: Depending on their weight in the superconductor, each of the subbands will obtain their own induced superconducting gap. Since the applied gate voltage is also used to control the number of active subbands in the nanowire, it can be used directly to control the induced gap in the density of states.

This is shown in figure 2.7c, where the induced gap shrinks as the gate voltage is increased. Figure 2.7d shows the correspondence between the induced gap in the nanowire and the corresponding weight in the superconductor.

We have seen that subbands are confined close to the semiconductor-superconductor interface for strongly negative gate values. Such confinement has the consequence of creating a strong coupling between the subband to the superconductor, resulting in a large induced gap. This is known as metalization or renormalization of the semiconductor [31, 32], and it has some profound consequences. It is, indeed, not only the value of the induced gap that gets renormalized - other parameters like the g-factor and spin-orbit coupling strength are also adjusted to become closer to their value in the superconductor. Such effects are vastly unfavorable for the transition into a topological phase, as the g-factor determines how quickly the gap can close and reopen upon the application of a magnetic field. Figure 2.7e shows simulations of a topological phase diagram as a function of gate voltage and magnetic field. The strongly-coupled bands, like the one around $V_g = -2.3\,\mathrm{V}$, only transition to a topological phase near $B = 4\,\mathrm{T}$ - a value which exceeds the Pauli limit for aluminum films with a realistic thickness. On the other hand, bands that are too weakly coupled essentially obtain no superconducting pairing and, by definition, can not give rise to a topological superconducting phase. However, there are some bands in between these two regimes which are characterized by an intermediate coupling. It is there that one should look for a topological phase transition and Majorana zero modes.

The above example provides quite the paradigm shift in the way one thinks about semiconductors coupled to superconductors. The fact that subbands get renormalized by the superconductor provides crucial information on where to look for Majorana zero modes and how the proximity effect works in these hybrids. In fact, it has become even more clear how important the properties of the materials are: the renormalization of the band structure is entirely governed by the band offset between the materials in combination with the exact geometry of the devices.

2.2.4 Detection methods: local and nonlocal spectroscopy

As we have seen, Majorana zero modes appear at the edges of a one-dimensional topological superconductor. In practice, if we fabricate a nanowire that is partially covered by a superconductor, we need to create probes near the edges of that superconductor in order to detect them. If we also create tunnel barriers in between the probe and the superconducting region, we can use the technique of tunneling spectroscopy to learn about the density of states underneath the superconductor. Moreover, we can make use of a nonlocal conductance measurement if we create one probe at each end and ground the superconducting material. Both techniques should reveal the presence of Majorana zero modes through specific signatures, which we will elucidate in the following section.

Local and nonlocal transport

In figure 2.8a, we show a schematic of a typical device. A hexagonal nanowire is shown in green and, in our case, is made of InSb - a semiconductor with a strong spin-orbit coupling and large g-factor, as required by the Lutchyn-Oreg model. Shown in grey-blue is the superconductor, which covers the central region on three nanowire facets. In our

case, Al is the material of choice - an *s*-wave superconductor. The superconductor extends onto the dielectric substrate (HfO_2, shown in transparent white), where it can be used as one of the electrical connections to the device. On the two sides of the device, we see two yellow contacts made of a non-superconducting metal: a Cr/Au bilayer. Both of these also provide an electrical contact, so the device has a total of three of them. A bare section of semiconductor remains in between the metallic contacts and the superconducting region. Here, the electron density can be tuned via electrostatic gating. This is done by applying a voltage to the set of gate electrodes underneath the dielectric layer, which are made from a Ti/Pd bilayer and shown in red. The two outer electrodes function to control the semiconducting junctions, whereas the central gate will allow us to adjust the Fermi level underneath the superconductor.

Inside the longitudinal cross-section of the nanowire in figure 2.8a, we have drawn an illustration of the relevant transport processes. We start by looking at the simple scenario in which no magnetic field and consequentially no Majorana zero modes are present. We will also assume that the superconducting region is sufficiently long, much longer than the superconducting coherence length. One typically applies a voltage bias V_b to one of the two normal metallic contacts while keeping the other normal and superconducting contacts grounded. One can then measure the local and nonlocal conductance: In the case of local conductance, one measures the current flowing through the biased contact as the response to the applied voltage. In contrast, the nonlocal signal only captures the part of the current which drains away via the unbiased normal contact and not via the superconductor [33].

In figure 2.8a, we have chosen the left contact to apply the voltage bias. A tunnel barrier is assumed to be present in the semiconducting junction, as indicated by the dashed orange line. Furthermore, we assume there is an induced gap Δ_i in the superconducting section of the semiconductor, which it obtains from the superconductor with a gap Δ_{SC}. Various transport mechanisms can take place depending on the value of the applied bias voltage. If the bias is larger than the gap of the superconductor $|eV_b| > \Delta_{SC}$, injected carriers will enter the proximitized region with enough energy to escape into the superconducting shell. As a consequence, they will contribute to the local conductance but not the nonlocal conductance. If the bias voltage falls in between the two gap parameters $\Delta_i > |eV_b| > \Delta_{SC}$, the carriers do not possess enough energy to escape via the shell and can only drain away via the opposing normal contact. They will thus contribute both to the local conductance and the nonlocal conductance. Finally, if the applied voltage is below the induced gap $|eV_b| < \Delta_i$, there are no single particle states available and carriers can only enter the superconducting region via Andreev reflection. The formed Cooper pairs can simply enter and drain away via the superconductor, only contributing to the local conductance.

The transparency of the tunnel barrier further determines the magnitude of the measured conductance. Examples of the resulting local signal for various barrier transparencies T are shown in figure 2.8b. In the ideal case of a single ballistic conduction channel and at energies far above the superconducting gap, the local conductance value is proportional to the transparency of the tunnel barrier $G_{local}(eV_b \gg \Delta_{SC}) = G_0 T$ - where $G_0 = 2e^2/h$ is the conductance quantum. It can intuitively be understood that the junction possesses a single quasiparticle channel of which the junction transparency sets the transmission - thus

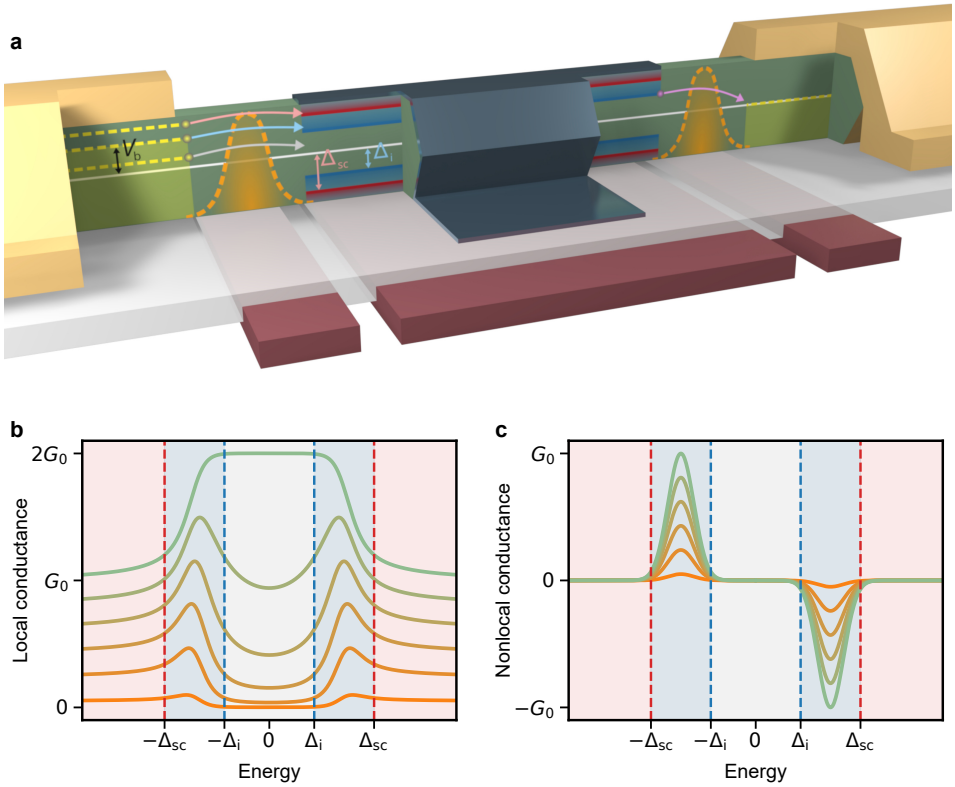

Figure 2.8: **Local and nonlocal spectroscopy of proximitized nanowires. a.** Schematic illustration of a proximitized nanowire and the transport processes. The nanowire (green) is contacted in the center by a superconductor (blue) and on the ends by normal metals (yellow). It is separated by a dielectric (transparent white) from a set of electrostatic gates (red). The superconductor has a gap Δ_{sc} and induces a gap Δ_i in the semiconductor. Tunnel barriers (orange dashed lines) are created through appropriate gate potentials. A voltage bias V_b controls the energy of the injected electrons. **b.** Local conductance for various tunnel barrier transparencies. Above Δ_{sc}, the conductance in units of the conductance quantum $G_0 = 2e^2/h$ approaches the transparency of the tunnel barrier. Below Δ_i, transport is governed by Andreev reflection, and conductance is enhanced for high transparencies. In between, a peak represents the density of states of the proximitized semiconductor. **c.** Only injected particles in between Δ_i and Δ_{sc} can escape via the opposing normal lead and contribute to the nonlocal conductance.

reaching a single conductance quantum when $T = 1$, with the factor 2 in the conductance quantum owing to the spin degeneracy of the channel. Below the induced gap, however, the conductance magnitude is governed by the Andreev reflection probability. At zero bias specifically, it is given by the Beenakker formula $G_{\text{local}}(eV_b = 0) = G_0 2T^2/(2-T)^2$ [34]. In between the induced and superconducting gaps, the exact structure can be quite complicated. We have seen in section 2.2.3 that multiple subbands, each with their own value of Δ_i, form in the superconducting region. They all contribute to the density of states, and

the result is that the peak structure in the local conductance depends on the exact details of the electrostatics, materials, and geometry. The general shape is some broadened or even multiple peaks - in stark contrast to the singularity in the density of states of a metallic superconductor.

The nonlocal conductance is affected similarly by the transparency of both semiconductor junctions. Figure 2.8c shows the nonlocal conductance for various barrier transparencies, assuming the receiving junction is fully transparent. As we have seen before, carriers injected either above Δ_{SC} or below Δ_i do not contribute to the nonlocal conductance. Only in between can we measure a nonlocal conductance. In the ideal case with both junctions fully transparent, each injected charge will exit via the opposing lead so that it contributes a single conductance quantum to the conductance [35]. Moreover, in the ideal case, the signal should be symmetric around zero energy. However, in reality, it is almost always antisymmetric, and the exact shape and even the sign of the signal depend on the details of the sample. In general, the signal increases in magnitude with increasing barrier transparencies.

The initial proposal to measure nonlocal conductance assumed that nonlocal transport was governed either through direct quasiparticle transport or via crossed Andreev reflection [33]. The two cases differ because, in the former, the sign of the charge is preserved, while in the latter, it is reversed. This has implications for the sign of the nonlocal conductance, which was predicted to exhibit rectifying effects near the topological phase transition [33] as a result. However, we have recently shown that nonlocal transport in long wires actually functions rather differently [36]: First, a charge carrier is injected into the superconducting region at some energy eV_b. The injected carrier is either an electron or a hole, depending on the sign of the applied bias, and thus has a charge of $-e$ or e. Such charges are, however, not the elementary excitations of a superconductor - as we have seen before, these are Bogoliubov quasiparticles. Thus, the injected charge excites the system both in energy and charge [37–39]. Inside the superconducting region, the charges are subjected to a few processes: If their injection energy allows it, they may drain away via the superconducting lead. Inelastic scattering causes the remaining charges to relax to the lowest available state at the edge of the induced gap. In addition, Andreev reflection at the interface with the superconductor drains away the excess charge and converts the injected particle into a Bogoliubov quasiparticle. The quasiparticles then diffuse around in the proximitized region, where they may recombine with other quasiparticles into Cooper pairs - allowing them to drain to ground via the superconductor. The remaining ones can reach the opposite normal contact, where they will exit and contribute to the nonlocal conductance. In reality, tunnel junctions often have different transmission amplitudes for electrons or holes - and as the quasiparticles are equal superpositions of both, the details of the receiving junction will determine which kind of charge they are projected onto [40]. Note that this does not depend on the sign of the injected charge due to the energy and charge relaxation. The measured current direction thus does not depend on the sign of the voltage bias, leading to an antisymmetric nonlocal conductance.

Signatures of the topological phase

We are now ready to consider the signatures of Majorana zero modes in local and nonlocal conductance measurements. As we have seen in section 2.2.2, Majorana zero modes appear

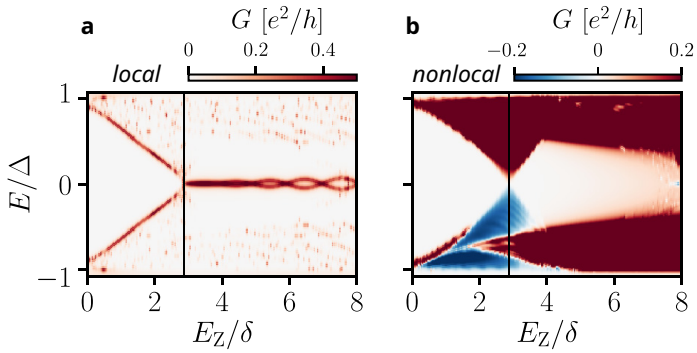

Figure 2.9: **Signatures of Majorana zero modes in local and nonlocal spectroscopy. a.** In the local spectrum, the superconducting gap closes, followed by the formation of a zero-bias peak. A gap reopening should also be visible, and the peak should exhibit specific features: Conductance quantization to $G = 2e^2/h$, and peak splitting and oscillations if the nanowire is short. **b.** In the nonlocal spectrum, no local states should be visible so that the zero-bias peak is absent. The closure and reopening of the induced gap should be well visible, and the conductance should be rectified near the topological phase transition. Adapted from [33].

at the ends of the superconducting segment of the nanowire after the Zeeman energy exceeds some critical value. Thus, we are interested in the evolution of the local and nonlocal spectra as a function of a magnetic field.

If we ignore the orbital effects of the magnetic field, the primary effect is to provide a Zeeman splitting of the states at low momentum. This will cause the induced gap in the semiconductor to close linearly. After the gap closes, Majorana zero modes form at the edges while the bulk states will become gapped again. The Majorana zero mode exists as part of the ground state manifold, so that exciting it costs no energy. As a result, it shows up as a state at zero energy in local spectroscopy measurements. The induced gap at that point reopens, such that the local measurement will feature a zero-bias peak amid a gapped region. The peak itself is predicted to possess some distinctive properties. Most prominently, the tunneling process into a Majorana zero mode is characterized by resonant Andreev reflection. This gives rise to a quantization of the zero-bias peak [41–43], which has a conductance value of $G = 2e^2/h$. In addition, the two Majorana zero modes at the two ends of the wire might have some overlapping wavefunctions. This splits the zero-bias peak and causes an oscillatory behavior as the magnetic field is increased further [44]. Finally, the local spectra on both ends of the superconducting section must simultaneously feature all these signatures. This predicted end-to-end correlation is a direct consequence of the Majorana zero modes appearing in pairs at both ends of the wire upon the topological phase transition. The characteristic signature of a topological phase transition as a function of a magnetic field in the local conductance measurements is shown in figure 2.9a. In practice, some of the signatures might be weakened in actual experiments: for example, thermal effects may reduce the zero-bias peak height below $G = 2e^2/h$. Moreover, the states that constitute the induced gap are bulk states, meaning they potentially couple weakly to the tunnel probes. Thus, the closing and reopening of the induced gap might not be visible in the local conductance measurements [45].

This is where the nonlocal conductance comes in. Zero-bias peaks can, unfortunately, also originate from various other physical sources [46–56]. For example, confinement happens naturally near the end of the superconducting section, as the electrostatic potential in the wire is disrupted both by the termination of the superconducting shell and the voltage on the tunnel barrier gate. Such confinement often results in discrete sub-gap states, which can also reach and stick to zero bias. Thus, the observation of zero-bias peaks in isolation is insufficient as a signature of a topological superconductor. Even the concomitant appearance of peaks at both ends of the device is insufficient. Indeed, their formation must necessarily be accompanied by a closing and reopening of the bulk gap. As we have seen, nonlocal conductance is sensitive to the induced gap in the semiconductor. Consequentially, this important signature of a topological phase transition is also visible in the nonlocal spectra. Moreover, nonlocal measurements are insensitive to any local states near the ends of the superconducting section. Neither the Majorana zero modes nor any other confinement- or disorder-induced zero-energy states will appear in the nonlocal conductance. The characteristic signature of a topological phase transition as a function of a magnetic field in the nonlocal conductance measurements is shown in figure 2.9b. A topological phase transition should simultaneously be observed in both local spectra as zero-bias peaks and in the nonlocal spectra as a closure and reopening of the induced gap.

2.3 The realistic Kitaev chain

Experimental work over the last decade has shown that it is challenging to realize a topological superconductor based on the semiconductor-superconductor nanowire model. It was already recognized shortly after the first nanowire experiments that instead, it may be advantageous to try to emulate a Kitaev chain in a system of coupled quantum dots [23–25]. This can be done with the same ingredients used for the continuous nanowire approach: a semiconductor coupled to a superconductor in the presence of spin-orbit interaction and a magnetic field.

2.3.1 The Kitaev chain in proximitized nanowires

The original Kitaev chain toy model consists of a chain of spinless fermionic sites. Such a chain can be physically realized in proximitized semiconductors, with an example of a five-site chain in a nanowire shown in figure 2.10. The closest analog of the fermionic sites are quantum dots, where three-dimensional confinement discretizes their energy spectrum. We are looking to consider such an energy level and make sure that the energy spacing to the next level is large compared to other energy scales in our system. This spacing is called the addition energy [57], which is given by $E_{\text{add}} = E_{\text{C}} + \delta E_{\text{L}}$. The first term describes the charging energy $E_{\text{C}} = e^2/C$, where C is the capacitance between the quantum dot and the environment. The second term is the level spacing $\delta E_{\text{L}} \propto 1/m^* L^2$, which is inversely proportional to the largest length of the dot L. We thus want to maximize the addition energy - and since both the charging energy and level spacing increase with a shrinking quantum dot size, we look to make the quantum dots as small as possible. The material of choice should have a small dielectric constant to minimize the capacitance to the environment. Furthermore, a large effective mass of the carriers is desired.

In general, though, the energy levels of a quantum dot are spin-degenerate, hosting a pair

of electrons with opposite spins. Indeed, this degeneracy will need to be removed, and we can do so through the application of a magnetic field. Recalling that the energy of spinfull states is adjusted by the Zeeman energy $E_Z = g\mu_B B/2$, we see that materials with a large g-factor are desired. The evolution of the addition energy as a function of a magnetic field is shown in figure 2.10a. At the very minimum, we require that the Zeeman splitting exceeds the thermal energy of the electrons $E_Z > k_B T$. If we tune the spin-polarized dot level close to the Fermi level via electrostatic gating, the quantum dot can be considered spinless [58].

The original model by Kitaev contains the three coupling parameters μ, t, and Δ, which are assumed to be uniform along the chain. In reality, however, each quantum dot n can be tuned via its on-site electrochemical potential μ_n, with generalized couplings t_n and Δ_n between the sites. The couplings can, in theory, be introduced to the chain via bulk superconductors separating adjacent quantum dots, as shown in figure 2.10b. In this case, electrons hopping from one dot to the next can do this via virtual occupation of quasiparticle excitations above the superconducting gap - a transport mechanism known as elastic co-tunneling (ECT) with amplitude t_n. Similarly, two electrons at adjacent sites can join the superconducting condensate together as a Cooper pair - via a transport mechanism known as crossed Andreev reflection (CAR) with amplitude Δ_n.

However, we face a similar problem as the Lutchyn-Oreg model: we can tune adjacent quantum dots to have the same spin species, which allows direct tunneling via t_n but prevents them from obtaining a superconducting pairing Δ_n from an s-wave superconductor. If we instead tune adjacent quantum dots to be of opposite spin species, the superconducting pairing is enabled, but the regular tunneling is forbidden. Thus, we need to tilt the spins in each quantum dot somehow so that they obtain both a parallel and an anti-parallel spin component. As we have seen before, this issue can be resolved by requiring the material to exhibit spin-orbit coupling and applying the magnetic field perpendicular to the spin-orbit field. The spin-orbit coupling can be present in the quantum dots themselves or the connecting superconductor.

Thus, we have seen that a Kitaev chain can be physically implemented in a system with the same ingredients as the Lutchyn-Oreg model: low-dimensional semiconductors with strong spin-orbit coupling coupled to superconductors in the presence of a magnetic field. However, the generalized Kitaev Hamiltonian is more complicated as it contains three tunable parameters per quantum dot in the chain. One might think that it demands very stringent tuning, requiring all the μ_n's to be zero and all the t_n's and Δ_n's to be equal. This defines the ideal scenario, but just like for the Kitaev toy model, it is unnecessary. It can be shown that if the chain contains N sites, it is robust again variations of $N-1$ parameters in the Hamiltonian [25]. However, the quasiparticle excitation gap in the bulk is limited by the smallest coupling in the chain.

The problem, however, with bulk superconductors is that in general, t_n and Δ_n cannot be independently controlled - making it difficult to realize any $t_n = \Delta_n$. Moreover, these processes can only occur if the length of the superconductor is sufficiently short - that is, much shorter than the coherence length ξ_0. This results in couplings which are generically too weak, especially in the case of Δ_n since it is a two-particle process [59]. Experimental

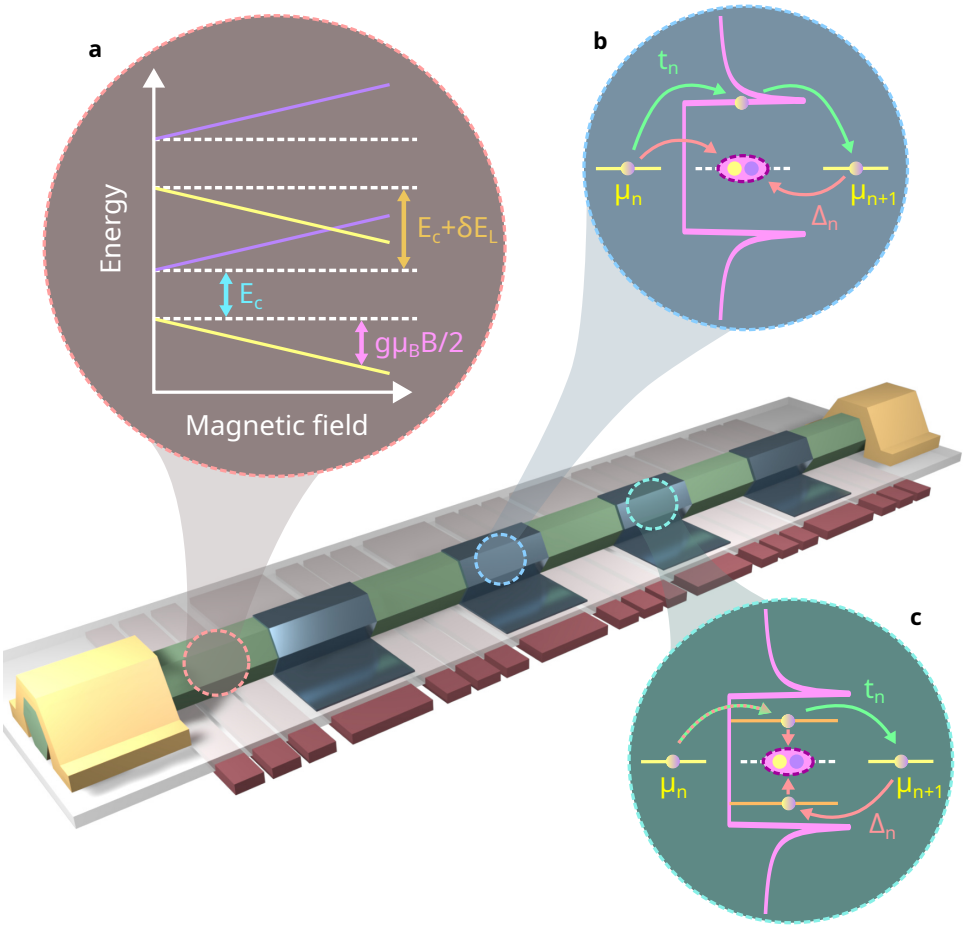

Figure 2.10: **Implementation of a (five-site) Kitaev chain in proximitized nanowires.** A nanowire (green) is coupled to short superconducting segments (blue). At the ends of the wire, normal metals (yellow) make contacts that can be used to probe the Majorana zero modes. The nanowire is separated by a gate dielectric (transparent white) from a set of bottom gates (red). Three narrow gates can create a confining potential to form quantum dots underneath the bare semiconducting segments. **a.** The quantum dots are characterized by a charging energy E_C and a level spacing δE_L. Upon including a magnetic field, the levels obtain a Zeeman splitting $E_Z = g\mu_B B/2$. **b.** Bulk superconductors were initially envisioned to mediate the coupling terms t_n and Δ_n, where t_n is a virtual hopping process via the quasiparticle continuum and Δ_n allows Cooper pairs from the condensate to split into two electrons at opposite sites. **c.** Instead, we can use short proximitized semiconductor sections in which Andreev bound states form to mediate the coupling. Both t_n and Δ_n use virtual excitations from the ground state to the excited states of the Andreev bound state. In both cases, t_n is referred to as elastic co-tunneling (ECT) and Δ_n as crossed Andreev reflection (CAR).

attempts at generating a coherent coupling via CAR using proximitized semiconductors have also proven to be unsuccessful, likely due to the absence of a hard induced gap in these systems [60–63].

2.3.2 Tunable coupling via Andreev bound states

Instead, we have developed an alternative way to introduce the two coupling mechanisms between quantum dots. This method utilizes the presence of Andreev bound states (ABSs) in short hybrid segments to mediate the coupling [64, 65], offering a versatile way to realize the Kitaev chain.

Andreev bound states in short hybrids

One can think of Andreev bound states as single-particle levels which have obtained a superconducting pairing via interaction with a superconductor, as schematically illustrated in figure 2.11a. Such levels can generally be formed by confining a material in all spatial dimensions. Indeed, the energy levels in a quantum dot are an example of such single-particle levels. Thus, all we have to do is create more quantum dots in our nanowires and couple them to superconductors. Like before, we will assume that the quantum dot is sufficiently small so that the level spacing is larger than the superconducting gap. This allows us to consider only a single energy level close to the Fermi level.

The single-particle level obtains the superconducting pairing through contact of the short semiconducting segment with an *s*-wave superconductor. Since the superconductor is typically a large body of metal that is connected to ground, the charging energy of the dot is strongly quenched. If we assume spin-orbit coupling to be weak as well, it can be described by the Hamiltonian

$$H_{\mathrm{ABS}} = \mu(c_\uparrow^\dagger c_\uparrow + c_\downarrow^\dagger c_\downarrow) + \Gamma(c_\uparrow^\dagger c_\downarrow^\dagger + c_\downarrow c_\uparrow) \tag{2.21}$$

where μ denotes the chemical potential and Γ the superconducting coupling strength [66]. Indeed, the latter can be understood as the analog of Δ in a regular superconductor, for example through comparison with equation 2.2. The ground state of this level is a spin-singlet state of the form $|S\rangle = u|0\rangle - v\left|\uparrow\downarrow\right\rangle$, which can be understood as the analog of a Cooper pair. Likewise, u and v denote the coherence factors which are given by $u^2 = 1 - v^2 = (1 + \mu/\sqrt{\mu^2 + \Gamma^2})/2$ as shown in figure 2.11b. Finally, excitations of the ABS are the doublet states $\left|\uparrow\right\rangle, \left|\downarrow\right\rangle$, whose excitation energy is depicted in figure 2.11a and given by $E = \sqrt{\mu^2 + \Gamma^2}$. Like Bogoliubov quasiparticles in a superconductor, the excitations are still gapped when $\mu = 0$ - justifying our interpretation of Γ as the induced gap. In fact, the doublet states are themselves Bogoliubov quasiparticles like those described in equation 2.8. This implies that the electron-like and hole-like components of the excitation can be controlled via the chemical potential. Unlike superconductors, however, the chemical potential can be controlled via electrostatic gating. This gives us a direct knob to manipulate the coherence factors and excitation energy of the ABS.

Crossed Andreev reflection and elastic co-tunneling

We are now ready to see how this state can be used to generate a coherent coupling between quantum dots. This is schematically illustrated in figure 2.10c and figure 2.11a. The ABS couples to the left and right quantum dots via the tunnel couplings t_{L} and t_{R}, respectively [64]. The singlet state of the ABS can be excited by the injection of an electron

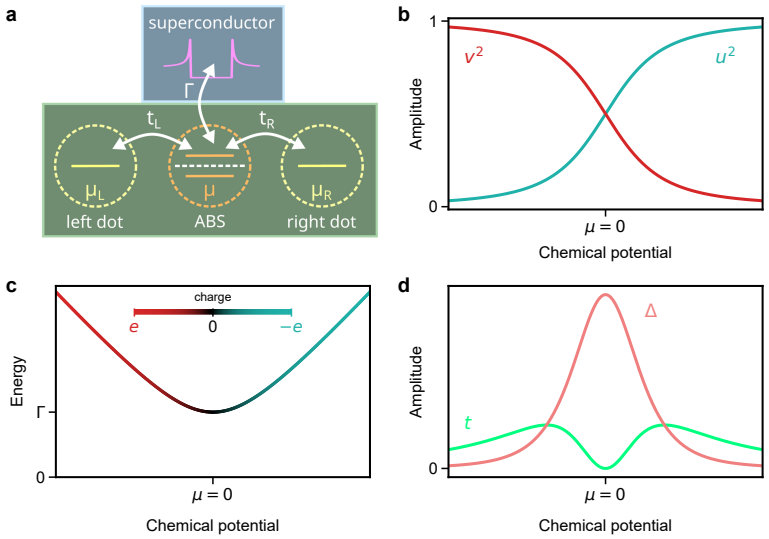

Figure 2.11: **Coupled quantum dots via an intermediate Andreev bound state. a.** Schematic illustration of two quantum dots coupled via an Andreev bound state. The central quantum dot obtains a superconducting pairing Γ from the superconductor and couples to the adjacent quantum dots with couplings t_L and t_R. **b.** Coherence factors of the ABS u and v near the minimum of the excitation energy. **c.** Excitation spectrum of a single ABS with induced gap Γ. The charge of the excitation can be tuned via the chemical potential μ. **d.** The left and right quantum dots obtain an effective coupling t and Δ, which can be controlled via the chemical potential of the ABS. Virtual paths can either interfere constructively or destructively near zero chemical potential, resulting in a peak for Δ and a dip for t. Tuning of the chemical potential can also equalize the two coupling parameters, as required for the topological phase in the Kitaev chain.

from one of the quantum dots, causing it to end up in one of the doublet states. Note that these electrons do not have the energy to excite the ABS, so it needs to be regarded as a virtual process. This makes use of the $|0\rangle$ part of the singlet state, thus the excitation is governed by the amplitude u. Next, the ABS can relax back to the ground state via two options: Either the electron can exit to the other dot, again using the $|0\rangle$ part of the singlet and hence the amplitude u. Alternatively, the electron can pair up with an electron from the second dot. This uses the $|\uparrow\downarrow\rangle$ part of the singlet state with amplitude v, which allows the pair to enter the superconducting condensate of the proximitizing superconductor as a Cooper pair. The first process described here is known as elastic co-tunneling, whereas the second is crossed Andreev reflection.

There is, however, a second virtual path available for both processes: An electron can first leave the ABS, using the $|\uparrow\downarrow\rangle$ part of the singlet state and thus amplitude v. Completing the ECT process then requires an electron to hop from the other dot into the ABS, again with amplitude v. Alternatively, completing CAR requires the second electron from the ABS to leave to the other quantum dot using amplitude u. This effectively splits a Cooper pair from the condensate of the bulk superconductor. Interestingly, the two paths for each process interfere - and in a strikingly different way. The two processes interfere

destructively for ECT, whereas for CAR they interfere constructively. Overall, the two quantum dots obtain effective coupling amplitudes t and Δ via the mediating ABS, which are described by

$$t \propto \left| \frac{u^2 - v^2}{\sqrt{\mu^2 + \Gamma^2}} \right|^2, \qquad \Delta \propto \left| \frac{2uv}{\sqrt{\mu^2 + \Gamma^2}} \right|^2 \tag{2.22}$$

Recalling that u and v are proportional to the chemical potential, we immediately see that Δ is only significant when μ is close to zero, when the ABS excitation energy is close to its minimum. This in contrast to t, which vanishes when $\mu = 0$. Their behavior versus chemical potential is shown in figure 2.11c, revealing a crossover between t-dominated coupling far from the energy minimum to Δ-dominated coupling close to it. Crucially, a value of the chemical potential for which the two are equal will always exist, allowing us to realize this fundamental requirement for the artificial Kitaev chain.

Note that the description here has assumed a weak spin-orbit coupling for the Andreev bound state. As mentioned before, spin-orbit coupling is required to be finite in order to couple spin-polarized quantum dots with both types of coupling. We have also excluded the effect of a magnetic field on the ABS in the above picture. Including it would modify the energies of the two doublet excitations via the Zeeman splitting and consequentially alters the amplitude of the various virtual paths between the coupled dots [64]. In addition, t and Δ also start to be affected by the choice of the quantum dot spin direction - making the exact form more complicated. The general conclusion, though, remains: constructive interference causes CAR to peak near $\mu = 0$, whereas ECT vanishes in its vicinity. We have experimentally verified the theory [65] and further used it to demonstrate the splitting of Cooper pairs into two electrons with equal spins [67]. In chapter 8, we use this to realize a minimal Kitaev chain, consisting of only two quantum dots coupled via an ABS - and demonstrate the formation of Majorana zero modes in the process.

References

[1] H. Onnes, *The resistance of pure mercury at helium temperatures,* Commun. Phys. Lab. Univ. Leiden **12** (1911).

[2] W. L.Ginzburg and L. D. Landau, *The resistance of pure mercury at helium temperatures,* Zh. Eksper. Teor. Fiz **20** (1950).

[3] J. Bardeen, L. N. Cooper, and J. R. Schrieffer, *Microscopic theory of superconductivity,* Physical Review **106**, 162 (1957).

[4] N. Bogolyubov, *On a new method in the theory of superconductivity,* Zh. Eksper. Teor. Fiz **6** (1958).

[5] P.-G. De Gennes, *Superconductivity of metals and alloys* (CRC press, 2018).

[6] M. Tinkham, *Introd. to Supercond. 2nd Ed.*, 2nd ed. (Dover, 2004).

[7] J. F. Cochran and D. E. Mapother, *Superconducting transition in aluminum,* Phys. Rev. **111**, 132 (1958).

[8] P. Fulde, *High field superconductivity in thin films,* Advances in Physics **22**, 667 (1973).

[9] P. M. Tedrow and R. Meservey, *Critical magnetic field of very thin superconducting aluminum films,* Phys. Rev. B **25**, 171 (1982).

[10] W. Meissner and R. Ochsenfeld, *Ein neuer effekt bei eintritt der supraleitfähigkeit,* Naturwissenschaften **21**, 787 (1933).

[11] S. Caplan and G. Chanin, *Critical-field study of superconducting aluminum,* Phys. Rev. **138**, A1428 (1965).

[12] J. F. Cochran and D. E. Mapother, *Superconducting transition in aluminum,* Phys. Rev. **111**, 132 (1958).

[13] K. Yosida, *Paramagnetic susceptibility in superconductors,* Physical Review **110**, 769 (1958).

[14] B. S. Chandrasekhar, *A note on the maximum critical field of high-field superconductors,* Appl. Phys. Lett. **1**, 7 (1962).

[15] A. M. Clogston, *Upper limit for the critical field in hard superconductors,* Phys. Rev. Lett. **9**, 266 (1962).

[16] R. Meservey and P. Tedrow, *Properties of very thin aluminum films,* Journal of Applied Physics **42**, 51 (1971).

[17] N. Read and D. Green, *Paired states of fermions in two dimensions with breaking of parity and time-reversal symmetries and the fractional quantum hall effect,* Phys. Rev. B **61**, 10267 (2000).

[18] S. Das Sarma, C. Nayak, and S. Tewari, *Proposal to stabilize and detect half-quantum vortices in strontium ruthenate thin films: Non-abelian braiding statistics of vortices in a $p_x + ip_y$ superconductor,* Phys. Rev. B **73**, 220502 (2006).

[19] M. Leijnse and K. Flensberg, *Introduction to topological superconductivity and majorana fermions,* Semiconductor Science and Technology **27**, 124003 (2012).

[20] R. Aguado, *Majorana quasiparticles in condensed matter,* La Rivista del Nuovo Cimento **40**, 523 (2017).

[21] P. Marra, *Majorana nanowires for topological quantum computation,* Journal of Applied Physics **132**, 231101 (2022).

[22] A. Y. Kitaev, *Unpaired majorana fermions in quantum wires,* Physics-uspekhi **44**, 131 (2001).

[23] J. D. Sau and S. D. Sarma, *Realizing a robust practical majorana chain in a quantum-dot-superconductor linear array,* Nature communications **3**, 964 (2012).

[24] M. Leijnse and K. Flensberg, *Parity qubits and poor man's majorana bound states in double quantum dots,* Phys. Rev. B **86**, 134528 (2012).

[25] I. C. Fulga, A. Haim, A. R. Akhmerov, and Y. Oreg, *Adaptive tuning of majorana fermions in a quantum dot chain,* New journal of physics **15**, 045020 (2013).

[26] R. M. Lutchyn, J. D. Sau, and S. D. Sarma, *Majorana fermions and a topological phase transition in semiconductor-superconductor heterostructures,* Physical review letters **105**, 077001 (2010).

[27] Y. Oreg, G. Refael, and F. Von Oppen, *Helical liquids and majorana bound states in quantum wires,* Physical review letters **105**, 177002 (2010).

[28] A. Andreev, *The thermal conductivity of the intermediate state in superconductors,* Journal of Experimental and Theoretical Physics **46**, 1823 (1964).

[29] G. Blonder, m. M. Tinkham, and k. T. Klapwijk, *Transition from metallic to tunneling regimes in superconducting microconstrictions: Excess current, charge imbalance, and supercurrent conversion,* Physical Review B **25**, 4515 (1982).

[30] S. Guéron, H. Pothier, N. O. Birge, D. Esteve, and M. H. Devoret, *Superconducting proximity effect probed on a mesoscopic length scale,* Phys. Rev. Lett. **77**, 3025 (1996).

[31] A. E. Antipov, A. Bargerbos, G. W. Winkler, B. Bauer, E. Rossi, and R. M. Lutchyn, *Effects of gate-induced electric fields on semiconductor majorana nanowires,* Phys. Rev. X **8**, 031041 (2018).

[32] C. Reeg, D. Loss, and J. Klinovaja, *Metallization of a rashba wire by a superconducting layer in the strong-proximity regime,* Phys. Rev. B **97**, 165425 (2018).

[33] T. O. Rosdahl, A. Vuik, M. Kjaergaard, and A. R. Akhmerov, *Andreev rectifier: A nonlocal conductance signature of topological phase transitions,* Phys. Rev. B **97**, 045421 (2018).

[34] C. W. J. Beenakker, *Quantum transport in semiconductor-superconductor microjunctions,* Phys. Rev. B **46**, 12841 (1992).

[35] M. P. Anantram and S. Datta, *Current fluctuations in mesoscopic systems with andreev scattering,* Phys. Rev. B **53**, 16390 (1996).

[36] G. Wang, T. Dvir, N. van Loo, G. P. Mazur, S. Gazibegovic, G. Badawy, E. P. A. M. Bakkers, L. P. Kouwenhoven, and G. de Lange, *Nonlocal measurement of quasiparticle charge and energy relaxation in proximitized semiconductor nanowires using quantum dots,* Phys. Rev. B **106**, 064503 (2022).

[37] J. Clarke, *Experimental observation of pair-quasiparticle potential difference in nonequilibrium superconductors,* Physical Review Letters **28**, 1363 (1972).

[38] M. Tinkham, *Tunneling generation, relaxation, and tunneling detection of hole-electron imbalance in superconductors,* Physical Review B **6**, 1747 (1972).

[39] M. Tinkham and J. Clarke, *Theory of pair-quasiparticle potential difference in nonequilibrium superconductors,* Physical Review Letters **28**, 1366 (1972).

[40] J. Danon, A. B. Hellenes, E. B. Hansen, L. Casparis, A. P. Higginbotham, and K. Flensberg, *Nonlocal conductance spectroscopy of andreev bound states: Symmetry relations and bcs charges,* Phys. Rev. Lett. **124**, 036801 (2020).

[41] K. T. Law, P. A. Lee, and T. K. Ng, *Majorana fermion induced resonant andreev reflection,* Physical review letters **103**, 237001 (2009).

[42] K. Flensberg, *Tunneling characteristics of a chain of majorana bound states,* Physical Review B **82**, 180516 (2010).

[43] C. Beenakker, J. Dahlhaus, M. Wimmer, and A. Akhmerov, *Random-matrix theory of andreev reflection from a topological superconductor,* Physical Review B **83**, 085413 (2011).

[44] S. D. Sarma, J. D. Sau, and T. D. Stanescu, *Splitting of the zero-bias conductance peak as smoking gun evidence for the existence of the majorana mode in a superconductor-semiconductor nanowire,* Physical Review B **86**, 220506 (2012).

[45] E. Prada, P. San-Jose, and R. Aguado, *Transport spectroscopy of n s nanowire junctions with majorana fermions,* Physical Review B **86**, 180503 (2012).

[46] E. J. H. Lee, X. Jiang, R. Aguado, G. Katsaros, C. M. Lieber, and S. De Franceschi, *Zero-bias anomaly in a nanowire quantum dot coupled to superconductors,* Phys. Rev. Lett. **109**, 186802 (2012).

[47] J. Liu, A. C. Potter, K. T. Law, and P. A. Lee, *Zero-bias peaks in the tunneling conductance of spin-orbit-coupled superconducting wires with and without majorana end-states,* Phys. Rev. Lett. **109**, 267002 (2012).

[48] D. I. Pikulin, J. Dahlhaus, M. Wimmer, H. Schomerus, and C. Beenakker, *A zero-voltage conductance peak from weak antilocalization in a majorana nanowire,* New Journal of Physics **14**, 125011 (2012).

[49] D. Bagrets and A. Altland, *Class d spectral peak in majorana quantum wires,* Phys. Rev. Lett. **109**, 227005 (2012).

[50] H. Pan and S. Das Sarma, *Physical mechanisms for zero-bias conductance peaks in majorana nanowires,* Phys. Rev. Res. **2**, 013377 (2020).

[51] T. D. Stanescu and S. Tewari, *Disentangling majorana fermions from topologically trivial low-energy states in semiconductor majorana wires,* Phys. Rev. B **87**, 140504 (2013).

[52] D. Rainis, L. Trifunovic, J. Klinovaja, and D. Loss, *Towards a realistic transport modeling in a superconducting nanowire with majorana fermions,* Phys. Rev. B **87**, 024515 (2013).

[53] D. Roy, N. Bondyopadhaya, and S. Tewari, *Topologically trivial zero-bias conductance peak in semiconductor majorana wires from boundary effects,* Phys. Rev. B **88**, 020502 (2013).

[54] H. Pan, W. S. Cole, J. D. Sau, and S. Das Sarma, *Generic quantized zero-bias conductance peaks in superconductor-semiconductor hybrid structures,* Phys. Rev. B **101**, 024506 (2020).

[55] S. Das Sarma and H. Pan, *Disorder-induced zero-bias peaks in majorana nanowires,* Phys. Rev. B **103**, 195158 (2021).

[56] H. Pan, C.-X. Liu, M. Wimmer, and S. Das Sarma, *Quantized and unquantized zero-bias tunneling conductance peaks in majorana nanowires: Conductance below and above* $2e^2/h$*,* Phys. Rev. B **103**, 214502 (2021).

[57] L. P. Kouwenhoven, D. Austing, and S. Tarucha, *Few-electron quantum dots,* Reports on Progress in Physics **64**, 701 (2001).

[58] R. Hanson, L. P. Kouwenhoven, J. R. Petta, S. Tarucha, and L. M. Vandersypen, *Spins in few-electron quantum dots,* Reviews of modern physics **79**, 1217 (2007).

[59] P. Recher, E. V. Sukhorukov, and D. Loss, *Andreev tunneling, coulomb blockade, and resonant transport of nonlocal spin-entangled electrons,* Phys. Rev. B **63**, 165314 (2001).

[60] L. Hofstetter, S. Csonka, J. Nygård, and C. Schönenberger, *Cooper pair splitter realized in a two-quantum-dot y-junction,* Nature **461**, 960 (2009).

[61] L. Herrmann, F. Portier, P. Roche, A. L. Yeyati, T. Kontos, and C. Strunk, *Carbon nanotubes as cooper-pair beam splitters,* Physical review letters **104**, 026801 (2010).

[62] A. Das, Y. Ronen, M. Heiblum, D. Mahalu, A. V. Kretinin, and H. Shtrikman, *High-efficiency cooper pair splitting demonstrated by two-particle conductance resonance and positive noise cross-correlation,* Nature communications **3**, 1165 (2012).

[63] A. Bordoloi, V. Zannier, L. Sorba, C. Schönenberger, and A. Baumgartner, *Spin cross-correlation experiments in an electron entangler,* Nature , 1 (2022).

[64] C.-X. Liu, G. Wang, T. Dvir, and M. Wimmer, *Tunable superconducting coupling of quantum dots via andreev bound states in semiconductor-superconductor nanowires,* Physical review letters **129**, 267701 (2022).

[65] A. Bordin, G. Wang, C.-X. Liu, S. L. ten Haaf, G. P. Mazur, N. van Loo, D. Xu, D. van Driel, F. Zatelli, S. Gazibegovic, *et al.*, *Controlled crossed andreev reflection and elastic co-tunneling mediated by andreev bound states,* arXiv (2022), 2212.02274 .

[66] J. Bauer, A. Oguri, and A. Hewson, *Spectral properties of locally correlated electrons in a bardeen–cooper–schrieffer superconductor,* Journal of Physics: Condensed Matter **19**, 486211 (2007).

[67] G. Wang, T. Dvir, G. P. Mazur, C.-X. Liu, N. van Loo, S. L. Ten Haaf, A. Bordin, S. Gazibegovic, G. Badawy, E. P. Bakkers, *et al.*, *Singlet and triplet cooper pair splitting in hybrid superconducting nanowires,* Nature , 1 (2022).

3

Methods and optimization of nanofabrication techniques

Over 2000 nanowires were brutally displaced from their motherchip during the course of this Ph.D.

Throughout this thesis, we make use of our novel nanofabrication technique of shadow-wall lithography. The design principles and characterization of basic quantum transport devices based on this method are presented in chapter 4. As a complement, this chapter provides a more in-depth description of the technique - starting from bare substrates and ending with fully fabricated devices. This includes the fabrication of two types of shadow-wall substrates, as well as the optimization of their fabrication processes. Next, the deposition of semiconductor nanowires is shown. Then, the process and optimization of hydrogen-radical cleaning are described - a process crucial to the creation of high-quality devices which is used to selectively remove the native nanowire oxides. The deposition of the superconductor is treated after that, before ending the chapter with a section on the creation of Ohmic contacts. Other experimental methods, such as the experimental setups, electrical circuits, measurement techniques, and data analysis, are described in detail in the supplemental information sections of the experimental chapters.

3.1 Shadow-wall substrate fabrication and optimization

A semiconductor-superconductor hybrid device typically contains several elements that are present regardless of the purpose of the device or the intended experiment. First of all, the semiconductor needs to be brought in contact with a superconductor in order to induce superconductivity in it. This forms a hybrid that needs to be contacted by Ohmic contacts, typically made of a stack of normal metals. Additional metallic electrodes are required nearby to control the chemical potential and electron density, often requiring an elaborate pattern to independently affect various parts of the hybrid. These electrodes are usually separated from the device by a gate dielectric. In addition, thick-metallic bond pads can be present to facilitate the wire-bonding connection between the sample chip and the measurement setup. Each of these elements requires precise patterning, which can be accomplished through the use of Electron-Beam Lithography (EBL) combined with deposition or etching techniques. Unfortunately, forming the interface between the semiconductor and superconductor is almost always the first step in fabrication. Yet, it is precisely this interface that plays a crucial role in the quality of the final device [1]. What is worse is that this interface is also extremely fragile [2], being adversely affected by the elevated temperature of the various fabrication processes. Moreover, the repeated processing inevitably adds contamination to the surface of the hybrids - which is also known to reduce their quality [3]. Indeed, the many fabrication steps after forming the semiconductor-superconductor interface (or post-fabrication for short) are detrimental, both to the performance as well as the reproducibility of hybrid devices.

We have developed the Shadow-Wall Lithography (SWL) technique in order to circumvent the drawbacks of post-fabrication. This is done by executing many of the fabrication steps prior to the deposition of the nanowire. Importantly, this avoids the thermal budget of the InSb/Al interface, allowing for a broader range of nanofabrication processes to be used as well as improving the performance of many fabrication steps. In addition, SWL eliminates the need to etch the superconductor by replacing it with a selective deposition. This requires the fabrication of pre-patterned dielectric structures in order to selectively block the deposition of superconducting material. SWL allows for a wide range of complex device architectures, although at the expense of a more challenging design process. Understanding the fabrication of SWL substrates and its limitations is crucial for the design of condensed matter experiments involving semiconductor-superconductor hybrids.

In figure 3.1, we present a Scanning-Electron Microscopy (SEM) image of an exemplary shadow-wall sample after measurements have concluded. This particular sample is used in the three-terminal experiments presented in chapter 7. A large-scale overview of the chip is shown in figure 3.1a. Here, 12 structures, each containing one device and consisting of 2×3 shapes, are visible within a $5x5$ mm area. The distance between the center of adjacent structures is approximately 1 mm. In figure 3.1b, we zoom in on one of these structures. The 4 diamond shapes and 2 trapezoid shapes are the bond pads, which are used to connect the sample to the measurement setup. On top of the pads, bond scraps from the removal of the bonds after measurement are visible. The brighter pads are connected to the two Ohmic contacts Ω_1 and Ω_2 of the device, whereas the pad in between them is connected to the central superconducting lead. The other three pads connect to the three electrostatic gates that control the hybrid. The faint lines between the pads are the shadow walls, which form

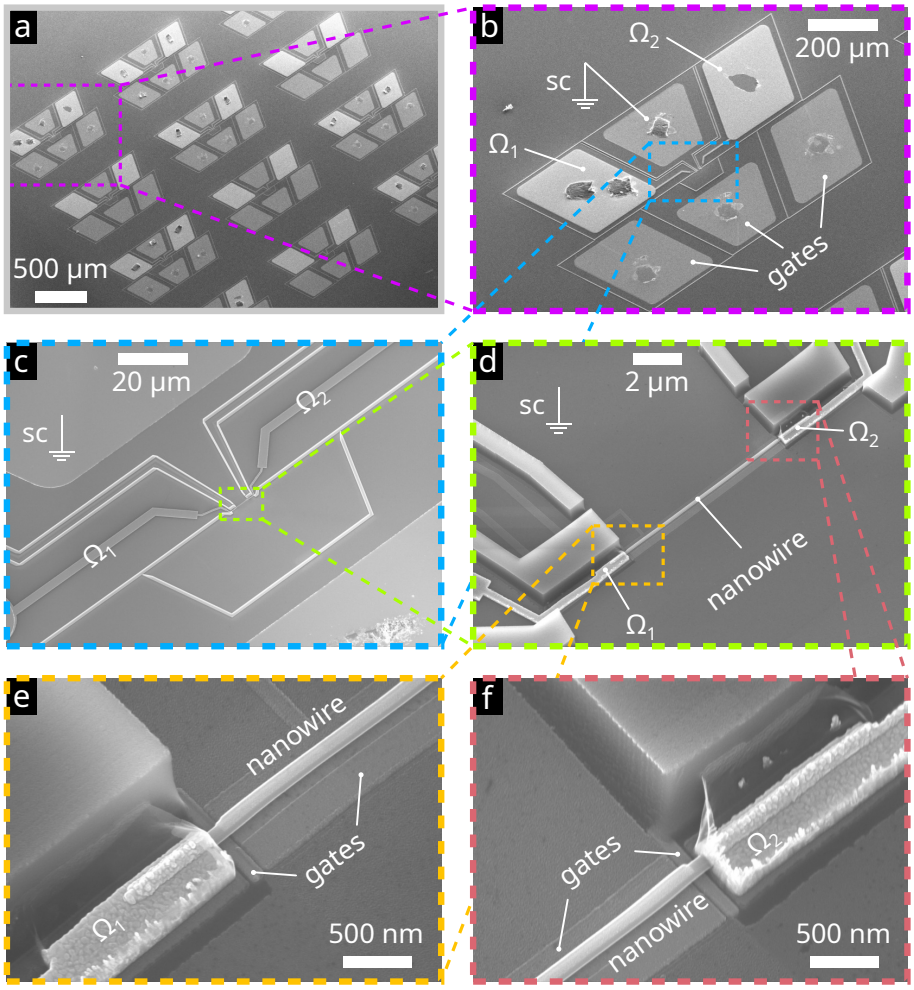

Figure 3.1: **Example of a shadow-wall substrate and 8μm nanowire hybrid. a**. Large-scale overview of a chip used for three-terminal measurements. The chip hosts 12 structures, separated approximately by 1 mm. **b**. Zoom-in on a single structure. The 6 pads are connected to the three leads (denoted by Ω_1, Ω_2, and *sc*) and three electrostatic gates of the device. Shadow walls are used to galvanically isolate the various elements of the structure. **c**. The central area of the structure hosts an isolated pocket in which the nanowire is placed. **d**. The nanowire is placed on a set of gate electrodes in the center of the structure. The middle lead of the device, in the top-left corner, connects directly to one of the bond pads. The normal leads are routed via the shadow of the walls and through gaps in the walls to their respective bond pockets. **e,f**. The two semiconductor junctions separate the Al-covered part of the device from the normal leads. Individual narrow gates control the junction transmissions, while the larger central gate controls the chemical potential in the hybrid segment of the device.

bond pockets that galvanically isolate the bond pads. In the center, a small isolated pocket can be seen. A zoom-in of this pocket is shown in figure 3.1c, where the shadow walls are presented as brighter lines. In addition, the Ohmic contacts are shown as narrow strips moving from the bottom-left and top-right to the center of the structure. In the center, the nanowire is placed on top of the gate array as displayed in figure 3.1d. It is contacted by the superconducting film on the top-left side, forming a 8 μm long superconducting hybrid. The film connects directly to one of the bond pads. Various gaps in the shadow walls can be seen, which are crucial elements to ensure electrical isolation between the bond pads. The Ohmic contacts are routed through such gaps in the walls in the bottom-left and top-right corner. Further zoom-ins on the Ohmic contacts on the nanowire are shown in figure 3.1e and f. The hybrid segment of the nanowire is separated from the Ohmic contacts by a section of uncovered nanowire. Underneath this section is a narrow finger gate, which can be used to form a tunnel barrier through electrostatic gating. The hybrid segment itself is positioned on top of a larger gate, which is used to tune the chemical potential in the segment.

In this thesis, two SWL substrate fabrication methods are used. In chapter 4, substrates are fabricated using a top-down approach which involves the growth of separate layers and their subsequent etching. On the other hand, chapters 5, 6, 7, 8 and 9 use bottom-up substrates for which the individual layers are selectively deposited. Both methods have 4 fabrication stages in common, as shown in figure 3.2. The left and right columns give an overview of the various nanofabrication steps used to transition between the stages for the top-down and bottom-up approaches, respectively. Details of these steps are elucidated in the following two sections. In both cases, we start with initial substrates made from (usually intrinsic) Si covered by a 285 nm layer of SiO_2, as shown in figure 3.2a. The first round of fabrication involves the formation of patterned gate electrodes, which are used for electrostatic gating of the devices. This results in the stage depicted in figure 3.2b. In the next round, bond pads are deposited at the ends of the gate electrodes as well as at the eventual termination of the Ohmic leads. This results in the stage shown in figure 3.2c. Subsequently, the entire chip is covered in a high-quality gate dielectric before fabricating the shadow walls, as displayed in figure 3.2d. A final round of cleaning primes the substrates for nanowire deposition.

3.1.1 Top-down substrates

Top-down: gate layer and bond pads

The top-down approach for the fabrication of shadow-wall substrates relies on the growth and subsequent etching of the different materials. Before the first fabrication round, the substrates are covered by a layer of Al_2O_3using Atomic Layer Deposition (ALD)[1]. This layer acts as a stopping layer for the various etching steps in the fabrication flow. At this point the fabrication of the gate layer can begin. This requires a total of 7 steps (including ALD), which are shown in figure 3.3a. First, a thin layer of W is sputtered[2] globally on the chip, as shown in figure 3.3a(ii). Next, the W layer is covered by a thin layer of

[1] 17 nm Al_2O_3 grown at T = 300°C

[2] 17 nm W grown using RF sputtering at P = 150 W in a 20 μbar Ar pressure

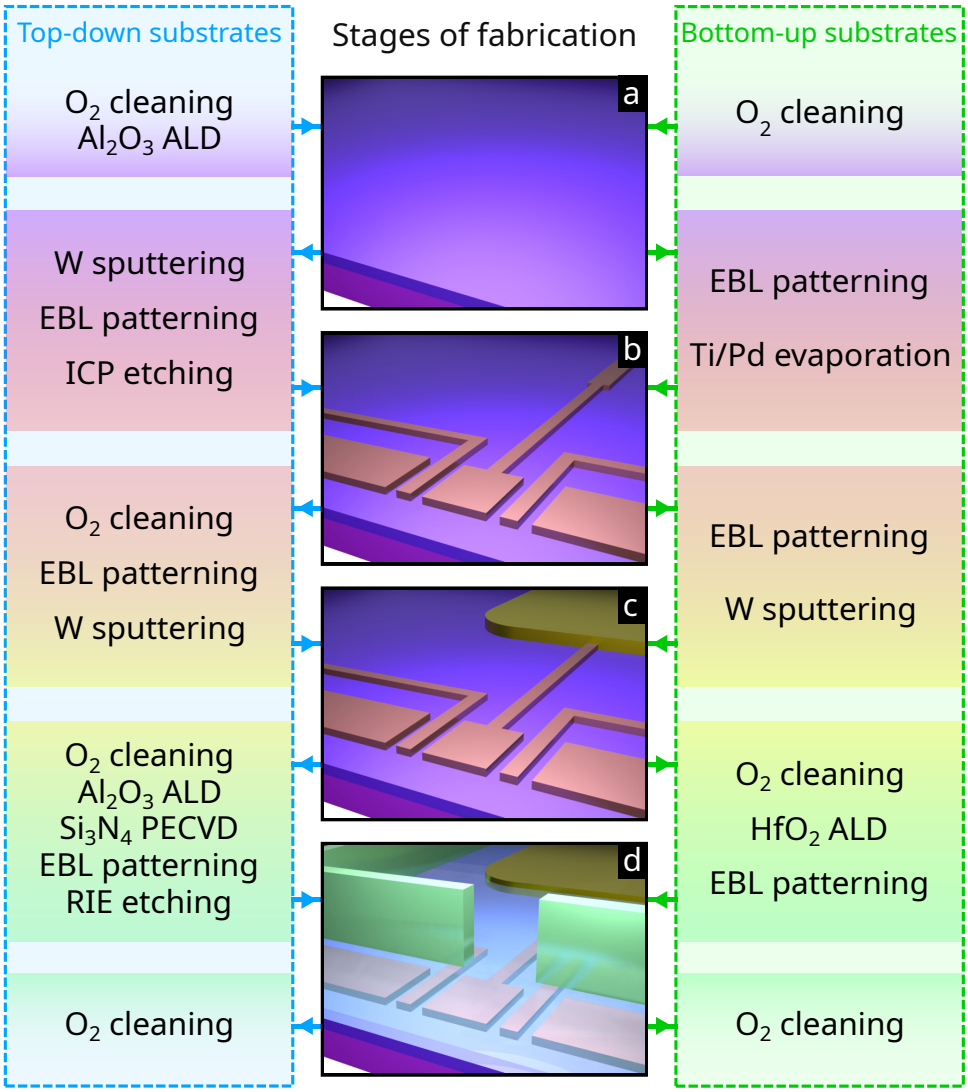

Figure 3.2: **Fabrication flow of shadow-wall substrates.** The left column (blue) shows the flow for top-down fabrication, whereas the right column (green) depicts the bottom-up approach. **a**. The base substrates consist of (intrinsic) silicon (light purple) covered by 285 nm silicon oxide (dark purple). **b**. After an initial round of fabrication, the substrates are covered with arrays of thin (~ 17nm) gate electrodes (red). **c**. Large and thicker (~ 50nm) metallic pads (dark yellow) are connected to the gates to facilitate wire bonding of the samples. **d**. The substrates are covered in a gate dielectric (light blue) before fabricating the shadow walls (green), which define the shadow lithography pattern for the deposition of the superconducting layer.

negative EBL resist[3] (figure 3.3a(iii)). The resist layer is subsequently exposed in the shape of the gate pattern using EBL. After exposure, the resist is developed[4] which removes the unexposed parts of the resist layer. Both exposure and development of the resist layer are depicted in figure 3.3a(iv). The desired pattern is then dry-etched into the W layer (figure 3.3a(v)), using Reactive-Ion Etching (RIE)[5]. Afterward, the resist layer, which covers the remaining W, is removed using the appropriate stripper[6] (figure 3.3a(vi)). However, this may leave undesirable resist residues on top of the gates as the etching process can harden the resist layer through heating, making it difficult to remove. Thus, an aggressive O_2 plasma cleaning[7] is used as a final step to remove any residues from the sample (figure 3.3a(vii)).

While we found initial success in this approach of gate fabrication, the reliance on etching does come with limitations. On the one hand, organic material (EBL resist) on top of the gates can be problematic if it is not properly removed. In this case, resist residues could be present between the gate electrode and the gate dielectric, and inevitably underneath the hybrid device. Such residues are essentially very poor-quality dielectric, which is filled with charge traps [4]. Consequentially, they can result in an undesirable loss of electrical stability of the hybrid devices. In addition, our etching process turned out to have poor reproducibility. For example, in figure 3.3b and c, we show two examples of a shadow-wall structure with etched gates. In figure 3.3b, a properly-formed structure is shown where the fine gate (blue box) is well-separated from the other two gates. However, the similar structure in figure 3.3c shows an example where the three gates are merged. As a result, various parts of the hybrid can not be individually controlled with the gates, rendering the structure useless. What is more concerning is that these two structures were adjacent on a single chip, with a spacing between them on the order of 950 μm. The non-uniformity of the etching process causes such a low reliability that chips essentially can only be fabricated one at a time. Furthermore, this also limits the spatial resolution and size of the gate pattern. A fine set of narrow gates, such as the ones used to form quantum dots, is difficult to realize using this specific fabrication recipe.

After the fabrication of the gate layer, bond pads are created to facilitate the wire bonding of the sample to the measurement setup. First, the substrates are covered in positive EBL resist[8]. The bond pad areas are exposed in the EBL, after which the sample is developed[9]. Next, the W is sputtered[10] which covers the exposed parts of the chip, forming the bond pads. The sample is then put in liftoff[11] to remove the excess resist and W. At this point, the gate layer and bond pads are finished and need to be covered by the gate dielectric. Before growing this layer, the sample is again subjected to an aggressive O_2 plasma cleaning[12]. This ensures no organic residues remain between the gate electrodes and the dielectric

[3] AR-N 7500.08 spun at 4 krpm for 1 min, hot-baked at T = 85°C for 3 min
[4] AR 300-47 for 2 min, followed by 30 s in H_2O and post-baking at T = 120°C for 1 min
[5] RIE etching using SF_6 at T = 20°C for 1 min
[6] AR 600-71 overnight (~ 18 h), followed by 30 s in H_2O
[7] O_2 plasma at a pressure of p = 0.7 mbar and P = 600 W for 40 min
[8] PMMA 950k A6 spun at 4 krpm for 1 min, hot-baked at T = 185°C for 10 min
[9] 3 : 1 mixture of IPA:MIBK for 1 min, followed by IPA for 1 min
[10] 50 nm W grown using RF sputtering at P = 150 W in a 20 μbar Ar pressure
[11] 30 min in acetone at T = 50°C followed by 5 minutes of low-power ultrasonic bath
[12] O_2 plasma at a pressure of p = 0.7 mbar and P = 600 W for 40 min

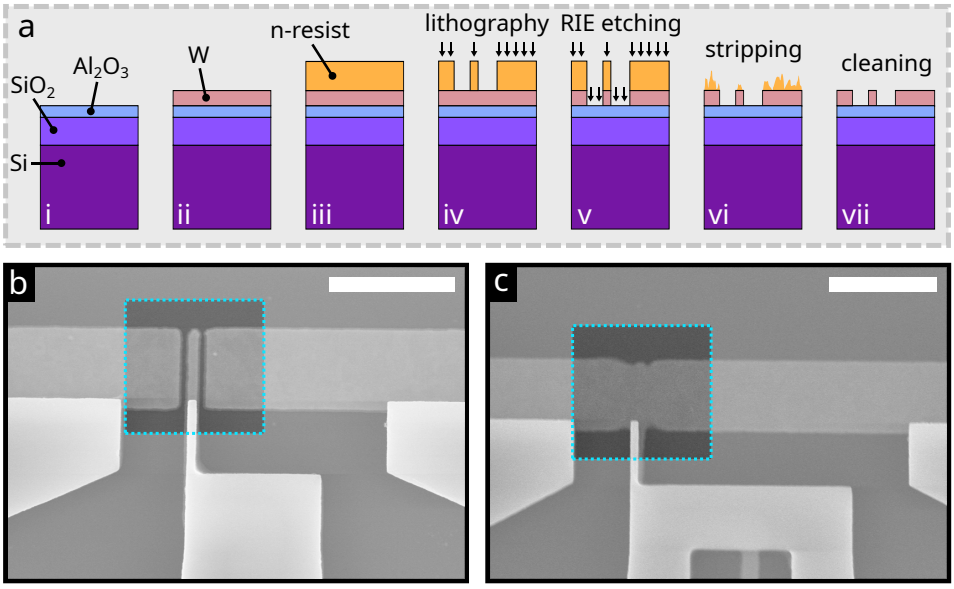

Figure 3.3: **Fabrication procedure of W bottom gates.** **a**. W gates are fabricated by first sputtering a full W film on the substrate and subsequently etching down the layer to achieve the desired pattern. **b**. Example SEM image of the desired gate pattern with successful etching. **c**. Example SEM image of unsuccessful gate fabrication due to nonuniform etching. Notably, the two structures in **b** and **c** are adjacent on the same chip, only 950 μm apart. Scale bars represent 1 μm.

layer. The Al_2O_3 gate dielectric is grown directly afterward, using ALD[13]. The samples are now ready for the fabrication of the shadow walls.

Top-down: shadow walls

The shadow walls themselves are made from a dielectric material in order to facilitate electrical isolation between various parts of the chip. The 6 fabrication steps involved are shown in figure 3.4a. First, a ~ 700 nm thick Si_3N_4 layer is grown globally on the chip using Plasma-Enhanced Chemical Vapor Deposition[14] (PECVD), as shown in figure 3.4a(ii). The Si_3N_4 layer is then covered by a thin layer of negative EBL resist[15] (figure 3.4a(iii)). The resist layer is subsequently exposed in the shape of the shadow-wall pattern using EBL. After exposure, the resist is developed[16] which removes the unexposed parts of the resist layer. Both exposure and development of the resist layer are depicted in figure 3.4a(iv). The desired pattern is then dry-etched into the Si_3N_4 layer (figure 3.4a(v)), using RIE[17] (RIE). Here, the time is calibrated to slightly over-etch the Si_3N_4 layer, whereas the Al_2O_3 acts as a stopping layer to protect the gate electrodes. Finally, the resist layer which covers

[13] 17 nm Al_2O_3 grown at T = 300°C
[14] 700 nm Si_3N_4 grown at T = 300°C
[15] AR-N 7500.18 spun at 4 krpm for 1 min, hot-baked at T = 85°C for 3 min
[16] AR 300-47 for 2 min, followed by 30 s in H_2O and post-baking at T = 120°C for 1 min
[17] RIE etching using CHF_3/O_2 gases at p = 8.0 mtorr and P = 50 W

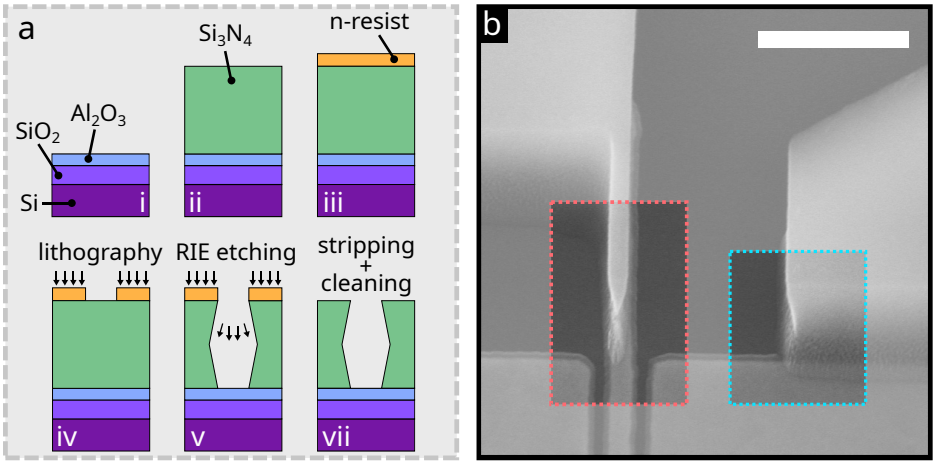

Figure 3.4: **Fabrication procedure of Si_3N_4 shadow walls. a**. Shadow walls are grown by globally depositing a thick (~ 700 nm) Si_3N_4 layer using PECVD before etching it down to achieve the desired pattern. **b**. Example SEM of Si_3N_4 shadow walls. Lateral etching can damage fine structures such as nozzles (red) and alter the shape of the walls (blue). Scalebar represents 500 nm. Image taken at 60° angle from the substrate.

the remaining Si_3N_4 is removed[18] and the substrates are cleaned with an aggressive O_2 plasma[19] (figure 3.4a(vii)). At this point, the substrate is ready for nanowire deposition.

The RIE process is typically only partially directional. As a result, the etching of thick layers might suffer from lateral etching, as demonstrated in figure 3.4b. The lateral etching can lead to deformation or even a complete removal for narrow features. This is shown, for example, in the red box, where a nozzle used to create nanowire junctions is depicted. The width of the nozzle using this process is limited, as narrower nozzles would collapse more quickly due to the lateral etching. Similarly, a thicker Si_3N_4 layer results in a more-significant lateral etching as the required etching time increases with the layer thickness. Thus, the Si_3N_4 thickness is also limited, which in turn affects the length of the shadow cast by the shadow walls. This can make the deposition of the nanowires quite challenging, as they need to be placed in close proximity to the walls.

3.1.2 Bottom-up substrates

Bottom-up: gate layer and bond pads

In the bottom-up approach, the various layers of the shadow-wall substrates are directly deposited. The main advantage is that the least reliable fabrication step, the etching of various layers, is avoided. At the start of the fabrication, no etch-stop layer in the form of ALD-deposited Al_2O_3 is required. The formation of the gate layer is thus reduced to 4 steps, which are depicted in figure 3.5a. First, a thin layer of positive EBL resist is spun across

[18] AR 600-71 over night (~ 18 h), followed by 30 s in H_2O

[19] O_2 plasma at a pressure of p = 0.7 mbar and P = 600 W for 40 min

the sample[20] (figure 3.5a(ii)). The pattern of the bottom gate array is then exposed in the EBL and subsequently developed[21], as shown in figure 3.5a(iii). Next, the gate metals are deposited using an electron-beam evaporator (EBE). First, a thin layer of Ti is deposited as a sticking layer, followed by a thin Pd film[22]. The sample is then put in acetone for the lift-off process[23], which removes the EBL resist as well as the Ti/Pd layer on top (figure 3.5a(iv)). The bond pads are fabricated afterward, using the same fabrication as for the top-down substrates (see section 3.1.1).

With this method, the gate metals are deposited in the desired pattern onto the substrate and require no etching. A correct dose for the EBL process is, in this case, the most critical process parameter. For example, if the dose is too low, the positive resist does not get fully exposed, which results in resist residues after the development. These residues then remain during the gate metal deposition, resulting in non-flat gate electrodes as shown in figure 3.5b. On the other hand, none of these residues should remain if the dose is correct. This results in flat gate electrodes, as shown in figure 3.5c. The roughness of the films can be investigated using Atomic Force Microscopy (AFM). An example is shown in figure 3.5d, for which a roughness of R_a = 0.25 nm is estimated.

[20] PMMA 950k A2 spun at 4 krpm for 1 min, hot-baked at T = 185°C for 10 min
[21] 3 : 1 mixture of IPA:MIBK for 1 min, followed by IPA for 1 min and 1 min post-baking at T = 110°C
[22] 3 nm Ti evaporated at 0.5 Å/s followed by 17 nm Pd evaporated at 1.0 Å/s
[23] Room temperature acetone overnight (~ 18 h) or in T = 50°C Acetone for 1 h, followed by a low-power ultrasonic bath for 5 min

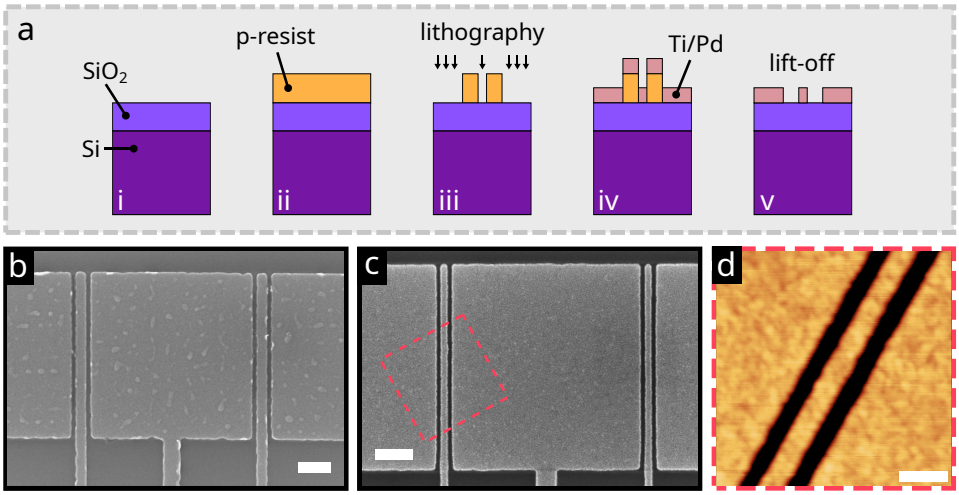

Figure 3.5: **Fabrication procedure of Ti/Pd bottom gates. a**. Ti/Pd gates are fabricated by first patterning the desired shape before depositing a Ti/Pd film using electron-beam evaporation. **b**. Underdosing during lithography can lead to resist residues on the substrate, resulting in non-flat gates. **c**. With the correct dose, small feature sizes can be achieved, and the gate roughness is limited by grains in the film. **d**. AFM image of the gates depicted in panel c around the red dashed box. The films have a roughness of Ra = 0.25 nm. Scalebars represent 200 nm.

For the optimized EBL dose, we can obtain gate arrays with features sizes as small as 20 nm spacing between the gates and a gate width of 30 nm. This allows the formation of narrow gate-defined quantum dots in the semiconductor. The size of the dots determines the orbital level spacing E_n, which is inversely proportional to its length L ($E_n \propto 1/L^2$). Thus, small dots have a large orbital level spacing, which, together with a large g-factor, opens up the possibility to spin-polarize the dot levels. The ability to do this is a crucial requirement for the experiment done in chapter 8 on the unit-cell Kitaev chain (see also the theory in section 2.3). This would likely be difficult to implement with our recipe for etched W gates (see section 3.1.1). Thus, the direct deposition of Ti/Pd gates forms an essential improvement over the etched W gates, which enabled a vast number of new device architectures and experiments.

Similarly, the direct deposition of Ti/Pd gates with the correct EBL dose significantly improved the reproducibility of the substrate fabrication. For example, substrates are made with this technique on a 2 × 2 cm chip containing 4 dies of 1 × 1 cm. Each die contains 12 shadow-wall structures, allowing for an equal number of devices to be made per die. Thus a total of 48 gate arrays are present on the chip. With the optimized recipe, we typically obtain a yield close to 100% for the gate layer. In contrast to the etched W gates, the deposited Ti/Pd gates allow the creation of a large number of identical and fully functional substrates. This improvement is essential for optimizing recipes for a new superconductor, as done in chapter 5, as well as the large-scale studies of many samples in chapter 6.

Bottom-up: shadow walls

In contrast to the top-down approach, this method uses a different gate dielectric: HfO_2 instead of Al_2O_3. The shadow walls themselves are fabricated in 2 steps, as shown in figure 3.6a. First, an ~ 800 nm thick layer of Hydrogen Silsesquioxane (HSQ) is spin-coated on the chip[24]. The HSQ acts as a negative resist, which forms a silicon-rich oxide upon exposure to the EBL. Development[25] removes the unexposed HSQ, leaving only the shadow walls. While the samples can typically be blown dry with an N_2 gun, small features with large aspect ratios can benefit from drying using a Critical Point Dryer (CPD) to avoid them from collapsing. Note that the developer is based on TMAH, which is used to etch Al_2O_3. While we typically use HfO_2 as the gate dielectric, it can be replaced with Al_2O_3 but only if the walls are fabricated before the gate dielectric is grown. Prior to nanowire deposition, the substrates are cleaned using a moderate O_2 plasma[26] to remove organic residues.

The optimization of HSQ shadow-wall fabrication relies on the correct dosing in the EBL. For example, if the dose is too high, the electron backscattering on the substrate can cause narrow gaps in the walls to merge, as shown in figure 3.6b. On the other hand, a low dose results in the malformation or removal of narrow features such as nozzles (figure 3.6c). With the correct dose, figure 3.6d shows that narrow features can be fully formed without merging at the base. However, such features with large aspect ratios can collapse upon each other if patterned close together and not dried using the CPD - or if exposed to the

[24] FOx-25 spun at 1.5 krpm for 1 min, hot-baked at $T = 180^\circ$C for 2 min

[25] 5 min in MF-321 at $T = 50^\circ$C, followed by rinsing for 30 s in H_2O and 30 s in IPA.

[26] O_2 plasma at a pressure of $p = 0.7$ mbar and $P = 600$ W for 5 min

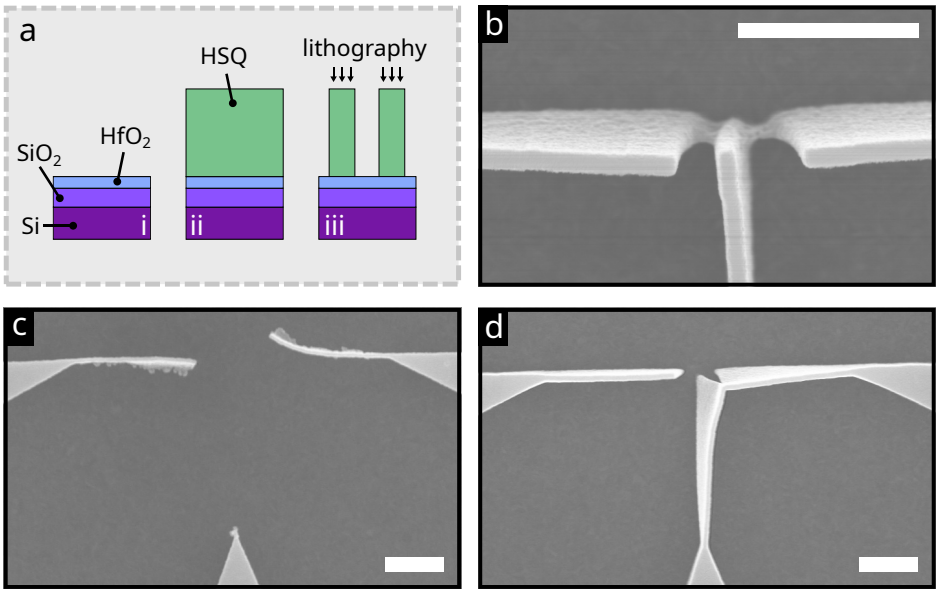

Figure 3.6: **Fabrication procedure of HSQ shadow walls. a**. HSQ walls are fabricated by spin-coating an HSQ layer and exposing the desired pattern using EBL. **b**. Too high doses can merge small gaps in the wall structure. **c**. Too low doses are detrimental to fine structures such as nozzles. **d**. With the correct dose, narrow features with large aspect ratios can fully form without merging at the base. However, CPD might be required to dry chips with such features, and SEM exposure can also cause them to collapse, as seen in this image. Scalebars represent 500 nm.

electron beam of an SEM. In comparison to the etched Si_3N_4 walls, the minimal feature size of HSQ walls is only limited by the EBL resolution. We have found that nozzles with a small width of ~ 20 nm can be reliably fabricated using this method. This enables the creation of extremely short nanowire Josephson junctions [5], essential for the experiments presented in chapter 9 on the superconducting diode effect.

3.2 Nanowire deposition

After the preparation of the substrates, nanowires need to be deposited on top of the gate electrodes. For the shadow-wall lithography to function correctly, the nanowires must be placed in close vicinity to the shadow walls. Depending on the height of the walls and the deposition angle, the maximum allowed distance from the wall can vary between ~ 500 nm and ~ 1400 nm. It is beneficial to calculate the estimated shadow length of the walls for a given superconductor recipe, and adjust the size of the gate array such that the gate electrodes themselves fall within the shadow length of the wall. This way, it is assured that the proper parts of the nanowire are shadowed by the walls during the superconductor deposition whenever the nanowire is placed on top of the gates.

Throughout this thesis, we make use of stemless InSb nanowires [6]. These nanowires offer relatively high mobility, can be as long as 15 μm, and can have diameters as small

as 80 nm. The length can be exploited to make extremely long hybrids, up to 8 μm in chapter 7. On the other hand, the small diameter is beneficial to increase the level spacing of the nanowire subbands and energy levels.

The nanowires are deposited using an optical nanomanipulator setup. This technique uses a sharp needle to mechanically transfer nanowires from the growth chip to a target substrate [7]. However, the addition of shadow walls on the substrate poses a new challenge: the target area for landing the nanowire is small and close to the shadow walls, which makes direct placement very challenging. Here, we show step-by-step how the nanowires are placed on shadow-wall substrates.

The nanowire deposition process is illustrated in figure 3.7. In figure 3.7a, the manual controller is shown. It possesses three rotating knobs which can be used to maneuver the needle in three orthogonal directions. The needle itself and the arm on which it is mounted are shown in figure 3.7b. A tightening screw can be used to clamp or release the needle. By releasing it, the needle can be manually rotated around its axis. Figure 3.7c depicts the tip of the needle, which has an apex of around 100 nm. It is close to a growth field of nanowires, depicted as black dots in this image. The coordinate system is also shown, and corresponds to the rotational knobs in figure 3.7a. Movements of the needle in figure 3.7 are represented by a white arrow, whereas black arrows are used to highlight the chosen nanowire.

First, the nanowire has to be picked up from the growth chip. This is depicted in the red panels of figure 3.7. The needle is initially brought close to the nanowire, as shown in figure 3.7d. In addition, it needs to be relatively close to the surface of the growth chip. Then, the needle is pushed sideways into the nanowire, causing it to bend as shown in figure 3.7e. If the needle is positioned too far from the surface, the nanowire will fully bend and slip underneath the needle. This is a consequence of their large aspect ratios. However, if the needle is low enough, the nanowire will usually break at the connection to the growth chip. While thicker nanowires may stick to the needle directly due to van der Waals forces, thinner nanowires often jump away a small distance before sticking upright to the substrate. This is depicted in figure 3.7f. As the mechanical connection between the nanowire and the substrate is broken, it is now easier to pick up by combining a sideways and upward motion of the needle. This typically results in the nanowire sticking vertically to the tip, as depicted in figure 3.7g.

At this point, the nanowire can be deposited onto the substrate, as illustrated in the blue panels of figure 3.7. To facilitate a correct landing, it is helpful to manually rotate the needle such that the nanowire is positioned horizontally on the bottom of the tip, as shown in figure 3.7h. In addition, a reticle in one of the ocular lenses of the microscope can be aligned with the nanowire, depicted as the white cross-hair in figure 3.7h. Next, the aligned reticle serves as a reference for the target substrate. The substrate can be manually rotated to align the shadow walls with the reticle. This, in turn, ensures that the nanowire is oriented parallel to the shadow walls. The needle is then brought close to the center of the structure, a little bit above the surface of the substrate, as shown in figure 3.7j. Once the nanowire is close to the electrostatic gates, depicted in orange here, the needle can be lowered as depicted in figure 3.7k. Van der Waals forces will then cause the nanowire to

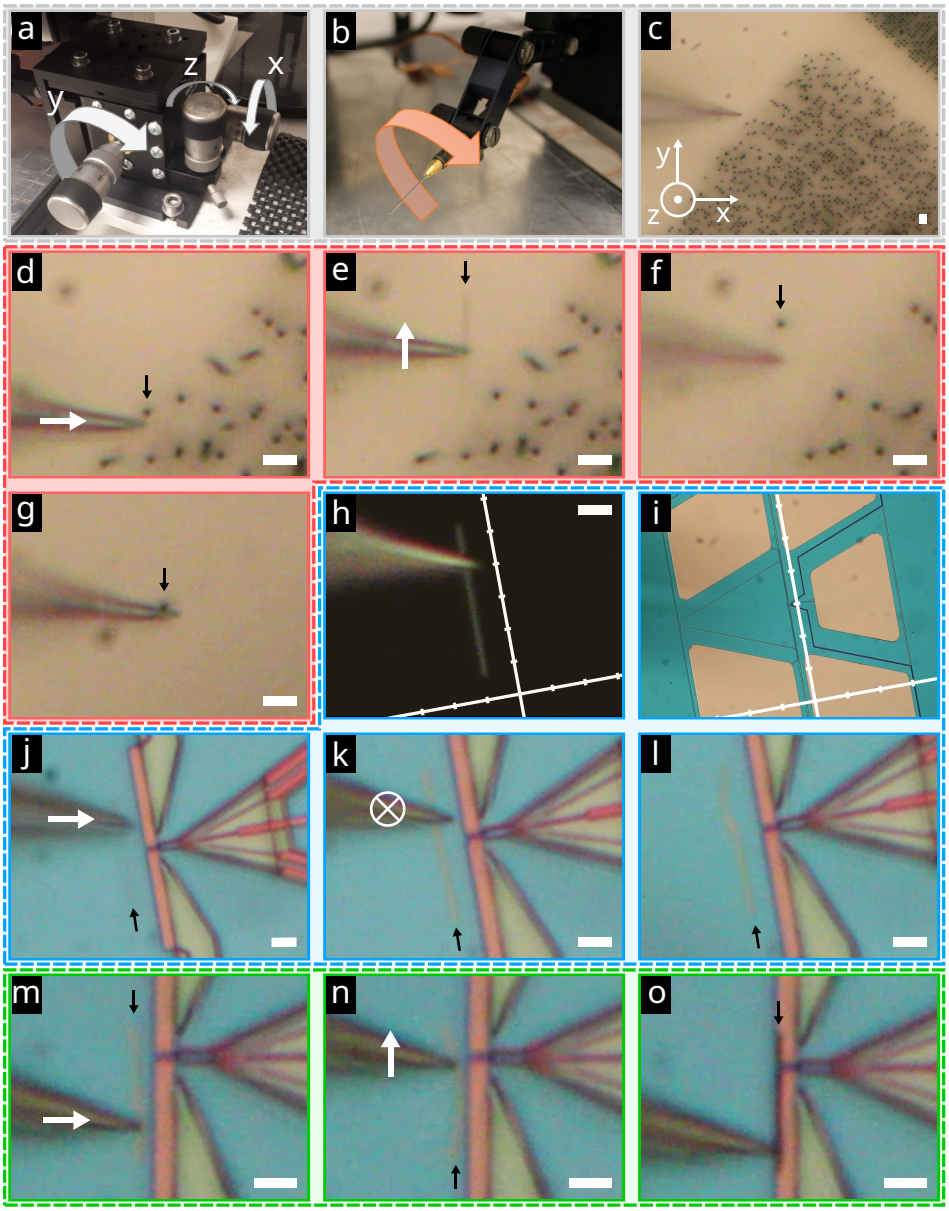

Figure 3.7: **Nanowire deposition on shadow-wall substrates. a**. The nanomanipulator setup possesses individual control over three movement axes. **b**. The needle used for nanowire transfer can be manually rotated. **c**. Optical microscope image of the manipulator needle close to a field of nanowires (black dots). **d-g**. Red panels show how nanowires are picked up from the growth chip. **h-l**. Blue panels depict the various steps during nanowire deposition. **m-o**. Green panels illustrate the nanowire pushing process. In all panels, the used nanowire is highlighted with a black arrow. White arrows represent the movement of the manipulator needle. Scale bars correspond to 2 μm.

snap to the substrate, finishing the deposition process (figure 3.7l). Note that depending on the size of the gates and the position of the nanowire on the needle, it can be possible to directly deposit the nanowire on top of the gates. However, the vicinity of the gates near the shadow walls (shown in green) can cause the nanowire to attach to the walls instead - effectively causing a loss of the nanowire and disabling the structure from being used.

Instead, we often rely on the process of nanowire pushing to bring the nanowire on top of the gates. This is demonstrated in the green panels of figure 3.7. The needle is first brought close to the substrate, allowing it to touch weakly. The needle is then moved across the substrate, pushing on the ends of the nanowire to move it slightly closer to the gates (figure 3.7m). Subsequently, the nanowire is straightened out by moving the needle in the orthogonal direction, as shown in figure 3.7n. This cycle of slightly pushing and straightening is repeated until the nanowire is on top of the gates. The final position is displayed in figure 3.7o.

3.3 Interface cleaning and metal deposition

3.3.1 Semiconductor surface treatment

Once all nanowires are placed on the shadow-wall substrate, the sample is ready for the superconductor deposition. However, the nanowires possess a native oxide layer which prevents making good contact. Thus, it first needs to be removed, which we achieve through atomic hydrogen cleaning [8].

The hydrogen-cleaning process is executed inside the load lock of a custom electron-beam evaporator. This is schematically depicted in figure 3.8a. The sample itself is mounted onto a heatable stage, which can rotate freely about its axis. The stage temperature is set to $T = 550\,\mathrm{K}$, where the sample is thermalized at this temperature for 2 h before starting the cleaning process. H_2 gas is injected into the chamber at a flow of 2 mln/min. A fraction of the H_2 molecules is dissociated into H^* radicals through the use of a W filament at a temperature of $T = 1700^\circ\mathrm{C}$. This results in a chamber pressure of $p = 6.3 \cdot 10^{-5}\,\mathrm{mbar}$. The created H^* radicals are volatile and react with the native nanowire oxide [9]. This reaction results in the formation of H_2O, which is pumped out of the process chamber. The cleaning angle φ can be adjusted by rotating the stage. During the cleaning, we use a combination of two cleaning angles $\varphi = 30^\circ$ and $\varphi = 120^\circ$ as depicted in figure 3.8b. Both angles receive an equal hydrogen cleaning time t_{cleaning}, which is the main parameter over which we optimize the cleaning process.

To optimize the cleaning time, we investigate the transport characteristics of InSb/Al Josephson junctions [10]. Such devices can be measured either in a voltage-bias configuration or in a current-bias configuration, of which the circuits are schematically depicted in figure 3.8c and d. In the case of a voltage bias, a DC voltage $V_{\mathrm{dc}} = 1\,\mathrm{mV}$ is applied across the device while measuring the resulting current I. The nanowire conductance G is then calculated as $G = I/(V_{\mathrm{dc}} - I \cdot R_{\mathrm{s}})$, where R_{s} is the series resistance of the circuit. In addition, the doped Si layer on the back of the chip can be used as a gate by applying a back-gate voltage V_{BG}. The nanowire conductance is then measured as a function of V_{BG}, resulting in a pinch-off curve as shown in figure 3.8e. At high back-gate voltages, the conductance tends to saturate to a saturation conductance G_{sat}. This value is obtained from the mea-

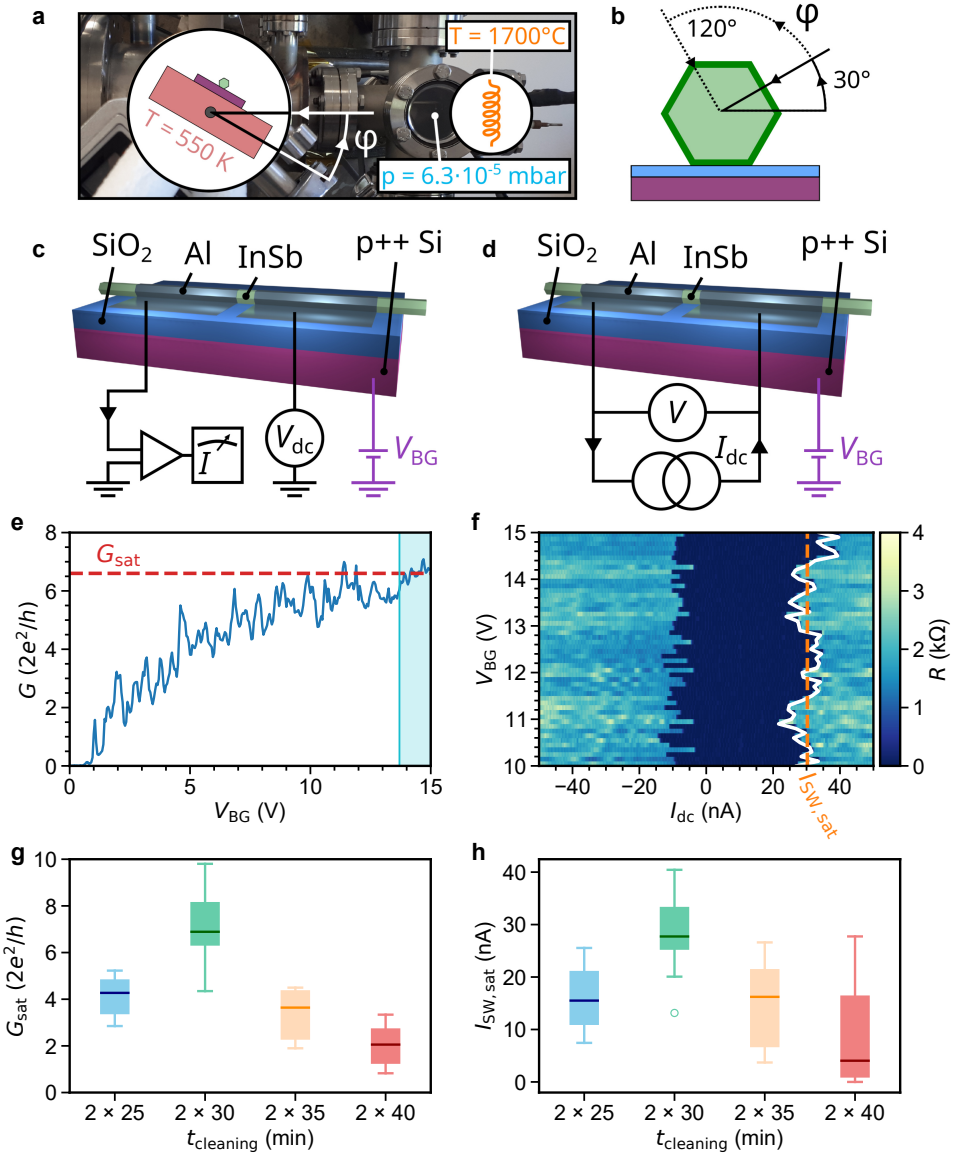

Figure 3.8: **Optimization of the hydrogen cleaning process. a**. Illustration of the cleaning setup. The holder and substrate can be rotated to adjust the cleaning angle φ. **b**. A mix of two cleaning angles (30°C and 120°C with respect to the substrate) is used to remove the native oxide (dark green) from the nanowires. **c**. A nanowire Josephson junction in the voltage-bias configuration, used for panels **e** and **g**. **d**. A nanowire Josephson junction in the current-bias configuration, used for panels **f** and **h**. **e**. Example pinch-off trace to determine the saturation conductance G_{sat} (red dashed line) by averaging the conductance in between $13.7\,V < V_{BG} < 15\,V$ (light blue area). **f**. Example switching current map to determine the saturation switching current $I_{SW,sat}$ (orange dashed line) by averaging switching current values (white line) in between $10\,V < V_{BG} < 15\,V$. **g**. Box plots of G_{sat} as a function of H*-cleaning time. **h**. Box plots of $I_{SW,sat}$ as a function of H*-cleaning time.

surements by averaging conductance values in a window 13.7 V < V_{BG} < 15 V, depicted as the light-blue rectangle. The saturation conductance serves as one of the metrics for characterizing the hydrogen cleaning process.

On the other hand, Josephson junctions can also be measured by using a current bias (figure 3.8d). A current I_{dc} is applied to the device, resulting in a voltage drop V. At low values of I_{dc}, the current across the junction is a supercurrent which results in no voltage dropping across the device. As the current is increased, the junction switches to a resistive state at a current value I_{SW}. This value typically increases and saturates at high back-gate voltages. In addition, the differential resistance $R \equiv dV/dI_{dc}$ is measured using standard lock-in techniques. The sample resistance is measured as a function of I_{dc} and V_{BG}, as shown in figure 3.8f. The switching current is depicted as a white curve on top. We define the saturation switching current $I_{SW,sat}$ as the average value of the switching current in a window of 13.7 V < V_{BG} < 15 V, depicted as the dashed orange line. This serves as the second metric for characterizing the hydrogen cleaning process.

Both saturation conductance and switching current can vary between different nanowires. In particular, they rely on microscopic details as well as the diameter of the used nanowire, as this influences their mobility [6]. Thus, to optimize the cleaning process, we prepare several chips, each with a large number of nanowires, all from the same growth field. Picking nanowires from the same field ensures that the spread in diameters is minimal, on the order of 20 nm. The substrates accommodate up to 16 nanowires, so a statistical analysis of the results on a single chip can be used.

In figure 3.8g, the saturation conductance is shown for 4 chips while varying the cleaning time. Here, a cleaning time of $t_{cleaning} = 2 \times 25$ min means a combination of 25 min cleaning at an angle of $\varphi = 30^\circ$ followed by 25 min cleaning at $\varphi = 120^\circ$. Results are presented as box plots, displaying the median and spread of the saturation conductance across multiple nanowires on the same chip. The 4 chips contain data of 10, 10, 6 and 9 nanowires for the cleaning times of 2×25 min, 2×30 min, 2×35 min and 2×40 min respectively. Likewise, results of the saturation switching current are shown in figure 3.8h. Both panels display a maximum value of the respective metric for a cleaning time of $t_{cleaning} = 2 \times 30$ min. As the two parameters G_{sat} and $I_{SW,sat}$ are indicative of the interface transparency between InSb and Al, this cleaning time achieves an optimal removal of the native oxide of the nanowires. This was verified by analyzing samples using Energy-dispersive X-ray spectroscopy (EDX) in a Transmission electron microscope (TEM); see also chapter 4. We note that the interface quality apparently decreases when the sample is cleaned for 2×35 min and 2×40 min. We suspect that over-cleaning results in the removal of Sb molecules at the surface after the oxide has been completely removed. This increases the surface roughness, and combined with the presence of In droplets, the transparency between the InSb and Al can be adversely affected.

3.3.2 Superconductor deposition

After removing the nanowire oxide, the sample is cooled down through active liquid nitrogen (LN_2) cooling. The heater is then used to stabilize the stage temperature at $T = 138$ K, where the sample is allowed to thermalize for 1 h. At the same time, a shroud surrounding the evaporator chamber is filled with LN_2, which reduces the chamber pressure from

$p =\sim 2 \cdot 10^{-8}$ mbar to $p =\sim 2 \cdot 10^{-9}$ mbar. Then, we precondition the chamber by evaporating ~ 20 nm of getter material (such as Ti, V or Nb), which reacts with residual gas species in the chamber (such as O_2, H_2O and N_2). This reduces the pressure even further, bringing it down to $p =\sim 2 \cdot 10^{-10}$ mbar. The Al film is then deposited onto the sample at a rate of 0.05 Å/s, with the deposition angle and film thickness depending on the sample requirements (see supplemental information of the various chapters for details). After this, for some samples, a thin Pt deposition is included (see chapters 6 and 7). To prevent the films from deforming during the warm-up to room temperature, they are protected either through the deposition of a capping layer (20 nm AlO_x deposited at ~ 0.2 Å/s) or through cold oxidation of the film in the load lock of the evaporator. This is done by exposing the samples to an O_2 pressure of 200 mTorr for 5 min.

The deposition process is schematically depicted in figure 3.9. In figure 3.9a, the substrate is shown with a nanowire placed on top of the gates. In addition, it illustrates the deposition of Al at an angle with respect to the substrate. A typical deposition angle is $\varphi = 30^\circ$, which results in a shadow length of ~ 1.4 μm for a shadow wall height of 800 nm. The red and yellow bars indicate the location of two cross-sections displayed in figure 3.9d and e,

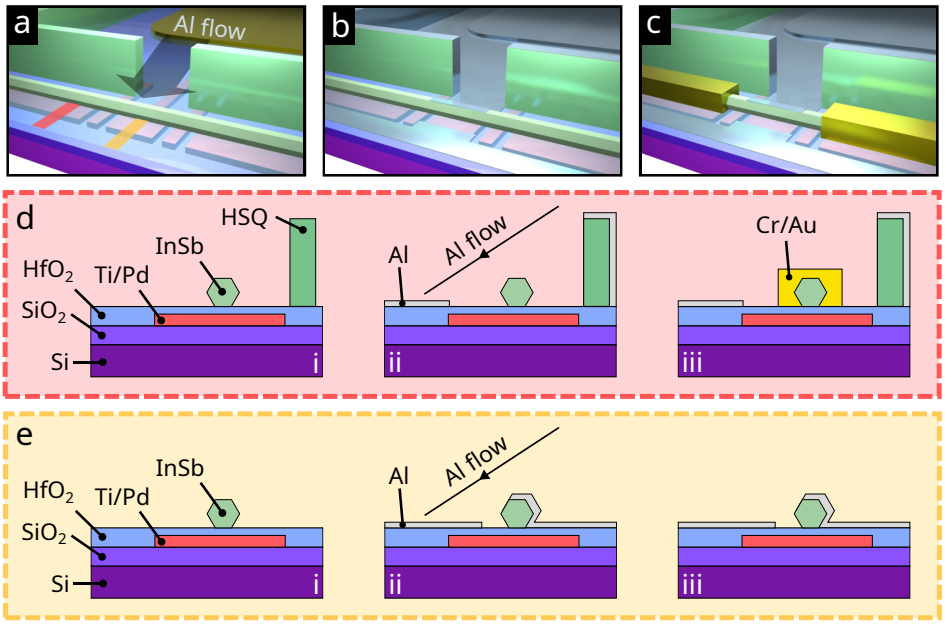

Figure 3.9: **Deposition of the superconducting and normal metals for a three-terminal device. a**. A nanowire (green) is placed on top of the gates in the vicinity of the shadow walls. The direction of the Al flow is indicated with a black arrow. The red and yellow bars indicate the locations of the cross-sections taken in **d** and **e**. **b**. After H^*-cleaning and superconductor deposition, part of the nanowire is covered by the Al (grey) while other parts are unexposed. **c**. Normal metal contacts (yellow) can be formed in the shadow of the walls, where no Al film is present. **d,e**. Cross-sectional cuts in the shadow of the walls (**d**) and outside the shadow (**e**), showing the position of the nanowire (i), Al film deposition (ii) and normal contact placement (iii).

and the situation before deposition is shown in subpanel (i). The deposition itself covers a predefined section of the nanowire with Al, forming the hybrid segment wherever there is a gap in the shadow walls (see figure 3.9b, d(ii) and e(ii)). The parts of the nanowire which lie in the shadow of the walls can later be used to form nanowire junctions and normal metal contacts. Some device archetypes, such as Josephson junctions and Superconducting Quantum Interference Devices (SQUIDs), do not require any Ohmic contacts and are ready for loading into the measurement setup at this point.

3.3.3 Normal contact deposition

As a final step, some samples may require the formation of Ohmic contacts made from a normal metal. In principle, this can be achieved in the same chamber as the superconductor deposition without breaking the vacuum. It requires the use of shadow-wall deposition at 2 different angles [11]. However, making contact with InSb is difficult due to the formation of a Schottky barrier when a mild interface treatment is used. This problem can, in principle, be alleviated by including an additional gate underneath [12]. It can instead be beneficial to create the Ohmic contacts in a different evaporator while using standard EBL techniques - avoiding both the added complexity of designing a substrate for double-angle deposition, as well as the requirement of additional gates underneath the contacts.

In order to do so, the sample is first coated in a layer of positive EBL resist[27]. The pattern of the Ohmic contacts is then exposed in the EBL and subsequently developed[28]. Since this process requires the sample to move between evaporators, a newly-formed oxide layer needs to be removed from the nanowire. This is done through aggressive Ar ion milling[29], which locally destroys the semiconductor crystal and leaves the surface of the nanowire covered with In droplets. While normal metals typically form a Schottky barrier with InSb [12], this facilitates a good Ohmic contact between the nanowire and the contact metal. An electron-beam evaporator (EBE) is used first to deposit a sticking layer of Cr or Ti, followed by the evaporation of a thick Au film[30]. The sample is then put in acetone for the lift-off process[31]. At this point, the sample is ready for loading into the measurement setup. An example of the sample after deposition of the normal metal is schematically depicted in figure 3.9c, with cross-sections in figure 3.9d(iii) and e(iii).

References

[1] P. Krogstrup, N. Ziino, W. Chang, S. Albrecht, M. Madsen, E. Johnson, J. Nygård, C. M. Marcus, and T. Jespersen, *Epitaxy of semiconductor–superconductor nanowires,* Nature materials **14**, 400 (2015).

[2] R. Sporken, P. Xhonneux, R. Caudano, and J.-P. Delrue, *The formation of the al-insb (110) interface,* Surface Science **193**, 47 (1988).

[3] Ö. Gül, D. J. Van Woerkom, I. van Weperen, D. Car, S. R. Plissard, E. P. Bakkers, and

[27] PMMA 950k A6 spun at 4 krpm for 1 min, soft-baked in a vacuum oven at room temperature for > 2 h
[28] 3 : 1 mixture of IPA:MIBK for 1 min, followed by IPA for 1 min
[29] 2×20 s at $p = 1.5 \cdot 10^{-3}$ mbar
[30] 10 nm Cr or Ti evaporated at 0.5 Å/s followed by 120-140 nm Au evaporated at 1.5 Å/s
[31] Room temperature Acetone overnight (~ 18 h)

L. P. Kouwenhoven, *Towards high mobility insb nanowire devices,* Nanotechnology **26**, 215202 (2015).

[4] A. V. Kuhlmann, J. Houel, A. Ludwig, L. Greuter, D. Reuter, A. D. Wieck, M. Poggio, and R. J. Warburton, *Charge noise and spin noise in a semiconductor quantum device,* Nature Physics **9**, 570 (2013).

[5] V. Levajac, G. P. Mazur, N. van Loo, F. Borsoi, G. Badawy, S. Gazibegovic, E. P. Bakkers, S. Heedt, L. P. Kouwenhoven, and J.-Y. Wang, *Impact of junction length on supercurrent resilience against magnetic field in insb-al nanowire josephson junctions,* arXiv preprint arXiv:2211.07858 (2022).

[6] G. Badawy, S. Gazibegovic, F. Borsoi, S. Heedt, C.-A. Wang, S. Koelling, M. A. Verheijen, L. P. Kouwenhoven, and E. P. Bakkers, *High mobility stemless InSb nanowires,* Nano Lett. **19**, 3575 (2019).

[7] K. Flöhr, M. Liebmann, K. Sladek, H. Y. Günel, R. Frielinghaus, F. Haas, C. Meyer, H. Hardtdegen, T. Schäpers, D. Grützmacher, *et al.*, *Manipulating inas nanowires with submicrometer precision,* Review of scientific instruments **82**, 113705 (2011).

[8] J. L. Webb, J. Knutsson, M. Hjort, S. Gorji Ghalamestani, K. A. Dick, R. Timm, and A. Mikkelsen, *Electrical and surface properties of inas/insb nanowires cleaned by atomic hydrogen,* Nano Letters **15**, 4865 (2015).

[9] S. Vangalaa, H. Dauplaiseb, C. Santeufemioa, C. Lynchb, P. Alcorna, L. Allenc, G. Dallasc, K. Vaccarob, D. Blissb, and W. Goodhuea, *Atomic hydrogen cleaning of epiready insb (100),(111) b, and gcib processed insb (111) b surfaces,* CS MANTECH Conference , 113 (2007).

[10] H. Nilsson, P. Samuelsson, P. Caroff, and H. Xu, *Supercurrent and multiple andreev reflections in an insb nanowire josephson junction,* Nano letters **12**, 228 (2012).

[11] F. Borsoi, G. P. Mazur, N. van Loo, M. P. Nowak, L. Bourdet, K. Li, S. Korneychuk, A. Fursina, J.-Y. Wang, V. Levajac, E. Memisevic, G. Badawy, S. Gazibegovic, K. van Hoogdalem, E. P. A. M. Bakkers, L. P. Kouwenhoven, S. Heedt, and M. Quintero-Pérez, *Single-shot fabrication of semiconducting–superconducting nanowire devices,* Adv. Func. Mater. , 2102388 (2021), https://onlinelibrary.wiley.com/doi/pdf/10.1002/adfm.202102388 .

[12] D. Fan, N. Kang, S. G. Ghalamestani, K. A. Dick, and H. Xu, *Schottky barrier and contact resistance of insb nanowire field-effect transistors,* Nanotechnology **27**, 275204 (2016).

4

Shadow-wall lithography of ballistic superconductor-semiconductor quantum devices

The realization of hybrid superconductor–semiconductor quantum devices, in particular a topological qubit, calls for advanced techniques to readily and reproducibly engineer induced superconductivity in semiconductor nanowires. Here, we introduce an on-chip fabrication paradigm based on shadow walls that offers substantial advances in device quality and reproducibility. It allows for the implementation of hybrid quantum devices and ultimately topological qubits while eliminating fabrication steps such as lithography and etching. This is critical to preserve the integrity and homogeneity of the fragile hybrid interfaces. The approach simplifies the reproducible fabrication of devices with a hard induced superconducting gap and ballistic normal-/superconductor junctions. Large gate-tunable supercurrents and high-order multiple Andreev reflections manifest the exceptional coherence of the resulting nanowire Josephson junctions. Our approach enables the realization of 3-terminal devices, where zero-bias conductance peaks emerge in a magnetic field concurrently at both boundaries of the one-dimensional hybrids.

This chapter has been published as *Shadow-wall lithography of ballistic superconductor-semiconductor quantum devices*, S. Heedt[†], M. Quintero-Pérez[†], F. Borsoi[†], A. Fursina, **N. van Loo**, G.P. Mazur, M.P. Nowak, M. Ammerlaan, K. Li, S. Korneychuk, J. Shen, M.A.Y. van de Poll, G. Badawy, S. Gazibegovic, N. de Jong, P. Aseev, K. van Hoogdalem, E.P.A.M. Bakkers and L.P. Kouwenhoven in Nature Communications 12, 4914 (2021).
[†] These authors contributed equally to this work.

4.1 Introduction

Hybrid superconducting/semiconducting nanowires are a promising material platform for the formation of one-dimensional topological superconductors bounded by pairs of Majorana modes [1–3]. Owing to their non-Abelian exchange statistics, these localized Majorana bound states (MBS) are the fundamental constituents for fault-tolerant topological quantum computing [4, 5]. Individual qubits comprise at least four MBS in several interconnected nanowire segments with a hard induced superconducting gap [6, 7]. Residual fermionic states within the gap would compromise the topological protection of the Majorana modes. Hence, a fundamental challenge in the development of topological qubits is the engineering of complex, interconnected hybrid devices with hard superconducting gaps and clean, homogeneous interfaces [8, 9].

Here, we introduce a fabrication technique that resolves these challenges and provides high-quality hybrid quantum devices, reflected by the absence of chemical intermixing, a high interface transparency and hard induced gaps, while involving minimal nanofabrication steps compared with previously established methods [10, 11]. Our approach is based on the deposition of superconducting thin films at a shallow angle onto semiconducting nanowires, which have been selectively placed on substrates with pre-patterned gates and shadow-wall structures. It enables complex hybrid devices while eliminating lithography, etching, and other fabrication steps after the deposition of the superconductor, in the following referred to as post-interface fabrication. While shadow-wall lithography is compatible with a large variety of materials, we utilize InSb nanowires coated with Al half-shells to induce superconducting correlations – a suitable material combination to study Majorana physics [11, 12]. The homogeneity of the interface between InSb and Al ultimately determines the device quality, but it is known to have very limited chemical and thermal stability [9, 13]. Therefore, the reduction or elimination of post-interface fabrication steps represents a paradigm shift that enables pristine hybrid interfaces. Similar advances in quality and reproducibility (Supplementary Note 1) were made possible by the reverse fabrication process established for carbon nanotube devices [14].

In this article, we investigate the transport properties of hybrid nanowire shadow-wall devices. Initially, we examine Josephson junctions and detect subharmonic gap features that arise from multiple Andreev reflections [15]. These junctions exhibit gate-tunable supercurrents of up to 90 nA, which is exceptionally large for InSb/Al nanowires compared to previous works on InSb Josephson junction devices [9, 16, 17]. The shadow-wall method also facilitates 3-terminal hybrid devices with two normal metal/superconductor (N–S) interfaces, which are crucial to corroborate earlier Majorana signatures [18–20]. We investigate the transport at a single N–S interface and observe a crossover between a hard induced gap and pronounced Andreev enhancement upon increasing the junction transparency, consistent with the expected behaviour for ballistic junctions [21, 22]. Finally, we report the emergence of discrete subgap states in the tunnelling conductance at both nanowire ends and detect stable zero-energy conductance peaks that coexist at certain magnetic fields and chemical potentials.

Our fabrication method paves the way for more advanced nanowire devices, including qubit implementations [6, 7, 23] and other multi-terminal devices that are essential for fun-

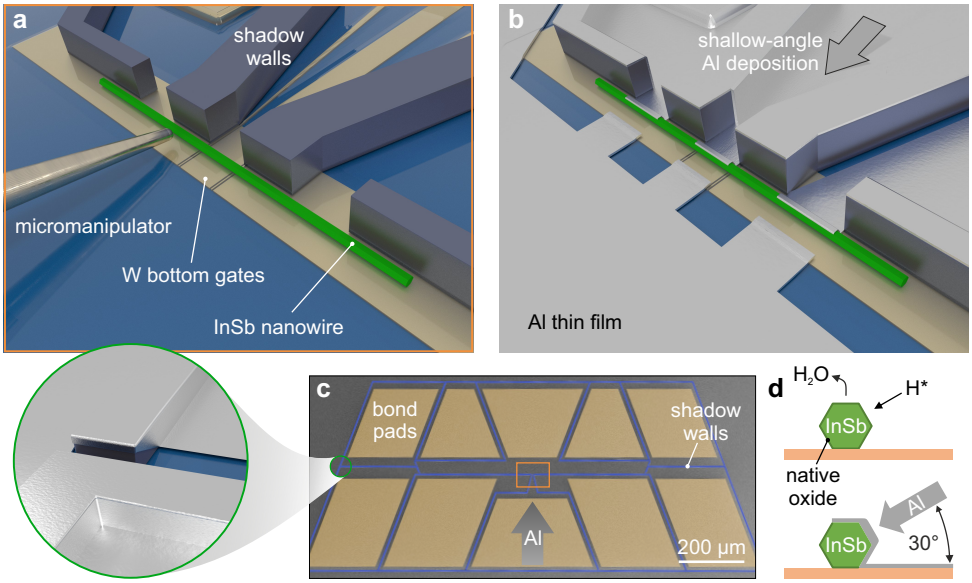

Figure 4.1: **Illustration of the shadow-wall technique.** **a** Micromechanical transfer of the nanowires onto local bottom gates (covered by Al_2O_3 dielectric) in the proximity of the Si_3N_4 shadow walls. **b** Illustration of a final device following the H radical cleaning and Al deposition at a shallow angle. **c** False-colour SEM image of an exemplary sample prior to Al deposition. Shadow walls are designated in blue and bond pads, which are enclosed by the shadow walls, are shaded in dark yellow. Gaps are placed at critical locations along the shadow walls (cf. green circle and the illustration in the blow-up following Al deposition). This ensures that bond pads with leads are isolated from each other after the Al deposition. The area illustrated in panel (**a**) is indicated by the orange box. **d** Schematic of the InSb nanowire cross-section during H radical cleaning (top). The native oxide of the semiconductor is denoted by a dark green layer. The Al thin film deposited at a shallow angle of 30° forms an electrical connection from the nanowire to the substrate (bottom).

damental research on topological superconductors [18, 24]. The versatility of the shadow-wall technique introduces a convenient and quick way to implement new device geometries with various combinations of semiconductor and superconductor materials.

4.2 Results

4.2.1 Shadow-Wall Lithography

A well-established approach to realize hybrid devices is based on the epitaxial growth of nanowires followed by the in-situ evaporation of a superconductor [10, 25]. This method requires a subsequent etching step to expose gate-tunable wire segments without metal. Nanowires have also been grown on opposite crystal facets of etched trenches [11, 26], which enables the formation of shadowed junctions without the need to etch the superconductor [11]. The native oxide that forms during the ex-situ processing is removed prior to the deposition of the superconductor. Another recent study employed growth chips with bridges and trenches that act as selectively shadowing objects during the evaporation of a superconductor [27]. Common to those methods is that the hybrid nanowires are removed from the growth substrate following the evaporation and undergo several post-interface

fabrication steps such as alignment via scanning electron microscopy (SEM), electron-beam lithography involving resist coating, or etching. The latter, in particular, degrades the electrical device performance compared with shadowed junctions [13]. Moreover, hybrid devices are prone to degradation. High-temperature processing (e.g. certain dielectric deposition methods or resist baking) cannot be performed, as it would lead to chemical intermixing at the super-/semiconductor interface [28, 29]. The limited chemical stability of the interface requires sample storage in vacuum at a temperature $T < 0\,^{\circ}\mathrm{C}$, which is hardly compatible with standard fabrication methods. The low thermal budget and the additional fabrication steps limit the achievable device performance in terms of electrical noise, lithographical alignment accuracy, contamination and disorder. The considerable variation from device to device imposes singular rather than standardized designs and results in a limited reproducibility of basic transport measurements.

In contrast, the core principle of our approach is to minimize or eliminate post-interface fabrication. We have engineered scalable substrates that comprise all desired functionalities without being subject to any fabrication restrictions (e.g. thermal budget limitations) since the semiconductor nanowires are only introduced right before the superconductor deposition. As depicted in Fig. 4.1a, we transfer InSb nanowires [30] to these substrates onto pre-patterned bottom gates covered by a continuous dielectric layer in the vicinity of shadow-wall structures. The nanowires are loaded into a customized evaporation chamber where the native oxide is removed at $T = 550\,\mathrm{K}$ by exposure to a directed flow of atomic hydrogen radicals. Without breaking the vacuum, Al is subsequently deposited onto the samples at $T = 140\,\mathrm{K}$. The superconductor is evaporated at a shallow angle of 30° with respect to the substrate plane, which creates a 3-facet nanowire shell that is connected to the leads and bond pads on the substrate (Fig. 4.1d). As illustrated in Fig. 4.1b, the shadow walls enable selective deposition on both the nanowires and the substrate. Adding gaps at critical locations along the shadow walls (Fig. 4.1c) ensures that the leads are electrically isolated from one another while eliminating the need for post-interface fabrication such as lift-off patterning or Al etching. Fig. 4.2a shows an exemplary device without local gates that is directly bonded to a printed circuit board for low-temperature transport measurements. Here, the p^+-doped Si substrate enables back-gate control of the electron density in the nanowire (see Fig. 4.2b).

4.2.2 Materials Analysis

The quality of the InSb nanowires, Al thin films, and InSb/Al interfaces is assessed by transmission electron microscopy (TEM) of cross-sectional lamellae prepared via focused ion beam (FIB). These lamellae are cut out from devices like the one depicted in Fig. 4.2a (cf. dashed line). A continuous high-quality polycrystalline Al layer is formed on three facets of the InSb nanowires and the samples exhibit a sharp superconductor–semiconductor interface (see Figs. 4.2c,e and Supplementary Fig. 4.7). No oxide formation is observed between the Al grains, which is evident in the elemental energy-dispersive X-ray spectroscopy (EDX) composite image (Fig. 4.2c). The middle facet has twice the Al layer thickness (16 nm) compared to the top and bottom facets (8 nm) due to the evaporation angle of 30° with respect to the substrate plane. The InSb/Al interface is clean and there is no residual native oxide (see Figs. 4.2d,e), which confirms that our procedure of atomic hydrogen radical cleaning can effectively remove the oxide without damaging the InSb crystal

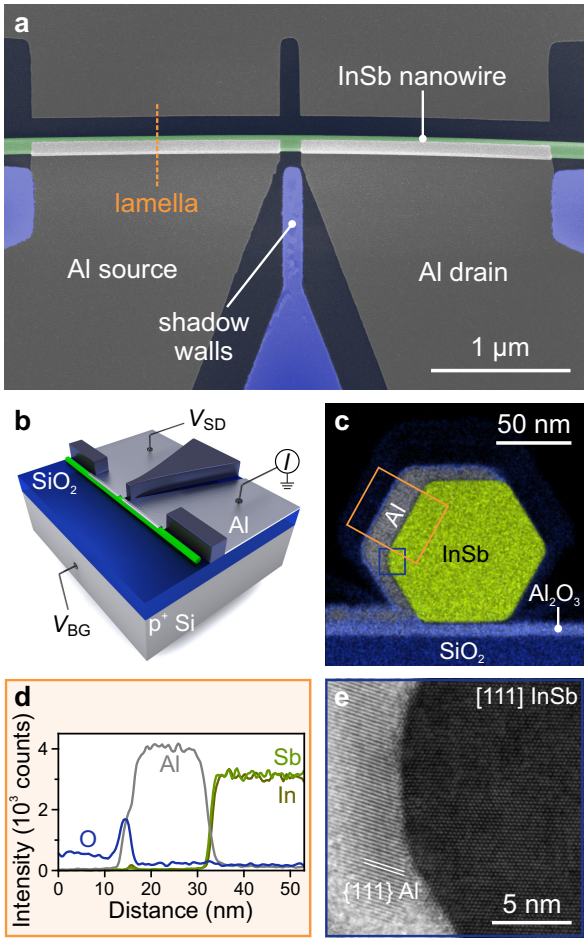

Figure 4.2: **TEM analysis of the InSb/Al interface. a** False-colour SEM image of an InSb nanowire Josephson junction. **b** Schematic of the measurement setup. The back-gate voltage, V_{BG}, is applied to the p^+-doped Si substrate to tune the electron density in the nanowire. **c** Cross-sectional EDX elemental composite image of the [111] InSb nanowire covered with the Al layer and a protective layer of SiN_x. **d** Line-cuts of the integrated elemental counts within the orange box in panel (**c**). **e** High-resolution bright-field scanning TEM image of the InSb/Al interface at the location indicated by the blue box in panel (**c**).

structure. The nanowires are single-crystalline, defect-free, and exhibit a hexagonal geometry. The polycrystalline Al layer forms a continuous metallic connection from the nanowire to the substrate. This connection is crucial for the contact between the shell and the thin Al lead on the substrate and it is fundamental for more complex devices such as superconducting interferometers (see Supplementary Fig. 4.36) and 3-terminal Majorana devices that can reveal the opening of a topological gap [18].

4.2.3 Highly Transparent Josephson Junctions

We employ mesoscopic InSb/Al Josephson junctions like the one depicted in Fig. 4.2a to study the induced superconductivity in the nanowires. Each device comprises two Al contacts (1.8 µm wide) separated by a 110–150 nm long bare nanowire segment that is tunable by the back-gate voltage, V_{BG}. The source–drain voltage, V_{SD}, is applied or measured between the two Al electrodes (Fig. 4.2b). Fig. 4.3a shows the differential resistance, $R = \mathrm{d}V_{SD}/\mathrm{d}I_{SD}$, as a function of bias current, I_{SD}, and temperature for a typical device. The blue region ($R = 0\,\Omega$) denotes the superconducting phase, which persists up to ~ 1.8 K, consistent with the enhanced superconducting critical temperature for thin films with respect to bulk Al [31]. At low temperatures ($T < 0.6$ K), the hysteretic behaviour of the asymmetric V_{SD}–I_{SD} traces is caused by self-heating of the junction. This effect disappears at higher temperatures ($T > 0.6$ K), which can be attributed to enhanced thermalization via electron–phonon coupling [32]. Remarkably, at $T = 30$ mK, the switching current, I_{sw}, i.e. the observable supercurrent, ranges from 30 to 90 nA across all devices in the open-channel regime. The magnitude of the intrinsic supercurrent, I_c, in ballistic and short junctions can be predicted via the Ambegaokar–Baratoff formula: $I_c R_N = \pi\Delta_{ind}/2e$, with the normal-state resistance R_N, the induced gap Δ_{ind}, and the electron charge e [33]. Here, the typical $I_{sw}R_N$ product is ~ 110 µV, i.e. only one-third of $\pi\Delta_{ind}/2e$ ~ 360 µV. The discrepancy between I_{sw} and I_c is consistent with previous experiments [16, 17, 34] and can be explained by premature switchings due to thermal activation and current fluctuations [35, 36]. We note that the magnitude of I_{sw} as well as the normalized quantity $eI_{sw}R_N/\Delta_{ind}$ ~ 0.5 are significantly larger than in previous reports on InSb Josephson junctions [9, 16, 17].

In Fig. 4.3b, we show the differential conductance, $G = \mathrm{d}I_{SD}/\mathrm{d}V_{SD}$, as a function of V_{SD} (red curves) for the same Josephson junction (top) and for a second device (bottom). The traces display subharmonic conductance peaks originating from multiple Andreev reflection (MAR) processes [15]. By fitting the conductance with a coherent scattering model (green curves), we can estimate the induced superconducting gap, Δ_{ind} (235 µeV and 229 µeV for device 1 and 2, respectively), and the gate-tunable tunnelling probability of the different subbands (see Supplementary Figs. 8–10) [37].

In Fig. 4.3c, we report the evolution of the MAR pattern as a function of magnetic field, $B_\parallel$, parallel to the nanowire axis of device 2. Here, the presence of subgap states close to the gap edge alters the typical MAR pattern and gives rise to an intricate energy dispersion in magnetic field that is further discussed in Supplementary Note 3. Eventually, the magnetic field quenches the superconductivity at a critical value of B_c = 1.2–1.3 T. This limit can be enhanced to about 2 T by using a thinner Al shell (Supplementary Fig. 4.20). These values are well above the magnetic field at which a topological phase transition should occur in hybrid InSb/Al nanowires [38]. In Fig. 4.3c, the out-of-gap conductance displays a dense pattern of faint peaks with an average spacing of about 30 µV and an effective Landé g factor of ~ 20 (extracted from the energy dispersion in magnetic field). This g factor is larger than in Al ($|g| = 2$) but smaller than in InSb ($|g| = 30$–50), which indicates that these peaks stem from discrete states of the nanowire hybridized with the ones in the metal [39]. The observation of this structure might be correlated with our choice of nanowire surface treatment. In fact, the gentle atomic hydrogen cleaning preserves the pristine semiconductor crystal quality, unlike the invasive chemical or physical etching

methods adopted in previous works [9, 16, 17, 34, 40].

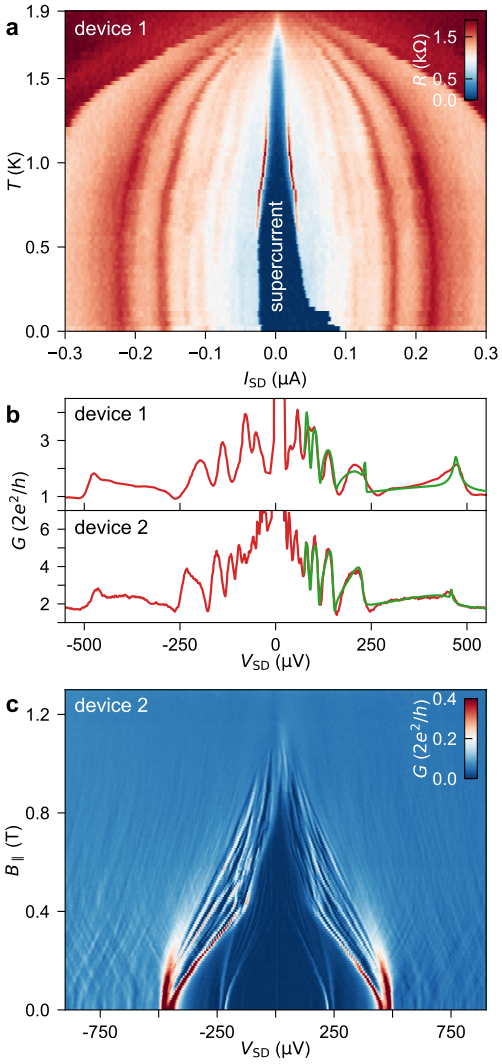

Figure 4.3: **Multiple Andreev reflections and supercurrent in InSb/Al Josephson junctions. a** Differential resistance, R, as a function of I_{SD} (upward sweep direction) and T for device 1 at V_{BG} = 13.65 V. The switching current reaches a maximum of ~ 90 nA at T = 30 mK and persists up to 1.8 K. The peaks at $I_{SD} > I_{sw}$ arise from quasiparticle transport via multiple Andreev reflections. **b** Conductance line traces (red) versus source–drain voltage for device 1 at V_{BG} = 5.1 V (top) and for device 2 at V_{BG} = 3.0 V (bottom). The theoretical fits (green) yield the transmissions, T_n, of the one-dimensional subbands with index n: T_1 = 0.91, T_2 = 0.17 (top) and T_1 = 0.93, T_2 = 0.71, T_3 = 0.01 (bottom). **c** Differential conductance, G, as a function of V_{SD} and magnetic field, $B_\parallel$, which is oriented along the nanowire, for device 2 at V_{BG} = −0.9 V.

4.2.4 Hard Induced Gap and Ballistic Superconductivity

A common technique to search for evidence of Majorana bound states is N–S tunnelling spectroscopy, which probes the local density of states. Signatures of MBS in proximitized InSb nanowires are zero-bias peaks (ZBPs) in the differential conductance at moderately large magnetic fields [41]. The ZBP height in the zero-temperature limit is predicted to be $G_0 = 2e^2/h$, independent of the tunnel-coupling strength, due to resonant Andreev reflection via a Majorana zero mode [42]. ZBPs of non-topological origin, which mimic the subgap behaviour of MBS, may arise from disorder or potential inhomogeneities [43]. A major challenge is to reduce the detrimental role of disorder at the superconductor–semiconductor interface, which determines the final device quality. The measure of success is a hard induced gap at a finite magnetic field and quantized Andreev enhancement as a signature of ballistic transport [44, 45].

An exemplary N–S device is depicted in Fig. 4.4a. Here, the N contact to the InSb nanowire was formed in a post-interface fabrication step, similar to the contacting of conven-

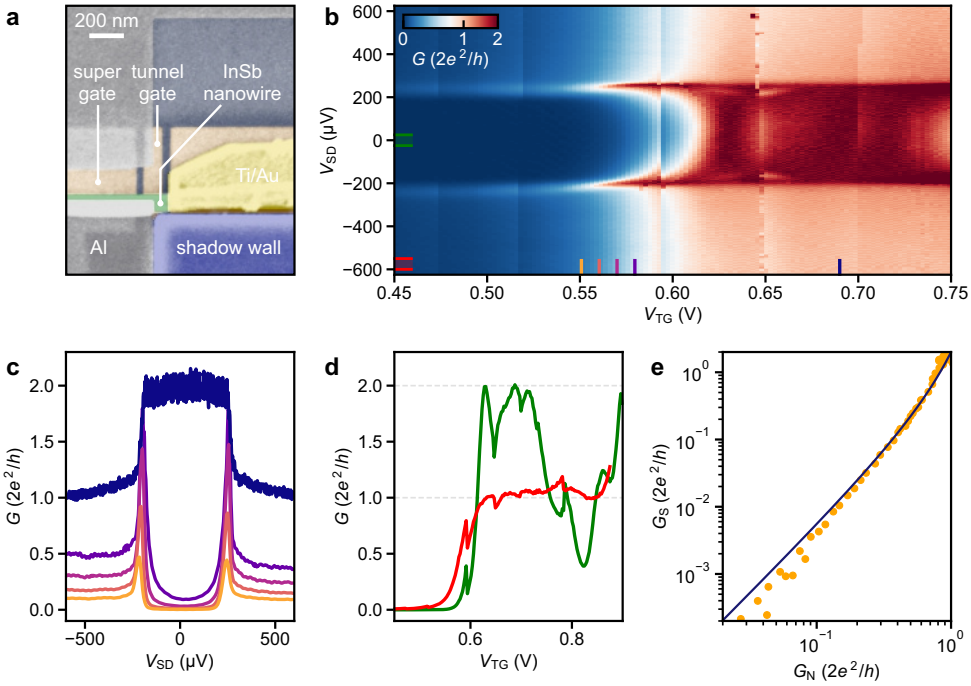

Figure 4.4: **Ballistic Andreev transport.** **a** False-colour SEM image of an exemplary N–S junction. The W bottom gates (brown) underneath the 100 nm wide InSb nanowire (green) are covered by 18 nm of Al_2O_3 dielectric. **b** Differential conductance, G, as a function of source–drain voltage, V_{SD}, and bottom tunnel-gate voltage, V_{TG}. The so-called super gate, which controls the chemical potential of the hybrid nanowire segment, is grounded. **c** G versus V_{SD} line-cuts of the data in panel (**b**) at the locations designated by the coloured lines. **d** Subgap conductance (green) and above-gap conductance (red) averaged over the V_{SD} intervals designated in panel (**b**). **e** G_S (subgap conductance at zero bias) as a function of G_N (normal-state conductance at $V_{SD} = 650\,\mu V$) together with the theoretically predicted dependence, which assumes Andreev-dominated transport in a single channel (blue line trace).

tional shadow junctions (Supplementary Note 1). Alternatively, Al leads that are defined by the shadow walls – microns away from the N–S junction – can serve as N contacts but require additional bottom gates to render all nanowire segments fully conducting (cf. Fig. 4.1b). Another option to fabricate N contacts in situ involves using two deposition angles, which we describe in detail elsewhere [46]. In Fig. 4.4b, we present voltage-bias spectroscopy of the N–S junction in Fig. 4.4a where the transmission is tunable via a pre-fabricated bottom tunnel gate. The line-cuts in Fig. 4.4c at low tunnel-gate voltage, V_{TG}, highlight the pronounced suppression of the subgap conductance, G_S, by about two orders of magnitude compared with the normal-state conductance, G_N (cf. Supplementary Fig. 4.29). As the first one-dimensional subband starts to conduct fully at $V_{TG} > 0.6\,V$, the above-gap conductance reaches the conductance quantum, $2e^2/h$, and the quantization manifests itself as a plateau in the tunnel-gate dependence (Fig. 4.4d). At the same time, the conductance below the gap edge reaches $4e^2/h$ owing to two-particle transport via Andreev reflection [21]. This pronounced doubling of the normal-state conductance together with the quantization of G_N signifies a very low disorder strength in the junction and a strong coupling at the nanowire/Al interface [47]. While the subgap conductance reaches up to $2G_0$, it drops again at $V_{TG} \sim 0.8\,V$, possibly due to inter-subband scattering as a result of residual disorder [44, 47–49]. The plot of G_S versus G_N (Fig. 4.4e) follows the Beenakker model [22] reasonably well without any fitting parameter, which shows that in the single-subband regime electrical transport below the gap edge is dominated by Andreev processes. The data are well-described by the BTK theory [21] across the entire gate voltage range, demonstrating a hard induced gap of $\Delta_{ind} \sim 230\,\mu eV$ (see Methods and Supplementary Fig. 4.31). Discrete subgap states and ZBPs appear at a finite magnetic field and field-dependent voltage-bias spectroscopy for this N–S device is presented in Supplementary Fig. 4.32.

4.2.5 Emergence of Zero-Bias Peaks at Both Nanowire Ends

The shadow-wall technique enables 3-terminal Majorana devices for nonlocal correlation experiments [18, 19] by harnessing the continuous connection of the Al shell to the substrate, as depicted in Fig. 4.5a. Here, the Al thin film serves as the superconducting drain lead. Established fabrication methods do not allow for the implementation of such devices since etching away the superconductor causes disorder at the InSb surface and contacting the Al shell requires selective removal of the native oxide of Al, which affects the integrity of the thin film. As shown in Fig. 4.5a, optional Ti/Au contacts are again added at both nanowire ends in the same fabrication run and on the same substrate as the sample in Fig. 4.4. With this device type, we can study the simultaneous emergence of ZBPs at both N–S boundaries in a magnetic field oriented along the wire. Here, the hybrid nanowire segment is 1 µm long and the chemical potential, μ, is controlled via a bottom gate (super gate) at potential V_{SG}. The differential conductance is measured concurrently at both N–S boundaries by alternating the V_{SD} sweep between the left and right N terminals for every increment of $B_\parallel$ or V_{SG}. Using this technique, we demonstrate the formation of zero-energy subgap states at both nanowire ends for $V_{SG} = 0\,V$ (see Figs. 4.5e,f). The effective g factor extracted from the linear energy dispersion at the two boundaries is ~ 10, albeit the values of g can be strongly gate-dependent [12]. Many experiments have demonstrated ZBPs in tunnelling spectroscopy at a single N–S boundary, indicating the

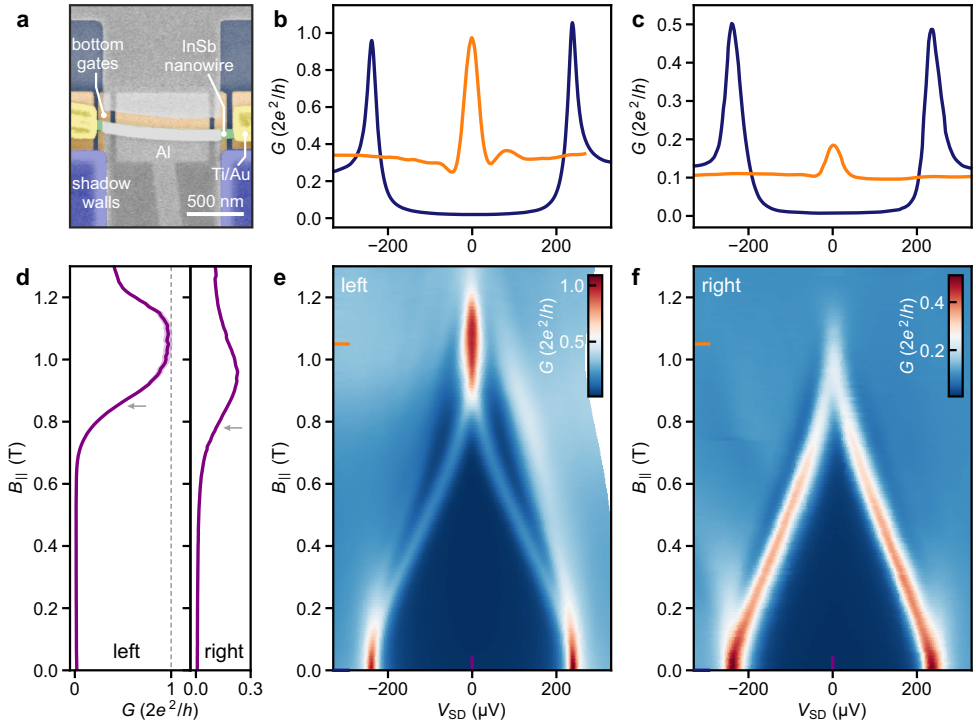

Figure 4.5: **Zero-bias conductance peaks at two opposite N–S boundaries. a** False-colour SEM image of the correlation device based on an 80 nm wide InSb nanowire with a 1 µm long hybrid segment. **b**, **c** Line-cuts of the differential conductance at zero field (blue) and at $B_\parallel = 1.05\,\mathrm{T}$ (orange) taken from panel (**e**) and (**f**), respectively. **d** G versus $B_\parallel$ line-cut at $V_{SD} = 0\,\mu\mathrm{V}$ taken from panel (**e**) (left) and (**f**) (right). Shaded areas (light purple) illustrate the variation in conductance assuming an uncertainty of $\pm 0.5\,\mathrm{k}\Omega$ in the series resistance. For the line-cut at the right N–S junction, this variation is less than the line width. **e**, **f** Differential conductance, $G = \mathrm{d}I_{SD}/\mathrm{d}V_{SD}$, as a function of bias voltage, V_{SD}, and magnetic field, $B_\parallel$, measured concurrently at the left and right junction, respectively. Here, the super gate underneath the hybrid nanowire segment is grounded ($V_{SG} = 0\,\mathrm{V}$).

presence of a robust state at zero energy [41, 49–51]. The robustness of ZBPs in the parameter space (defined by chemical potential and magnetic field) has been used to substantiate their topological origin [52].

So far, no experiment has revealed the emergence of ZBPs concurrently at both boundaries of a long hybrid nanowire. Recent experimental studies reported correlations between bound states at both ends of short (up to 400 nm long) hybrid nanowire devices [53, 54]. ZBPs often originate from trivial Andreev bound states (ABS). In topological nanowires, ABS can form by overlapping MBS due to local variations in the chemical potential or random disorder, which emphasizes the need for long and pristine hybrids [43]. A topological phase with well-separated MBS requires that potential inhomogeneities along the hybrid segment, $\Delta\mu$, are much smaller than the width of the topological phase, $2\sqrt{E_Z^2 - \Delta_{ind}^2}$, where E_Z is the Zeeman energy [1, 55]. We see in Figs. 4.5e,f that the ZBPs at the two boundaries do not exhibit the same onset field, which is defined as the field where the zero-bias

conductance reaches half of its maximum value. In Fig. 4.5d, this corresponds to 0.85 T on the left and 0.78 T on the right side (grey arrows). This observation could be explained by the presence of long-range inhomogeneities that result in a difference in $\Delta\mu$ at the two nanowire ends of about 70 µeV, considering $g = 10$. A possible origin of this inhomogeneity might be a variation in the deformation potential along the length of the hybrid due to a slight bend in the nanowire [56]. At larger values of μ, potential variations are expected to be suppressed due to screening. This might be supported by another data set measured at a larger chemical potential ($V_{SG} \sim 0.5$ V) presented in Supplementary Fig. 4.35, where we observe the same ZBP onset field at both N–S boundaries. The concomitant evolution as a function of V_{SG} at both nanowire ends is shown in Supplementary Figs. 28 and 29. This observation might corroborate the signatures of MBS [19, 55], but it cannot be regarded as conclusive evidence for truly separated MBS [43].

Figs. 4.5b,c show differential conductance line-cuts, which reveal a zero-bias conductance close to $2e^2/h$ for the ZBP at the left boundary of the device, as highlighted in Fig. 4.5d. While ZBP conductance close to G_0 has been observed for several N–S junctions, it depends on the fine-tuning of the tunnel barriers, which can be strongly affected by transmission resonances. Experimentally, ZBPs are in general substantially lower than the expected value of G_0 [42, 50]. Theoretical studies recently pointed out that partially or fully overlapping MBS can cause quantized ZBPs, indistinguishable from those resulting from isolated MBS [55, 57, 58]. Hence, the quantized ZBP conductance is a critical but not sufficient hallmark of MBS [54, 58].

4.3 Discussion

The 3-terminal hybrid nanowire devices provide a fundamental tool to study the evolution of the induced superconducting gap in the bulk of the hybrid, where electron- and hole-type bands become inverted at the topological phase transition. There, the closing and reopening of the induced gap are accompanied by the emergence of delocalized MBS, hallmarked by ZBPs at both boundaries of the hybrid nanowire [20]. Here, we demonstrate hard-gap N–S junctions in a magnetic field where only discrete subgap states move to zero energy to form ZBPs at both boundaries and that respond similarly to variations in the chemical potential. While these are critical signatures of MBS, upcoming studies will attempt to correlate the local tunnelling conductance with the evolution of the induced bulk gap via the non-local conductance between the two N terminals [18].

Our approach promotes the development of intriguing nanowire-based quantum devices. The ballistic hard-gap N–S junctions together with the thin Al connections across the substrate represent a vital starting point for realizing a topological qubit. A qubit implementation with a single read-out loop [7] would allow for measuring the projection of the qubit state on one axis of the Bloch sphere. A schematic of the loop qubit is presented in Fig. 4.6a. It is made from a single nanowire with two superconductor–semiconductor segments connected via a superconducting loop that encircles a central shadow-wall pillar. Bottom gates at the centre of the device are used to define a read-out quantum dot in the nanowire with tunable tunnel couplings to the MBS denoted as γ_2 and γ_3 in the schematic. Parity read-out will be performed by measuring the quantum capacitance via radio-frequency gate reflectometry [6, 7, 59]. In Fig. 4.6b, we present an exemplary real-

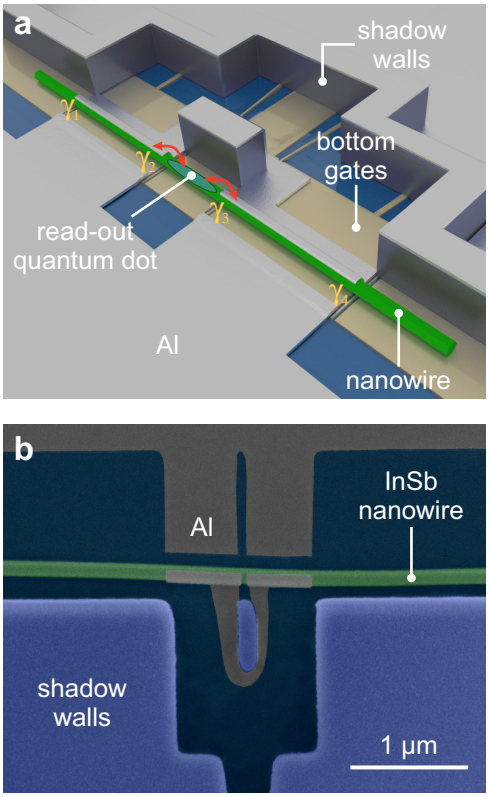

Figure 4.6: **Illustration of the proposed Majorana loop qubit. a** Schematic of a single-nanowire loop-qubit device. The presumable locations of the MBS at the boundaries of the two hybrid segments are denoted by γ_i, where $i \in \{1,2,3,4\}$. The electron parity is fixed due to the finite charging energy of the loop qubit. This configuration offers the desired ground-state degeneracy for a single qubit and can provide information on decoherence and quasiparticle poisoning. **b** False-colour SEM image of an InSb nanowire following the shadow-wall deposition. Two segments of the nanowire are covered with a superconducting 3-facet Al shell. These hybrid segments are interconnected via an Al loop running across the substrate.

ization of the basic elements of such a device via the shadow-wall technique. It comprises a superconducting loop to provide a connection for the exchange of Cooper pairs that acts as a blocker for quasiparticle transport between the two hybridized nanowire segments. The shadow-wall technique is ideally suited to realize these superconducting interconnects across the substrate for multi-terminal devices without the need for post-interface fabrication.

4.4 Methods

4.4.1 Nanowire growth

The InSb nanowires are grown on InSb (111)B substrates covered with a pre-patterned SiN_x mask via metalorganic vapour-phase epitaxy (MOVPE). These nanowires are not grown on top of InP stems but nucleate instead directly on the growth substrate at Au catalyst

droplets [30]. The investigated nanowires have an average diameter of 100 nm, which is controlled by the Au droplet size and the growth mask openings, and a typical length in the order of 10 µm.

4.4.2 Device fabrication

Bottom gates are fabricated on Si/SiO_2 substrates via dry-etching of W thin films, which are subsequently covered by Al_2O_3 gate dielectric via atomic layer deposition (ALD). Shadow walls of ~ 600 nm height are created via reactive-ion etching of thick layers of Si_3N_4 formed via plasma-enhanced chemical vapour deposition (PECVD). Using a micromanipulator, individual nanowires are placed deterministically next to the shadow walls. The native oxide of the nanowires is removed via atomic hydrogen radical cleaning (see Supplementary Note 1). The Al thin films are deposited by evaporation under a shallow angle that forms continuous contacts between the nanowires and the substrate and creates segments on the chip that are electrically isolated from one another. This allows to immediately cool down the devices without the need for additional post-interface fabrication steps. We have not observed a decreased stability or performance of devices that were made with an extra fabrication step to create N contacts. We attribute this to the fact that the hybrid segments are not directly exposed and resist baking is avoided during the fabrication of the contacts.

4.4.3 TEM analysis

The cross-sectional lamellae for TEM are prepared using the focused ion beam technique with a Helios G4 UX FIB/SEM from Thermo Fisher Scientific after capping the devices with a protective layer of sputtered SiN_x. TEM analysis is carried out at an acceleration voltage of 200 kV with a Talos electron microscope from Thermo Fisher Scientific equipped with a Super-X EDX detector.

4.4.4 Transport measurements

Electrical transport measurements are carried out in dilution refrigerators equipped with 3-axes vector magnets. The base temperature is approximately 15 mK, corresponding to an electron temperature of about 30 mK measured with a metallic N–S tunnel junction thermometer. The sample space is evacuated by a turbomolecular pump for at least one day prior to the cool-down to remove surface adsorbates that limit the device performance. Conductance measurements are performed using a standard low-frequency lock-in technique. For voltage-bias measurements, the excitation voltage is $V_{AC} \leq 20\,\mu V$ at a lock-in frequency of at least 20 Hz. For all two-terminal conductance measurements we only subtract setup-related series resistances without making any assumptions about additional contact resistances of the metal–semiconductor interface. Current-driven measurements are carried out in a four-point configuration. After taking the data, we became aware of the relatively low bandwidth of the employed current-to-voltage amplifiers. Hence, we recalibrated the lock-in data via a mapping according to the measured DC conductance that does not suffer from any bandwidth limitations and is insensitive to the reactive response of the circuit (Supplementary Note 4).

4.4.5 Superconducting gap extraction

The BCS–Dynes term is given by a smeared BCS density of states with the broadening parameter Γ [60]:

$$\frac{dI_{SD}}{dV_{SD}}(V_{SD}) = G_N \mathrm{Re}\left[\frac{eV_{SD} - i\Gamma}{\sqrt{(eV_{SD} - i\Gamma)^2 - \Delta_{ind}^2}}\right].$$

For all of our N–S devices, the fit of the BCS–Dynes term yields typical broadening parameters of less than 10 μeV. The model by Blonder, Tinkham, and Klapwijk (BTK) incorporates the transition between BCS tunnelling and Andreev reflection in the open channel regime [21]. Fits of the BCS–Dynes term and of the BTK model to the N–S junction data (including the data in Fig. 4.4b) are presented in Supplementary Note 4. The subgap conductance for a ballistic N–S junction with a single subband, where the transport is dominated by Andreev processes, has been described by Beenakker [22]. At a large enough chemical potential [61], it is given by

$$G_S = \frac{4e^2}{h}\frac{T^2}{(2-T)^2} = 2\frac{G_N^2}{(2G_0 - G_N)^2},$$

where the transmission probability, T, has been substituted with the normal-state conductance, G_N, in units of $2e^2/h$. This function is plotted together with the measured data in Fig. 4.4e.

Data availability

The data that support the plots within this paper and other findings of this study are available at `https://doi.org/10.5281/zenodo.5034524`.

4.5 Supplementary information

4.5.1 Fabrication Details

Chips without Bottom Gates

Chips that contain devices with a global back-gate like the ones presented in Figs. 4.2 and 4.3 of the main text are fabricated on p^+-doped Si wafers covered with 285 nm of thermal SiO_2. The first fabrication step consists of patterning the bond pads via electron-beam lithography (EBL), W sputtering and lift-off in acetone. Afterwards, plasma-enhanced chemical vapour deposition (PECVD) of 600 nm of Si_3N_4 is performed followed by EBL, reactive-ion etching (RIE) with CHF_3/O_2 gases, resist lift-off and an oxygen plasma descum step to remove carbon residues. Eventually, nanowires are deposited under an optical microscope using a micromanipulator equipped with tungsten needles [62].

Chips with Bottom Gates

Chips with additional local bottom gates (used e.g. for the experiments in Figs. 4.4 and 4.5 of the main text) are fabricated by sputtering 17 nm of W on Si wafers covered with 285 nm of thermal SiO_x (protected by an Al_2O_3 etch-stop layer), followed by EBL patterning and

RIE of the W layer with SF_6 gas. Next, 18 nm of a high-quality Al_2O_3 layer are deposited by atomic layer deposition (ALD), acting as the bottom-gate dielectric. Shadow walls on top of the bottom gates are created by first depositing 600 nm of Si_3N_4 by PECVD, followed by EBL patterning with precise alignment of the shadow walls with respect to the underlying fine bottom gates. Then, RIE with CHF_3/O_2 gases is used to selectively etch Si_3N_4 while the Al_2O_3 gate dielectric acts as an etch-stop layer. Finally, after the resist strip, an oxygen plasma descum step is used to remove carbon residues from the chips. The nanowires are then mechanically transferred on top of the bottom gates under an optical microscope using a micromanipulator equipped with tungsten needles [62].

Additional Fabrication Steps for N–S Devices

For devices with additional Ti/Au normal-metal contacts, such as the ones presented in Figs. 4.4 and 4.5 of the main text, an extra post-interface fabrication step is included. It consists of EBL patterning (solvents are removed from the resist via vacuum pumping instead of conventional resist baking to accommodate the low thermal budget), 40 s of argon ion milling at $1.5 \cdot 10^{-3}$ mbar with a commercial Kaufmann source in the load lock of an electron-beam evaporator, and in-situ evaporation of 10 nm/120 nm of Ti/Au at a pressure of $8 \cdot 10^{-8}$ mbar followed by lift-off in acetone. Note that this step is not strictly essential and could have been omitted. Bottom gates underneath the nanowire can open up the channels and tune the conductance. Combining this electrostatic gate control with additional Al contacts that are defined by shadow walls microns away from the N–S junction allows to entirely avoid post-interface fabrication for these devices.

Semiconductor Surface Treatment

To obtain a pristine, oxide-free semiconductor surface, we accomplish a gentle oxygen removal via atomic hydrogen radical cleaning. For this purpose, a custom-made H radical generator is installed in the load lock of our aluminium electron-gun evaporator. It consists of a gas inlet for H_2 molecules connected to a mass-flow controller and a tungsten filament at a temperature of about 1700 °C that dissociates a fraction of the molecules into hydrogen radicals [63].

The cleaning process is evaluated via the transport characteristics of InSb/Al nanowire Josephson junctions and TEM analysis of the same devices. In particular, we consider the magnitude of the supercurrents and the amount of interfacial oxide, measured by EDX, as critical indicators of the interface transparency. During optimization, we vary the process duration and the hydrogen flow, and keep the substrate temperature constant at 550 K. It has been demonstrated in the literature that this temperature results in an efficient cleaning of InSb, allowing for indium- and antimony-based oxides to be removed with similar efficiency [64, 65].

The optimal removal of the native oxide is achieved for a process duration of 30 mins and a hydrogen flow of 2 mln/min. During atomic hydrogen cleaning, the H_2 pressure is $6.3 \cdot 10^{-5}$ mbar. This recipe, which is used for all the devices shown in this paper, results in a constant EDX count of oxygen at the interface (i.e. the traces do not show oxygen peaks, see Fig. 4.2d of the main text) and yields the highest supercurrents in the Josephson junction devices (~ 90 nA).

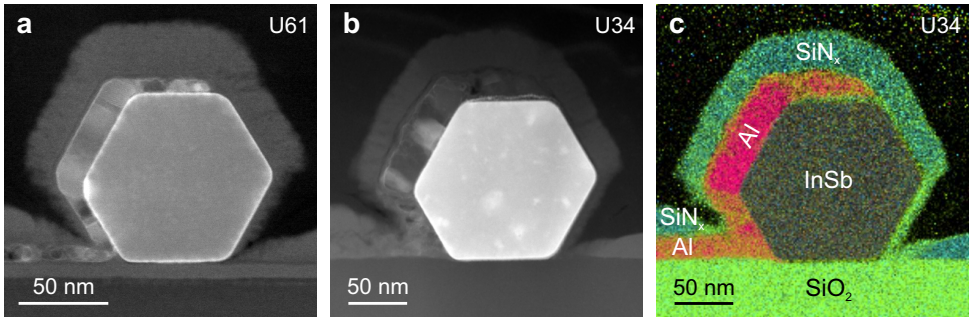

Figure 4.7: Cross-sectional TEM images of InSb nanowires covered by a thin layer of Al. SiN_x was sputter-coated as a protective layer before focused ion beam (FIB) lamella preparation. **a** Annular dark-field (ADF) scanning TEM image of a nanowire cross-section. This sample is identical to the device presented in Figs. 4.2c–e of the main text (sample ID: U61). Al is deposited at an angle of 30° with respect to the substrate plane at T = 140 K. **b** ADF scanning TEM image of another nanowire cross-section (sample ID: U34). Here, 30 nm of Al are deposited at an angle of 25° with respect to the substrate plane at T = 80 K. **c** EDX elemental composite image of the device in panel (**b**) identifying the individual compounds and the Al thin film.

4

Superconductor Deposition

After cleaning the semiconductor surface, the chips are loaded into the main chamber of the evaporator and cooled down by actively circulating liquid nitrogen through the sample holder. After one hour of thermalization, aluminium is deposited by electron-beam evaporation at a typical rate of 0.2 nm/min.

The aluminium growth conditions are optimized by studying the quality of thin films deposited on Si substrates – typically also containing transferred InSb nanowires – at different evaporation rates, temperatures and angles. It is observed that evaporation angles close to 90° with respect to the substrate plane are favourable for aluminium thin-film growth, whereas at shallower angles the self-shadowing effect of Al atoms on the surface becomes more prominent, giving rise to columnar growth, possible voids in the film, and greater roughness [66, 67]. To minimize this angle-dependent self-shadowing effect, the substrate temperature can be slightly increased to give the atoms arriving at the substrate enough momentum to rearrange into a crystal before the next atoms arrive at the substrate. Our results and the work by Dong *et al.* [66] indicate that, for a fixed deposition rate, the temperature optimum depends on the evaporation angle.

In this work, a temperature optimum of around 140 K is found for Al growth at 30° with respect to the substrate plane, allowing for homogeneous 3-facet coverage of the hexagonal nanowires as well as a connection from the nanowires to the substrate. The Josephson junctions made at this growth temperature exhibit roughly four times higher supercurrents than similar devices produced when Al was deposited at a substrate temperature of ~ 80 K. Cross-sectional TEM images of FIB lamellae from nanowires with Al grown at 140 K and 80 K are presented in Supplementary Figure 4.7a (as well as Figs. 4.2c,e of the main text) and Supplementary Figures 4.7b,c, respectively. Comparing these figures, the superior quality of the deposition at 140 K is evident; the nanowire facets are more uniformly covered and form a continuous film, the crystalline quality of the Al is higher and

the oxidation of the Al facets is much less prominent than in the case of the deposition at 80 K (in Supplementary Figure 4.7c, the abundant oxide formation in the aluminium film at the top and bottom-left nanowire facets is especially noticeable).

In addition, Supplementary Figure 4.8 illustrates a comparison between a higher Al growth temperature (160 K) and Al grown at 140 K. The former results in both granular Al covering the middle nanowire facet, which is better observed in the tilt-view image in Supplementary Figure 4.8b, and a film on the substrate where the different grains are clearly distinguishable. In comparison, images corresponding to deposition at 140 K instead show a featureless Al film on the middle facet, where roughness is indiscernible under these SEM conditions (Supplementary Figure 4.8d), and a granular but more uniform Al structure on the substrate.

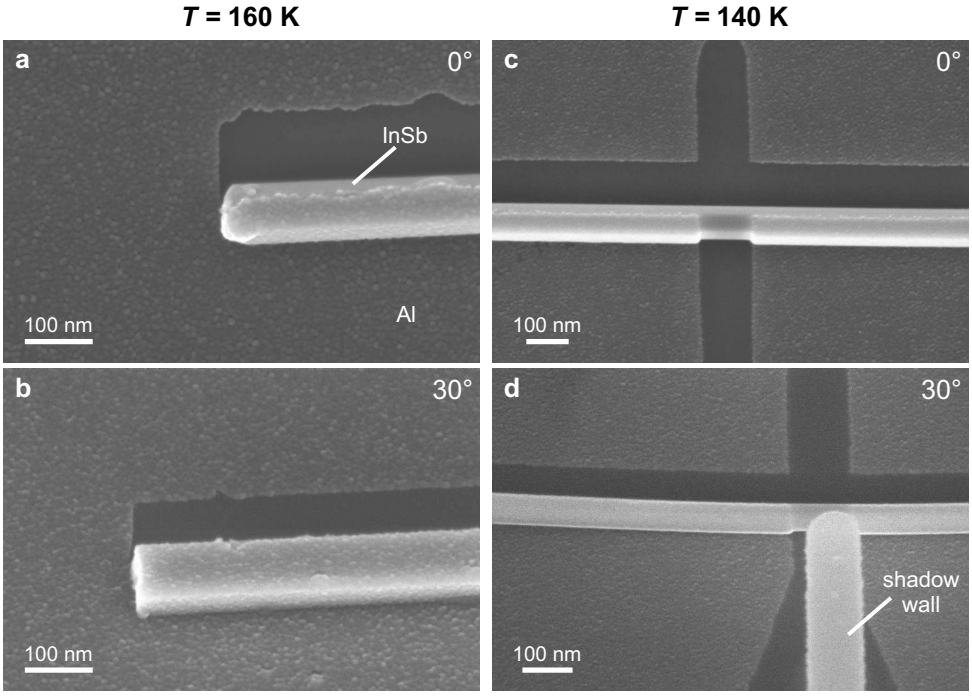

Figure 4.8: SEM images of InSb nanowires with Al thin films deposited at different temperatures. For both samples the evaporation angle is 30° relative to the substrate plane. **a**, **b** Top-view and tilt-view (tilt angle: 30°) SEM images of InSb nanowires covered with an Al thin film deposited at 160 K. The maximum film thickness, which corresponds to the thin film on the middle nanowire facet, is 20 nm. **c**, **d** Top-view and tilt-view (tilt angle: 30°) SEM images of a nanowire Josephson junction. Here, the Al thin film is deposited at 140 K and the film thickness at the middle nanowire facet is 15 nm. Panel (**d**) exhibits a featureless Al shell on the middle wire facet, whereas grains are visible on the middle facet in the case of Al grown at 160 K (panel (**b**)).

Reproducibility and Typical Yield of Shadow-Wall Devices

As shown in Supplementary Figure 4.9, there are 4 unique orientations of a 3-facet Al shell on hexagonal nanowires. This rotational configuration has major implications for the electrostatics of the junctions, for the screening of the gates and it determines whether

the electronic wave functions are pushed away from or towards the superconductor by the gates [39], renormalizing key parameters such as spin–orbit coupling, g factors and possibly gap hardness. To some degree, this random variation can be mitigated by post-selecting certain wire rotations after detailed SEM inspections, but it is very difficult to eliminate. Moreover, this would reduce the device yield by up to 75%. In contrast, the shadow-wall lithography method resolves this issue by removing any random variation in rotational configuration and enforcing the scenario in Supplementary Figure 4.9a.

Another source of random variation inherent in conventional fabrication methods is the design customization required for every device based on SEM images of individual nanowires. Shadow-wall lithography, however, relies on standardized designs and allows for convenient blind fabrication, which eliminates imaging and alignment steps. It offers inherently good alignment between the gates and the edges of the superconductors, resulting in low variability in device dimensions with many nearly identical devices made in a single deposition step.

By design, all nanowires are aligned along the same direction on the chip. This is an important bonus feature of the shadow-wall technique that ensures that the largest possible magnetic field of the vector magnet can be applied along every nanowire axis, which is critical for finding a topological phase transition.

As presented in Supplementary Note 2 for the Josephson junctions as well as in Supplementary Note 4 and Figs. 4.4 and 4.5 of the main text for the N–S devices, the magnitude of the induced gap is consistent across all devices. The atomic hydrogen cleaning yields pristine interfaces with high interface transparency resulting in hard-gap superconductivity on a par with state-of-the-art shadow-deposition methods. By omitting all or in some cases all but one fabrication steps, our approach avoids the ageing of the superconductor–semiconductor interface and yields many nominally identical devices.

Beyond the reduced variations among devices, a qualitatively new feature not offered by other techniques is the significant flexibility in device designs, such as the arbitrary shadow lengths and fundamentally new device geometries (e.g. 3-terminal Majorana devices or SQUIDs, see Supplementary Note 5). Depending on the layout, our pre-patterned chips typically accommodate up to 16 nanowire devices. It is readily viable to have around 10 fully functional devices on a single chip to consistently optimize the fabrication parameters. The yield per chip can be affected by the accidental transfer of multiple wires at once or by nanowires breaking during the transfer. In Supplementary Figures 4.11, 4.12 and 4.13, we show scanning electron micrographs taken prior to the cool-down of the Josephson junctions. On the first chip (sample ID: U12) 13 nanowires are transferred and result in 12 working devices, i.e. where the junctions are well-defined. On the second chip (sample ID: U51) in total 12 nanowires are transferred, which yield 11 working devices. However, 2 turned out to be narrow nano-flakes [68, 69], which can be indistinguishable from nanowires in optical microscopy. On a third chip (sample ID: U55) 12 nanowires are positioned and yield 9 working devices. Among those, 7 are hexagonal-shaped nanowires and 2 turned out to be narrow nano-flakes. In Supplementary Figure 4.10, the reproducibility of the device dimensions within each chip and among two of the chips is illustrated by box plots of the extracted junction lengths.

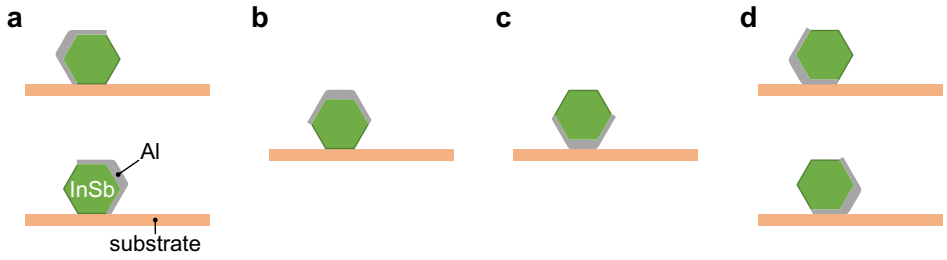

Figure 4.9: The 4 unique orientations of the Al-covered facets on hexagonal nanowires.

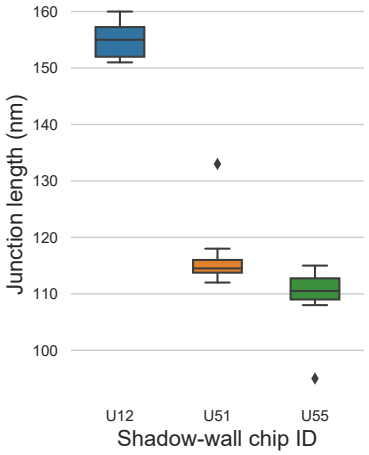

Figure 4.10: Box plots showing the distribution of the Josephson junction length across the devices on chips U12 (Supplementary Figure 4.11), U51 (Supplementary Figure 4.12) and U55 (Supplementary Figure 4.13). The boxes denote the lower and upper quartiles of the distributions, the central horizontal lines denote the medians, and the whiskers show the minimum and maximum values of the junction length. The two diamonds are determined as outliers due to physical damage to the shadow walls. Chips U51 and U55 have been prepared using nominally the same shadow-wall layout and the median junction length differs by only 4 nm. For chip U12 the junction length is larger by design.

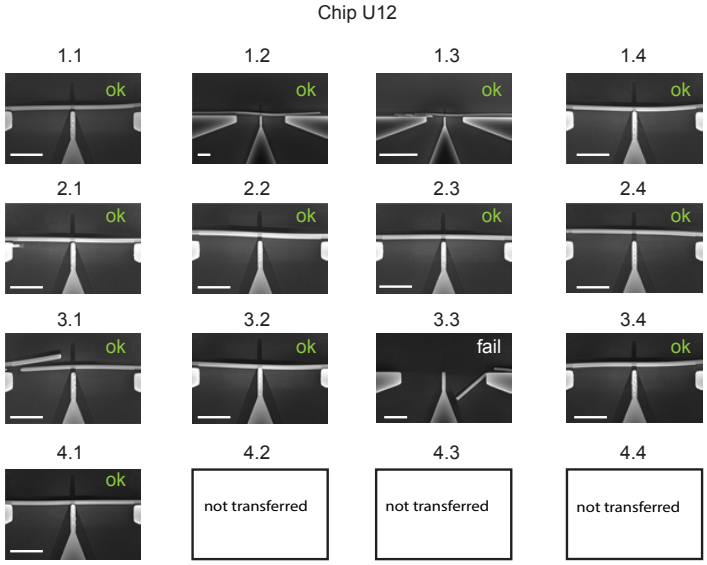

Figure 4.11: Typical yield of the nanowire transfer for Josephson junction devices: Scanning electron micrographs of all Josephson junction devices on a typical chip (sample ID: U12) taken after the Al deposition. Out of 13 nanowire transfer attempts, 12 nanowires are perfectly positioned, and only in one case the transfer failed (device 3.3). The scale bars indicate 1 µm.

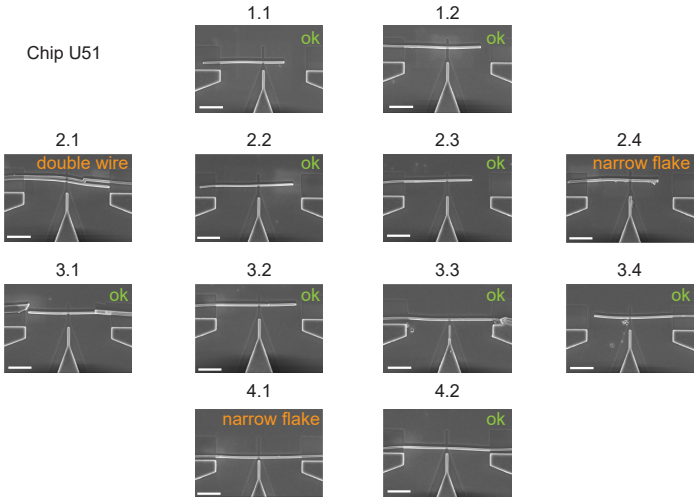

Figure 4.12: Typical yield of the nanowire transfer for Josephson junction devices: Scanning electron micrographs of all Josephson junction devices on a typical chip (sample ID: U51) taken after the Al deposition. Out of 12 nanowire transfer attempts, 9 nanowires are perfectly positioned, 2 narrow flakes – rather than nanowires – are accidentally transferred (devices 2.4 and 4.1), and in one case, two nanowires are transferred in the same location (device 2.1). The scale bars indicate 1 µm.

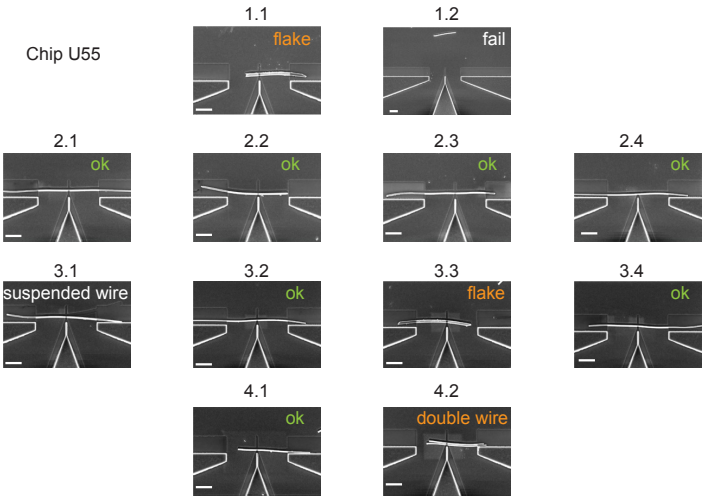

Figure 4.13: Typical yield of the nanowire transfer for Josephson junction devices: Scanning electron micrographs of all Josephson junction devices on a typical chip (sample ID: U55) taken after the Al deposition. Out of 12 nanowire transfer attempts, 7 nanowires are perfectly positioned, 2 of them are not (devices 1.2 and 3.1), 2 narrow flakes – rather than nanowires – are accidentally transferred (devices 1.1 and 3.3), and in one case, two nanowires are transferred in the same location (device 4.2). The scale bars indicate 1 µm.

4.5.2 Additional Transport Measurements of Josephson Junctions

In this section, we summarize the characteristics of the Josephson junction devices listed in Supplementary Table 4.1. All devices are fabricated by evaporating an Al thin film at an angle of 30° with respect to the substrate plane. Device 3 differs from the other samples in the thickness of the Al shell. We note that despite such a low shell thickness, all nanowire devices on sample U59 are in electrical contact with the Al film on the substrate.

Josephson junction	Sample ID/ device name	Evaporation angle	Channel width (nm)	Maximum Al thickness (nm)	Oxidation
device 1	U55/2.3	30°	100	16	in O_2 atmosphere
device 2	U51/1.2	30°	100	16	in O_2 atmosphere
device 3	U59/2.3	30°	100	11	Al_2O_3 capping
device 4	U55/3.3	30°	160	16	in O_2 atmosphere

Table 4.1: Summary of the Josephson junction devices presented in this study. Devices 1, 2, and 3 are all nominally identical in their geometries with a nanowire diameter of 100 nm and a separation between the Al contacts of 115 nm. Device 3 was made with a thinner Al shell thickness and capped in situ with around 20 nm of Al_2O_3. Device 4 is a Josephson junction formed in an InSb nano-flake. Here, the channel width is 160 nm.

Device 1

The current and differential conductance in the normal state (V_{SD} = 10 mV) display a step-like increase as a function of V_{BG} (Supplementary Figures 4.14a,b). The first two steps approximately align with the quantized values expected for one-dimensional transport, providing possible hints for ballistic transport at zero magnetic field. At lower bias voltage, features of the induced superconductivity appear such as the conductance peaks due to multiple Andreev reflections and the zero-bias supercurrent peak (Supplementary Figures 4.14c,d). A line-cut of Supplementary Figure 4.14c is presented in Fig. 4.4b of the main text, whereas a line-cut of Supplementary Figure 4.14d is shown in panel (e). Here, the experimental data (red trace) is fitted with the theoretical model (green trace) to identify the number and the transmissions of the nanowire subbands, which are plotted in Supplementary Figure 4.14f. Similarly, in Supplementary Figure 4.15a, we illustrate the extracted transmission probabilities of the three lowest subbands in the back-gate voltage range of Supplementary Figure 4.14c. The sum of these transmission probabilities extracted from the MAR pattern is compared to the normal-state conductance in Supplementary Figure 4.15b.

Device 2

The normal-state current and conductance (V_{SD} = 10 mV) as a function of back-gate voltage are displayed in Supplementary Figures 4.16a,b. While conductance plateaus are more difficult to identify than in the case of device 1, the presence of an induced superconducting gap is clear from the MAR conductance peaks and the supercurrent peak (Supplementary Figures 4.16c,d). By fitting each line-cut of panel (c) (just like in panel (d)), we can extract the transmissions of the nanowire subbands across the full measurement range (Supplementary Figure 4.16e). The closing of the superconducting gap and the suppression of the switching current with the magnetic field aligned along three perpendicular orientations are shown in Supplementary Figure 4.17 and Supplementary Figure 4.18, respectively.

Device 3
Device 3 differs from the first two samples by having a significantly thinner Al shell. To protect the thin film from oxidation, the device is capped in situ with a 20 nm Al_2O_3 layer. This results in a large zero-field switching current of more than 50 nA (Supplementary Figure 4.19) and a critical magnetic field of ~ 2 T (Supplementary Figure 4.20).

Device 4
In this nano-flake device, the normal-state current manifests sharp steps and the differential conductance features quantized plateaus owing to ballistic transport in the junction (Supplementary Figures 4.21a,b). The presence of a moderate supercurrent (Supplementary Figure 4.21c) demonstrates that our fabrication technique can be used not only to proximitize one-dimensional nanowires, but also other types of nanostructures such as quasi-two-dimensional nano-flakes.

Voltage-biased conductance measurements in the tunnelling regime for 7 Josephson junctions (including devices 1–3) are depicted in Supplementary Figure 4.22. The average induced gap extracted for these devices is $\Delta_{ind} = 248 \pm 10\,\mu eV$. It is slightly higher than in the more transmissive regime at more positive gate voltages since the global back gate to some degree also tunes the coupling to the superconductor, in agreement with the literature [12].

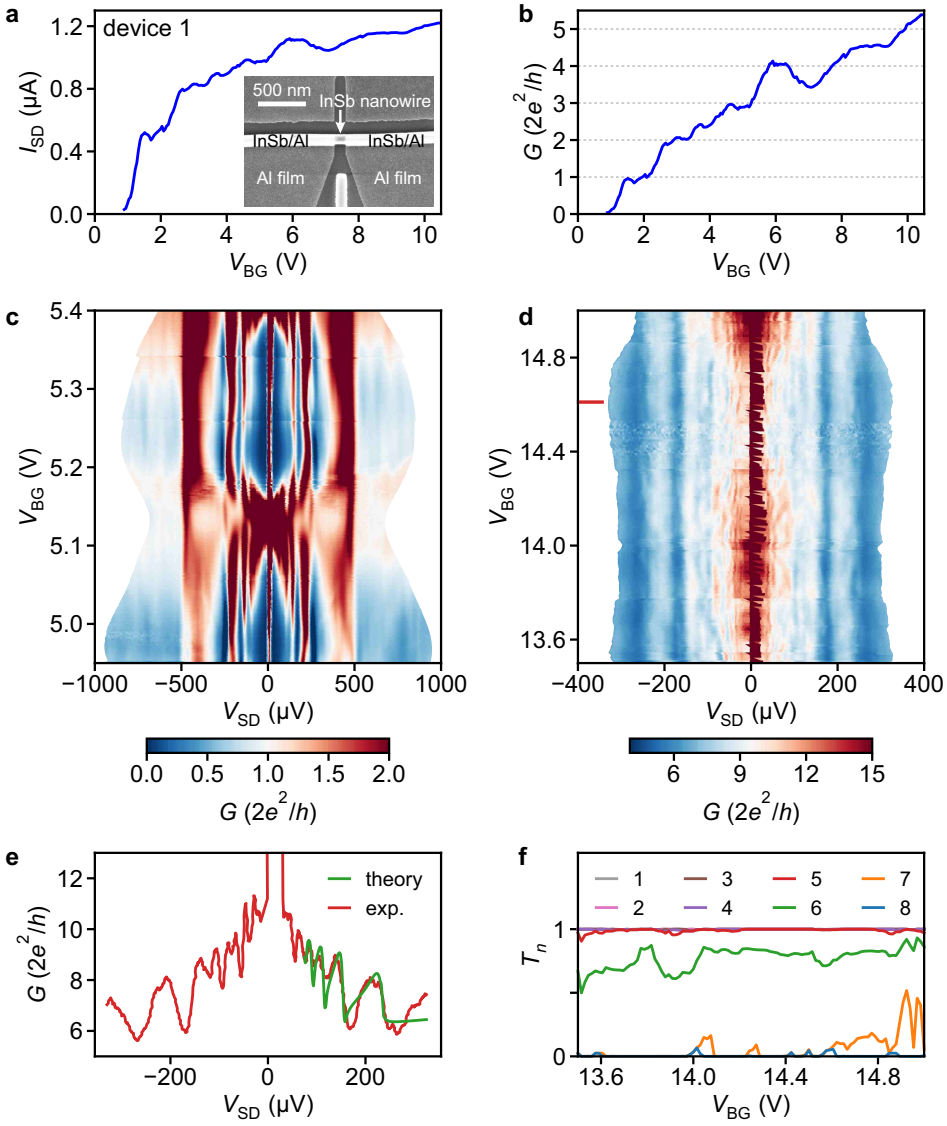

Figure 4.14: Additional transport measurements of the first Josephson junction device. **a** I_{SD} vs. V_{BG} sweep at V_{SD} = 10 mV, showing the field-effect tunability of the junction. Inset: scanning electron micrograph of the device. **b** DC conductance, G, after subtracting the series resistance of the setup, as a function of V_{BG} at 10 mV bias voltage. **c**, **d** G vs. V_{SD} and V_{BG} in the few-subbands and many-subbands regime, respectively: vertical features in both scans at constant bias voltages are the characteristic peaks originating from MARs. **e** Line-cut of (**d**) at V_{BG} = 14.61 V in red and best fit of the trace in green according to the coherent scattering model in Supplementary Note 3. **f** Extracted transmission probabilities, T_n, as a function of V_{BG} in the multi-subbands regime, with $n \in \{1, 2, \ldots, 8\}$. In this back-gate voltage range, the transmission of the first five subbands is already saturated at $T_n = 1$.

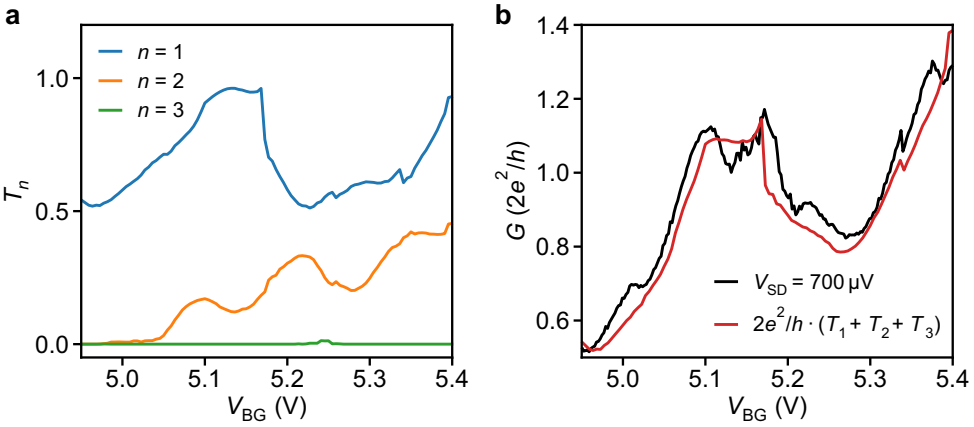

Figure 4.15: Tunability of the subbands of the first Josephson junction device. **a** Transmission probabilities, T_n, of the first three subbands as a function of V_{BG}. The parameters are extracted by fitting the conductance map of Supplementary Figure 4.14c with the coherent scattering model described in Supplementary Note 3. **b** Out-of-gap conductance as a function of V_{BG} in black (i.e. vertical line-cut of Supplementary Figure 4.14c at $V_{SD} = 700\,\mu V$) together with the sum of the transmission probabilities in red.

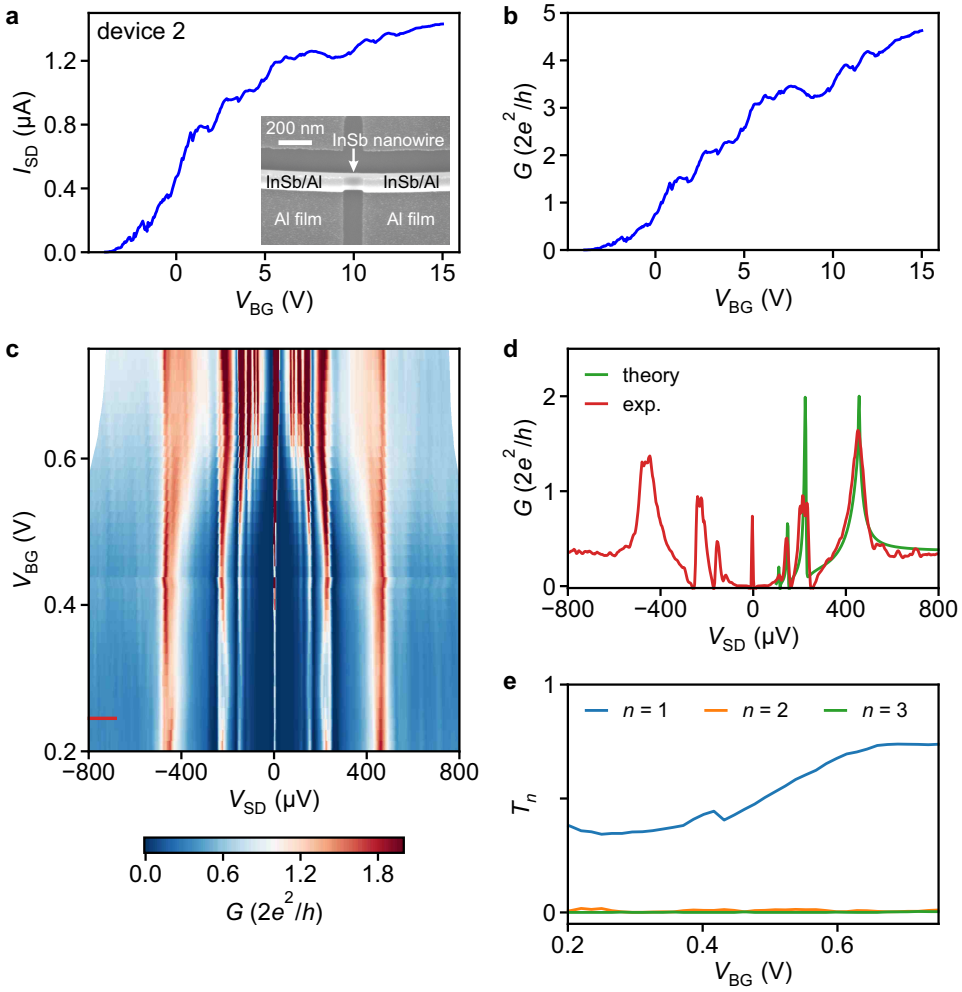

Figure 4.16: Additional transport measurements of the second Josephson junction device. **a** I_{SD} vs. V_{BG} sweep at V_{SD} = 10 mV, showing the field-effect tunability of the junction. Inset: scanning electron micrograph of the device. **b** DC conductance, G, after subtracting the series resistance of the setup, as a function of V_{BG} at 10 mV bias voltage. **c** G vs. V_{SD} and V_{BG} in the weak-tunnelling regime: subharmonic gap features correspond to different orders of MARs. **d** Line-cut of (**c**) at V_{BG} = 0.25 V in red and best fit of the trace in green according to the coherent scattering model in Supplementary Note 3. **e** Extracted transmission probabilities, T_n, depicted as a function of V_{BG} with $n \in \{1, 2, 3\}$.

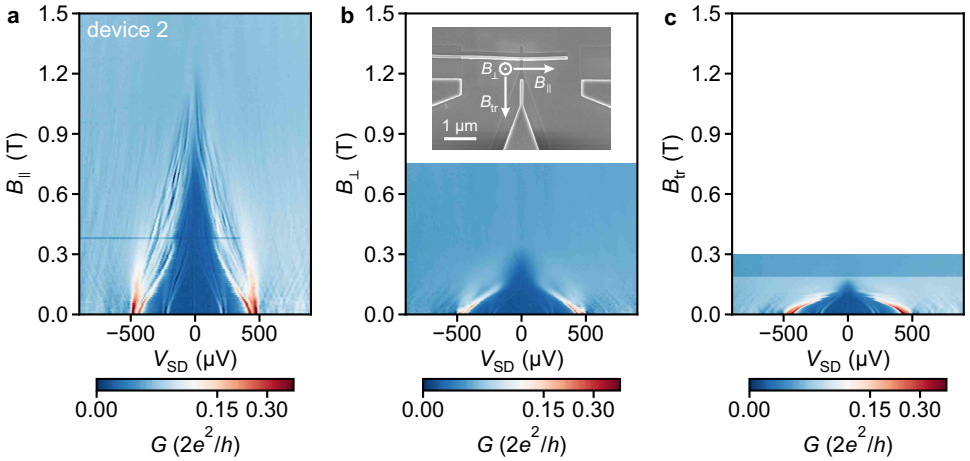

Figure 4.17: Superconducting critical magnetic fields of the second Josephson junction device. Colour maps of G vs. V_{SD} and magnetic field taken at V_{BG} = 1.45 V for different magnetic field orientations: in **a** the field $B_{\parallel}$ is oriented parallel to the nanowire direction, in **b** $B_{\perp}$ is orthogonal to the plane of the substrate, and in **c** the transversal field B_{tr} is orthogonal to the nanowire direction but in the substrate plane. The inset in panel (**b**) shows a scanning electron micrograph of the device together with the different magnetic field directions.

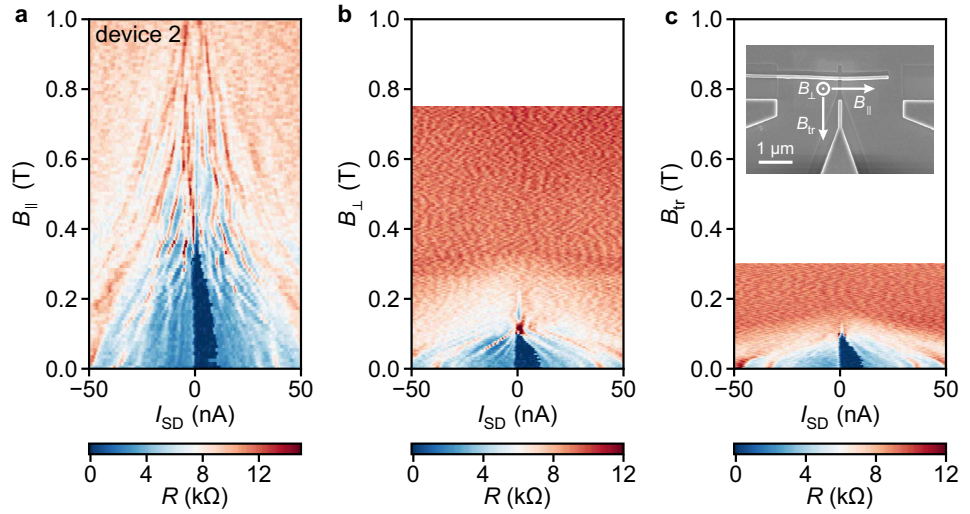

Figure 4.18: Switching current of the second Josephson junction device in the open-channel regime (V_{BG} = 5.7 V). Differential resistance, R, as a function of I_{SD} and magnetic field in three different orientations: **a** Magnetic field, $B_{\parallel}$, aligned parallel to the nanowire, **b** magnetic field, $B_{\perp}$, oriented out-of-plane, and **c** transversal in-plane magnetic field, B_{tr}. The vectors in the inset of panel (**c**) illustrate the three field orientations.

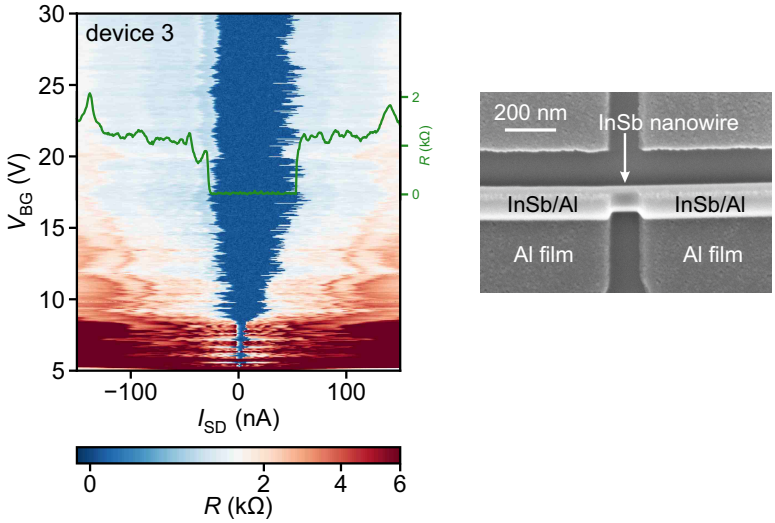

Figure 4.19: Back-gate dependence of the switching current of the third Josephson junction device. Colour map of R as a function of I_{SD} and V_{BG}; the green trace is taken at V_{BG} = 13.82 V. The switching current (in dark blue) is suppressed in the low back-gate voltage regime. The inset on the right shows a scanning electron micrograph of the device. The Al segments are capped with a protective layer of Al_2O_3 evaporated at an angle of 30°.

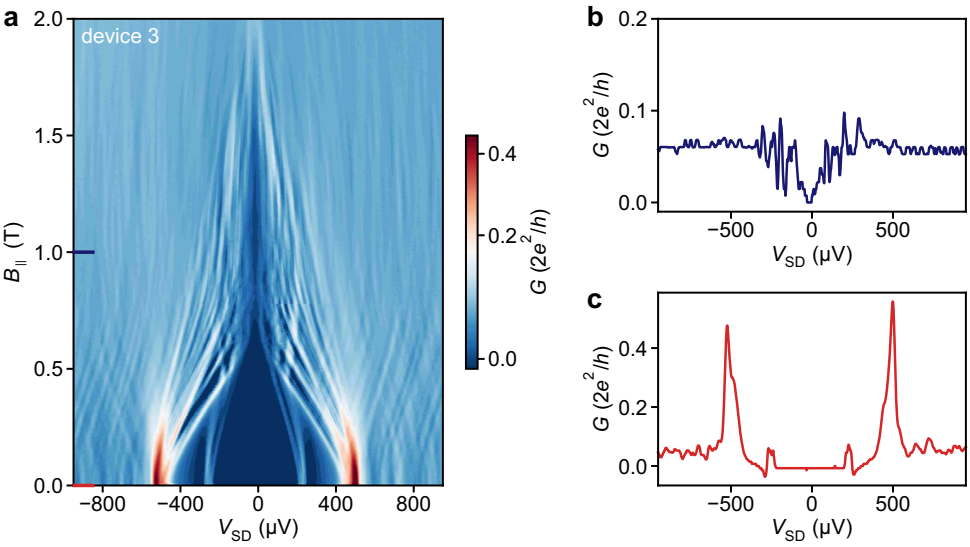

Figure 4.20: Transport measurements of the third Josephson junction device. **a** V_{SD} vs. $B_{\parallel}$ in the tunnelling regime. Owing to the thinner Al shell, the superconducting critical field is $B_c \sim 2$ T, much larger than for the previous two junctions. The tunnelling conductance peaks at $\pm 2\Delta_{ind}$ split into a manifold of resonances at a finite magnetic field due to the different g factors of the discrete quasiparticle states at the gap edge. **b**, **c** Line-cuts of (**a**) at the positions indicated by the two lines.

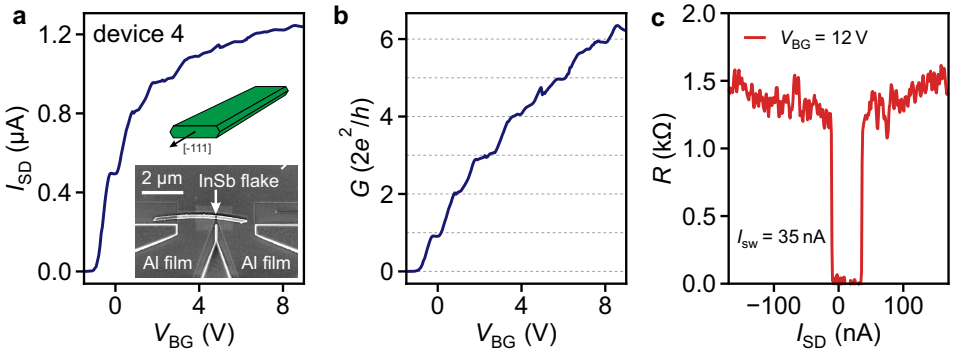

Figure 4.21: Ballistic transport and supercurrent in an InSb flake Josephson junction (device 4) at zero magnetic field. **a** I_{SD} vs. V_{BG} at V_{SD} = 10 mV. Bottom inset: scanning electron micrograph of the nano-flake Josephson junction. Top inset: schematic of the cross-section of the nano-flake [69]. **b** G vs. V_{BG} at V_{SD} = 10 mV. The conductance displays distinct plateaus at multiples of $2e^2/h$, indicating the stepwise population of the one-dimensional subbands in the nanowire. **c** R vs. I_{SD} at V_{BG} = 12 V. The device exhibits a switching current of ~ 35 nA in the open-channel regime.

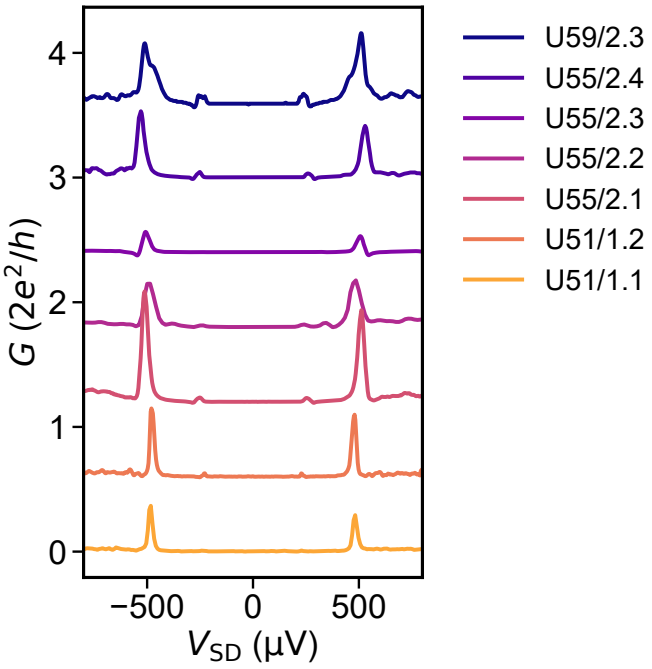

Figure 4.22: Voltage-biased induced gap measurements on 7 different Josephson junction devices in the tunnelling regime (cf. Supplementary Table 4.1). Neighbouring traces are offset in conductance by $0.6 \cdot 2e^2/h$ for clarity. The average nanowire diameter of these Josephson junctions is 99 ± 5 nm. The average induced gap for these devices of $\Delta_{ind} = 248 \pm 10$ μeV is extracted from the best fits of these traces according to the coherent scattering model in Supplementary Note 3 and it corresponds to the conductance peaks where the coherence peaks on both sides of the junctions are aligned.

4.5.3 Modelling of Andreev Transport

Modelling of the Conductance of a Biased Josephson Junction and the Fitting Procedure

We calculate the conductance of a voltage-biased Josephson junction following the approach of ref. [70]. In the model, we account for the electrons and holes propagating through the normal region of the junction with the transparency T. The quasiparticles are accelerated by the voltage V_{SD} applied to the structure and are Andreev reflected at the superconducting leads with the induced superconducting gap Δ_{ind}. The sequential Andreev reflections imprint the conductance with the subgap features appearing at $V_{SD} = 2\Delta_{ind}/Ne$, where N is integer – see Supplementary Figure 4.23.

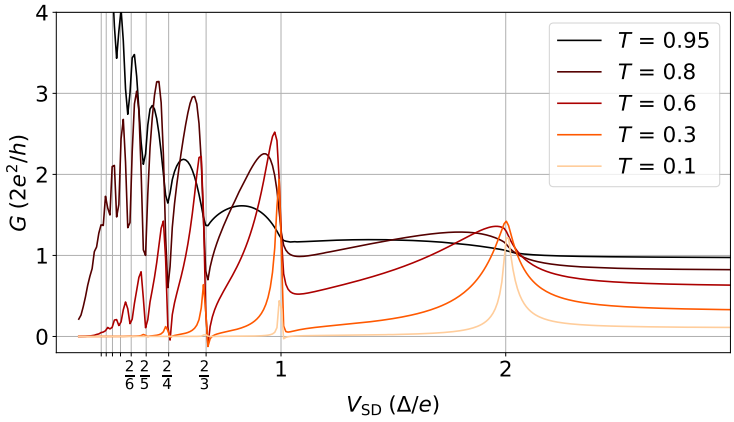

Figure 4.23: Conductance, G, of a single-mode Josephson junction versus bias voltage, V_{SD}, for five transparencies (T) of the normal region.

For the analysis of the experimental conductance traces, we estimate the total conductance $G_{theory}(V_{SD})$ of a multimode nanowire Josephson junction as a sum of M single-mode contributions resulting from the presence of M modes of the transverse quantization [71]:

$$G_{theory}(V_{SD}) = \sum_{i=1}^{M} G_i\left(V_{SD}, T_i, \Delta_{ind}\right), \tag{4.1}$$

where T_i is the transmission probability for the i-th mode. We obtain T_i and Δ_{ind} (induced in the nanowire by the presence of the Al shell) by fitting the numerically calculated conductance to the experimental one by minimizing $\chi = \int[G_{exp}(V_{SD}) - G_{theory}(V_{SD})]^2 dV_{SD}$. M is a free parameter of the fitting procedure and it is chosen as the smallest number for which at least one of the parameters T_i is zero.

Theory for Multiple Andreev Reflections in the Presence of Subgap States
The original theory developed in ref. [70] assumes a bulk superconducting density of states in the leads. To account for different properties of the two leads, especially the presence of subgap states in one of the contacts, we extend this theory as follows.

We consider a Josephson junction consisting of two superconducting electrodes connected through a normal scattering region. We assume that the first contact is kept at zero voltage, while the second one is biased at V_{SD}. In the normal region, adjacent to the L-th lead, the quasiparticle wave function takes the form,

$$\Psi_L = \sum_n \left[\begin{pmatrix} A_n^L \\ B_n^L \end{pmatrix} e^{ikx} + \begin{pmatrix} C_n^L \\ D_n^L \end{pmatrix} e^{-ikx} \right] e^{-i[E+neV_{\mathrm{SD}}]t/\hbar}, \tag{4.2}$$

where A_n^L, C_n^L (B_n^L, D_n^L) correspond to the electron (hole) amplitudes, the time dependence stems from the voltage applied to the leads and x points in the direction opposite to the scattering region. We describe the scattering properties of the normal region by the scattering matrix:

$$S_0 = \begin{pmatrix} r & t \\ t & -r \end{pmatrix}, \tag{4.3}$$

which sets the transmission probability through the scattering region with the transmission amplitude $t = \sqrt{T}$ and the reflection amplitude $r = \sqrt{1-T}$. We rely on the short-junction approximation and use the energy-independent S_0 to setup the matching conditions for the wave functions Ψ_L. The electron and hole coefficients are related by:

$$\begin{pmatrix} A_n^1 \\ A_{n+1}^2 \end{pmatrix} = S_0 \begin{pmatrix} C_n^1 \\ C_{n+1}^2 \end{pmatrix}, \tag{4.4}$$

and

$$\begin{pmatrix} D_n^1 \\ D_{n-1}^2 \end{pmatrix} = S_0^* \begin{pmatrix} B_n^1 \\ B_{n-1}^2 \end{pmatrix}, \tag{4.5}$$

respectively. The shifts of the indexes correspond to the changes of quasiparticle energies due to the bias voltage. At each superconductor–normal-conductor interface we take into account the Andreev reflection:

$$\begin{pmatrix} C_n^L \\ B_n^L \end{pmatrix} = \begin{pmatrix} a_n & 0 \\ 0 & a_n \end{pmatrix} \begin{pmatrix} D_n^L \\ A_n^L \end{pmatrix}, \tag{4.6}$$

with the amplitude $a_n \equiv a(E + neV_{\mathrm{SD}})$, where,

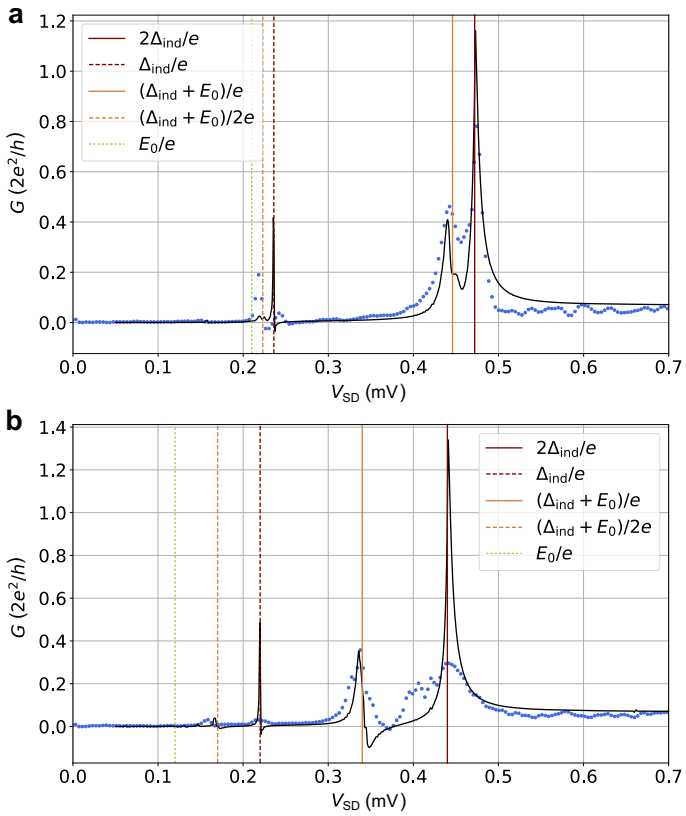

Figure 4.24: Experimental (blue dots) and theoretical (black curves) conductance traces of a Josephson junction with a subgap state in one of the superconducting leads. **a** is for $B_\parallel = 0$ and **b** is for $B_\parallel = 0.2\,\mathrm{T}$.

$$a(E) = \frac{1-\delta_{L,1}\Gamma(E)}{\Delta_{\mathrm{ind}}} \begin{cases} E - \mathrm{sgn}(E)\sqrt{E^2-\Delta_{\mathrm{ind}}^2} & |E| > \Delta_{\mathrm{ind}} \\ E - i\sqrt{\Delta_{\mathrm{ind}}^2 - E^2} & |E| \le \Delta_{\mathrm{ind}}. \end{cases} \tag{4.7}$$

The Andreev reflection amplitude is modified by the factor $[1-\delta_{L,1}\Gamma(E)]$ where,

$$\Gamma(E) = \frac{\gamma^2}{(E \pm E_0)^2 + \gamma^2}, \tag{4.8}$$

is the Lorentzian distribution that accounts for absorption of the quasiparticles in the subgap states (with the energy $\pm E_0$) in the first lead. We set $\gamma = 4\,\mu\mathrm{eV}$.

The electronic excitations in the normal part of the junction originate from the quasiparticles incoming from the nearby superconducting contacts. We therefore write down equation (4.6) including the quasiparticle source terms [72]:

$$\begin{aligned}\begin{pmatrix} C_n^L \\ B_n^L \end{pmatrix} = &\begin{pmatrix} a_n & 0 \\ 0 & a_n \end{pmatrix}\begin{pmatrix} D_n^L \\ A_n^L \end{pmatrix} \\ &+\begin{pmatrix} J(E+eV_L) \\ 0 \end{pmatrix}\frac{1}{\sqrt{2}}\delta_{p,e}\delta_{s,L}\kappa_L^+ \\ &+\begin{pmatrix} 0 \\ J(E-eV_L) \end{pmatrix}\frac{1}{\sqrt{2}}\delta_{p,h}\delta_{s,L}\kappa_L^-,\end{aligned} \tag{4.9}$$

with $J(E) = \sqrt{[1-a(E)^2]F_D(E)}$, where $F_D(E, T = 30\,\text{mK})$ is the Fermi distribution. In equation (4.9) p sets the injected quasiparticle type, s determines the lead in which we consider the source term, $\kappa_1^\pm = \delta_{n,0}$, $\kappa_2^\pm = \delta_{n,\pm1}$ keep track of the quasiparticle energy shifts due to the bias, and where $V_1 = 0$ and $V_2 = V_{\text{SD}}$. We calculate the current I^L in the L-th lead as:

$$I^L = \sum_{\imath=-I_{\text{max}}}^{I_{\text{max}}} I_\imath^L e^{\imath V_{\text{SD}} e i t/\hbar}, \tag{4.10}$$

with the Fourier components,

$$I_\imath^L = \frac{e}{\hbar\pi}\sum_{s=1,2}\sum_{p=e,h}\int_{-\infty}^{\infty} dE \sum_{n=-N_{\text{max}}}^{N_{\text{max}}} (\mathbf{U}_{\imath+n}^{L*}\mathbf{U}_n^L - \mathbf{V}_{\imath+n}^{L*}\mathbf{V}_n^L). \tag{4.11}$$

$\mathbf{U}_n^L = \left(A_n^L, B_n^L\right)^T$ and $\mathbf{V}_n^L = \left(C_n^L, D_n^L\right)^T$ are vectors that consist of the electron and hole amplitudes. The DC current is obtained for $\imath = 0$ and subsequently used to calculate the conductance, $G = dI^L/dV_{\text{SD}}$. To efficiently sample the non-uniform conductance trace we use the Adaptive package [73].

In Supplementary Figure 4.24, we show the calculated MAR conductance traces (black curves) together with two cross-sections (blue dots) from the experimental map in Fig. 4.3c of the main text. We focus here on two cases: $B_\parallel = 0$ and $B_\parallel = 0.2\,\text{T}$ with the parameters used for the calculations given in the first and second row of Supplementary Table 4.2, respectively. The calculated traces agree qualitatively well with the data: they capture the peak positions and the overall line shape. In particular, we observe two ordinary MAR peaks at $V_{\text{SD}} = 2\Delta_{\text{ind}}/Ne$ with $N = 1, 2$ and two peaks induced by the presence of the subgap state at $V_{\text{SD}} = (\Delta_{\text{ind}} + E_0)/Ne$ with $N = 1, 2$. The increase of the magnetic field significantly alters the energy of the subgap state causing a further splitting between the MAR and the subgap-induced peaks.

To better understand the transport features in Fig. 4.3c of the main text, we simulate the conductance assuming a single subgap state whose energy evolves linearly in the magnetic field as $E_0 = \pm(E_{B_\parallel=0} - \frac{1}{2}g\mu_B B_\parallel)$, where g = 18 and $E_{B_\parallel=0} = 210\,\mu\text{eV}$. The result is shown in Supplementary Figure 4.25a, where we have assumed a junction transmission of $T_1 = 0.065$ and a magnetic field dependence of the gap given by $\Delta_{\text{ind}} = \Delta_0(1 - B_\parallel^2/B_c^2)$ [74, 75] with B_c

$B_{\parallel}$ (T)	Δ_{ind} (μeV)	T_1	E_0 (μeV)
0	236	0.065	210
0.2	220	0.065	120

Table 4.2: Parameters used for the calculation of the conductance traces in Supplementary Figure 4.24.

= 1.1 T and Δ_0 = 236 μeV. In Supplementary Figures 4.25b–d, we illustrate the quasiparticle transport processes for different magnetic fields. The conductance peaks at $V_{\mathrm{SD}} = \pm 2\Delta_{\mathrm{ind}}/e$ correspond to an energy difference of $2\Delta_{\mathrm{ind}}$ as denoted by the red arrows. If the electron transfer involves a subgap state at energy E_0 on one side of the junction, the corresponding bias voltage is $V_{\mathrm{SD}} = \left(\Delta_{\mathrm{ind}} + E_0\right)/e$ (Supplementary Figure 4.25d). As the magnetic field is increased, the subgap state moves to lower energies. Once the state is at zero energy ($E_0 = 0$), electrons only require an energy of $eV_{\mathrm{SD}} = \Delta_{\mathrm{ind}}$ (Supplementary Figure 4.25c). In Fig. 4.3c of the main text, this occurs around $B_{\parallel} = 0.4$ T. As the subgap state crosses zero energy, electrons again require an energy of $eV_{\mathrm{SD}} = \Delta_{\mathrm{ind}} + E_0$ to cross the junction via this state (Supplementary Figure 4.25b). If the junction is more transmissive, as is the case for Fig. 4.3c of the main text, also a MAR process occurs, identified by the conductance peak that emerges at $V_{\mathrm{SD}} \sim 0.24$ mV at zero field and is associated with an energy Δ_{ind}. In addition, when the subgap state moves to lower energies due to the Zeeman effect,

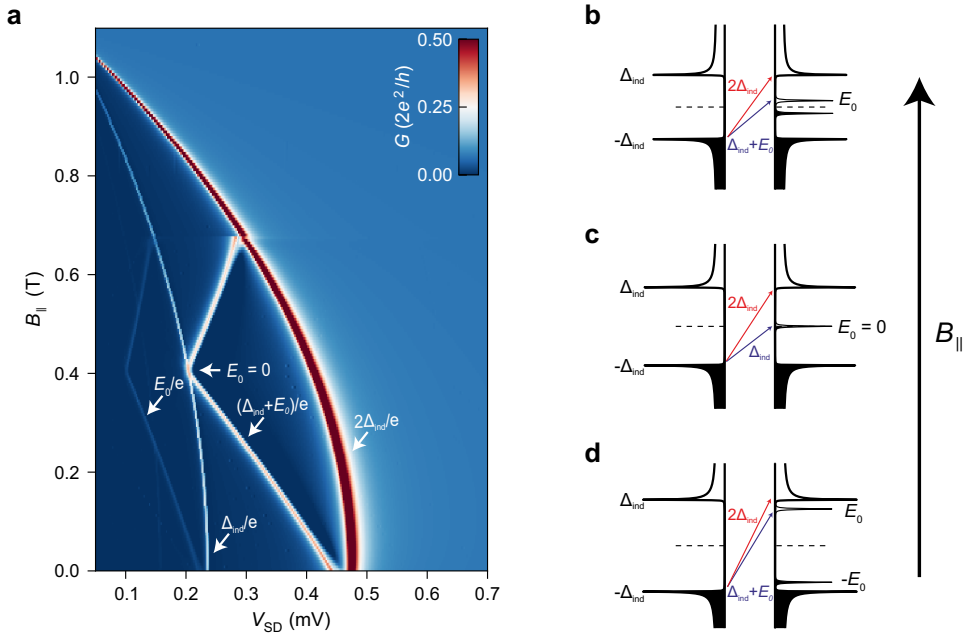

Figure 4.25: Multiple Andreev reflections in the presence of a subgap state. **a** Calculated conductance in the presence of a subgap state at energy E_0. Both quantities Δ_{ind} and E_0 vary with magnetic field. **b**–**d** Schematics of the first-order multiple Andreev reflection processes for different magnetic fields increasing from the bottom to the top panel. The superconducting gap is varied accordingly.

it also allows for a MAR process to occur, which results in a splitting of the MAR peak. With increasing magnetic field, the superconducting gap on both sides of the junction shrinks, resulting in the scenario shown in Supplementary Figure 4.25a, where the subgap state moves as a function of $B_{\parallel}$ from $V_{\mathrm{SD}} = 2\Delta_{\mathrm{ind}}/e$ down to Δ_{ind}/e and back up to $2\Delta_{\mathrm{ind}}/e$. Considering that multiple subgap states can peel off from the gap edge with different associated g factors, a rich and complex pattern can occur. This interpretation of the involved transport processes is supported by the numerical simulation.

4.5.4 Additional Transport Measurements in Normal Metal/Superconductor Junctions

Calibrating the AC conductance

The AC conductance is measured using a standard low-frequency lock-in technique. Some of the employed current-to-voltage amplifiers have been found to suffer from a relatively low bandwidth. This required a recalibration of the measured differential conductance of the N–S devices. The approach shown here is similar to a calibration procedure developed by Jouri Bommer, Guanzhong Wang and Michiel de Moor (see also guidelines on lock-in measurements by the same authors:
`http://homepage.tudelft.nl/q40r9/lockin-meas-guide-v20200603.pdf`).

Supplementary Figure 4.26 shows the raw conductance data from Fig. 4.4 of the main text prior to the subtraction of any series resistance. For the mapping of the lock-in conductance, G_{LI}, to the numerical DC conductance, G_{num}, the data is binned into a two-dimensional histogram (resolution $0.003 \cdot 2e^2/h$). Since the numerical conductance suffers from noise, we determine the centre of the distribution for each bin of G_{LI} by fitting a Gaussian distribution to the histogram of G_{num} (see right panel of Supplementary Figure 4.26). Data points that are more than 5 standard deviations from the centre of the distributions are discarded as outliers. Here, the mapping yields the parametrization $G_{\mathrm{num}} = -0.016 \cdot G_{\mathrm{LI}}^2 + 0.995 \cdot G_{\mathrm{LI}}$.

Supplementary Figure 4.27 shows the calibration for the left junction of the correlation device in Fig. 4.5e of the main text. In Supplementary Figure 4.28, the calibration is presented for the right junction of the correlation device in Fig. 4.5f of the main text. This is the only N–S junction device that was measured at a relatively large lock-in frequency ($f = 72\,\mathrm{Hz}$). The right panels of Supplementary Figure 4.27 and Supplementary Figures 4.28a–c show exemplary fits of the histograms using a Gaussian. The red traces represent the fitting by the least-squares method using the polynomial regression function $G_{\mathrm{num}} = A \cdot G_{\mathrm{LI}}^2 + B \cdot G_{\mathrm{LI}} + C$. The mapping in Supplementary Figure 4.27 yields the parametrization $G_{\mathrm{num}} = -0.108 \cdot G_{\mathrm{LI}}^2 + 1.043 \cdot G_{\mathrm{LI}} - 0.003$. In Supplementary Figure 4.28, the weighted average of the fitting functions yields the mapping function $G_{\mathrm{num}} = 0.023 \cdot G_{\mathrm{LI}}^2 + 1.034 \cdot G_{\mathrm{LI}} - 0.040$, where the residuals of the individual measurements provide the weights. Supplementary Figure 4.28d summarizes the parabolic (A) and linear (B) fit parameters from Supplementary Figures 4.28a–c. The black data point indicates the weighted average of the fit parameters.

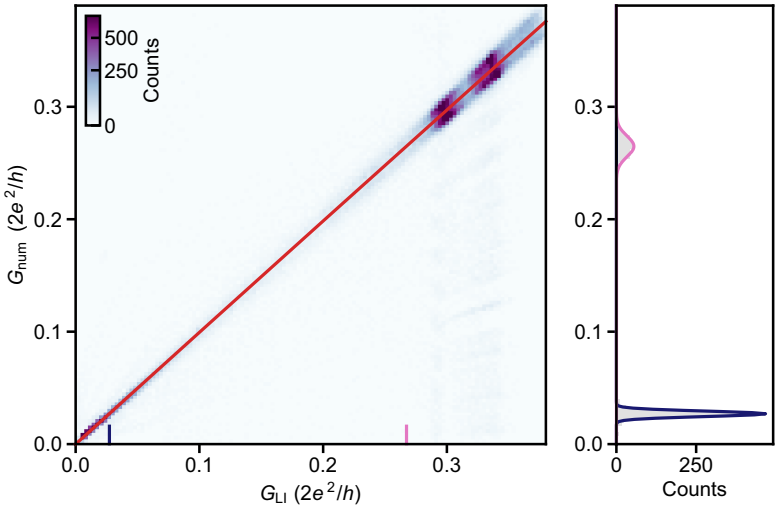

Figure 4.26: Calibration function extracted from the conductance data of the N–S junction presented in Fig. 4.4 of the main text. Numerical differential conductance, G_{num}, vs. AC differential conductance, G_{LI}. Here, the lock-in frequency is $f = 23\,\text{Hz}$.

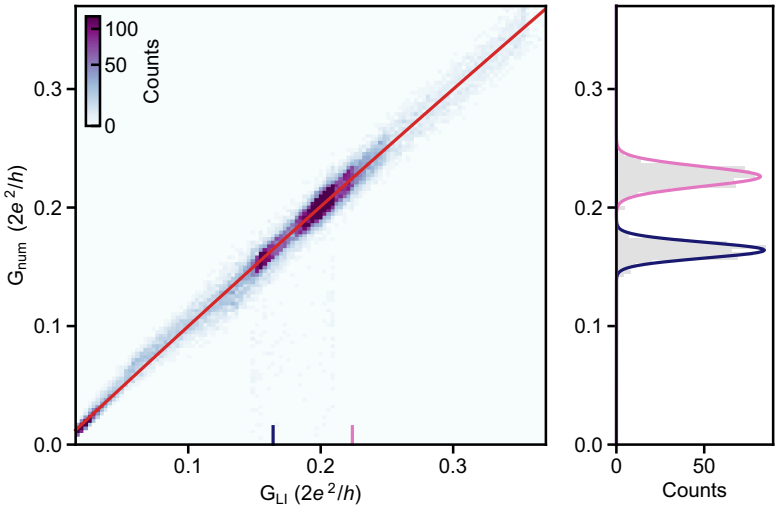

Figure 4.27: Calibration function extracted from the conductance data of the N–S junction presented in Fig. 4.5e of the main text. Numerical differential conductance, G_{num}, vs. AC differential conductance, G_{LI}. Here, the lock-in frequency is $f = 23\,\text{Hz}$.

List of N–S Devices

The specifications of the N–S junction devices studied in this work are listed in Supplementary Table 4.3. All devices are fabricated by evaporating an Al thin film at 30° with respect to the substrate plane.

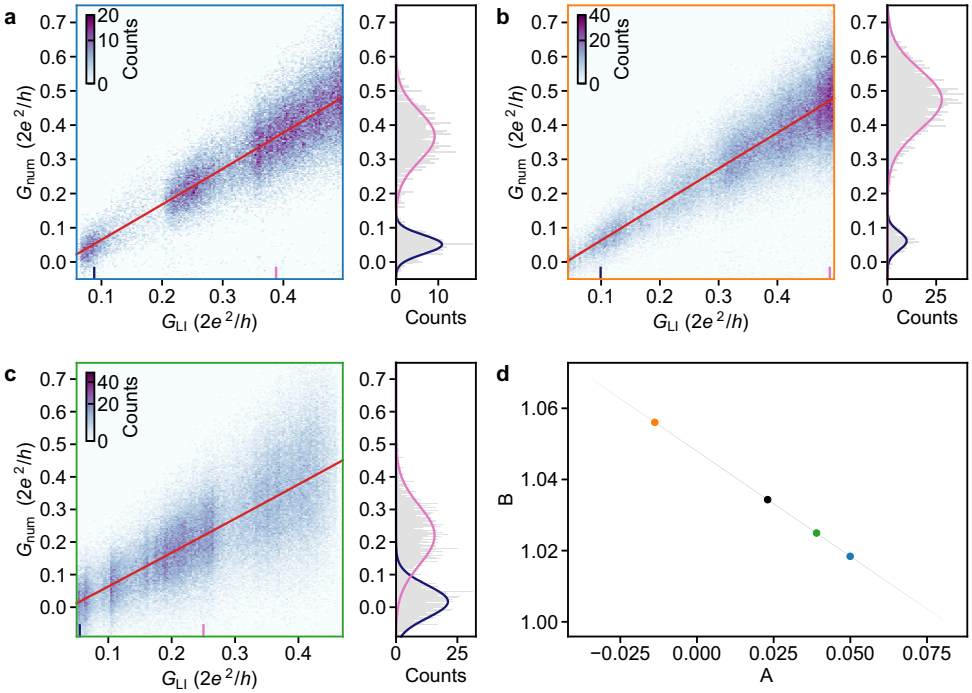

Figure 4.28: Calibration functions extracted for the N–S junction presented in Fig. 4.5f of the main text. **a**–**c** Numerical differential conductance, G_{num}, vs. AC differential conductance, G_{LI}. Each of the three panels is from separate data set. Here, the lock-in frequency is $f = 72\,\text{Hz}$. **d** Summary of the parabolic (A) and linear (B) fit parameters in panels (**a**–**c**). The colors of the data points correspond to the axis colors of the respective panels. The black data point denotes the weighted average fit parameters, where the weights are determined by the residuals of the individual fits. The grey area designates the 95% confidence interval.

N–S device	Sample ID/ device name	Evaporation angle	Nanowire diameter (nm)	Maximum Al thickness (nm)	Oxidation
device 1	U53/1.3	30°	100	16	in O_2 atmosphere
device 2	U53/1.1	30°	100	16	in O_2 atmosphere
device 3	U48/2.3	30°	105	16	in O_2 atmosphere
device 4	U53/1.2, left	30°	80	16	in O_2 atmosphere
device 5	U53/1.2, right				

Table 4.3: Summary of the N–S devices presented in this study. Device 1 is the sample presented in Fig. 4.4 of the main text. Devices 4 and 5 correspond to the left and right N–S junctions, respectively, of the sample presented in Fig. 4.5 of the main text.

N–S Junction Spectroscopy

Deep in the tunnelling regime, the subgap conductance is strongly suppressed. As illustrated in Supplementary Figure 4.29, the ratio of the above-gap conductance and the subgap conductance is approximately a factor of 100. In Supplementary Figures 4.29a,b, the differential conductance line-cut for N–S device 1 (i.e. the same device as in Fig. 4.4 of the main text) is fitted using the BCS–Dynes term (red) and the BTK model (green). The data

in Supplementary Figures 4.29c,d shows a line-cut for another N–S junction (device 2), which is not presented in the main text. The fitting parameters of the BTK model are the induced gap, Δ_{ind}, the normal-state conductance, G_{N}, and the temperature, T. For device 1 it yields an induced gap of $\Delta_{\text{ind}} = 231\,\mu\text{eV}$ and for device 2 the extracted gap is $\Delta_{\text{ind}} = 241\,\mu\text{eV}$. In the BTK model the only effective broadening parameter is the temperature, which for both devices yields $T \approx 0.1\,\text{K}$. The two N–S junctions presented in Fig. 4.5 of the main text (devices 4 and 5) also exhibit comparable values of the induced gap of $\Delta_{\text{ind}} \sim 230$–$240\mu\text{eV}$.

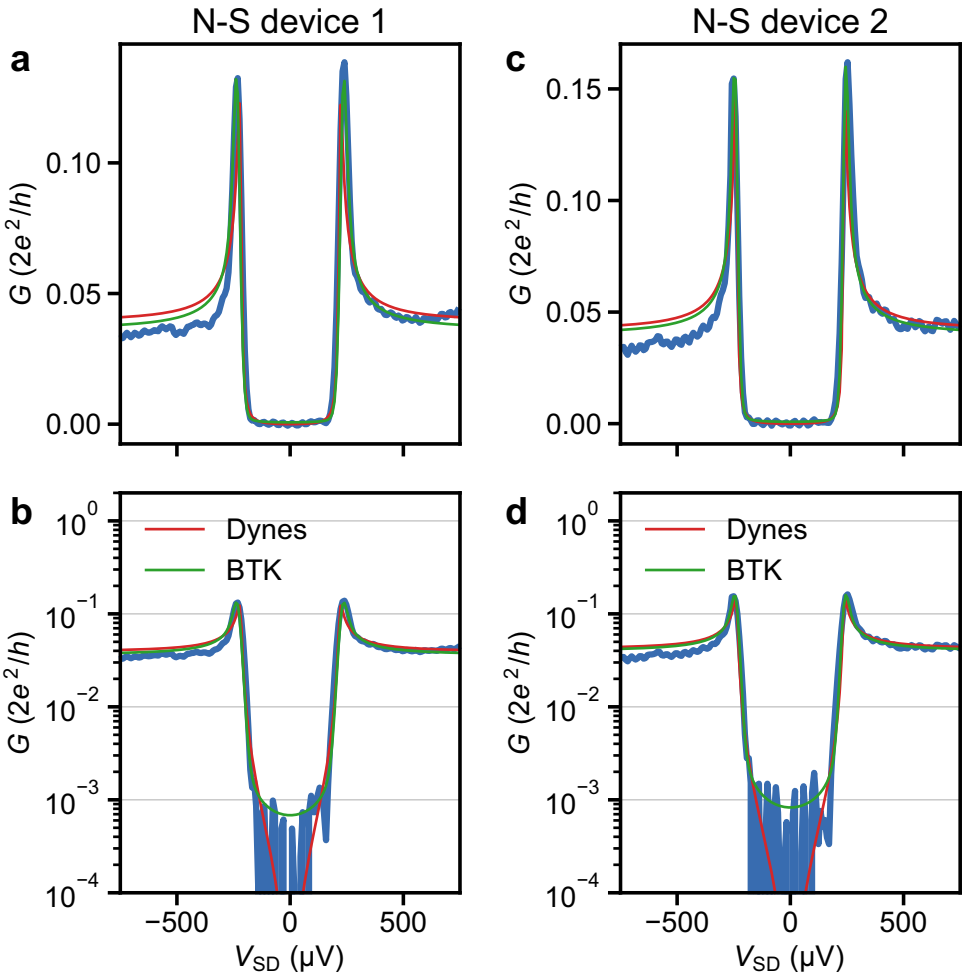

Figure 4.29: **a**, **b** Differential conductance vs. source–drain voltage line-cut for N–S device 1 (same as in Fig. 4.4 of the main text) on a linear scale in (**a**) and on a logarithmic scale in (**b**). Here, the tunnel-gate voltage is $V_{\text{TG}} = 0.530\,\text{V}$ and the super-gate voltage is $V_{\text{SG}} = 0\,\text{V}$. **c**, **d** Differential conductance vs. source–drain voltage line-cut for N–S device 2 (not presented in the main text) on a linear scale in (**c**) and on a logarithmic scale in (**d**). Here, the tunnel-gate voltage is $V_{\text{TG}} = 2.004\,\text{V}$ and the super-gate voltage is $V_{\text{SG}} = 7.0\,\text{V}$. The fit of the BCS–Dynes term and of the BTK model are shown in red and green, respectively.

Temperature Dependence of the Induced Gap

In Supplementary Figure 4.30, we present the temperature dependence for another device (N–S device 3), which is not presented in the main text. In the limit $k_B T \ll \Delta_{ind}$, the subgap conductance, G_S, scales with temperature, T, as [36]

$$G_S(V_{SD} = 0) = G_N \sqrt{\frac{2\pi\Delta_{ind}}{k_B T}} e^{-\Delta_{ind}/k_B T}, \tag{4.12}$$

where G_N is the normal-state conductance and k_B is the Boltzmann constant. The purple trace in Supplementary Figure 4.30a measured at $T = 18\,\text{mK}$ is well described by the BTK model with an induced gap of $\Delta_{ind} = 237\,\mu\text{eV}$. This is very similar to the magnitude of the induced gap of the other two N–S devices shown in Supplementary Figure 4.29, albeit those junctions are formed in a separate Al deposition step on another substrate. The theoretical model in equation (4.12) can describe the smearing of the density of states with temperature. It yields a fit parameter of $\Delta_{ind} \approx 210\,\mu\text{eV}$, which is a bit smaller than the gap directly extracted from the tunnelling spectroscopy.

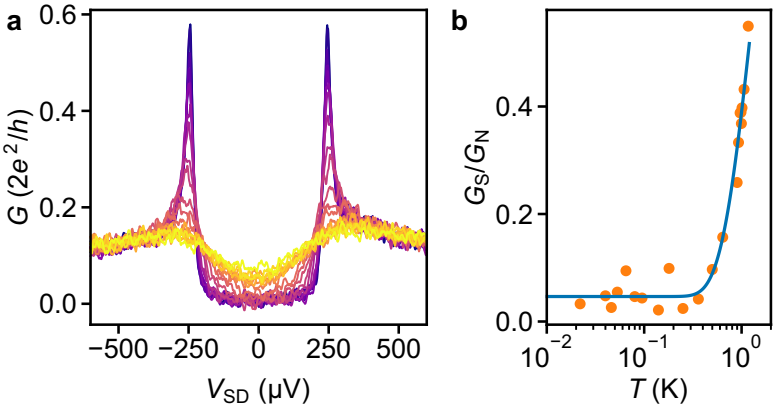

Figure 4.30: Temperature dependence of the induced gap (N–S device 3). **a** Tunnelling conductance vs. source–drain voltage between $T = 18\,\text{mK}$ (purple) and $T = 1.17\,\text{K}$ (yellow). **b** Subgap conductance averaged between $V_{SD} = \pm 30\,\mu\text{V}$ (G_S) divided by the normal-state conductance (G_N) as a function of T. The blue trace is a fit to equation (4.12).

Hard Induced Gap

In Supplementary Figure 4.31, we report the fit of the BTK model to the data shown in Fig. 4.4b of the main text (N–S device 1). The extracted induced superconducting gap is $\Delta_{ind} \sim 230\,\mu\text{eV}$.

Zero-Bias Peaks in the N–S Device

In Supplementary Figure 4.32, we present additional data for the first N–S device (cf. Fig. 4.4 of the main text) in a parallel magnetic field for two different super-gate voltages. In the main text, we present ballistic transport and pronounced Andreev enhancement for the same N–S device. Here, we show the evolution of discrete subgap states as a function

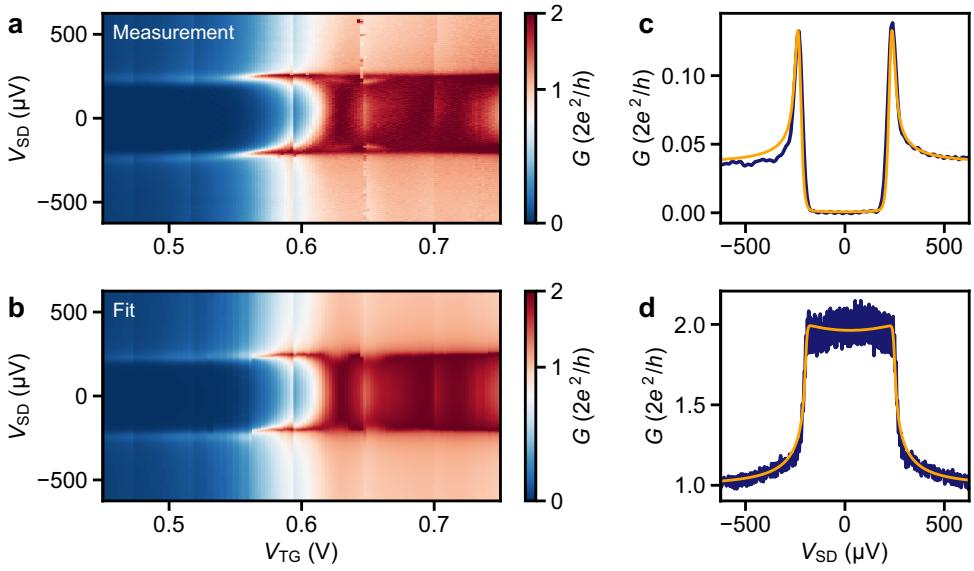

Figure 4.31: N–S junction voltage-bias spectroscopy and the corresponding fit of the BTK model [21] for N–S device 1. **a** Differential conductance, G, as a function of source–drain voltage, V_{SD}, and bottom tunnel-gate voltage, V_{TG}, from Fig. 4.4b of the main text. **b** Fit of the BTK model to the data set in panel (**a**). The fit parameters include the induced gap, the temperature, and the barrier strength Z, wich is given by the transmission $(1+Z^2)^{-1}$. **c**, **d** Line-cut of the data in panel (**a**) (dark blue) at $V_{TG} = 0.53\,\mathrm{V}$ and at $V_{TG} = 0.69\,\mathrm{V}$, respectively. The orange traces show the corresponding fits to the BTK model.

of magnetic field and the formation of ZBPs, which in some cases can reach a conductance close to $2e^2/h$.

Zero-Bias Peaks and Super-Gate Dependence

Additional N–S spectroscopy measurements of the left N–S junction of the device presented in Fig. 4.5 of the main text are shown in Supplementary Figure 4.33. Here, the voltage at the super gate – the bottom gate controlling the electrochemical potential in the hybrid nanowire segment – is larger ($V_{SG} = 0.525\,\mathrm{V}$ vs. $0\,\mathrm{V}$). The differential conductance vs. V_{SD} and $B_\parallel$ is depicted in Supplementary Figure 4.33a, the bias-voltage line-cut in Supplementary Figure 4.33b illustrates the pronounced zero-bias conductance peak at large magnetic fields. However, the magnitude of the ZBP conductance depends on the tuning of the tunnel-gate and super-gate voltages (cf. Supplementary Figure 4.33c).

In Supplementary Figure 4.34 additional data from the high-field regime are presented (here $B_\parallel = 0.85 - 1.15\,\mathrm{T}$). For the same bottom-gate settings as in Supplementary Figure 4.33 we observe ZBPs that emerge concurrently at both boundaries of the superconductor–semiconductor nanowire segment (cf. Supplementary Figures 4.34a,b). By fixing the magnetic field at $B_\parallel = 1.0\,\mathrm{T}$ we can observe the evolution of the ZBPs at the left and right N–S junctions as a function of the voltage on the super gate underneath the hybrid nanowire segment (see Supplementary Figures 4.34c,d). The asymmetry in the conductance of Supplementary Figure 4.34d with respect to bias polarity is presumably related to energy-

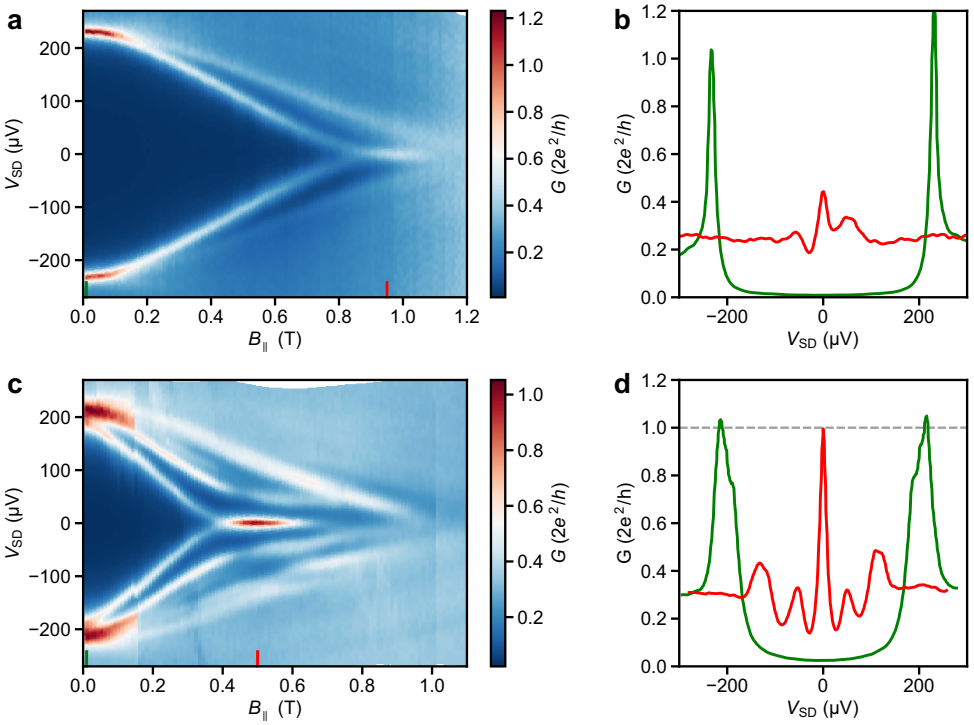

Figure 4.32: Magnetic-field-dependent voltage-bias spectroscopy for N–S device 1 from Fig. 4.4 of the main text, demonstrating the formation of zero-bias peaks in the differential conductance. **a** G as a function of V_{SD} and $B_{\parallel}$. The super-gate voltage is $V_{SG} = 7.5\,V$ and the tunnel-gate voltage is $V_{TG} = 0.5\,V$. **b** Line-cuts from panel (**a**) at the positions indicated by the two lines. **c** G as a function of V_{SD} and $B_{\parallel}$. Here, $V_{SG} = 2.97\,V$ and $V_{TG} = 0.417\,V$. **d** Line-cuts from panel (**c**) at the positions indicated by the two lines.

dependent tunnel barrier transmission at the right N–S junction. The concurrent evolution of the ZBPs at both N–S boundaries of the correlation device as a function of the super-gate voltage is also depicted in Supplementary Figure 4.35 for same tunnel-gate settings as in Fig. 4.5 of the main text.

4.5.5 Realization of Advanced Hybrid Devices

In this section, we present another example of more advanced nanowire devices that can be realized using the shadow-wall technique. In the main text, we have introduced the necessary ingredients to realize the basic implementation of a topological qubit using the shadow-wall technique. In Supplementary Figure 4.36, we show another application of the shadow-wall concept, which is intended as an experimental implementation of a theoretical proposal by Schrade and Fu [76]. It represents a superconducting quantum interference device (SQUID) formed by two InSb nanowires (green) placed deterministically in close vicinity of shadow walls (blue). Previous realizations of nanowire SQUIDs relied on electron-beam lithography and standard lift-off technique [77]. Here, top gates (yellow) are fabricated to form a single Josephson junction (JJ) on the left side of the device

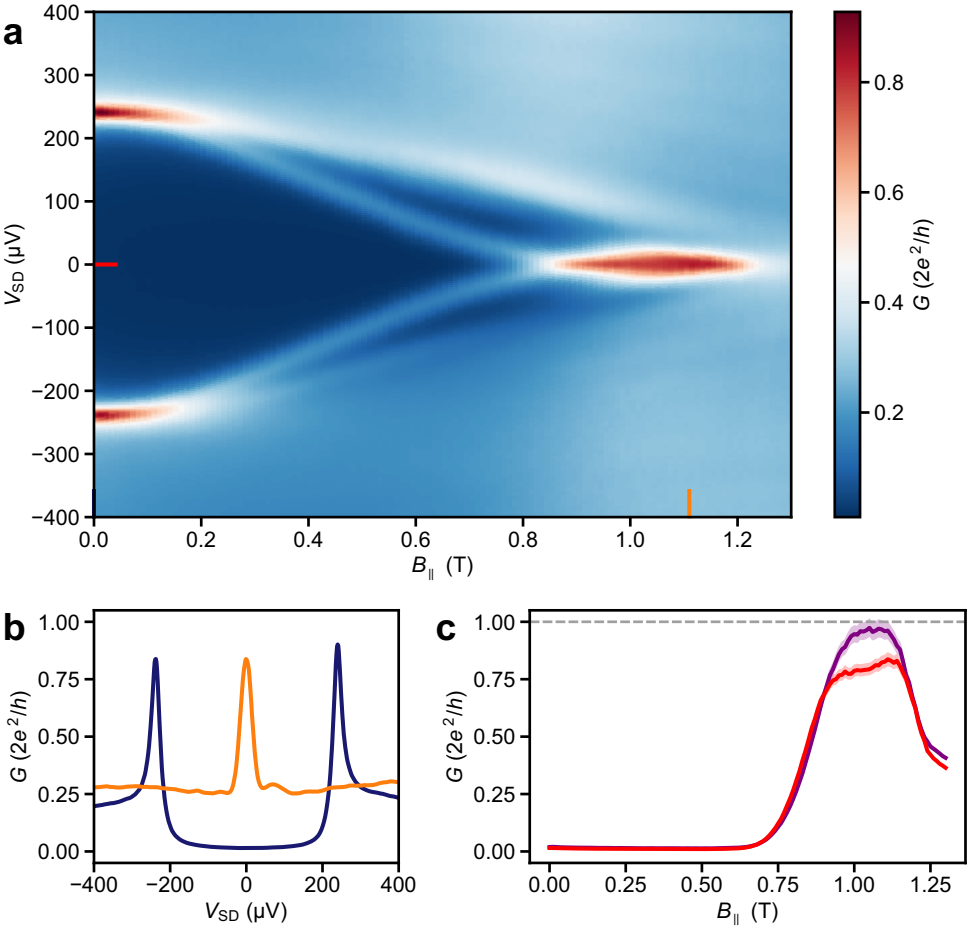

Figure 4.33: Voltage-bias spectroscopy of a subgap state with a large zero-bias peak conductance close to $2e^2/h$ (measured at the left N–S junction of the device presented in Fig. 4.5 of the main text). Here, the super-gate voltage $V_{SG} = 0.525\,V$. **a** Differential conductance, G, as a function of the bias voltage at the left terminal, V_{SD}, and the magnetic field along the wire axis. **b** Voltage-bias line-cut of the differential conductance at zero field (blue) and at $B_{\parallel} = 1.11\,T$ (orange). **c** G vs. $B_{\parallel}$ line-cuts at $V_{SD} = 0\,\mu V$ from panel (**a**) (red, at $V_{SG} = 0.525\,V$) and from Fig. 4.5e of the main text (purple, at $V_{SG} = 0\,V$). The shaded areas behind the solid traces correspond to the variation in conductance assuming an uncertainty of $\pm 0.5\,k\Omega$ in estimating the actual series resistance.

and a superconducting island is defined by two tunnel gates and one plunger gate on the right side of the device. Source and drain electrodes are created by bonding directly to the Al film (grey) at the bottom and at the top of the SQUID loop, respectively. By utilizing shadow-wall substrates with bottom gates, this SQUID sample can be realized without any post-interface fabrication steps.

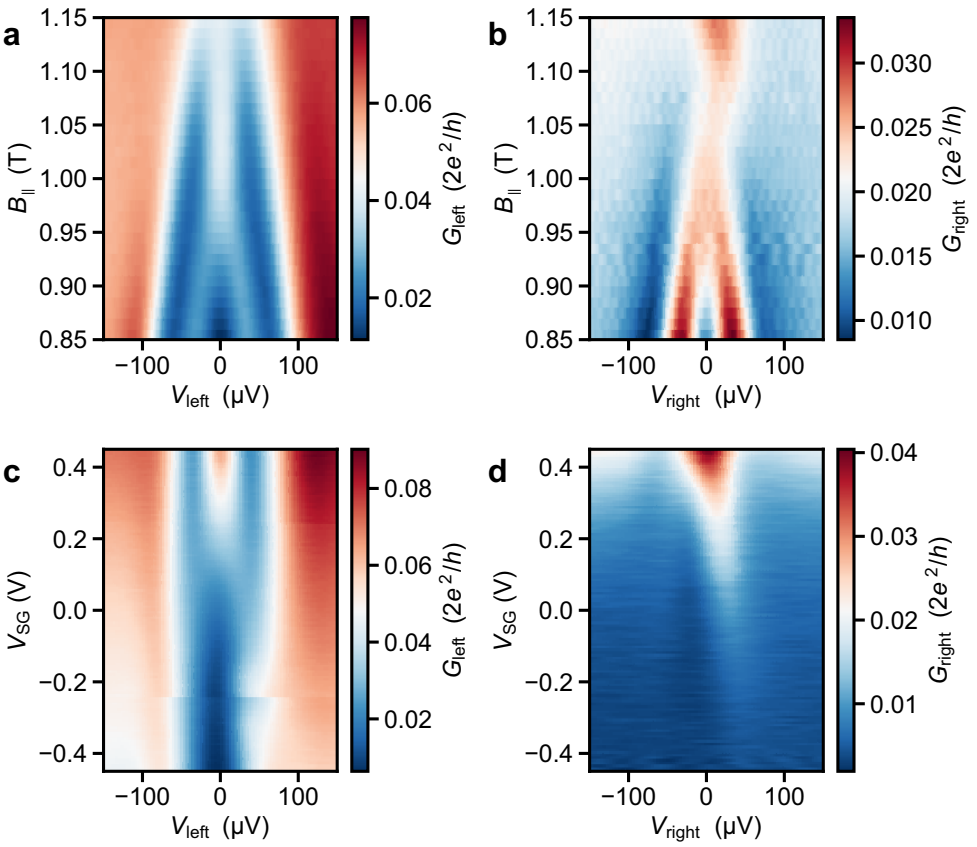

Figure 4.34: Simultaneous appearance of zero-bias peaks at both hybrid boundaries (same device as in Fig. 4.5 of the main text). The two tunnel gates are set to $V_{\text{TG,left}} = 0.47\,\text{V}$ and $V_{\text{TG,right}} = 0.13\,\text{V}$. **a**, **b** Differential conductance, $G_{\text{left/right}}$, as a function of magnetic field, $B_\parallel$, and bias voltage at the left and right terminal, respectively. Here, the super-gate voltage $V_{\text{SG}} = 0.525\,\text{V}$, i.e. identical as for the data in Supplementary Figure 4.33a. **c**, **d** Differential conductance, $G_{\text{left/right}}$, at $B_\parallel = 1.0\,\text{T}$ as a function of V_{SG} and bias voltage at the left and right terminal, respectively.

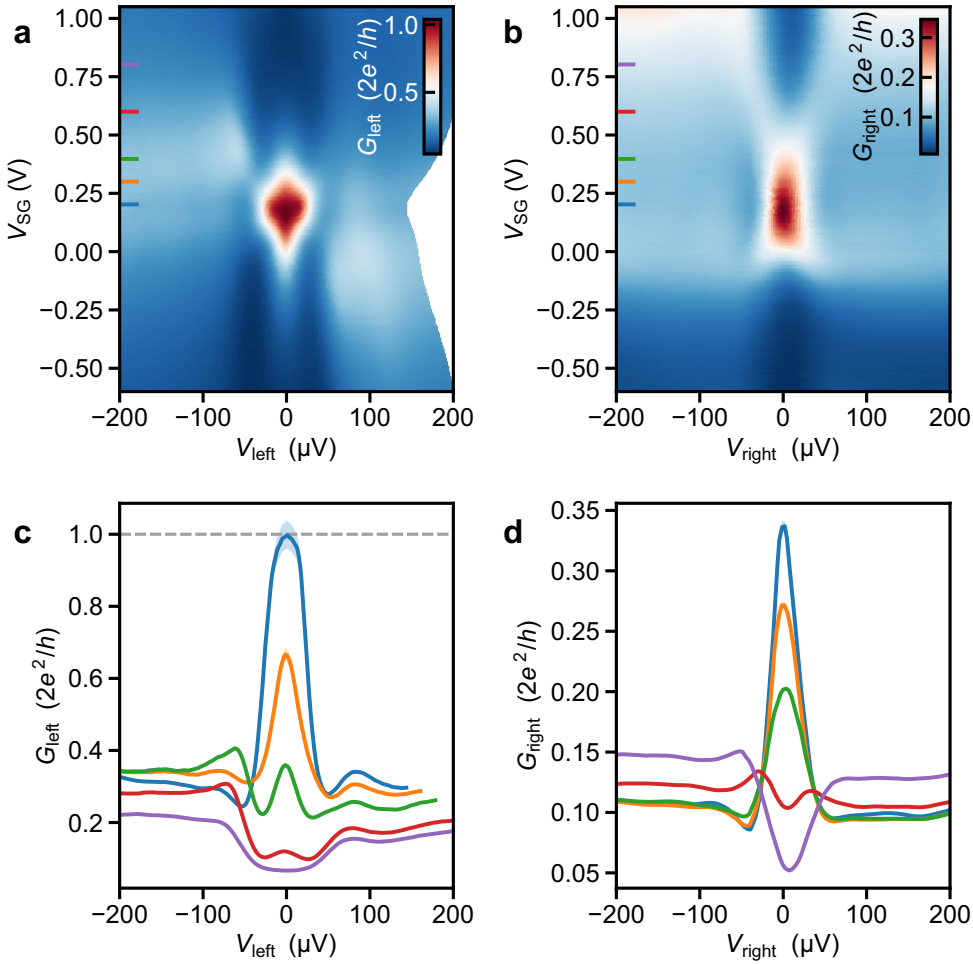

Figure 4.35: Simultaneous appearance of zero-bias peaks at both hybrid boundaries (same device and same tunnel-gate settings as in Fig. 4.5 of the main text). The two tunnel gates are set to $V_{TG,left} = 0.52\,V$ and $V_{TG,right} = 0.21\,V$. **a**, **b** Differential conductance, $G_{left/right}$, at $B_{\parallel} = 1.0\,T$ as a function of V_{SG} and bias voltage at the left and right terminal, respectively. **c**, **d** Line-cuts from panels (**a**) and (**b**) at the values of V_{SG} designated by the coloured lines. The shaded areas behind the solid traces correspond to the variation in conductance assuming an uncertainty of $\pm 0.5\,k\Omega$ in estimating the actual series resistance.

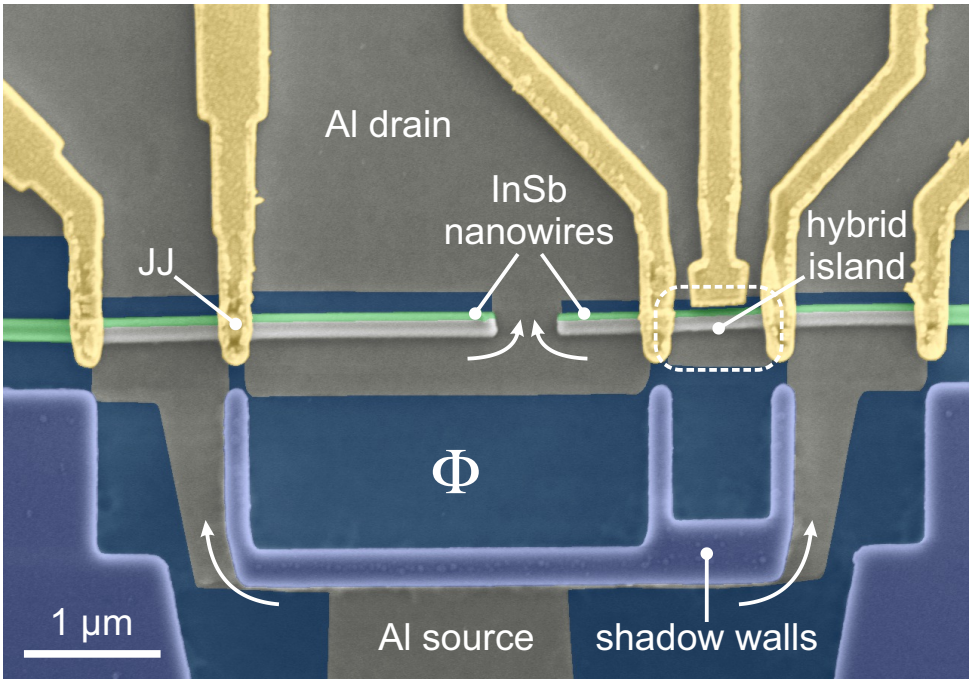

Figure 4.36: SQUID sample formed by placing two InSb nanowires next to each other in the shadow region of the dielectric walls. Electrical current flows from source to drain via the Josephson junction (denoted as JJ) and the hybrid charge island as indicated by the white arrows. The magnetic flux threading through the SQUID loop is denoted as Φ. The bottom of the SQUID loop is partly formed by the Al thin film covering the side of the central shadow wall.

References

[1] Y. Oreg, G. Refael, and F. Von Oppen, *Helical liquids and majorana bound states in quantum wires,* Physical review letters **105**, 177002 (2010).

[2] R. M. Lutchyn, J. D. Sau, and S. D. Sarma, *Majorana fermions and a topological phase transition in semiconductor-superconductor heterostructures,* Physical review letters **105**, 077001 (2010).

[3] R. M. Lutchyn, E. P. Bakkers, L. P. Kouwenhoven, P. Krogstrup, C. M. Marcus, and Y. Oreg, *Majorana zero modes in superconductor–semiconductor heterostructures,* Nature Reviews Materials **3**, 52 (2018).

[4] A. Y. Kitaev, *Unpaired majorana fermions in quantum wires,* Physics-uspekhi **44**, 131 (2001).

[5] C. Nayak, S. H. Simon, A. Stern, M. Freedman, and S. D. Sarma, *Non-abelian anyons and topological quantum computation,* Reviews of Modern Physics **80**, 1083 (2008).

[6] S. Plugge, A. Rasmussen, R. Egger, and K. Flensberg, *Majorana box qubits,* New Journal of Physics **19**, 012001 (2017).

[7] T. Karzig, C. Knapp, R. M. Lutchyn, P. Bonderson, M. B. Hastings, C. Nayak, J. Alicea, K. Flensberg, S. Plugge, Y. Oreg, *et al.*, *Scalable designs for quasiparticle-poisoning-protected topological quantum computation with majorana zero modes,* Physical Review B **95**, 235305 (2017).

[8] S. Takei, B. M. Fregoso, H.-Y. Hui, A. M. Lobos, and S. D. Sarma, *Soft superconducting gap in semiconductor majorana nanowires,* Physical review letters **110**, 186803 (2013).

[9] O. Gül, H. Zhang, F. K. de Vries, J. van Veen, K. Zuo, V. Mourik, S. Conesa-Boj, M. P. Nowak, D. J. van Woerkom, M. Quintero-Pérez, *et al.*, *Hard superconducting gap in insb nanowires,* Nano letters **17**, 2690 (2017).

[10] P. Krogstrup, N. Ziino, W. Chang, S. Albrecht, M. Madsen, E. Johnson, J. Nygård, C. M. Marcus, and T. Jespersen, *Epitaxy of semiconductor–superconductor nanowires,* Nature materials **14**, 400 (2015).

[11] S. Gazibegovic, D. Car, H. Zhang, S. C. Balk, J. A. Logan, M. W. De Moor, M. C. Cassidy, R. Schmits, D. Xu, G. Wang, *et al.*, *Epitaxy of advanced nanowire quantum devices,* Nature **548**, 434 (2017).

[12] M. W. De Moor, J. D. Bommer, D. Xu, G. W. Winkler, A. E. Antipov, A. Bargerbos, G. Wang, N. v. Loo, R. L. Op het Veld, S. Gazibegovic, *et al.*, *Electric field tunable superconductor-semiconductor coupling in majorana nanowires,* New Journal of Physics **20**, 103049 (2018).

[13] S. A. Khan, C. Lampadaris, A. Cui, L. Stampfer, Y. Liu, S. J. Pauka, M. E. Cachaza, E. M. Fiordaliso, J.-H. Kang, S. Korneychuk, *et al.*, *Highly transparent gatable superconducting shadow junctions,* ACS nano **14**, 14605 (2020).

[14] J. Cao, Q. Wang, and H. Dai, *Electron transport in very clean, as-grown suspended carbon nanotubes,* Nature materials **4**, 745 (2005).

[15] M. Octavio, M. Tinkham, G. Blonder, and T. Klapwijk, *Subharmonic energy-gap structure in superconducting constrictions,* Physical Review B **27**, 6739 (1983).

[16] H. Nilsson, P. Samuelsson, P. Caroff, and H. Xu, *Supercurrent and multiple andreev reflections in an insb nanowire josephson junction,* Nano letters **12**, 228 (2012).

[17] S. Li, N. Kang, D. Fan, L. Wang, Y. Huang, P. Caroff, and H. Xu, *Coherent charge transport in ballistic insb nanowire josephson junctions,* Scientific Reports **6**, 24822 (2016).

[18] T. Rosdahl, A. Vuik, M. Kjaergaard, and A. Akhmerov, *Andreev rectifier: A nonlocal conductance signature of topological phase transitions,* Physical Review B **97**, 045421 (2018).

[19] Y.-H. Lai, J. D. Sau, and S. D. Sarma, *Presence versus absence of end-to-end nonlocal conductance correlations in majorana nanowires: Majorana bound states versus andreev bound states,* Physical Review B **100**, 045302 (2019).

[20] H. Pan, J. D. Sau, and S. D. Sarma, *Three-terminal nonlocal conductance in majorana nanowires: Distinguishing topological and trivial in realistic systems with disorder and inhomogeneous potential,* Physical Review B **103**, 014513 (2021).

[21] G. Blonder, m. M. Tinkham, and k. T. Klapwijk, *Transition from metallic to tunneling regimes in superconducting microconstrictions: Excess current, charge imbalance, and supercurrent conversion,* Physical Review B **25**, 4515 (1982).

[22] C. Beenakker, *Quantum transport in semiconductor-superconductor microjunctions,* Physical Review B **46**, 12841 (1992).

[23] S. Vijay and L. Fu, *Teleportation-based quantum information processing with majorana zero modes,* Physical Review B **94**, 235446 (2016).

[24] B. Béri and N. Cooper, *Topological kondo effect with majorana fermions,* Physical review letters **109**, 156803 (2012).

[25] M. Bjergfelt, D. J. Carrad, T. Kanne, M. Aagesen, E. M. Fiordaliso, E. Johnson, B. Shojaei, C. J. Palmstrøm, P. Krogstrup, T. S. Jespersen, *et al.*, *Superconducting vanadium/indium-arsenide hybrid nanowires,* Nanotechnology **30**, 294005 (2019).

[26] T. Rieger, D. Rosenbach, D. Vakulov, S. Heedt, T. Schäpers, D. Grützmacher, and M. I. Lepsa, *Crystal phase transformation in self-assembled inas nanowire junctions on patterned si substrates,* Nano letters **16**, 1933 (2016).

[27] D. J. Carrad, M. Bjergfelt, T. Kanne, M. Aagesen, F. Krizek, E. M. Fiordaliso, E. Johnson, J. Nygård, and T. S. Jespersen, *Shadow epitaxy for in situ growth of generic semiconductor/superconductor hybrids,* Advanced Materials **32**, 1908411 (2020).

[28] F. Boscherini, Y. Shapira, C. Capasso, C. Aldao, M. del Giudice, and J. Weaver, *Exchange reaction, clustering, and surface segregation at the al/insb (110) interface,* Physical Review B **35**, 9580 (1987).

[29] C. Thomas, R. E. Diaz, J. H. Dycus, M. E. Salmon, R. E. Daniel, T. Wang, G. C. Gardner, and M. J. Manfra, *Toward durable al-insb hybrid heterostructures via epitaxy of 2ml interfacial inas screening layers,* Physical Review Materials **3**, 124202 (2019).

[30] G. Badawy, S. Gazibegovic, F. Borsoi, S. Heedt, C.-A. Wang, S. Koelling, M. A. Verheijen, L. P. Kouwenhoven, and E. P. Bakkers, *High mobility stemless insb nanowires,* Nano letters **19**, 3575 (2019).

[31] R. Meservey and P. Tedrow, *Properties of very thin aluminum films,* Journal of Applied Physics **42**, 51 (1971).

[32] H. Courtois, M. Meschke, J. Peltonen, and J. P. Pekola, *Origin of hysteresis in a proximity josephson junction,* Physical review letters **101**, 067002 (2008).

[33] V. Ambegaokar and A. Baratoff, *Tunneling between superconductors,* Physical Review Letters **10**, 486 (1963).

[34] Y.-J. Doh, J. A. van Dam, A. L. Roest, E. P. Bakkers, L. P. Kouwenhoven, and S. De Franceschi, *Tunable supercurrent through semiconductor nanowires,* science **309**, 272 (2005).

[35] T. Fulton and L. Dunkleberger, *Lifetime of the zero-voltage state in josephson tunnel junctions,* Physical Review B **9**, 4760 (1974).

[36] M. Tinkham, *Introduction to superconductivity* (Courier Corporation, 2004).

[37] E. Scheer, P. Joyez, D. Esteve, C. Urbina, and M. H. Devoret, *Conduction channel transmissions of atomic-size aluminum contacts,* Physical Review Letters **78**, 3535 (1997).

[38] B. Nijholt and A. R. Akhmerov, *Orbital effect of magnetic field on the majorana phase diagram,* Physical Review B **93**, 235434 (2016).

[39] A. E. Antipov, A. Bargerbos, G. W. Winkler, B. Bauer, E. Rossi, and R. M. Lutchyn, *Effects of gate-induced electric fields on semiconductor majorana nanowires,* Physical Review X **8**, 031041 (2018).

[40] S. Abay, H. Nilsson, F. Wu, H. Xu, C. Wilson, and P. Delsing, *High critical-current superconductor-inas nanowire-superconductor junctions,* Nano letters **12**, 5622 (2012).

[41] V. Mourik, K. Zuo, S. M. Frolov, S. Plissard, E. P. Bakkers, and L. P. Kouwenhoven, *Signatures of majorana fermions in hybrid superconductor-semiconductor nanowire devices,* Science **336**, 1003 (2012).

[42] K. T. Law, P. A. Lee, and T. K. Ng, *Majorana fermion induced resonant andreev reflection,* Physical review letters **103**, 237001 (2009).

[43] H. Pan and S. D. Sarma, *Physical mechanisms for zero-bias conductance peaks in majorana nanowires,* Physical Review Research **2**, 013377 (2020).

[44] W. Chang, S. Albrecht, T. Jespersen, F. Kuemmeth, P. Krogstrup, J. Nygård, and C. M. Marcus, *Hard gap in epitaxial semiconductor–superconductor nanowires,* Nature nanotechnology **10**, 232 (2015).

[45] M. Kjærgaard, F. Nichele, H. Suominen, M. Nowak, M. Wimmer, A. Akhmerov, J. Folk, K. Flensberg, J. Shabani, w. C. Palmstrøm, *et al.*, *Quantized conductance doubling and hard gap in a two-dimensional semiconductor–superconductor heterostructure,* Nature communications **7**, 12841 (2016).

[46] F. Borsoi, G. P. Mazur, N. van Loo, M. P. Nowak, L. Bourdet, K. Li, S. Korneychuk, A. Fursina, J.-Y. Wang, V. Levajac, *et al.*, *Single-shot fabrication of semiconducting–superconducting nanowire devices,* Advanced Functional Materials **31**, 2102388 (2021).

[47] H. Zhang, Ö. Gül, S. Conesa-Boj, M. P. Nowak, M. Wimmer, K. Zuo, V. Mourik, F. K. De Vries, J. Van Veen, M. W. De Moor, *et al.*, *Ballistic superconductivity in semiconductor nanowires,* Nature communications **8**, 16025 (2017).

[48] S. Heedt, A. Manolescu, G. Nemnes, W. Prost, J. Schubert, D. Grutzmacher, and T. Schäpers, *Adiabatic edge channel transport in a nanowire quantum point contact register,* Nano letters **16**, 4569 (2016).

[49] Ö. Gül, H. Zhang, J. D. Bommer, M. W. de Moor, D. Car, S. R. Plissard, E. P. Bakkers, A. Geresdi, K. Watanabe, T. Taniguchi, *et al.*, *Ballistic majorana nanowire devices,* Nature nanotechnology **13**, 192 (2018).

[50] F. Nichele, A. C. Drachmann, A. M. Whiticar, E. C. O'Farrell, H. J. Suominen, A. Fornieri, T. Wang, G. C. Gardner, C. Thomas, A. T. Hatke, *et al.*, *Scaling of majorana zero-bias conductance peaks,* Physical review letters **119**, 136803 (2017).

[51] A. Grivnin, E. Bor, M. Heiblum, Y. Oreg, and H. Shtrikman, *Concomitant opening of a bulk-gap with an emerging possible majorana zero mode,* Nature communications **10**, 1940 (2019).

[52] J. Chen, P. Yu, J. Stenger, M. Hocevar, D. Car, S. R. Plissard, E. P. Bakkers, T. D. Stanescu, and S. M. Frolov, *Experimental phase diagram of zero-bias conductance peaks in superconductor/semiconductor nanowire devices,* Science advances **3**, e1701476 (2017).

[53] G. Anselmetti, E. Martinez, G. Ménard, D. Puglia, F. Malinowski, J. Lee, S. Choi, M. Pendharkar, C. Palmstrøm, C. Marcus, *et al.*, *End-to-end correlated subgap states in hybrid nanowires,* Physical Review B **100**, 205412 (2019).

[54] P. Yu, J. Chen, M. Gomanko, G. Badawy, E. Bakkers, K. Zuo, V. Mourik, and S. Frolov, *Non-majorana states yield nearly quantized conductance in proximatized nanowires,* Nature Physics **17**, 482 (2021).

[55] C. Moore, T. D. Stanescu, and S. Tewari, *Two-terminal charge tunneling: Disentangling majorana zero modes from partially separated andreev bound states in semiconductor-superconductor heterostructures,* Physical Review B **97**, 165302 (2018).

[56] A. Gielen and F. V. Mackenzie, *Thermo-mechanical effects in majorana type quantum devices,* Microelectronics Reliability **62**, 50 (2016).

[57] A. Vuik, B. Nijholt, A. R. Akhmerov, and M. Wimmer, *Reproducing topological properties with quasi-majorana states,* SciPost Physics **7**, 061 (2019).

[58] H. Pan, W. S. Cole, J. D. Sau, and S. D. Sarma, *Generic quantized zero-bias conductance peaks in superconductor-semiconductor hybrid structures,* Physical Review B **101**, 024506 (2020).

[59] D. De Jong, J. Van Veen, L. Binci, A. Singh, P. Krogstrup, L. P. Kouwenhoven, W. Pfaff, and J. D. Watson, *Rapid detection of coherent tunneling in an in as nanowire quantum dot through dispersive gate sensing,* Physical Review Applied **11**, 044061 (2019).

[60] R. C. Dynes, V. Narayanamurti, and J. P. Garno, *Direct measurement of quasiparticle-lifetime broadening in a strong-coupled superconductor,* Physical Review Letters **41**, 1509 (1978).

[61] C.-X. Liu, F. Setiawan, J. D. Sau, and S. D. Sarma, *Phenomenology of the soft gap, zero-bias peak, and zero-mode splitting in ideal majorana nanowires,* Physical Review B **96**, 054520 (2017).

[62] K. Flöhr, M. Liebmann, K. Sladek, H. Y. Günel, R. Frielinghaus, F. Haas, C. Meyer, H. Hardtdegen, T. Schäpers, D. Grützmacher, *et al.*, *Manipulating inas nanowires with submicrometer precision,* Review of scientific instruments **82**, 113705 (2011).

[63] J. L. Webb, J. Knutsson, M. Hjort, S. Gorji Ghalamestani, K. A. Dick, R. Timm, and A. Mikkelsen, *Electrical and surface properties of inas/insb nanowires cleaned by atomic hydrogen,* Nano Letters **15**, 4865 (2015).

[64] L. Haworth, J. Lu, D. Westwood, and J. E. Macdonald, *Atomic hydrogen cleaning, nitriding and annealing insb (100),* Applied surface science **166**, 253 (2000).

[65] R. Tessler, C. Saguy, O. Klin, S. Greenberg, E. Weiss, R. Akhvlediani, R. Edrei, and A. Hoffman, *Oxide-free insb (100) surfaces by molecular hydrogen cleaning,* Applied physics letters **88**, 031918 (2006).

[66] L. Dong, R. W. Smith, and D. J. Srolovitz, *A two-dimensional molecular dynamics simulation of thin film growth by oblique deposition,* Journal of Applied Physics **80**, 5682 (1996).

[67] A. Barranco, A. Borras, A. R. Gonzalez-Elipe, and A. Palmero, *Perspectives on oblique angle deposition of thin films: From fundamentals to devices,* Progress in Materials Science **76**, 59 (2016).

[68] F. K. de Vries, M. L. Sol, S. Gazibegovic, R. L. op het Veld, S. C. Balk, D. Car, E. P. Bakkers, L. P. Kouwenhoven, and J. Shen, *Crossed andreev reflection in insb flake josephson junctions,* Physical Review Research **1**, 032031 (2019).

[69] S. Gazibegovic, G. Badawy, T. L. Buckers, P. Leubner, J. Shen, F. K. de Vries, S. Koelling, L. P. Kouwenhoven, M. A. Verheijen, and E. P. Bakkers, *Bottom-up grown 2d insb nanostructures,* Advanced Materials **31**, 1808181 (2019).

[70] D. Averin and A. Bardas, *ac josephson effect in a single quantum channel,* Physical review letters **75**, 1831 (1995).

[71] A. Bardas and D. V. Averin, *Electron transport in mesoscopic disordered superconductor–normal-metal–superconductor junctions,* Physical Review B **56**, R8518 (1997).

[72] M. Nowak, M. Wimmer, and A. Akhmerov, *Supercurrent carried by nonequilibrium quasiparticles in a multiterminal josephson junction,* Physical Review B **99**, 075416 (2019).

[73] B. Nijholt, J. Weston, JornHoofwijk, A. Akhmerov, and A. E. Antipov, *python-adaptive/adaptive: version 0.9.0,* (2019).

[74] D. Morris and M. Tinkham, *Effect of magnetic field on thermal conductivity and energy gap of superconducting films,* Physical Review Letters **6**, 600 (1961).

[75] V. Mathur, N. Panchapakesan, and R. Saxena, *Magnetic-field dependence of the energy gap in superconductors,* Physical Review Letters **9**, 374 (1962).

[76] C. Schrade and L. Fu, *Andreev or majorana, cooper finds out,* arXiv preprint arXiv:1809.06370 (2018).

[77] D. Szombati, S. Nadj-Perge, D. Car, S. Plissard, E. Bakkers, and L. Kouwenhoven, *Josephson ϕ 0-junction in nanowire quantum dots,* Nature Physics **12**, 568 (2016).

5

Parametric exploration of zero-energy modes in three-terminal InSb-Al nanowire devices

Lasciate ogne speranza, voi ch'intrate.

Dante Alighieri

We systematically study three-terminal InSb-Al nanowire devices by using radio-frequency reflectometry. Tunneling spectroscopy measurements on both ends of the hybrid nanowires are performed while systematically varying the chemical potential, magnetic field and junction transparencies. Identifying the lowest-energy state allows for the construction of lowest- and zero-energy state diagrams, which show how the states evolve as a function of the aforementioned parameters. Importantly, comparing the diagrams taken for each end of the hybrids enables the identification of states which do not coexist simultaneously, ruling out a significant amount of the parameter space as candidates for a topological phase. Furthermore, altering junction transparencies filters out zero-energy states sensitive to a local gate potential. Such a measurement strategy significantly reduces the time necessary to identify a potential topological phase and minimizes the risk of falsely recognizing trivial bound states as Majorana zero modes.

This chapter has been published as *Parametric exploration of zero-energy modes in three-terminal InSb-Al nanowire devices*, J.-Y. Wang, **N. van Loo**, G.P. Mazur, V. Levajac, F.K. Malinowski, M. Lemang, F. Borsoi, G. Badawy, S. Gazibegovic, E.P.A.M. Bakkers, M. Quintero-Pérez, S. Heedt and L.P. Kouwenhoven in Physical Review B 106, 075306 (2022).

5.1 Introduction

Superconductor-semiconductor hybrids have attracted great interest in recent years for their potential applications in creating Majorana zero modes (MZMs) [1–3]. Extensive experiments have been carried out on such hybrid nanowires [4–11] and hybrid two-dimensional electron gases (2DEGs) [12–14]. Zero-bias peaks (ZBPs), observed at the ends of such hybrids, were initially considered as evidence for the existence of MZMs. However, such ZBPs could also originate from alternative trivial mechanisms, such as quasi-Majoranas [15], disorder [16–20], or a combination of Zeeman and Little-Parks effects [21]. On the other hand, end-to-end correlations are a unique property of paired MZMs in a topological superconductor, and could be used to distinguish MZMs from trivial Andreev bound states in three-terminal architectures [22–25].

Simulations taking into account the physical details of experimental devices (i.e. superconductor-semiconductor coupling, band offset at the interface, multiple subbands, and disorder effects) predict a significantly reduced and complex topological phase space [26]. Therefore, finding such a phase in the large parameter space requires the development of a detection method capable of scanning the entire parameter space within a practical time [27]. Radio-frequency (rf) techniques have been succesfully implemented on superconducting qubits [28], spin qubits [29] and hybrid devices [30, 31]. Compared to traditional dc conductance measurements, it enables a fast and high-resolution exploration of all essential parameters in hybrid devices.

Three-terminal InSb-Al nanowire devices are systematically investigated using rf reflectometry. Local tunneling spectroscopy is performed at two ends of the hybrid nanowires, while exploring the chemical potential (controlled by the so-called 'super gate') and external magnetic field. The lowest-energy states (LESs) and zero-energy states (ZESs) are extracted as a function of super gate voltage and magnetic field, forming LES or ZES diagrams. As MZMs in an idealized model feature end-to-end correlations, the extracted diagrams of the two sides are compared to filter out uncorrelated ZESs. Stability of ZESs to transparency variation is studied by altering barrier gate settings, and zero-energy Andreev states residing around junctions are successfully identified. In addition, induced superconductivity on two ends of the hybrid nanowires is extracted, helpful for quantifing superconductor-semiconductor coupling in the hybrid nanowires. By applying the aforementioned experimental procedure, typical patterns of ZBPs are indentified in the studied devices, but after a closer inspection non-topological explanations are more likely. The approach is able to significantly accelerate the idenfication on a potential topological phase.

5.2 Experimental Setup

Fig. 5.1(a) shows a circuit diagram of the measurement setup together with a false-color scanning electron microscope (SEM) image of Device 1. Three-terminal devices are fabricated from InSb nanowires [32] using the recently developed shadow-wall lithography technique, enabling high-quality semiconductor-superconductor quantum devices [33, 34]. In the SEM image, an Al film (blue) is connected from the substrate to the nanowire to serve as a superconducting drain lead, while Ti/Au contacts (yellow) are fabricated on

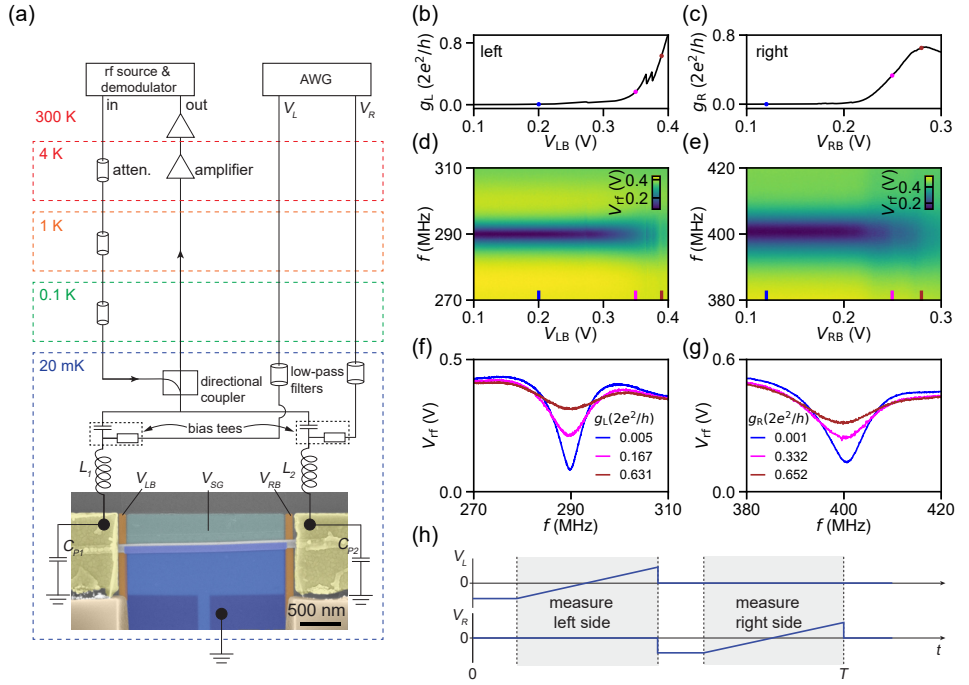

Figure 5.1: Rf reflectometry measurement setup and its basic characteristics. **(a)** Measurement circuit together with a false-color SEM image of a three-terminal InSb-Al device. The superconducting lead (blue) is made from Al, connecting from the substrate to the nanowire. The superconductor-semiconductor hybrid is ~2 μm long. Two probe leads (yellow), made from Ti/Au, are bonded to two superconducting inductors L_1, L_2. Voltages V_{LB} and V_{RB} are applied to bottom gates (orange) for tuning the left and right tunneling barriers, respectively. The chemical potential of the hybrid nanowire is tuned by the super gate (turquoise) with voltage V_{SG}. **(b)** and **(c)** Dc conductance of left and right junction (g_{L}, g_{R}) versus corresponding barrier gate voltage (V_{LB}, V_{RB}). **(d)** and **(e)** Corresponding rf response as a function of barrier gates in the same range as **(b)** and **(c)**. **(f)** and **(g)** Line cuts at specific gate voltages from **(d)** and **(e)**. In **(d)-(g)**, V_{rf} is the amplitude of the reflected rf signal with ~30 dB amplification at 4 K and ~65 dB amplification at room temperature. **(h)** Bias-voltage waveforms applied at two probe leads as a function of time. In the shaded time period, voltage-bias spectroscopy of either side is performed. T is the time period for measuring bias-spectroscopy traces on both sides.

both ends of the hybrid nanowire to serve as probe leads. Voltages V_{LB}, V_{RB} are applied onto barrier gates (orange) to tune the transparency of the tunneling junctions. The voltage on the super gate (turquoise), V_{SG}, is changing the chemical potential of the hybrid nanowire. In Fig. 5.10, we show SEM pictures of two additional measured devices and a schematic of the cross-section of the device. The hybrids in all three devices are ~2 μm long.

In order to accelerate tunneling spectroscopy at both junctions, an rf-conductance measurement scheme is employed [30, 35, 36]. The left and right probe lead of the device are connected to two superconducting spiral inductors (L_1, L_2) [29]. Together with parasitic capacitors (C_{P1}, C_{P2}) to ground, the inductors form two rf resonant circuits with typical

resonance frequencies 250-450 MHz (see optical images of inductor chips with devices in Fig. 5.11). Each resonator acts as an impedance transformer for the corresponding tunneling junction. On resonance, the typical junction impedance (~150 kΩ) is converted towards 50 Ω, which is the characteristic impedance of the transmission lines in the cryostat. Consequently, the reflection of the rf circuits at resonance displays a sensitive dependence on the differential conductance of the tunneling junctions. Fig. 5.1(b) and Fig. 5.1(c) present the pinch-off curves of the junctions at the two ends of the hybrid nanowire, at 10 mV dc bias, while Fig. 5.1(d)-(g) show corresponding response of the resonator circuits. The rf reflection has a sensitive response to conductance changing from 0.005 G_0 to 0.6 G_0 (G_0=$2e^2/h$). Such a broad conductance response allows sensitive rf detection at different tunneling transparencies.

The integration time per data point is about 1 ms, approximately two orders of magnitude less than the integration time of a conventional lock-in conductance measurement. To take advantage of the reduced integration time, we employ a rastering scheme [36, 37] to rapidly sweep the dc voltage bias applied at the tunneling junctions. Fig. 5.1(h) shows the waveforms generated by an arbitrary waveform generator (AWG). To perform the tunneling spectroscopy measurements at the two ends of the nanowire, the AWG generates a pair of triangular pulses, each sweeping the dc voltage bias at one of the junctions. The waveforms are accompanied by triggers, synchronizing the data aquisition with the voltage sweeps. Throughout the experiment, we perform pairs of tunneling spectroscopy measurement (typically 200 data points for each side with a total duration of ~0.4 s), which we repeat while varying gate voltages and the external magnetic field.

5.3 Results

5.3.1 Tunneling spectroscopy

Initially, basic characterization of devices and resonators is performed before moving to tunneling spectroscopy with rf. First, cross-talk between the super gate and barrier gates is measured at a fixed dc voltage bias. While sweeping V_{SG}, barrier gate voltages are changed accordingly to maintain a constant junction conductance (see Fig. 5.12(a) and Fig. 5.12(b)). Next, the magnetic field is aligned along the nanowire axis. Furthermore, the resonator frequency shift in an external magnetic field is characterized (see Fig. 5.12(c) and Fig. 5.12(d)). As the external magnetic field is swept, the probing frequencies are adjusted to maintain a high sensitivity of the rf conductance measurement. Finally, tunneling spectroscopy is performed on both sides of the device by applying the dc bias waveform illustrated in Fig. 5.1(h), while stepping V_{SG} and the parallel magnetic field, $B_{\parallel}$.

Fig. 5.2 shows segments of tunneling spectroscopy measurements on two nanowire ends at different $B_{\parallel}$. Fig. 5.2(a) and Fig. 5.2(c) show the results as a function of V_{SG} at $B_{\parallel}$=0. Line cuts at different V_{SG} are presented in Fig. 5.2(b) and Fig. 5.2(d). Suppressed conductance in between two pronounced coherence peaks suggests a hard superconducting gap. The superconducting gap is ~260 μeV, consistent with previous report based on the same fabrication platform [33, 34]. Fig. 5.2(e) and Fig. 5.2(g) present an example of sub-gap features at $B_{\parallel}$=0.48 T for the same V_{SG} range as Fig. 5.2(a) and Fig. 5.2(c). ZBPs are formed at both ends between V_{SG} = −0.23 V and V_{SG} = −0.15 V (see Fig. 5.2(f) and Fig. 5.2(h) for

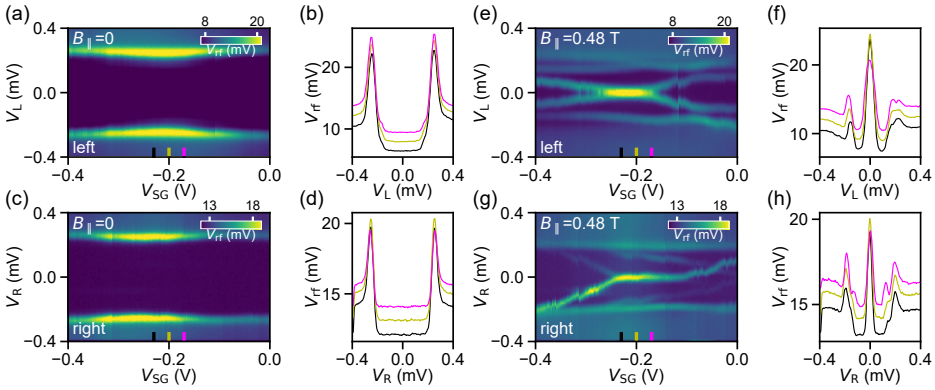

Figure 5.2: **(a)** and **(e)** Selected segments of tunneling spectroscopy at the left junction at $B_\parallel = 0$ T and $B_\parallel = 0.48$ T, respectively. Line cuts are taken at colored bars and shown in **(b)** and **(f)**. **(c)** and **(g)** are similar as **(a)** and **(e)**, but for the right junction. **(d)** and **(h)** show line cuts from **(c)** and **(g)**. Line cuts at zero magnetic field show a hard gap on both sides. Results at $B_\parallel = 0.48$ T illustrate the coexistence of zero-bias peaks on two sides. Note that the curves shown in **(b)**, **(d)**, **(f)** and **(h)** are shifted vertically for better visibility.

5

line cuts). ZBPs, peaks in differential conductance at zero energy, indicate the existence of ZESs, which are states with zero energy. Having established our setup for tunneling spectroscopy at both nanowire ends, we start mapping ZESs as a function of multiple parameters over a large range with high resolution.

5.3.2 Diagrams of lowest- and zero-energy states

For a given combination of $B_\parallel$ and V_{SG}, the presence of ZBPs is validated by analyzing one V_{rf}-$V_{L/R}$ trace (see Fig. 5.15 for details). This is repeated for all measured parameter values and presented as ZES diagrams, as shown in Fig. 5.3. Fig. 5.3(c) shows coexisting ZESs on both ends of the hybrid nanowire. In these diagrams, three distinct regimes can be observed. (1) For negative super gate voltages ($V_{SG} < -0.8$ V), ZESs only appear at high magnetic field (on the order of $B_\parallel = 0.8$ T) and there are no coexistent ZESs. (2) For positive super gate voltages ($V_{SG} > 0.5$ V), ZESs are ubiquitous at fields as low as $B_\parallel = 0.2$ T (An example of bias spectroscopy in this regime is shown in Fig. 5.13). Here, coexistent ZESs are sparsely distributed in parameter space. (3) In an intermediate regime (-0.8 V < $V_{SG} < 0.5$ V), ZESs emerge at moderate magnetic fields compared to the other two regimes. Notably, ZESs form regular shapes in parameter space and there is a significant amount of coexisting ZESs. This behavior is reproduced for two other InSb-Al hybrid nanowires presented in this work (see Fig. 5.21 and Fig. 5.23). A recent work on InSb-Al hybrid islands reports three similar regimes in V_{SG} [38]. It is explained by a tunable superconductor-semiconductor coupling with V_{SG} [26, 39, 40]. The intermediate regime is identified to be the most promising region to search for a topological superconducting phase. We focus the subsequent measurements on this intermediate super gate regime (marked by magenta rectangles in Fig. 5.3).

Fig. 5.4 presents high-resolution diagrams obtained in the intermediate super gate regime.

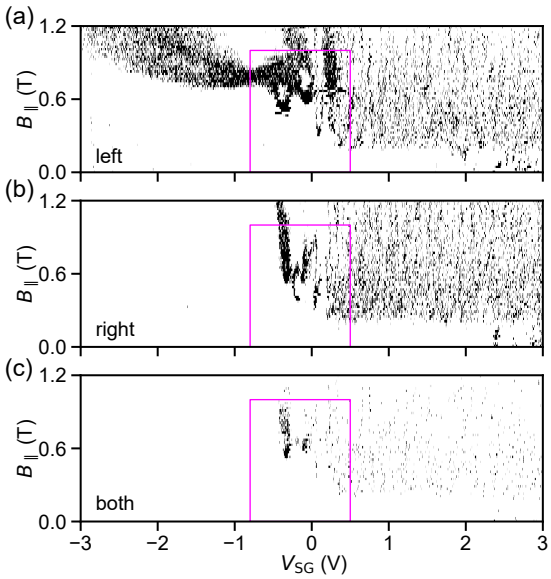

Figure 5.3: ZES diagrams as a function of V_{SG} and $B_{||}$ for the left junction **(a)** and right junction **(b)**. Black and white pixels indicate the presence and absence of ZESs, respectively. **(c)** Diagram with black pixels indicating the coexistence of ZESs on both ends. In each panel, there are 2523 data points along V_{SG} and 61 along $B_{||}$ (i.e. total number of pixels is 2523×61). The full data set is acquired in ~142 hours. Magenta rectangles mark the region with a relatively large density of coexistent ZESs. Calibration measurements, including Fig. 5.1(d), Fig. 5.1(e) and Fig. 5.12, take ~13.5 hours.

Fig. 5.4(a) and Fig. 5.4(b) show the energy of LESs probed at the two junctions, E_0^L and E_0^R, versus V_{SG} and $B_{||}$ (LES extraction method is shown in Fig. 5.15). At zero magnetic field, $E_0^{L/R}$ is close to the superconducting gap (~260 μeV). As $B_{||}$ increases, $E_0^{L/R}$ starts to drop due to the emergence of sub-gap states. In order to illustrate the dependence of $E_0^{L/R}$ on $B_{||}$, examples of two vertical line cuts are shown in Fig. 5.4(d) and Fig. 5.4(e). These are picked to illustrate two types of behavior: For the blue line cuts (V_{SG} = −0.18 V), the behavior on both sides of the nanowire is similar. Sub-gap states emerge and drop to zero energy, with a comparable effective g-factor (solid green lines are fitting traces to the linear part of the data). On the other hand, the magenta line cuts (V_{SG} = −0.6 V) show an example where on one junction, a sub-gap state drops to zero energy while on the other side no sub-gap states emerge. In order to identity LESs that may extend between the two ends of the hybrid nanowire, the energy difference between LESs, $|E_0^L - E_0^R|$, is calculated and shown in Fig. 5.4(c). Fig. 5.4(f) shows the line cuts at the same V_{SG} as in Fig. 5.4(d) and Fig. 5.4(e). Notably, for the blue line cut the energy difference of the LESs on both ends is close to zero within a large range of field, indicating a potential correlation. In contrast, the magenta line cut shows a large energy difference for almost all field values, which signifies uncorrelated behavior.

From the LES diagrams, states with zero energy are identified. These states are presented in ZES diagrams, shown in Fig. 5.4(g)-Fig. 5.4(i) (see the example of the extraction process

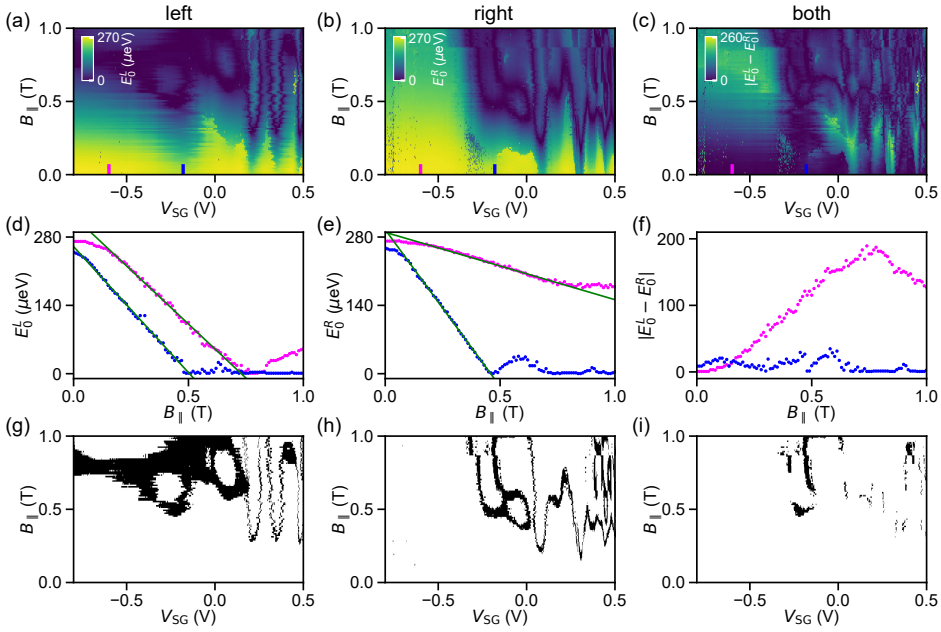

Figure 5.4: High-resolution LES and ZES diagrams. **(a)** Energy of LESs, E_0^L, probed on the left junction as a function of V_{SG} and $B_{||}$. **(b)** Energy of LESs, E_0^R, probed on the right junction versus V_{SG} and $B_{||}$. **(c)** Energy difference between the LESs probed on the two ends. **(d)-(f)** Line cuts taken at different V_{SG} from **(a)-(c)**. In **(d)** and **(e)**, solid green lines are linear fits. **(g)** and **(h)** ZES diagrams for the left and right junction, respectively. **(i)** Diagram of coexisting ZESs on both ends. Gates are swept by following the cyan dashed lines (g_L ~0.035 G_0, g_R ~0.064 G_0) in Fig. 5.14. In **(a)-(c)** and **(g)-(i)**, each panel includes 522×101 pixels. The dataset is acquired in ~35 hours.

in Fig. 5.15). Similar to Fig. 5.3, black pixels in Fig. 5.4(g) and Fig. 5.4(h) represent the presence of ZESs, while white pixels indicate the absence of ZESs. Regular features are observed in these diagrams, including parabolic and oscillatory shapes, as well as clusters of black pixels. The intersection of the two diagrams yields a diagram (Fig. 5.4(i)) consisting of ZESs which coexist on both sides. Around $V_{SG} \sim -0.2$ V and $B_{||} > 0.5$ T, a high density of coexistent ZESs is observed which indicates a potential candidate region for a topological phase. In the following section, this region and several of the regular patterns will be further analyzed.

5.3.3 Detailed analysis of ZES and LES diagrams

Coexisting ZBP clusters

ZES diagrams constructed in the previous section identify a region with coexisting ZESs on both ends of the nanowire hybrid. Fig. 5.5(a)-Fig. 5.5(c) show a zoom-in of Fig. 5.4(g)-Fig. 5.4(i). At fixed $V_{SG} = -0.18$ V, tunneling spectroscopy on both ends of the hybrid nanowire shows a sub-gap state reaching zero energy around 0.5 T (Fig. 5.5(d) and Fig. 5.5(e)). After a single oscillation, it sticks to zero energy for ~300 mT. On the other hand, when the magnetic field is fixed at 0.82 T, a stable ZES is observed only on the left side (Fig. 5.5(f)).

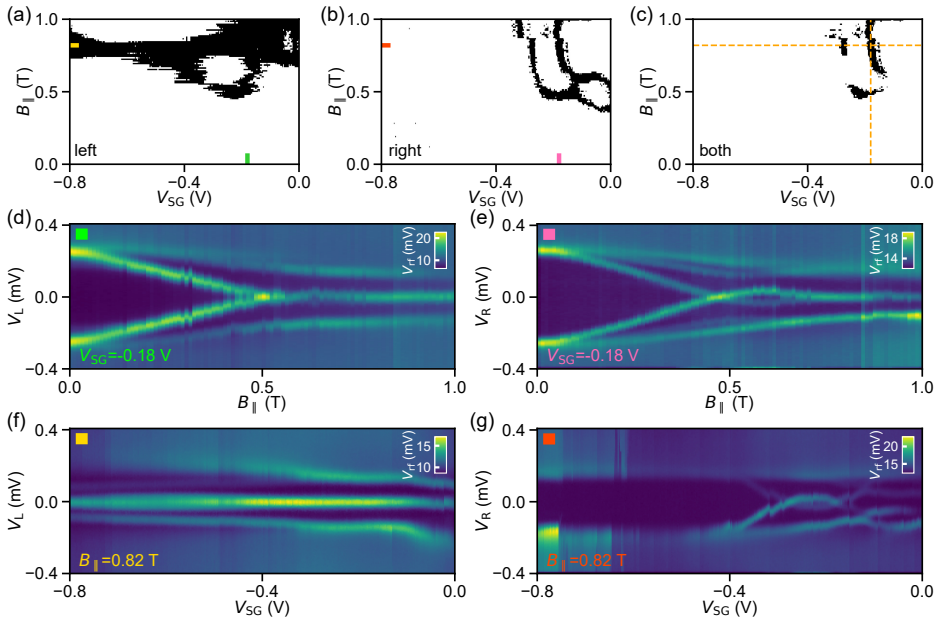

Figure 5.5: Clusters of ZBPs with respect to super gate and magnetic field. **(a)-(c)** ZES diagrams for the left junction, the right junction, and coexistence in both junctions (same as Fig. 5.4(g)-Fig. 5.4(i), but with reduced super gate range). In **(a)**, the green mark indicates the position of $V_{SG} = -0.18$ V and corresponding tunneling spectroscopy data is shown in **(d)**. The results at $B_\parallel = 0.82$ T (yellow mark) is shown in **(f)**. In **(b)**, tunneling spectroscopy data of the vertical (pink mark) and horizontal (red mark) line cut is shown in **(e)** and **(g)**, respectively. In **(c)**, the horizontal and vertical dashed line indicates $B_\parallel = 0.82$ T and $V_{SG} = -0.18$ V, respectively.

Remarkably, it persists for more than 800 mV in V_{SG}. Considering that the dielectric layer is made from 20 nm HfO_x, chemical potential is changed by a significant amount in this super gate range. Such stable ZBPs as a function of super gate voltage and magnetic field, together with similar behavior on both sides of the device as a function of magnetic field, have been previously interpreted as evidence of MZMs. However, robust ZBPs can also originate from Andreev bound states formed in quantum dots near the junction [41], as well as due to disorder [20]. Indeed, tunneling spectroscopy along super gate on the right side of the device (Fig. 5.5(g)) reveals a strikingly different behavior, with only two crossings through zero energy. The different behaviors on the two sides of the device can be recognized as well from ZES diagrams in Fig. 5.5(a)-Fig. 5.5(c). Such clearly distinct behavior with respect to changes in the chemical potential implies that the ZESs on the two sides of the device do not originate from an unbroken topological superconducting phase.

Parabolic patterns in ZES diagrams

In Fig. 5.4, ZESs form parabolic patterns in the V_{SG}-$B_\parallel$ space. Such parabolic patterns can represent the onset of a topological phase when Majorana zero modes at two ends of a short hybrid nanowire strongly interact [9, 42]. In Fig. 5.6, an example of such a parabola is shown and its tunneling spectroscopy data is presented. In Fig. 5.6(a), an orange rectangle

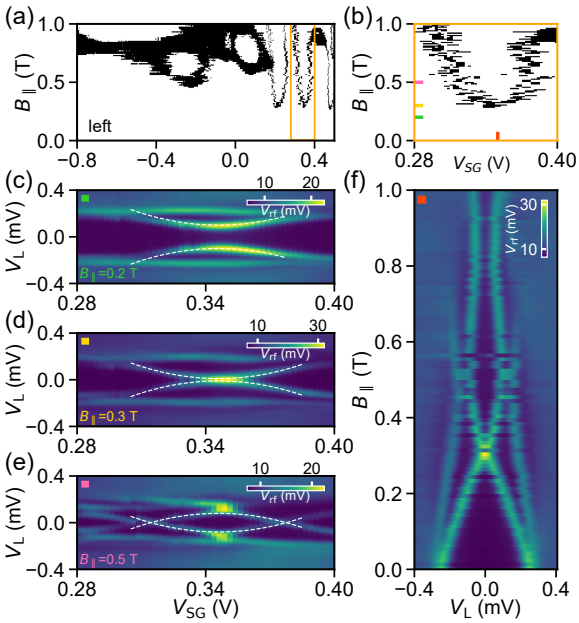

Figure 5.6: Parabolic patterns in ZES diagrams. **(a)** ZES diagram for the left junction (same as Fig. 5.4(g)). The region marked by the orange rectangle is re-plotted in **(b)**. Three line cuts are made at different $B_{||}$ and corresponding tunneling spectroscopy data is displayed in **(c)-(e)**. White dashed lines serve as guide to the eye. **(f)** Evolution of sub-gap levels in magnetic field at V_{SG} = 0.35 V (red vertical line cut from **(b)**).

marks the region with such a parabolic pattern. This region is re-plotted in Fig. 5.6(b). In order to understand the pattern, three line cuts are made at different magnetic fields and corresponding spectroscopic results are plotted in Fig. 5.6(c)-Fig. 5.6(e). At $B_{||}$ = 0.2 T (Fig. 5.6(c)), there is a pair of levels emerging below the superconducting gap, marked by white dashed lines. Once the magnetic field is increased to 0.3 T (Fig. 5.6(d)), the pair of sub-gap levels merges at zero energy, forming ZBPs. This field corresponds to the onset of ZESs in Fig. 5.6(b). At higher $B_{||}$, for example $B_{||}$ = 0.5 T (Fig. 5.6(e)), the sub-gap levels form two crossings at zero energy. The evolution of these sub-gap levels in $B_{||}$ at V_{SG} = 0.35 V is shown in Fig. 5.6(f). In Fig. 5.16, another parabolic pattern which has similar properties as Fig. 5.6 is presented. This behavior is fully explained by Zeeman-driven Andreev level splitting in a quantum dot proximitized by a superconducting lead [43].

Oscillatory patterns in LES diagrams

The oscillation of LESs in magnetic field with an increasing amplitude and period is consistent with the prediction of smoking gun evidence for MZMs [42]. This type of behavior would result in oscillatory patterns in LES and ZES diagrams. An example of such patterns is shown in Fig. 5.7(a) and Fig. 5.7(b). A line cut through such a circle, shown in Fig. 5.7(c) (V_{SG} = −0.08 V), shows the energy of a LES dropping to zero before oscillating with increasing amplitude and period, thus matching the smoking gun predictions. The tunneling spectroscopy data as a function of $B_{||}$ corresponding to this particular line cut

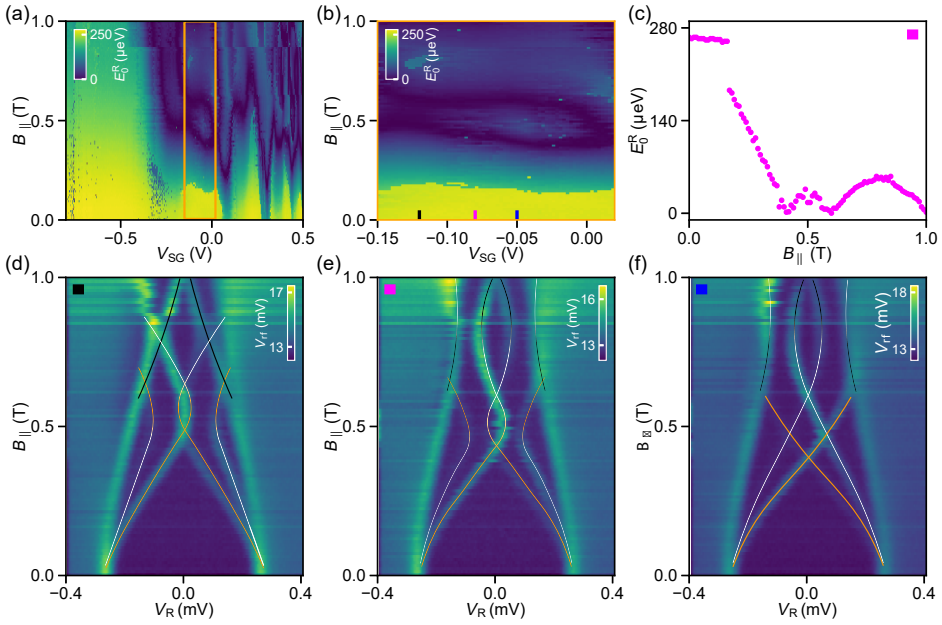

Figure 5.7: Oscillatory patterns in LES diagrams. **(a)** LES diagram for the right junction (same as Fig. 5.4(b)). The region marked by the orange rectangle is plotted in **(b)**. **(c)** Example of an oscillating LES, showing E_0^R versus $B_{\parallel}$ for the line cut taken at $V_{SG} = -0.08$ V (marked by the magenta bar in **(b)**). Tunneling spectroscopy data taken at $V_{SG} = -0.12$ V (black bar), $V_{SG} = -0.08$ V (magenta bar), and $V_{SG} = -0.05$ V (blue bar) is shown in **(d)**, **(e)** and **(f)**, respectively. In **(d)-(f)**, three sub-gap states are marked by orange, white, and black lines which serve as a guide to the eye. Gradient colors indicate interaction between states.

is shown in Fig. 5.7(e). In this map, three discrete sub-gap states are observed and marked with an orange, white, and black lines. The LES (orange) first comes down in energy and crosses through zero energy, before interacting with another state (white). Interaction between these states results in an anti-crossing, which can be attributed to the mixing of different spin species of two states via spin-orbit interaction [44], and is represented by a gradient color. The LES crosses through zero once more, and subsequently interacts with another state (black). In addition, two spectroscopy results at a lower ($V_{SG} = -0.12$ V) and higher ($V_{SG} = -0.05$ V) super gate voltage are presented in Fig. 5.7(d) and Fig. 5.7(f), respectively. By changing the super gate voltage, the magnitude of the interaction between the states can be tuned. Consequently, the interactions can become negligible which results in states crossing rather than anti-crossing. This indicates that the results in Fig. 5.7(e) or Fig. 5.7(c) arise from several sub-gap states interacting with each other. Thus, while the behavior of LESs in Fig. 5.7(e) and Fig. 5.7(c) is consistent with the predicted evidence of MZMs, such oscillations can originate from anti-crossings between the LES and other states. The analysis made above suggests that although oscillatory patterns in LES and ZES diagrams are expected for interacting MZMs, they may also originate from interactions between topologically trivial Andreev bound states.

Induced superconductivity

In addition to extracting the energy of various sub-gap states in the system, two other important parameters can be determined from the data: the superconducting gap size Δ and the effective g-factor g^*. From the local tunneling spectroscopy measurements, the superconducting gap can be estimated by fitting zero-field $g_{L/R}$-$V_{L/R}$ traces with the BCS–Dynes formula [45], where $g_{L/R}$ is obtained from V_{rf}-$g_{L/R}$ correspondence in Fig. 5.1. On the other hand, the effective g-factor is determined by making a linear fit to the energy dependence of the LES as a function of magnetic field [44, 46]. In Fig. 5.8, the evolution of these two parameters is shown as a function of super gate voltage. At both ends of the nanowire, the estimated gap size behaves similarly and remains largely unaffected by the super gate. It only shows a small dip in the vicinity of V_{SG}= −0.25 V, and from the spectra shown in Fig. 5.2 it can be seen that these dips correspond to the energy minima of two LESs. However, if we instead look at the field evolution it becomes apparent that the extracted g-factors do not behave in a similar way. This indicates that the LESs at two ends are uncorrelated. The right side of the device shows an absence of sub-gap states below V_{SG}=−0.4 V (see an example in Fig. 5.17). The corresponding g-factor is estimated from the gap edge and remains close to 2, as the measured properties are dominated by the Al film. It is worth to note that with local tunneling spectroscopy, only the superconducting properties in the vicinity of the junctions are detected while leaving the bulk properties inaccessible. In contradiction to our observations, the induced gap size and effective g-factor should behave similarly if they represent bulk properties [39]. Thus, we conclude that the behavior shown in Fig. 5.8 belongs to Andreev bound states formed locally in the vicinity of the junctions [47]. Nonlocal measurements are required in order to investigate induced superconductivity, including gap closing, in the bulk of the hybrids [27].

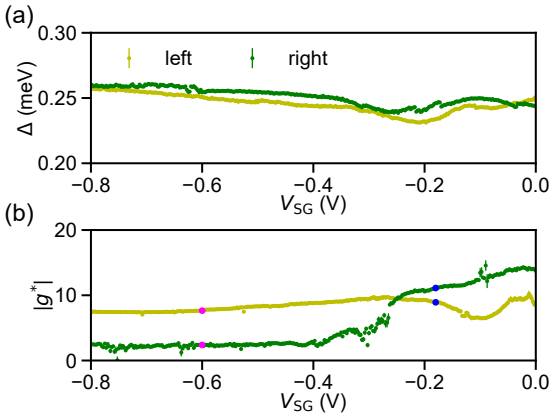

Figure 5.8: Gate-dependent induced superconductivity. **(a)** Superconducting gap as a function of super gate voltage V_{SG} extracted from the left (yellow) and right (green) junction. **(b)** Effective g-factor versus V_{SG} for the left (yellow) and right (green) end of the hybrid nanowire. Magenta and blue points correspond to the data extracted from the traces in Fig. 5.4(d) and Fig. 5.4(e). g-factors are extracted by fitting the linear part of the traces $E_0^{L/R}$ vs $B_\parallel$.

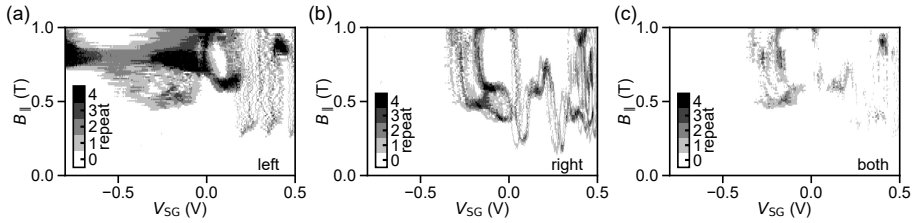

Figure 5.9: Overlapping ZES diagrams taken at different barrier gate settings for the left junction **(a)**, right junction **(b)**, and coexistence in both junctions **(c)**. The panels are obtained by overlapping ZES diagrams from Fig. 5.18 (g_L ~ 0.027 G_0, g_R ~ 0.025 G_0), Fig. 5.19 (g_L ~ 0.029 G_0, g_R ~ 0.004 G_0), Fig. 5.4 (g_L ~ 0.03 G_0, g_R ~ 0.064 G_0), and Fig. 5.20 (g_L ~ 0.047 G_0, g_R ~ 0.129 G_0).

5.3.4 Influence of barrier gates

ZESs formed in the vicinity of the junction can mimic MZM behavior with respect to magnetic field and chemical potential variations [48]. Tunnel transparency is an important experimental parameter which can be used for distinguishing MZMs from trivial Andreev bound states. To investigate the stability of ZESs shown in Fig. 5.4, similar measurements are performed with three different barrier gate settings. The corresponding processed diagrams are plotted in Fig. 5.18, Fig. 5.19, and Fig. 5.20 in the supplementary material. ZES diagrams obtained for four different barrier gate settings are overlapped to form ZES histograms in Fig. 5.9. As shown in Fig. 5.9(a), the left end of the hybrid exhibits clusters of ZESs in the space of chemical potential and magnetic field. As those ZESs are stable against variation of all experimentally accessible parameters, they are compatible with MZMs. However, as shown in Fig. 5.9(b), the right side of the studied hybrid does not show similar stability and thus indicates that the device does not exhibit an unbroken topological superconducting phase. As expected, the uncorrelated behavior between left and right end of the hybrid is recognized as well in the histogram of coexisting ZESs (Fig. 5.9(c)). Similar studies have been performed on the other two devices and details are presented in Fig. 5.21-Fig. 5.24 in the supplementary material. The results do not yield evidence for correlated MZMs either.

5.4 Discussion

In this work, three-terminal InSb-Al hybrid nanowire devices have been systematically studied using rf reflectometry. This approach introduces a critical experimental technique to quickly map out a large phase space at both ends of superconductor-semiconductor hybrid nanowires, which is crucial for searching for candidate regions of a topological phase. A wide range of chemical potential can be mapped out in high resolution by varying the super gate voltage, and consequently the chance of missing topologically non-trivial regions is minimized. Tunneling spectroscopy depending on super gate voltage and magnetic field enables the extraction of LESs and ZESs, as well as induced superconducting gap and effective g-factor. Constructed diagrams of ZESs and LESs indicate the most promising regions for searching for MZMs [27]. Combined with the tunneling-spectroscopy data, clusters of ZPBs, parabolic and oscillatory patterns in ZES and LES diagrams are analyzed for the first time in large scale and high resolution. While such patterns mimic the predicted

behavior of MZMs, the systematic exploration of all accessible experimental parameters suggest a non-topological origin. Further analysis by altering barrier gates indicate that the ZESs and LESs observed in this work are likely localized in the vicinity of the tunnel junctions. Additionally, the simultaneous detection of LESs at both ends of the hybrid enables the possibility to look for correlated ZESs, which is a prerequisite to prove the existence of paired MZMs. Yet, the observation of correlated ZBPs can also originate from trivial mechanisms such as Andreev bound states with a long localized length [49]. Even so, no indication of correlated behavior is observed in this work.

The absence of an unbroken topological superconducting phase in these samples can be attributed to several physical origins. Possible reasons include disorder, inhomogeneous interface band bending, local chemical potential fluctuations and a non-perfect detection method. Here, these four possible shortcomings are elaborated. (1) In addition to forming trivial sub-gap levels which can mimic MZMs, disorder effects could push the Majorana wavefunctions away from the ends of the hybrid nanowires [20, 22]. In this case, even if a topological phase is formed in the bulk, the MZM wavefunction cannot be probed by tunneling probes at the end of the hybrid nanowire. (2) Local chemical potential fluctuations with an energy above the helical gap can break a single topological phase into segments. In this case, the two ends of a hybrid nanowire are not necessarily correlated. In real devices, such fluctuations can originate from non-uniform gating effects, grain boundaries in aluminium, and disorder from impurities. (3) Recently, the interface band bending between the superconductor and semiconductor was recognized as an important ingredient for tuning the properties of the hybrid [26, 39, 40]. In particular, band bending can lead to the occupation of multiple subbands, and for the InSb-Al system the experimental implications are still unknown. This makes it difficult to predict the experimental conditions to achieve a topological superconducting phase. (4) The experimental protocol in this work is specifically designed to search for paired MZMs at two ends of an extended topological phase. If for any reason, a topological phase would not be continuous across the entire hybrid, it is possible that MZMs can be probed on one end but not on the other. In this case, the protocol applied in this work would miss a potential topological phase in the parameter space. Such a false negative cannot be ruled out by these measurements. We would note that a more general conclusion, like if topological phase is achievable in InSb-Al hybrid nanowires, cannot be drawn before exploring a large number of such devices to achieve statistical relevance.

For the aforementioned problems, several solutions can be proposed. (1) The InSb nanowires in this work have transport mobilities of $\sim 4 \times 10^4$ cm^2/V·s [32]. The introduction of capping layers on top of the semiconductor could alleviate disorder and improve transport mobilities [50]. (2) In order to improve resilience against local chemical potential fluctuations, alternative superconductors with larger superconducting gaps can be considered. Recent reports have successfully realized growth of Sn ($\Delta \sim 700\,\mu$eV) [51] and Pb ($\Delta \sim 1.25$ meV) [52] on semiconductor nanowires. These hybrids may have a higher chance to achieve an uninterrupted topological phase in spite of the challenges in fabrication. (3) Band bending at the interface between superconductors and semiconductors can be engineered by inserting modulation layers [50]. Simultaneously, proper engineering of these layers can also be used as a tool to influence the magnitude of the induced superconducting

gap. (4) Nonlocal measurements, proposed to probe the superconducting gap on three-terminal devices [53], can complement the fast rf reflectometry used in this work [27]. Corresponding experimental work established its capability of detecting bulk properties beyond the local characteristics [54, 55], though the measurement speed was slow. Combining our present protocol with nonlocal measurement would strike a balance between measurement speed and detection reliability.

The experimental protocol developed in this work, together with possible improvements discussed above, will pave the way for unambiguously detecting MZMs in superconductor-semiconductor hybrid systems in the future.

Data availability.
The authors declare that all relevant raw data together with analysis files are available at `https://doi.org/10.5281/zenodo.5938281`

5.5 Supplementary material

5.5.1 Methods and additional data

Device fabrication.
The InSb nanowires, with a typical diameter of 100 nm, are grown on InSb (111)B substrates covered with pre-patterned SiN_x mask via metalorganic vapour-phase epitaxy (MOVPE) [32]. InSb nanowires are transfered onto pre-patterned substrates with a micro-manipulator. Hydrogen cleaning is used to remove the native oxide on the nanowire surface. Subsequently, a thin aluminum film (~ 15 nm) is evaporated at 138 K and a 30 degree angle with respect to the substrate using shadow-wall lithography [33]. Finally, e-beam evaporation is used to make Ti/Au (10/120 nm) contacts on the nanowire ends right after the removal of the NW oxide using argon ion milling.

Transport measurements.
Samples are measured at a base temperature of ~20 mK in a dilution refrigerator equipped with a 6/2/2 T vector magnet. Two different measurement techniques are used in this work. (1) Conductance measurements are performed with standard dc technique. (2) For the rf measurements, resonators typically have resonance frequencies in the range of 250-450 MHz. For resonators, the inductors have inductances of 300-730 nH and a parasitic capacitance of ~0.5 pF. The acquisition time for each data point is typically 1 ms. In each tunneling spectroscopy line trace, there are typically 201 or 401 data points. The rf signals are generated and demodulated by UHFLI from Zurich Instruments. Within the measurements presented in this work, the junction conductances on the two sides are kept at relatively low values (below 0.3 G_0) in order to minimize voltage divider effects from serial resistances in the setup while assuring sensitivity to rf detection. An arbitrary waveform generator Tektronix 5014C generates the waveforms which serve as bias voltages.

Correspondence between rf reflection and differential conductance.
In our data, zero-field rf reflection results can be converted into differential conductance. Converting rf reflection data at finite magnetic field is difficult due to inadequate calibra-

tion on resonators in field, which has little influence on this article as we focus on the energy of sub-gap states rather than conductance amplitude of these states.

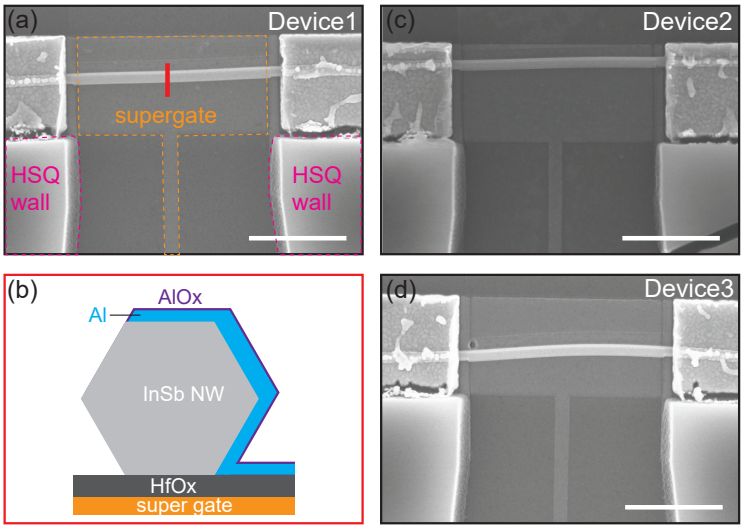

Figure 5.10: Scanning-electron microscope (SEM) images of the three InSb-Al nanowire devices presented in this work (**(a)**, **(c)** and **(d)**). The length of the InSb-Al hybrids is ~2 μm. Scale bars in the pictures are 1 μm. In **(a)**, the super gate and insulating nanostructures (HSQ wall) for the shadow-wall evaporation are outlined in orange and magenta, respectively. **(b)** Schematic cross-section of an InSb-Al nanowire hybrid.

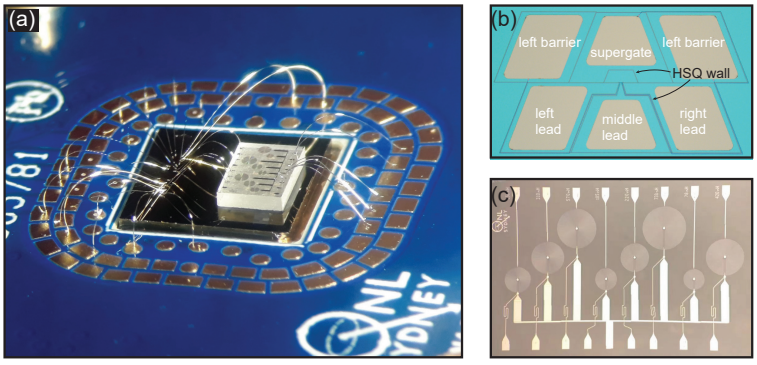

Figure 5.11: **(a)** Optical image of a PCB board with a sample chip and a frequency multiplexing chip [29] after bonding. **(b)** Optical image of a representative device. Bonding pads for different gates and leads are labelled. **(c)** Optical image of a frequency multiplexing chip.

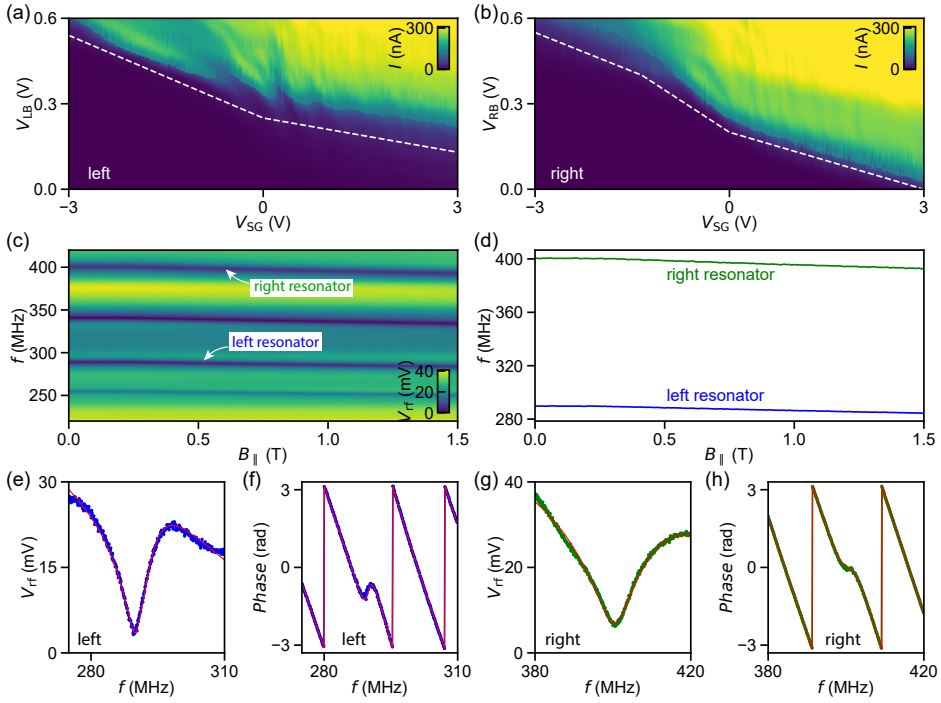

Figure 5.12: Basic characteristics of **Device 1**. **(a)** Current through the left junction, I, as a function of barrier gate voltage V_{LB} and V_{SG} at 10 mV bias voltage. **(b)** Current through the right junction, I, as a function of barrier gate voltage V_{RB} and V_{SG} at 10 mV bias voltage. In Fig. 5.3 in the main text, the super gate is swept while compensating the two barrier gate voltages by following the white dashed lines in **(a)** and **(b)**. **(c)** Dependence of the resonators on parallel magnetic field. Four resonators are visible in this panel, of which two are bonded to **Device 1**. **(d)** Extracted resonant frequencies of the left and right resonators as a function of $B_\parallel$. **(e)-(h)** Resonator reflection spectra (blue and green solid dots) and corresponding fitted curves (red solid lines) for two resonators based on a hanger superconducting resonator model [56]. **(e)** and **(f)** show respectively the amplitude and phase of the left resonator. **(g)** and **(h)** show respectively the amplitude and phase of the right resonator. Internal quality factors of the two resonators, Q_L and Q_R, are fitted to be ~ 47 and ~ 28, respectively.

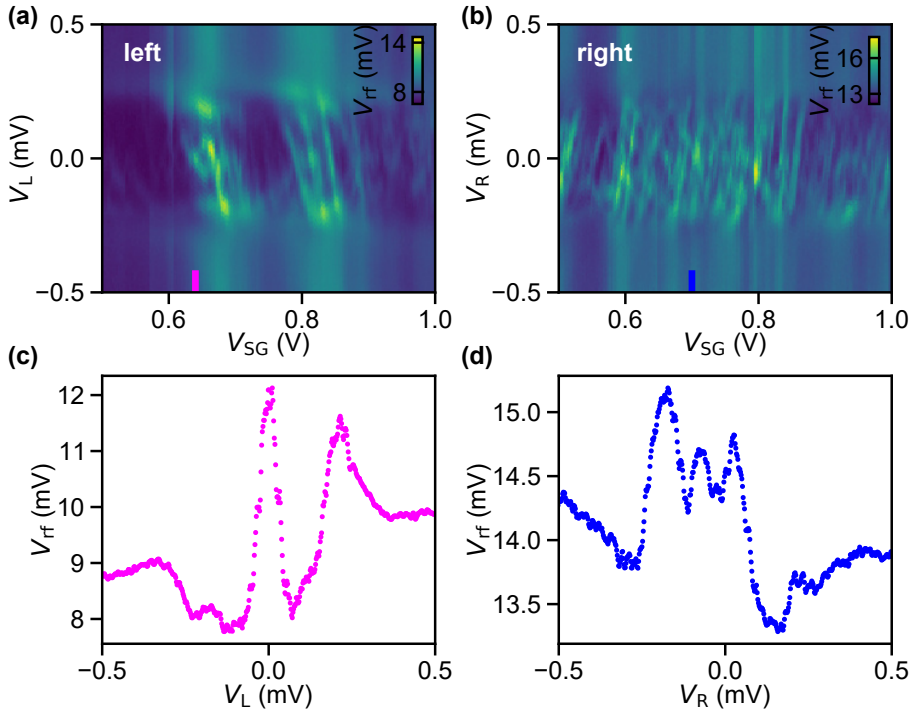

Figure 5.13: Tunneling spectroscopy results at relatively positive super gate voltage (**Device 1**). **(a)** Tunneling spectroscopy of the left junction at $B_{\parallel}$=0.3 T. A line cut is made at V_{SG}=0.64 V and the data is shown in **(c)**. **(b)** Tunneling spectroscopy of the right junction at $B_{\parallel}$=0.3 T. A line cut is made at V_{SG}=0.7 V and the data is shown in **(d)**. The sub-gap features in such a super gate voltage range is more crowded as compared with the results at less positive super gate value (Fig. 5.15).

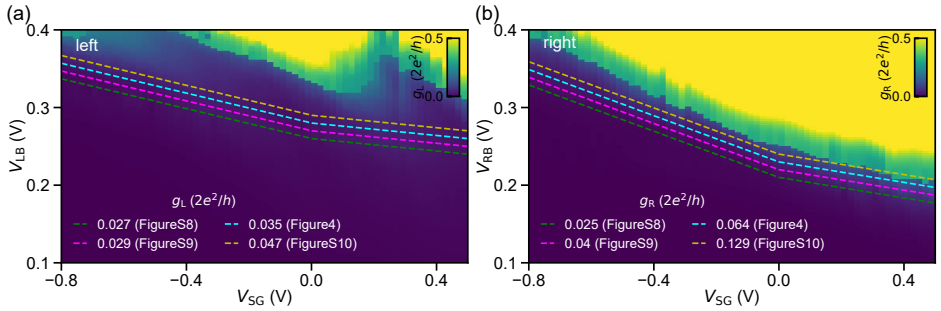

Figure 5.14: Conductance measurements of the two junctions in **Device 1**, together with gate-compensation lines used in tunneling spectroscopy measurements. **(a)** Calculated conductance of the left junction, g_L, from Fig. 5.12(a) **(b)** Calculated conductance of the right junction, g_R, from Fig. 5.12(b). In **(a)** and **(b)**, dashed lines with different colors illustrate how gates are swept during corresponding measurements. Data is taken from the data set of Fig.3 in the main text.

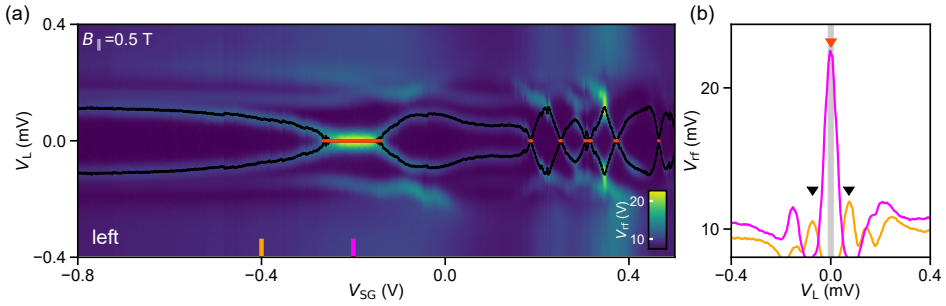

Figure 5.15: Example of the energy extraction for LESs and ZESs. Data from **Device 1**. **(a)** Tunneling spectroscopy versus super gate voltage at $B_\parallel$ = 0.5 T, taken from the data set of Fig. 5.4 in the main text. Black and red dots mark the extracted LESs and ZESs, respectively. Line cuts, taken at V_{SG} = −0.4 V (orange) and V_{SG} = −0.2 V (magenta), are shown in **(b)**. Black triangles mark the position of the extracted LESs, whilst red triangle marks the position of the extracted ZESs. The grey area displays the bias window from −10 μV to 10 μV used for the extraction of ZESs. The concrete procedure of extracting LESs is (1) The data of V_{rf} vs bias is smoothed with the function "savgol_filter", which belongs to a python package "scipy.signal"; (2) All peaks are found from the smoothed data with the function "find_peaks", which also belongs to the python package "scipy.signal"; (3) The peak with minimum absolute energy is considered as the LES.

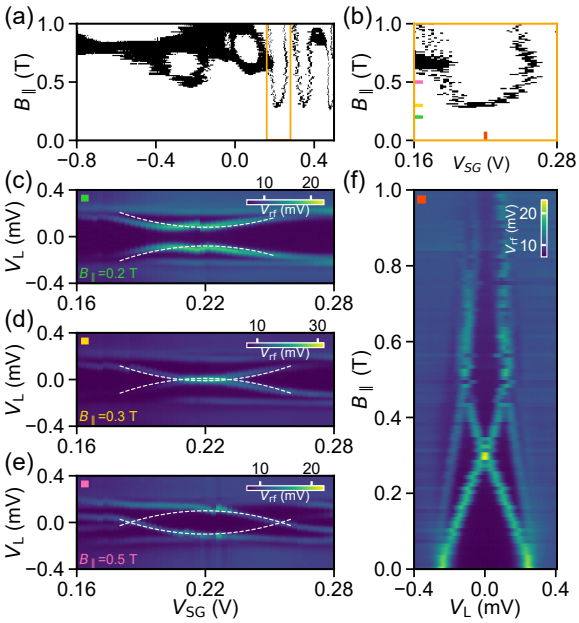

Figure 5.16: Another example of parabolic patterns in ZES diagrams for **Device 1**. **(a)** ZES diagram for the left junction (same as Fig. 5.4(g) in the main text). The region marked by the orange rectangle is shown in **(b)**. Three line cuts are made at different magnetic fields and corresponding tunneling spectroscopy data is shown in **(c)-(e)**. White dashed lines serve as a guide to the eye for a pair of sub-gap levels. **(f)** Evolution of sub-gap levels in magnetic field at V_{SG} = 0.22 V. Together with Fig. 5.6 in the main text, we show that parabolic patterns in ZES diagrams, consistent with onset of a topological phase in short hybrid nanowires [42], can be fully explained by Zeeman-driven Andreev level splitting in a quantum dot–superconducting lead architecture [43].

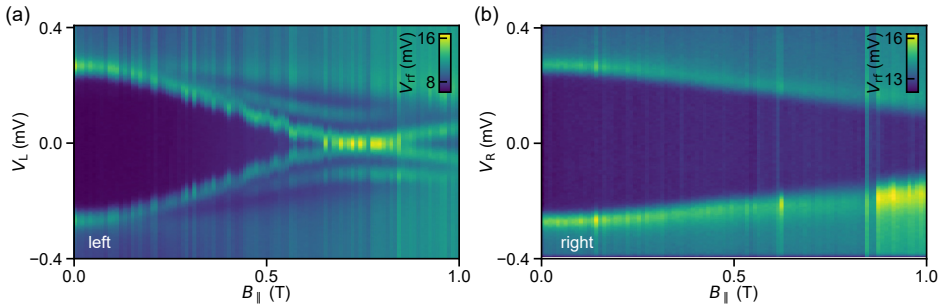

Figure 5.17: Tunneling spectroscopy results at $V_{SG} = -0.5$ V for the left **(a)** and right **(b)** junction. For the left side, sub-gap states are present whilst they are absent for the right side. Data is taken from the data set of Fig. 5.4 in the main text (**Device 1**).

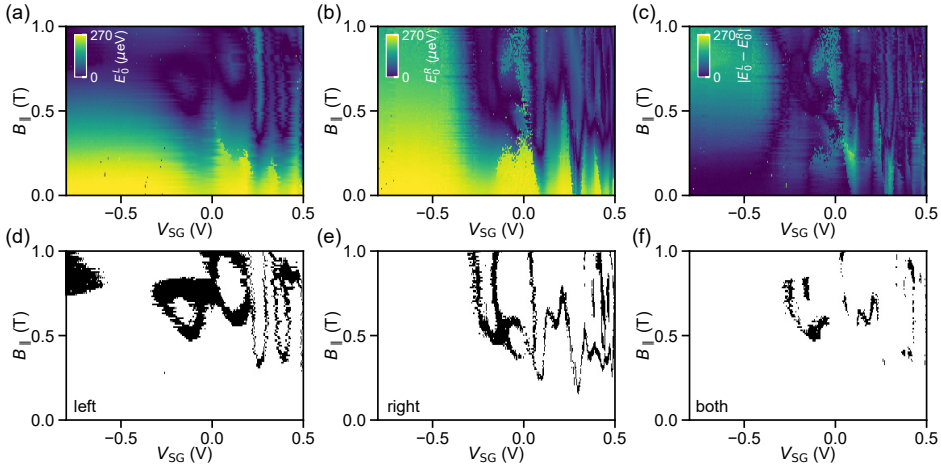

Figure 5.18: LES and ZES diagrams for $g_L \sim 0.027\ G_0$, $g_R \sim 0.025\ G_0$. Data comes from **Device 1**. Gates are swept by following the green dashed lines in Fig. 5.14. Compared with Fig. 5.4 in the main text, both barrier gates are shifted to more negative value by 20 mV, in order to confirm the stability of the LESs and ZESs against varying tunneling transparency. **(a)** LES diagram in V_{SG}–$B_\parallel$ space on the left end of the hybrid nanowire. **(b)** LES diagram in V_{SG}–$B_\parallel$ space on the right end of the hybrid nanowire. **(c)** Energy difference between LESs probed on the two sides. **(d)** and **(e)** ZES diagrams for the left and right junctions, respectively. **(f)** Diagram of coexisting ZESs on both ends. In **(a)-(f)**, each panel includes 522×101 pixels. The data set is taken in ~35 hours.

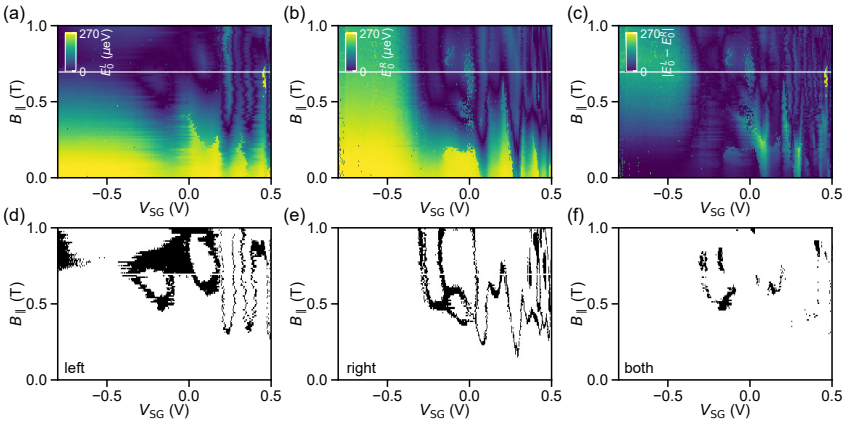

Figure 5.19: LES and ZES diagrams for $g_L \sim 0.029\, G_0$, $g_R \sim 0.04\, G_0$. Data comes from **Device 1**. Gates are swept by following the magenta dashed lines in Fig. 5.14. Compared with Fig. 5.4 in the main text, both barrier gates are shifted to more negative value by 10 mV, in order to confirm the stability of the LESs and ZESs against varying tunneling transparency. **(a)** LES diagram in super gate-magnetic field space on the left end of the hybrid nanowire. **(b)** LES diagram in super gate-magnetic field space on the right end of the hybrid nanowire. **(c)** Energy difference between ZESs probed on the two sides. **(d)** and **(e)** ZES diagrams for the left and right junctions, respectively. **(f)** Diagram of coexistent ZESs on both ends. In **(a)-(f)**, each panel includes 522×100 pixels. The dataset is taken in ~34.5 hours. Note that compared with data sets in Fig. 5.4 in the main text, Fig. 5.18 and Fig. 5.20, in this data set the results at $B_\parallel = 0.69$ T was not taken because of technical errors. In **(a)-(c)**, data at $B_\parallel = 0.69$ T is set to NaN and panels display a white line at this field value.

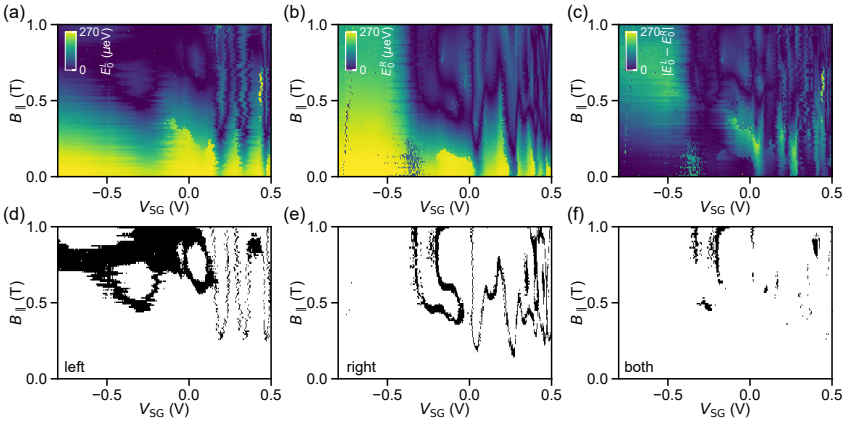

Figure 5.20: LES and ZES diagrams for $g_R \sim 0.047\, G_0$, $g_R \sim 0.129\, G_0$. Data comes from **Device 1**. Gates are swept by following the yellow dashed lines in Fig. 5.14. Compared with Fig. 5.4 in the main text, both barrier gates are shifted to more positive value by 10 mV, in order to confirm the stability of the LESs and ZESs against varying tunneling transparency. **(a)** LES diagram in super gate-magnetic field space on the left end of the hybrid nanowire. **(b)** LES diagram in super gate-magnetic field space on the right end of the hybrid nanowire. **(c)** Energy difference between ZESs probed on both ends. **(d)** and **(e)** ZES diagrams for left and right junctions, respectively. **(f)** Diagram of coexistent ZESs on both ends. In **(a)-(f)**, each panel includes 522×101 pixels. The data set is taken in ~35 hours.

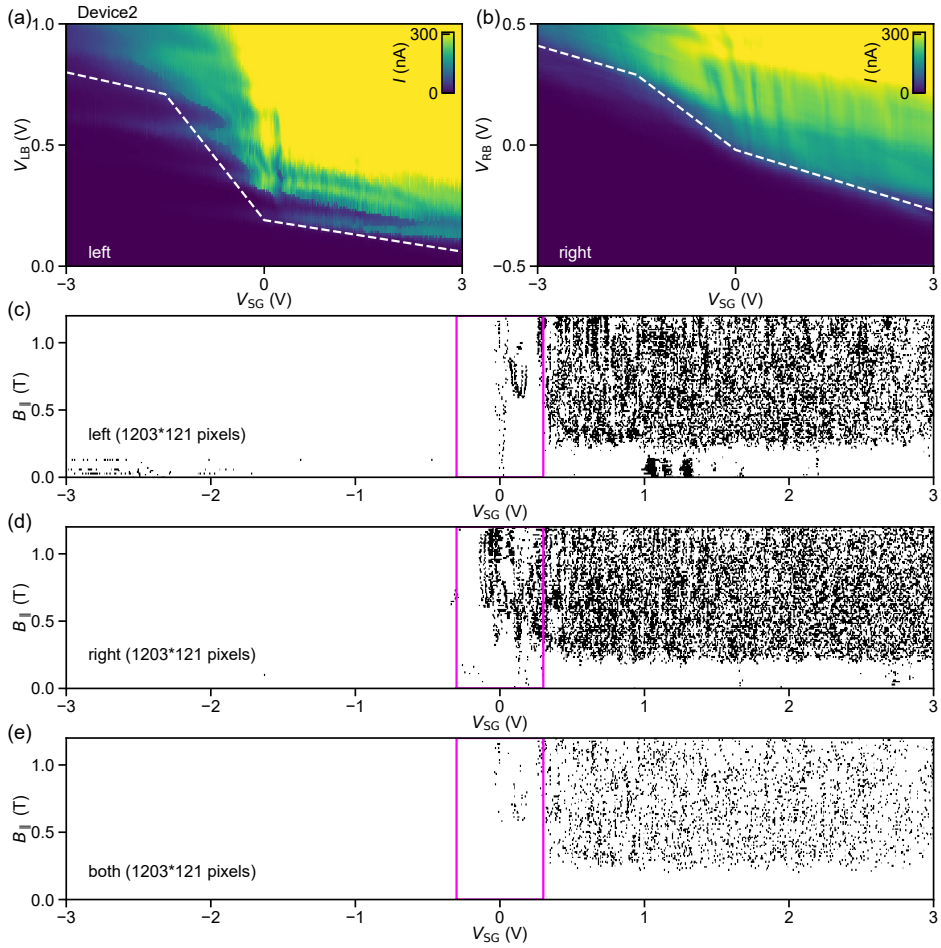

Figure 5.21: Cross-talk properties of **Device 2** and large-scale ZES diagrams. **(a)** Current through the left junction, I, as a function of barrier gate voltage V_{LB} and V_{SG} at 10 mV bias voltage. **(b)** Current through the right junction, I, as a function of barrier gate voltage V_{RB} and V_{SG} at 10 mV bias voltage. ZES diagrams in parameter space of super gate voltage V_{SG} and parallel magnetic field $B_\parallel$ for the left junction **(c)**, right junction **(d)**, and coexistence in both junctions **(e)**. Gates are scanned by following the white dashed lines in **(a)** and **(b)**. In **(c)-(e)**, each panel includes 1203×121 pixels. The data set is taken in ~ 96.8 hours. Similar as Fig. 5.3 in the main text (**Device 1**), three distinct regimes along V_{SG} can be identified and the intermediate supergate regime (marked by magenta rectangles) is further investigated in Fig. 5.22.

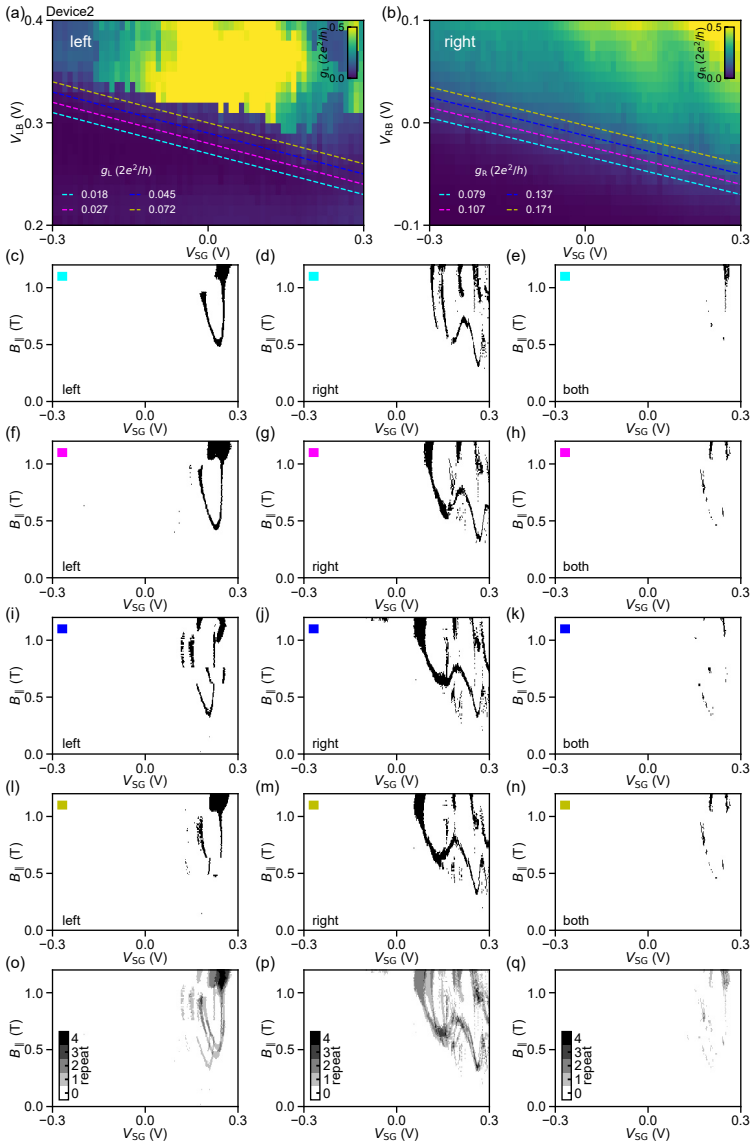

Figure 5.22: Conductance measurements of the two junctions in **Device 2**, together with gate-compensation lines used in tunneling spectroscopy measurements. **(a)** Calculated conductance of the left junction, g_L, from Fig. 5.21(a) **(b)** Calculated conductance of the right junction, g_R, from Fig. 5.21(b). In **(a)** and **(b)**, dashed lines with different colors illustrate how gates are swept during corresponding measurements. The dashed lines have a difference of 10 mV in each barrier gate with respect to each other. **(c)**-**(n)** ZES diagrams at various barrier gate settings. **(c)**, **(f)**, **(i)**, and **(l)** show results for the left junction. **(d)**, **(g)**, **(j)**, and **(m)** show results for right junction. **(e)**, **(h)**, **(k)**, and **(n)** show the diagram of coexistent ZESs on both sides. **(c)**-**(e)** are taken at $g_L \sim 0.018\ G_0$ and $g_R \sim 0.079\ G_0$, marked with a cyan color. **(f)**-**(h)** are taken at $g_L \sim 0.027\ G_0$ and $g_R \sim 0.107\ G_0$, marked with a magenta color. **(i)**-**(k)** are taken at $g_L \sim 0.045\ G_0$ and $g_R \sim 0.137\ G_0$, marked with a blue color. **(l)**-**(n)** are taken at $g_L \sim 0.072\ G_0$ and $g_R \sim 0.171\ G_0$, marked with a yellow color. From these data sets, overlapping ZES diagrams are constructed which are shown for the left **(o)** and right **(p)** junction, as well as coexistence in both junctions **(q)**. In **(c)**-**(n)**, each panel includes 601×121 pixels. The total data set is taken in ~ 193.6 hours.

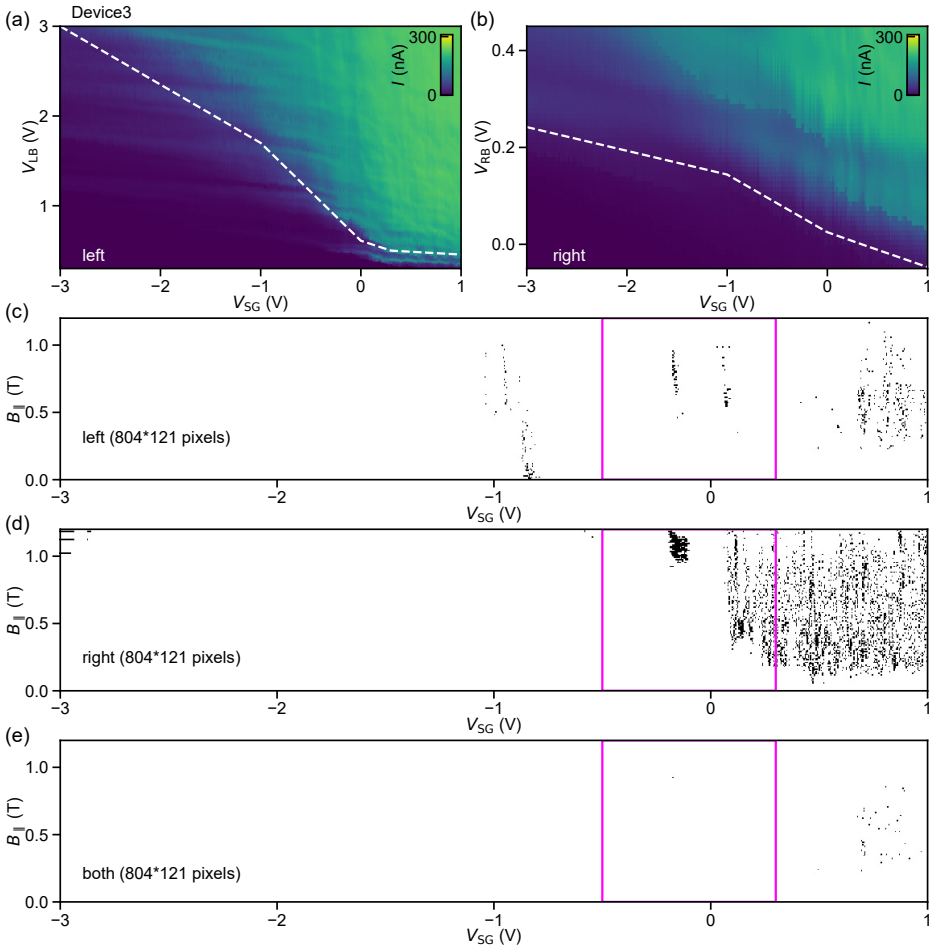

Figure 5.23: Cross-talk properties of **Device 3** and large-scale ZES diagrams. **(a)** Current through the left junction, I, as a function of barrier gate voltage V_{LB} and V_{SG} at 5 mV bias voltage. **(b)** Current through the right junction, I, as a function of barrier gate voltage V_{RB} and V_{SG} at 5 mV bias voltage. ZES diagrams in parameter space of super gate voltage V_{SG} and parallel magnetic field $B_{\parallel}$ for the left junction **(c)**, right junction **(d)**, and their intersection **(e)**. Gates are scanned by following the white dashed lines in **(a)** and **(b)**. In **(c)-(e)**, each panel includes 804×121 pixels. The data set is taken in ~ 42.3 hours. Similar as Fig. 5.3 in the main text (**Device 1**) and Fig. 5.21 (**Device 2**), there are three different regimes along V_{SG} for right side, while left side does not have such clear characteristics. Nonethless, we still focus on similar intermediate super gate region (within magenta rectangles) and do further investigation in Fig. 5.24.

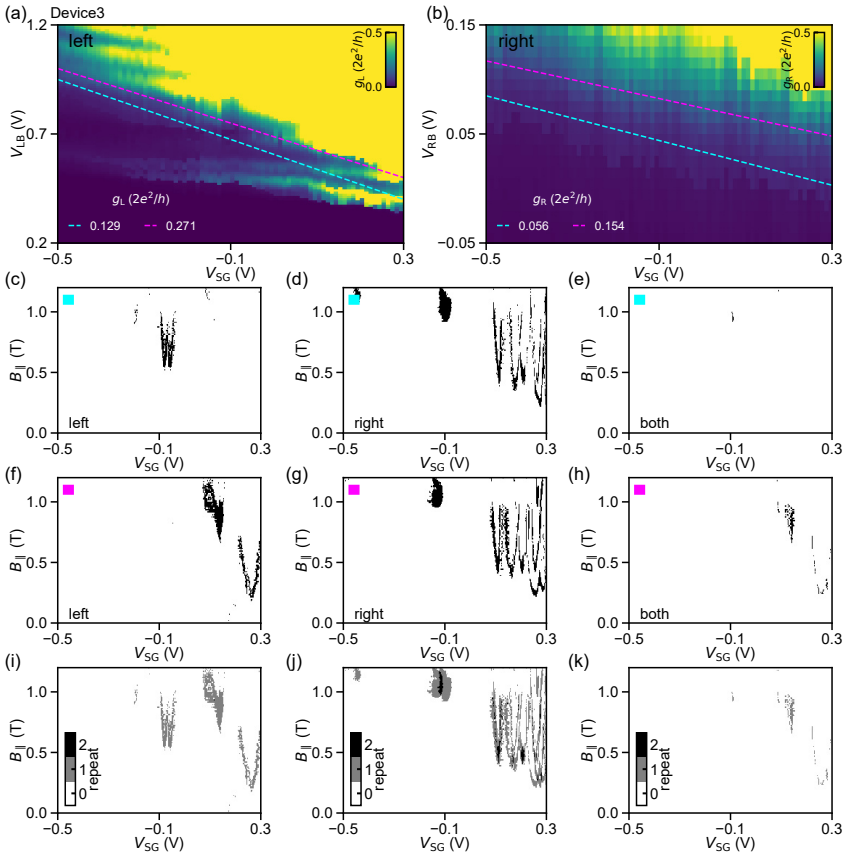

Figure 5.24: Conductance measurements of the two junctions in **Device 3**, together with gate-compensation lines used in tunneling spectroscopy measurements. **(a)** Calculated conductance of the left junction, g_L, from Fig. 5.23(a) **(b)** Calculated conductance of the right junction, g_R, from Fig. 5.23(b). In **(a)** and **(b)**, dashed lines with different colors illustrate how gates are swept during corresponding measurements. **(c)-(h)** ZES diagrams at various barrier gate settings. **(c)** and **(f)** show results for the left junction. **(d)** and **(g)** show results for right junction. **(e)** and **(h)** show the diagram of coexistent ZESs on both sides. **(c)-(e)** are taken at $g_L \sim 0.129\, G_0$ and $g_R \sim 0.056\, G_0$, marked with a cyan color. **(f)-(h)** are taken at $g_L \sim 0.271\, G_0$ and $g_R \sim 0.154\, G_0$, marked with a magenta color. From these data sets, overlapping ZES diagrams are constructed which are shown for the left **(i)** and right **(j)** junction, as well as coexistence in both junctions **(k)**. In **(c)-(k)**, each panel includes 601×121 pixels. The total data set is taken in ~ 83 hours. Notably, left side has dramatic changes in ZES diagrams with varying barrier gates (see **(c)** and **(f)**), while the right side just undergoes moderate changes (see **(d)** and **(g)**). The origins could be found from conductance measurement in **(a)** and **(b)**. Conductance of the left junction has quite distinct modulations along cyan and magenta dashed line, whereas for the right side conductance has similar modulations along two dashed lines.

References

[1] L. Fu and C. L. Kane, *Superconducting proximity effect and majorana fermions at the surface of a topological insulator,* Physical review letters **100**, 096407 (2008).

[2] R. M. Lutchyn, J. D. Sau, and S. D. Sarma, *Majorana fermions and a topological phase transition in semiconductor-superconductor heterostructures,* Physical review letters **105**, 077001 (2010).

[3] Y. Oreg, G. Refael, and F. Von Oppen, *Helical liquids and majorana bound states in quantum wires,* Physical review letters **105**, 177002 (2010).

[4] V. Mourik, K. Zuo, S. M. Frolov, S. Plissard, E. P. Bakkers, and L. P. Kouwenhoven, *Signatures of majorana fermions in hybrid superconductor-semiconductor nanowire devices,* Science **336**, 1003 (2012).

[5] M. Deng, C. Yu, G. Huang, M. Larsson, P. Caroff, and H. Xu, *Anomalous zero-bias conductance peak in a nb–insb nanowire–nb hybrid device,* Nano letters **12**, 6414 (2012).

[6] A. Das, Y. Ronen, Y. Most, Y. Oreg, M. Heiblum, and H. Shtrikman, *Zero-bias peaks and splitting in an al–inas nanowire topological superconductor as a signature of majorana fermions,* Nature Physics **8**, 887 (2012).

[7] H. Churchill, V. Fatemi, K. Grove-Rasmussen, M. Deng, P. Caroff, H. Xu, and C. M. Marcus, *Superconductor-nanowire devices from tunneling to the multichannel regime: Zero-bias oscillations and magnetoconductance crossover,* Physical Review B **87**, 241401 (2013).

[8] M. Deng, S. Vaitiekėnas, E. B. Hansen, J. Danon, M. Leijnse, K. Flensberg, J. Nygård, P. Krogstrup, and C. M. Marcus, *Majorana bound state in a coupled quantum-dot hybrid-nanowire system,* Science **354**, 1557 (2016).

[9] J. Chen, P. Yu, J. Stenger, M. Hocevar, D. Car, S. R. Plissard, E. P. Bakkers, T. D. Stanescu, and S. M. Frolov, *Experimental phase diagram of zero-bias conductance peaks in superconductor/semiconductor nanowire devices,* Science advances **3**, e1701476 (2017).

[10] H. Zhang, M. W. de Moor, J. D. Bommer, D. Xu, G. Wang, N. van Loo, C.-X. Liu, S. Gazibegovic, J. A. Logan, D. Car, *et al.*, *Large zero-bias peaks in insb-al hybrid semiconductor-superconductor nanowire devices,* arXiv preprint arXiv:2101.11456 (2021).

[11] S. Vaitiekėnas, G. Winkler, B. Van Heck, T. Karzig, M.-T. Deng, K. Flensberg, L. Glazman, C. Nayak, P. Krogstrup, R. Lutchyn, *et al.*, *Flux-induced topological superconductivity in full-shell nanowires,* Science **367**, eaav3392 (2020).

[12] F. Nichele, A. C. Drachmann, A. M. Whiticar, E. C. O'Farrell, H. J. Suominen, A. Fornieri, T. Wang, G. C. Gardner, C. Thomas, A. T. Hatke, *et al.*, *Scaling of majorana zero-bias conductance peaks,* Physical review letters **119**, 136803 (2017).

[13] A. Fornieri, A. M. Whiticar, F. Setiawan, E. Portolés, A. C. Drachmann, A. Keselman, S. Gronin, C. Thomas, T. Wang, R. Kallaher, *et al.*, *Evidence of topological superconductivity in planar josephson junctions,* Nature **569**, 89 (2019).

[14] H. Ren, F. Pientka, S. Hart, A. T. Pierce, M. Kosowsky, L. Lunczer, R. Schlereth, B. Scharf, E. M. Hankiewicz, L. W. Molenkamp, *et al.*, *Topological superconductivity in a phase-controlled josephson junction,* Nature **569**, 93 (2019).

[15] A. Vuik, B. Nijholt, A. R. Akhmerov, and M. Wimmer, *Reproducing topological properties with quasi-majorana states,* SciPost Physics **7**, 061 (2019).

[16] J. Liu, A. C. Potter, K. T. Law, and P. A. Lee, *Zero-bias peaks in the tunneling conductance of spin-orbit-coupled superconducting wires with and without majorana end-states,* Physical review letters **109**, 267002 (2012).

[17] H. Pan and S. D. Sarma, *Disorder effects on majorana zero modes: Kitaev chain versus semiconductor nanowire,* Physical Review B **103**, 224505 (2021).

[18] H. Pan, C.-X. Liu, M. Wimmer, and S. D. Sarma, *Quantized and unquantized zero-bias tunneling conductance peaks in majorana nanowires: Conductance below and above 2 e 2/h,* Physical Review B **103**, 214502 (2021).

[19] H. Pan and S. D. Sarma, *Crossover between trivial zero modes in majorana nanowires,* arXiv preprint arXiv:2102.07296 (2021).

[20] S. D. Sarma and H. Pan, *Disorder-induced zero-bias peaks in majorana nanowires,* Physical Review B **103**, 195158 (2021).

[21] M. Valentini, F. Peñaranda, A. Hofmann, M. Brauns, R. Hauschild, P. Krogstrup, P. San-Jose, E. Prada, R. Aguado, and G. Katsaros, *Nontopological zero-bias peaks in full-shell nanowires induced by flux-tunable andreev states,* Science **373**, 82 (2021).

[22] J. Liu, F.-C. Zhang, and K. Law, *Majorana fermion induced nonlocal current correlations in spin-orbit coupled superconducting wires,* Physical Review B **88**, 064509 (2013).

[23] H.-F. Lü, H.-Z. Lu, and S.-Q. Shen, *Current noise cross correlation mediated by majorana bound states,* Physical Review B **90**, 195404 (2014).

[24] Y.-H. Lai, J. D. Sau, and S. D. Sarma, *Presence versus absence of end-to-end nonlocal conductance correlations in majorana nanowires: Majorana bound states versus andreev bound states,* Physical Review B **100**, 045302 (2019).

[25] G. Anselmetti, E. Martinez, G. Ménard, D. Puglia, F. Malinowski, J. Lee, S. Choi, M. Pendharkar, C. Palmstrøm, C. Marcus, *et al.*, *End-to-end correlated subgap states in hybrid nanowires,* Physical Review B **100**, 205412 (2019).

[26] A. E. Antipov, A. Bargerbos, G. W. Winkler, B. Bauer, E. Rossi, and R. M. Lutchyn, *Effects of gate-induced electric fields on semiconductor majorana nanowires,* Physical Review X **8**, 031041 (2018).

[27] D. I. Pikulin, B. van Heck, T. Karzig, E. A. Martinez, B. Nijholt, T. Laeven, G. W. Winkler, J. D. Watson, S. Heedt, M. Temurhan, *et al.*, *Protocol to identify a topological superconducting phase in a three-terminal device,* arXiv preprint arXiv:2103.12217 (2021).

[28] A. Wallraff, D. I. Schuster, A. Blais, L. Frunzio, R.-S. Huang, J. Majer, S. Kumar, S. M. Girvin, and R. J. Schoelkopf, *Strong coupling of a single photon to a superconducting qubit using circuit quantum electrodynamics,* Nature **431**, 162 (2004).

[29] J. Hornibrook, J. Colless, A. Mahoney, X. Croot, S. Blanvillain, H. Lu, A. Gossard, and D. Reilly, *Frequency multiplexing for readout of spin qubits,* Applied Physics Letters **104**, 103108 (2014).

[30] D. Razmadze, D. Sabonis, F. K. Malinowski, G. C. Ménard, S. Pauka, H. Nguyen, D. M. van Zanten, C. Eoin, J. Suter, P. Krogstrup, *et al.*, *Radio-frequency methods for majorana-based quantum devices: Fast charge sensing and phase-diagram mapping,* Physical Review Applied **11**, 064011 (2019).

[31] J. Van Veen, D. De Jong, L. Han, C. Prosko, P. Krogstrup, J. D. Watson, L. P. Kouwenhoven, and W. Pfaff, *Revealing charge-tunneling processes between a quantum dot and a superconducting island through gate sensing,* Physical Review B **100**, 174508 (2019).

[32] G. Badawy, S. Gazibegovic, F. Borsoi, S. Heedt, C.-A. Wang, S. Koelling, M. A. Verheijen, L. P. Kouwenhoven, and E. P. Bakkers, *High mobility stemless insb nanowires,* Nano letters **19**, 3575 (2019).

[33] S. Heedt, M. Quintero-Pérez, F. Borsoi, A. Fursina, N. van Loo, G. P. Mazur, M. P. Nowak, M. Ammerlaan, K. Li, S. Korneychuk, *et al.*, *Shadow-wall lithography of ballistic superconductor–semiconductor quantum devices,* Nature Communications **12**, 4914 (2021).

[34] F. Borsoi, G. P. Mazur, N. van Loo, M. P. Nowak, L. Bourdet, K. Li, S. Korneychuk, A. Fursina, J.-Y. Wang, V. Levajac, *et al.*, *Single-shot fabrication of semiconducting–superconducting nanowire devices,* Advanced Functional Materials **31**, 2102388 (2021).

[35] R. Schoelkopf, P. Wahlgren, A. Kozhevnikov, P. Delsing, and D. Prober, *The radio-frequency single-electron transistor (rf-set): A fast and ultrasensitive electrometer,* science **280**, 1238 (1998).

[36] D. Reilly, C. Marcus, M. Hanson, and A. Gossard, *Fast single-charge sensing with a rf quantum point contact,* Applied Physics Letters **91**, 162101 (2007).

[37] J. Stehlik, Y.-Y. Liu, C. Quintana, C. Eichler, T. Hartke, and J. R. Petta, *Fast charge sensing of a cavity-coupled double quantum dot using a josephson parametric amplifier,* Physical Review Applied **4**, 014018 (2015).

[38] J. Shen, G. Winkler, F. Borsoi, S. Heedt, V. Levajac, J.-Y. Wang, D. van Driel, D. Bouman, S. Gazibegovic, R. O. H. Veld, *et al.*, *Full parity phase diagram of a proximitized nanowire island,* Physical Review B **104**, 045422 (2021).

[39] C. Reeg, D. Loss, and J. Klinovaja, *Metallization of a rashba wire by a superconducting layer in the strong-proximity regime,* Physical Review B **97**, 165425 (2018).

[40] A. E. Mikkelsen, P. Kotetes, P. Krogstrup, and K. Flensberg, *Hybridization at superconductor-semiconductor interfaces,* Physical Review X **8**, 031040 (2018).

[41] C. Reeg, O. Dmytruk, D. Chevallier, D. Loss, and J. Klinovaja, *Zero-energy andreev bound states from quantum dots in proximitized rashba nanowires,* Physical Review B **98**, 245407 (2018).

[42] S. D. Sarma, J. D. Sau, and T. D. Stanescu, *Splitting of the zero-bias conductance peak as smoking gun evidence for the existence of the majorana mode in a superconductor-semiconductor nanowire,* Physical Review B **86**, 220506 (2012).

[43] E. J. Lee, X. Jiang, M. Houzet, R. Aguado, C. M. Lieber, and S. De Franceschi, *Spin-resolved andreev levels and parity crossings in hybrid superconductor–semiconductor nanostructures,* Nature nanotechnology **9**, 79 (2014).

[44] M. W. De Moor, J. D. Bommer, D. Xu, G. W. Winkler, A. E. Antipov, A. Bargerbos, G. Wang, N. v. Loo, R. L. Op het Veld, S. Gazibegovic, *et al.*, *Electric field tunable superconductor-semiconductor coupling in majorana nanowires,* New Journal of Physics **20**, 103049 (2018).

[45] R. C. Dynes, V. Narayanamurti, and J. P. Garno, *Direct measurement of quasiparticle-lifetime broadening in a strong-coupled superconductor,* Physical Review Letters **41**, 1509 (1978).

[46] S. Vaitiekėnas, M.-T. Deng, J. Nygård, P. Krogstrup, and C. Marcus, *Effective g factor of subgap states in hybrid nanowires,* Physical review letters **121**, 037703 (2018).

[47] O. Dmytruk, D. Chevallier, D. Loss, and J. Klinovaja, *Renormalization of the quantum dot g-factor in superconducting rashba nanowires,* Physical Review B **98**, 165403 (2018).

[48] C.-X. Liu, J. D. Sau, T. D. Stanescu, and S. D. Sarma, *Andreev bound states versus majorana bound states in quantum dot-nanowire-superconductor hybrid structures: Trivial versus topological zero-bias conductance peaks,* Physical Review B **96**, 075161 (2017).

[49] R. Hess, H. F. Legg, D. Loss, and J. Klinovaja, *Local and nonlocal quantum transport due to andreev bound states in finite rashba nanowires with superconducting and normal sections,* Physical Review B **104**, 075405 (2021).

[50] J. Shabani, M. Kjaergaard, H. J. Suominen, Y. Kim, F. Nichele, K. Pakrouski, T. Stankevic, R. M. Lutchyn, P. Krogstrup, R. Feidenhans'l, S. Kraemer, C. Nayak, M. Troyer, C. M. Marcus, and C. J. Palmstrøm, *Two-dimensional epitaxial superconductor-semiconductor heterostructures: A platform for topological superconducting networks,* Phys. Rev. B **93**, 155402 (2016).

[51] M. Pendharkar, B. Zhang, H. Wu, A. Zarassi, P. Zhang, C. Dempsey, J. Lee, S. Harrington, G. Badawy, S. Gazibegovic, *et al.*, *Parity-preserving and magnetic field–resilient superconductivity in insb nanowires with sn shells,* Science **372**, 508 (2021).

[52] T. Kanne, M. Marnauza, D. Olsteins, D. J. Carrad, J. E. Sestoft, J. de Bruijckere, L. Zeng, E. Johnson, E. Olsson, K. Grove-Rasmussen, *et al.*, *Epitaxial pb on inas nanowires for quantum devices,* Nature Nanotechnology **16**, 776 (2021).

[53] T. Rosdahl, A. Vuik, M. Kjaergaard, and A. Akhmerov, *Andreev rectifier: A nonlocal conductance signature of topological phase transitions,* Physical Review B **97**, 045421 (2018).

[54] G. Ménard, G. Anselmetti, E. Martinez, D. Puglia, F. Malinowski, J. Lee, S. Choi, M. Pendharkar, C. Palmstrøm, K. Flensberg, *et al.*, *Conductance-matrix symmetries of a three-terminal hybrid device,* Physical Review Letters **124**, 036802 (2020).

[55] D. Puglia, E. Martinez, G. Ménard, A. Pöschl, S. Gronin, G. Gardner, R. Kallaher, M. Manfra, C. Marcus, A. P. Higginbotham, *et al.*, *Closing of the induced gap in a hybrid superconductor-semiconductor nanowire,* Physical Review B **103**, 235201 (2021).

[56] M. S. Khalil, M. Stoutimore, F. Wellstood, and K. Osborn, *An analysis method for asymmetric resonator transmission applied to superconducting devices,* Journal of Applied Physics **111**, 054510 (2012).

6

Spin-mixing enhanced proximity effect in aluminum-based superconductor-semiconductor hybrids

In superconducting quantum circuits, aluminum is one of the most widely used materials. It is currently also the superconductor of choice for the development of topological qubits. In this application, however, aluminum-based devices suffer from poor magnetic field compatibility. In this article, we resolve this limitation by showing that adatoms of heavy elements (e.g. platinum) increase the critical field of thin aluminum films by more than a factor of two. Using tunnel junctions, we show that the increased field resilience originates from spin-orbit scattering introduced by Pt. We exploit this property in the context of the superconducting proximity effect in semiconductor-superconductor hybrids, where we show that InSb nanowires strongly coupled to Al/Pt films can maintain superconductivity up to 7 T. The two-electron charging effect, a fundamental requirement for topological quantum computation, is shown to be robust against the presence of heavy adatoms. Additionally, we use non-local spectroscopy in a three-terminal geometry to probe the bulk of hybrid devices, showing that it remains free of sub-gap states. Finally, we demonstrate that semiconductor states which are proximitized by Al/Pt films maintain their ability to Zeeman-split in an applied magnetic field. Combined with the chemical stability and well-known fabrication routes of aluminum, Al/Pt emerges as the natural successor to Al-based systems and is a compelling alternative to other superconductors, whenever high-field resilience is required.

This chapter has been published as *Spin-mixing enhanced proximity effect in aluminum-based superconductor-semiconductor hybrids*, G.P. Mazur[†], **N. van Loo**[†], J.-Y. Wang, T. Dvir, G. Wang, A. Khindanov, S. Korneychuk, F. Borsoi, R.C. Dekker, G. Badawy, P. Vinke, S. Gazibegovic, E.P.A.M. Bakkers, M. Quintero-Pérez, S. Heedt and L.P. Kouwenhoven in Advanced Materials 2022, 34, 2202034. [†] These authors contributed equally to this work.

6.1 Introduction

Topological superconductivity can arise in hybrid material stacks containing a conventional superconductor and a semiconductor with strong Rashba spin-orbit coupling [1, 2]. Narrow-gap semiconductors with a large g-factor and low carrier density (such as InAs and InSb) are most commonly used, either as 1D nanowires [3] or 2D electron gases [4]. The first generation of semiconductor-superconductor hybrids was made using Nb [5] and NbTiN [6] as the superconductor. While these materials offer a large superconducting gap and resilience to high magnetic fields, the hybrids suffered from a finite in-gap conductance (often described as "soft-gap"). In addition, Nb-based hybrids have not been shown to host parity-conserving transport - a key ingredient for the development of topological qubits [7]. These drawbacks remained even after substantial improvements of the fabrication, such as epitaxial growth of the superconductor [8].

In the meantime, aluminum has emerged as the material of choice. Thin shells made of this metal combined with an oxide-free interface result in clean electronic transport [9, 10]. This includes suppressed sub-gap tunneling conductance (hard induced gap) and parity-conserving transport [11], which enables the search for topological superconductivity. For a topological phase to emerge, the minimal condition states that the Zeeman energy $V_Z = g\mu_B B$ must be larger than the induced superconducting gap Δ, where g is the Landé g-factor, μ_B is the Bohr magneton and B is the applied magnetic field. It was demonstrated recently that the properties of the semiconductor, such as spin-orbit coupling and g-factor, are renormalized by the presence of a proximitizing metal [12, 13]. As a result, stronger magnetic fields than initially anticipated are required to close and reopen the induced superconducting gap [14]. Typical aluminum-based hybrids, however, have a zero-field superconducting gap Δ_0 ranging from 200 to 300 μeV [6], which results in poor field compatibility. This has fueled the search for alternative superconducting systems, with recent works reporting superconductivity and parity-conserving transport in InSb/Sn [15], InAs/Pb [16, 17] and InAs/In [18] hybrids. These superconductors offer higher field compatibility than aluminum, yet they bring different challenges such as chemical instability and fabrication constraints [19, 20]. To avoid these constraints, in this work we present a different approach by eliminating the main drawback of aluminum: its poor resilience against magnetic fields.

For a Bardeen-Cooper-Schrieffer (BCS) type superconductor like aluminum, there are two dominant mechanisms which quench superconductivity in a finite magnetic field. The first of these is orbital depairing, which results from the cyclotron motion of conduction electrons due to the magnetic field. If the superconductor is grown as a thin film, this mechanism can be suppressed when the field is applied in the plane of the film. For light elements such as Al, there is a second contribution arising from spin physics. Once the magnetic field reaches a certain value, the paramagnetic ground state becomes energetically favourable. This results in a first-order phase transition into the normal state. The field for which this happens is known as the Chandrasekhar-Clogston [21, 22] or Pauli limit, and is given by $B_P = \Delta_0/(\sqrt{2}\mu_B)$. In addition, the quasiparticle excitation spectrum spin-splits upon applying a magnetic field. In their seminal experiment [23], Tedrow and Meservey demonstrate that Zeeman splitting can be quenched and eventually suppressed completely through the addition of heavy metal impurities, such as platinum (Pt). These

heavy atoms introduce spin-orbit scattering, which prevents spins from being polarized by an external magnetic field. As a result, superconductors made of lightweight elements can reach unprecedentedly high critical fields. This has straightforward applications in the field of semiconductor-superconductor hybrids, where large Zeeman energies are a necessary condition for achieving a topological superconducting phase.

6.2 Al/Pt thin films and tunnel junctions

We begin this study by evaluating the properties of aluminum films with a thickness of 6 nm, coated with varying amounts of platinum. We define the platinum thickness d_{Pt} as measured by the quartz balance in the deposition chamber (For details of the calibration see section 6.7.1 of the supporting information). Figure 6.1 presents the superconducting transitions of Al/Pt films as a function of temperature (Fig. 6.1a) and in-plane magnetic field (Fig. 6.1b). Importantly, the addition of Pt does not affect the shape and sharpness of the superconducting transitions, which indicates that the films do not become strongly disordered or inhomogeneous [24]. The bare aluminum film has a critical temperature T_c = 1.79 K and in-plane critical field B_c = 2.6 T. Upon the addition of platinum, the critical field is increased above the bare aluminum's Chandrasekhar-Clogston limit already

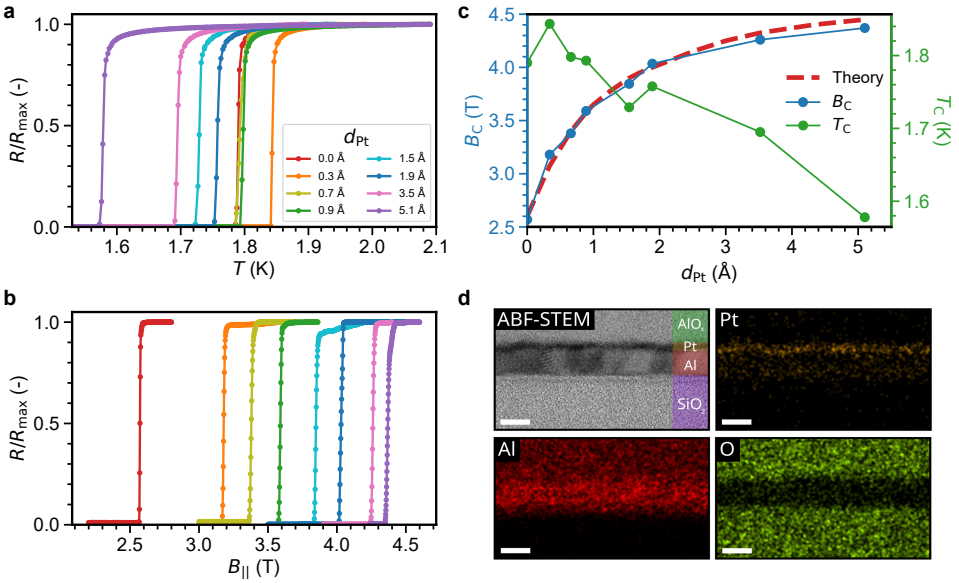

Figure 6.1: **Properties of Al/Pt thin films.** Four-point measurements of resistance R normalized to its value in the normal state R_N as a function of temperature (**a**) and in-plane magnetic field (**b**). Measurements have been performed for 6 nm thick aluminum films with varying amount of platinum d_{Pt}. **c.** In-plane critical magnetic field and temperature as a function of Pt thickness, together with the predicted critical field from theory calculations. **d.** Annular bright field scanning-tunneling electron micrograph and energy-dispersive X-ray images of the Al film with 1.89 Å of Pt. The thin layer of platinum (orange) is visible on top of aluminum film (red). The film is grown on top of amorphous SiO_2 and amorphous AlO_x on top of the film serves as the capping layer. Scale bars are 5 nm.

for $d_{Pt} \approx 1$ Å, while leaving T_c unaffected. In agreement with previous studies on Al/Pt bilayers [23], the critical field starts to saturate for $d_{Pt} \approx 2$ Å and increases only by an additional 300 mT for $d_{Pt} \approx 5.1$ Å (see Fig. 6.1c). At these thicknesses, however, T_c starts to decrease as a result of the inverse proximity effect, as shown for Au/Be bilayers [25]. Our theoretical model based on the Usadel equation (see section 6.7.3 of the supporting information) captures the increase of B_c as a direct result of including spin-orbit scattering (Fig. 6.1c). The calculated spin-orbit scattering energies increase linearly with d_{Pt}, in agreement with previous experiments [23]. In addition, we perform a structural analysis of the films. Fig. 6.1d presents the cross-section of an Al/Pt film with $d_{Pt} \approx 1.9$ Å, which reveals the poly-crystalline structure of the Al. The results of electron energy loss spectroscopy (EELS) performed on the studied samples indicate that aluminum and platinum do not form an alloy, in agreement with the bulk phase diagram [26].

Furthermore, we investigate the impact of Pt atoms on the Al quasiparticle density of states through normal-metal/insulator/superconductor (NIS) tunneling measurements. A

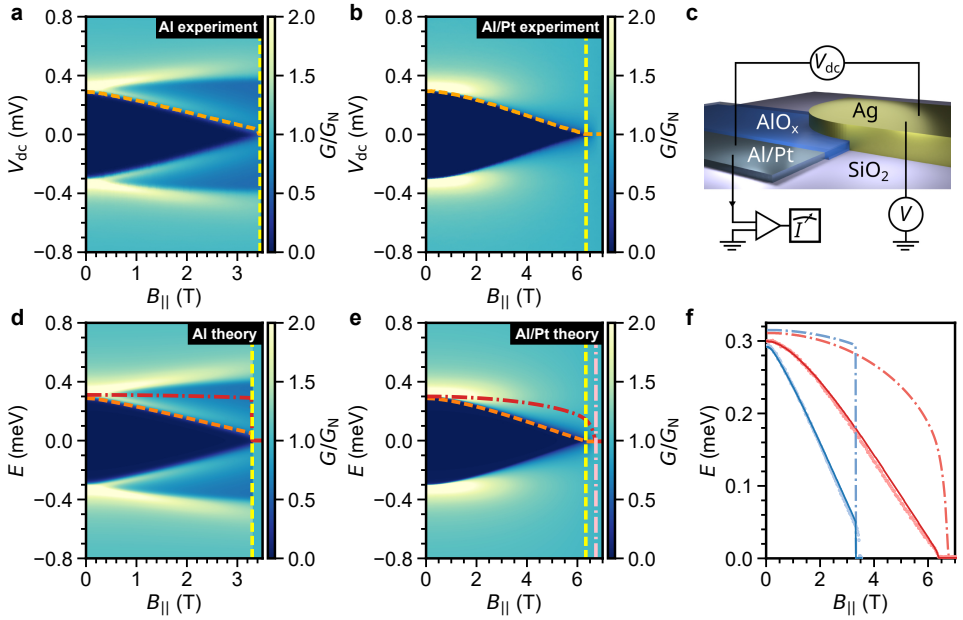

Figure 6.2: **Conductance spectroscopy on Al and Al/Pt NIS tunnel junctions. a.** Experimental tunneling conductance of a ~ 4.5 nm Al tunnel junction. **b.** Experimental tunneling conductance of a ~ 4.5 nm Al + 1.9 Å Pt tunnel junction. **c.** Schematic and measurement circuit of a NIS tunnel junction. The tunnel barrier is formed by the AlO_x layer between the Al/Pt and Ag electrodes. **d.** Tunneling conductance from theory calculations of the Al tunnel junction. **e.** Tunneling conductance from theory calculations of the Al/Pt tunnel junction. The dashed orange lines present the energy gap E_g. The order parameter Δ which is extracted from theory is presented by dashed red lines. Dashed yellow lines show the magnetic field B_{c1} for which the energy gap is closed, and the dashed pink lines indicate the magnetic field B_{c2} for which the order parameter is calculated to vanish. **f.** Overview of the extracted energy gap from experiments (dots), the predicted energy gap from theory (solid line) and the corresponding order parameter (dash-dotted line) of the Al (blue) and Al/Pt (red) films.

schematic illustration together with the used measurement circuit for these experiments is shown in Figure 6.2c. Further details on the fabrication and measurements can be found in section 6.7.2 of the supporting information. For the aluminum film, we observe a Zeeman splitting of the quasiparticle coherence peaks (Fig. 6.2a). At an in-plane magnetic field of $B_{\parallel} = 3.45\,\mathrm{T}$, the film undergoes a first-order phase transition to the normal state. Our theoretical model reproduces these two key features (Fig. 6.2d), where the first-order transition is reflected in an abrupt collapse of the order parameter. The critical field extracted from the model is 200 mT smaller than the experimentally measured value. This discrepancy between theory and experiment can be explained by the hysteretic behavior of the order parameter near the transition [27] (see Fig. 6.8 in the supporting information). A metastable superconducting state can persist for magnetic fields slightly above the calculated critical value.

For the Al/Pt film with $d_{\mathrm{Pt}} = 1.9\,\text{Å}$, Zeeman splitting is not observed. Instead, the film undergoes a second-order phase transition at $B_{\parallel} = 6.34\,\mathrm{T}$ induced primarily by orbital effects (Fig. 6.2b). Importantly, the energy gap in the film remains free of quasiparticle states (for log-scale linecuts, see Fig. 6.9 in the supporting information). Theoretical modelling of the film reveals a small magnetic field range with gapless superconductivity close to the transition (Fig. 6.2e), which is an expected feature when the transition from the superconducting into the normal state is of second order[28]. For both Al and Al/Pt films, the model yields diffusion constants which correspond to a mean free path of $l_{\mathrm{mfp}} \approx 7\,\text{Å}$. This value is consistent with reports on Al films grown under similar conditions [29, 30]. Since the addition of Pt does not seem to affect the mean free path, the increase in critical magnetic field cannot be attributed to increased disorder. The suppression of Zeeman splitting instead demonstrates that spin mixing is the dominant mechanism. From the model, the increased spin-orbit scattering energy of the Al/Pt film is extracted to be $\Gamma_{\mathrm{SO}} = 7.5\,\mathrm{meV}$, corresponding to a spin-orbit scattering time of $\tau_{\mathrm{SO}} = 1.3 \cdot 10^{-13}\,\mathrm{s}$. We note, however, that this extracted value of the spin-orbit scattering energy could be overestimated due to the presence of Fermi-liquid effects [31] (see discussion in section 6.7.4 of the supporting information). In Fig. 6.2f, the measured energy gap is shown together with the energy gap extracted from theory, as well as the corresponding order parameter. We observe good quantitative agreement between the model and our experiment.

6.3 Spectroscopy and Coulomb blockade of InSb/Al/Pt hybrids

The next step of our study is to induce superconductivity in InSb nanowires using Al/Pt films. In order for any material combination to be considered for Majorana experiments and topological qubits, two fundamental properties need to be demonstrated. In tunneling spectroscopy, a proximity-induced gap free of sub-gap states (i.e. a hard gap) should be observed. While this is conventionally done on hybrids with a grounded superconductor, designs of topological qubits typically contain superconducting segments which are floating [7]. These have a finite charging energy, and it is energetically favorable to add charges to such an island in pairs if the low-energy excitation spectrum of the hybrid is free of single-charge states (i.e. $2e$ charging). Both a hard superconducting gap and $2e$ charging have already been demonstrated for Al-based hybrids [3, 11, 32]. In order to con-

firm that platinum does not compromise these properties, for example through hosting single-electron states [33], hybrids with a grounded superconducting shell as well as with a floating shell have been investigated.

In Figure 6.3, we show the results of both tunneling spectroscopy and Coulomb blockade measurements on InSb/Al/Pt nanowires. The fabrication follows our shadow-wall lithography method [9, 10], of which details can be found in the supporting information (sections 6.7.5, 6.7.6 and 6.7.7). In Fig. 6.3a, schematic illustrations and measurement circuits of a tunneling spectroscopy device (top) and a superconducting island device (bottom) are shown. SEM images of all the measured devices are shown in Fig. 6.12 and 6.13. The measurements are conducted by applying a bias voltage between the source and drain contacts. The chemical potential in the hybrid is controlled by the so-called super gate voltage V_{SG}, while the tunnel gate voltages V_{TG} are used to induce tunnel barriers in the nanowire junctions. Details of the measurements can be found in section 6.7.8 of the supporting information.

In order to measure the spectroscopy device, the semiconducting nanowire junction is tuned into the tunneling regime. Under this condition, the measured differential conductance reflects the quasiparticle density of states (DOS) in the proximitized section of the nanowire. Here, the super gate voltage is set to V_{SG} = -1 V, where a strong coupling between the nanowire and the superconducting shell is expected [13, 34]. The differential conductance is shown as a function of magnetic field parallel to the nanowire axis in Fig. 6.3c, with linecuts taken at B = 0.0 T and B = 4.5 T presented in Fig. 6.3e. At zero magnetic field, a large superconducting gap of Δ = 304 μeV is observed. This is significantly larger than in the case of conventional Al-based hybrids, which is a direct consequence of the reduced thickness (~ 4.5 nm) of the Al shell [23]. In addition, the in-gap conductance is suppressed by two orders of magnitude and the differential conductance matches the BTK theory [35], indicating that the superconducting gap is free of sub-gap states (i.e. a hard gap). Importantly, at B = 4.5 T the superconducting gap is still on the order of ~ 100 μeV, which allows to look for Majorana signatures at Zeeman energies which were not accessible before. Remarkably, as can be seen from the in-gap and out-of-gap linecuts in Fig. 6.3f, the superconducting gap remains hard up to B = 6.0 T. The field compatibility offered by Al/Pt hybrids opens up the opportunity to study high-field signatures of Majorana zero modes, like Majorana oscillations [36]. The superconducting island device is studied by inducing tunnel barriers in the semiconducting nanowire junctions, which separate the island from the leads. The voltage on the super gate is then swept to tune the charge on the island, as shown in Fig. 6.3b. This results in a periodic sequence of 2e Coulomb diamonds with a charging energy $E_c \approx 30\,\mu$eV. Linecuts are shown in Fig. 6.3d, where at finite bias the Coulomb peak periodicity has doubled due to the onset of single-electron transport in the quasiparticle excitation spectrum. The magnetic field evolution is shown in Fig. 6.18 of the supporting information. The observation of 2e charging demonstrates that semiconductors coupled to Al/Pt are a suitable replacement of Al-based hybrids, capable to be used for the development of parity-protected topological qubits. Additional data on tunneling spectroscopy devices and superconducting islands is shown in section 6.8 of the supporting information.

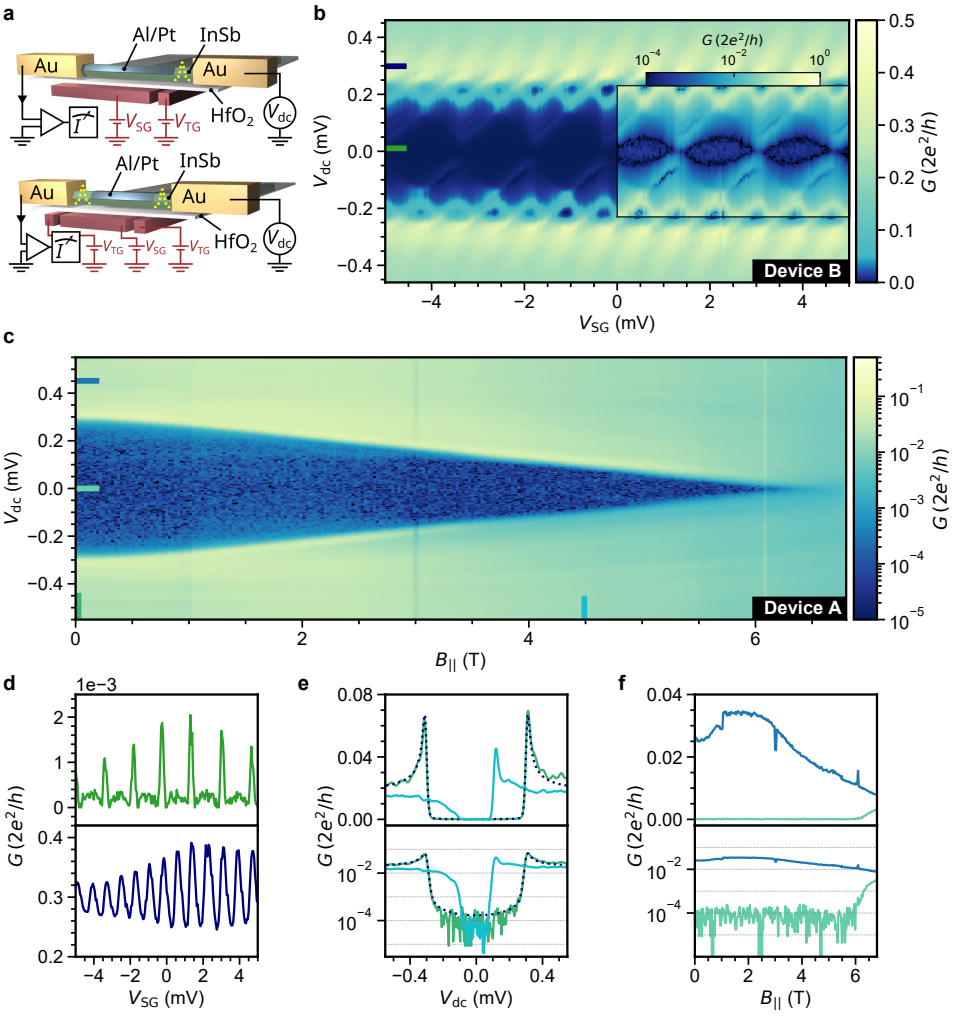

Figure 6.3: **Transport data on 2-terminal InSb/Al/Pt hybrids (devices A and B). a.** Schematics of devices used for tunneling spectroscopy (top, Device A) and Coulomb blockade spectroscopy (bottom, Device B). Device A has a grounded superconducting shell of 1.8 μm long, while the floating shell of Device B is 0.8 μm long. Dashed yellow potentials indicate the formation of tunnel barriers in the semiconducting junctions. **b.** 2e-periodic Coulomb diamonds measured on device B. The inset is a logarithmic overlay of the Coulomb diamonds, highlighting the 2e periodicity at low biases. **c.** Differential conductance from tunneling spectroscopy of device A in logarithmic scale, taken at V_{SG} = -1 V as a function of parallel magnetic field. **d.** Linecuts from the Coulomb-blockade measurements in panel **b** at the locations designated by the colored lines. **e.** Linecuts from the tunneling spectroscopy measurement in panel **c** at the locations designated by the colored lines, shown in linear (top) and logarithmic (bottom) scale. The dashed lines show conductance from BTK theory, with Δ = 304 μeV, temperature T = 70 mK and transmission G_N = 0.018 G_0. **f.** Differential conductance taken from the tunneling spectroscopy measurement in panel **c** at the locations designated by the colored lines, shown in linear (top) and logarithmic (bottom) scale.

6.4 Non-local measurements of three-terminal hybrids

The experiments presented above are a prerequisite for investigating topological superconductivity. Most of the research to date has focused on the study of zero-bias anomalies and their evolution as a function of chemical potential and magnetic field [6, 37]. However, it is becoming increasingly clear that spectroscopy of the density of states at the ends of a nanowire is inconclusive when it comes to identifying an extended topological superconducting phase [38, 39]. While conventional tunneling experiments can provide information on the local density of states at both ends of a wire, the induced gap in the bulk of the hybrid can instead be probed by measuring the non-local conductance in a three-terminal geometry [40]. Consequently, the observation of correlated zero-bias peaks at both ends of a wire should be accompanied by the closing and reopening of the induced superconducting gap in the non-local spectra [41].

In Fig. 6.4a we present a schematic of such a three-terminal device, together with the measurement circuit. The Al/Pt shell covers three facets of the InSb nanowire and is directly connected to the film on the substrate. This forms the third lead of the device, which we connect to ground in the presented measurements. The super gate voltage V_{SG} controls the chemical potential in the hybrid, and the tunnel gate voltages, V_{TL} and V_{TR}, are used to control the left and right semiconducting nanowire junction conductances, respectively. In this work, we fix the super gate voltage to be V_{SG} = -2 V, where the nanowire is expected to be strongly coupled to the superconducting shell [13, 34]. Bias voltages are applied to the left (V_L) or right (V_R) normal contact while keeping the middle lead grounded. The local (g_{LL}, g_{RR}) and non-local (g_{LR}, g_{RL}) conductances are measured to form the full conductance matrix of the system, where they are defined as $g_{ij} \equiv dI_i/dV_j$. Figure 6.4(c-f) shows an example of such a conductance matrix, measured as a function of parallel magnetic field. The critical field in this device is reduced to ~ 4 T in comparison to the single-facet device in the previous section. This is a direct consequence of the thicker Al/Pt shell (~ 8 nm), in which the orbital depairing is more pronounced. The local spectrum on the right junction exhibits a few sub-gap states, which are not present in the local spectrum on the left junction. This suggests that these states are confined locally near the right junction. The corresponding non-local conductances are zero everywhere inside the gap, confirming the local nature of these sub-gap states. This is emphasized in Fig. 6.4b, which displays the extracted energy gap E_g in the hybrid (top panel) as well as the non-local slope $S \equiv d^2I_i/dV_j^2|_{V_j=0}$ (bottom panel). The non-local slope stays close to zero only while there is an energy gap present in the bulk of the hybrid. It starts to deviate from zero around $B_\parallel \approx 3.4$ T, indicating the gap in the system becomes soft before closing eventually around $B_\parallel \approx 3.8$ T. Remarkably, the induced superconducting gap in the bulk of these hybrids can be free of sub-gap states up to high magnetic fields. The effect of the super gate voltage on the proximity effect in these hybrids will be explored in chapter 7. The extraction procedure for the energy gap and the non-local slope is described in section 6.7.8 of the supporting information.

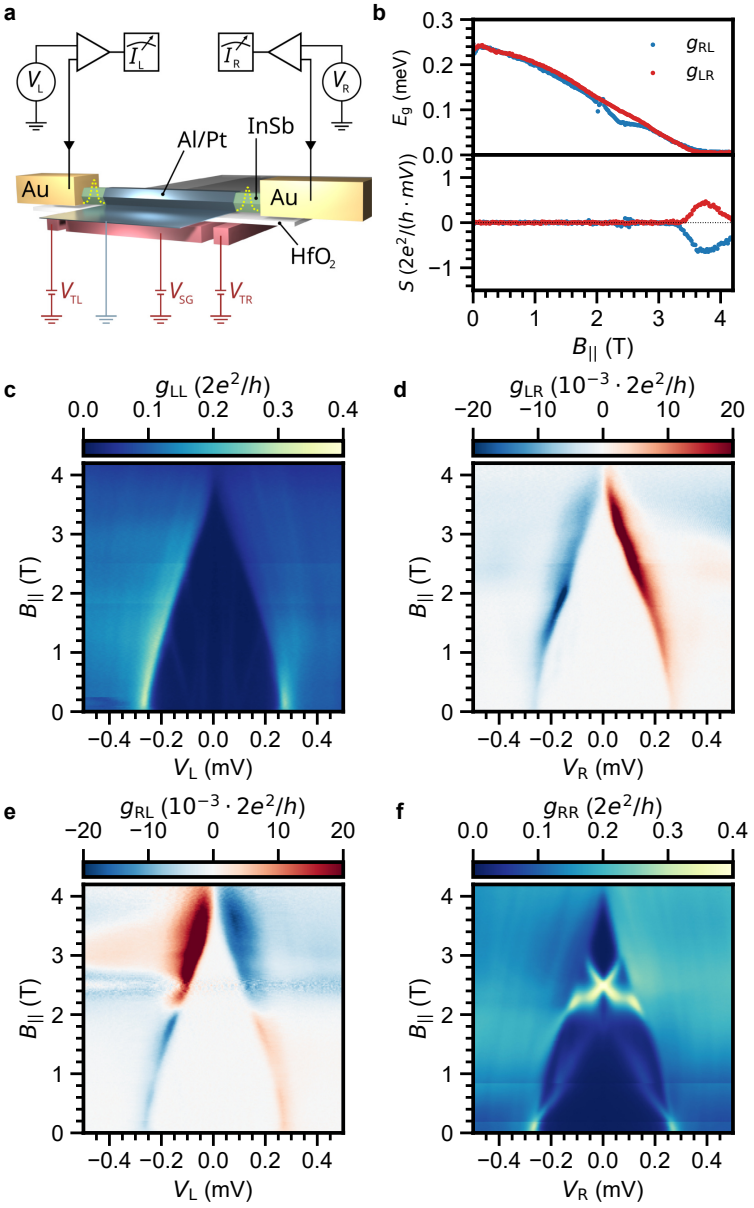

Figure 6.4: **Three-terminal measurements on InSb/Al/Pt hybrids (device C). a.** Schematic of a three-terminal hybrid device and the measurement circuit. The hybrid has a superconducting shell of 1 μm in length, which is grounded through its connection to the film on the substrate. Yellow dashed potentials indicate the formation of tunnel barriers in the semiconducting junctions. **b.** Extracted energy gap in the bulk of the hybrid (top), together with the non-local slope at zero bias (bottom). **c-f.** Differential-conductance matrix measurements as a function of parallel magnetic field. Panels **c,f** show the local conductances g_{LL} and g_{RR}, respectively, whereas panels **d,e** present the non-local conductances g_{LR} and g_{RL}. Conductances are defined as $g_{ij} \equiv dI_i/dV_j$. Data is taken at V_{SG} = -2 V.

6.5 Zeeman splitting inside the hybrid

Having shown that the addition of Pt adatoms quenches the Zeeman effect in the Al shell, we turn our attention to the semiconductor part of the hybrid device. Breaking the Kramers degeneracy through Zeeman splitting of the DOS of the hybrid segment lies at the heart of the proposed schemes to reach the topological regime [1, 2]. Tunneling into a discrete Andreev bound state (ABS) in the hybrid nanowire involves a transition between a spinless singlet state and spinful doublet states. The doublet state splits under the effect of an external magnetic field [42, 43]. Thus, measuring the evolution of the ABS spectrum in a magnetic field would show whether the effect of spin mixing leaks to the proximitized semiconductor.

Figure 6.5a shows a schematic illustration and the measurement circuit of another three-terminal device, with a hybrid segment 150 nm long. The local conductance g_{LL} as a function of V_{SG} and V_L taken at zero field is shown in Fig. 6.5b. We observe a clean superconducting gap, in addition to a series of sub-gap resonances. They appear only when setting $V_{SG} > 0\,V$, and reflect the presence of discrete states in the confined semiconductor. These states hybridize with the superconductor to form Andreev bound states. In Fig. 6.5c-f, we track the evolution of the ABSs in an applied magnetic field by measuring the conductance matrix. We set $V_{SG} = 0\,V$, so that the energy of one of the ABSs is reduced below the quasiparticle continuum. To verify that the ABS is located in the hybrid segment and is not a local resonance on the left junction, we notice that it appears at the same energy on both sides, in g_{LL} and g_{RR}. We also note that it shows up in the non-local signals, g_{RL} and g_{RL}, consistent with a state which is extended along the entire hybrid. Upon application of the magnetic field, the ABS splits into two peaks that move with the same slope in opposite directions. The outgoing peaks are soon merged with the quasiparticle continuum, but the peaks shifting to lower energy cross at $B = 0.34\,T$, where the ABS ground state turns from even to odd [42]. We extract its gyromagnetic ratio to be $g = 20.0 \pm 0.3$, showing only a moderate amount of renormalization of the semiconducting properties [12, 13]. Thus, the effect of spin mixing from Pt enhances the critical field of the Al shell, but does not negatively influence the spin properties in the semiconductor. This is evidenced by the picture of an extended ABS in the hybrid segment, which Zeeman splits with a high g factor in the presence of a magnetic field. This demonstration is of crucial importance, as a spin-mixed hybrid would be fundamentally incapable of transitioning into a topological phase. It is still an open question if hybrids would preserve these properties when the semiconductors are coupled to high-atomic-number superconductors, like Sn, In or Pb [15, 17, 18].

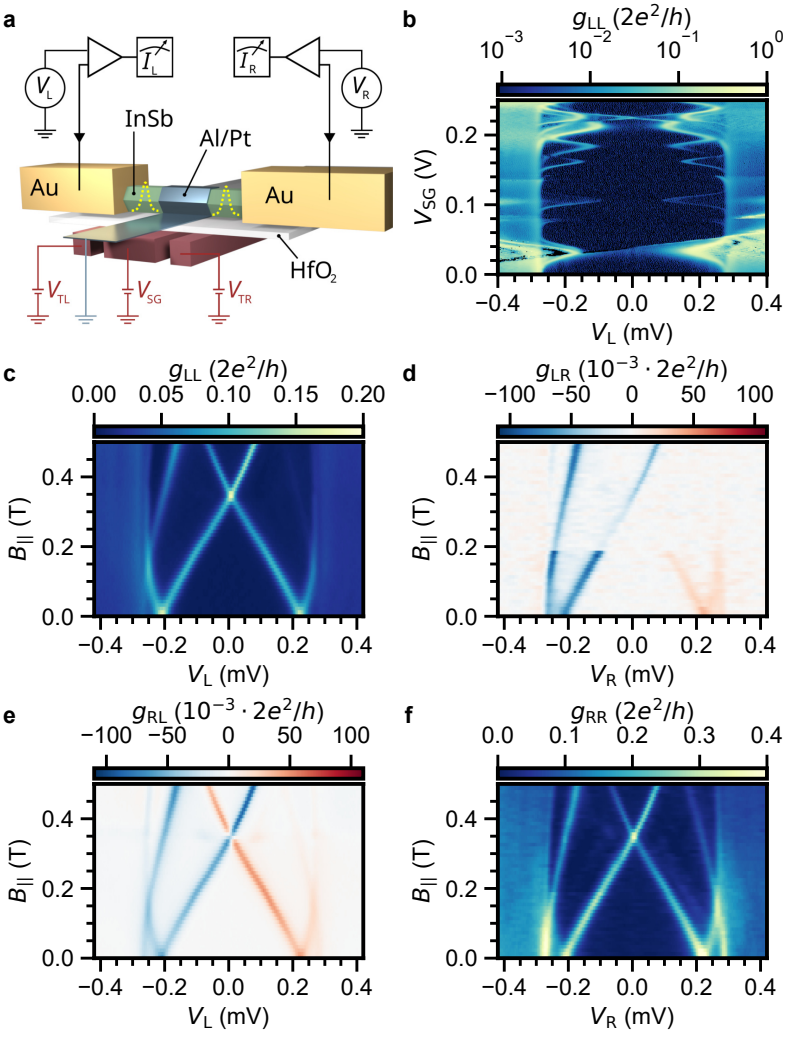

Figure 6.5: **Spin splitting of Andreev bound states in InSb/Al/Pt hybrids (device D). a.** Schematic of a three-terminal hybrid and the measurement circuit. The hybrid has a superconducting shell of 150 nm in length, which is grounded through its connection to the film on the substrate. Yellow dashed potentials indicate the formation of tunnel barriers in the semiconducting junctions. **b.** Local differential conductance as a function of super gate voltage taken at zero applied magnetic field. **c-f.** Differential-conductance matrix measurements as a function of parallel magnetic field. Panels **c,f** show the local conductances g_{LL} and g_{RR}, respectively, whereas panels **d,e** illustrate the non-local conductances g_{LR} and g_{RL}. Data is taken at $V_{SG} = 0.0\,V$.

6.6 Conclusion

In this work, we have examined the properties of thin aluminum films coated with sub-monolayer amounts of platinum, as well as semiconductor nanowires proximitized by Al/Pt bilayers. By measuring the critical temperature and parallel magnetic field of thin films, we have found that ~ 2 Å of Pt can increase the critical field above the Chandrasekhar-Clogston limit without having a significant effect on the size of the superconducting gap. We show, using our theoretical model, that the spin-orbit scattering rate of Pt-covered films is drastically increased. At the same time, various critical parameters of the films, such as the mean free path and coherence length, remain unaffected. When coupling InSb nanowires to these Pt-enhanced films, we observe a hard superconducting gap up to magnetic fields as high as 6 T. Additionally, parity-conserving transport results in the formation of $2e$-periodic diamonds in Coulomb-blockade experiments. Upon switching to a three-terminal geometry, non-local measurements provide evidence of a bulk energy gap which is free of sub-gap states. Furthermore, the spin splitting of extended Andreev bound states in a short hybrid is observed. This evidences that the spin mixing from Pt does not adversely affect the semiconducting properties of a hybrid. Crucially, like Al, the Al/Pt system satisfies all the necessary requirements for investigating Majorana zero modes and topological qubits.

What should also be considered is that the fabrication of aluminum/platinum samples can be straightforwardly executed, with minimal modifications of the well-established aluminum technology. Importantly, aluminum and platinum are non-toxic materials suited for most UHV deposition chambers. As a result, the development of scalable quantum systems can be readily implemented using Al/Pt bilayers - which is still a major challenge for heavy elements with a low melting point like Sn and Pb. Thus, we expect that Al covered with Pt will be the natural successor to Al-based hybrids. Furthermore, since Al can be grown especially thin in planar geometries, we anticipate that Al/Pt will be particularly attractive for proximitizing two-dimensional semiconductors and van der Waals materials. Future works involving Al/Pt hybrids will focus on investigating Majorana physics, exploring their behavior as a function of chemical potential and high Zeeman energies.

Data Availability and Code availability

Raw data presented in this work and the data processing/plotting codes are available at `https://doi.org/10.5281/zenodo.5835794`. Theory simulation code is available upon reasonable request.

6.7 Supporting information: Methods and materials

6.7.1 Platinum thickness calibration

In this work we use sub-nanometric amounts of platinum to enhance the magnetic field resilience of aluminum. As platinum and aluminum do not form an abrupt interface, the thickness estimation from TEM analysis is not reliable. Instead, atom-force microscopy (AFM) was used to calibrate the tooling factor of the quartz crystal balance. Prior to the deposition of platinum, the deposition rate was stabilized between a value of 0.01 Å/s to 0.03 Å/s. Upon opening of the shutter, there is an apparent sharp drop of the deposition

rate due to thermal effects on the quartz crystal monitor (QCM). The rate relaxes back to its initial value after few tens of seconds when the monitor re-cools again. This thermal effect makes it difficult to accurately estimate the thickness of deposited metal during the deposition. To precisely estimate how much Pt was deposited, the deposition rate as a function of time was recorded. Knowing the rate before opening the sample shutter, we calculated the deposition time to obtain the desired thickness. This way we minimized the impact of the thermal effect caused on the estimated thickness by the QCM. After the deposition is complete, the closing of the shutter induces a similar spike on the rate. The rate was allowed to stabilize again at this point. The exact amount of Platinum deposited was then calculated using a linear fit between the stabilized rate before and after the deposition, which accounts for possible drifts in the deposition rate. The curves were then integrated between the opening and closing of the shutter, with the area under the curve corresponding to the deposited Pt thickness. This process is presented in Fig. 6.6.

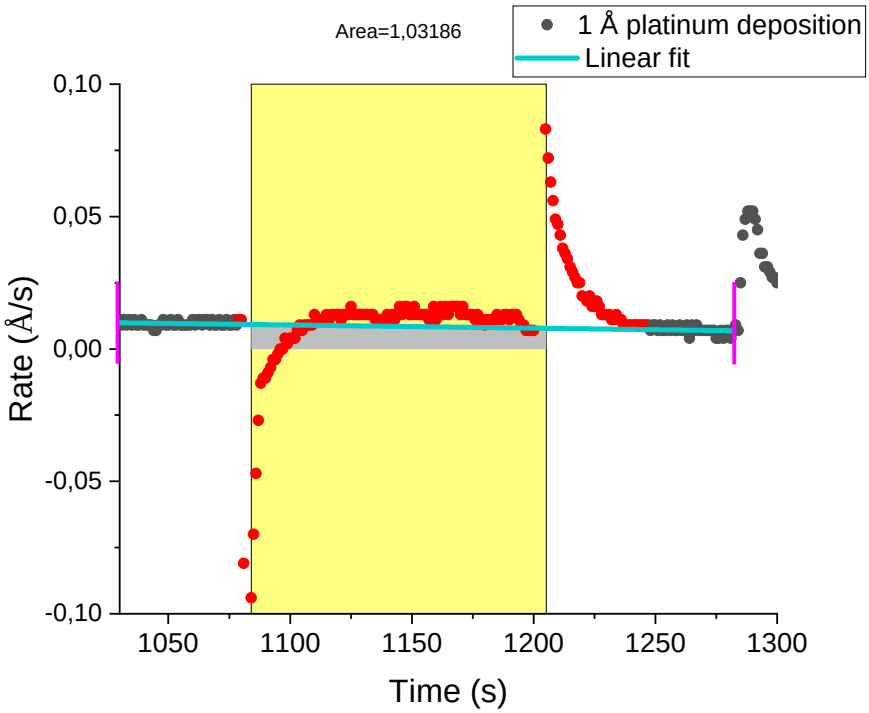

Figure 6.6: Example of a fitting procedure to precisely estimate the platinum thickness. Dark gray points correspond to the raw rate measured by the quartz crystal monitor. Red points are masked and excluded from the fit. Purple markers indicate the range of the fit, and the cyan line is the fitted linear curve. The yellow rectangle marks the range of integration and the integrated light gray area corresponds to the evaporated platinum thickness.

6.7.2 Al films

The Al films presented in this work have been deposited with a rate of 0.05 Å/s on an intrinsic silicon substrate with 285 nm thermally oxidized SiO_2. Prior to the aluminum deposition, the substrate was kept at 138 K for 1 hour to achieve good thermalization. Metals were evaporated at an angle of 30° from the normal. After aluminum deposition, platinum was deposited with the above mentioned procedure. AlOx was deposited at 0.1-0.2 Å/s. All materials were deposited at a substrate temperature of 138 K. The critical temperature and magnetic field of the films was measured in a 4-terminal geometry, with 4 probes in a line separated by 1 mm. The thickness of the films is 6 nm as estimated from the quartz crystal monitor (QCM) and transmission electron microscopy (TEM). The films are subsequently capped with a layer of evaporated AlO_x, which protects them from oxidation when exposed to air. We note however that the observed thickness of platinum from TEM appears larger than indicated by QCM in the deposition chamber.

The tunnel junctions in this work have been grown under similar conditions. A 6 nm Al film is deposited at 138 K with 30° angle from the normal. The films are oxidized at 138 K with an oxygen pressure of 10 Torr. Without breaking the vacuum, 40 nm Ag is evaporated at 0.5 Å/s as the counter electrode at −30° from the normal. The samples are subsequently protected with an AlO_x capping layer. They are measured in a 4-terminal geometry: 2 probes are used to provide the source and drain contacts, where a voltage V is applied to one probe and the current I through the junction is measured on the other probe. At the same time, 2 additional probes are used to directly measure the voltage drop V_{dc} on the junction.

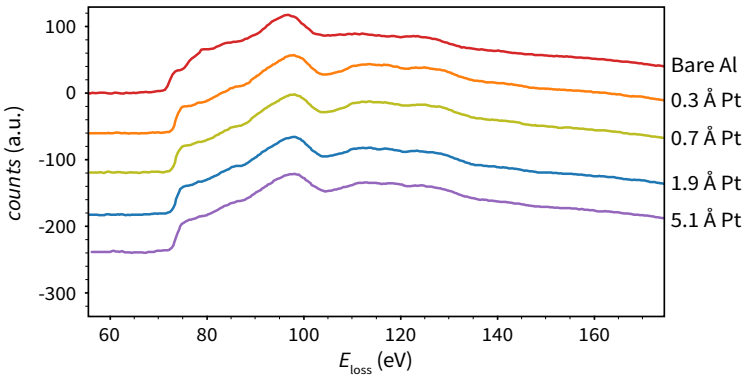

Figure 6.7: Electron energy-loss spectroscopy extracted at the center of the studied films. The spectra do not change with the increase of Pt thickness. This indicates that Al and Pt do not form a compound, despite the detection of Pt inside the Al layer with EDX. Based on the shape of the spectra we conclude that Pt is physically implanted inside the Al layer during deposition. Values on the y axis have been offset by -60 a.u. for clarity.

6.7.3 Usadel equation and theory fitting

We use the Usadel equation [44] to calculate the critical fields of the films and fit the tunneling spectroscopy data. The Usadel equation is written in terms of the quasiclassical Green's function [45, 46] $\check{g}(i\omega_n, r)$ and is valid in the limit of dirty superconductors, $l_{\mathrm{mfp}} \ll \xi$, where l_{mfp} is the electronic mean free path and ξ is the superconducting coherence length. Introducing Pauli matrices $\hat{\sigma}(\hat{\tau})$ in spin (Nambu) space, the Usadel equation for a superconductor with spin-orbit impurities in external magnetic field can be written as

$$D\partial\cdot(\check{g}\partial\check{g}) - \left[\omega_n\hat{\tau}_z + iV_{\mathrm{Z}}\cdot\hat{\sigma}\hat{\tau}_z + \Delta\hat{\tau}_+ + \Delta^*\hat{\tau}_- + \check{\Sigma}_{\mathrm{SO}}, \check{g}\right] = 0, \tag{6.1}$$

where the covariant derivative is defined as $\partial\cdot = \nabla - i[A\hat{\tau}_z, \cdot]$, A is the vector potential, ω_n are Matsubara frequencies, $V_{\mathrm{Z}} = g_{\mathrm{el}}\mu_{\mathrm{B}}B/2$ is the Zeeman field originating from the external magnetic field B, g_{el} is the electronic g-factor, μ_{B} is the Bohr magneton, Δ is the superconducting pair potential, and $\hat{\tau}_\pm = (\hat{\tau}_x \pm \hat{\tau}_y/2)$. The diffusion constant D corresponds to scattering on non-magnetic impurities and is given by $D = v_{\mathrm{F}}l_{\mathrm{mfp}}/3$, where v_{F} is Fermi velocity in the superconductor. The quasiclassical Green's function is subject to a normalization condition $\check{g}^2 = 1$. As it was first shown in Ref. [31], scattering on spin-orbit impurities produces the self-energy term $\check{\Sigma}_{\mathrm{SO}} = \hat{\sigma}\check{g}\hat{\sigma}/(8\tau_{\mathrm{SO}})$ in the Usadel equation, where τ_{SO} is scattering time. For convenience, we introduce the spin-orbit scattering energy as $\Gamma_{\mathrm{SO}} = 3\hbar/(2\tau_{\mathrm{SO}})$. In general, the Usadel equation has to be supplemented with appropriate boundary conditions, which for a superconductor-insulator interface read $\partial\check{g}|_{\mathrm{interface}} = 0$, and the resulting boundary problem has to be solved. However, for very thin superconductors (with thickness $d_{\mathrm{SC}} \ll \xi, \lambda_{\mathrm{London}}$, where $\lambda_{\mathrm{London}}$ is the London penetration depth) in a parallel magnetic field the spatial dependencies of the Green's function and the order parameter can be neglected [47], and the order parameter can be chosen real. In that case, the Usadel equation (6.1) becomes an algebraic equation:

$$\left[\omega_n\hat{\tau}_z + iV_{\mathrm{Z}}\cdot\hat{\sigma}\hat{\tau}_z + \Delta\hat{\tau}_1 + \check{\Sigma}_{\mathrm{SO}} + \check{\Sigma}_{\mathrm{ORB}}, \check{g}\right] = 0, \tag{6.2}$$

where orbital effects of the magnetic field lead to an additional contribution to the self-energy:

$$\check{\Sigma}_{\mathrm{ORB}} = \Gamma_{\mathrm{ORB}}\frac{\hat{\tau}_z\check{g}\hat{\tau}_z}{4}, \tag{6.3}$$

and the orbital depairing energy is given by

$$\Gamma_{\mathrm{ORB}} = \frac{De^2B^2d_{\mathrm{SC}}^2}{3\hbar c^2}. \tag{6.4}$$

Equation (6.4) is a familiar result for thin superconducting films subjected to a parallel magnetic field [28, 48].

To calculate the order parameter self-consistently, Eq. (6.2) needs to be solved together with the gap equation,

$$\Delta\log\left(\frac{T}{T_{c0}}\right) = 2\pi T\sum_{\omega_n>0}\left(\frac{1}{4}\mathrm{Tr}(\hat{\tau}_x\check{g}) - \frac{\Delta}{\omega_n}\right), \tag{6.5}$$

Independent parameters				Extracted Parameters		
T (mK)	d_{SC} (nm)	g_{el}	v_F (m/s)	Δ_0 (meV)	l_{mfp} (nm)	Γ_{SO} (meV)
20	6	2	2×10^6	0.27	0.9	see Fig. 6.11a

Table 6.1: Values of parameters used in critical field simulations of Al and Al/Pt films (see Fig. 1 of the main text). Extracted parameters were obtained by fitting experimental data.

where T is temperature and T_{c0} is critical temperature of the bare superconductor. In addition, to appropriately identify first-order transitions one needs to ensure that the free energy difference between the superconducting and the normal state is negative throughout the calculation [49–51]. Once the self-consistent value of the order parameter and the corresponding Green's function are obtained, the density of states in the superconductor can be calculated using

$$N(E) = \frac{1}{8} N_0 \mathrm{Re}[\mathrm{Tr}(\hat{\tau}_z \check{g}|_{\omega_n \to -iE^+})], \tag{6.6}$$

where N_0 is the density of states at the Fermi level. The differential conductance in the SIN junction is related to the density of states through convolution [30],

$$\frac{dI}{dV}(V) \propto \int_{-\infty}^{\infty} N(E) K(E + eV) dE, \tag{6.7}$$

where V is a voltage bias and the convolution kernel is given by

$$K(x) = \frac{\beta e^{\beta x}}{(1 + e^{\beta x})^2} \tag{6.8}$$

with the inverse temperature $\beta = 1/k_B T$.

6.7.4 Simulation details

We use Eqs. (6.2)-(6.5) to calculate the values of the pair potential and to simulate the critical fields of the Al and Al/Pt films considered in Fig. 6.1 of the main text. We take the critical temperature to be $T_{c0} = 1.79$ K for all simulated samples. Using the critical field of the bare Al film (which we assume has a negligible amount of spin-orbit impurities) measured in the experiment, $B_c \approx 2.6$ T, we extract the value of the mean free path in the film by solving the Usadel equation (6.2)-(6.5) with $\check{\Sigma}_{SO} = 0$ and obtain $l_{mfp} \approx 0.9$ nm. We further use this value to simulate the critical fields of the Pt-covered samples (see red dashed curve in Fig. 1c of the main text) and extract the respective values of the spin-orbit scattering rate (see Fig. 6.11a). Values of the parameters used in these simulations, both independent and extracted by fitting experimental data, are given in Table 6.1.

Conductance spectroscopy on the Al and Al/Pt films presented in Fig. 2 of the main text is simulated using Eqs. (6.2),(6.5),(6.6) and (6.7). Table 6.2 summarizes values of the parameters, both independent and extracted by fitting experimental data, used in conductance simulations.

Similarly to initial studies of the Al/Pt system, our theoretical model yields a linear dependence of Γ_{SO} on d_{Pt}. We note however that even for $d_{Pt} = 5.1$ Å, the extracted value of Γ_{SO}

	Independent parameters				Extracted Parameters		
	T (mK)	d_{SC} (nm)	g_{el}	v_F (m/s)	Δ_0 (meV)	l_{mfp} (nm)	Γ_{SO} (meV)
Al	110	4.5	2	2×10^6	0.31	0.68	0.0
Al/Pt	30	4.5	2	2×10^6	0.306	0.68	7.5

Table 6.2: Values of parameters used in conductance spectroscopy simulations of Al and Al/Pt tunnel junctions (see Fig. 2 of the main text). Extracted parameters were obtained by fitting experimental data.

is smaller than Γ_{SO} = 7.5 meV, which we extract from the tunneling measurements. Initial studies of Al/Pt revealed unphysically large spin-orbit scattering rates [23]. In the case of the above mentioned experiment, the extracted spin-orbit scattering rate was higher than the momentum scattering rate, which indicated that the increase of critical field was not fully understood. It was pointed out later [31] that, due to Fermi liquid effects, the g-factor of such a thin Al films is being reduced [30]. We plot the energy difference between the spin-up and spin-down quasiparticle peaks in a 4.5-nm Al film as a function of magnetic field in Fig. 6.11. The analysis is made for fields larger then 1 T. In our case, we do not observe a clear deviation from a g-factor of 2 (indicated by the orange curve). The slight discrepancy observed near the transition can be a result of the peak broadening, rather than Fermi-liquid effects. We note, however, that the Fermi-liquid correction becomes more relevant at higher magnetic field values, and we cannot fully exclude the presence of these effects in Al/Pt devices.

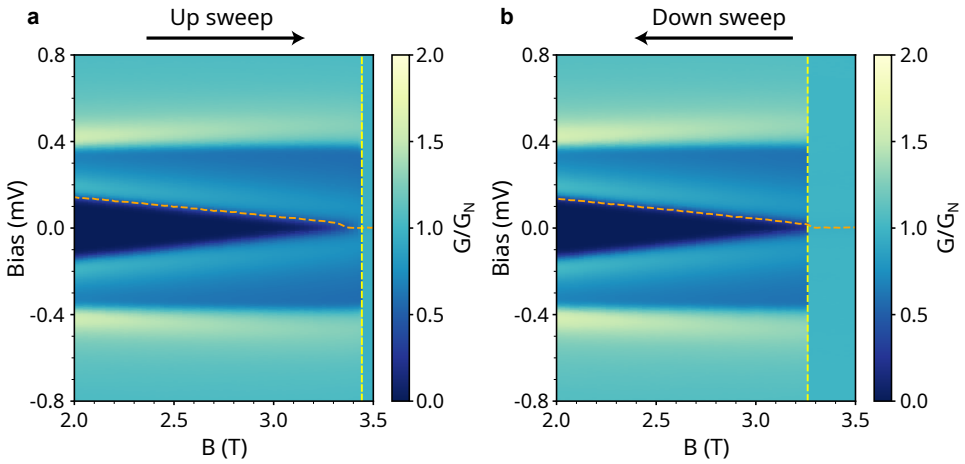

Figure 6.8: Additional experimental tunnel junction data in the vicinity of the critical field of the Al tunnel junction. Panels illustrate the magnetic field up (**a**) and down (**b**) sweeps, respectively. Measurements show a clear difference in the critical field value, evidencing hysteresis as expected for the first order phase transition. Orange lines depict the gap edge and yellow lines mark the critical field extracted from experimental data.

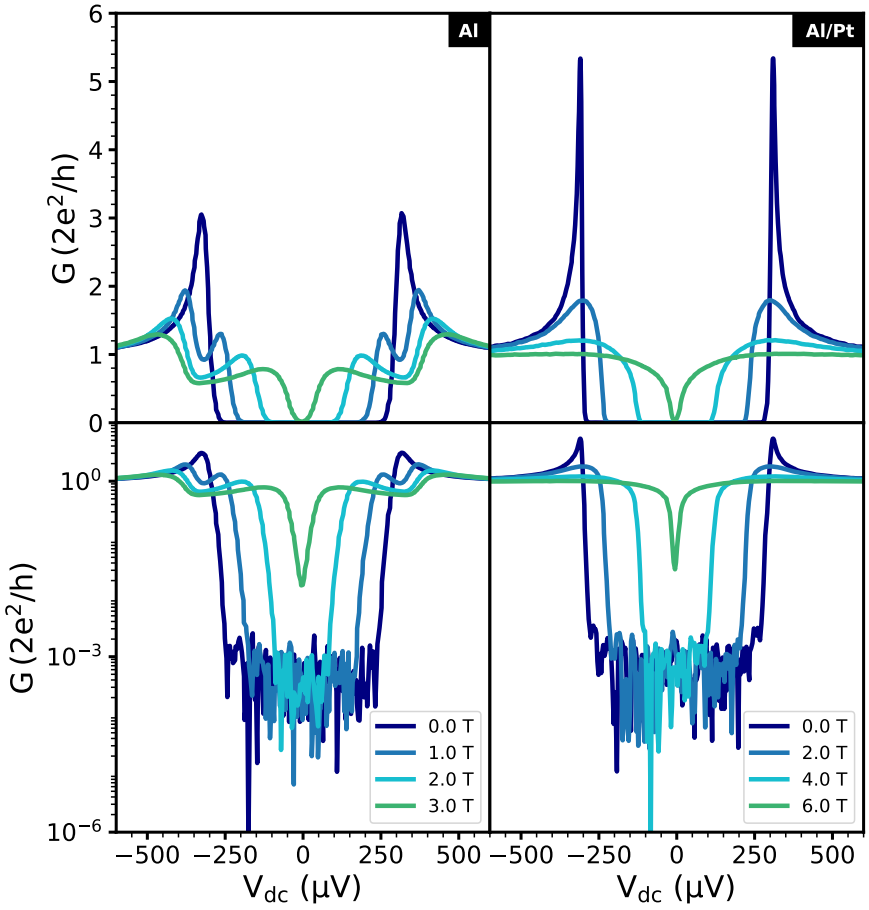

Figure 6.9: Linecuts of the tunnel junction data presented in main text Fig. 6.2. Plots in the left column show linecuts of the Al/AlO_x/Ag NIS tunnel junction, presented in linear and logarithmic scale. In the right column, linecuts of the Al/Pt/AlO_x/Ag NIS tunnel junction are presented in linear and logarithmic scale.

6.7.5 Nanowire hybrids: substrate fabrication

The nanowire hybrids presented in this work are fabricated on pre-patterned substrates, following the shadow-wall lithography technique described in [9, 10]. Intrinsic silicon wafers ($2\,k\Omega\cdot$cm) with 285 nm thermal SiO_x serve as the base for the device substrates. Local bottom gates are patterned with standard electron-beam litography (EBL) techniques, using PMMA 950k A2 spun at 4 krpm for one minute followed by 10 minutes of baking on

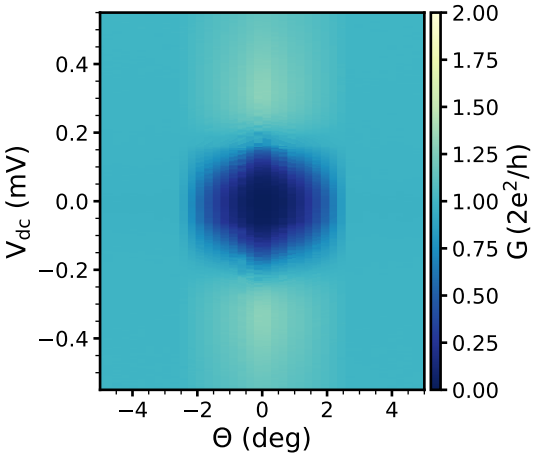

Figure 6.10: Field rotation scan taken at 3.5 T for Al/Pt/AlO_x/Ag NIS tunnel junction. The angle Θ is defined as the angle between the substrate plane and the normal, where 0 degrees is the substrate plane. A misalignment between the substrate plane and the applied field of only 2 degrees is enough to turn the film normal.

a 185 °C hot plate. After development of the resist using a 3:1 solution of IPA and MIBK, 3 nm Ti and 17 nm Pd are deposited as the gate metal using e-beam evaporation at 0.5 Å/s and 1 Å/s, respectively. Subsequently, bond pads are patterned with EBL using PMMA 950k A6 spun at 4 krpm for one minute and hot-baked at 185 °C for 10 minutes. After development, 50 nm of W is sputtered using RF-sputtering at 150 W in an Ar pressure of 20 μbar. Next, the substrates are covered with high-quality HfO_x gate dielectric grown at 110 °C using atomic layer deposition (ALD). Finally, shadow walls are patterned on top of the dielectric. FOx-25 (HSQ) is spun at 1.5 krpm for one minute, followed by 2 minutes of hot baking at 180 °C and patterning with EBL. The HSQ is then developed with MF-321 at 60 °C for 5 minutes and the substrates are subsequently dried using critical point dryer (CPD). Nanowires are deposited onto the gates using an optical nanomanipulator setup. For some devices, a modified version of the fabrication flow presented above was used. For devices H and I, the shadow walls are grown using a double-layer process. First, PMMA 950k A8 is spun at 4 krpm and hot baked at 185 °C for 10 minutes. After EBL and development, FOx-25 (HSQ) is spun at 2 krpm for one minute, followed by 2 minutes of hot baking at 180 °C and patterning with EBL. HSQ is developed for 15 minutes using MF-321 at 60 °C, followed by stripping of the PMMA using acetone at 50 °C for 10 minutes and drying of the substrates using CPD. For device H, bottom gates are instead fabricated using sputtered W, etched down using reactive ion etching (RIE). Details are described in [9, 10]. For devices B, H and I, AlO_x grown at 300 °C using ALD was used as the gate dielectric instead of HfO_x. Since the HSQ developer etches AlO_x, the ALD is moved in the fabrication flow to be done after the shadow walls are fabricated. For device J, p++ doped Si wafers (0.02 Ω · cm) with 285 nm thermal SiO_x were used. The Si serves as a global back gate, and so no local gates were patterned. Instead, only the bond pads and shadow walls were fabricated onto the substrate.

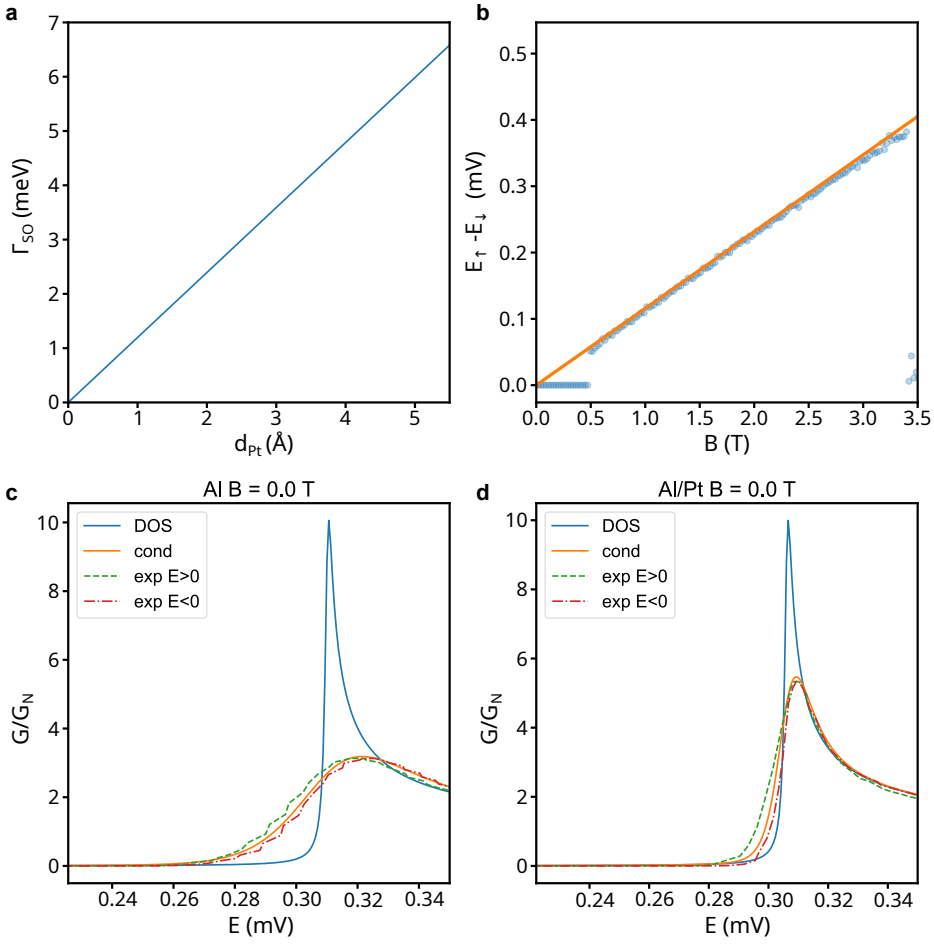

Figure 6.11: **a.** Spin-orbit scattering energy Γ_{SO} as a function of platinum thickness fitted to experimental film data presented in the main text. **b.** Experimentally extracted energy difference between Zeeman-split quasiparticle peaks (blue dots), and the corresponding Zeeman energy with $g = 2$. **c.** Calculated DOS (blue) and thermally broadened conductance (orange) for the Al tunnel junction. Green and red curves correspond to positive and negative bias respectively. **d.** Same curves for the Al/Pt tunnel junction.

6.7.6 Nanowire hybrids: superconductor deposition

To obtain a pristine, oxide-free semiconductor surface, a gentle oxygen removal is accomplished via atomic hydrogen radical cleaning. For this purpose, a custom-made H radical generator is installed in the load lock of an aluminium electron-gun evaporator. It consists of a gas inlet for H_2 molecules connected to a mass-flow controller and a tungsten filament at a temperature of about 1700 °C that dissociates a fraction of the molecules into hydrogen radicals. The optimal removal of the native oxide is achieved for a process duration of 60 mins and at a H_2 pressure of $6.3{\cdot}10^{-5}$ mbar. This recipe, which is used for all the devices

shown in this paper, results in a constant EDX count of oxygen at the interface as shown in the previous works utilizing our shadow wall lithography technique (see Refs[9, 10]).

After the native oxide removal, the samples are cooled down to 138 K and thermalized for one hour. The Al is then deposited with a rate of 0.05 Å/s. The various samples presented in this work are shown in Fig. 6.8, and can be separated into three categories based on the facet coverage of the nanowire. For nanowires with a single covered facet (pink outline in Fig. 6.8), a thin Al film is grown with a 30° angle with respect to the substrate. After Pt deposition at the same angle, the film is oxidized while still cold at an oxygen pressure of 200 mTorr for 5 minutes. With these growth conditions, the top and botom-side facets of the nanowire are covered with extremely thin granular Al and are expected to fully oxidize. Similarly, 2 nanowire facets can be covered with Al (cyan outline in Fig. 6.8) by growing a slightly thicker film at 50° – 60° from the substrate. On the other hand, nanowires with 3-facet coverage (orange outline in Fig. 6.8) can be grown at 30° (or a mix of 15° and 45°) with thicker films. In that case, there is a continuous connection between the nanowire shell and the film on the substrate. This can serve as a ground or source/drain contact to the nanowire. These samples are typically capped with evaporated AlO_x (~ 0.2 Å/s) to prevent oxidation of the shell-substrate connection. Details on the growth conditions of all presented samples are shown in Table 6.3.

6.7.7 Nanowire hybrids: contacts

For most devices presented in this work, contacts are fabricated ex-situ after the superconductor deposition. PMMA 950k A6 is spun at 4 krpm and subsequently cured at room temperature in a vacuum oven to prevent intermixing at the pristine InSb-Al interface. Contacts are patterned using EBL, and Ar milling is used to remove the native oxide prior to deposition of 10 nm Cr and 120 nm Au using e-beam evaporation at 0.5 Å/s and 1.5 Å/s, respectively. For devices H and I, contacts are deposited in-situ. Using the single-shot fabrication technique presented in [10], 50 nm Pt is deposited at a 30° angle with respect to the substrate to form metallic contacts. For device J, the Al/Pt shell is deposited at a 30° angle with respect to the substrate, forming the source and drain contacts.

6.7.8 Nanowire hybrids: measurements

Transport measurements are conducted in dilution refrigerators with a base temperature of ~ 20 mK. All magnetic field measurements presented in this work have the magnetic field aligned parallel to the nanowire using 3-axis vector magnets. Voltage-bias measurements were conducted in a 2-terminal geometry (with the exception of devices C and D) using standard lock-in techniques. The used excitation voltages are between 10 μV and 20 μV, with frequencies between 15 Hz and 40 Hz. To calculate the voltage drop on the sample and the corresponding conductance, a setup-specific series resistance is taken into account (see Table 6.3). The used series resistances consist of the input resistance of the current amplifier, output resistance of the voltage source and resistance of the RC filters present in the dilution fridge (no contact resistance is assumed in any of the measurements).

Measurements in the 3-terminal geometry on devices C and D are conducted using the circuit described in [52]. When measuring the conductance matrix, the bias on the left contact of the device V_L is swept first while the bias on the other side V_R is set to zero.

Device	# facets	Angle (°)	d_{Al} (nm)	Oxidation	d_{Pt} (Å)	Figure	R_{series} (Ω)
A	1	30	5.5	200 mTorr O_2	1.8	3d	15134
						3e	15134
						3f	15134
						S8	15134
						S9	6134
B	2	60	7.5	AlO_x capping	2	3b	6134
						3c	6134
						S12	6134
C	3	15 + 45	4 + 4	AlO_x capping	2	4	6778
D	3	15 + 45	4 + 4	AlO_x capping	2	5	0
E	1	30	5.5	200 mTorr O_2	1.8	S10	15134
F	1	30	5.5	200 mTorr O_2	1.8	S11	6134
G	1	30	8	200 mTorr O_2	1.8	S13	6144
H	2	50	7.5	200 mTorr O_2	2	S14	8668
I	2	50	7.5	200 mTorr O_2	2	S15	15134
J	3	30	12.5	200 mTorr O_2	5	S16	6778

Table 6.3: Overview of sample fabrication parameters. The deposition angle is specified with respect to the substrate. The # facets column indicates the amount of nanowire facets covered with Al/Pt, of which cross-section illustrations are shown in Fig. 6.13. Right two columns show the subtracted series resistance from the raw data for each plot, which consists of the input resistance of the current amplifier, output resistance of the voltage source and resistance of the RC filters present in the dilution fridge. For devices C & D, we refer to the main body of the manuscript, as the series resistance varies for the grounding and biasing lines.

The corresponding matrix elements g_{LL} and g_{RL} are recorded. Next, the right-contact bias V_R is swept while setting the bias on the left contact V_L to zero and the remaining two conductance matrix elements g_{RR} and g_{LR} are recorded. All three-terminal measurements are conducted with low junction conductances compared to the circuit resistances, such that voltage-divider effects are negligible [52]. For the data presented on device C, only the DC voltage drop on each junction is corrected by performing the standard two-terminal correction $V_L = V_L^{\text{applied}} - I_L R_{\text{series}}$. Measurements taken on device D are not corrected for any series resistances.

To extract the induced gap size from measurements on device C, each voltage-bias line trace is first smoothed by applying a Savitzky-Golay filter. Subsequently, the data is split into positive bias and negative bias, before being normalized by the peak non-local conductance value in the corresponding half. The induced gap is then determined separately for positive and negative bias values, by calculating the voltage value for which the signal crosses 20% of the peak value. The energy gap E_g shown in the main text Fig. 6.4b is the average of these two values. See Fig. 6.22 for the non-local data with an overlay of the extracted E_g values, as well as the processed data with overlay. The non-local slope is calculated by averaging the gradient of the Savitzky-Golay filtered data within a $\pm 9\,\mu$V window around zero bias.

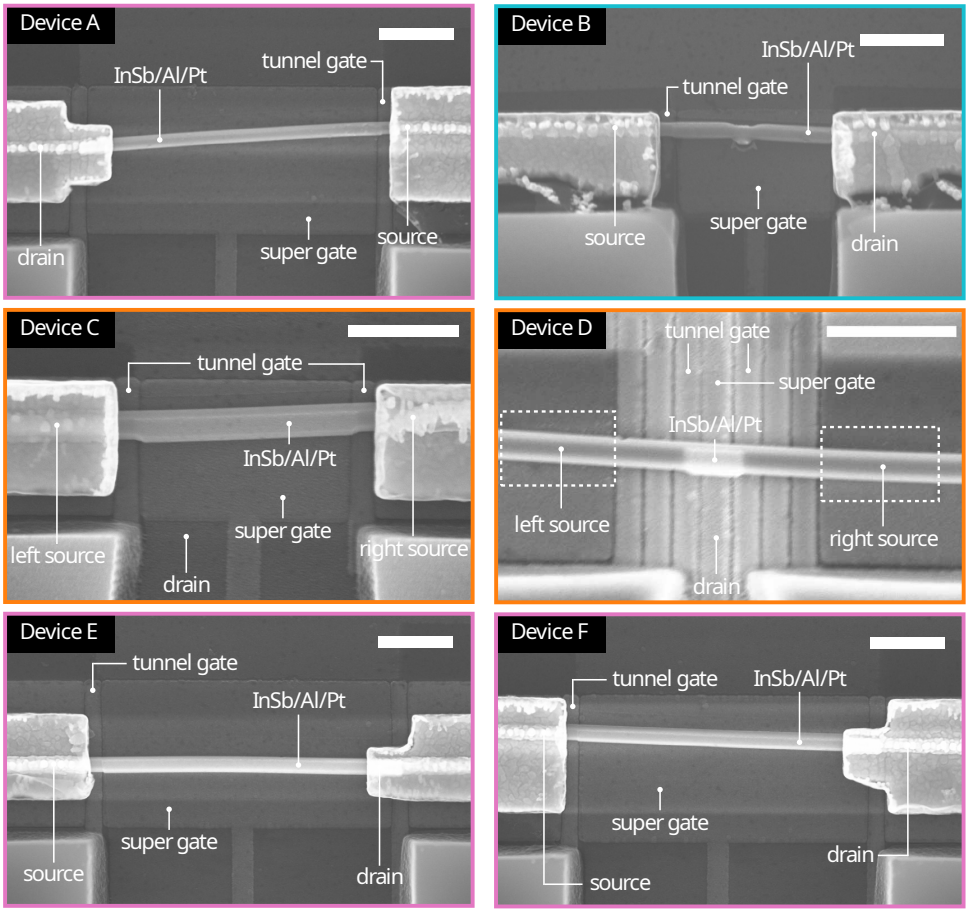

Figure 6.12: SEM images of some of the nanowire hybrid devices presented in this work. Scale bars are 500 nm. The borders of each panel are color-coded corresponding to the three bottom panels in Fig. 6.13, which show illustrations of the intended cross-section of various fabrication recipes used in this work. Device B, which showed Coulomb oscillations, was not intended to be an island device; we suspect a second barrier was present at the grounding contact due to incomplete Ar milling of the AlO_x capping layer. Additionally, it shows signs of ESD which we suspect happened during unloading from the fridge. The image of device D was taken prior to contact deposition - dashed rectangles indicate the designed contact location.

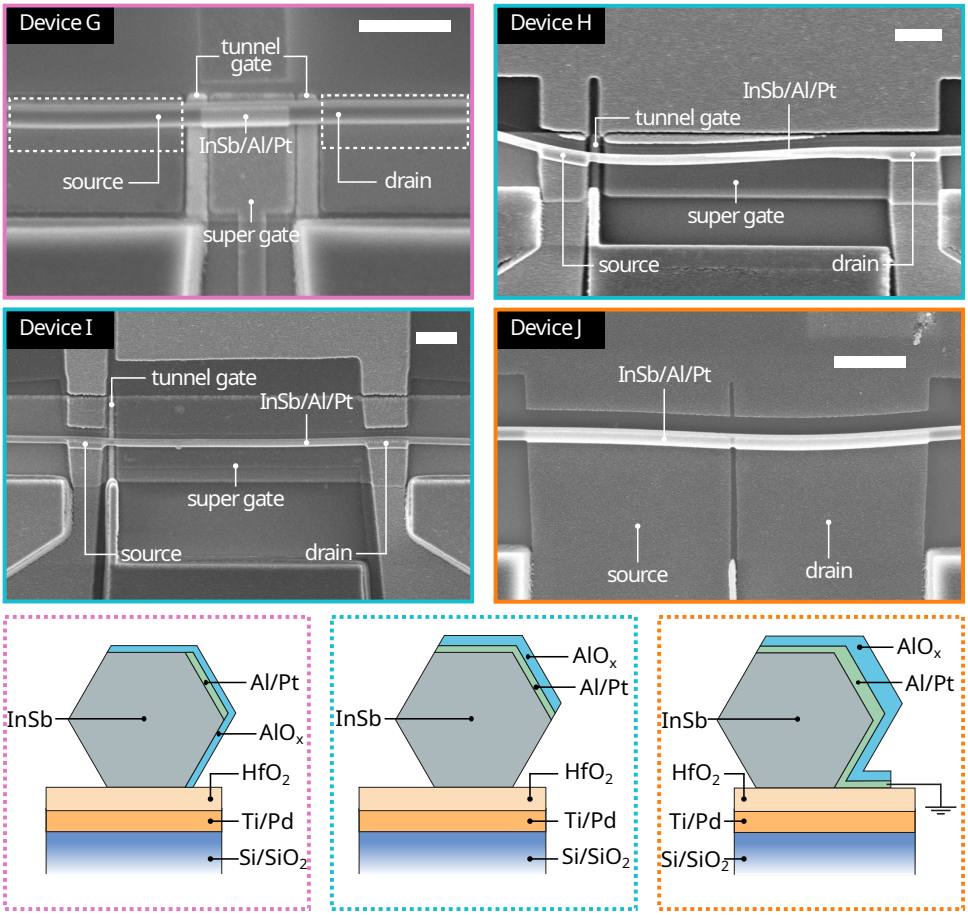

Figure 6.13: SEM images of the other nanowire hybrid devices presented in this work. Scale bars are 500 nm. The borders of each panel are color-coded corresponding to the three bottom panels, which show illustrations of the intended cross-section of various fabrication recipes used in this work. The image of device G was taken prior to contact deposition - dashed rectangles indicate the designed contact location.

6.8 Supporting information: Additional data on nanowire hybrids

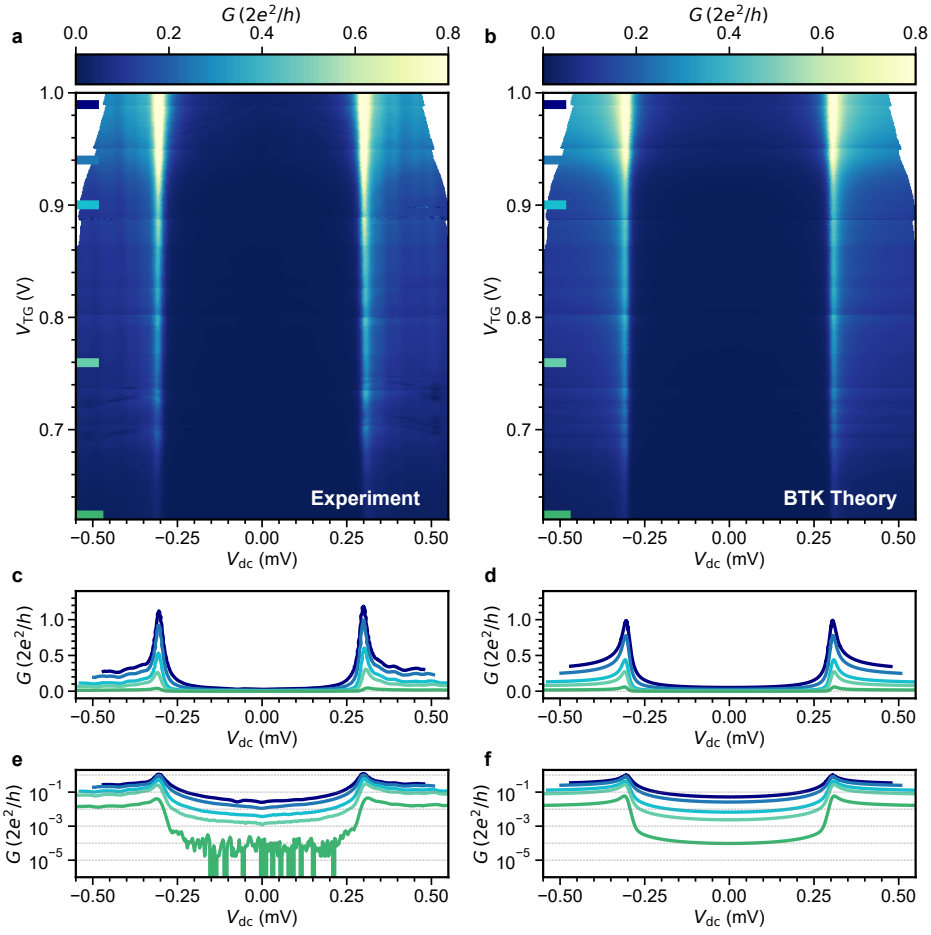

Figure 6.14: **Device A** additional data. **a.** Differential conductance as a function of tunnel gate voltage, taken at $V_{SG} = -0.8$ V. **b.** BTK theory, with $\Delta = 304\,\mu$eV, $T = 50$ mK and transmission G_N estimated from the experimental data. Bottom panels show conductance traces at various transmissions, taken at the locations designated by the colored lines, of the experiment (**c**) and theory (**d**) in a linear scale. The same traces are shown in logarithmic scale in panels **e,f**.

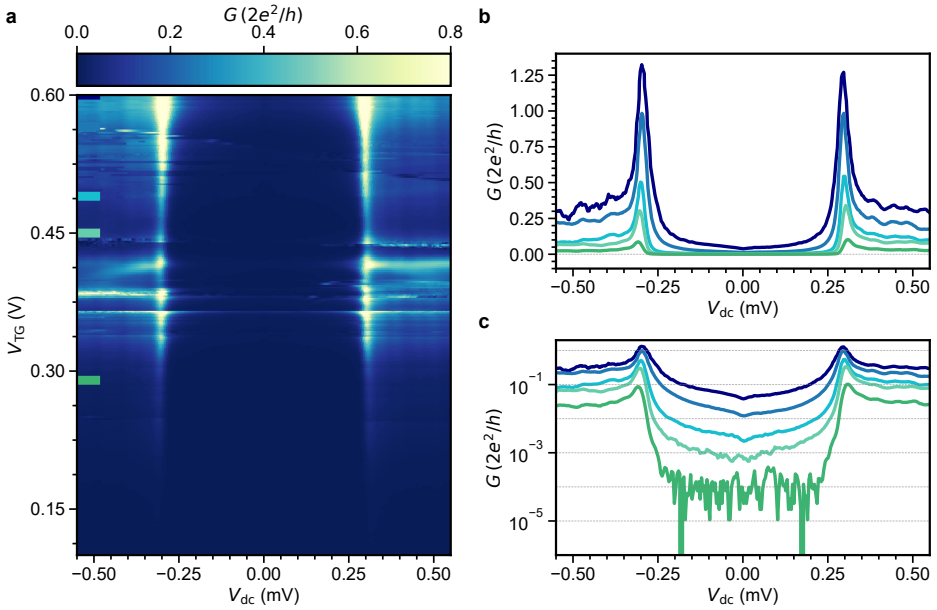

Figure 6.15: **Device A** additional data. **a.** Differential conductance as a function of tunnel gate voltage, taken at $V_{SG} = -2.0$ V. At this super gate voltage, an unfavorable electrostatic potential leads to more disordered transport in the tunnel junction. Line cuts taken at different transmission values of the tunnel junction, at the locations designated by the colored lines, are shown in the linear (**b**) and logarithmic (**c**) scale.

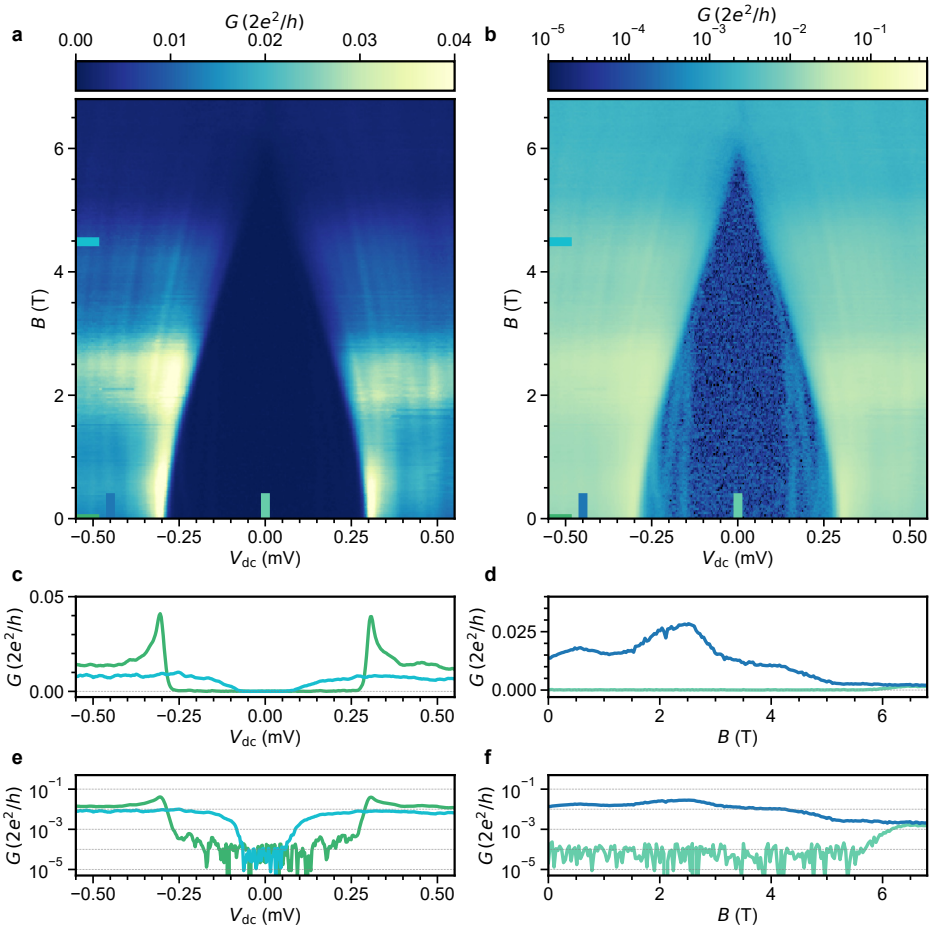

Figure 6.16: **Device E.** Additional data on magnetic field compatibility of single-facet devices. Differential conductance vs parallel magnetic field map presented in the linear (**a**) and logarithmic (**b**) scale. Panel **b** reveals a few discrete sub-gap states, which typically originate from disorder in the semiconducting junction. Panels **c** and **d** depict linecuts taken at B = 0 T (green) and B = 4.5 T (cyan). Out-of-gap and in-gap conductances as a function of magnetic field are shown in the linear (**d**) and logarithmic (**f**) scale. The length of the studied device is about 1.8 μm, similar to a device presented in the main text in Fig 2. The data is taken at V_{SG} = -2 V.

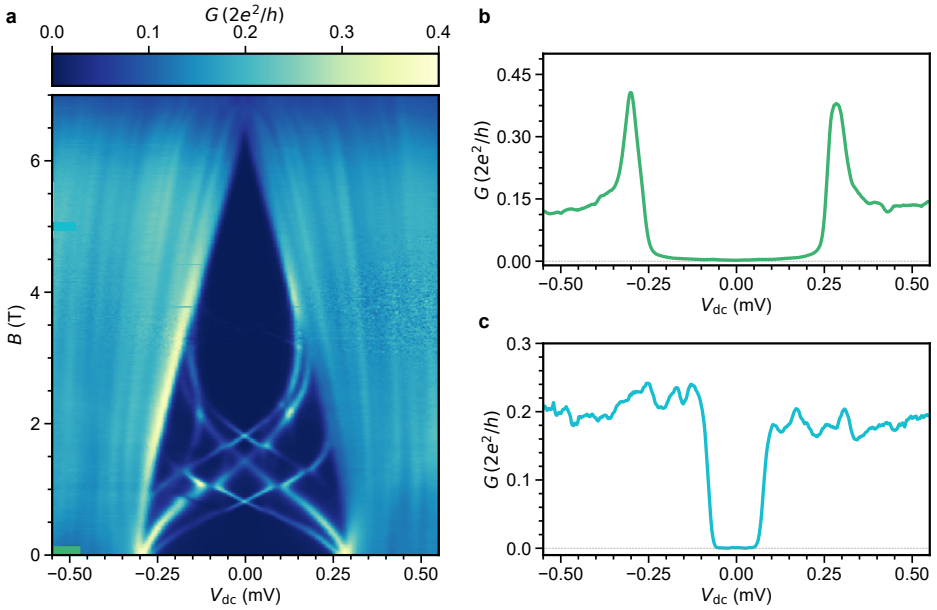

Figure 6.17: **Device F.** Additional data on magnetic field compatibility of single-facet devices. **a.** Differential conductance as a function of parallel magnetic field at $V_{SG} = 0$ V. Discrete Andreev bound states cross and anti-cross inside the gap. Above $B = 4$ T, the gap is hard again. Panels **b** and **c** depict differential conductance scans at $B = 0$ T and $B = 5$ T.

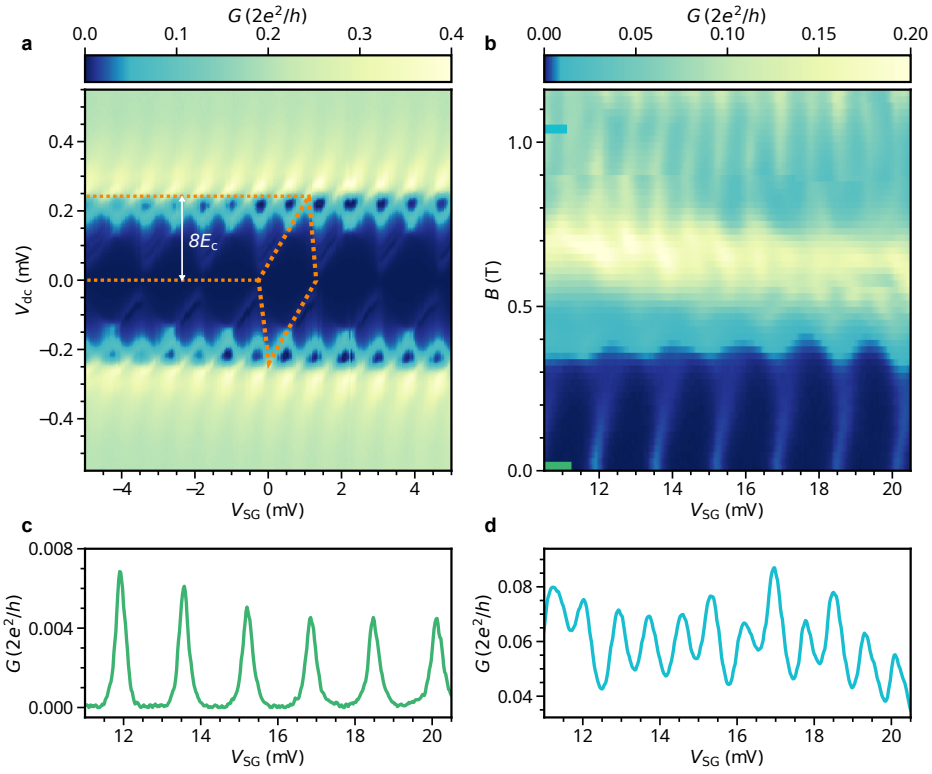

Figure 6.18: **Device B. a.** $2e$ coulomb diamonds with estimated diamond size in dashed orange lines. **b.** Parallel magnetic field dependence of $2e$ transport presented in Fig. 6.3 in the main text. A $2e$ to $1e$ transition is observed when the energy of the lowest energy sub-gap state drops below the charging energy of the island. **c,d** Linecuts of the magnetic field measurements, showing $2e$ periodic coulomb peaks at low magnetic field.

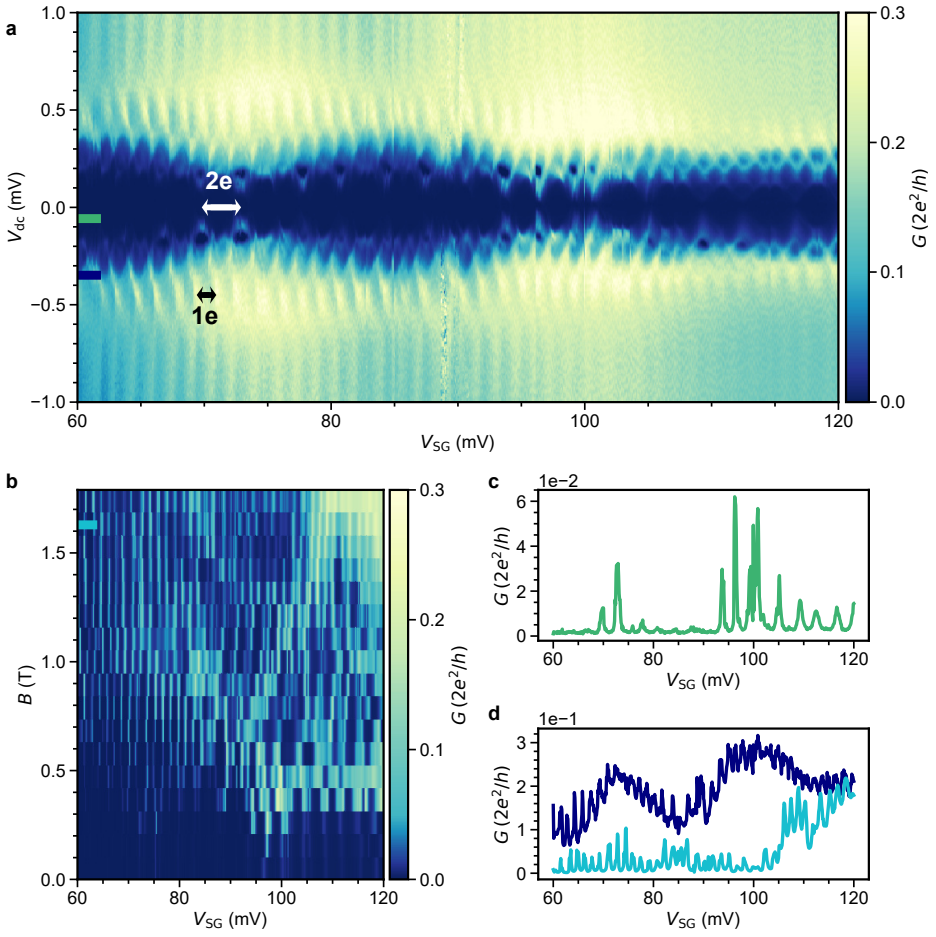

Figure 6.19: **Device G.** Additional data presenting $2e$ charging on a single-facet device. **a.** Voltage-bias spectroscopy, showing clear $2e$ and $1e$ charging processes. **b.** Magnetic field dependence of $2e$ transport. **c.** Linecut taken at zero bias and zero magnetic field. **d.** Linecuts at higher bias (B = 0 T) and B = 1.6 T (zero bias).

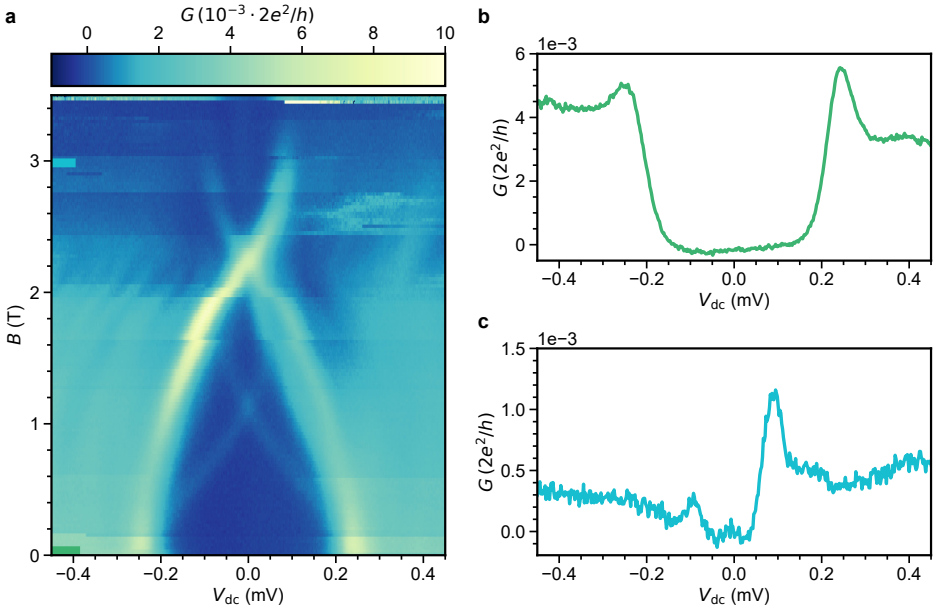

Figure 6.20: **Device H.** Example of a 2-facet device fabricated with the single-shot technique. **a.** Voltage bias spectroscopy as a function of magnetic field, which resembles the closing and reopening of the superconducting gap followed by the formation of a faint but stable zero-bias peak. Panels **b** and **c** depict differential conductance scans at $B = 0$ and $B = 3$ T. Due to non-functioning super gate and dielectric instability, the device could not be further investigated.

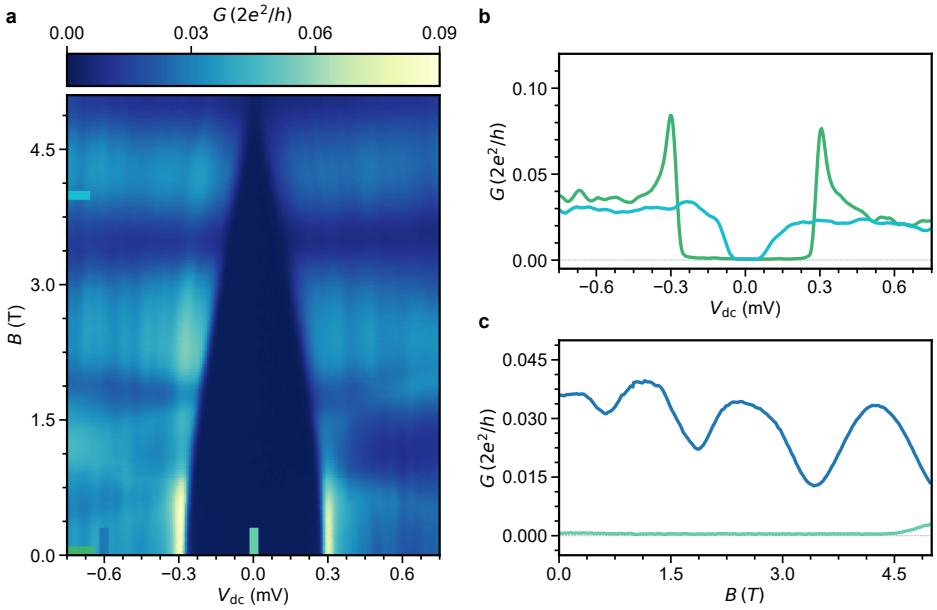

Figure 6.21: **Device I.** Example of a 2-facet device fabricated with the single-shot technique. **a.** Differential conductance map as a function of magnetic field, with a hard gap up to $B = 4.5\,\mathrm{T}$. **b.** Linecuts of the differential conductance at $B = 0\,\mathrm{T}$ and $B = 4\,\mathrm{T}$. **c.** Evolution of the out-of-gap ($V_{\mathrm{dc}} = 0.6\,\mathrm{mV}$) and in-gap ($V_{\mathrm{dc}} = 0\,\mathrm{mV}$) conductance as a function of parallel magnetic field. Oscillatory behavior of the out-of-gap conductance indicates the presence of a quantum dot in the vicinity of the tunnel junction.

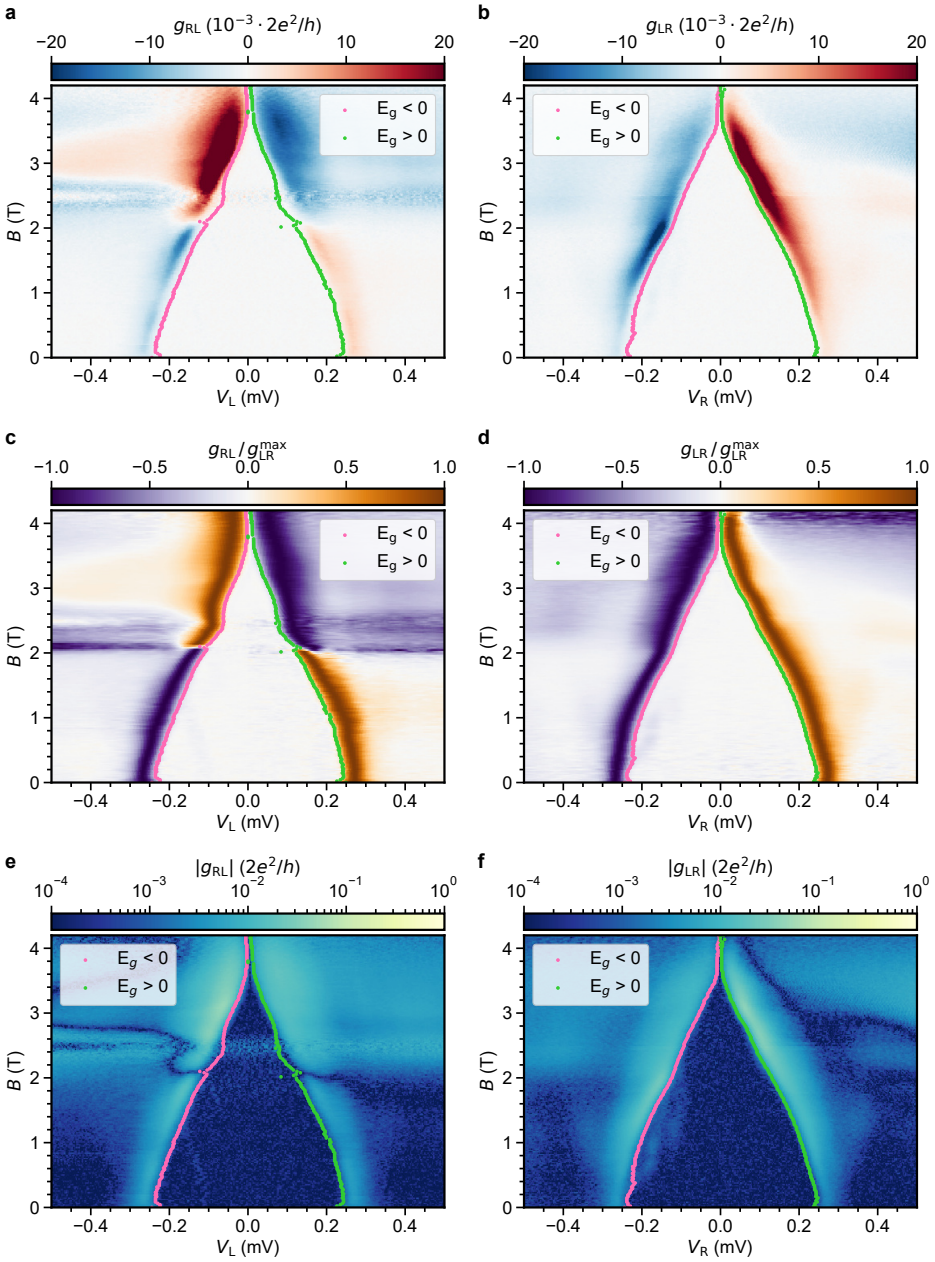

Figure 6.22: **Device C.** Extraction of the induced gap size from non-local signals g_{LR} **a** and g_{LR} **b**. Negative energy values are shown in pink, positive energy values in green. In panels **c** and **d**, the extracted gap values are overlayed with the normalized and Savitzky-Golay filtered data. Panels **e** and **f** show the absolute value of both non-local signals in a logarithmic scale.

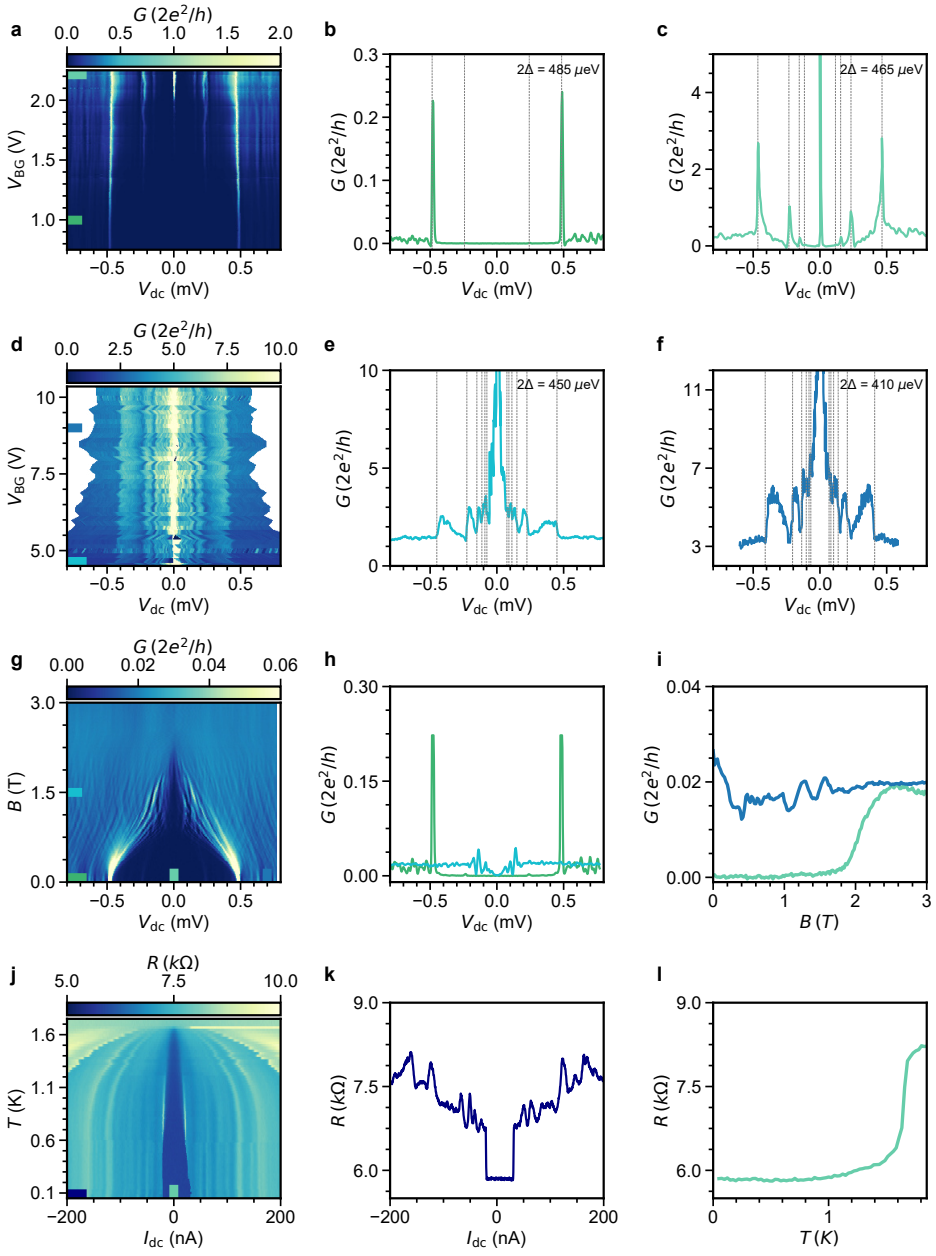
a
b
c
d
e
f
g
h
i
j
k
l
$G\,(2e^2/h)$
V_{BG} (V)
V_{dc} (mV)
2Δ = 485 μeV
2Δ = 465 μeV
2Δ = 450 μeV
2Δ = 410 μeV
B (T)
B (T)
R (kΩ)
T (K)
I_{dc} (nA)
R (kΩ)
T (K)

Figure 6.23: **Device J.** Collection of data on a nanowire Josephson junction with Al/Pt. **a.** Differential conductance as a function of back-gate voltage in a low-transmission regime. **b,c.** Differential conductance traces as a function of voltage bias. Linecuts are taken from panel **a** at the locations designated by the colored lines. **d.** Differential conductance at a higher transmission. **e,f.** Differential conductance traces as a function of voltage bias. Linecuts are taken from panel **d** at the locations designated by the colored lines. **g.** Parallel magnetic field evolution of the differential conductance, with a critical field of $B_c = 2$ T. **h.** Linecuts showing the zero-field and finite field spectroscopy, taken from panel **g** at the locations designated by the colored lines. **i.** Linecuts showing the in-gap and out-of-gap conductance, taken from panel **g** at the locations designated by the colored lines. **j.** Temperature evolution of the switching current. **k.** show the differential resistance trace at $T = 50$ mK. **l.** In-gap resistance versus temperature, indicating a critical temperature of $T_c = 1.6$ K. About 5.8 kΩ resistance in panels **j-l** corresponds to the resistance of the fridge lines. In comparison to InSb-Al Josephson junctions [9, 10], the reduced T_c in combination with a modest increase in B_c indicates that the orbital contribution of the magnetic field dominates the behavior of devices with relatively thick (12.5 nm) Al shells.

References

[1] R. M. Lutchyn, J. D. Sau, and S. Das Sarma, *Majorana fermions and a topological phase transition in semiconductor-superconductor heterostructures,* Phys. Rev. Lett. **105**, 077001 (2010).

[2] Y. Oreg, G. Refael, and F. Von Oppen, *Helical liquids and majorana bound states in quantum wires,* Phys. Rev. Lett. **105**, 177002 (2010).

[3] P. Krogstrup, N. Ziino, W. Chang, S. Albrecht, M. Madsen, E. Johnson, J. Nygård, C. M. Marcus, and T. Jespersen, *Epitaxy of semiconductor–superconductor nanowires,* Nat. Mater. **14**, 400 (2015).

[4] J. Shabani, M. Kjaergaard, H. J. Suominen, Y. Kim, F. Nichele, K. Pakrouski, T. Stankevic, R. M. Lutchyn, P. Krogstrup, R. Feidenhans'l, S. Kraemer, C. Nayak, M. Troyer, C. M. Marcus, and C. J. Palmstrøm, *Two-dimensional epitaxial superconductor-semiconductor heterostructures: A platform for topological superconducting networks,* Phys. Rev. B **93**, 155402 (2016).

[5] M. Deng, C. Yu, G. Huang, M. Larsson, P. Caroff, and H. Xu, *Anomalous zero-bias conductance peak in a Nb–InSb nanowire–Nb hybrid device,* Nano letters **12**, 6414 (2012).

[6] R. M. Lutchyn, E. P. Bakkers, L. P. Kouwenhoven, P. Krogstrup, C. M. Marcus, and Y. Oreg, *Majorana zero modes in superconductor–semiconductor heterostructures,* Nat. Rev. Mater. **3**, 52 (2018).

[7] S. Plugge, A. Rasmussen, R. Egger, and K. Flensberg, *Majorana box qubits,* New J. Phys. **19**, 012001 (2017).

[8] D. J. Carrad, M. Bjergfelt, T. Kanne, M. Aagesen, F. Krizek, E. M. Fiordaliso, E. Johnson, J. Nygård, and T. S. Jespersen, *Shadow epitaxy for in situ growth of generic semiconductor/superconductor hybrids,* Advanced Materials **32**, 1908411 (2020).

[9] S. Heedt, M. Quintero-Pérez, F. Borsoi, A. Fursina, N. van Loo, G. P. Mazur, M. P. Nowak, M. Ammerlaan, K. Li, S. Korneychuk, *et al.*, *Shadow-wall lithography of ballistic superconductor–semiconductor quantum devices,* Nat. Commun. **12**, 1 (2021).

[10] F. Borsoi, G. P. Mazur, N. van Loo, M. P. Nowak, L. Bourdet, K. Li, S. Korneychuk, A. Fursina, J.-Y. Wang, V. Levajac, E. Memisevic, G. Badawy, S. Gazibegovic, K. van Hoogdalem, E. P. A. M. Bakkers, L. P. Kouwenhoven, S. Heedt, and M. Quintero-Pérez, *Single-shot fabrication of semiconducting–superconducting nanowire devices,* Adv. Func. Mater. , 2102388 (2021), https://onlinelibrary.wiley.com/doi/pdf/10.1002/adfm.202102388 .

[11] J. Shen, S. Heedt, F. Borsoi, B. Van Heck, S. Gazibegovic, R. L. O. het Veld, D. Car, J. A. Logan, M. Pendharkar, S. J. Ramakers, *et al.*, *Parity transitions in the superconducting ground state of hybrid InSb–Al Coulomb islands,* Nat. Commun. **9**, 1 (2018).

[12] A. E. Antipov, A. Bargerbos, G. W. Winkler, B. Bauer, E. Rossi, and R. M. Lutchyn, *Effects of gate-induced electric fields on semiconductor majorana nanowires,* Phys. Rev. X **8**, 031041 (2018).

[13] M. W. A. de Moor, J. D. S. Bommer, D. Xu, G. W. Winkler, A. E. Antipov, A. Bargerbos, G. Wang, N. van Loo, R. L. M. O. het Veld, S. Gazibegovic, D. Car, J. A. Logan, M. Pendharkar, J. S. Lee, E. P. A. M. Bakkers, C. J. Palmstrøm, R. M. Lutchyn, L. P. Kouwenhoven, and H. Zhang, *Electric field tunable superconductor-semiconductor coupling in majorana nanowires,* New J. Phys. **20**, 103049 (2018).

[14] S. Ahn, H. Pan, B. Woods, T. D. Stanescu, and S. Das Sarma, *Estimating disorder and its adverse effects in semiconductor majorana nanowires,* Phys. Rev. Materials **5**, 124602 (2021).

[15] M. Pendharkar, B. Zhang, H. Wu, A. Zarassi, P. Zhang, C. P. Dempsey, J. S. Lee, S. D. Harrington, G. Badawy, S. Gazibegovic, R. L. M. Op het Veld, M. Rossi, J. Jung, A.-H. Chen, M. A. Verheijen, M. Hocevar, E. P. A. M. Bakkers, C. J. Palmstrøm, and S. M. Frolov, *Parity-preserving and magnetic field–resilient superconductivity in InSb nanowires with Sn shells,* Science **372**, 508 (2021), https://science.sciencemag.org/content/372/6541/508.full.pdf .

[16] J. Paajaste, M. Amado, S. Roddaro, F. Bergeret, D. Ercolani, L. Sorba, and F. Giazotto, *Pb/InAs nanowire josephson junction with high critical current and magnetic flux focusing,* Nano Lett. **15**, 1803 (2015).

[17] T. Kanne, M. Marnauza, D. Olsteins, D. J. Carrad, J. E. Sestoft, J. de Bruijckere, L. Zeng, E. Johnson, E. Olsson, K. Grove-Rasmussen, *et al.*, *Epitaxial Pb on InAs nanowires for quantum devices,* Nat. Nanotechnol. , 1 (2021).

[18] M. S. Bjergfelt, D. J. Carrad, T. Kanne, E. Johnson, E. M. Fiordaliso, T. S. Jespersen, and J. Nygård, *Superconductivity and parity preservation in as-grown In islands on InAs nanowires,* Nano letters **21**, 9875 (2021).

[19] J. M. Baker, C. J. Kircher, and J. Matthews, *Structure of tunnel barrier oxide for Pb-alloy josephson junctions,* IBM Journal of Research and Development **24**, 223 (1980).

[20] S. A. Khan, C. Lampadaris, A. Cui, L. Stampfer, Y. Liu, S. J. Pauka, M. E. Cachaza, E. M. Fiordaliso, J.-H. Kang, S. Korneychuk, T. Mutas, J. E. Sestoft, F. Krizek, R. Tanta, M. C.

Cassidy, T. S. Jespersen, and P. Krogstrup, *Highly transparent gatable superconducting shadow junctions,* ACS Nano **14**, 14605 (2020).

[21] B. S. Chandrasekhar, *A note on the maximum critical field of high-field superconductors,* Appl. Phys. Lett. **1**, 7 (1962).

[22] A. M. Clogston, *Upper limit for the critical field in hard superconductors,* Phys. Rev. Lett. **9**, 266 (1962).

[23] P. M. Tedrow and R. Meservey, *Critical magnetic field of very thin superconducting aluminum films,* Phys. Rev. B **25**, 171 (1982).

[24] P. Monceau, *Resistive transitions of superconducting thin films in strong electric fields,* Phys. Lett. A **47**, 193 (1974).

[25] X. S. Wu, P. W. Adams, Y. Yang, and R. L. McCarley, *Spin proximity effect in ultrathin superconducting Be-Au bilayers,* Phys. Rev. Lett. **96**, 127002 (2006).

[26] A. McAlister and D. Kahan, *The Al- Pt (aluminum-platinum) system,* Bulletin of Alloy Phase Diagrams **7**, 47 (1986).

[27] W. Wu and P. Adams, *Avalanches and slow relaxation: dynamics of ultrathin granular superconducting films in a parallel magnetic field,* Phys. Rev. Lett. **74**, 610 (1995).

[28] M. Tinkham, *Introd. to Supercond. 2nd Ed.*, 2nd ed. (Dover, 2004).

[29] L. D. Alegria, C. G. Bøttcher, A. K. Saydjari, A. T. Pierce, S. H. Lee, S. P. Harvey, U. Vool, and A. Yacoby, *High-energy quasiparticle injection into mesoscopic superconductors,* Nat. Nanotechnol. **16**, 404 (2021).

[30] R. Meservey and P. Tedrow, *Spin-polarized electron tunneling,* Phys. Rep. **238**, 173 (1994).

[31] J. Alexander, T. Orlando, D. Rainer, and P. Tedrow, *Theory of fermi-liquid effects in high-field tunneling,* Phys. Rev. B **31**, 5811 (1985).

[32] S. M. Albrecht, A. P. Higginbotham, M. Madsen, F. Kuemmeth, T. S. Jespersen, J. Nygård, P. Krogstrup, and C. Marcus, *Exponential protection of zero modes in majorana islands,* Nature **531**, 206 (2016).

[33] A. Savin, M. Meschke, J. P. Pekola, Y. A. Pashkin, T. Li, H. Im, and J.-S. Tsai, *Parity effect in Al and Nb single electron transistors in a tunable environment,* Appl. Phys. Lett. **91**, 063512 (2007).

[34] J. Shen, G. W. Winkler, F. Borsoi, S. Heedt, V. Levajac, J.-Y. Wang, D. van Driel, D. Bouman, S. Gazibegovic, R. L. M. Op Het Veld, D. Car, J. A. Logan, M. Pendharkar, C. J. Palmstrøm, E. P. A. M. Bakkers, L. P. Kouwenhoven, and B. van Heck, *Full parity phase diagram of a proximitized nanowire island,* Phys. Rev. B **104**, 045422 (2021).

[35] G. E. Blonder, M. Tinkham, and T. M. Klapwijk, *Transition from metallic to tunneling regimes in superconducting microconstrictions: Excess current, charge imbalance, and supercurrent conversion,* Phys. Rev. B **25**, 4515 (1982).

[36] S. Das Sarma, J. D. Sau, and T. D. Stanescu, *Splitting of the zero-bias conductance peak as smoking gun evidence for the existence of the majorana mode in a superconductor-semiconductor nanowire,* Phys. Rev. B **86**, 220506 (2012).

[37] E. Prada, P. San-Jose, M. W. de Moor, A. Geresdi, E. J. Lee, J. Klinovaja, D. Loss, J. Nygård, R. Aguado, and L. P. Kouwenhoven, *From Andreev to Majorana bound states in hybrid superconductor–semiconductor nanowires,* Nat. Rev. Phys. **2**, 575 (2020).

[38] H. Pan, C.-X. Liu, M. Wimmer, and S. Das Sarma, *Quantized and unquantized zero-bias tunneling conductance peaks in majorana nanowires: Conductance below and above* $2e^2/h$*,* Phys. Rev. B **103**, 214502 (2021).

[39] D. Puglia, E. A. Martinez, G. C. Ménard, A. Pöschl, S. Gronin, G. C. Gardner, R. Kallaher, M. J. Manfra, C. M. Marcus, A. P. Higginbotham, and L. Casparis, *Closing of the induced gap in a hybrid superconductor-semiconductor nanowire,* Phys. Rev. B **103**, 235201 (2021).

[40] T. O. Rosdahl, A. Vuik, M. Kjaergaard, and A. R. Akhmerov, *Andreev rectifier: A nonlocal conductance signature of topological phase transitions,* Phys. Rev. B **97**, 045421 (2018).

[41] D. I. Pikulin, B. van Heck, T. Karzig, E. A. Martinez, B. Nijholt, T. Laeven, G. W. Winkler, J. D. Watson, S. Heedt, M. Temurhan, V. Svidenko, R. M. Lutchyn, M. Thomas, G. de Lange, L. Casparis, and C. Nayak, *Protocol to identify a topological superconducting phase in a three-terminal device,* arXiv e-prints **2103.12217** (2021).

[42] E. J. Lee, X. Jiang, M. Houzet, R. Aguado, C. M. Lieber, and S. De Franceschi, *Spin-resolved Andreev levels and parity crossings in hybrid superconductor–semiconductor nanostructures,* Nat. Nanotechnol. **9**, 79 (2014).

[43] A. Jellinggaard, K. Grove-Rasmussen, M. H. Madsen, and J. Nygård, *Tuning Yu-Shiba-Rusinov states in a quantum dot,* Phys. Rev. B **94**, 064520 (2016).

[44] K. D. Usadel, *Generalized diffusion equation for superconducting alloys,* Phys. Rev. Lett. **25**, 507 (1970).

[45] G. Eilenberger, *Transformation of Gorkov's equation for type II superconductors into transport-like equations,* Zeitschrift für Phys. **214**, 195 (1968).

[46] A. Larkin and Y. Ovchinnikov, *Quasiclassical Method in the Theory of Superconductivity,* Sov Phys JETP **28**, 1200 (1969).

[47] P. G. de Gennes, *Superconductivity of Metals and Alloys*, 1st ed. (CRC Press, 1999).

[48] K. Maki, *The Behavior of Superconducting Thin Films in the Presence of Magnetic Fields and Currents*),* Progress of Theoretical Physics **31**, 731 (1964), https://academic.oup.com/ptp/article-pdf/31/5/731/5322574/31-5-731.pdf .

[49] F. Aikebaier, P. Virtanen, and T. Heikkilä, *Superconductivity near a magnetic domain wall,* Phys. Rev. B **99**, 104504 (2019), arXiv:1812.08410 .

[50] T. T. Heikkilä, M. Silaev, P. Virtanen, and F. S. Bergeret, *Thermal, electric and spin transport in superconductor/ferromagnetic-insulator structures,* Progress in Surface Science **94**, 100540 (2019).

[51] A. Khindanov, J. Alicea, P. Lee, W. S. Cole, and A. E. Antipov, *Topological superconductivity in nanowires proximate to a diffusive superconductor–magnetic-insulator bilayer,* Phys. Rev. B **103**, 134506 (2021).

[52] E. A. Martinez, A. Pöschl, E. B. Hansen, M. A. Y. van de Poll, S. Vaitiekėnas, A. P. Higginbotham, and L. Casparis, *Measurement circuit effects in three-terminal electrical transport measurements,* arXiv e-prints **2104.02671** (2021).

7

Electrostatic control of the proximity effect in the bulk of semiconductor-superconductor hybrids

The proximity effect in semiconductor-superconductor nanowires is expected to generate an induced gap in the semiconductor. The magnitude of this induced gap, together with the semiconductor properties like spin-orbit coupling and g-factor, depends on the coupling between the materials. It is predicted that this coupling can be adjusted through the use of electric fields. We study this phenomenon in InSb/Al/Pt hybrids using nonlocal spectroscopy. We show that these hybrids can be tuned such that the semiconductor and superconductor are strongly coupled. In this case, the induced gap is similar to the superconducting gap in the Al/Pt shell and closes only at high magnetic fields. In contrast, the coupling can be suppressed which leads to a strong reduction of the induced gap and critical magnetic field. At the crossover between the strong-coupling and weak-coupling regimes, we observe the closing and reopening of the induced gap in the bulk of a nanowire. Contrary to expectations, it is not accompanied by the formation of zero-bias peaks in the local conductance spectra. As a result, this cannot be attributed conclusively to the anticipated topological phase transition and we discuss possible alternative explanations.

This chapter has been published as *Electrostatic control of the proximity effect in the bulk of semiconductor-superconductor hybrids*, **N. van Loo**[†], G.P. Mazur[†], T. Dvir, G. Wang, R.C. Dekker, J.-Y. Wang, M. Lemang, C. Sfiligoj, A. Bordin, D. van Driel, G. Badawy, S. Gazibegovic, E.P.A.M. Bakkers and L.P. Kouwenhoven in Nature Communications 14, 3325 (2023).
[†] These authors contributed equally to this work.

7.1 Introduction

When a semiconductor is coupled to a superconductor, the resulting hybrid is expected to inherit properties of both. The combination of these properties can be exploited to create exotic phases of matter [1, 2]. For example, a magnetic field can trigger the transition to a phase of topological superconductivity in semiconducting nanowires with strong spin-orbit coupling [3, 4]. In theory, this should be accompanied by the formation of Majorana zero modes (MZMs) at the ends, together with a closing and reopening of the superconducting gap in the bulk of the hybrid [5, 6]. In general, the proximity effect induces superconductivity in the semiconductor as a result of Andreev reflection at the interface between the materials. This effect manifests itself as the emergence of an induced superconducting gap Δ_i in the semiconductor. The size of this gap depends on the size of the proximitizing superconductor Δ_{SC}, as well as the coupling between the materials [7]. Importantly, the coupling also affects various other properties of the hybrid, such as the spin-orbit coupling and g - factor. Moreover, it is expected to be tunable through the use of electric fields [8, 9].

In experiments, a modest tunability of the superconducting gap [10, 11] and the g - factor of Andreev bound states (ABSs) [12, 13] have been reported. However, most experiments to date rely on tunnelling measurements at the end of a nanowire, which only provide information on the local density of states. Yet, it remains unknown what information these observations provide about the proximity effect in the bulk of a hybrid. Advances in nanofabrication now enable the study of semiconductor-superconductor hybrids in a three-terminal geometry [14–16]. In addition to the local density of states at the two ends of a nanowire, such devices allow the nonlocal conductance to be measured. Nonlocal transport is fundamentally carried by states in the nanowire that couple to both leads. Moreover, it requires their energy to reside in an energy window between the gap of the superconductor and the induced gap in the semiconductor [5], and thus can be used to directly determine the induced gap in the bulk of the hybrid [17]. Measurements in this geometry have been used to observe the closing of the induced gap [18], map the local charge of ABSs [19, 20], investigate the quasiparticle wavefunction composition [21] and search for topological superconductivity in a variety of platforms [22, 23].

In this article, we investigate the effect of gate-induced electric fields on the bulk of InSb nanowires, proximitized by Al/Pt films [24]. To do this, we utilize nonlocal spectroscopy. We demonstrate that the devices can be tuned into a strongly-coupled regime with an induced gap close to that of the Al/Pt shell. Likewise, gate voltages can be used to significantly reduce the induced gap and eventually fully close it. By applying a parallel magnetic field, we show that wires in the strong-coupling regime can have critical magnetic fields close to that of the superconducting shell. On the other hand, a gate-reduced coupling drastically lowers the critical field.

The three-terminal devices presented in this work are fabricated using our shadow-wall lithography technique [15, 16]. In Fig. 7.1a we depict the device schematic of a nanowire hybrid used in these experiments. A set of pre-patterned bottom gates is separated from the InSb nanowire by a thin layer of HfO_2. Voltages on the two tunnel gates, V_{TL} and

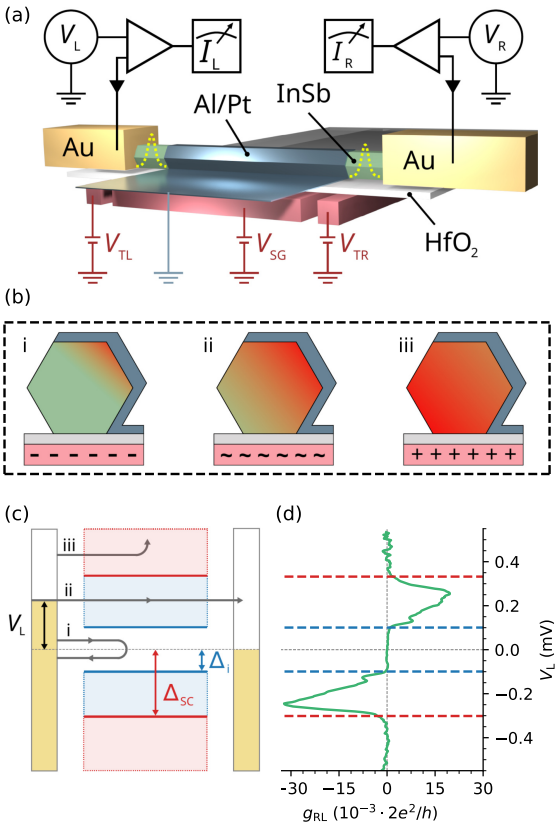

Figure 7.1: (a) Schematic of a three-terminal hybrid device and the measurement circuit. The superconducting shell is grounded through its connection to the film on the substrate. Yellow dashed potentials indicate the formation of tunnel barriers in the semiconducting junctions. (b) Illustration of three different coupling regimes between the superconductor and semiconductor. (i) Strong-coupling: electrons (red) are confined at the interface which results in a renormalization of the semiconducting properties. (ii) Crossover: predicted to be optimal for the formation of a topological superconductor. (iii): Weak-coupling: electrons accumulate far from the interface, which can result in unproximitized states. (c) Transport schematic of nonlocal measurements. (i) Below Δ_i (blue), only local processes are possible. (ii) In between Δ_i and Δ_{SC}, nonlocal transport can occur. (iii) Above Δ_{SC}, electrons are drained to ground. (d) Example of measured nonlocal conductance g_{RL} taken on device A, corresponding to the diagram in (c). Blue and red dashed lines indicate the induced and superconductor gap, respectively.

V_{TR}, are used to induce tunnel barriers in the exposed semiconducting segments. The super gate voltage V_{SG} is used to apply an electric field in the bulk of the hybrid. The nanowire is covered on three facets by an Al/Pt film, where the Pt serves to enhance the critical magnetic field of the Al film [24]. This superconducting shell extends onto the substrate, forming the connection to ground. Two Cr/Au contacts are fabricated at the ends of the wire. The devices are measured by individually applying bias voltages, V_L and V_R, to the left and right leads. The conductance matrix is obtained by measuring the differential conductances $g_{ij} \equiv dI_i/dV_j$, with $i, j = L, R$ using standard lock-in techniques

(see Supplementary section I and II for details of device fabrication and measurement).

In Fig. 7.1b, we illustrate the expected effect of electric fields on the bulk of the hybrid as calculated by [25]. For negative gate voltages (Fig. 7.1b(i)), electrons accumulate near the semiconductor-superconductor interface which results in a strong coupling to the superconductor. As a consequence, the semiconducting properties of the hybrid are strongly renormalized. We refer to this as the strong-coupling regime in the rest of this work. On the other hand, electrons can accumulate far from the interface through the application of positive gate voltages (Fig. 7.1b(iii)). This results in a diminished coupling with unproximitized states in the hybrid, to which we refer as the weak-coupling regime. Finally, there is a crossover between these two regimes (Fig. 7.1b(ii)) where electrons still maintain superconducting correlations, while their semiconducting properties are only moderately renormalized. As a result, this crossover is expected to be optimal for the emergence of topological superconductivity [25]. Furthermore, the application of an electric field also changes the electron density in the hybrid. Due to quantum confinement we expect the formation of discrete subbands, each with their own coupling strength. Thus, applied gate voltages should be able to tune the hybrid between the different subbands.

To characterize the different coupling regimes, we determine the induced gap in our devices using nonlocal spectroscopy. The transport mechanisms involved in such measurements are schematically depicted in Fig. 7.1c, together with an example of the resulting nonlocal conductance g_{RL} in Fig. 7.1d. If the applied bias V_{L} is below the induced gap Δ_{i}, electrons from the lead can only enter the superconducting region through Andreev reflection (Fig. 7.1c(i)). This results in the formation of Cooper pairs, which drain away into the superconducting lead. As a consequence, no nonlocal conductance is observed below the induced gap (Fig. 7.1d). Similarly, electrons injected above the gap of the superconductor Δ_{SC} are likely to drain to the ground without reaching the other side [26] (Fig. 7.1c(iii)). However, if the applied bias is larger than Δ_{i} but below Δ_{SC}, injected electrons can reach the opposite lead of the device. This results in a finite nonlocal conductance as shown in Fig. 7.1d, from which Δ_{i} (dashed blue lines) and Δ_{SC} (dashed red lines) can be estimated. In Supplementary section III, we describe how these parameters are determined from the data. While this picture helps to understand three-terminal measurements, we note that nonlocal processes can involve energy relaxation of the injected electrons as well as non-equilibrium effects not captured by the single-particle transport theory [21]. We further elaborate on this in Supplementary section II.B.

7.2 Results and Discussion

First, we investigate the gate tunability of the induced gap. We measure the full conductance matrix of a device as a function of super gate voltage V_{SG} at zero magnetic field. In Fig. 7.2, we show such a measurement on a long nanowire hybrid (device B, 8 μm long). Panels c and d depict the nonlocal signals g_{RL} and g_{LR}, in which the induced gap is directly visible as the white area between two anti-symmetric peaks. For a large range of low gate voltages, the peaks in the nonlocal signal are relatively sharp. This indicates that the difference between Δ_{i} and Δ_{SC} is small, and so it is associated with the

strong-coupling regime. Above a certain gate voltage $V_{SG} > 3.5\,V$, the peaks gradually become wider. This signals the reduction of the induced gap, as the coupling between the semiconductor and superconductor is decreased. The induced gap fully closes above $V_{SG} > 6\,V$, which means that at this point there reside states in the bulk of the nanowire which do not couple at all to the superconductor. To better visualize the effect of V_{SG}, in the top panel of Fig. 7.2e we plot the behavior of the induced gap in the bulk (blue) and the gap of the superconducting shell (red). In addition, we show in the bottom panel the nonlocal slope at zero bias [18]. This parameter is defined as $S_{ij} \equiv d^2I_i/dV_j^2|_{V_j=0}$, with S_{RL} presented in purple and S_{LR} in orange. Indeed, their deviation from zero above $V_{SG} > 6\,V$ confirms that the hybrid has become gapless. We generically observe the tunability of the induced gap, and hence the coupling between the semiconductor and superconductor. However, the application of an electric field does not exclusively tune the coupling but also controls the density in the hybrid. Typically, we observe a sudden onset of the reduction of Δ_i while the magnitude of the nonlocal signal increases concurrently.This behavior has theoretically been related to the occupation of an additional subband with a reduced coupling [8]. Still, it remains unknown how many sub-bands are active in our hybrids.

It is particularly interesting how the reduction of the induced gap is also reflected in the local signals g_{LL} and g_{RR}, which are displayed in Fig. 7.2a and b. In the strong-coupling regime, the local signals exhibit two sharp coherence peaks and for the majority of the gate voltages, a clean superconducting gap. However, some states can be seen in these spectra which do not correlate between the two panels nor show up in the nonlocal signals - a confirmation that these states are confined to the local tunnel junctions. Exemplary linecuts in this regime of the full conductance matrix are shown in Fig. 7.2f. In g_{LL} and g_{RR}, we see a typical local spectrum which in literature is referred to as a hard superconducting gap. While the sub-gap conductance does not actually go to zero, we note that the junctions are relatively transparent. This results in a significant amount of Andreev reflection [27], which contributes only to the local conductance. To confirm this, we have repeated similar measurements in the tunneling regime (see Supplementary information Fig. 7.14). Indeed, the hard gap is also visible in g_{RL} and g_{LR}, which show zero response outside of the two anti-symmetric peaks. As V_{SG} increases, the semiconductor-superconductor coupling is reduced. Linecuts in the regime of weak coupling are shown in Fig. 7.2f. The coherence peaks visible in g_{LL} and g_{RR} have now broadened significantly, while the sub-gap conductance still only contains contributions from Andreev reflection. The peaks in g_{RL} and g_{LR} have also broadened accordingly, while the absence of signal in between still evidences a hard gap. This changes when V_{SG} is increased further, as show in Fig. 7.2g. The absence of a flat part in g_{RL} and g_{LR} now indicates that an induced gap is absent in the system. This is also seen in g_{LL} and g_{RR}, where the conductance close to zero bias is now increased beyond what can be explained by Andreev reflection. Indeed, the nanowire now exhibits a soft gap as measured from the local spectra, while the nonlocal signals demonstrate that the hybrid is gapless. Such a soft gap has long been attributed only to the quality of the semiconductor-superconductor interface [28]. Yet, here we show that this is not the full story: a soft gap can equally well exist in hybrids with a pristine interface. In this

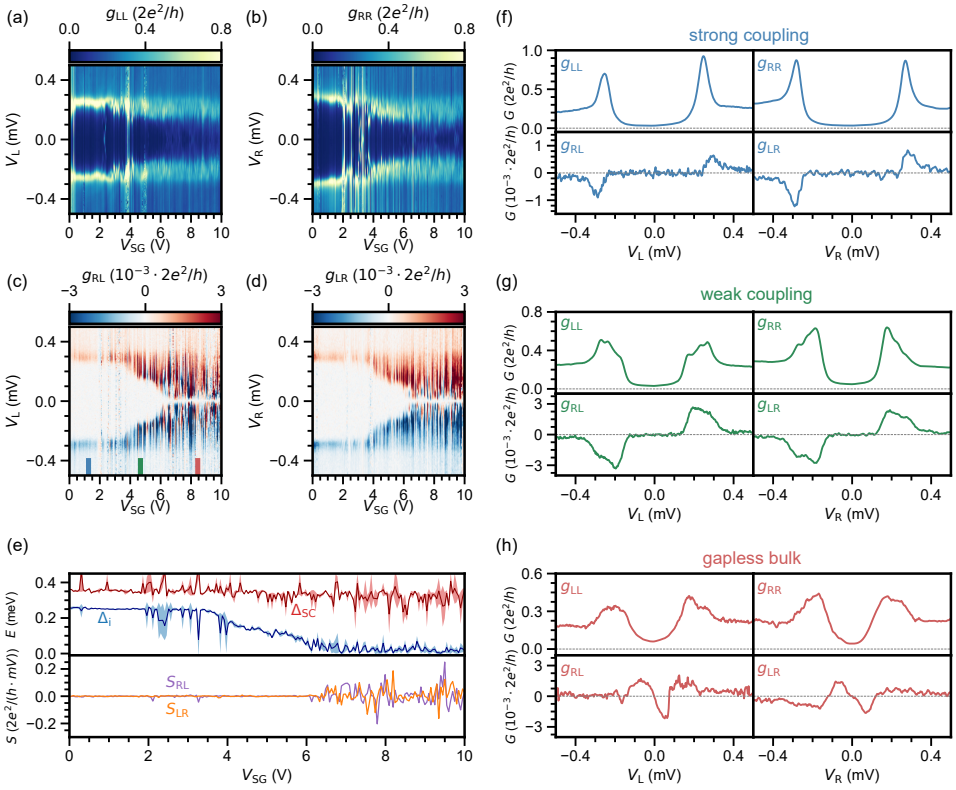

Figure 7.2: (a-d) Conductance matrix measured as a function of V_{SG} in the absence of a magnetic field on device B (8 μm long hybrid). At low V_{SG}, a large induced gap is observed in g_{RL} and g_{LR} (panels c,d). For increasing V_{SG}, the induced gap gradually decreases and eventually fully closes. At the same time, the superconducting gap in g_{LL} and g_{RR} (panels a,b) becomes soft. (e) Top: Δ_i (blue) and Δ_{SC} (red). Dark colors represent the mean of four values, obtained from the positive and negative biases of the two nonlocal signals. Similarly, the shaded areas correspond to the standard deviation. Bottom: calculated nonlocal slope at zero bias for g_{RL} (purple) and g_{LR} (orange). (f) Linecuts of the conductance matrix taken at V_{SG} = 1.26 V in the strong-coupling regime, where a large induced gap is observed. (g) Linecuts of the conductance matrix taken at V_{SG} = 4.67 V in the weak-coupling regime, where the induced gap is significantly reduced. (h). Linecuts of the conductance matrix taken at V_{SG} = 8.44 V. The induced gap is closed as visible in g_{RL} and g_{LR}, whereas the superconducting gap in g_{LL} and g_{RR} has turned soft.

case, it is caused by a combination of a weak semiconductor-superconductor coupling and increasing electron density in the nanowire. Since a high electron density and weak or absent semiconductor-superconductor coupling are unfavorable conditions for the formation of a topological superconducting phase, this demonstrates that hybrids with a soft gap in the local spectra are unlikely to undergo a topological phase transition. Moreover, topological superconductivity has to be realized by a Zeeman-driven gap closing and reopening, which is not possible to realize in devices gapless already at zero field.

We proceed by exploring the effect of parallel magnetic fields $B_\parallel$ on the induced gap of a 1 μm long hybrid (device C). In Fig. 7.3, we present two field sweeps of the nanowire in the two extreme regimes. In the strong-coupling regime (Fig. 7.3a-e), the induced gap decreases slowly with magnetic field. For g_{RL} and g_{LR} it can be seen that the white area between the anti-symmetric peaks persists up to almost $B_\parallel = 4\,\mathrm{T}$. At the same time, a few states can be observed in g_{LL} and g_{RR}. Again, the absence of correlation between the two sides and the absence of these states from the nonlocal signals confirms they are confined locally near the tunnel junctions. By looking at the estimated induced gap and the nonlocal slope in Fig. 7.3e, we observe an induced critical field $B_\parallel^{\mathrm{c}} = 3.5\,\mathrm{T}$. The outer ridge of the nonlocal signal decreases more slowly, which indicates that the shell maintains a superconducting gap (red) up to higher fields. By fitting the linear part of the induced-gap closing to the Zeeman energy $E_{\mathrm{Z}} = g\mu_{\mathrm{B}}B/2$, we estimate the g - factor to be $g = 2.3$ (see Supplementary section IV). This demonstrates that the semiconductor properties are indeed strongly renormalized in this regime [8, 9]. Such a low g - factor and the absence of any states below Δ_{i} may suggest that the semiconductor is depleted. Yet, we observe that the induced critical field in the strong-coupling regime varies significantly from wire to wire, and likely depends on the microscopic details (see Supplementary section IV). Moreover, we note that the addition of Pt in the shell causes its g - factor to be reduced close to zero, so that the effective g - factor in the hybrid can be reduced below $g = 2$ [24]. In the weak-coupling regime (Fig. 7.3f-j) on the contrary, the induced gap closes quickly upon the application of the magnetic field. Thereafter, the spectrum remains gapless and filled with a plethora of states. This is also reflected in g_{LL} and g_{RR}, where the same states are visible. From both the induced gap and the nonlocal slope in Fig. 7.3j, we observe an induced critical field $B_\parallel^{\mathrm{c}} = 0.16\,\mathrm{T}$. We estimate a g - factor of $g = 54$, although this value can be overestimated as orbital effects of the magnetic field are more prominent in this regime [29–31]. The rapid closing of the induced gap confirms that the hybrid inherits more of the semiconductor properties in the weak-coupling regime.

We next turn our attention to the crossover between these two regimes, which is expected to be optimal for the formation of a topological superconducting phase [25]. In Fig. 7.4a-d, the conductance matrix of the same nanowire (device C, 1 μm) taken at $V_{\mathrm{SG}} = -0.3\,V$ is shown. In the nonlocal spectra (Fig. 7.4c and d), we see a collection of states moving down in energy as the magnetic field is increased. The induced gap closes around $B_\parallel^{\mathrm{c}} = 0.8\,\mathrm{T}$ and reopens around $B_\parallel^{\mathrm{c}} = 1.6\,\mathrm{T}$. The induced gap (blue) and nonlocal slope are presented in Fig. 7.4e. Here, the closing and reopening of the induced gap is directly visible. The reopened gap reaches energies of $\Delta_{\mathrm{i}} = 50\,\mu\mathrm{eV}$, which is similar to predictions of the gap size in topological systems [6]. The reopening is also reflected in the behavior of the nonlocal slope, which deviates from zero around $B_\parallel = 1\,\mathrm{T}$ before returning to zero again at higher fields. Fig. 7.4f-h provide linecuts from g_{RL}, emphasizing that the induced gap is finite at zero field, closed at intermediate field, and reopened at higher fields. However, neither of the local signals (Fig. 7.4a and b) exhibit zero-bias peaks. This suggests that the observed feature does not originate from a topological phase with Majorana zero modes at the ends, extended over the full length of the hybrid. Yet, it may be possible that the presence of tunnel gates generates a smooth potential profile near the ends of the wire. In this case, the local spectra only represent the presence of bound states formed

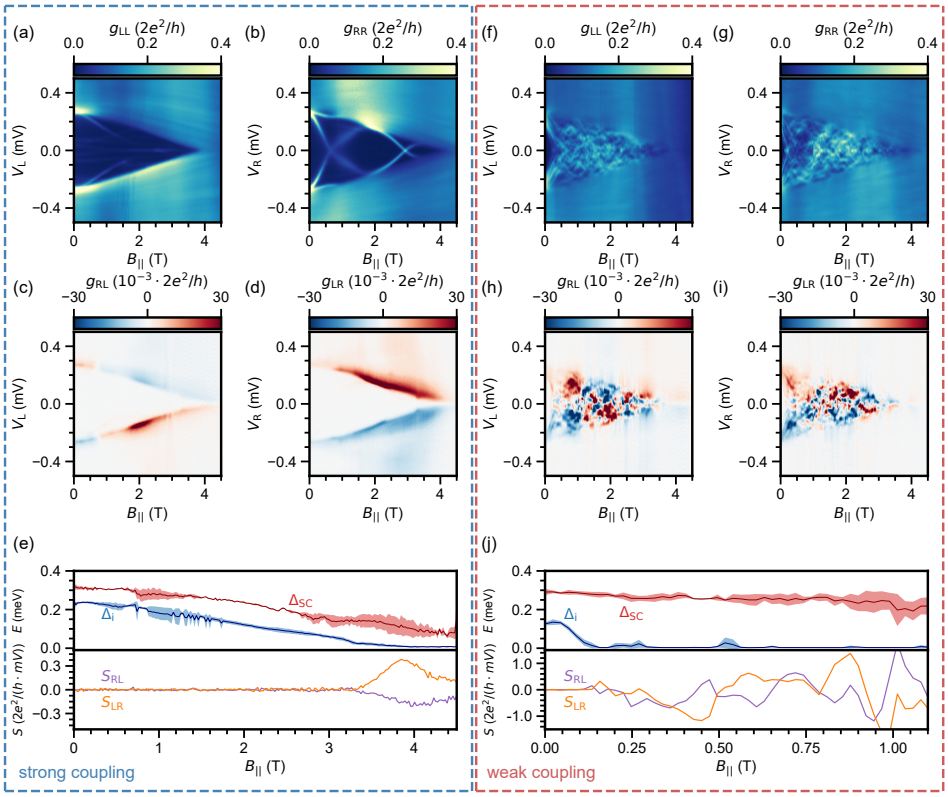

Figure 7.3: (a-d) Conductance matrix measured as a function of $B_{\|}$ for device C (1 μm hybrid) in the strong-coupling regime (V_{SG} = −0.75 V), where the induced gap only closes at large magnetic fields as visible in g_{RL} and g_{LR} (panels c,d). In g_{LL} and g_{RR} (panels a,b), a few sub-gap states localized in the vicinity of the tunnel junctions are observed. (e) Top panel: Δ_i (blue) and Δ_{SC} (red) In the strong-coupling regime . Bottom panel: Nonlocal slope extracted from g_{RL} (purple) and g_{LR} (orange). (f-i) Conductance matrix measured as a function of $B_{\|}$ for device C (1 μm hybrid) in the weak-coupling regime (V_{SG} = 0.5 V.), where the induced gap instead closes at small magnetic fields as visible in g_{RL} and g_{LR} (panels h,i). This is also reflected in g_{LL} and g_{RR} (panels f,g). (j) Top panel: Δ_i (blue) and Δ_{SC} (red) In the strong-coupling regime . Bottom panel: Nonlocal slope extracted from g_{RL} (purple) and g_{LR} (orange).

on the smooth potential, while pushing the Majorana zero modes towards the center of the hybrid - effectively decoupling them from the leads [32, 33]. Similar effects are expected to be caused by the device disorder independent of the tunnel gate voltage [34]. Accordingly, the gap reopening in the bulk should remain visible in the nonlocal spectra as this effectively measures the largest gap in the system, while no zero-bias peaks are observed in the local signals (see Supplementary section IIB). This scenario is supported by the observation that the local signals g_{LL} and g_{RR} do not appear to depend on the length of the hybrid and are not always correlated, as we elaborate on Supplementary section IV. On the contrary, it is also possible that the reopening of the gap has a topologically trivial origin. The hybrid segment of this device is only 1 μm long, so that it is likely to be

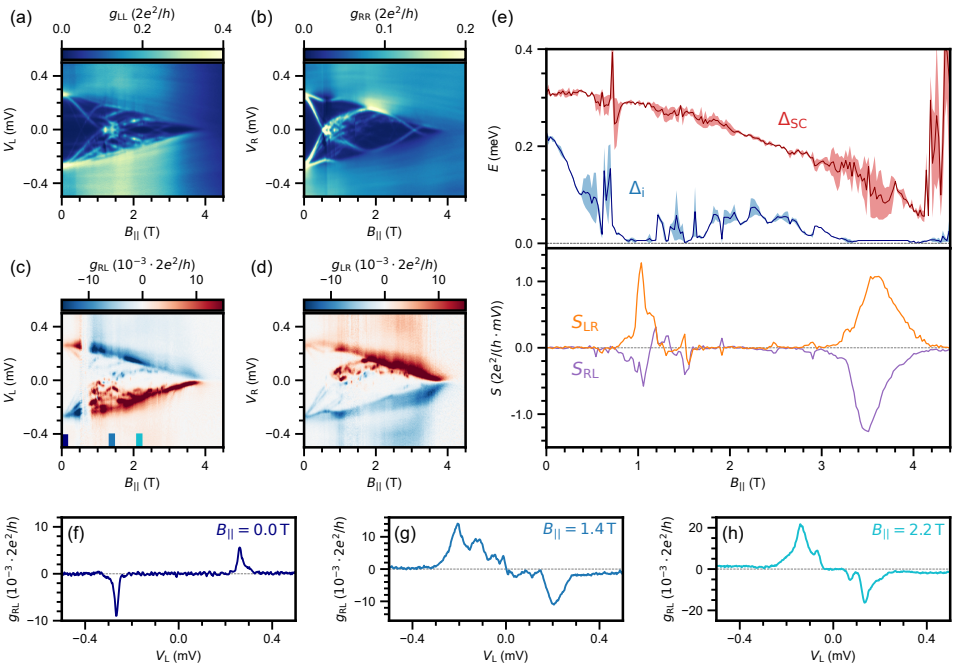

Figure 7.4: (a-d) Conductance matrix measured as a function of $B_{||}$ at $V_{SG} = -0.3$ V for device C (1 μm hybrid). A closing and reopening of the induced gap is observed in g_{RL} and g_{LR} (panels c,d), but it is not accompanied by the formation of zero-bias peaks in g_{LL} and g_{RR} (panels a,b). (e) Δ_i (blue) and Δ_{SC} (red) corresponding to the conductance matrix in (a-d). Bottom: Nonlocal slope extracted from g_{RL} (purple) and g_{LR} (orange). (f-h) Nonlocal conductance g_{RL} presented for (f) $B_{||} = 0$ T with a large induced gap, (g) $B_{||} = 1.4$ T illustrating a closed induced gap, (h) $B_{||} = 2.2$ T showing flat nonlocal conductance around zero-bias corresponding to a reopening of the induced gap.

within the short wire limit. In this case, the resulting spectrum is comprised of discrete energy levels with a small energy spacing. Both the Zeeman and orbital contributions of the magnetic field allow these states to come down and cross zero energy. However, in this limit there is no band structure forming in the nanowire, making the concept of topology ill-defined [35]. Alternatively, the observed gap reopening can originate from two sets of trivial ABSs localized near the nanowire junctions. In this case, spatial overlap due to a long localization length can enable transport through the hybrid [36]. Likewise, such states can cross zero energy without invoking a topological phase transition.

Finally, to enhance the picture we map out the induced gap of a nanowire as a function of parallel magnetic field and super gate voltage. In Fig. 7.5a, we present such an induced gap diagram for the same 1 μm long hybrid (device C). To complement this diagram, we show the corresponding normalized nonlocal slope S_{Norm} at zero bias in Fig. 7.5b. This quantity captures the collective behavior of the nonlocal slope from the two nonlocal signals, remaining close to zero whenever an induced gap is present in the hybrid. It is defined as $S_{Norm} = |S_{RL}S_{LR}|/\sqrt{|S_{RL}S_{LR}|}$ where the normalization is done independently

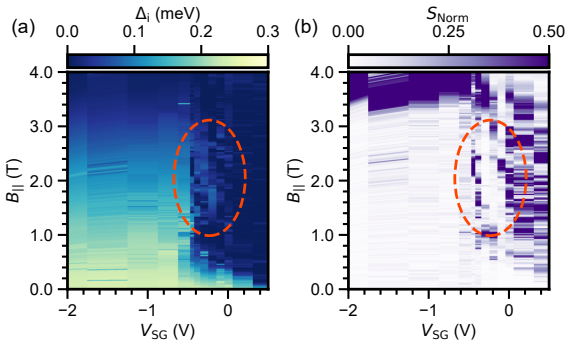

Figure 7.5: Induced gap and nonlocal slope diagrams for device C (1 μm long hybrid). (a) Induced gap as a function of V_{SG} and $B_{\parallel}$. (b) Normalized nonlocal slope S_{Norm} as a function of V_{SG} and $B_{\parallel}$. Dashed orange ellipses highlight the reopening of the induced gap, which occurs in a small but finite range of V_{SG} values.

for every gate voltage. In the strong-coupling regime below $V_{SG} < -0.5\,V$, we see that Δ_i decays slowly when the magnetic field is increased. It closes around $B_{\parallel}^{c} = 3.5\,T$, which is also reflected in S_{Norm} as it deviates from zero. In contrast, above $V_{SG} > -0.1\,V$ the semiconductor-superconductor coupling is strongly diminished which results in a significant reduction of Δ_i and $B_{\parallel}^{c}$. Near the crossover between $-0.4\,V < V_{SG} < -0.1\,V$ as indicated by the dashed orange ellipses, the closing of Δ_i is followed by its reopening at higher magnetic fields. This is also visible in the behavior of S_{Norm}, which becomes finite when the gap closes and returns to zero at the reopening. Importantly, the reopening occurs in a finite but narrow range of gate voltages. While a strong reduction of $B_{\parallel}^{c}$ is generically observed in our hybrids, only one out of the eleven nanowires studied in detail showed a subsequent reopening of the induced gap. In Supplementary section IV, we show phase diagrams and representative overviews of additional nanowires studied in this work.

In conclusion, we have demonstrated that electric fields can be used to control the bulk properties of InSb nanowires proximitized by Al/Pt films, using a three-terminal geometry. Even though this has been attempted in the past using two-terminal experiments [10, 12], local tunneling spectroscopy does not allow for discriminating between states localized in the junction area which are known to possess a gate-tunable coupling [37]. Such states are present in virtually all our local spectra, which demonstrates that nonlocal measurements are truly necessary to properly investigate the bulk properties of semiconductor-superconductor hybrids. On the one hand, a strong-coupling regime can be achieved where the induced gap is large and closes only at high magnetic fields. This corresponds to a metallized nanowire which has a strong renormalization of the semiconducting properties. In contrast, a weak-coupling regime can be realized where the induced gap and critical field are strongly reduced. In particular, the induced gap can be fully closed at zero magnetic field. We have demonstrated that under these conditions the system also exhibits a soft gap in the local spectra of the nanowire. Thus, the presence of a soft gap is a clear indication that the bulk of the hybrid posesses a

high electron density with a weak (or absent) semiconductor-superconductor coupling. Indeed, the strong-coupling regime acts too much like a regular superconductor whereas the weak-coupling regime acts too much like an ordinary semiconductor. Neither of these regimes have an interesting combination of both properties - making a large part of the gate voltage range irrelevant for the realization of a topological superconductor. Only at the crossover one can hope to find the right combination of semiconductor and superconductor properties.

By mapping out the induced gap diagram of a 1 μm nanowire near the crossover, we do observe a closing and reopening of the induced gap in a finite range of magnetic fields and gate voltages. However, the corresponding local signals reveal an absence of zero-bias peaks. As a consequence, the gap reopening cannot be conclusively attributed to the existence of a topological phase. We speculate that the density in the hybrids is too high whenever the coupling is weakened [8]. In fact, it is currently unclear what are the optimal density and coupling for reaching a topological phase in InSb/Al based hybrids. Thus, a desireable future improvement would be to decouple the semiconductor and superconductor via an epitaxial barrier, such that density in the wire and the coupling could be tuned independently [38].

7.3 Methods

7.3.1 Device fabrication

The nanowire hybrids presented in this work are fabricated on pre-patterned substrates, following the shadow-wall lithography technique described in [15, 16]. Intrinsic silicon wafers (2 $k\Omega \cdot$cm) with 285 nm thermal SiO_x serve as the base for the device substrates. Local bottom gates are patterned with standard electron-beam lithography (EBL) techniques, using PMMA 950k A2 spun at 4 krpm for one minute followed by 10 minutes of baking on a 185 °C hot plate. After development of the resist using a 3:1 solution of IPA and MIBK, 3 nm Ti and 17 nm Pd are deposited as the gate metal using e-beam evaporation at 0.5 Å/s and 1 Å/s, respectively. Subsequently, bond pads are patterned with EBL using PMMA 950k A6 spun at 4 krpm for one minute and hot-baked at 185 °C for 10 minutes. After development, 50 nm of W is sputtered using RF-sputtering at 150 W in an Ar pressure of 20 μbar. Next, the substrates are covered with 17 nm high-quality HfO_x gate dielectric grown at 110 °C using atomic layer deposition (ALD). Finally, shadow walls are patterned on top of the dielectric. FOx-25 (HSQ) is spun at 1.5 krpm for one minute, followed by 2 minutes of hot baking at 180 °C and patterning with EBL. The HSQ is then developed with MF-321 at 60 °C for 5 minutes and the substrates are subsequently dried using critical point dryer (CPD).

Nanowires are placed on top of the gates using an optical nanomanipulator setup. Samples are placed in a custom e-beam evaporator, where the native nanowire oxide is removed and the superconductor is deposited. To obtain a pristine, oxide-free semiconductor surface, a gentle oxygen removal is accomplished via atomic hydrogen radical cleaning. For this purpose, a custom-made H radical generator is installed in the load lock of an aluminium electron-gun evaporator. It consists of a gas inlet for H_2 molecules connected

to a mass-flow controller and a tungsten filament at a temperature of about 1700 °C that dissociates a fraction of the molecules into hydrogen radicals. The optimal removal of the native oxide is achieved for a process duration of 60 mins and at a H_2 pressure of $6.3{\cdot}10^{-5}$ mbar. This recipe, which is used for all the devices shown in this paper, results in a constant EDX count of oxygen at the interface as shown in the previous works utilizing our shadow wall lithography technique (see Refs[15, 16]). After the native oxide removal, the samples are cooled down to 138 K and thermalized for one hour. The Al is then deposited with a rate of 0.05 Å/s, alternating 2 nm at 15° and 45° angles with respect to the substrate for a total of 8 nm. Subsequently, a 2 ÅPt layer is deposited at 30° following the approach of [24]. Finally, the samples are capped with evaporated AlO_x (~ 0.2 Å/s) to prevent oxidation of the shell-substrate connection.

Ohmic contacts are fabricated ex-situ after the superconductor deposition. PMMA 950k A6 is spun at 4 krpm and subsequently cured at room temperature in a vacuum oven to prevent intermixing at the pristine InSb-Al interface. Contacts are patterned using EBL, and Ar milling is used to remove the native oxide prior to deposition of 10 nm Cr and 120 nm Au using e-beam evaporation at 0.5 Å/s and 1.5 Å/s, respectively.

7.3.2 Measurement details

Transport measurements are conducted in dilution refrigerators with a base temperature of ~ 20 mK. All magnetic field measurements presented in this work have the magnetic field aligned parallel to the nanowire using 3-axis vector magnets. We have used two adaptations of the three-terminal circuit presented in [39], which are shown in supplementary Fig. 7.10. For the measurements on device C, the Al/Pt film is grounded at room temperature, so that there is a finite resistance originating from the fridge line and filters in between the ground and the sample. This can give rise to voltage-divider effects, which we correct. We do this using formula (14) of ref [39]:

$$G(\mathbf{V}) = G'(\mathbf{V}^{\text{applied}})(\mathbb{I} - Z\,G'(\mathbf{V}^{\text{applied}}))^{-1} \tag{7.1}$$

Here, $G(\mathbf{V})$ is the corrected conductance matrix, $G'(\mathbf{V}^{\text{applied}})$ is the measured conductance matrix, $\mathbf{V} = (V_L, V_R)^T$ is the bias on the sample, $\mathbf{V}^{\text{applied}} = (V_L^{\text{applied}}, V_R^{\text{applied}})^T$ is the bias applied by the voltage sources and Z is the impedance matrix:

$$Z = \begin{bmatrix} R_L + R_g & R_g \\ R_g & R_R + R_g \end{bmatrix} \tag{7.2}$$

For device C, the circuit uses a grounding line resistance $R_g = 2834\,\Omega$ and biasing line resistances $R_L = R_R = 3944\,\Omega$. In addition, the DC voltage drop on the sample is corrected by measuring the current $\mathbf{I} = (I_L, I_R)^T$ using

$$\mathbf{V} = \mathbf{V}^{\text{applied}} - Z\,\mathbf{I} \tag{7.3}$$

The other samples in this work have used an adapted circuit, where the Al/Pt film is directly connected to the cold ground in the fridge as well as the ground at room temperature. The drawback is that the thermal voltage V_{th} introduces an offset in the bias voltages applied to the left and right lead, which needs to be corrected. The connection of the Al/Pt

film to ground at room temperature enables the direct measurement of this thermal voltage. Yet, this largely eliminates voltage-divider effects from the measurements. The DC voltage drop is also corrected using equation 7.3 with $R_g = 0\,\Omega$. By maintaining a low conductance compared to the line resistances, we can use the simplified correction of formula (16) of ref [39]:

$$G(\mathbf{V}) = G'(\mathbf{V}^{\text{applied}}) + \begin{bmatrix} R_L\, g_{LL}^2 & 0 \\ 0 & R_R\, g_{RR}^2 \end{bmatrix} \tag{7.4}$$

Note that this simplification can give an error in the nonlocal signals when the zero-bias conductance in the receiving junction is large, either due to the presence of a sub-gap state or Andreev reflection. This leads to a bias-independent offset, which in some measurements we correct by subtracting the offset as calculated from sub-gap or finite-bias conductance values.

When measuring the conductance matrix, the bias on the left contact of the device V_L is swept first while the bias on the other side V_R is set to zero. Before sweeping the bias, the thermal voltage is measured and the bias offsets is calibrated accordingly. The corresponding matrix elements g_{LL} and g_{RL} are recorded. Next, the right-contact bias V_R is swept while setting the bias on the left contact V_L to zero and the remaining two conductance matrix elements g_{RR} and g_{LR} are recorded. For the super gate sweeps presented in this work, we aim to maintain a constant transmission in both the nanowire junctions. To do this, the two tunnel gate voltages V_{TL} and V_{TR} are automatically adjusted each time the super gate voltage is changed. This is done by looking at the out-of-gap local conductances g_{LL} and g_{RR}. If one of the conductances is found to deviate more than $0.005 \times 2e^2/h$ from the specified value, the respective tunnel gate voltage is tuned to bring the out-of-gap local conductance back to the specified value.

7.3.3 Data analysis

We extract the induced gap Δ_i and the gap of the superconducting film Δ_{SC} from the nonlocal spectra g_{RL} and g_{LR}, as a function of various device parameters like as the super gate voltage V_{SC} and the parallel magnetic field $B_\parallel$. In such spectra, the nonlocal conductance is finite only in an energy window between Δ_{SC} and Δ_i. For a given trace of the nonlocal conductance as a function of bias voltage, we determine an adaptive threshold based on the noise level at a large bias voltages. Δ_{SC} and Δ_i are estimated by checking when the nonlocal conductance exceeds the threshold value. This is done independently for both g_{RL} and g_{LR} as well as both positive and negative bias values. This results in four estimates of Δ_{SC} and Δ_i each, from which the mean and standard deviation are calculated and presented in the figures. Values of the nonlocal slope S_{RL} and S_{LR} are estimated as the numerical derivative of the data at zero bias voltage, after application of a Savitzky-Golay filter. A detailed description and examples can be found in the supplementary information.

Data Availability

Raw data presented in this work and the data processing/plotting codes are available at `https://doi.org/10.5281/zenodo.6913897`.

7.4 Supplemental information

7.4.1 Analysis details

Determination of the induced gap and gap in the superconducting shell

In Fig. 7.6 we show how we extract Δ_i and Δ_{SC} from the nonlocal conductance. Fig. 7.6a shows the nonlocal conductance g_{LR} from the 8 μm device, which is also shown in the main text Fig. 7.2b. We show examples of the extraction algorithm for two linecuts, presented in the middle column (yellow) and right column (orange) for a large gap and a closed gap, respectively. In panels Fig. 7.6c and g, the two linecuts are shown. We first split the signal into two separate traces for positive (red) and negative (blue) biases and take its absolute value, as shown in Fig. 7.6d and h. Next, the two traces are normalized by their peak value. We then look at the noise level of each trace for biases larger than Δ_{SC}, as shown in dark blue and dark red in Fig. 7.6e and i. The maximum of the noise level is then used to set a threshold value, shown as the horizontal lines in dark blue and dark red in Fig. 7.6e and i. We then apply this threshold value to the Savitzky-Golay filtered version of the data as shown in Fig. 7.6f and j, which estimates Δ_i individually for positive and negative bias as shown in light green and pink vertical lines. Similarly, the threshold is used to estimate Δ_{SC} as shown in dark green and purple vertical lines in Fig. 7.6f and j. Finally, we show the filtered and renormalized data in Fig. 7.6b, together with the four estimated energy values Δ_i and Δ_{SC} at positive and negative biases. We see that the algorithm estimates them very well from the nonlocal signal, but sometimes deviates. This is usually the result of a linecut with a weak signal, which cannot be avoided during these measurements. We always check by eye if the obtained energy values match the nonlocal signals well. We occasionally increase the threshold for the estimation of the gaps by a factor of ~ 1.2 - 3 in order to avoid false triggers on noise, which is typically needed for longer nanowires where the magnitude of the nonlocal signal is small. Similarly, we apply a maximum to the threshold of ~ 0.4 - 0.8 to prevent the algorithm from failing to find a value.

We apply the above algorithm to both nonlocal signals g_{RL} and g_{LR} of a given measurement. From this we obtain four estimates of Δ_i: one at positive and one at negative bias, for both g_{RL} and g_{LR}. This is shown in Fig. 7.7a, which displays both nonlocal conductances from device B (8 μm) together with the extracted Δ_i estimates. In the top panel of Fig. 7.7b, the four Δ_i traces are displayed as a function of super gate voltage V_{SG}. We take the mean value of these traces as Δ_i, which is shown in dark blue in the bottom panel of Fig. 7.7b. In addition, we take the standard deviation of the four traces and plot it as the shaded blue area. A small standard deviation means the four estimates agree well to one another, which increases our confidence that the algorithm extracts the correct values. However in some cases, the nonlocal signal is strongly asymmetric in terms of signal strength which can hinder the correct estimation of one of the four traces. We always check by eye if this happens, in which case we adjust the procedure to first omit the strongly deviating trace out of the two positive-bias and negative-bias traces for a single nonlocal matrix element. Subsequently, one trace for g_{RL} and one trace for g_{LR} remain of which the mean and standard deviation are calculated. This is done, for example, in Fig. 5 of the main text as g_{LR} would overestimate the size of Δ_i due to asymmetries

in the signal strength. In most of the data however, both nonlocal signals look similar and result in similar estimations for Δ_i even if the visibility of one of the signals is weak.

The gap in the superconducting shell Δ_{SC} is determined from the measurement in a similar way. Four traces at positive and negative bias are obtained from g_{RL} and g_{LR}, as shown in Fig. 7.8a. The top panel in Fig. 7.8b shows the traces as a function of super gate voltage V_{SG}. We determine Δ_{SC} by calculating their mean, which is shown in the bottom panel of Fig. 7.8b as the dark red curve. Similarly, the standard deviation is shown as the red shaded area. We note that the algorithm we apply to estimate Δ_i and Δ_{SC} does have its limitations. For instance, Δ_{SC} should remain constant but in some cases the nonlocal signal close to this value is weak in comparison to the rest of the trace. This usually happens in the weak-coupling regime, where the majority of the quasiparticle transport across the hybrid is carried by low-energy states. As a result, the outer edge of the nonlocal signal can become almost invisible. For example, this happens in the main text in Fig. 7.2b for the 640 nm long hybrid. We suspect that energy relaxation in the hybrid plays a role in this [21].

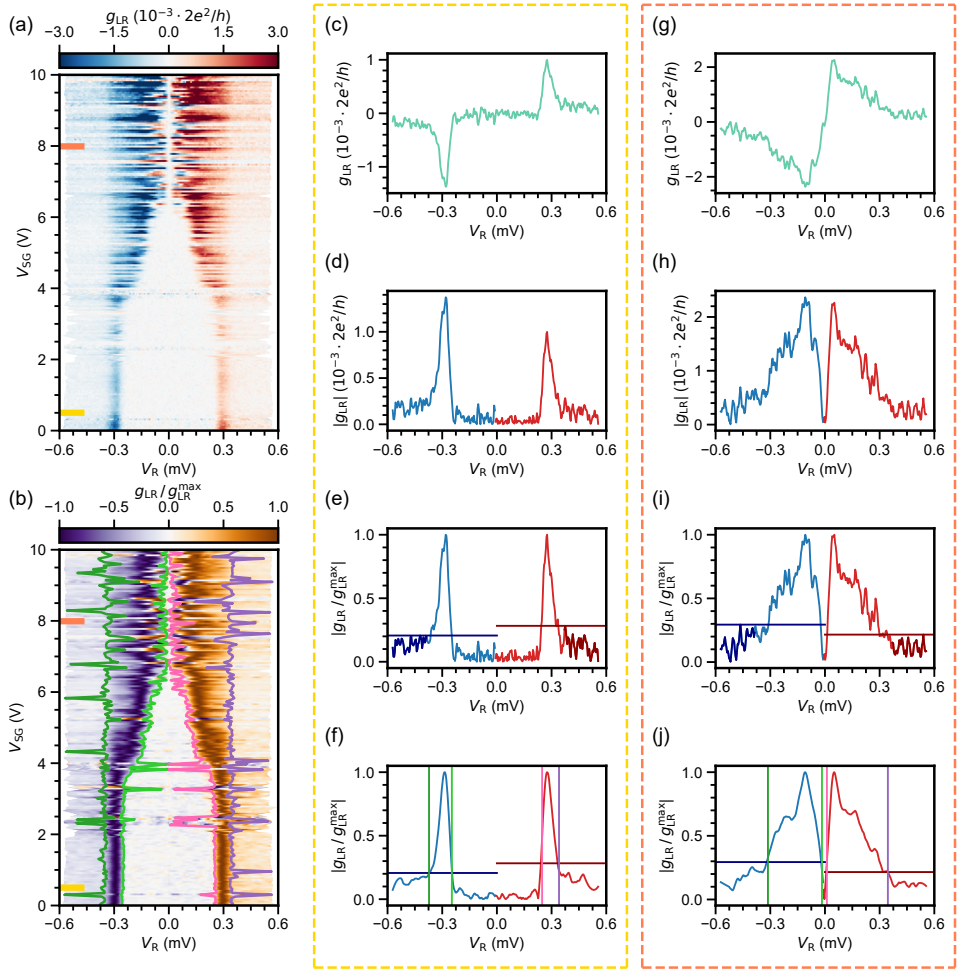

Figure 7.6: Example of the gap extraction algorithm used in this work, with data on device B (8 μm). Middle and right columns show linecuts taken at locations specified by the color bars in panel (a) for various stages during the analysis. (a) Nonlocal conductance matrix element g_{LR}. (b) g_{LR} after processing, including the estimates for Δ_i and Δ_{SC}. (c,g) Linecuts of g_{LR} taken with a large induced gap (c) and a closed gap (g). (d,h) The g_{LR} data is split into positive (red) and negative (blue) bias values and the absolute value is taken. (e,i) The positive and negative bias traces are normalized by their maximum value. The out-of-gap signal is used to set separate thresholds for positive (dark red) and negative (dark blue) biases relative to the maximum of the signal. (f,j) The data is smoothened using a Savitzky-Golay filter. The thresholds obtained in panels (e,i) are used to determine the Δ_i for positive (pink) and negative (light green) biases, as well as for Δ_{SC} for positive (purple) and negative (dark green) biases.

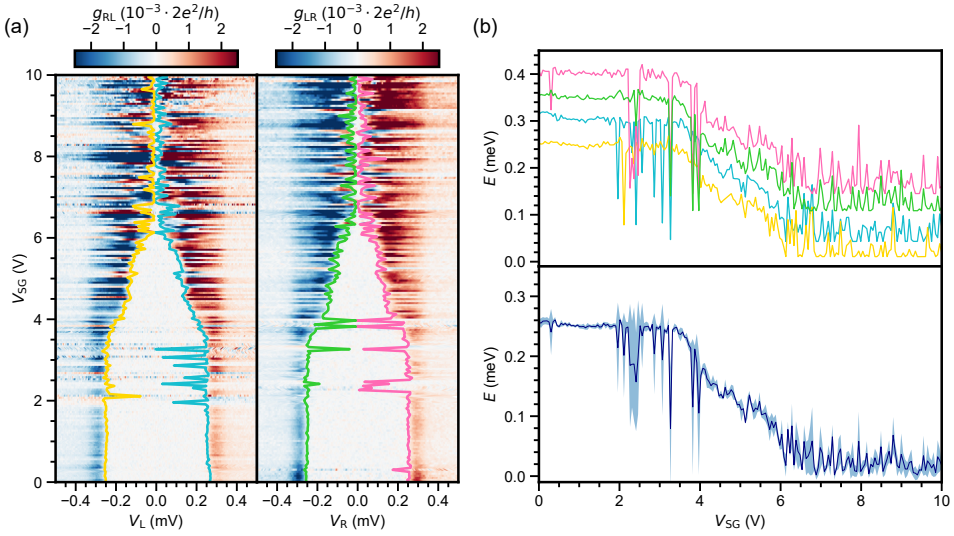

Figure 7.7: Example of the induced gap extraction. (a) g_{RL} and g_{LR} taken on device B, together with the four estimates for Δ_i: negative bias for g_{RL} (yellow) and g_{LR} (light green), and positive bias for g_{RL} (cyan) and g_{LR} (pink). (b) Top: the four estimated values of Δ_i, offset by 0.05 meV. Bottom: Mean of the four traces (dark blue) and their standard deviation (blue shaded area).

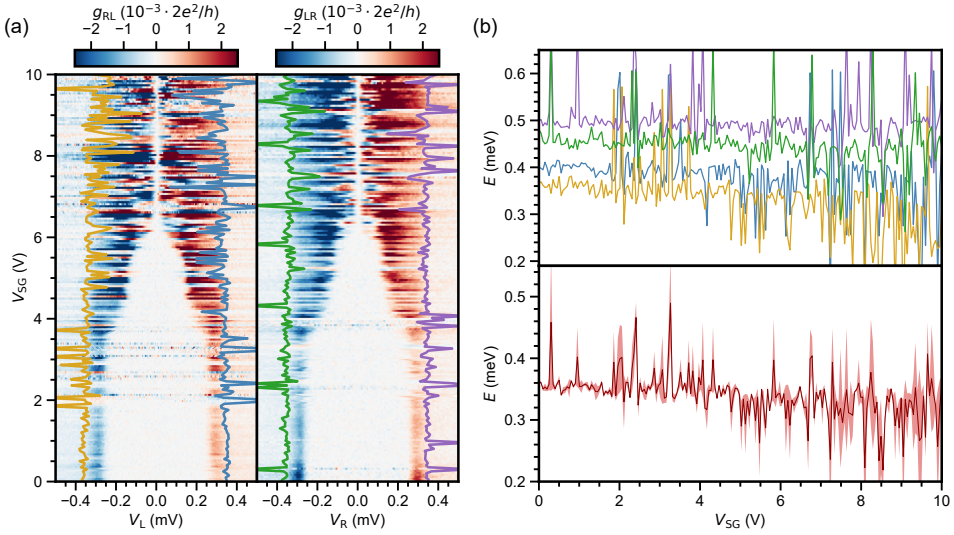

Figure 7.8: Example of extraction of the superconducting gap in the shell. (a) g_{RL} and g_{LR} taken on device B, together with the four estimates for Δ_{SC}: negative bias for g_{RL} (dark yellow) and g_{LR} (dark green), and positive bias for g_{RL} (blue) and g_{LR} (purple). (b) Top: the four estimated values ofΔ_{SC}, offset by 0.05 meV. Bottom: Mean of the four traces (dark red) and their standard deviation (red shaded area).

Extraction of the nonlocal slope

Estimation of Δ_i is challenging when the magnitude of the nonlocal signal is small, which is typically the case for long hybrids. In particular, problems arise when the induced gap is closed. This results in residual fluctuations as shown in Fig. 7.6 above $V_{SG} > 6$ V. Thus, we always complement the gap estimation algorithm by looking at the nonlocal slopes S_{RL} and S_{LR}. In Fig. 7.9 we show an example of how these are obtained from the nonlocal data. Examples are shown for two linecuts, presented in the middle column (yellow) and right column (orange) for a large gap and a closed gap, respectively. We first apply a Savitzky-Golay filter, as is shown in dark green in Fig. 7.9b and d. We subsequently calculate the derivative of the filtered data, of which we take the value at zero bias to be the nonlocal slope. In Fig. 7.9c and e, we show the filtered data together with the tangent at zero bias as a dashed orange line. We see that the nonlocal slope at zero bias is significantly larger when the gap is closed. As can be seen in the various plots of the nonlocal slope in the main text, S_{RL} and S_{LR} behave similar in the sense that once the induced gap closes, both of them start to deviate from zero.

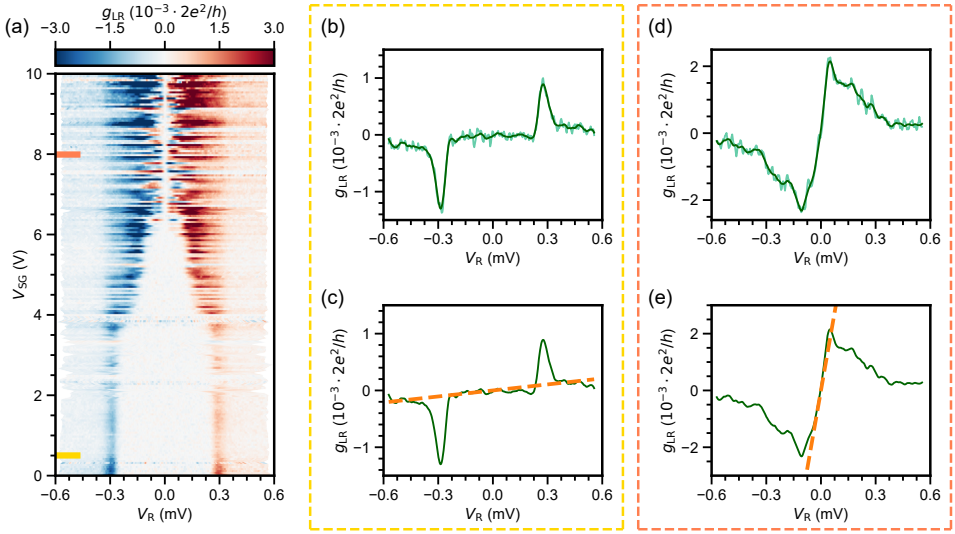

Figure 7.9: Example of the determination of the nonlocal slope. Middle and right columns show linecuts taken at locations specified by the color bars in panel (a) for various stages during the analysis. Linecuts are the same as the ones used in Fig. 7.6. (a) Nonlocal conductance matrix element g_{LR} taken on device B. (b,d) Linecuts of g_{LR} taken with a large induced gap (b) and a closed gap (d). The signals are smoothened using a Savitzky-Golay filter, shown in dark green. (c,e) Filtered signals together with the tangent of the nonlocal slope at zero bias (orange dashed line).

7.4.2 Additional data and discussion

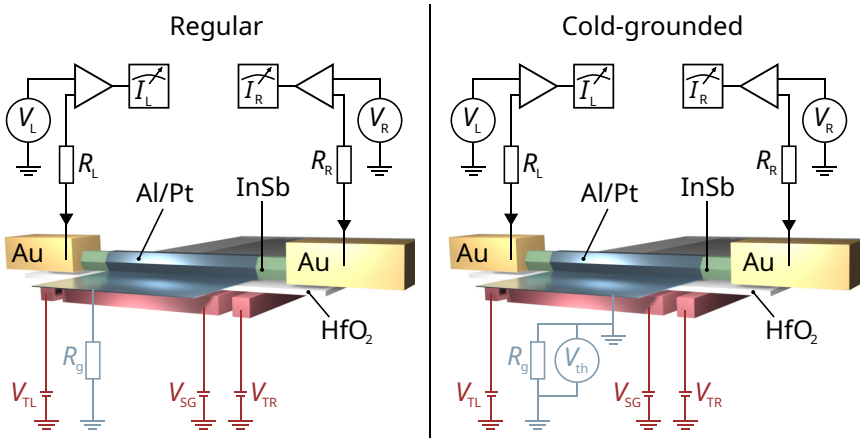

Figure 7.10: Schematic of the used measurement circuit, including fridge line resistance R_L,R_R and R_g. Left side shows the regular circuit used for device C, which has the fridge line resistance between the Al/Pt film and the ground. This results in potential voltage-divider effects, which need to be corrected. Right side shows the cold-grounded adaptation of the measurement circuit used for devices A and B. The cold grounding helps circumvent voltage-divider effects, but introduces a thermal voltage V_{th} on the applied biases. This is measured by also grounding the sample at room temperature and is actively compensated for during the measurements.

7

Overview of devices

In this work, we show data on six nanowire hybrids (see Fig. 7.11). Two of these devices are presented in the main text, with additional data on those and four other devices in this section. In total, we fabricated 7 chips on which a total of 36 nanowires were cooled down for measurement. Due to fabrication issues, some of these chips were non-functional which resulted in 15 nanowires working (defined as fully gate-controllable and with a hard induced gap). We performed a detailed study on 11 of these nanowires, with hybrid lengths varying from 240 nm up to 8 μm. In this section, we present the full conductance matrices corresponding to the main text figures in Fig. 7.16 and Fig. 7.17. We also show two additional induced gap diagrams without a reopening of the induced gap in Fig. 7.13, Fig. 7.20. We elaborate on the soft gap versus hard gap nomenclature in Fig. 7.14. We also show a comparison on the local spectra g_{LL} and g_{RR} for short and long wires in Fig. 7.15. Finally, we give a representative device overview of hybrids for which we did not map out the induced gap diagram in Fig. 7.12, Fig. 7.18 and Fig. 7.19.

We systematically observe the gate-tunable reduction of the induced gap in the explored nanowires. While in short devices Δ_i cannot be closed at zero field, we do observe that discrete states can cross zero energy. This is shown in Fig. 7.21 and Fig. 7.19(a-d). In such devices, the induced gap consists of a collection of discrete Andreev bound states (ABS). We suspect that some of these states can acquire a finite charging energy as their wave function is pulled away from the semiconductor-superconductor interface due to strongly positive super gate voltages. The presence of a charging energy can allow them to cross

zero energy [40], resembling the closing of the induced gap. However, this only happens for a finite range of gate voltages, in contrast to the long hybrids where the induced gap can be fully closed. It is not yet clear why this happens for some short devices (device E and F) but not for others (device A and D).

Similarly, we observe a strong reduction of the induced critical field as a function of super gate voltage. However, in some devices the critical induced field in the strong-coupling regime can be significantly lower than the critical field of the superconducting shell. For example, Fig. 7.12(e-h) shows that the induced critical field in the strong-coupling regime for device A reaches only $B_{\parallel}^{c} = 1.5\,\mathrm{T}$, while Δ_{SC} closes only above $B > 4\,\mathrm{T}$.

Hard and soft induced superconducting gaps

In literature on the proximity effect, various definitions are used to judge on the presence of an induced gap in a proximitized system. An induced gap is typically referred to as a hard gap, while the absence of a gap (but with a reduced conductance at low bias) is referred to as a soft gap. Typically, a local signal is used and the sub-gap to out-of-gap ratio is used to claim a hard induced gap. However, such a metric is unable to distinguish between the presence of a true induced gap or, for example, the reduction of local sub-gap conductance due to coulomb blockade in the semiconducting junctions. Fortunately, nonlocal conductance can be used to determine if an induced gap is present in a hybrid. For example, in Fig. 7.14 we show additional data on device B where a voltage on the

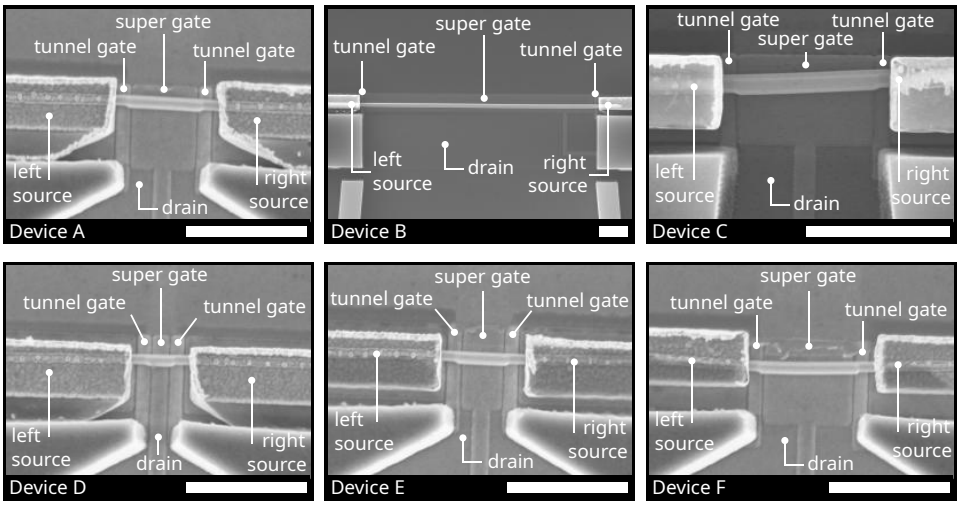

Figure 7.11: SEM images of the devices presented in this work. The white scalebar in each panel represents 1 μm. The top row shows the two devices used for the main text. The length of the hybrid section of each device is: Device A - length: 640 nm, diameter: 79 nm, Device B - length: 8 μm, diameter: 120 nm, Device C - length: 1 μm, diameter: 126 nm, Device D - length: 240 nm, diameter: 75 nm, Device E - length: 450 nm, diameter: 77 nm, Device F - length: 840 nm, diameter: 81 nm.

super gate is used to close the induced gap. In Fig. 7.14e, we show the conductance matrix at $V_{SG} = 6.05\,\text{V}$. Here, Δ_i is on the order of $\Delta_i = 120\,\mu\text{eV}$, which is visible in the nonlocal conductances g_{RL} and g_{LR} as the flat part between the two peaks. At the same time, the local conductances g_{LL} and g_{RR} show a broadening of the coherence peaks which corresponds to the reduction of Δ_i. At higher super gate voltages, Δ_i closes. For example, Fig. 7.14f shows the conductance matrix at $V_{SG} = 7.45\,\text{V}$. From the local signal g_{LL} it may appear as if the hybrid still has a hard gap, while g_{RR} shows a finite sub-gap conductance. In this case, the nonlocal signals g_{RL} and g_{LR} both show an absence of a flat part between the two peaks (i.e. a finite nonlocal slope at zero bias) which confirms that the hybrid is gapless.

We note that the induced gap in short hybrids does not close at zero magnetic field, as can be seen for example in Fig. 7.12. This is a consequence of the short length of this hybrid: while states without any semiconductor-superconductor coupling may form in the weak-coupling regime, in practice these can obtain a finite energy gap if they are allowed to mix with proximitized states. Such mixing can occur due to disorder and, in this particular case of short hybrids, due to the presence of tunnel junctions at the ends of the hybrid segment.

Absence of end-to-end correlation in local spectra

One striking feature we observe is that the local conductance spectra g_{LL} and g_{RR} do not seem to change significantly as the length of a nanowire hybrid is increased. In Fig. 7.15, we compare the spectra of device F (800 nm) and device B ($8\,\mu$m) in the weak-coupling regime. The local spectra of device F (Fig. 7.15(a,b)) show the field evolution of a discrete number of states, as expected for a short nanowire hybrid [41]. For device B, the increased length is expected to reduce the level spacing of these states such that they form a continuum. However, the local spectra show a similar field evolution of a discrete number of states (Fig. 7.15(g,h)). In addition, the local spectra g_{LL} and g_{RR} generically appear to be uncorrelated. These observations both indicate that the tunnel junctions significantly disrupt the potential profile at the ends of the hybrid, leading to the formation of localized states. This suggests that the local spectra are only looking at an effective short nanowire segment located in the vicinity of the tunnel junctions. Such a scenario could potentially give rise to dark Majoranas, which would not show up as zero-bias peaks in the local end spectra but still be visible in the nonlocal signals as a reopening in the bulk of the nanowire. This in contrast to the formation of quasi-Majoranas, which form on the smooth potential of the tunnel barriers - resulting in a zero-bias peak without a reopening of the bulk gap.

Interpretation of nonlocal transport measurements

In this work, we use nonlocal spectroscopy to investigate the bulk properties of three-terminal InSb/Al/Pt nanowire hybrids. In particular, nonlocal transport is facilitated through the density of states between Δ_{SC} and Δ_i. However, several processes complicate this simple picture. For example, the visibility of nonlocal signals is affected strongly by the non-ideal injection and detection processes in the tunnel junctions [21]. Moreover, relaxation from above to below Δ_{SC} is sometimes visible in the nonlocal spectra [21]. In addition, Δ_i can potentially vary along the length of the hybrid. As a result, the nonlo-

cal signal may reflect the largest induced gap somewhere in the bulk. However, nonlocal transport is likely insensitive to fluctuations of Δ_i on a short length scale as quasiparticles can cross such areas through various tunneling mechanisms. Despite the above-mentioned complications, we systematically observe a good correspondence between the two nonlocal signals g_{RL} and g_{LR}, which supports the assumption that nonlocal transport can be used to evaluate bulk properties.

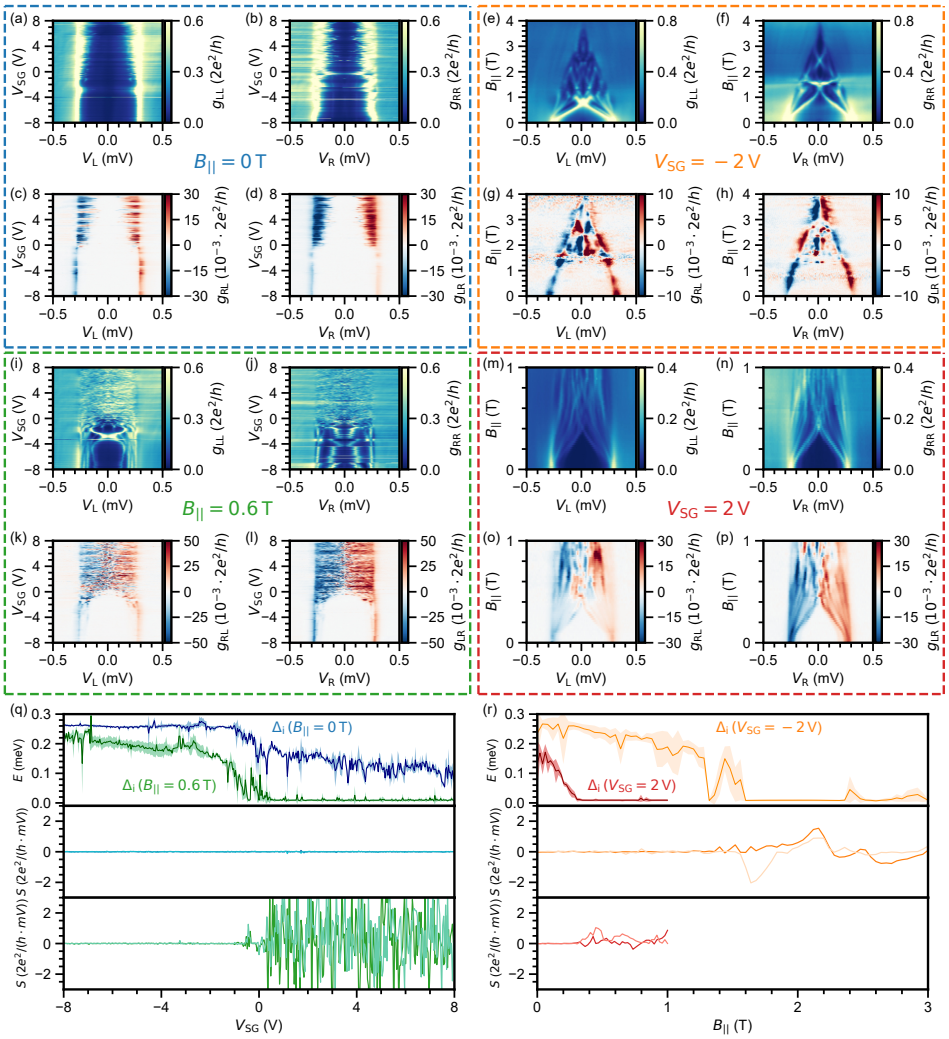

Figure 7.12: Representative overview of device A (640 nm). (a-d: Blue) Conductance matrix as a function of V_{SG} taken at $B_{\parallel} = 0$ T. This corresponds to panels (a,b) of Fig. 7.2 in the main text. (e-h: Orange) Conductance matrix as a function of $B_{\parallel}$ in the strong-coupling regime, taken at $V_{SG} = -2$ V. (i-l: Green) Conductance matrix as a function of V_{SG} taken at $B_{\parallel} = 0.6$ T. (m-p: Red) Conductance matrix as a function of $B_{\parallel}$ in the weak-coupling regime, taken at $V_{SG} = 2$ V. (q) Top: Δ_i as function of V_{SG} at $B_{\parallel} = 0$ T (blue) and $B_{\parallel} = 0.6$ T (green). Middle: Nonlocal slope as function of V_{SG} at $B_{\parallel} = 0$ T, indicating the nanowire maintains an induced gap at all gate values. Bottom: Nonlocal slope as function of V_{SG} at $B_{\parallel} = 0.6$ T, showing the induced gap closing around $V_{SG} = -1$ V. (r) Top: Δ_i as function of $B_{\parallel}$ at $V_{SG} = -2$ V (orange) and $V_{SG} = +2$ V (red). Middle: Nonlocal slope as function of $B_{\parallel}$ taken at $V_{SG} = -2$ V, showing the induced gap closing at $B_{\parallel}^c = 1.5$ T. Bottom: Nonlocal slope as function of $B_{\parallel}$ taken at $V_{SG} = 2$ V, showing the induced gap closing at $B_{\parallel}^c = 0.3$ T.

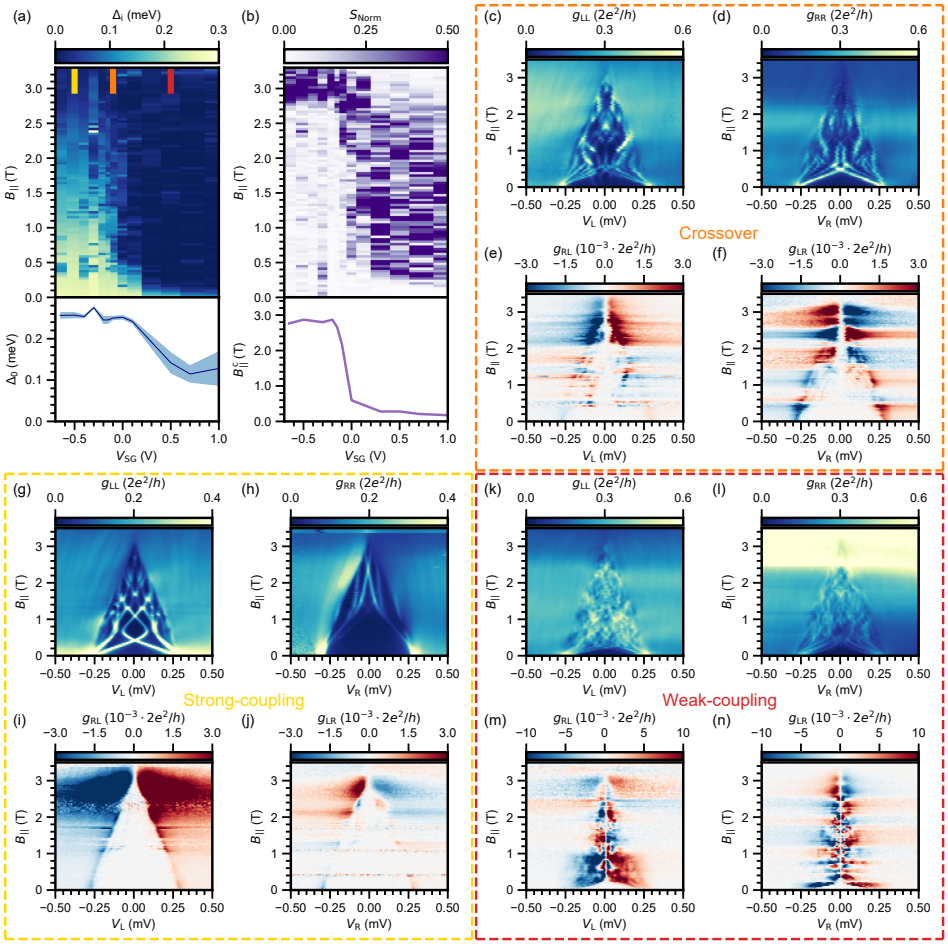

Figure 7.13: Induced gap and nonlocal slope diagrams for device B (8 μm long hybrid). (a) Top: Δ_i as a function of V_{SG} and $B_\parallel$. Bottom: Δ_i at $B_\parallel$ = 0 T. We note that the gate voltage for which Δ_i starts to decrease is quite different from the data presented in the main text (Fig. 7.2(c-d)). This is the result of dielectric hysteresis, as the gate voltages are swept over a large voltage range. (b) Top: S_{Norm} as a function of V_{SG} and $B_\parallel$. Bottom: $B_\parallel^c$ as a function of V_{SG}. (c-f: Orange) Conductance matrix as a function of $B_\parallel$ taken at V_{SG} = −0.1 V. (g-j: Yellow) Conductance matrix as a function of $B_\parallel$ taken at V_{SG} = −0.5 V. (c-f: Red) Conductance matrix as a function of $B_\parallel$ taken at V_{SG} = 0.5 V.

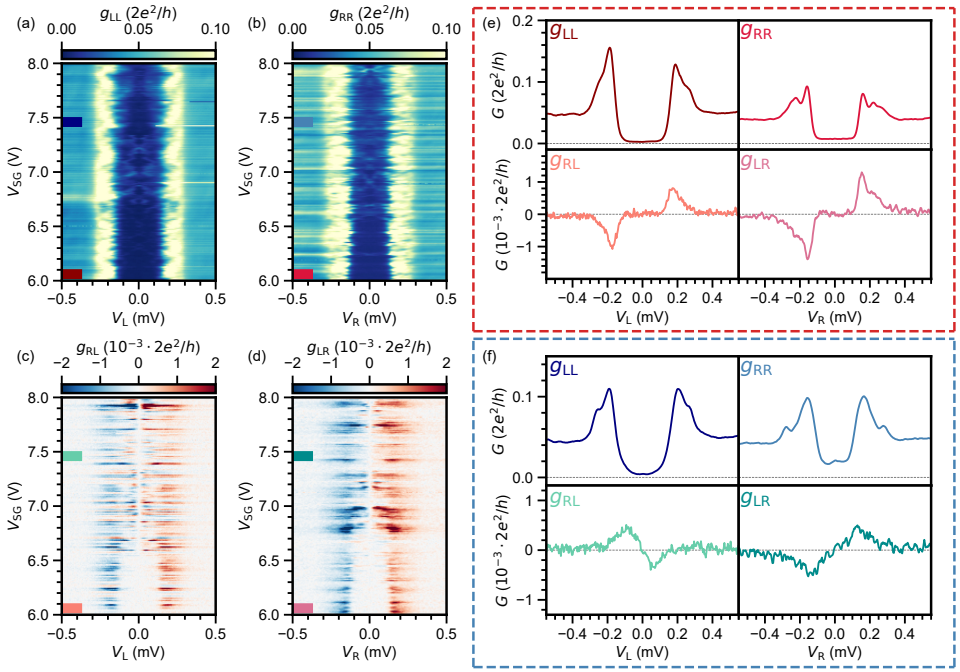

Figure 7.14: Full conductance matrix of device B (8 μm) as a function of V_{SG} taken at $B_{\parallel} = 0$ T. (a,b) Local conductances g_{LL} and g_{RR}. (c,d) Nonlocal conductances g_{RL} and g_{LR}. (e) Linecuts of the local and nonlocal spectra taken at $V_{SG} = 6.05$ V where the nanowire has a (hard) induced gap. (f) Linecuts of the local and nonlocal spectra taken at $V_{SG} = 7.45$ V where the induced gap in the nanowire is closed (i.e. a soft gap).

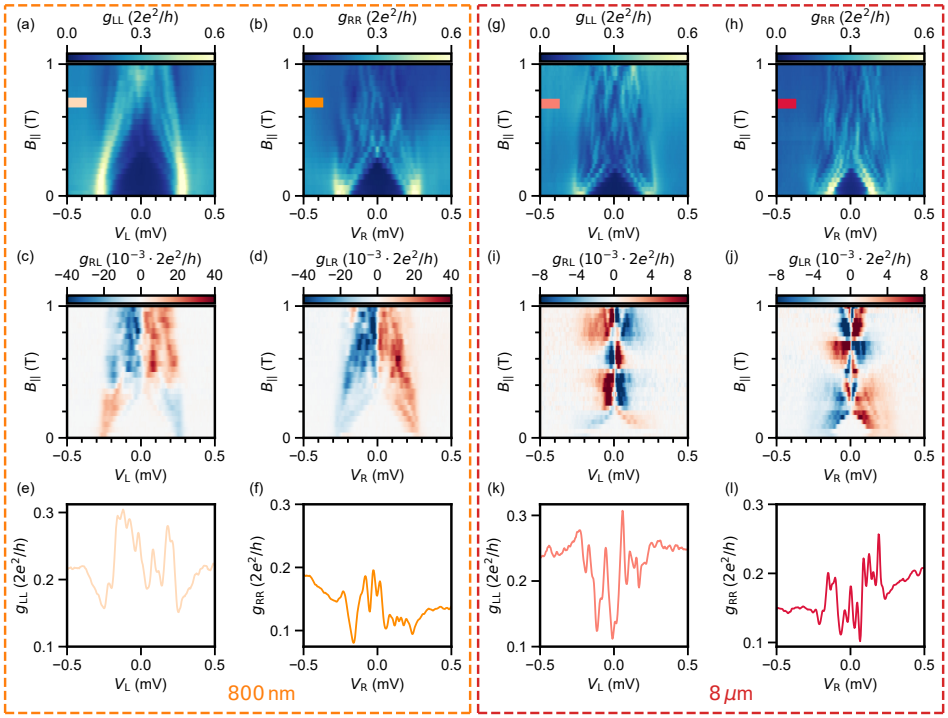

Figure 7.15: Comparison of the spectra between short (device F, 800 nm) and long (device B, 8 μm) hybrids in the weak-coupling regime. Both short (left) and long (right) nanowires form similar-sized fragmented segments in the nanowire near the junctions, as a result of the identical feature size of the tunnel gate geometry. Accordingly, both spectra exhibit a similar number of discrete states which are formed near the junctions. (a-d) Conductance matrix of device F as a function of $B_\parallel$ in the weak-coupling regime, taken at V_{SG} = 1.75 V. (e,f) linecuts of the local spectra g_{LL} and g_{RR} taken at $B_\parallel$ = 0.7 T. (g-j) Conductance matrix of device B as a function of $B_\parallel$ in the weak-coupling regime, taken at V_{SG} = 1 V. (k,l) linecuts of the local spectra g_{LL} and g_{RR} taken at $B_\parallel$ = 0.7 T.

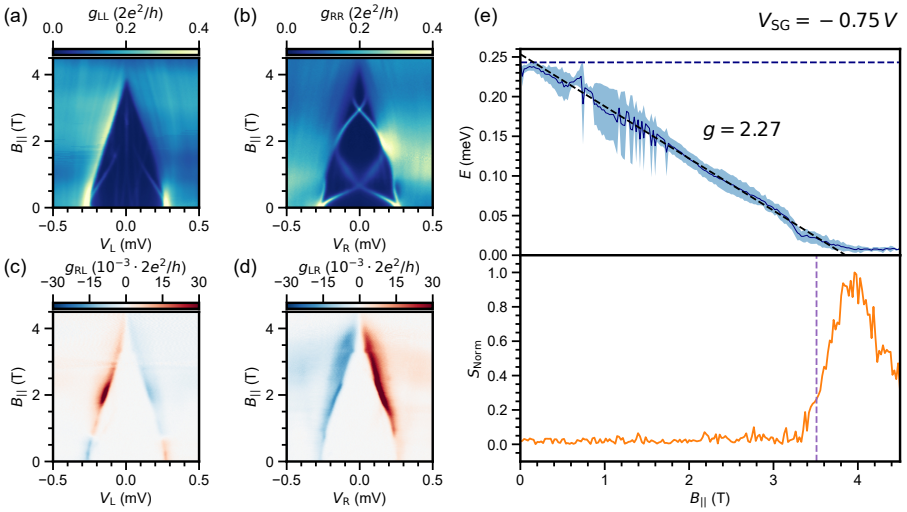

Figure 7.16: Full conductance matrix of device C (1 μm) as a function of parallel magnetic field in the strong-coupling regime, corresponding to panels (a,b) of Fig. 7.3 in the main text. (a,b) Local conductances g_{LL} and g_{RR}. (c,d) Nonlocal conductances g_{RL} and g_{LR}. (e) Top: Δ_i as a function of parallel magnetic field. The dashed black line indicates the fit of the Zeeman energy to the linear part of the data with $g = 2.27$. The dashed blue line indicates the zero-field induced gap Δ_0. Bottom: Normalized nonlocal slope $S_{Norm} = |S_{RL}S_{LR}|/\sqrt{|S_{RL}S_{LR}|}$ normalized by its maximum value. The dashed purple line indicates the estimated induced critical field $B_{||}^c$.

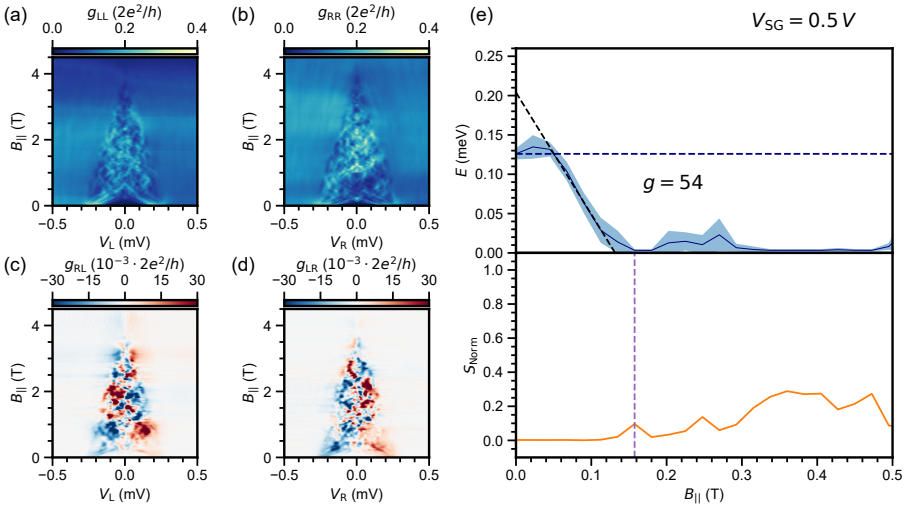

Figure 7.17: Full conductance matrix of device C (1 μm) as a function of parallel magnetic field in the weak-coupling regime, corresponding to panels (c,d) of Fig. 7.3 in the main text. (a,b) Local conductances g_{LL} and g_{RR}. (c,d) Nonlocal conductances g_{RL} and g_{LR}. (e) Top: Δ_i as a function of parallel magnetic field. The dashed black line indicates the fit of the Zeeman energy to the linear part of the data with $g = 54$. The dashed blue line indicates the zero-field induced gap Δ_0. Bottom: Normalized nonlocal slope $S_{Norm} = |S_{RL}S_{LR}|/\sqrt{|S_{RL}S_{LR}|}$ normalized by its maximum value. The dashed purple line indicates the estimated induced critical field $B_{||}^c$

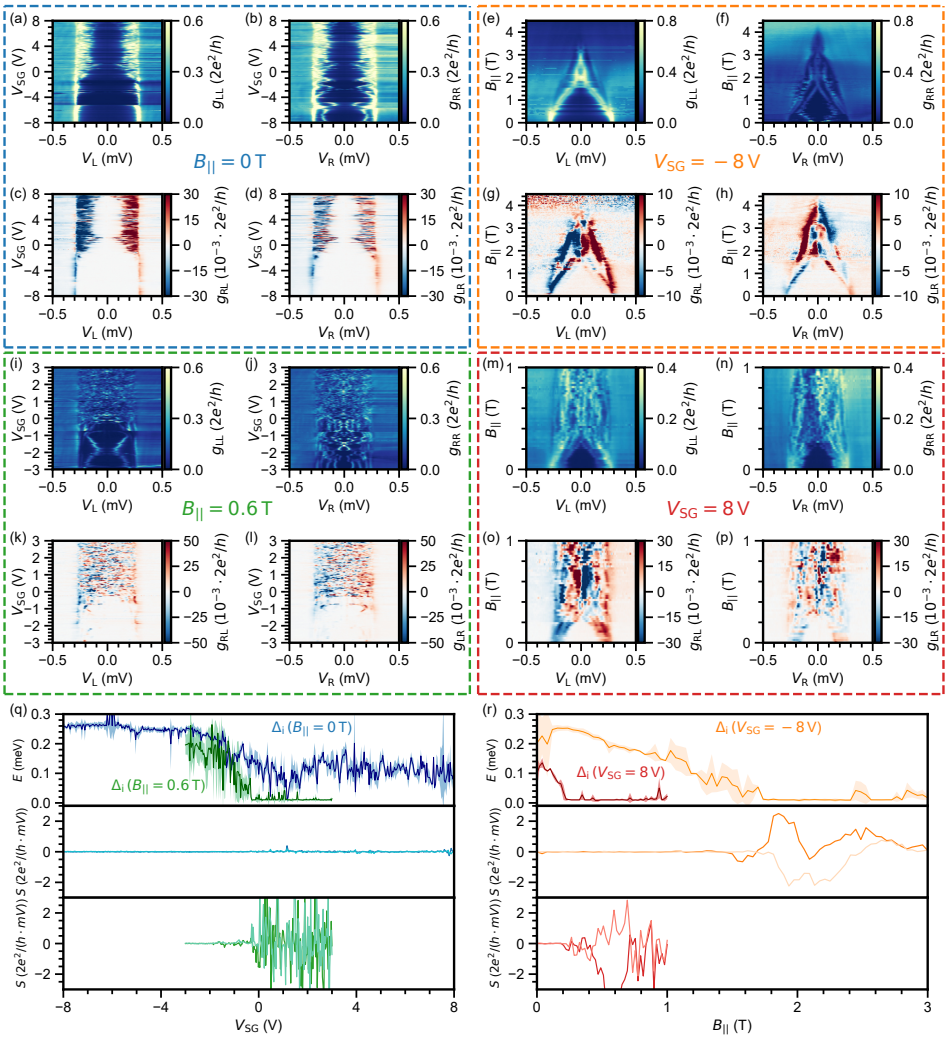

Figure 7.18: Representative overview of device D (240 nm hybrid). (a-d: Blue) Conductance matrix as a function of V_{SG} taken at $B_{\parallel} = 0\,\mathrm{T}$. (e-h: Orange) Conductance matrix as a function of $B_{\parallel}$ in the strong-coupling regime, taken at $V_{SG} = -8\,\mathrm{V}$. (i-l: Green) Conductance matrix as a function of V_{SG} taken at $B_{\parallel} = 0.6\,\mathrm{T}$. (m-p: Red) Conductance matrix as a function of $B_{\parallel}$ in the weak-coupling regime, taken at $V_{SG} = 8\,\mathrm{V}$. (q) Top: Δ_i as function of V_{SG} at $B_{\parallel} = 0\,\mathrm{T}$ (blue) and $B_{\parallel} = 0.6\,\mathrm{T}$ (green). Middle: Nonlocal slope as function of V_{SG} at $B_{\parallel} = 0\,\mathrm{T}$, indicating the nanowire maintains an induced gap at all gate values. Bottom: Nonlocal slope as function of V_{SG} at $B_{\parallel} = 0.6\,\mathrm{T}$, showing the induced gap closing around $V_{SG} = -0.5\,\mathrm{V}$. (r) Top: Δ_i as function of $B_{\parallel}$ at $V_{SG} = -8\,\mathrm{V}$ (orange) and $V_{SG} = -8\,\mathrm{V}$ (red). Middle: Nonlocal slope as function of $B_{\parallel}$ taken at $V_{SG} = -8\,\mathrm{V}$, showing the induced gap closing at $B_{\parallel}^{c} = 1.6\,\mathrm{T}$. Bottom: Nonlocal slope as function of $B_{\parallel}$ taken at $V_{SG} = 8\,\mathrm{V}$, showing the induced gap closing at $B_{\parallel}^{c} = 0.2\,\mathrm{T}$.

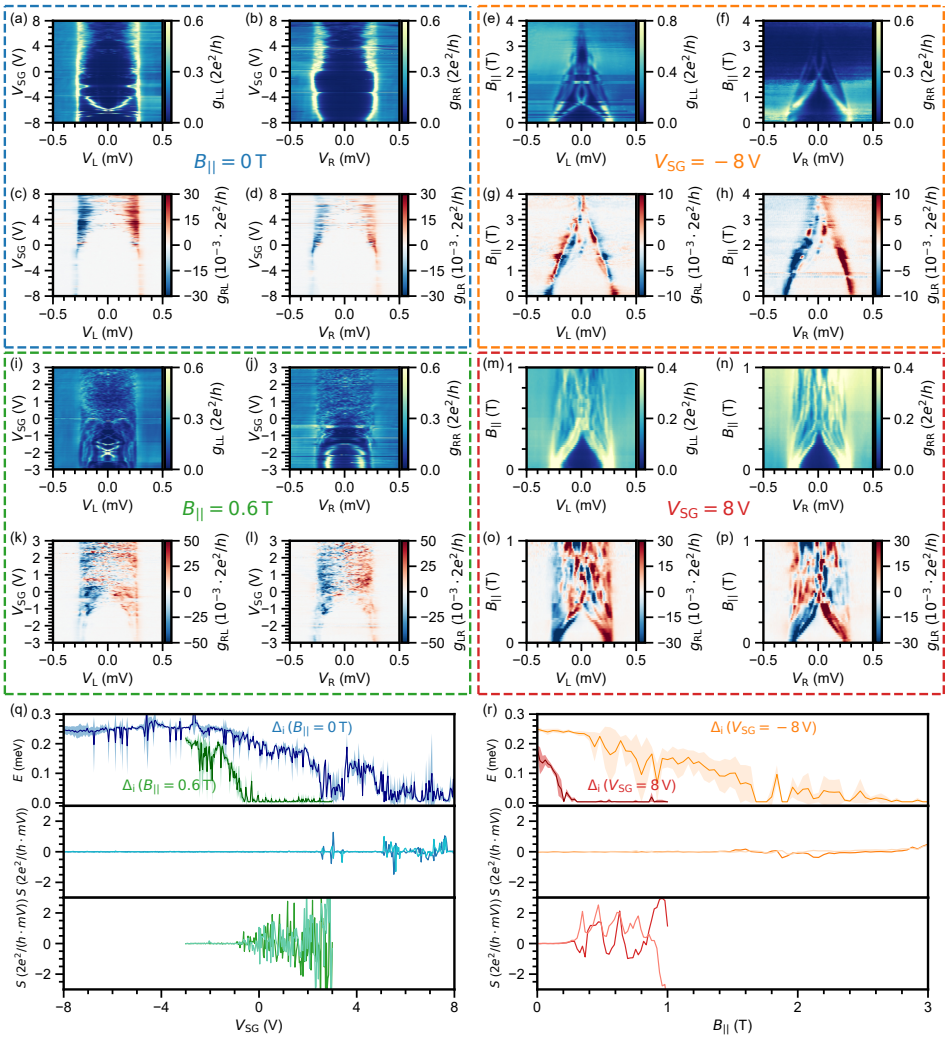

Figure 7.19: Representative overview of device E (450 nm hybrid). (a-d: Blue) Conductance matrix as a function of V_{SG} taken at $B_\parallel = 0$ T. (e-h: Orange) Conductance matrix as a function of $B_\parallel$ in the strong-coupling regime, taken at $V_{SG} = -8$ V. (i-l: Green) Conductance matrix as a function of V_{SG} taken at $B_\parallel = 0.6$ T. (m-p: Red) Conductance matrix as a function of $B_\parallel$ in the weak-coupling regime, taken at $V_{SG} = 8$ V. (q) Top: Δ_i as function of V_{SG} at $B_\parallel = 0$ T (blue) and $B_\parallel = 0.6$ T (green). Middle: Nonlocal slope as function of V_{SG} at $B_\parallel = 0$ T, showing an occational closing of the induced gap due to discrete states crossing zero energy. Bottom: Nonlocal slope as function of V_{SG} at $B_\parallel = 0.6$ T, showing the induced gap closing around $V_{SG} = -1$ V. (r) Top: Δ_i as function of $B_\parallel$ at $V_{SG} = -8$ V (orange) and $V_{SG} = -8$ V (red). Middle: Nonlocal slope as function of $B_\parallel$ taken at $V_{SG} = -8$ V, showing the induced gap closing at $B_\parallel^c = 1.6$ T. Bottom: Nonlocal slope as function of $B_\parallel$ taken at $V_{SG} = 8$ V, showing the induced gap closing at $B_\parallel^c = 0.23$ T.

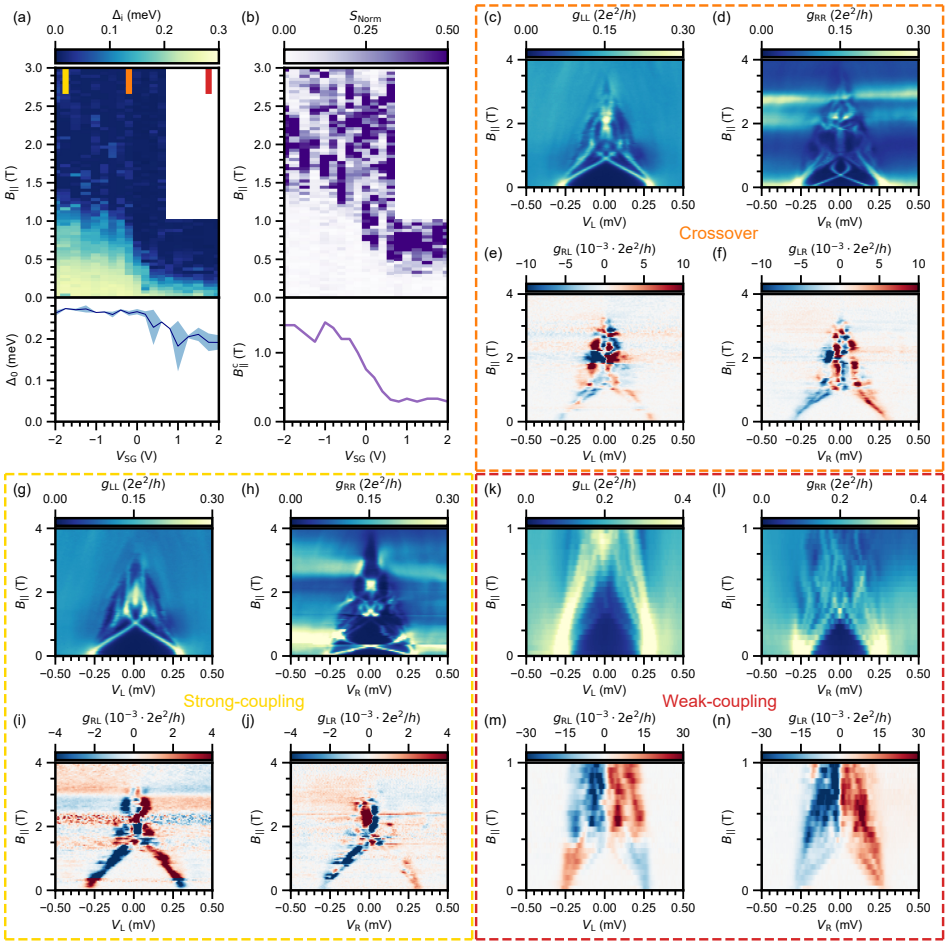

Figure 7.20: Induced gap and nonlocal slope diagrams for device F (800 nm long hybrid). (a) Top: Δ_i as a function of V_{SG} and $B_\parallel$. Bottom: Δ_i at $B_\parallel = 0$ T. (b) Top: Normalized nonlocal slope S_{Norm} as a function of V_{SG} and $B_\parallel$. Bottom: Parallel induced critical field $B_\parallel^c$ as a function of V_{SG}. (c-f: Orange) Conductance matrix as a function of $B_\parallel$ taken at $V_{SG} = -0.1$ V. (g-j: Yellow) Conductance matrix as a function of $B_\parallel$ taken at $V_{SG} = -1.75$ V. (c-f: Red) Conductance matrix as a function of $B_\parallel$ taken at $V_{SG} = 1.75$ V.

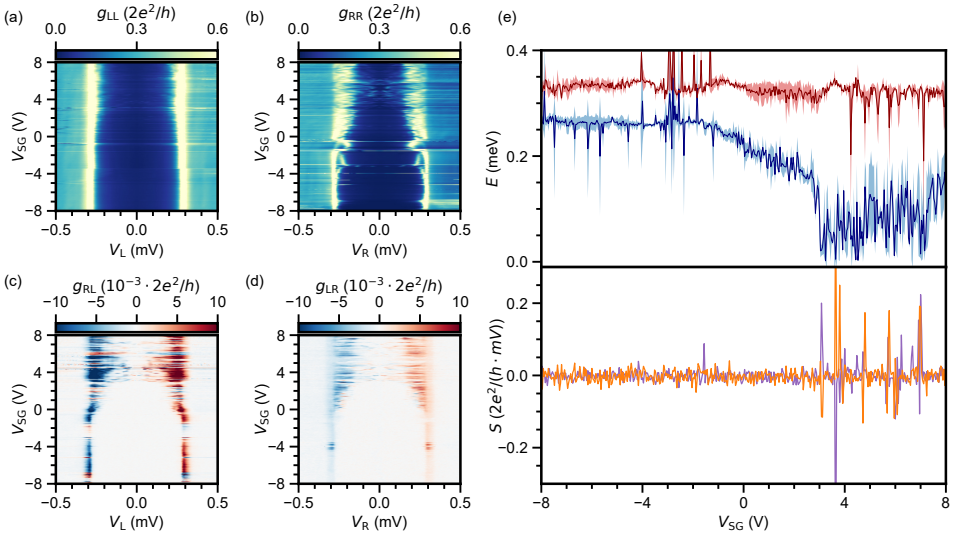

Figure 7.21: Full conductance matrix of device F as a function of V_{SG} taken at $B_{\parallel} = 0$ T. (a,b) Local conductances g_{LL} and g_{RR}. (c,d) Nonlocal conductances g_{RL} and g_{LR}. (e) Top: Δ_i (blue) and Δ_{SC} (red) as a function of V_{SG}. Bottom: calculated nonlocal slope at zero bias for g_{RL} (purple) and g_{LR} (orange). Here, Δ_i occasionally reaches zero but always returns to a finite value. We speculate this is the result of individual states in the hybrid attaining a finite charging energy due.

References

[1] R. M. Lutchyn, E. P. Bakkers, L. P. Kouwenhoven, P. Krogstrup, C. M. Marcus, and Y. Oreg, *Majorana zero modes in superconductor–semiconductor heterostructures,* Nat. Rev. Mater. **3**, 52 (2018).

[2] E. Prada, P. San-Jose, M. W. de Moor, A. Geresdi, E. J. Lee, J. Klinovaja, D. Loss, J. Nygård, R. Aguado, and L. P. Kouwenhoven, *From Andreev to Majorana bound states in hybrid superconductor–semiconductor nanowires,* Nat. Rev. Phys. **2**, 575 (2020).

[3] R. M. Lutchyn, J. D. Sau, and S. Das Sarma, *Majorana fermions and a topological phase transition in semiconductor-superconductor heterostructures,* Phys. Rev. Lett. **105**, 077001 (2010).

[4] Y. Oreg, G. Refael, and F. Von Oppen, *Helical liquids and majorana bound states in quantum wires,* Phys. Rev. Lett. **105**, 177002 (2010).

[5] T. O. Rosdahl, A. Vuik, M. Kjaergaard, and A. R. Akhmerov, *Andreev rectifier: A nonlocal conductance signature of topological phase transitions,* Phys. Rev. B **97**, 045421 (2018).

[6] D. I. Pikulin, B. van Heck, T. Karzig, E. A. Martinez, B. Nijholt, T. Laeven, G. W. Winkler, J. D. Watson, S. Heedt, M. Temurhan, V. Svidenko, R. M. Lutchyn, M. Thomas, G. de Lange, L. Casparis, and C. Nayak, *Protocol to identify a topological superconducting phase in a three-terminal device,* arXiv e-prints **2103.12217** (2021).

[7] J. Shabani, M. Kjaergaard, H. J. Suominen, Y. Kim, F. Nichele, K. Pakrouski, T. Stankevic, R. M. Lutchyn, P. Krogstrup, R. Feidenhans'l, S. Kraemer, C. Nayak, M. Troyer, C. M. Marcus, and C. J. Palmstrøm, *Two-dimensional epitaxial superconductor-semiconductor heterostructures: A platform for topological superconducting networks,* Phys. Rev. B **93**, 155402 (2016).

[8] A. E. Antipov, A. Bargerbos, G. W. Winkler, B. Bauer, E. Rossi, and R. M. Lutchyn, *Effects of gate-induced electric fields on semiconductor majorana nanowires,* Phys. Rev. X **8**, 031041 (2018).

[9] C. Reeg, D. Loss, and J. Klinovaja, *Metallization of a rashba wire by a superconducting layer in the strong-proximity regime,* Phys. Rev. B **97**, 165425 (2018).

[10] M. W. A. de Moor, J. D. S. Bommer, D. Xu, G. W. Winkler, A. E. Antipov, A. Bargerbos, G. Wang, N. van Loo, R. L. M. O. het Veld, S. Gazibegovic, D. Car, J. A. Logan, M. Pendharkar, J. S. Lee, E. P. A. M. Bakkers, C. J. Palmstrøm, R. M. Lutchyn, L. P. Kouwenhoven, and H. Zhang, *Electric field tunable superconductor-semiconductor coupling in majorana nanowires,* New J. Phys. **20**, 103049 (2018).

[11] L. J. Splitthoff, A. Bargerbos, L. Grünhaupt, M. Pita-Vidal, J. J. Wesdorp, Y. Liu, A. Kou, C. K. Andersen, and B. van Heck, *Gate-tunable kinetic inductance in proximitized nanowires,* Phys. Rev. Appl. **18**, 024074 (2022).

[12] S. Vaitiekėnas, M.-T. Deng, J. Nygård, P. Krogstrup, and C. Marcus, *Effective g factor of subgap states in hybrid nanowires,* Physical review letters **121**, 037703 (2018).

[13] J.-Y. Wang, N. van Loo, G. P. Mazur, V. Levajac, F. K. Malinowski, M. Lemang, F. Borsoi, G. Badawy, S. Gazibegovic, E. P. A. M. Bakkers, M. Quintero-Pérez, S. Heedt, and L. P. Kouwenhoven, *Parametric exploration of zero-energy modes in three-terminal insb-al nanowire devices,* Phys. Rev. B **106**, 075306 (2022).

[14] G. Ménard, G. Anselmetti, E. Martinez, D. Puglia, F. Malinowski, J. Lee, S. Choi, M. Pendharkar, C. Palmstrøm, K. Flensberg, *et al.*, *Conductance-matrix symmetries of a three-terminal hybrid device,* Physical Review Letters **124**, 036802 (2020).

[15] S. Heedt, M. Quintero-Pérez, F. Borsoi, A. Fursina, N. van Loo, G. P. Mazur, M. P. Nowak, M. Ammerlaan, K. Li, S. Korneychuk, *et al.*, *Shadow-wall lithography of ballistic superconductor–semiconductor quantum devices,* Nat. Commun. **12**, 1 (2021).

[16] F. Borsoi, G. P. Mazur, N. van Loo, M. P. Nowak, L. Bourdet, K. Li, S. Korneychuk, A. Fursina, J.-Y. Wang, V. Levajac, E. Memisevic, G. Badawy, S. Gazibegovic, K. van Hoogdalem, E. P. A. M. Bakkers, L. P. Kouwenhoven, S. Heedt, and M. Quintero-Pérez, *Single-shot fabrication of semiconducting–superconducting nanowire devices,* Adv. Func. Mater. , 2102388 (2021).

[17] G. L. R. Anselmetti, E. A. Martinez, G. C. Ménard, D. Puglia, F. K. Malinowski, J. S. Lee, S. Choi, M. Pendharkar, C. J. Palmstrøm, C. M. Marcus, L. Casparis, and A. P. Higginbotham, *End-to-end correlated subgap states in hybrid nanowires,* Phys. Rev. B **100**, 205412 (2019).

[18] D. Puglia, E. A. Martinez, G. C. Ménard, A. Pöschl, S. Gronin, G. C. Gardner, R. Kallaher, M. J. Manfra, C. M. Marcus, A. P. Higginbotham, and L. Casparis, *Closing of the induced gap in a hybrid superconductor-semiconductor nanowire,* Phys. Rev. B **103**, 235201 (2021).

[19] J. Danon, A. B. Hellenes, E. B. Hansen, L. Casparis, A. P. Higginbotham, and K. Flensberg, *Nonlocal conductance spectroscopy of andreev bound states: Symmetry relations and BCS charges,* Phys. Rev. Lett. **124**, 036801 (2020).

[20] A. Pöschl, A. Danilenko, D. Sabonis, K. Kristjuhan, T. Lindemann, C. Thomas, M. J. Manfra, and C. M. Marcus, *Nonlocal conductance spectroscopy of andreev bound states in gate-defined inas/al nanowires,* Phys. Rev. B **106**, L241301 (2022).

[21] G. Wang, T. Dvir, N. van Loo, G. P. Mazur, S. Gazibegovic, G. Badawy, E. P. A. M. Bakkers, L. P. Kouwenhoven, and G. de Lange, *Nonlocal measurement of quasiparticle charge and energy relaxation in proximitized semiconductor nanowires using quantum dots,* Phys. Rev. B **106**, 064503 (2022).

[22] A. Banerjee, O. Lesser, M. Rahman, C. Thomas, T. Wang, M. Manfra, E. Berg, Y. Oreg, A. Stern, and C. Marcus, *Local and nonlocal transport spectroscopy in planar josephson junctions,* arXiv preprint arXiv:2205.09419 (2022).

[23] M. Aghaee, A. Akkala, Z. Alam, R. Ali, A. A. Ramirez, M. Andrzejczuk, A. E. Antipov, M. Astafev, B. Bauer, J. Becker, *et al.*, *InAs-Al hybrid devices passing the topological gap protocol,* arXiv preprint arXiv:2207.02472 (2022).

[24] G. P. Mazur, N. van Loo, J.-Y. Wang, T. Dvir, G. Wang, A. Khindanov, S. Korneychuk, F. Borsoi, R. C. Dekker, G. Badawy, *et al.*, *Spin-mixing enhanced proximity effect in aluminum-based superconductor–semiconductor hybrids,* Advanced Materials , 2202034 (2022).

[25] J. Shen, G. W. Winkler, F. Borsoi, S. Heedt, V. Levajac, J.-Y. Wang, D. van Driel, D. Bouman, S. Gazibegovic, R. L. M. Op Het Veld, D. Car, J. A. Logan, M. Pendharkar, C. J. Palmstrøm, E. P. A. M. Bakkers, L. P. Kouwenhoven, and B. van Heck, *Full parity phase diagram of a proximitized nanowire island,* Phys. Rev. B **104**, 045422 (2021).

[26] A. Denisov, A. Bubis, S. Piatrusha, N. Titova, A. Nasibulin, J. Becker, J. Treu, D. Ruhstorfer, G. Koblmüller, E. Tikhonov, *et al.*, *Charge-neutral nonlocal response in superconductor-InAs nanowire hybrid devices,* Semiconductor Science and Technology **36**, 09LT04 (2021).

[27] G. E. Blonder, M. Tinkham, and T. M. Klapwijk, *Transition from metallic to tunneling regimes in superconducting microconstrictions: Excess current, charge imbalance, and supercurrent conversion,* Phys. Rev. B **25**, 4515 (1982).

[28] P. Krogstrup, N. Ziino, W. Chang, S. Albrecht, M. Madsen, E. Johnson, J. Nygård, C. M. Marcus, and T. Jespersen, *Epitaxy of semiconductor–superconductor nanowires,* Nat. Mater. **14**, 400 (2015).

[29] B. Nijholt and A. R. Akhmerov, *Orbital effect of magnetic field on the Majorana phase diagram,* Phys. Rev. B **93**, 235434 (2016).

[30] G. W. Winkler, D. Varjas, R. Skolasinski, A. A. Soluyanov, M. Troyer, and M. Wimmer, *Orbital contributions to the electron g factor in semiconductor nanowires,* Phys. Rev. Lett. **119**, 037701 (2017).

[31] G. W. Winkler, A. E. Antipov, B. van Heck, A. A. Soluyanov, L. I. Glazman, M. Wimmer, and R. M. Lutchyn, *Unified numerical approach to topological semiconductor-superconductor heterostructures,* Phys. Rev. B **99**, 245408 (2019).

[32] B. D. Woods, S. Das Sarma, and T. D. Stanescu, *Charge-impurity effects in hybrid majorana nanowires,* Phys. Rev. Applied **16**, 054053 (2021).

[33] E. Prada, P. San-Jose, and R. Aguado, *Transport spectroscopy of ns nanowire junctions with Majorana fermions,* Phys. Rev. B **86**, 180503 (2012).

[34] S. Ahn, H. Pan, B. Woods, T. D. Stanescu, and S. Das Sarma, *Estimating disorder and its adverse effects in semiconductor majorana nanowires,* Phys. Rev. Materials **5**, 124602 (2021).

[35] H. Pan, C.-X. Liu, M. Wimmer, and S. Das Sarma, *Quantized and unquantized zero-bias tunneling conductance peaks in majorana nanowires: Conductance below and above* $2e^2/h$, Phys. Rev. B **103**, 214502 (2021).

[36] R. Hess, H. F. Legg, D. Loss, and J. Klinovaja, *Local and nonlocal quantum transport due to andreev bound states in finite rashba nanowires with superconducting and normal sections,* Phys. Rev. B **104**, 075405 (2021).

[37] E. J. Lee, X. Jiang, M. Houzet, R. Aguado, C. M. Lieber, and S. De Franceschi, *Spin-resolved Andreev levels and parity crossings in hybrid superconductor–semiconductor nanostructures,* Nat. Nanotechnol. **9**, 79 (2014).

[38] G. Badawy, B. Zhang, T. Rauch, J. Momand, S. Koelling, J. Jung, S. Gazibegovic, O. Moutanabbir, B. J. Kooi, S. Botti, *et al.*, *Electronic structure and epitaxy of CdTe shells on InSb nanowires,* Advanced Science **9**, 2105722 (2022).

[39] E. A. Martinez, A. Pöschl, E. B. Hansen, M. A. Y. van de Poll, S. Vaitiekėnas, A. P. Higginbotham, and L. Casparis, *Measurement circuit effects in three-terminal electrical transport measurements,* arXiv e-prints **2104.02671** (2021).

[40] J. Pillet, C. Quay, P. Morfin, C. Bena, A. L. Yeyati, and P. Joyez, *Andreev bound states in supercurrent-carrying carbon nanotubes revealed,* Nature Physics **6**, 965 (2010).

[41] T. D. Stanescu, R. M. Lutchyn, and S. D. Sarma, *Dimensional crossover in spin-orbit-coupled semiconductor nanowires with induced superconducting pairing,* Physical Review B **87**, 094518 (2013).

8

Realization of a minimal Kitaev chain in coupled quantum dots

Majorana bound states constitute one of the simplest examples of emergent non-Abelian excitations in condensed matter physics. A toy model proposed by Kitaev shows that such states can arise at the ends of a spinless *p*-wave superconducting chain [1]. Practical proposals for its realization [2, 3] require coupling neighboring quantum dots in a chain via both electron tunneling and crossed Andreev reflection [4]. While both processes have been observed in semiconducting nanowires and carbon nanotubes [5–8], crossed-Andreev interaction was neither easily tunable nor strong enough to induce coherent hybridization of dot states. Here we demonstrate the simultaneous presence of all necessary ingredients for an artificial Kitaev chain: two spin-polarized quantum dots in an InSb nanowire strongly coupled by both elastic co-tunneling and crossed Andreev reflection. We fine-tune this system to a sweet spot where a pair of Poor Man's Majorana states is predicted to appear. At this sweet spot, the transport characteristics satisfy the theoretical predictions for such a system, including pairwise correlation, zero charge and stability against local perturbations. While the simple system presented here can be scaled to simulate a full Kitaev chain with an emergent topological order, it can also be used imminently to explore relevant physics related to non-Abelian anyons.

This work has been published as *Realization of a minimal Kitaev chain in coupled quantum dots*, T. Dvir[†], G. Wang[†], **N. van Loo**[†], C.-X. Liu, G.P. Mazur, A. Bordin, S.L.D. ten Haaf, J.-Y. Wang, D. van Driel, F. Zatelli, X. Li, F.K. Malinowski, S. Gazibegovic, G. Badawy, E.P.A.M. Bakkers, M. Wimmer and L.P. Kouwenhoven in Nature 614, 445–450 (2023).

[†] These authors contributed equally to this work.

Engineering Majorana bound states in condensed matter systems is an intensively pursued goal, both for their exotic non-Abelian exchange statistics and for potential applications in building topologically protected qubits [1, 9, 10]. The most investigated experimental approach looks for Majorana states at the boundaries of topological superconducting materials, made of hybrid semiconducting-superconducting heterostructures [11–15]. However, the widely-relied-upon signature of Majorana states, zero-bias conductance peaks, is by itself unable to distinguish topological Majorana states from other trivial zero-energy states induced by disorder and smooth gate potentials [16–21]. Both problems disrupting the formation or detection of a topological phase originate from a lack of control over the microscopic details of the electron potential landscape in these heterostructure devices.

In this work, we realize a minimal Kitaev chain [1] using two quantum dots (QDs) coupled via a short superconducting-semiconducting hybrid [2]. By controlling the electrostatic potential on each of these three elements, we overcome the challenge imposed by random disorder potentials. At a fine-tuned sweet spot where Majorana states are predicted to appear, we observe end-to-end correlated conductance that signals emergent Majorana properties such as zero charge and robustness against local perturbations. We note that these Majorana states in a minimal Kitaev chain are *not* topologically protected and have been dubbed "Poor Man's Majorana" (PMM) states [3].

8.1 Realization of a minimal Kitaev chain

The elementary building block of the Kitaev chain is a pair of spinless electronic sites coupled simultaneously by two mechanisms: elastic co-tunneling (ECT) and crossed Andreev reflection (CAR). Both processes are depicted in Figure 8.1a. ECT involves a single electron hopping between two sites with an amplitude t. CAR refers to two electrons from both sites tunneling back and forth into a common superconductor with an amplitude Δ (not to be confused with the superconducting gap size), forming and splitting Cooper-pairs [4]. To create the two-site Kitaev chain, we utilize two spin-polarized QDs where only one orbital level in each dot is available for transport. In the absence of tunneling between the QDs, the system is characterized by a well-defined charge state on each QD: $|n_{\mathrm{LD}}\ n_{\mathrm{RD}}\rangle$, where $n_{\mathrm{LD}}, n_{\mathrm{RD}} \in \{0,1\}$ are occupations of the left and right QD levels. The charge on each QD depends only on its electrochemical potential μ_{LD} or μ_{RD}, schematically shown in Figure 8.1b.

In the presence of inter-dot coupling, the eigenstates of the combined system become superpositions of the charge states. ECT couples $|10\rangle$ and $|01\rangle$, resulting in two eigenstates of the form $\alpha|10\rangle - \beta|01\rangle$ (Figure 8.1c), both with odd combined charge parity. These two bonding and anti-bonding states differ in energy by $2t$ when both QDs are at their charge degeneracy, i.e., $\mu_{\mathrm{LD}} = \mu_{\mathrm{RD}} = 0$. Analogously, CAR couples the two even states $|00\rangle$ and $|11\rangle$ to produce bonding and anti-bonding eigenstates of the form $u|00\rangle - v|11\rangle$, preserving the even parity of the original states. These states differ in energy by 2Δ when $\mu_{\mathrm{LD}} = \mu_{\mathrm{RD}} = 0$ (Figure 8.1d). If the amplitude of ECT is stronger than CAR ($t > \Delta$), the odd bonding state has lower energy than the even bonding state near the joint charge

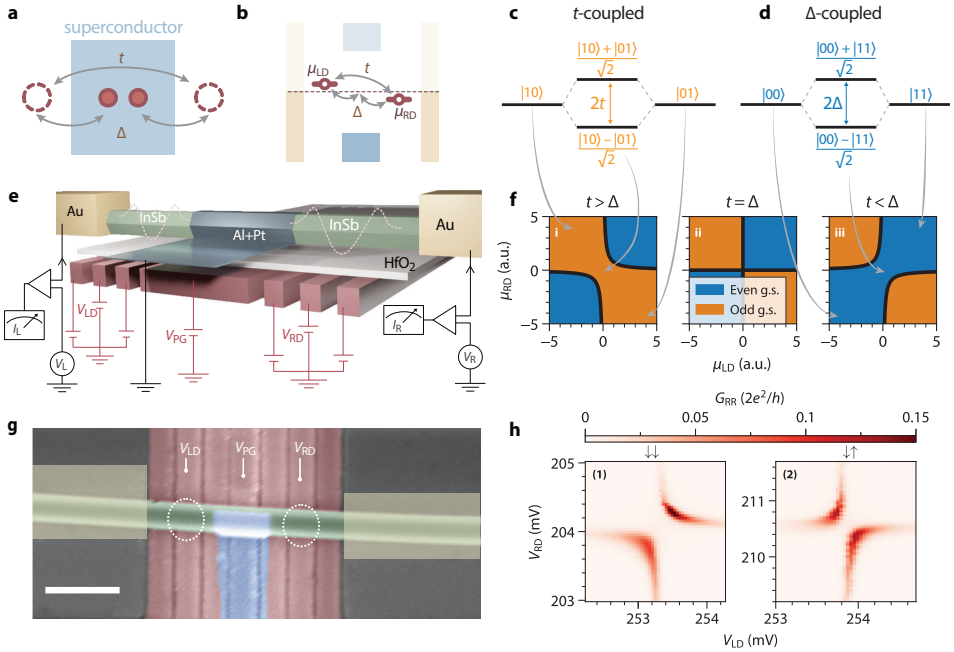

Figure 8.1: **Coupling quantum dots through elastic co-tunneling (ECT) and crossed Andreev reflection (CAR). a.** Illustration of the basic ingredients of a Kitaev chain: two QDs simultaneously coupled via ECT with amplitude t and via CAR with amplitude Δ through the superconductor in between. **b.** Energy diagram of a minimal Kitaev chain. Two QDs with gate-controlled chemical potentials are coupled via both ECT and CAR. The two ohmic leads enable transport measurements from both sides. **c.** Energy diagram showing that coupling the $|01\rangle$ and $|10\rangle$ states via ECT leads to a bonding state $(|10\rangle - |01\rangle)/\sqrt{2}$ and anti-bonding state $(|10\rangle + |01\rangle)/\sqrt{2}$. **d.** Same showing how CAR couples $|00\rangle$ and $|11\rangle$ to form the bonding state $(|00\rangle - |11\rangle)/\sqrt{2}$ and anti-bonding state $(|00\rangle + |11\rangle)/\sqrt{2}$. **e.** Illustration of the N-QD-S-QD-N device and the measurement circuit. Dashed potentials indicate QDs defined in the nanowire by finger gates. **f.** Charge stability diagram of the coupled-QD system, in the cases of $t > \Delta$ (i), $t = \Delta$ (ii) and $t < \Delta$ (iii). Blue marks regions in the (μ_{LD}, μ_{RD}) plane where the ground state is even and orange where the ground state is odd. **g.** False-colored scanning electron microscopy image of the device, prior to the fabrication of the normal leads. InSb nanowire is colored green. QDs are defined by bottom finger gates (in red) and their locations are circled. The gates controlling the two QD chemical potentials are labeled by their voltages, V_{LD} and V_{RD}. The central thin Al/Pt film, in blue, is grounded. The proximitized nanowire underneath is gated by V_{PG}. Two Cr/Au contacts are marked by yellow boxes. The scale bar is 300 nm. **h.** Right-side zero-bias local conductance G_{RR} in the (V_{LD}, V_{RD}) plane when the system is tuned to $t > \Delta$ (1) and $t < \Delta$ (2). The arrows mark the spin polarization of the QD levels. The DC bias voltages are kept at zero, $V_L = V_R = 0$, and an AC excitation of 6 μV RMS is applied on the right side.

degeneracy $\mu_{LD} = \mu_{RD} = 0$ (see Methods for details). The system thus features an odd ground state in a wider range of QD potentials, leading to a charge stability diagram shown in Figure 8.1f(i) [22]. The opposite case of CAR dominating over ECT, i.e., $t < \Delta$, leads to a charge stability diagram shown in Figure 8.1f(iii), where the even ground state is more prominent. Fine-tuning the system such that $t = \Delta$ equalizes the two avoided crossings, inducing an even-odd degenerate ground state at $\mu_{LD} = \mu_{RD} = 0$ (Figure 8.1f(ii)). This degeneracy gives rise to two spatially separated PMMs, each localized at one QD [3].

Figure 8.1e illustrates our coupled QD system and the electronic measurement circuit. An InSb nanowire is contacted on two sides by two Cr/Au normal leads (N). A 200 nm-wide superconducting lead (S) made of a thin Al/Pt film covering the nanowire is grounded and proximitizes the central semiconducting segment. The chemical potential of the proximitized semiconductor can be tuned by gate voltage V_{PG}. This hybrid segment shows a hard superconducting gap accompanied by discrete, gate-tunable Andreev bound states (Figure 8.5). Two QDs are defined by finger gates underneath the nanowire. Their chemical potentials μ_{LD}, μ_{RD} are linearly tuned by voltages on the corresponding gates V_{LD}, V_{RD}. Bias voltages on the two N leads, V_L, V_R, are applied independently and currents through them, I_L, I_R, are measured separately. Transport characterization shows charging energies of 1.8 meV on the left QD and 2.3 meV on the right (Figure 8.5). Standard DC+AC lock-in technique allows measurement of the full conductance matrix:

$$G = \begin{pmatrix} G_{LL} & G_{LR} \\ G_{RL} & G_{RR} \end{pmatrix} = \begin{pmatrix} \frac{dI_L}{dV_L} & \frac{dI_L}{dV_R} \\ \frac{dI_R}{dV_L} & \frac{dI_R}{dV_R} \end{pmatrix}. \tag{8.1}$$

Measurements were conducted in a dilution refrigerator in the presence of a magnetic field $B = 200\,\mathrm{mT}$ applied approximately along the nanowire axis. The combination of Zeeman splitting E_Z and orbital level spacing allows single-electron QD transitions to be spin-polarized. Two neighbouring Coulomb resonances correspond to opposite spin orientations, enabling the QD spins to be either parallel ($\uparrow\uparrow$ and $\downarrow\downarrow$) or anti-parallel ($\uparrow\downarrow$ and $\downarrow\uparrow$). We report on two devices, A in the main text and B in Extended Data (Figure 8.11 and Figure 8.12). A scanning electron microscope image of Device A is shown in Figure 8.1g.

Transport measurements are used to characterize the charge stability diagram of the system. In Figure 8.1h(1), we show G_{RR} as a function of QD voltages V_{LD}, V_{RD} when both QDs are set to spin-down ($\downarrow\downarrow$). The measured charge stability diagram shows avoided crossing which indicates the dominance of ECT. In Figure 8.1h(2), we change the spin configuration to $\downarrow\uparrow$. The charge stability diagram now develops the avoided crossing of the opposite orientation, indicating the dominance of CAR for QDs with anti-parallel spins. This is, to our knowledge, the first verification of the prediction that spatially separated QDs can coherently hybridize via CAR coupling to a superconductor [23]. Thus, we have introduced all the necessary ingredients for a two-site Kitaev chain.

8.2 Tuning the relative strength of CAR and ECT

Majorana states in long Kitaev chains are present under a wide range of parameters due to topological protection [1]. Strikingly, even a chain consisting of only two sites can host a pair of PMMs despite a lack of topological protection, if the fine-tuned sweet spot $t = \Delta$ and $\mu_{LD} = \mu_{RD} = 0$ can be achieved [3]. This, however, is made challenging by the above-mentioned requirement to have both QDs spin-polarized. If spin is conserved, ECT can only take place between QDs with $\downarrow\downarrow$ or $\uparrow\uparrow$ spins, while CAR is only allowed for $\uparrow\downarrow$ and $\downarrow\uparrow$. Rashba spin-orbit coupling in InSb nanowires solves this dilemma [2, 24, 25], allowing finite ECT even in anti-parallel spin configurations and CAR between QDs with equal spins.

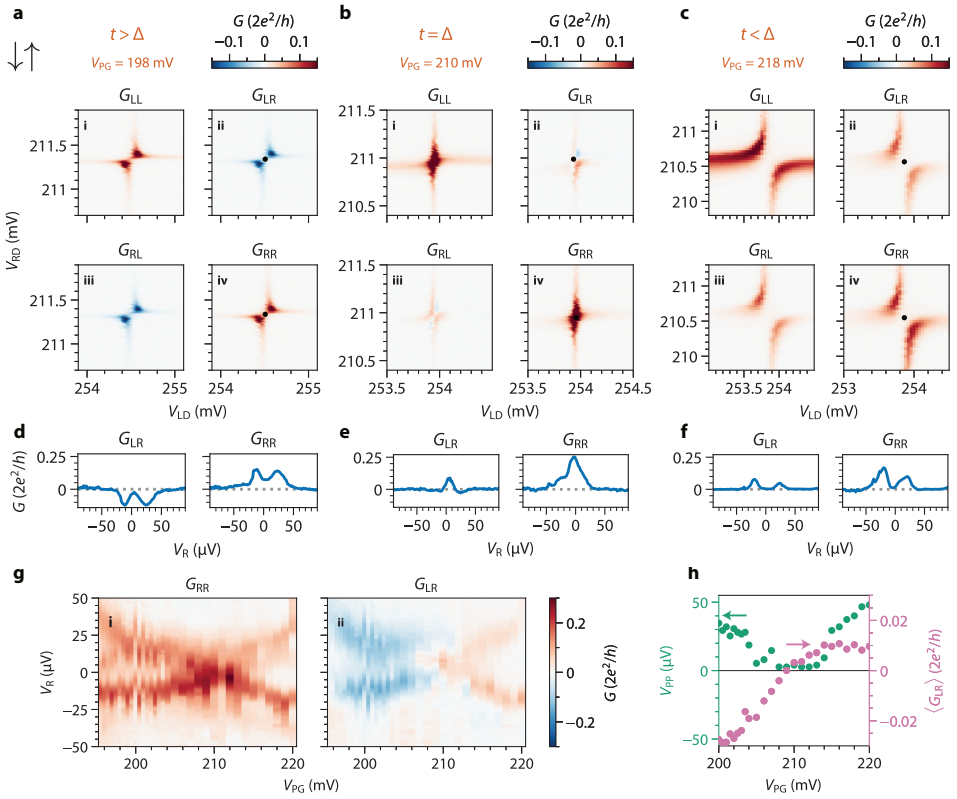

Figure 8.2: **Tuning the relative strength of CAR and ECT for the ↓↑ spin configuration. a-c.** Conductance matrices measured with $V_{PG} = (198, 210, 218)$ mV, respectively. **d-f.** G_{LR} and G_{RR} as functions of V_R when V_{LD}, V_{RD} are set to the center of each charge stability diagram in panels a to c, indicated by the black dots in the corresponding panels above them. **g.** Local (G_{RR}) and nonlocal (G_{LR}) conductance as a function of V_R and V_{PG} while keeping $\mu_{LD} \approx \mu_{RD} \approx 0$, showing the continuous crossover from $t > \Delta$ to $t < \Delta$. **h.** Green dots: peak-to-peak distance (V_{PP}) between the positive- and negative-bias segments of G_{RR}, showing the closing and re-opening of QD avoided crossings. Purple dots: average G_{LR} ($\langle G_{LR} \rangle$) as a function of V_{PG}, showing a change in the sign of the nonlocal conductance.

A further challenge is to make the two coupling strengths equal for a given spin combination. Refs. [24–26] show that both CAR and ECT in our device are virtual transitions through intermediate Andreev bound states residing in the short InSb segment underneath the superconducting film. Thus, varying V_{PG} changes the energy and wavefunction of said Andreev bound states and thereby t, Δ. We search for the V_{PG} range over which Δ changes differently than t and look for a crossover in the type of charge stability diagrams.

Figure 8.2a-c shows the resulting charge stability diagrams for the ↓↑ spin configuration at different values of V_{PG}. The conductance matrix $G(V_L = 0, V_R = 0)$ at $V_{PG} = 198\,\text{mV}$ is shown in Figure 8.2a. The local conductance on both sides, G_{LL} and G_{RR}, exhibit level repulsion indicative of $t > \Delta$. We emphasize that ECT can become stronger than CAR even

though the spins of the two QD transitions are anti-parallel due to the electric gating mentioned above. The dominance of ECT over CAR can also be seen in the negative sign of the nonlocal conductance, G_{LR} and G_{RL}. During ECT, an electron enters the system through one dot and exits through the other, resulting in negative nonlocal conductance. CAR, in contrast, causes two electrons to enter or leave both dots simultaneously, producing positive nonlocal conductance [27]. The residual finite conductance in the center of the charge stability diagram can be attributed to level broadening due to finite temperature and dot-lead coupling (see Figure 8.14). In Figure 8.2d, we show the conductance spectrum measured as a function of V_R, with V_{LD} and V_{RD} tuned to $\mu_{LD} \approx \mu_{RD} \approx 0$ (black dots in panels c(ii, iv)). A pair of conductance peaks or dips is visible on either side of zero energy.

Figure 8.2c shows G at $V_{PG} = 218\,\mathrm{mV}$ (the G_{RR} component is also used for Figure 8.1h(2)). Here, all the elements of G exhibit CAR-type avoided crossings. The spectrum shown in panel f, obtained at the joint charge degeneracy point (black dots in panels c(ii, iv)), similarly has two conductance peaks surrounding zero energy. The measured nonlocal conductance is positive as predicted for CAR. The existence of both $t > \Delta$ and $t < \Delta$ regimes, together with continuous gate tunability, allows us to approach the $t \approx \Delta$ sweet spot. This is shown in panel b, taken with $V_{PG} = 210\,\mathrm{mV}$. Here, G_{RR} and G_{LL} exhibit no avoided crossing while G_{LR} and G_{RL} fluctuate around zero, confirming that CAR and ECT are in balance. Accordingly, the spectrum in panel e confirms the even and odd ground states are degenerate and transport can occur at zero excitation energy via the appearance of a zero-bias conductance peak. The crossover from the $t > \Delta$ regime to the $t < \Delta$ regime can be seen across multiple QD resonances (Figure 8.13).

To show that gate-tuning of the t/Δ ratio is indeed continuous, we repeat charge stability diagram measurements (Figure 8.7) and bias spectroscopy at more V_{PG} values. As before, each bias sweep is conducted while keeping both QDs at charge degeneracy. Figure 8.2g shows the resulting composite plot of G_{RR} (i) and G_{LR} (ii) vs bias voltage and V_{PG}. The X-shaped conductance feature indicates a continuous evolution of the excitation energy, with a linear zero-energy crossing agreeing with predictions in Ref. [3]. Following analysis described in Methods, we extract the peak spacing and average nonlocal conductance in Figure 8.2h in order to visualize the continuous crossover from $t > \Delta$ to $t < \Delta$.

8.3 Poor Man's Majorana sweet spot

Next, we study the excitation spectrum in the vicinity of the $t = \Delta$ sweet spot. The predicted zero-temperature experimental signature of the PMMs is a pair of quantized zero-bias conductance peak on both sides of the devices. These zero-bias peaks are persistent even when one of the QD levels deviates from charge degeneracy [3]. We focus on the $\uparrow\uparrow$ spin configuration since it exhibits higher t, Δ values when they are equal (see Figure 8.8). Figure 8.3a shows the charge stability diagram measured via I_R under fixed $V_L = 0, V_R = 10\,\mu\mathrm{V}$. No level repulsion is visible, indicating $t \approx \Delta$. Panel b(i) shows the excitation spectrum when both dots are at charge degeneracy. The spectra on both sides show zero-bias peaks accompanied by two side peaks. The values of t, Δ can be read directly from the position of the side peaks, which correspond to the anti-bonding excited states at energy $2t = 2\Delta \approx 25\,\mu\mathrm{eV}$. The height of the observed zero-bias peaks is

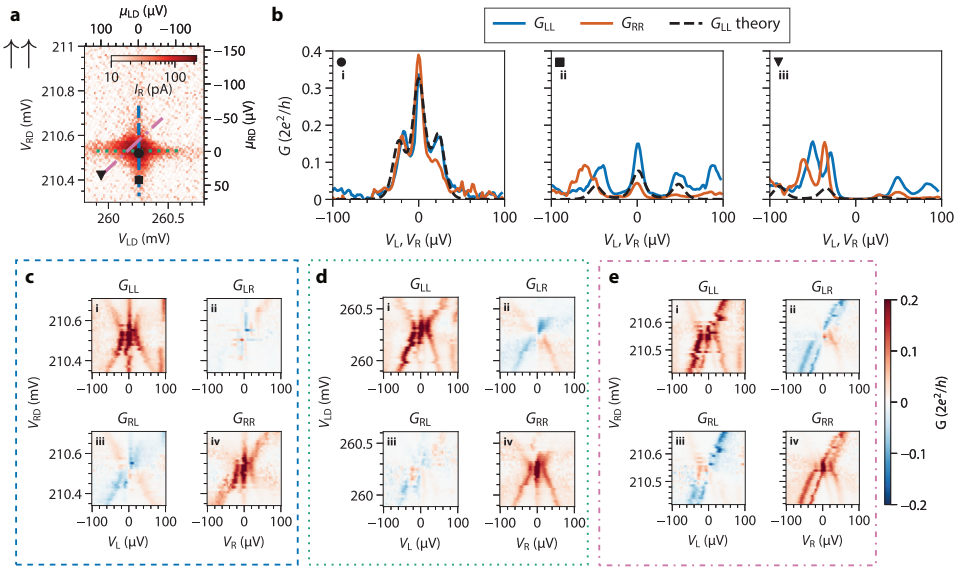

Figure 8.3: **Conductance spectroscopy at the $t = \Delta$ sweet spot for the ↑↑ spin configuration.** **a.** I_R vs V_{LD}, V_{RD} under $V_L = 0$, $V_R = 10\,\mu V$. The spectra in panel b are taken at values of V_{LD}, V_{RD} marked by corresponding symbols. The gate vs bias sweeps are taken along the dashed, dotted, dash-dot lines in panels c,d,e respectively. Data are taken with fixed $V_{PG} = 215.1\,mV$. **b.** Spectra taken under the values of V_{LD}, V_{RD} marked in panel a. The dashed lines are theoretical curves calculated with $t = \Delta = 12\,\mu eV$, $\Gamma_L = \Gamma_R = 4\,\mu eV$, $T = 45\,mK$ and at QD energies converted from V_{LD}, V_{RD} using measured lever arms (see Methods for details). **c, d.** G as a function of the applied bias and V_{RD} (c) or V_{LD} (d), taken along the paths indicated by the dashed blue line and the dotted green line in panel a, respectively. **e.** G as a function of the applied bias and along the diagonal indicated by the dashed-dotted pink line in panel a. This diagonal represents $500\,\mu V$ of change in V_{LD} and $250\,\mu V$ of change in V_{RD}.

8

0.3 to $0.4 \times 2e^2/h$, likely owing to a combination of tunnel broadening and finite electron temperature (Figure 8.6). Figure 8.3b(ii) shows the spectrum when the right QD is moved away from charge degeneracy while μ_{LD} is kept at 0. The zero-bias peaks persist on both sides of the device, as expected for a PMM state. In contrast, tuning both dots away from charge degeneracy, shown in Figure 8.3b(iii), splits the zero-bias peaks.

In Figure 8.3c,d, we show the evolution of the spectrum when varying V_{RD} and V_{LD}, respectively. The vertical feature appearing in both G_{LL} and G_{RR} shows correlated zero-bias peaks in both QDs, which persist when one QD potential departs from zero. This crucial observation demonstrates the robustness of PMMs against local perturbations. The excited states disperse in agreement with the theoretical predictions [3]. Nonlocal conductance, on the other hand, reflects the local charge character of a bound state on the side where current is measured [28–30]. Near-zero values of G_{LR} in panel c and G_{RL} in panel d are consistent with the prediction that the PMM mode on the unperturbed side remains an equal superposition of an electron and a hole and therefore chargeless.

Finally, when varying the chemical potential of both dots simultaneously (panel e), we see that the zero-bias peaks split away from zero energy. This splitting is not linear, in

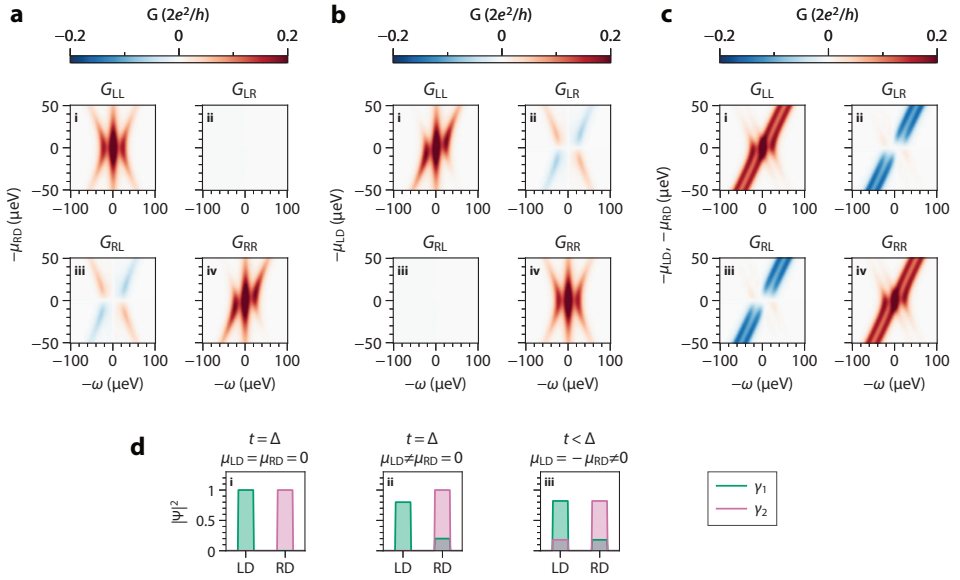

Figure 8.4: **Calculated conductance and Majorana localization. a.** Numerically calculated G as a function of energy ω and μ_{RD} at the $t = \Delta$ sweet spot. **b.** Numerically calculated G as a function of ω and μ_{LD} at the $t = \Delta$ sweet spot. **c.** Numerically calculated G as a function of ω and μ_{RD}, μ_{LD} along the diagonal corresponding to $\mu_{LD} = \mu_{RD}$ at $t = \Delta$. All of the numerical curves use the same value of $t, \Delta, \Gamma_L, \Gamma_R$ as those in Figure 8.3. **d.** Illutrations of the localization of two zero-energy solutions for the following set of parameters: $t = \Delta$, $\mu_{LD} = \mu_{RD} = 0$ (sub-panel i), $t = \Delta$, $\mu_{RD} = 0$, $\mu_{LD} > 0$ (sub-panel ii), $t < \Delta$, $\mu_{LD} = -\mu_{RD} = \sqrt{\Delta^2 - t^2}$ (sub-panel iii).

contrast to the case when $\Delta \neq t$ (see Figure 8.9). The profile of the peak splitting is consistent with the predicted quadratic protection of PMMs against chemical potential fluctuations [3]. This quadratic protection is expected to develop into topological protection in a long-enough Kitaev chain [2].

8

8.4 Discussion

To facilitate comparison with data, we develop a transport model (see Methods) and plot in Figure 8.4a-c the calculated conductance matrices as functions of excitation energy, ω, vs μ_{RD} (panel a), μ_{LD} (panel b), and $\mu \equiv \mu_{LD} = \mu_{RD}$ (panel c). These conditions are an idealization of those in Figure 8.3 (a more realistic simulation of the experimental conditions is presented in Figure 8.10). The numerical simulations capture the main features appearing in the experiments discussed above.

Particle-hole symmetry ensures that zero-energy excitations in this system always come in pairs. These excitations can extend over both QDs or be confined to one of them. In Figure 8.4d we show the calculated spatial extent of the zero-energy excitations for three scenarios. The first, in Figure 8.4d(i), illustrates Figure 8.3b(i) and shows that the sweet-spot zero-energy solutions are two PMMs, each localized on a different QD. The second

scenario in Figure 8.4d(ii), illustrating Figure 8.3b(ii), is varying μ_{LD} while keeping $\mu_{\mathrm{RD}} = 0$. This causes some of the wavefunction localized on the perturbed left side, γ_1, to leak into the right QD. Since the right-side γ_2 excitation has no weight on the left, it does not respond to this perturbation and remains fully localized on the right QD. As the theory confirms [3], it stays a zero-energy PMM state. Since Majorana excitations always come in pairs, the excitation on the left QD must also remain at zero energy. This provides an intuitive understanding of the remarkable stability of the zero-energy modes at the sweet spot in Figure 8.3c,d when moving one of the QDs' chemical potentials away from zero. Finally, zero-energy solutions can be found away from the sweet spot, $t \neq \Delta$, as illustrated in Figure 8.4d(iii). These zero-energy states are only found when both QDs are off-resonance and none of them are localized Majorana states, extending over both QDs and exhibiting no gate stability. Measurements under these conditions are shown in Figure 8.9, where zero-energy states can be found in a variety of gate settings (panels a, c therein).

8.5 Conclusion

In summary, we realize a minimal Kitaev chain where two QDs in an InSb nanowire are separated by a hybrid semiconducting-superconducting segment. Compared to past works, our approach solves three challenges: strong hybridization of QDs via CAR, simultaneous coupling of two single spins via both ECT and CAR, and continuous tuning of the coupling amplitudes. This is made possible by the two QDs as well as the middle Andreev bound state mediating their couplings all being discrete, gate-tunable quantum states. The result is the creation of a new type of nonlocal states that host Majorana-type excitations at a fine-tuned sweet spot. The zero-bias peaks at this spot are robust against variations of the chemical potential of one QD and quadratically protected against simultaneous perturbations of both. This discrete and tunable way of assembling Kitaev chains shows good agreement between theory and experiment by avoiding the most concerning problems affecting the continuous nanowire experiments: disorder, smooth gate potentials and multi-subband occupation [31]. The QD-S-QD platform discussed here opens up a new frontier to the study of Majorana physics. In the long term, this approach can generate topologically protected Majorana states in longer chains [2]. A shorter term approach is to use PMMs as an immediate playground to study fundamental non-Abelian statistics, e.g., by fusing neighboring PMMs in a device with two such copies.

8.6 Methods

8.6.1 Device fabrication

The nanowire hybrid devices presented in this work were fabricated on pre-patterned substrates, using the shadow-wall lithography technique described in Refs. [32, 33]. Nanowires were deposited onto the substrates using an optical micro-manipulator setup. 8 nm of Al was grown at a mix of 15° and 45° angles with respect to the substrate. Subsequently, Device A was coated with 2 Å of Pt grown at 30°. No Pt was deposited for Device B. Finally, all devices were capped with 20 nm of evaporated AlO_x. Details of the substrate fabrication, the surface treatment of the nanowires, the growth conditions of the superconductor, the thickness calibration of the Pt coating and the ex-situ fabrication of

the ohmic contacts can be found in Ref. [34]. Devices A and B also slightly differ in the length of the hybrid segment: 180 nm for A and 150 nm for B.

8.6.2 Transport measurement and data processing

We have fabricated and measured six devices with similar geometry. Two of them showed strong hybridization of the QD states by means of CAR and ECT. We report on the detailed measurements of Device A in the main text and show qualitatively similar measurements from Device B in Figure 8.11 and Figure 8.12. All measurements on Device A were done in a dilution refrigerator with base temperature 7 mK at the cold plate and electron temperature of 40~50 mK at the sample, measured in a similiar setup using an NIS metallic tunnel junction. Unless otherwise mentioned, the measurements on Device A were conducted in the presence of a magnetic field of 200 mT approximately oriented along the nanowire axis with a 3° offset. Device B was measured similarly in another dilution refrigerator under B = 100 mT along the nanowire with 4° offset.

Figure 8.1e shows a schematic depiction of the electrical setup used to measure the devices. The middle segment of the InSb nanowire is covered by a thin Al shell, kept grounded throughout the experiment. On each side of the hybrid segment, we connect the normal leads to a current-to-voltage converter. The amplifiers on the left and right sides of the device are each biased through a digital-to-analog converter that applies DC and AC biases. The total series resistance of the voltage source and the current meter is less than 100 Ω for Device A and 1.11 kΩ for Device B. Voltage outputs of the current meter are read by digital multimeters and lock-in amplifiers. When DC voltage V_L is applied, V_R is kept grounded and vice versa. AC excitations are applied on each side of the device with different frequencies (17 Hz on the left and 29 Hz on the right for Device A, 19 Hz on the left and 29 Hz on the right for Device B) and with amplitudes between 2 and 6 μV RMS. In this manner, we measure the DC currents I_L, I_R and the conductance matrix G in response to applied voltages V_L, V_R on the left and right N leads, respectively. The conductance matrix is corrected for voltage divider effects (see Ref. [35] for details) taking into account the series resistance of sources and meters and in each fridge line (1.85 kΩ for Device A and 2.5 kΩ for Device B), except for the right panel of Figure 8.1h and Figure 8.2d. There, the left half of the conductance matrix was not measured and correction is not possible. We verify that the series resistance is much smaller than device resistance and the voltage divider effect is never more than ~ 10% of the signal.

8.6.3 Characterization of QDs and the hybrid segment

To form the QDs described in the main text, we pinch off the finger gates next to the three ohmic leads, forming two tunnel barriers in each N-S junction. V_{LD} and V_{RD} applied on the middle finger gates on each side accumulate electrons in the QDs. We refer to the associated data repository for the raw gate voltage values used in each measurement. See Figure 8.5a-f for results of the dot characterizations.

Characterization of the spectrum in the hybrid segment is done using conventional tunnel spectroscopy. In each uncovered InSb segment, we open up the two finger gates next to the N lead and only lower the gate next to the hybrid to define a tunnel barrier. The results of

the tunnel spectroscopy are shown in Figure 8.5g,h and the raw gate voltages are available in the data repository.

8.6.4 Determination of QD spin polarization

Control of the spin orientation of QD levels is done via selecting from the even vs odd charge degeneracy points following the method detailed in Ref. [36]. At the charge transition between occupancy $2n$ and $2n+1$ (n being an integer), the electron added to or removed from the QD is polarized to spin-down ($\downarrow$, lower in energy). The next level available for occupation, at the transition between $2n+1$ and $2n+2$ electrons, has the opposite polarization of spin-up ($\uparrow$, higher in energy). To ensure the spin polarization is complete, the experiment was conducted with $E_Z \approx 400\,\mu\text{eV} > |eV_L|, |eV_R|$ (see Figure 8.5 for determination of the spin configuration). In the experiment data, a change in the QD spin orientation is visible as a change in the range of V_{LD} or V_{RD}.

8.6.5 Controlling ECT and CAR via electric gating

Ref. [24] describes a theory of mediating CAR and ECT transitions between QDs via virtual hopping through an intermediate Andreev bound state. Ref. [26] experimentally verifies the applicability of this theory to our device. To summarize the findings here, we consider two QDs both tunnel-coupled to a central Andreev bound state in the hybrid segment of the device. The QDs have excitation energies lower than that of the Andreev bound state and thus transition between them is second-order. The wavefunction of an Andreev bound state consists of a superposition of an electron part, u, and a hole part, v. Both theory and experiment conclude that the values of t and Δ depend strongly and differently on u, v. Specifically, CAR involves converting an incoming electron to an outgoing hole and thus depends on the values of u and v jointly as $|uv|^2$. ECT, however, occurs over two parallel channels (electron-to-electron and hole-to-hole) and its coupling strength depends on u, v independently as $|u^2 - v^2|^2$. As the composition of u, v is a function of the chemical potential of the middle Andreev bound state, the CAR to ECT ratio is strongly tunable by V_{PG}. We thus look for a range of V_{PG} where Andreev bound states reside in the hybrid segment, making sure that the energies of these states are high enough so as not to hybridize with the QDs directly (Figure 8.5). Next, we sweep V_{PG} to find the crossover point between t and Δ as described in the main text.

8.6.6 Additional details on the measurement of the coupled QD spectrum

The measurement of the local and nonlocal conductance shown in Figure 8.2g was conducted in a series of steps. First, the value of V_{PG} was set, and a charge stability diagram was measured as a function of V_{LD} and V_{RD}. Representative examples of such diagrams are shown in Figure 8.7. Second, each charge stability diagram was inspected and the joint charge degeneracy point ($\mu_{LD} = \mu_{RD} = 0$) was selected manually (V^0_{LD}, V^0_{RD}). Lastly, the values of V_{LD} and V_{RD} were set to those of the joint degeneracy point and the local and nonlocal conductance were measured as a function of V_R.

The continuous transition from $t > \Delta$ to $t < \Delta$ is visible in Figure 8.2g via both local and nonlocal conductance. G_{RR} shows that level repulsion splits the zero-energy resonance

peaks both when $t > \Delta$ (lower values of V_{PG}) and when $t < \Delta$ (higher values of V_{PG}). The zero-bias peak is restored in the vicinity of $t = \Delta$, in agreement with theoretical predictions [3]. The crossover is also apparent in the sign of G_{LR}, which changes from negative ($t > \Delta$) to positive ($t < \Delta$).

To better visualize the transition between the ECT- and CAR-dominated regimes, we extract V_{PP}, the separation between the conductance peaks under positive and negative bias voltages, and plot them as a function of V_{PG} in Figure 8.2h. When tuning V_{PG}, the peak spacing decreases until the two peaks merge at $V_{PG} \approx 210\,\mathrm{mV}$. Further increase of V_{PG} leads to increasing V_{PP}. In addition, to observe the change in sign of the nonlocal conductance, we follow $\langle G_{LR} \rangle$, the value of G_{LR} averaged over the bias voltage V_R between −100 and 100 μV at a given V_{PG}. We see that $\langle G_{LR} \rangle$ turns from negative to positive at $V_{PG} \approx 210\,\mathrm{mV}$, in correspondence to a change in the dominant coupling mechanism.

Figure 8.3c-e presents measurements where the conductance was measured against applied biases along some paths within the charge stability diagram (panel a). Prior to each of these measurements, a charge stability diagram was measured and inspected, based on which the relevant path in the (V_{LD}, V_{RD}) plane was chosen. Following each bias spectroscopy measurement, another charge stability diagram was measured and compared to the one taken before to check for potential gate instability. In case of noticeable gate drifts between the two, the measurement was discarded and the process was repeated. The values of μ_{LD} and μ_{RD} required for theoretical curves appearing in panel b were calculated by $\mu_i = \alpha_i(V_i - V_i^0)$ where $i = \mathrm{LD}, \mathrm{RD}$ and α_i is the lever arm of the corresponding QD. The discrepancy between the spectra measured with G_{LL} and G_{RR} likely results from gate instability, since they were not measured simultaneously. Finite remaining G_{LR} in panel c and G_{RL} in panel d most likely result from small deviations of μ_{LD}, μ_{RD} from zero during these measurements.

8.6.7 Model of the phase diagrams in Figure 8.1f

To calculate the ground state phase diagram in Figure 8.1f, we write the Hamiltonian in the many-body picture, with the four basis states being $|00\rangle, |11\rangle, |10\rangle, |01\rangle$:

$$H_{\mathrm{mb}} = \begin{pmatrix} 0 & \Delta & 0 & 0 \\ \Delta & \varepsilon_L + \varepsilon_R & 0 & 0 \\ 0 & 0 & \varepsilon_L & t \\ 0 & 0 & t & \varepsilon_R \end{pmatrix} \tag{8.2}$$

in block-diagonalized form. The two 2 × 2 matrices yield the energy eigenvalues separately for the even and odd subspaces:

$$E_{o,\pm} = \frac{\varepsilon_L + \varepsilon_R}{2} \pm \sqrt{\left(\frac{\varepsilon_L - \varepsilon_R}{2}\right)^2 + t^2} \tag{8.3}$$

$$E_{e,\pm} = \frac{\varepsilon_L + \varepsilon_R}{2} \pm \sqrt{\left(\frac{\varepsilon_L + \varepsilon_R}{2}\right)^2 + \Delta^2} \tag{8.4}$$

The ground state phase transition occurs at the boundary $E_{o,-} = E_{e,-}$. This is equivalent to

$$\varepsilon_L \varepsilon_R = t^2 - \Delta^2 \tag{8.5}$$

8.6.8 Transport model in Figure 8.3 and Figure 8.4

We describe in this section the model Hamiltonian of the minimal Kitaev chain and the method we use for calculating the differential conductance matrices when the Kitaev chain is tunnel-coupled to two external N leads.

The effective Bogoliubov-de-Gennes Hamiltonian of the double-QD system is

$$H = \varepsilon_L c_L^\dagger c_L + \varepsilon_R c_R^\dagger c_R + t c_L^\dagger c_R + t c_R^\dagger c_L + \Delta c_L c_R + \Delta c_R^\dagger c_L^\dagger \quad = \frac{1}{2}\Psi^\dagger \begin{pmatrix} \varepsilon_L & t & 0 & -\Delta \\ t & \varepsilon_R & \Delta & 0 \\ 0 & \Delta & -\varepsilon_L & -t \\ -\Delta & 0 & -t & -\varepsilon_R \end{pmatrix} \Psi, \tag{8.6}$$

where $\Psi = (c_L, c_R, c_L^\dagger, c_R^\dagger)^\top$ is the Nambu spinor, $\varepsilon_{L/R}$ is the level energy in dot-L/R relative to the superconducting Fermi surface, t and Δ are the ECT and CAR amplitudes. Here we assume t and Δ to be real without loss of generality [3]. The presence of both t and Δ in this Hamiltonian implies breaking spin conservation during QD-QD tunneling via either spin-orbit coupling (as done in the present experiment) or non-collinear magnetization between the two QDs (as proposed in [3]). Without one of them, equal-spin QDs cannot recombine into a Cooper pair, leading to vanishing Δ, while opposite-spin QDs cannot support finite t. The exact values of t and Δ depend on the spin-orbit coupling strength and we refer to Ref. [24] for a detailed discussion.

To calculate the differential conductance for the double-QD system, we use the S-matrix method [37]. In the wide-band limit, the S matrix is

$$S(\omega) = \begin{pmatrix} s_{ee} & s_{eh} \\ s_{he} & s_{hh} \end{pmatrix} = 1 - iW^\dagger \left(\omega - H + \frac{1}{2} i W W^\dagger\right)^{-1} W, \tag{8.7}$$

where $W = \mathrm{diag}\{\sqrt{\Gamma_L}, \sqrt{\Gamma_R}, -\sqrt{\Gamma_L}, -\sqrt{\Gamma_R}\}$ is the tunnel matrix, with Γ_α being the tunnel coupling strength between dot-α and lead-α. The zero-temperature differential conductance is given by

$$G^0_{\alpha\beta}(\omega) = \mathrm{d}I_\alpha/\mathrm{d}V_\beta = \frac{e^2}{h}\left(\delta_{\alpha\beta} - |s_{ee}^{\alpha\beta}(\omega)|^2 + |s_{he}^{\alpha\beta}(\omega)|^2\right), \tag{8.8}$$

where $\alpha, \beta = L/R$. Finite-temperature effect is included by a convolution between the zero-temperature conductance and the derivative of Fermi-Dirac distribution, i.e.,

$$G^T(\omega) = \int dE \frac{G^0(E)}{4k_B T \cosh^2[(E-\omega)/2k_B T]}. \tag{8.9}$$

The theoretical model presented above uses five input parameters to calculate the conductance matrix under given $\mu_{\mathrm{LD}}, \mu_{\mathrm{RD}}, V_{\mathrm{L}}, V_{\mathrm{R}}$. The input parameters are: $t, \Delta, \Gamma_L, \Gamma_R, T$.

To choose the parameters in Figure 8.3b(i), we fix the temperature to the measured value $T = 45\,\mathrm{mK}$ and make the simplification $t = \Delta$, $\Gamma \equiv \Gamma_L = \Gamma_R$. This results in only two free parameters t, Γ, which we manually choose and compare with data. While oversimplified, this approach allows us to obtain a reasonable match between theory and data taken at $\mu_{\mathrm{LD}} = \mu_{\mathrm{RD}} = 0$ without the risk of overfitting. To obtain the other numerical curves shown in Figure 8.3, we keep the same choice of t, Γ and vary $\mu_{\mathrm{LD}}, \mu_{\mathrm{RD}}, V_{\mathrm{L}}, V_{\mathrm{R}}$ along various paths in the parameter space. Similarly, to model the data shown in Figure 8.9, we keep $T = 45\,\mathrm{mK}$ and Γ the same as in Figure 8.3. The free parameters to be chosen are thus t and Δ. The theory panels are obtained with the same t, Δ, and only $\mu_{\mathrm{LD}}, \mu_{\mathrm{RD}}, V_{\mathrm{L}}, V_{\mathrm{R}}$ are varied in accordance with the experimental conditions.

Finally, we comment on the physical meaning of the theory predictions in Figure 8.4a-c. Tuning μ_{RD} leads to symmetric G_{LL} and asymmetric G_{RR}, as well as zero G_{LR} and finite G_{RL} with an alternating pattern of positive and negative values. As discussed in the main text, these features, also seen in the measurements, stem from the local charge of the system: keeping $\mu_{\mathrm{LD}} = 0$ maintains zero local charge on the left dot, while varying μ_{RD} creates finite local charge on the right dot. The complementary picture appears when varying μ_{LD} in panel b. The asymmetry in both G_{LL} and G_{RR} and the negative nonlocal conductance when tuning simultaneously $\mu_{\mathrm{LD}} = \mu_{\mathrm{RD}}$ are also captured in the numerical simulation in panel c. We note that while there is a qualitative agreement between the features in Figure 8.4c and Figure 8.3e, they were obtained under nominally different conditions. As mentioned, the theoretical curve follows $\mu_{\mathrm{LD}} = \mu_{\mathrm{RD}}$, while the experimental curve was taken through a path along which V_{LD} changed twice as much as V_{RD}, although the lever arms of both QDs are similar. In Figure 8.4c, we calculate the conductance along a path reproducing the experimental conditions. We speculate that the discrepancy between Figure 8.3e and Figure 8.4c could arise from some hybridization between the left QD and the superconducting segment as seen in Figure 8.5.

Data Availability and Code Availability

Raw data presented in this work, the data processing/plotting code and code used for the theory calculations are available at `https://doi.org/10.5281/zenodo.6594169`.

8.7 Extended data

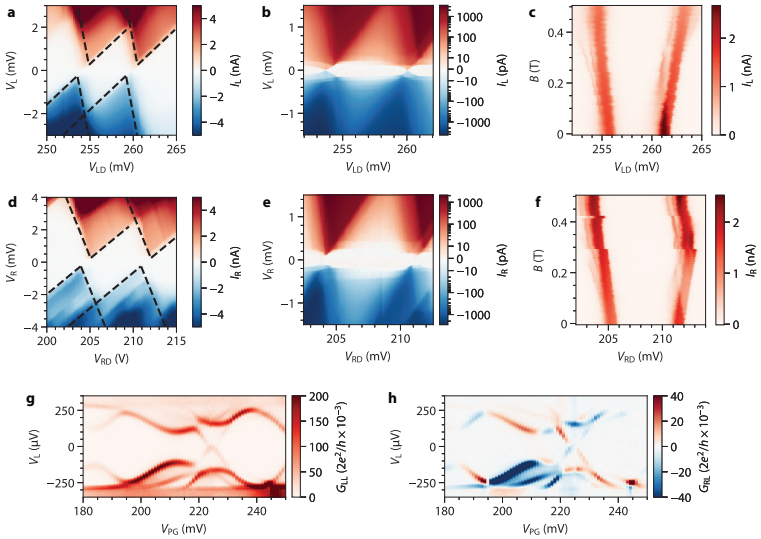

Figure 8.5: **Characterization of the QDs. a.** Coulomb blockade diamonds of the left QD when right QD is off resonance. I_L is measured as a function of V_L, V_{LD}. The data is overlaid with a constant interaction model [38] with 1.8 meV charging energy and gate lever arm of 0.32. **b.** A high-resolution scan of **a** with a symmetric-logarithmic color scale to show the presence of a small amount of Andreev current at sub-gap energies. This is due to the left QD being weakly proximitized by local Andreev coupling to Al. **c.** Field dependence of the Coulomb resonances. I_L is measured as a function of V_{LD} and B with a constant $V_L = 600\,\mu V$. The resonances of opposite spin polarization evolve in opposite directions with a g-factor of ~ 35, translating to Zeeman energy of 400 μeV at $B = 200$ mT. **d-f.** Characterization of the right QD, as described in the captions of panels a-c. Overlaid model in **d** has charging energy 2.3 meV and gate lever arm of 0.33. No sub-gap transport is detectable in **e**. B dispersion in **f** corresponds to $g = 40$. **g, h.** Bias spectroscopy results of the proximitized InSb segment under the thin Al/Pt film. I_L, I_R are measured as a function of V_L, V_{PG}. G_{LL}, G_{RL} are obtained by taking the numerical derivative of I_L, I_R along the bias direction after applying a Savitzky-Golay filter of window length 15 and order 1. The sub-gap spectrum reveals discrete, gate-dispersing Andreev bound states. The presence of nonlocal conductance correlated with the sub-gap states shows that these Andreev bound states extend throughout the entire hybrid segment, coupling to both left and right N leads [30]. Parts of this dataset are also presented in Ref. [34]

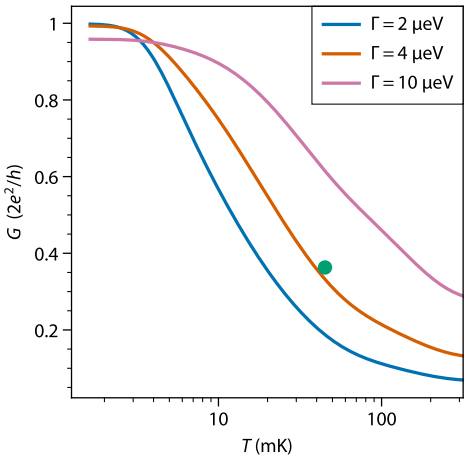

Figure 8.6: **Theoretical temperature dependence of the height of Majorana zero-bias conductance peaks.** The height of the Majorana zero-bias peaks is only quantized to $2e^2/h$ at zero temperature. At finite electron temperature T, the peak height is generally lower, with the exact value depending on T and tunnel broadening Γ_L, Γ_R due to coupling between QDs and N leads. The local zero-bias conductance G_{LL} at the sweet spot ($t = \Delta, \mu_{LD} = \mu_{RD} = 0$) is calculated and shown in this plot as a function of T, using the parameters presented in Figure 8.3: $t = \Delta = 12\,\mu eV$. Three curves are calculated assuming three different values of tunnel coupling $\Gamma = \Gamma_L = \Gamma_R$. The orange curve assumes a Γ value that matches the experimentally observed peak width (both of the zero-bias peaks and of generic QD resonant peaks at other conductance features), showing that conductance approaching quantization would only be realized at electron temperatures < 5 mK, unattainable in our dilution refrigerator. The blue curve, calculated with lower $\Gamma = 2\,\mu eV$, shows even lower conductance. Increasing Γ would not lead to conductance quantization either, since the zero-bias peaks would merge with the conductance peaks arising from the excited states (pink curve). The green dot marks the experimentally measured electron temperature and peak height (averaged between the values obtained on the left and right leads).

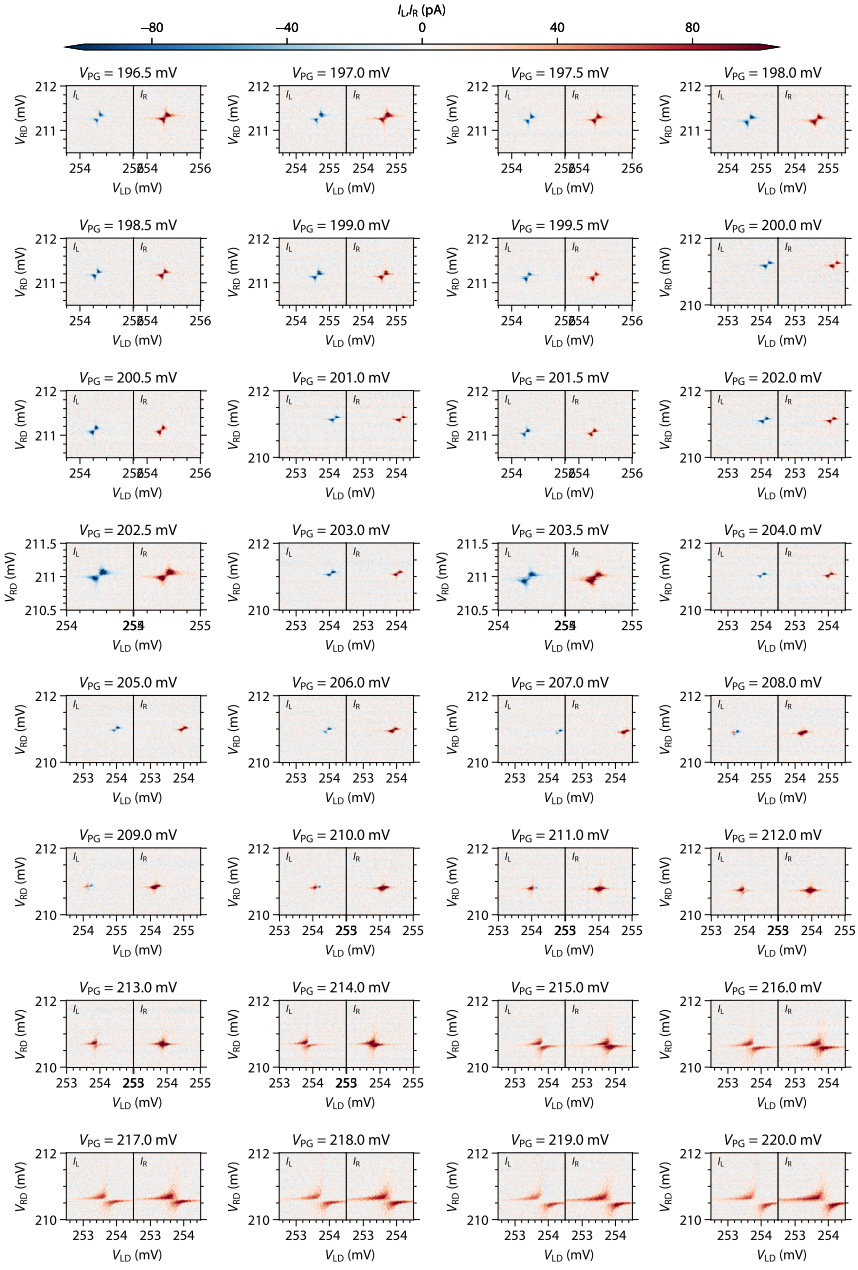

Figure 8.7: **Evolution of the charge stability diagram for the ↓↑ spin configuration.** Each panel shows I_L (nonlocal) and I_R (local) as functions of V_{LD}, V_{RD} measured under fixed biases $V_L = 0, V_R = 10\,\mu V$. V_{PG} is tuned from 196.5 mV, showing signatures of the $t > \Delta$ in both local and nonlocal currents, to 220 mV, featuring the opposite $t < \Delta$ regime.

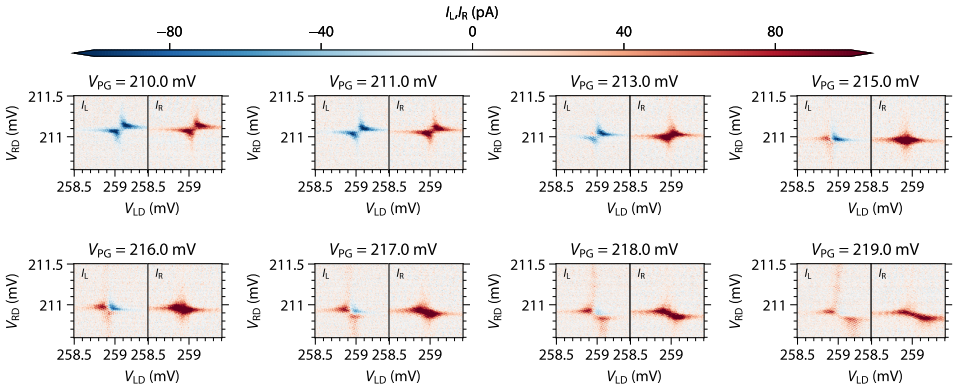

Figure 8.8: **Evolution of the charge stability diagram for the ↑↑ spin configuration.** Each panel shows I_L (nonlocal) and I_R (local) as functions of V_{LD}, V_{RD} measured under fixed biases $V_L = 0, V_R = 10\,\mu V$. V_{PG} is tuned from 210 mV, showing signatures of the $t > \Delta$ in both local and nonlocal currents, to 219 mV, featuring the opposite $t < \Delta$ regime.

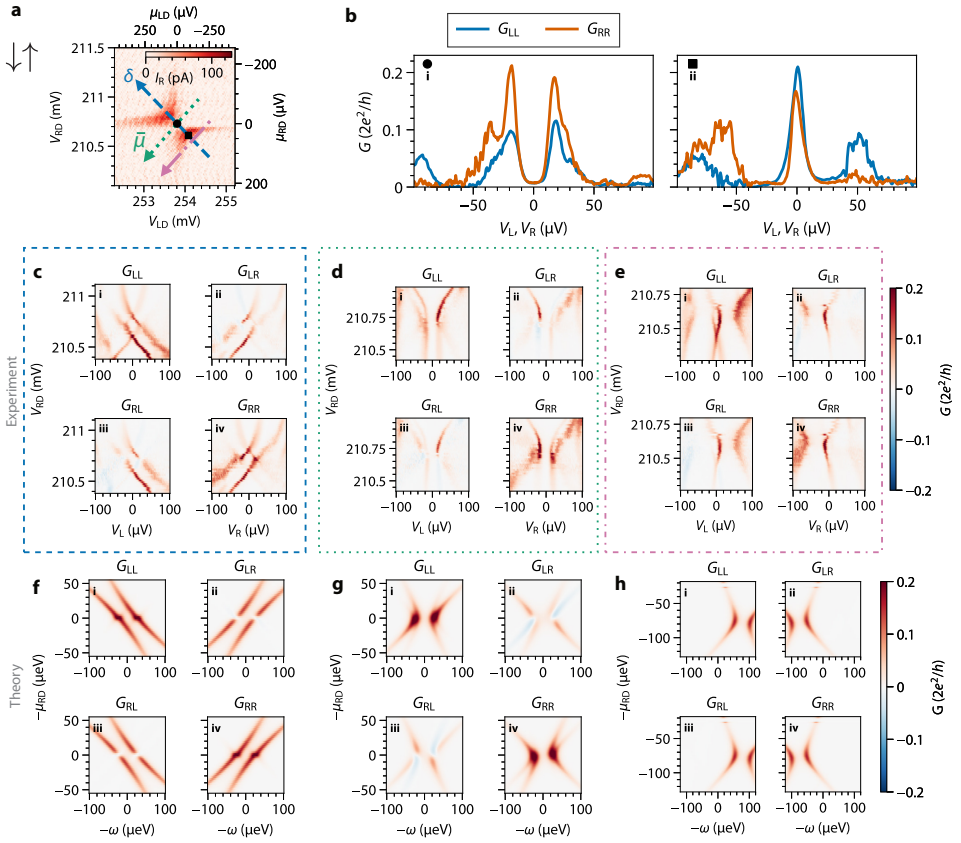

Figure 8.9: **Conductance spectroscopy when $t < \Delta$.** **a.** I_R vs μ_{LD}, μ_{RD} with $V_R = 10\,\mu V$. The evolution of the spectrum with the chemical potential is taken along the dashed, dashed-dotted and dotted lines in panels b,c,d respectively. Data taken at the $\downarrow\uparrow$ spin configuration with fixed $V_{PG} = 218\,mV$. **b.** Local conductance spectroscopy taken at gate setpoints marked by corresponding symbols in panel a. Insets mark schematically the spectrum of the QDs in the absence (brown dots) and the presence (grey lines) of hybridization via CAR and ECT. **c.** Conductance matrix as a function of bias and V_{LD}, taken along the dashed blue line in panel a, i.e., varying the detuning between the QDs $\delta = (\mu_{LD} - \mu_{RD})/2$ while keeping the average chemical potential $\bar{\mu} = (\mu_{LD} + \mu_{RD})/2$ close to 0. **d.** Conductance matrix as a function of bias and V_{LD}, taken along the dotted green line in panel a, keeping the detuning between the QDs around 0. **e.** Conductance matrix as a function of bias and V_{LD}, taken along the dashed-dotted pink line in panel a, keeping roughly constant non-zero detuning between the QDs. **f, g, h.** Numerically calculated G as a function of energy ω and μ_{LD}, μ_{RD} along the paths shown in panel a. All of the numerical curves assume the same parameters as those in Figure 8.3, except with $\Delta = 23\,\mu eV$ and $t = 6\,\mu eV$.

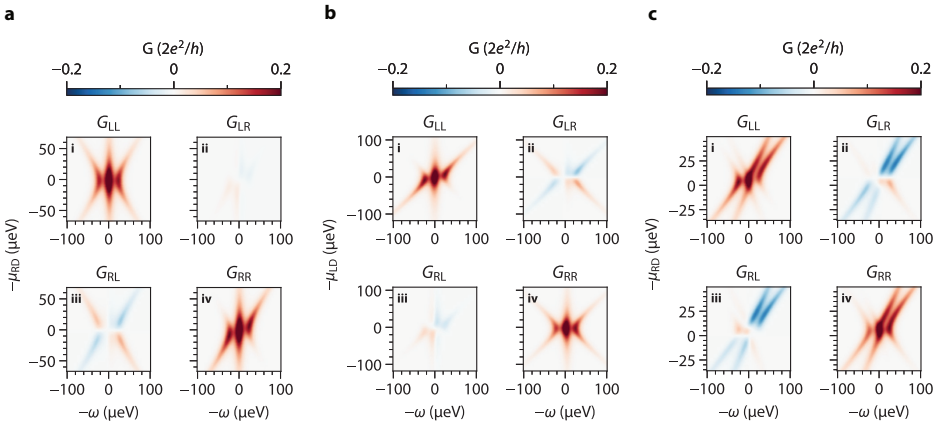

Figure 8.10: **Calculated conductance matrices at the $t = \Delta$ sweet spot** **a.** Numerically calculated G as a function of energy ω and μ_{LD}, μ_{RD} along the path shown in Fig 3c. The presence of finite G_{LR} and asymmetric G_{RL} result from a slight deviation from the $\mu_{LD} = 0$ condition which is depicted in Figure 8.4a. These features appear in the experimental data shown in Figure 8.3c. **b.** Numerically calculated G as a function of energy ω and μ_{LD}, μ_{RD} along the path shown in Fig 3d. The presence of finite G_{RL} and asymmetric G_{LR} result from a slight deviation from the $\mu_{RD} = 0$ condition which is depicted in Figure 8.4b. These features appear in the experimental data shown in Figure 8.3d. **c.** Numerically calculated G as a function of energy ω and μ_{LD}, μ_{RD} along the path shown in Fig 3e. Since the path does not obey $\mu_{LD} = \mu_{RD}$, the calculated spectral lines do not follow parallel trajectories, in slight disagreement with the experimental data. The conversion from V_{LD}, V_{RD} to μ_{LD}, μ_{RD} is done as explained in the Methods section with the measured lever-arms of both QDs.

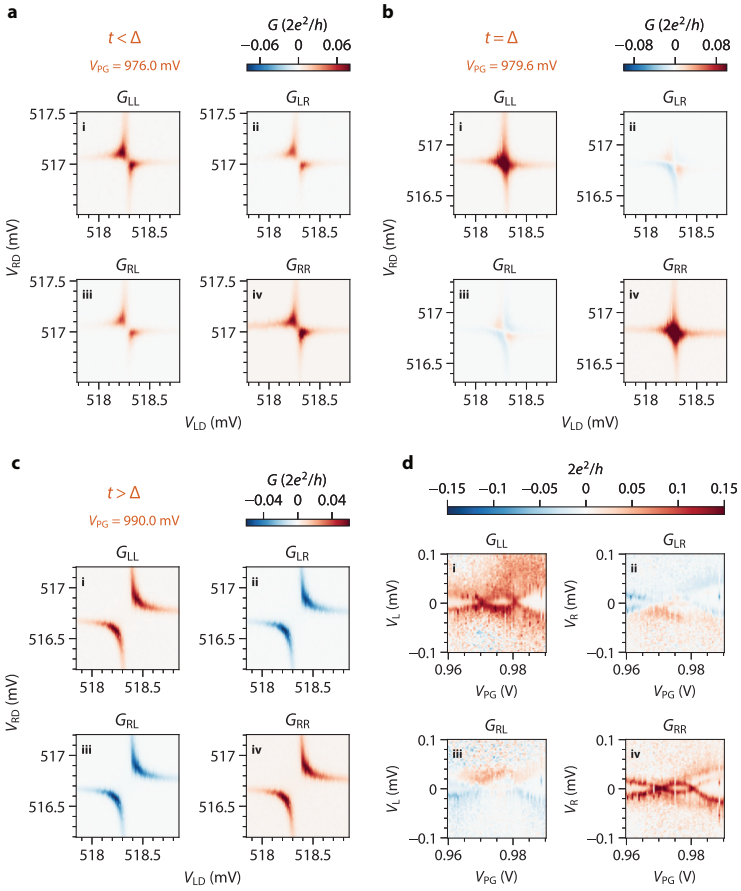

Figure 8.11: **Reproduction of the main results with Device B. a-c.** Conductance matrices measured at $V_{PG} = (976, 979.6, 990)$ mV, respectively. **d.** Conductance matrix as a function of V_L, V_R and V_{PG} while keeping $\mu_{LD} \approx \mu_{RD} \approx 0$. This device shows two continuous crossovers from $t > \Delta$ to $t < \Delta$ and again to $t > \Delta$.

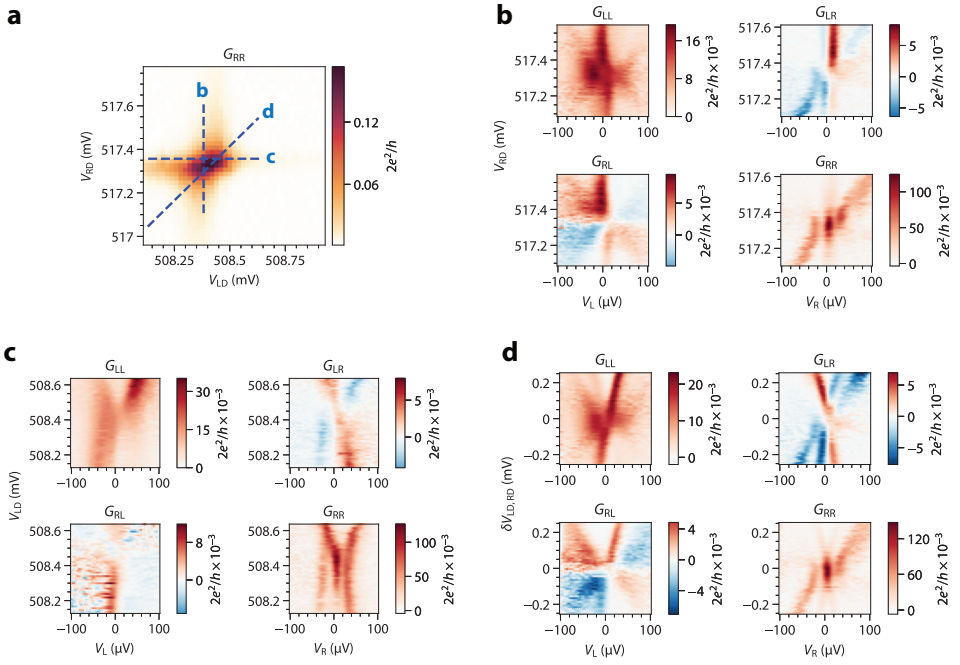

Figure 8.12: **Device B spectrum vs gates. a.** Charge stability diagram measured via G_{RR} of another $t = \Delta$ sweet spot of Device B, at $V_{PG} = 993$ mV. Dashed lines mark the gate voltage paths the corresponding panels are taken along. **b-d.** Conductance matrices when varying V_{RD} (b), V_{LD} (c) and the two gates simultaneously (d), similar to Figure 8.3 in the main text. The sticking zero-bias conductance peak feature when only one QD potential is varied around the sweet spot is clearly reproduced in G_{RR} of panel b. The quadratic peak splitting profile when both QD potentials are varied by the same amount is also reproduced the panel d. The left N contact of this device was broken and a distant lead belonging to another device on the same nanowire was used instead. This and gate jumps in V_{RD} complicate interpretation of other panels.

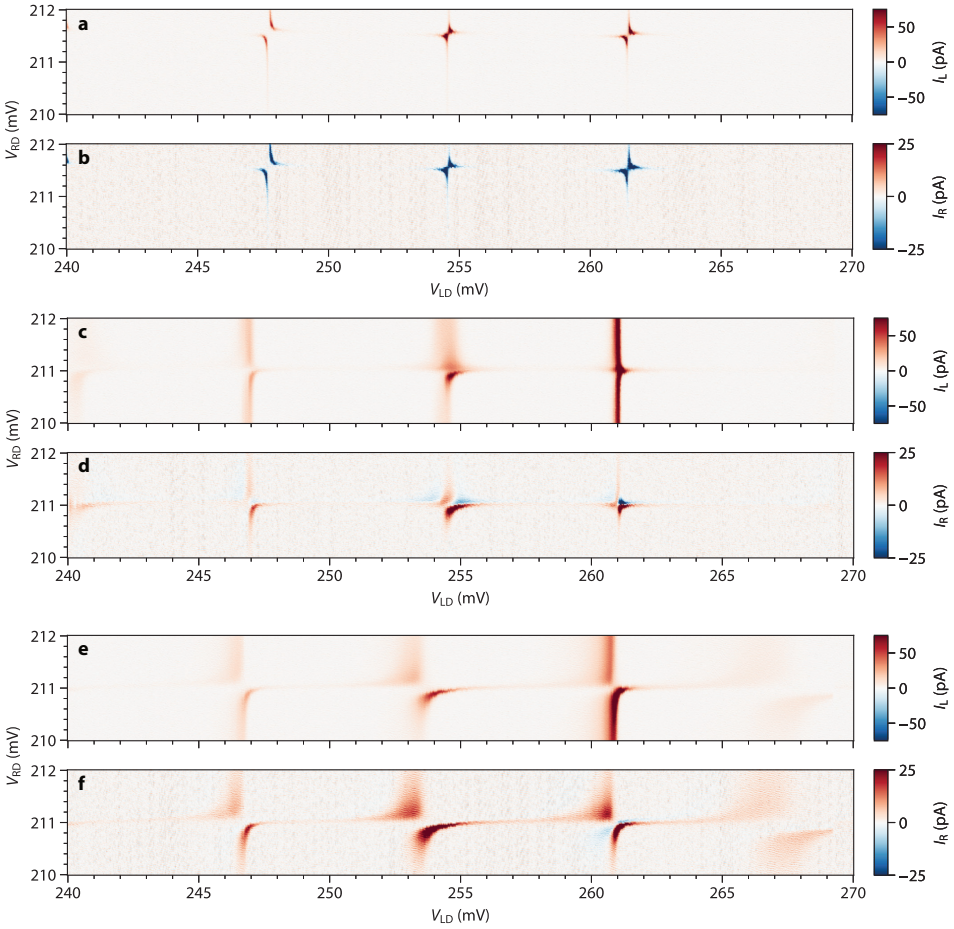

Figure 8.13: **CAR- and ECT-induced interactions across multiple QD resonances. a-b.** local (I_L) and nonlocal (I_R) currents as a function of V_{LD} and V_{RD} measured with V_{PG} = 200 mV and fixed V_L. All resonances show an ECT-dominated structure and a negative correlation between the local and the nonlocal currents. **c-d.** local (I_L) and nonlocal (I_R) currents as a function of V_{LD} and V_{RD} measured with V_{PG} = 218 mV and fixed V_L. Some resonances show the structure associated with the $t = \Delta$ sweet spot, showing both positive and negative correlations between the local and nonlocal currents. **e-f.** local (I_L) and nonlocal (I_R) currents as a function of V_{LD} and V_{RD} measured with V_{PG} = 200 mV and fixed V_L. All orbitals show a CAR-dominated structure and a positive correlation between the local and the nonlocal currents. All measurements were conducted with V_L = 10 µV, V_R = 0 and B = 100 mT.

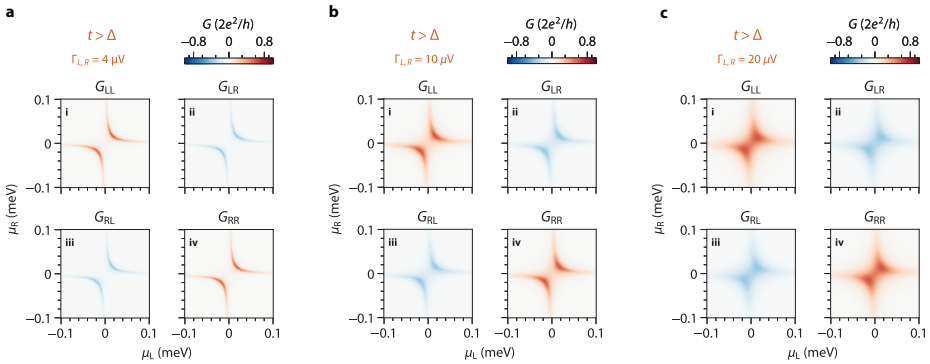

Figure 8.14: **Theoretical effect of tunnel broadening on the charge stability diagrams.** In some charge stability diagrams where level-repulsion is weak, e.g., Figure 8.2a and Figure 8.8, some residual conductance is visible even when $\mu_{LD} = \mu_{RD} = 0$. This creates the visual feature of the two conductance curves appearing to "touch" each other at the center. In the main text, we argued this is due to level broadening. Here, we plot the numerically simulated charge stability diagrams at zero temperature under various dot-lead tunnel coupling strengths. We use coupling strengths $t = 20\,\mu\text{V}, \Delta = 10\,\mu\text{V}$ as an example. From panel a to c, increasing the tunnel coupling and thereby level broadening reproduces this observed feature. When the level broadening is comparable to the excitation energy, $|t - \Delta|$, finite conductance can take place at zero bias. This feature is absent in, e.g., Figure 8.2c, where $|t - \Delta|$ is greater than the level broadening.

References

[1] A. Y. Kitaev, *Unpaired Majorana fermions in quantum wires,* Physics-Uspekhi **44**, 131 (2001), cond-mat/0010440 .

[2] J. D. Sau and S. D. Sarma, *Realizing a robust practical Majorana chain in a quantum-dot-superconductor linear array,* Nature Communications **3**, 964 (2012), 1111.6600 .

[3] M. Leijnse and K. Flensberg, *Parity qubits and poor man's Majorana bound states in double quantum dots,* Physical Review B **86**, 134528 (2012), 1207.4299 .

[4] P. Recher, E. V. Sukhorukov, and D. Loss, *Andreev tunneling, Coulomb blockade, and resonant transport of nonlocal spin-entangled electrons,* Physical Review B **63**, 165314 (2001), cond-mat/0009452 .

[5] L. Hofstetter, S. Csonka, J. Nygård, and Schönenberger, C, *Cooper pair splitter realized in a two-quantum-dot Y-junction,* **461**, 10.1038/nature08432.

[6] L. G. Herrmann, F. Portier, P. Roche, A. L. Yeyati, T. Kontos, and C. Strunk, *Carbon nanotubes as Cooper-pair beam splitters,* **104**, 026801, publisher: American Physical Society.

[7] A. Das, Y. Ronen, M. Heiblum, D. Mahalu, A. V. Kretinin, and H. Shtrikman, *High-efficiency Cooper pair splitting demonstrated by two-particle conductance resonance and positive noise cross-correlation,* **3**, 1165, publisher: Nature Publishing Group.

[8] J. Schindele, A. Baumgartner, and C. Schönenberger, *Near-unity Cooper pair splitting efficiency,* **109**, 157002.

[9] C. Nayak, S. H. Simon, A. Stern, M. Freedman, and S. D. Sarma, *Non-Abelian anyons and topological quantum computation,* Reviews of Modern Physics **80**, 1083 (2008), 0707.1889 .

[10] A. Kitaev, *Fault-tolerant quantum computation by anyons,* Annals of Physics **303**, 2 (2003), quant-ph/9707021 .

[11] V. Mourik, K. Zuo, S. M. Frolov, S. R. Plissard, E. P. A. M. Bakkers, and L. P. Kouwenhoven, *Signatures of Majorana fermions in hybrid superconductor-semiconductor nanowire devices,* Science **336**, 1003 (2012), 1204.2792 .

[12] M. T. Deng, S. Vaitiekėnas, E. B. Hansen, J. Danon, M. Leijnse, K. Flensberg, J. Nygård, P. Krogstrup, and C. M. Marcus, *Majorana bound state in a coupled quantum-dot hybrid-nanowire system,* Science **354**, 1557 (2016).

[13] A. Fornieri, A. M. Whiticar, F. Setiawan, E. Portolés, A. C. C. Drachmann, A. Keselman, S. Gronin, C. Thomas, T. Wang, R. Kallaher, G. C. Gardner, E. Berg, M. J. Manfra, A. Stern, C. M. Marcus, and F. Nichele, *Evidence of topological superconductivity in planar Josephson junctions,* Nature **569**, 89 (2019).

[14] H. Ren, F. Pientka, S. Hart, A. T. Pierce, M. Kosowsky, L. Lunczer, R. Schlereth, B. Scharf, E. M. Hankiewicz, L. W. Molenkamp, *et al.*, *Topological superconductivity in a phase-controlled Josephson junction,* Nature **569**, 93 (2019).

[15] S. Vaitiekėnas, G. W. Winkler, B. van Heck, T. Karzig, M.-T. Deng, K. Flensberg, L. I. Glazman, C. Nayak, P. Krogstrup, R. M. Lutchyn, and C. M. Marcus, *Flux-induced topological superconductivity in full-shell nanowires,* Science **367** (2020), 10.1126/science.aav3392.

[16] G. Kells, D. Meidan, and P. W. Brouwer, *Near-zero-energy end states in topologically trivial spin-orbit coupled superconducting nanowires with a smooth confinement,* Physical Review B **86** (2012), 10.1103/physrevb.86.100503.

[17] E. Prada, P. San-Jose, and R. Aguado, *Transport spectroscopy of NS nanowire junctions with Majorana fermions,* Physical Review B - Condensed Matter and Materials Physics **86**, 1 (2012).

[18] D. I. Pikulin, J. P. Dahlhaus, M. Wimmer, H. Schomerus, and C. W. J. Beenakker, *A zero-voltage conductance peak from weak antilocalization in a Majorana nanowire,* New Journal of Physics **14**, 125011 (2012).

[19] C.-X. Liu, J. D. Sau, T. D. Stanescu, and S. D. Sarma, *Andreev bound states versus Majorana bound states in quantum dot-nanowire-superconductor hybrid structures: Trivial versus topological zero-bias conductance peaks,* Physical Review B **96** (2017), 10.1103/physrevb.96.075161.

[20] A. Vuik, B. Nijholt, A. Akhmerov, and M. Wimmer, *Reproducing topological properties with quasi-Majorana states,* SciPost Physics **7**, 061 (2019), 1806.02801 .

[21] H. Pan and S. D. Sarma, *Physical mechanisms for zero-bias conductance peaks in Majorana nanowires,* Physical Review Research **2**, 013377 (2020), 1910.11413 .

[22] W. G. v. d. Wiel, S. D. Franceschi, J. M. Elzerman, T. Fujisawa, S. Tarucha, and L. P. Kouwenhoven, *Electron transport through double quantum dots,* Reviews of Modern Physics **75**, 1 (2003), cond-mat/0205350 .

[23] M.-S. Choi, C. Bruder, and D. Loss, *Spin-dependent Josephson current through double quantum dots and measurement of entangled electron states,* Physical Review B **62**, 13569 (2000).

[24] C. X. Liu, G. Wang, T. Dvir, and M. Wimmer, *Tunable superconducting coupling of quantum dots via Andreev bound states,* arXiv (2022), 2203.00107 .

[25] G. Wang, T. Dvir, G. P. Mazur, C.-X. Liu, N. van Loo, S. L. D. ten Haaf, A. Bordin, S. Gazibegovic, G. Badawy, E. P. A. M. Bakkers, M. Wimmer, and L. P. Kouwenhoven, *Singlet and triplet Cooper pair splitting in hybrid superconducting nanowires,* Nature , 1 (2022).

[26] A. Bordin, G. Wang, C.-X. Liu, S. L. ten Haaf, G. P. Mazur, N. van Loo, D. Xu, D. van Driel, F. Zatelli, S. Gazibegovic, *et al.*, *Controlled crossed andreev reflection and elastic co-tunneling mediated by andreev bound states,* arXiv (2022), 2212.02274 .

[27] D. Beckmann and H. v. Löhneysen, *Experimental evidence for crossed Andreev reflection,* in *AIP Conference Proceedings*, Vol. 850 (American Institute of Physics, 2006) pp. 875–876.

[28] J. Gramich, A. Baumgartner, and C. Schönenberger, *Andreev bound states probed in three-terminal quantum dots,* Physical Review B **96** (2017), 10.1103/physrevb.96.195418.

[29] J. Danon, A. B. Hellenes, E. B. Hansen, L. Casparis, A. P. Higginbotham, and K. Flensberg, *Nonlocal conductance spectroscopy of Andreev bound states: Symmetry relations and BCS charges,* Physical Review Letters **124**, 036801 (2020), 1905.05438 .

[30] G. C. Ménard, G. L. R. Anselmetti, E. A. Martinez, D. Puglia, F. K. Malinowski, J. S. Lee, S. Choi, M. Pendharkar, C. J. Palmstrøm, K. Flensberg, C. M. Marcus, L. Casparis, and A. P. Higginbotham, *Conductance-matrix symmetries of a three-terminal hybrid device,* Physical Review Letters **124**, 036802 (2020), 1905.05505 .

[31] H. Pan and S. D. Sarma, *Disorder effects on Majorana zero modes: Kitaev chain versus semiconductor nanowire,* Physical Review B **103**, 224505 (2021), 2012.12904 .

[32] S. Heedt, M. Quintero-Pérez, F. Borsoi, A. Fursina, N. van Loo, G. P. Mazur, M. P. Nowak, M. Ammerlaan, K. Li, S. Korneychuk, *et al.*, *Shadow-wall lithography of ballistic superconductor–semiconductor quantum devices,* Nat. Commun. **12**, 1 (2021).

[33] F. Borsoi, G. P. Mazur, N. van Loo, M. P. Nowak, L. Bourdet, K. Li, S. Korneychuk, A. Fursina, J.-Y. Wang, V. Levajac, E. Memisevic, G. Badawy, S. Gazibegovic, K. van Hoogdalem, E. P. A. M. Bakkers, L. P. Kouwenhoven, S. Heedt, and M. Quintero-Pérez, *Single-shot fabrication of semiconducting–superconducting nanowire devices,* Adv. Func. Mater. , 2102388 (2021).

[34] G. P. Mazur, N. van Loo, J.-Y. Wang, T. Dvir, G. Wang, A. Khindanov, S. Korneychuk, F. Borsoi, R. C. Dekker, G. Badawy, *et al.*, *Spin-mixing enhanced proximity effect in aluminum-based superconductor–semiconductor hybrids,* Advanced Materials **34**, 2202034 (2022).

[35] E. A. Martinez, . A. Pöschl, E. B. Hansen, M. A. Y. Van De Poll, S. Vaitiekenas, A. P. Higginbotham, and L. Casparis, *Measurement circuit effects in three-terminal electrical transport measurements,* arXiv 2104.02671 (2021), 10.48550/arXiv.2104.02671.

[36] R. Hanson, L. P. Kouwenhoven, J. R. Petta, S. Tarucha, and L. M. K. Vandersypen, *Spins in few-electron quantum dots,* Reviews of Modern Physics **79**, 1217 (2007), cond-mat/0610433 .

[37] S. Datta, *Quantum transport: atom to transistor* (Cambridge University Press, 2005).

[38] L. P. Kouwenhoven, D. G. Austing, and S. Tarucha, *Few-electron quantum dots,* Rep. Prog. Phys. **64**, 701 (2001).

9

The gate-tunable Josephson diode

Superconducting diodes are a recently-discovered quantum analogueue of classical diodes. The superconducting diode effect relies on the breaking of both time-reversal and inversion symmetry. As a result, the critical current of a superconductor can become dependent on the direction of the applied current. The combination of these ingredients naturally occurs in proximitized semiconductors under a magnetic field, which is also predicted to give rise to exotic physics such as topological superconductivity. In this work, we use InSb nanowires proximitized by Al to investigate the superconducting diode effect. Through shadow-wall lithography, we create short Josephson junctions with gate control of both the semiconducting weak link as well as the proximitized leads. When the magnetic field is applied perpendicular to the nanowire axis, the superconducting diode effect depends on the out-of-plane angle. In particular, it is strongest along a specific angle, which we interpret as the direction of the spin-orbit field in the proximitized leads. Moreover, the electrostatic gates can be used to drastically alter this effect and even completely suppress it. Finally, we also observe a significant gate-tunable diode effect when the magnetic field is applied parallel to the nanowire axis. Due to the considerable degree of control via electrostatic gating, the semiconductor-superconductor hybrid Josephson diode emerges as a promising element for innovative superconducting circuits and computation devices.

This chapter appears on arXiv as *The gate-tunable Josephson diode*, G.P. Mazur[†], **N. van Loo**[†], D. van Driel, J.-Y. Wang, G. Badawy, S. Gazibegovic, E.P.A.M. Bakkers and L.P. Kouwenhoven - arXiv:2211.14283 (2022).
[†] These authors contributed equally to this work.

9.1 Introduction

Semiconducting diodes are rectifiers that allow current to flow in only one direction. As such, they are ubiquitously used in conventional electronics. Recently, superconducting analogueues of diodes have been realized in V/Nb/Ta superlattices, where the value of critical current depends on the polarity of the applied current [1]. Consequently, it has been named the superconducting diode effect (SDE). The simultaneous breaking of both inversion symmetry and time-reversal symmetry has been identified as the critical ingredient for achieving the SDE [2, 3]. Time-reversal symmetry is conventionally broken either through the application of a magnetic field or by using magnetic materials [4]. Similarly, inversion symmetry is broken in systems with spin-orbit interaction (SOI), either through intrinsic structural asymmetry or via the application of electric fields. Interestingly, a correction to the critical current of superconducting films in the presence of an electric field was already proposed in the context of superconductors with an intrinsic polar axis [2]. It has the form of $\alpha(\mathbf{c} \times \mathbf{B}) \cdot \mathbf{J}$ where α is the Rashba spin-orbit constant, the unit vector $\mathbf{c}$ points along the electric field, $\mathbf{B}$ is an external magnetic field, and $\mathbf{J}$ is the supercurrent density. Such a correction can be obtained purely from the Ginzburg-Landau theory when both inversion symmetry and time-reversal symmetry are broken.

In order to give more insight into the microscopic mechanism behind non-reciprocal critical currents, models that go beyond the Ginzburg-Landau theory have been proposed [5, 6]. These models suggest that a finite Cooper pair momentum is the underlying physical mechanism. In this picture, the energy of left and right moving carriers develops a finite Doppler shift $\pm\ \mathbf{q}\mathbf{v}_\mathrm{F}$ due to the finite momentum $\mathbf{q}$ acquired by the Cooper pairs[6]. On the other hand, theoretical studies on Josephson Junctions (JJs) based on semiconducting nanowires predicted direction-dependent critical currents in the presence of SOI and time-reversal symmetry breaking [7, 8]. In this case, non-reciprocity of switching currents is caused by the interaction between multiple Andreev levels in the junction. In addition, the Meissner effect has been proposed [9] to give rise to non-reciprocal critical current. Finally, a small out-of-plane magnetic field also leads to an SDE in type-II elemental superconductors [10].

Most of the work to date has observed the SDE in metallic systems or van der Waals materials with a high electron density [11], which implies that such devices cannot be tuned electrostatically. In this context, proximitized semiconductors are a convenient platform on which various parameters can be tuned with electrostatic gates. This includes the transparency [12] and the number of active modes in the junction, as well as the density in the proximitized region [13]. Note that in proximitized semiconductors, superconducting correlations are carried by electron-hole pairs, as opposed to a Cooper pair condensate in regular metals. These pairs form Andreev bound states which can obtain a finite momentum due to the interplay between spin-orbit interaction and a Zeeman field [14–16]. The finite-momentum ABSs can be considered as the proximitized analogue of finite-momentum Cooper pairs. As a consequence, it is possible for an SDE to exist in a semiconductor in proximity to a regular superconductor, like Al. Indeed, recent works explored the SDE in weakly-proximitized InAs [17], either in the form of Josephson junctions [18, 19] or as a

metallic wire defined on the InAs stack [20]. Planar Josephson junctions based on InSb nanoflags are also reported to yield an SDE [21]. Most works do not report a strong effect of electrostatic gating on the SDE [18–21]. As such, superconducting diodes would have limited use as circuit elements of superconducting computation devices or quantum computers. Instead, a greater degree of control is desired [22, 23], similar to the electrical tunability of state-of-the-art quantum electronics based on semiconductors [24]. In this article, we demonstrate the presence and control of the SDE in semiconductor-superconductor hybrid Josephson junctions by means of electrostatic gating. Separate gate control of the electron density underneath the proximitized leads as well as in semiconducting weak link enables us to isolate their contribution to the observed SDE. Furthermore, we show that the efficiency of the SDE scales with the switching current in the JJ. In addition, we demonstrate that the SDE can also occur when a magnetic field is applied parallel to the nanowire axis and hence parallel to the current flow. Dual gating of the semiconducting weak link and the proximitized leads allows the InSb/Al JJ to act as a Josephson field-effect transistor as well as a superconducting diode. As such, it emerges as a promising platform for the development of superconducting circuits.

9.2 Methods

We study a Josephson junction made from an InSb nanowire coupled to an Al shell. Fig. 9.1A shows a schematic of such a device together with the measurement circuit. The InSb nanowire is placed on a HfO_2 dielectric, which separates the device from a set of local bottom gates. The device features two distinct gates: A voltage on the tunnel gate V_{TG} is used to control the semiconducting weak link, where it affects both the number of active modes as well as their transparency. On the other hand, a voltage on the super gates V_{SG} controls the electron density in the proximitized leads (that is, the InSb segments underneath the Al). In a recent work [13] we have shown that this gate can also be used to adjust the semiconductor-superconductor coupling, resulting in gate-tunable properties such as the induced gap and g-factor. A current-bias I is applied through the junction, and the resulting voltage drop V is measured. The sample is fabricated by means of our shadow-wall lithography technique[12, 25]. This fabrication method allows us to create semiconducting weak links as short as 50 nm [26] such that the device is expected to be in the short junction limit. Since the length of the semiconducting weak link is shorter than the coherence length, transport is dominated tunnel processes via Andreev bound states. In short junctions, transport is also sensitive to properties of the proximitized leads [27, 28]. Fig. 9.1B illustrates the cross-section of the hybrid together with the coordinate system used throughout this work.

To investigate the SDE, we apply a current bias to the sample and look for a difference in the detected critical current between the forward-bias and reverse-bias measurements. In Fig. 9.1C, we show an example I-V curve under conditions where an SDE should be observed (i.e. a finite magnetic field perpendicular to the nanowire axis). As I is swept from negative to positive (blue curve), the measured voltage first drops to zero at the retrapping current I_{rt}^{+}. At the positive switching event I^{+}, the measured voltage jumps again to a finite value. Similarly, the negative retrapping and switching events I_{rt}^{-} and I^{-} can be obtained by reversing the current bias polarity (red curve). In this case, a small

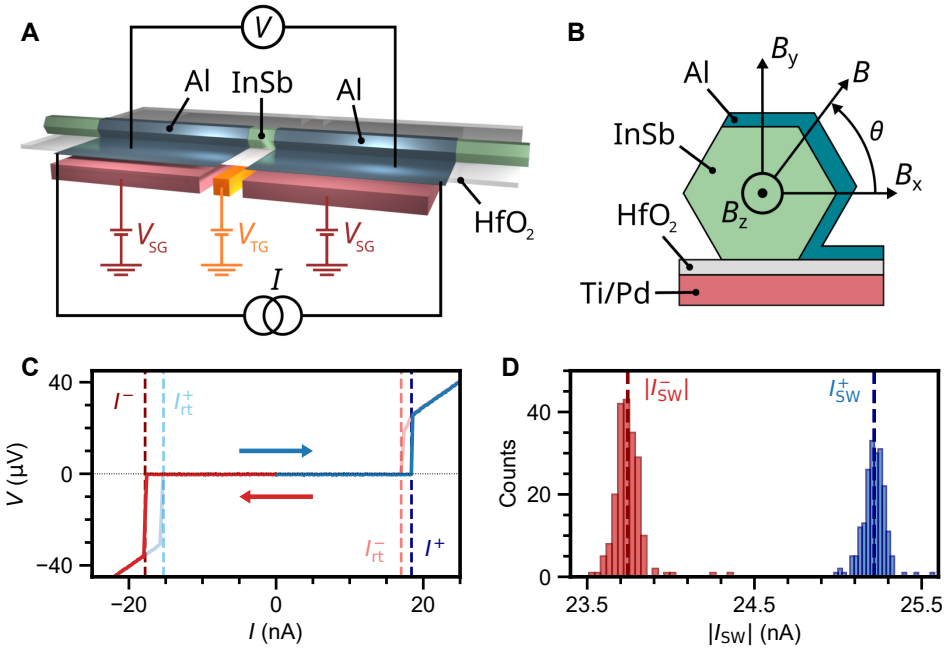

Figure 9.1: **Illustration of the device and measurement technique.** (**A**) Schematic of the measurement circuit, depicting a Josephson Junction in the current-bias configuration. The InSb nanowire (green) is covered by an Al shell (blue), which forms a connection to the film on the substrate. The electronic density underneath the shell is controlled via the super gates (red), and the junction transparency is tuned with the tunnel gate (orange). (**B**) Illustration of the hybrid cross-section. The magnetic field angle θ is defined as the angle in the plane perpendicular to the nanowire axis, starting at $\theta = 0^\circ$ when the applied magnetic field is along B_x. (**C**) Example of I-V curves showing non-reciprocal behavior. Blue and red curved display forward and reverse current bias, respectively. Positive and negative switching current (I^+,I^-) and retrapping current (I^+_{rt},I^-_{rt}) are marked with dashed lines. (**D**) Example of switching current histograms, each consisting of switching events (I^+,I^-) from 200 I-V curves. The average value of the distributions is labelled $|I^-_{SW}|$ and I^+_{SW} for the negative and positive switching currents, respectively.

difference between $I^+ = 18.4\,\text{nA}$ and $|I^-| = 17.7\,\text{nA}$ is observed, evidencing the SDE. As the switching current in Josephson junctions is stochastic [29, 30], we employ a fast-switching detection method [20, 31] in order to accurately resolve its value (see Section 1.3 of the supplemental information). An example of a switching current distribution obtained with this method is shown in Fig. 9.1D, where histograms for 200 switching events (I^+,I^-) are plotted. From these distributions, the average switching currents for the forward-bias I^+_{SW} and reverse-bias $|I^-_{SW}|$ are estimated. These values of the switching current are then used for calculating the SDE efficiency $\eta = (I^+_{SW} - |I^-_{SW}|)/(I^+_{SW} + |I^-_{SW}|)$.

9.3 Results

We start the investigation of the SDE in our system by rotating the magnetic field ($B = 12\,\text{mT}$) in the plane perpendicular to the nanowire axis, so that the direction of

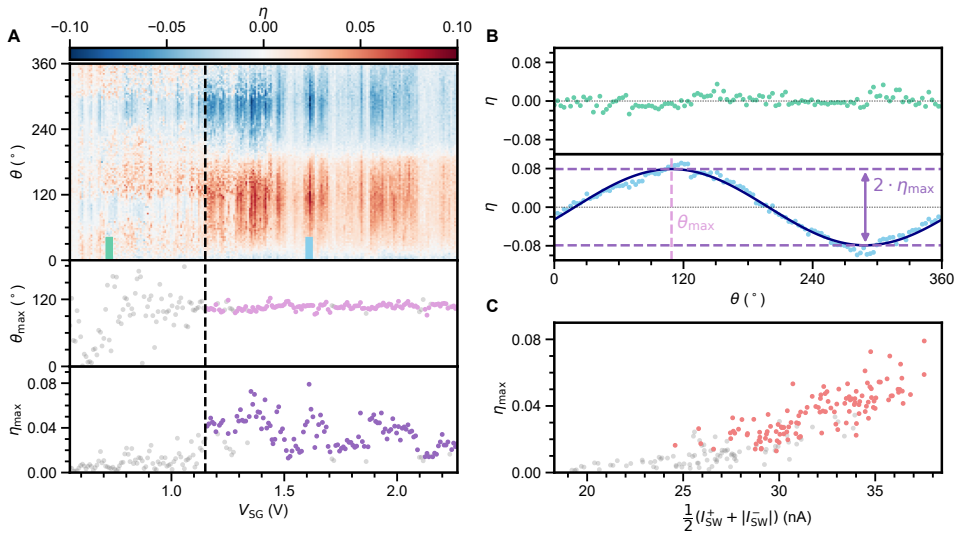

Figure 9.2: **Dependence of superconducting diode effect on super gate voltage.** (**A**) Top: η as a function of super gate voltage V_{SG} and θ, taken with $V_{TG} = 3.61\,V$ and $B = 12\,mT$. Middle: Estimation of θ_{max}. Bottom: η_{max} as a function of V_{SG}. The dashed black line indicates that the diode effect is suppressed below $V_{SG} < 1.15\,V$. (**B**) Top: lack of an SDE below $V_{SG} < 1.15\,V$. Bottom: presence of an SDE above $V_{SG} > 1.15\,V$. Linecuts taken from (**A**) top, at locations indicated by the colored bars. In the bottom panel, the dashed pink line specifies θ_{max}, whereas η_{max} is depicted by the dashed purple lines. (**C**) η_{max} as a function of average switching current, taken along $\theta = 105^{\circ}$. In all panels, grey data points correspond to a poor sinusoidal fit ($R^2 < 0.85$) of η as a function of θ.

the current remains perpendicular to the applied field. We set the tunnel gate voltage to a high $V_{TG} = 3.61\,V$, which ensures that the junction has around 5-10 active modes with a high transparency (see Fig. 9.18). Consequentially, this maximizes the switching current in the semiconducting weak link. The dependence of the diode efficiency on the magnetic field angle and super gate voltage is shown in Fig. 9.2A. In the top panel, we identify two distinct behaviors of the SDE. Above $V_{SG} > 1.15\,V$ we observe a finite diode efficiency which exhibits a sinusoidal dependence on the angle of the magnetic field. A line cut in this regime taken at $V_{SG} = 1.61\,V$ is shown in the bottom panel of Fig. 9.2B. A sinusoidal fit of $\eta(\theta)$ allows us to extract the angle with a maximum efficiency θ_{max} as well as the efficiency η_{max} at that angle (see supplemental information). From the fit for this particular line cut, we estimate $\theta_{max} = 105^{\circ}$ and $\eta_{max} = 0.08$. In contrast, the SDE is diminished and the field-angle dependence is almost absent for V_{SG} below $V_{SG} < 1.15\,V$. This is emphasized in the top panel of Fig. 9.2B, which shows a line cut taken at $V_{SG} = 0.72\,V$. We execute the fitting procedure for all values of V_{SG} in order to determine θ_{max} and η_{max} as we vary the gate voltage. These are presented in the middle and bottom panels of Fig. 9.2A, respectively. We see that the estimated θ_{max} angle remains roughly constant above $V_{SG} > 1.15\,V$ at $\theta_{max} \approx 105^{\circ}$. We interpret this angle to be the direction of the spin-orbit field in the proximitized leads $\theta_{max} = \theta_{SO}$, which we elaborate on in the discussion section. In contrast, η_{max} is modulated between ~ 1 % up to ~ 8 % and does not simply increase with V_{SG}. We note that in both panels, the grey data

points correspond to a poor sinusoidal fit of $\eta(\theta)$ with a R-squared value of $R^2 \leq 0.85$. We refer to Fig. 9.8 in the supplemental information for the underlying switching current maps and the estimation of the fitting error. As V_{SG} also modulates the magnitude of the switching current, we plot the maximum diode efficiency versus the average switching current in Fig. 9.2C. Interestingly, an increase in η_{max} appears to correlate to higher switching currents. This observation naturally raises the question whether the observed SDE can be attributed to the contribution from the proximitized leads of the device or to the increasing transparency of the junction due to capacitive coupling between the gates.

To answer this question, we note that the transparency of the junction can be adjusted directly through the use of the tunnel gate. We proceed by fixing the super gate voltage to $V_{SG} = 2\,V$, above the previously-identified threshold of $V_{SG} = 1.15\,V$. Next, the tunnel gate voltage V_{TG} is varied such that switching current is being modulated from $|I_{SW}| = 5\,nA$ up to $|I_{SW}| = 25\,nA$. We again vary the angle θ of the perpendicular magnetic field with an amplitude of $B = 12\,mT$, while measuring the diode efficiency. The results of this experiment are presented in the left panel of Fig. 9.3, where in panel A we show the evolution of the SDE. The effect is present for almost all gate values, while η is modulated with V_{TG}. Interestingly, the extracted θ_{max} remains constant as a function of the junction transparency around $\theta_{max} = 105^\circ$. In particular, η remains sinusoidal in θ (see, for

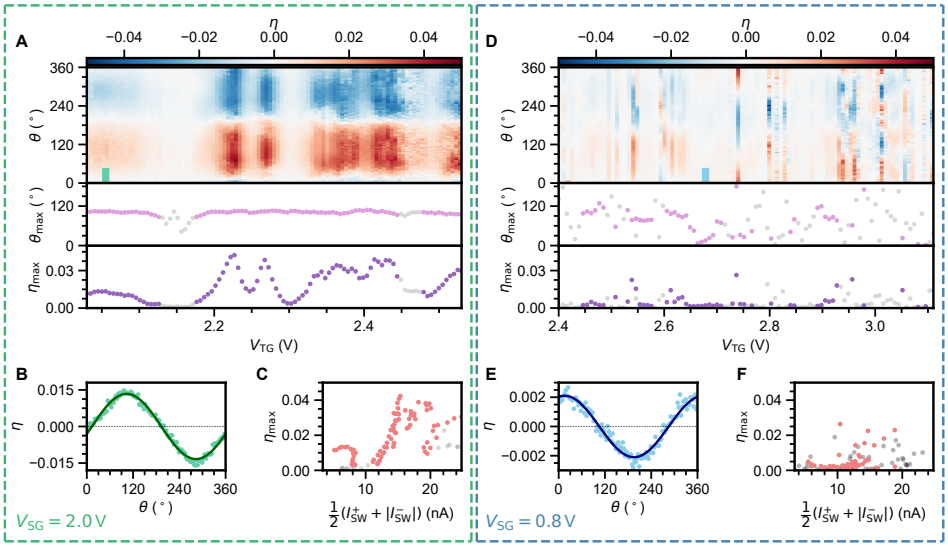

Figure 9.3: **Dependence of superconducting diode effect on tunnel gate voltage.** (**A-C**) Dependence on V_{TG} at a high super gate voltage $V_{SG} = 2.0\,V$. (**A**) Top: η as a function of V_{TG} and θ. Middle: Estimation of θ_{max}. Bottom: η_{max} as a function of V_{TG}. (**B**) Example of η taken at the location indicated by the colored bar in panel (**A**). (**C**) η_{max} as a function of average switching current, taken along $\theta = 105^\circ$. (**D-F**) Dependence on V_{TG} at a low super gate voltage $V_{SG} = 0.8\,V$. (**D**) Top: η as a function of V_{TG} and θ. Middle: Estimation of θ_{max}. Bottom: η_{max} as a function of V_{TG}. (**E**) Example of η taken at the location indicated by the colored bar in panel (**D**). (**F**) η_{max} as a function of average switching current, taken along $\theta = 105^\circ$. In all panels, grey data points correspond to a poor sinusoidal fit ($R^2 < 0.85$) of η as a function of θ. Data taken at $B = 12\,mT$.

example, Fig. 9.3B), and adjustments in V_{TG} only affect the amplitude. The scaling of η_{max} with I_{SW} is no longer monotonic, while the highest efficiency is still observed for high switching currents in the range of $|I_{SW}|$ = 15-20 nA (Fig. 9.3 C). Moreover, we are able to measure an appreciable SDE even at very low switching currents on the order of $|I_{SW}|$ = 5 nA. This confirms that the observed transition in Fig. 9.2 cannot be attributed to a reduced switching current as a result of, for example, capacitive coupling between the tunnel gate and the super gate. The situation is drastically different for V_{SG} = 0.8 V, which we present in the right panel of Fig. 9.3. Here, we adjust the tunnel gate voltage range such that it covers a similar range of switching currents, between $|I_{SW}|$ = 5 nA up to $|I_{SW}|$ = 25 nA. In Fig. 9.3D, we see that the efficiency of the SDE is generally weaker. It is often non-sinusoidal in θ and θ_{max} varies strongly with V_{TG}. An example is shown in Fig. 9.3E, where the angle with a maximum SDE is close to θ_{max} = 0°. The observed η_{max} is mainly below 1 %, even for the highest switching current values shown in Fig. 9.3F.

Next, we turn our attention to the dependence of the SDE on the magnitude of the

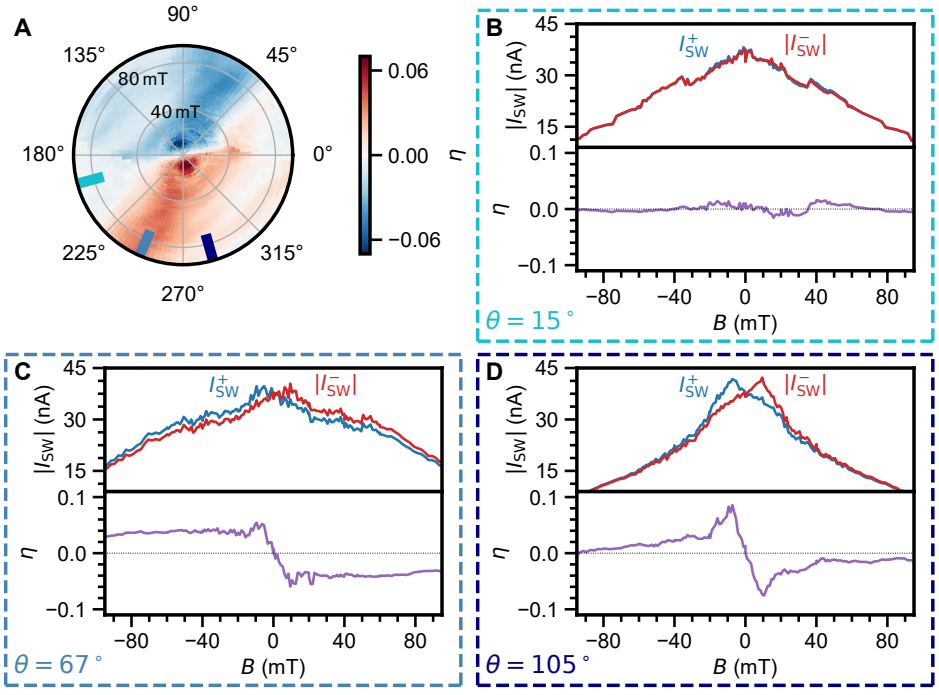

Figure 9.4: **Evolution of the superconducting diode effect as a function of magnetic field perpendicular to the nanowire axis.** (**A**) Polar plot of η as a function of θ (polar axis) and field magnitude B (radial axis), taken at V_{SG} = 2.21 V and V_{TG} = 3.60 V. (**B-D**) I_{SW}^{+}, $|I_{SW}^{-}|$ and η as a function of B taken at various angles. Perpendicular to the maximum-efficiency angle (θ = 15°, **B**), no SDE is observed. At θ = 67° (**C**), the SDE persists in a high magnetic field. Along the maximum-efficiency angle (θ = 105°, **D**), the SDE increases linearly around B = 0 T and reaches a maximum at B = 10 mT.

magnetic field. The results are shown in Fig. 9.4A, where the polar axis is the field angle θ and the radial axis represents the field magnitude B. Line cuts at various angles are shown in Fig. 9.4B-D. In the majority of the experiments to date, the efficiency of the diode does not simply increase linearly with magnetic field. Instead, the linear dependence only holds for low values of B, after which it peaks at a particular field value before it decays to zero as can be seen in Fig. 9.4D, where the field is applied along previously identified $\theta_{\text{max}} = 105^{\circ}$. In our device, we also find an unexpected deviation from that behavior when the magnetic field is applied along $\theta = 65^{\circ}$ (see Fig. 9.4C). Here, η increases linearly before saturating around $B = 10\,\text{mT}$ (see Fig. 9.16 for an extended magnetic field range). In addition, we note that the SDE is negligible whenever the magnetic field is applied perpendicular to θ_{max} at $\theta = 15^{\circ}$, as shown in Fig. 9.4B.

Lastly, we examine the impact of a parallel magnetic field on the SDE in our system. The results of this experiment are presented in Fig. 9.5. At zero magnetic field (top panel in Fig. 9.5B), the SDE is predominantly absent with occasional spikes at conductance resonances. Upon increasing B_z, the SDE becomes more pronounced and η exhibits multiple changes of sign as a function of V_{SG}, as shown in the bottom panel of Fig. 9.5B. Strikingly, our experimental data can once again be split into two different characteristic regimes. For the low super gate region below $V_{\text{SG}} < 1.15\,\text{V}$, the SDE exhibits frequent polarity flips as well as a high efficiency. At voltages above that threshold, the SDE is still present, however, in general with smaller intensity and with fewer polarity switches. This is best seen by comparing top and bottom panel of Fig. 9.5C. The top panel shows a line cut around $V_{\text{SG}} = 1.1\,\text{V}$, which exhibits a large η as well as a polarity switch. The bottom panel on the other hand presents a line cut along $V_{\text{SG}} = 1.3\,\text{V}$, where the SDE is strongly quenched.

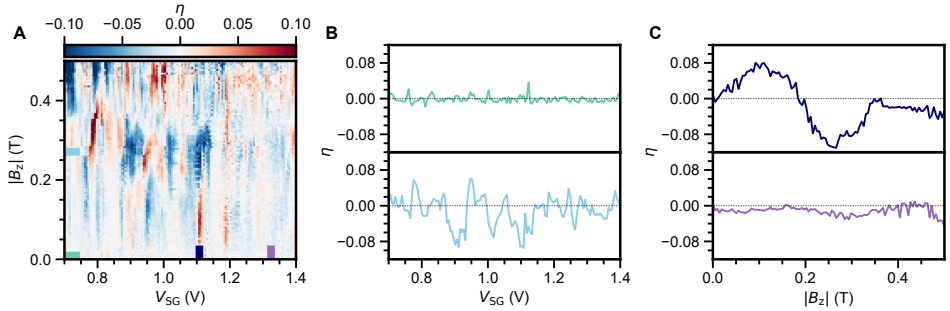

Figure 9.5: **Evolution of the superconducting diode effect as a function of magnetic field parallel to the nanowire axis.** (**A**) η as a function of V_{SG} and B_z. (**B**) Examples of η as a function of V_{SG} taken at locations indicated by the colored bars in panel (**A**). At finite field (bottom), the SDE frequently changes sign and the efficiency is strongly modulated by the tunnel gate voltage. (**C**) Examples of η as a function of B_z taken at locations indicated by the colored bars in panel (**A**). Depending on V_{SG}, the magnetic field can both enhance the diode efficiency and cause a sign inversion.

9.4 Discussion

One of the primary findings of our experimental work is a sinusoidal angle dependence of the SDE over a large range of positive V_{SG}. Such dependence can be interpreted by taking into account the role of spin-orbit interaction proposed in Edelstein's model for polar superconductors [2], which predicts a correction to the critical current in the form of $\alpha(\mathbf{c} \times \mathbf{B}) \cdot \mathbf{J}$. From this prediction we expect a diode efficiency of $\eta \propto \cos(\theta)$ that is accompanied by a maximum diode efficiency whenever the magnetic field aligns with the direction of the spin-orbit field. The spin-orbit interaction in our devices likely originates from the electric field applied on the super gates. As the Al film covers three facets of the hexagonal nanowire and extends onto the substrate (Fig. 9.1B), the electric field lines are expected to bend towards the metallic half-shell [33]. This agrees well with the observed maximum-efficiency angle of $\theta_{max} = 105^{\circ}$. On a second device (device B, see supplemental information), the extracted θ_{max} is similar at $\theta_{max} = 110^{\circ}$. This is also in agreement with previous results, which studied the dependence of spin-orbit interaction on the induced superconducting gap [33] for devices in the same geometry.

A related observation is the dependence of the SDE on the value of the super gate voltage V_{SG}. As depicted in Fig. 9.2A, we notice a sharp onset in the SDE efficiency η and the sinusoidal angular dependence. There is a striking similarity between this sharp onset of the SDE and the tunable semiconductor-superconductor coupling observed for InSb/Al hybrids [13]. The tunable coupling is reflected in a strong gate-tunability of the induced gap size as well as the g-factor. As the SOI is expected to be modulated by the coupling as well [34, 35], it may explain the difference between the low and high super gate regimes. We interpret our observations as follows. For high V_{SG} the system can be seen as S-S'-N-S'-S, where S is the Al shell, S' is the proximitized semiconductor, and N is the semiconducting weak link. In this regime, the hybrid inherits semiconducting properties such as a high g-factor and appreciable SOI. The presence of a finite SOI in addition to a Zeeman field results in a finite momentum of the ABSs that form in the proximitized leads [14–16]. In contrast, for low V_{SG} the hybrid can be seen as S-N-S where S represents the metallic (Al-like) leads with weak SOI. In the absence of SOI, the ABSs in the leads do not obtain a finite momentum - resulting in the suppression of the SDE. Still, the semiconducting weak link itself also possesses a strong SOI which can also lead to finite SDE. In this scenario, conductance resonances originating from confinement near the semiconducting weak link [36] yield a fluctuating spin-orbit direction [37]. Thus, we interpret the existence of erratic SDE in the low V_{SG} regime as originating from SOI in the semiconducting weak link.

It is worth to mention that recently, it was shown that the SDE can also arise in systems without SOI [9]. In this framework, screening currents present in the superconducting shell due to the Meissner effect lead to a spatially varying order parameter. This can equally well result in a formation of finite-momentum ABSs in proximitized material. In the case of our study, the maximum contribution from orbital effects in the Al shell is expected for a magnetic field direction perpendicular to the middle facet of the nanowire at $\theta = 30^{\circ}$ (see Fig. 9.1B). Yet, we observe a maximum η for a magnetic field angle $\theta_{max} = 105^{\circ}$, almost perpendicular to this direction. Moreover, η measured along $\theta = 15^{\circ}$

is close to zero in a magnetic field range of $\pm B = 100\,\mathrm{mT}$. Relating to those observations, we cannot identify the Meissner effect in the Al shell as the dominant mechanism explaining our results. Orbital effects might also have a direct effect on ABSs formed in the semiconductor, however it is presently unclear how this might influence the SDE.

The SDE dependence on the magnetic field magnitude (as shown in Fig. 9.4) is also pointing towards the presence of finite-momentum ABSs. In particular, the dependence of η on θ evolves from $\eta \propto \sin(\theta)$ to $\eta \propto \sin(\pi \cdot \sin(\theta))$ as the magnetic field amplitude is increased (see also supplemental information Fig. 9.12). The angular dependence of the diode efficiency measured as a function of the magnitude of the magnetic field looks nearly identical compared to the results reported for $NiTe_2$ [16]. There, this behavior was directly attributed to the presence of finite-momentum Cooper pairing. This observation suggests that the phenomenological theory of finite-momentum Cooper pairing can be universally applied to different material systems and may help to discriminate between various physical origins of the observed SDE. Proximitized InSb is particularly appealing in this context, as it has a fairly simple Fermi surface [38] and the proximity effect has been widely studied in this material [13, 39] which should lead to a simplification of theoretical studies.

Most of the models to date require the applied magnetic field to be parallel to the spin-orbit axis and perpendicular to the current flow [2, 6], with finite-momentum Cooper pairing as the microscopic origin. However, there are also several predictions regarding an SDE with the magnetic field applied parallel to the current flow. We will discuss applicability of those models to the experiment presented in Fig. 9.5. Short nanowire Josephson junctions with SOI in the presence of a Zeeman field were theoretically studied by Yokoyama et al. [7, 8]. When multiple conduction channels are formed within the semiconducting weak link, the Andreev levels interact and hybridize with each other due to interplay between disorder and SOI. Upon the application of an external magnetic field, they also become subject to a Zeeman splitting. As a result, time-reversal symmetry is broken and the energy of these levels is no longer equal with respect to sign inversion of the phase $E_N(-\varphi) \neq E_N(\varphi)$, where E_N is the energy of the Andreev levels and φ is a phase difference across the junction. This inequality also leads to an SDE. Similarly, a recent model [5] predicted that in the presence of a finite out-of-plane component, an in-plane Zeeman field is expected to drive subband transitions which should manifest as an enhancement of the SDE efficiency as well as inversion of the polarity. It is of particular interest for the study of topological superconductivity, as this information could be used to identify regions in parameter space where topological superconductivity is predicted to emerge.

We suspect that the SDE in a parallel magnetic field (as shown in Fig. 9.5) primarily originates from interaction between ABSs in the semiconducting weak link. To understand why, we note that the data can once again be divided into two sections. In contrast to the case of a perpendicular magnetic field, the SDE efficiency is the strongest at low V_{SG} while it remains strongly modulated with V_{TG} (see Fig. 9.21). In this regime, the electron density in the hybrid segments of the nanowire is expected to be low [13, 40, 41]. Conversely, we keep $V_{TG} = 3.615\,\mathrm{V}$ which ensures a high density in the InSb weak link. The

corresponding potential profile (e.g. a low V_{SG} in combination with a high V_{TG}) can result in additional confinement for the Andreev levels formed in the semiconducting weak link. A change in the confinement has been shown to change the magnitude and direction of the SOI [37], and also affects the scattering between different levels. Together, the interplay between these effects can modify the Andreev level spectrum in the weak link and, as a consequence, also affect the SDE. In particular, a phase shift $\varphi \approx \pi$ in the current-phase relation of the Andreev levels can generate a switch in the polarity of the SDE, as predicted by Yokoyama et al [8]. Such a phase shift can either originate from the changing confinement or Zeeman splitting of the Andreev levels in a magnetic field. On the other hand, Legg et al. [5] also predicted sign changes in the SDE polarity as the result of subband crossings in the hybrid. However, in this proposal a magnetic field component perpendicular to the nanowire axis is also required, which we do not apply in the current experiment. Thus, we cannot attribute our observations to subband physics. Furthermore, the addition of a small out-of-plane component does not significantly alter the picture (see supplemental information Fig. 9.19).

9.5 Conclusions

In conclusion, we have demonstrated the existence and gate-tunability of the Josephson diode effect in proximitized InSb nanowires. We have identified that it has a strong dependence both on the electronic density in the leads, as well as in the semiconducting weak link. For a high density in the leads, the angle for which diode efficiency is maximized is fixed. We interpret this angle as the direction of the spin-orbit field in the proximitized leads, which is in agreement with previous work on devices with similar geometry [33]. Likewise, the semiconducting weak link can give rise to the SDE, albeit with much weaker efficiency. There, the maximum angle is strongly modulated by the tunnel gate voltage, which we assign to a modification of the confinement potential. Our measurements at high magnetic fields point to finite-momentum Andreev bound states as a microscopic mechanism for the observed diode effect, in accordance with recent theoretical proposals and experiments [9, 16]. Finally, we show that the superconducting diode effect is also present when the field is applied parallel to the nanowire axis.

This work for the first time demonstrates the impact of the electronic density in the leads and semiconducting weak link on the SDE. As a consequence, gate-tunable superconducting diodes can be utilized as a building block of superconducting quantum devices. For example, proposals already exist which envision the use of these devices as on-chip gyrators and circulators [22]. Moreover, the gate-tunable switching current allows the InSb/Al JJ to act as a Josephson field-effect transistor - establishing it as a highly versatile and promising circuit element for superconducting electronics. In addition, this system can be readily used to create superconducting quantum interference devices (SQUIDs), in order to investigate the current-phase relation of a Josephson diode. In this case, one arm of the loop is tuned to the regime with a strong SDE and well defined maximum SDE angle, while the reference arm can be tuned to a trivial regime without any SDE. As theoretically proposed, gate-tunable junctions can also be embedded in many-loop interferometers to achieve unprecedentedly high efficiencies [42]. Further improvements to the circuits can be made through embedding quantum dots in the junction, which may allow for achieving

the SDE at zero magnetic field [43].

Data Availability and Code availability
Raw data presented in this work and the data processing/plotting codes are available at `https://doi.org/10.5281/zenodo.7351273`.

9.6 Supplemental information

9.6.1 Device fabrication

The InSb/Al hybrids presented in this work are fabricated on pre-patterned substrates, following the shadow-wall lithography technique described in [12, 25]. Specific details of the substrate fabrication, nanowire oxide removal and superconductor deposition can be found in the supplementary information of [13, 44].

9.6.2 Measurements setup

Samples are measured in a dilution refrigerator with a base temperature of ~ 20 mK, equipped with a three-axis vector magnet. We note that the switching current measured in a Josephson junction has a stochastic nature. As we are looking for quite small switching currents, a single I-V curve is not enough to systematically investigate the superconducting diode effect. Instead, we employ a setup which allows us to record a large number of switching events and look for the average of the obtained distributions. The circuit used for this is shown in Fig. 9.6A, together with a false-color scanning electron micrograph in Fig. 9.6B. We apply a current bias I with a triangular waveform and a frequency of 20 Hz. In Fig. 9.6C, we show a cartoon of a single period of this wave in the bottom panel, and the resulting voltage drop on the sample in the top panel. During the first half-period of the wave, the current is swept from negative to positive bias. The junction goes from a resistive state into the superconducting state, where the voltage drop $V = 0\,\mu$V. As the bias is increased, the junction switches again to the normal state which causes the voltage to jump to a finite value. Throughout the measurement, we employ a threshold voltage V_{th}^{+} (light blue line). The circuit detects the voltage drop on the sample surpassing the threshold voltage, and sends an optical trigger to the current meter at that time t^{+} (dotted dark blue line). The current meter records the current bias value I^{+} (dashed dark blue line). In the second half of the wave's period, the situation is reversed. The bias now sweeps from positive to negative, and at some point the junction switches from the superconducting state to normal state. At this time t^{-} the voltage drop on the sample drops below the negative threshold V_{th}^{-}, and the current meter records the current bias value I^{-}. For each data point (V_{SG},V_{TG},B,θ,B_{z}) presented in this work, 200 periods of the waveform are swept resulting in 200 recorded values of I^{+} and I^{-} each. In Fig. 9.7, four examples of resulting switching current distributions are shown for various values of the magnetic field. The reported switching current values I_{SW}^{+} and $|I_{\text{SW}}^{-}|$ in this work are calculated as the mean of each 200–datapoint distribution. We note that at low values of B, the switching current distributions are typically broader as evidenced by their standard deviation σ (Fig. 9.7A, bottom panel). We suspect this is the result of heating of the mixing chamber due to the presence of magnetic components in the sample puck.

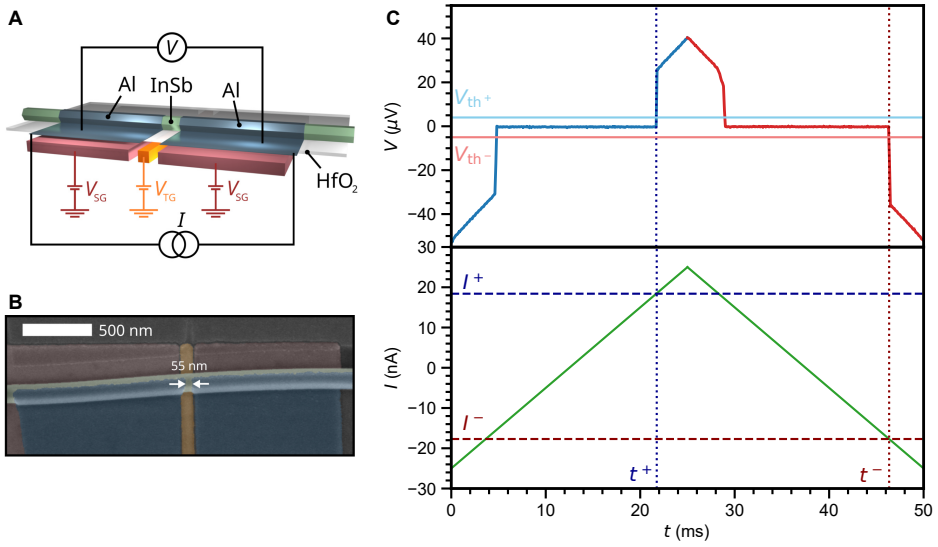

Figure 9.6: **Measurement circuit and technique.** (**A**) Electrical circuit used to measure switching current distributions. (**B**) False-color scanning electron micrograph of a Josephson junction which is lithographically identical to the measured devices. The junction is on the order of ~ 55 nm short, and the hybrid segments are on the order of ~ 1μm long. (**C**) Illustration of the acquirement of a single switching current event. Top: resulting voltage drop V on the junction. Bottom: applied triangular wave with a frequency of 20 Hz. On the up sweep, the circuits detects the surpassing of the threshold voltage V_{th}^{+} by the sample voltage. This sends an optical trigger to the current meter, which records the switching current event I^{+}. Similarly, I^{-} is recorded on the down sweep of the wave.

9.6.3 Data analysis

Whenever the magnetic field is applied in the plane perpendicular to the nanowire axis, the diode efficiency is modulated. The angle with a maximum SDE efficiency can be determined by fitting the diode efficiency $\eta(\theta)$;

$$\begin{aligned} \eta(\theta) &= a\sin(\theta + c) + d \\ \theta_{\text{max}} &= -c + 90^{\circ} \end{aligned} \tag{9.1}$$

Here the amplitude (a), phase (c) and offset (d) are free fitting parameters while the period of the sine is fixed to 360°. The fitting procedure is applied to various 2D maps of η versus θ and either V_{SG} or V_{TG}, notably in main text 9.2, main text 9.3, Fig. 9.14 and Fig. 9.23. In each figure, the typically-small offset is subtracted from the raw data. From the fits we also obtain the R^2 value, and set a threshold of $R^2 > 0.85$ for a good fit. In addition, we get the standard deviation of the three fitting parameters σ_{a}, σ_{c} and σ_{d}. Analysis and raw switching current maps of the four aforementioned figures is shown in Fig. 9.8, Fig. 9.9, Fig. 9.10, Fig. 9.15 and Fig. 9.24.

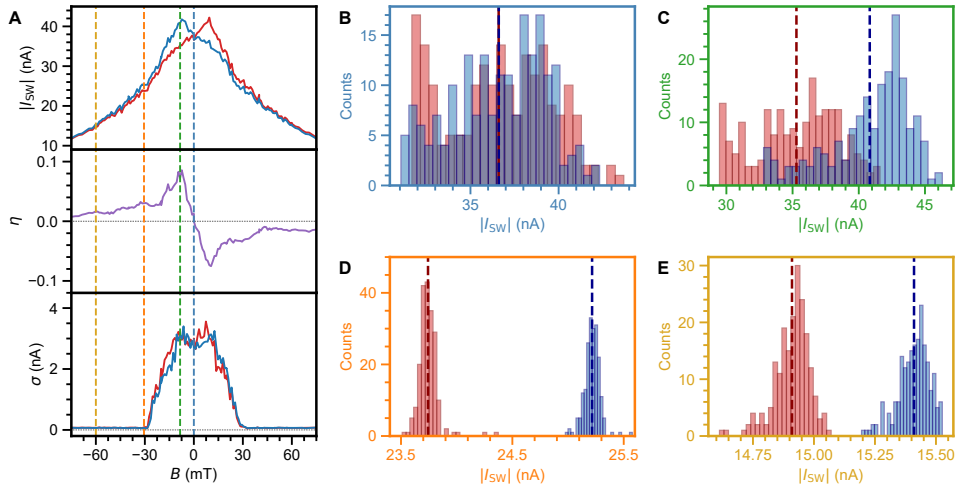

Figure 9.7: **Examples of switching current distributions at various magnetic field values.** (**A**) Top: Switching current I^{+}_{SW}, $|I^{-}_{SW}|$ as a function of magnetic field B, taken at $V_{SG} = 2.21\,V$, $V_{TG} = 3.60\,V$ and $\theta = 67^{\circ}$ (see also main text Fig. 9.4). Middle: SDE efficiency η as a function of B. Bottom: Standard deviation σ of the switching current distributions as a function of magnetic field. Below $|B| < 30\,mT$, the distributions have a larger spread. We presume this results from heating of the mixing chamber near $B = 0\,T$ due to the presence of magnetic components in the sample puck. (**B**) Switching current distributions at $B = 0\,T$. Despite the large spread of the distributions, the average switching current for both current bias polarities is the same. (**C**) At $B = 10\,mT$, I^{+}_{SW} and $|I^{-}_{SW}|$ differ significantly which results in a diode efficiency of almost $\eta = 0.1$. (**D**) At $B > 30\,mT$, heating effects are diminished which results in sharper distributions. Also displayed in main text 9.1. (**E**) At higher fields, the distributions remain sharp but move closer together as the SDE is diminished.

9.6.4 Additional data

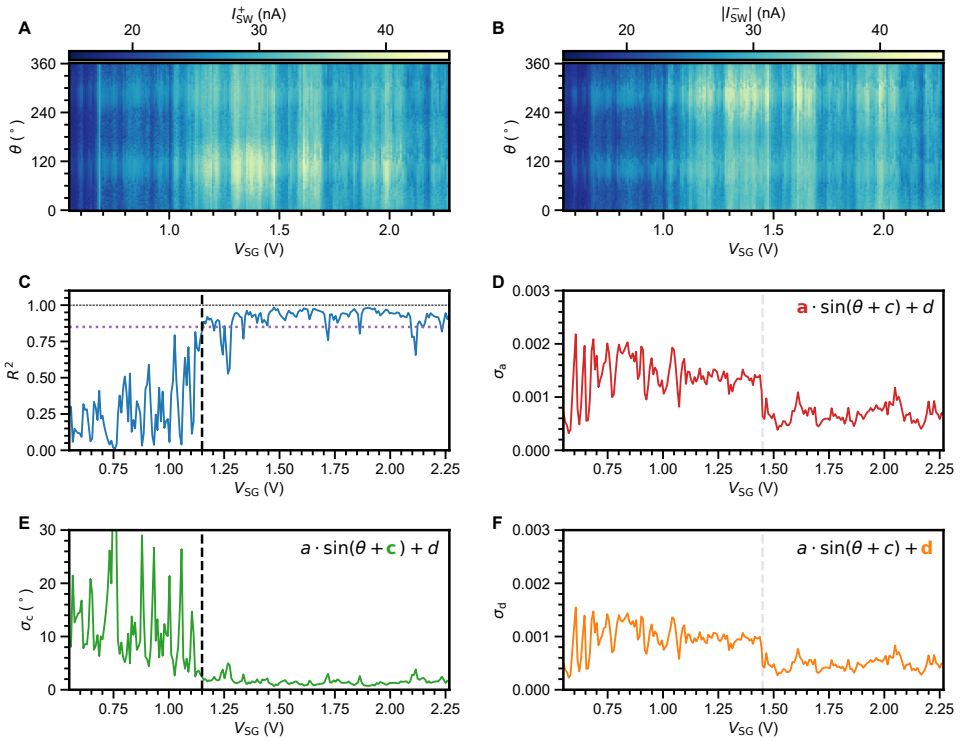

Figure 9.8: **Switching current and analysis underlying main text 9.2.** (**A,B**) I^+_{SW} and $|I^-_{SW}|$ versus V_{SG} and θ. (**C**) R^2 of the sinusoidal fit to the data. Below $V_{SG} < 1.15\,V$, R^2 quickly drops far below the threshold value of $R^2 = 0.85$, indicating a poor sinusoidal fit. (**D**) Standard deviation σ_a of the amplitude of the sine fits. (**E**) Standard deviation σ_c of the phase of the sine fits. Below $V_{SG} < 1.15\,V$, the phase becomes poorly defined. (**F**) Standard deviation σ_d of the offset of the sine fits. In panels (**D,F**), the dashed grey line corresponds to a change in the measurement setup where we switched from sequential detection of I^+_{SW} and $|I^-_{SW}|$ to simultaneous detection. As a result, the measurement time is halved and the thermal stability of the device improved, creating a more accurate fit of the amplitude and offset of the sine functions.

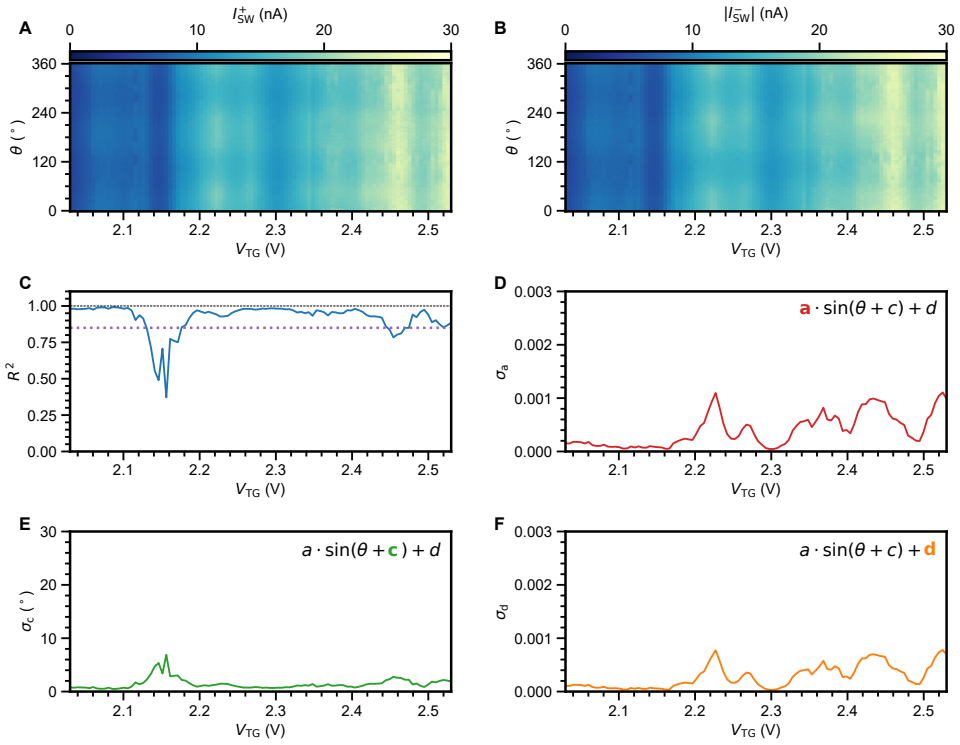

Figure 9.9: **Switching current and analysis underlying main text 9.3A-C at V_{SG} = 2.0 V (A,B)** I^+_{SW} and $|I^-_{SW}|$ versus V_{TG} and θ. **(C)** R^2 of the sinusoidal fit to the data. R^2 remains above $R^2 > 0.85$ over a large range of tunnel gate voltages and corresponding junction transmission, indicating a good sinusoidal fit. **(D)** Standard deviation σ_a of the amplitude of the sine fits. **(E)** Standard deviation σ_c of the phase of the sine fits. **(F)** Standard deviation σ_d of the offset of the sine fits.

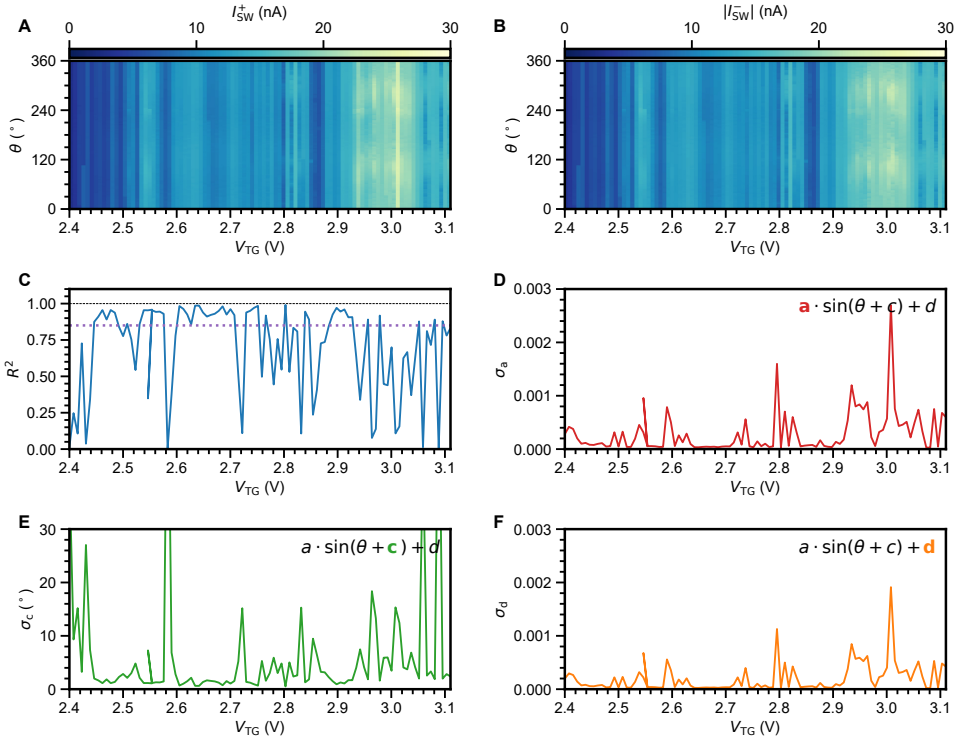

Figure 9.10: **Switching current and analysis underlying main text 9.3D-F at V_{SG} = 0.8 V (A,B)** I^+_{SW} and $|I^-_{SW}|$ versus V_{TG} and θ. **(C)** R^2 of the sinusoidal fit to the data. R^2 often drops below $R^2 < 0.85$, indicating a non-sinusoidal SDE resulting from junction physics. **(D)** Standard deviation σ_a of the amplitude of the sine fits. **(E)** Standard deviation σ_c of the phase of the sine fits. **(F)** Standard deviation σ_d of the offset of the sine fits.

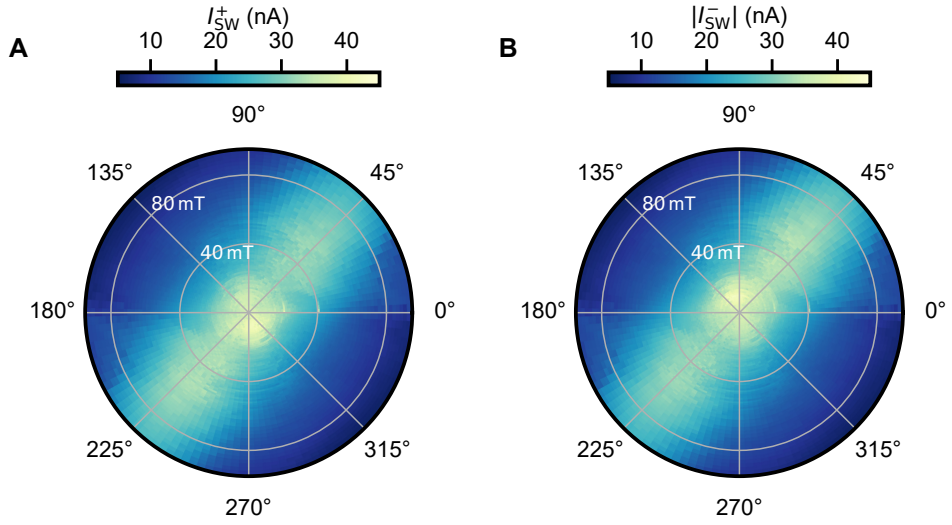

Figure 9.11: **Switching current and analysis underlying main text 9.4.** (**A**) Polar plot of I_{SW}^{+}, with θ on the polar axis and B on the radial axis. (**B**) Polar plot of $|I_{SW}^{-}|$, with θ on the polar axis and B on the radial axis.

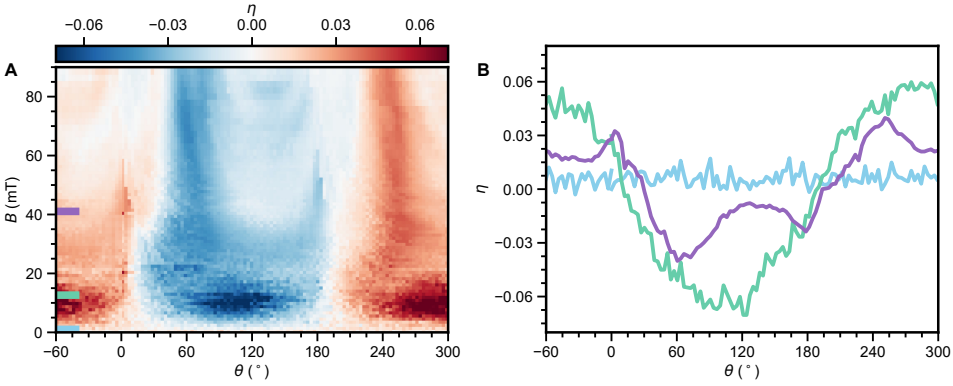

Figure 9.12: **Regular plot of the diode efficiency versus field magnitude, same data as main text 9.4.** (**A**) Regular plot of η as a function of rotating field with increasing magnitude. (**B**) Line cuts of η as a function of θ at various magnetic field values taken at the locations indicated by the colored bars in panel A. At $B = 0$ mT (light blue), the SDE is absent. At $B = 12$ mT (light green), the SDE is sinusoidal $\eta \propto \sin(\theta)$. At $B = 41$ mT (purple), the SDE becomes proportional to $\eta \propto \sin(\pi \cdot \sin(\theta))$, as predicted by [16].

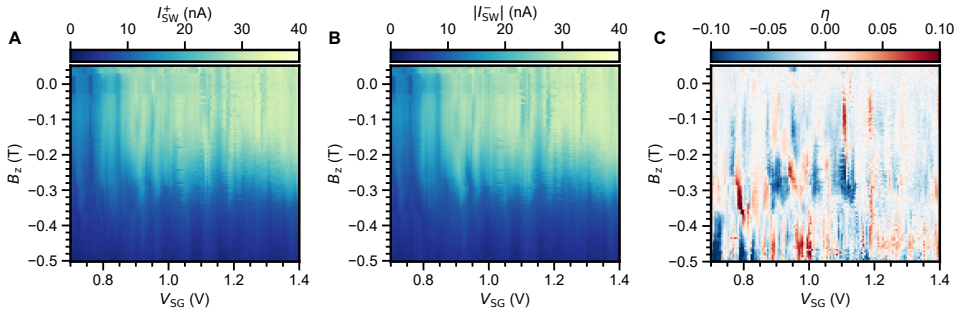

Figure 9.13: **Switching current and analysis underlying main text 9.5.** (**A,B**) I^+_{SW} and $|I^-_{SW}|$ versus V_{SG} and B_z. (**C**) η versus V_{SG} and B_z. Same plot as main text 9.5A, with the difference that 9.5A uses the absolute value of B_z presented here and is cropped at $B_z = 0$ T.

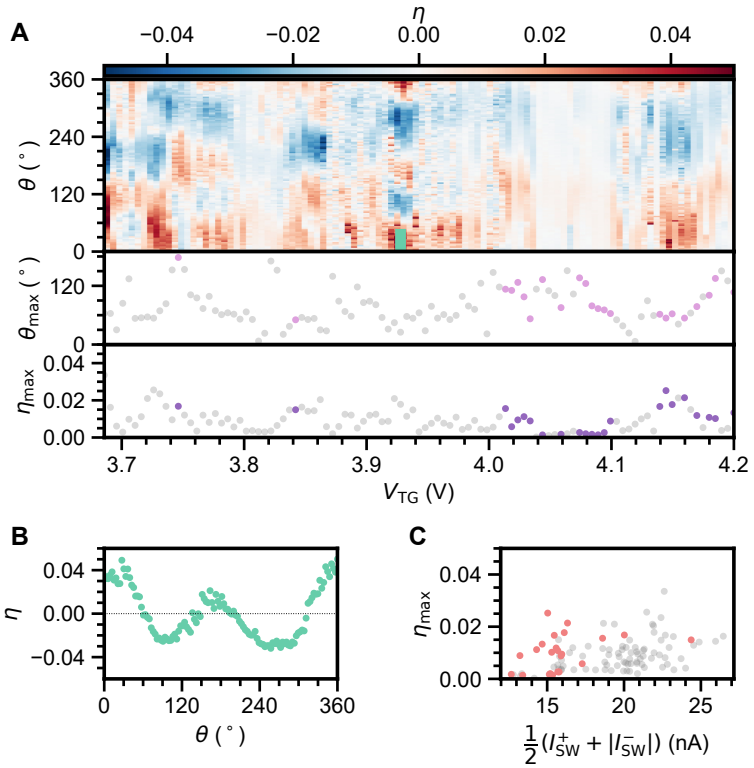

Figure 9.14: **Additional data: SDE dependence on tunnel gate voltage.** (**A**) Top: Diode efficiency η versus V_{TG} and θ. Taken at a low super gate voltage $V_{SG} = 0.7$ V and $B = 12$ mT. Middle: Estimation of the maximum efficiency angle θ_{max}. Bottom: Maximum diode efficiency η_{max}. (**B**) Example of the SDE taken at the location indicated by the colored bar in panel (**A**). The SDE is proportional to $\eta \propto \sin(\pi \cdot \sin(\theta))$. (**C**) η_{max} as a function of average switching current, taken along $\theta = 105^\circ$. In all panels, grey data points correspond to a poor sinusoidal fit ($R^2 < 0.85$) of η as a function of θ.

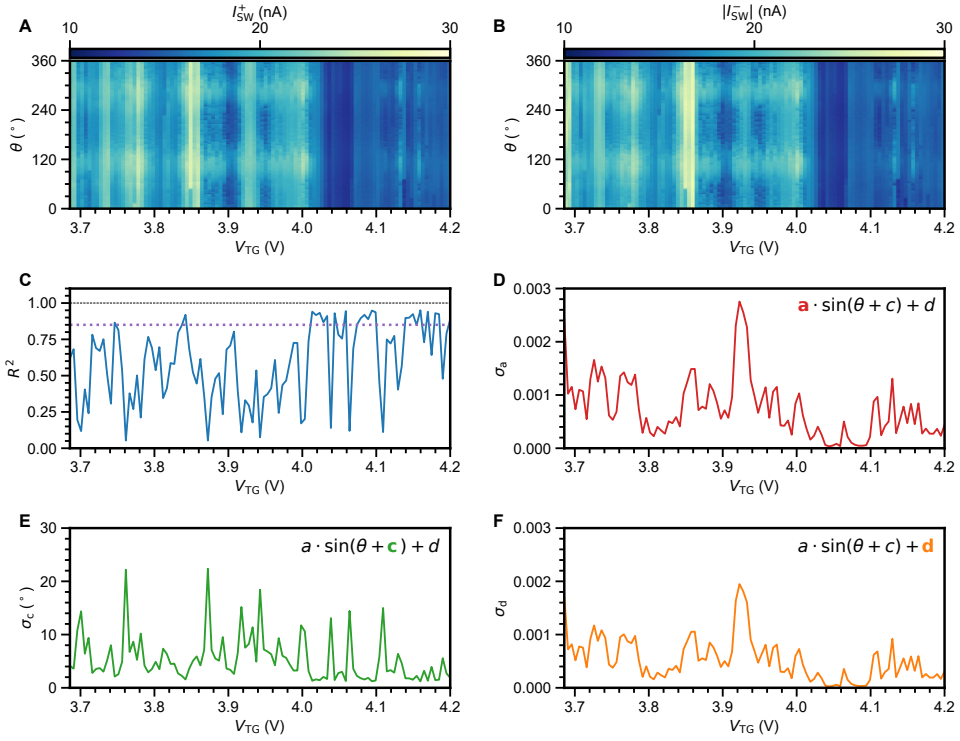

Figure 9.15: **Additional data: Switching current and analysis underlying Fig. 9.14.** **(A,B)** I^+_{SW} and $|I^-_{SW}|$ versus V_{TG} and θ. **(C)** R^2 of the sinusoidal fit to the data. R^2 mostly stays below $R^2 < 0.85$, indicating a non-sinusoidal SDE resulting from junction physics. **(D)** Standard deviation σ_a of the amplitude of the sine fits. **(E)** Standard deviation σ_c of the phase of the sine fits. **(F)** Standard deviation σ_d of the offset of the sine fits.

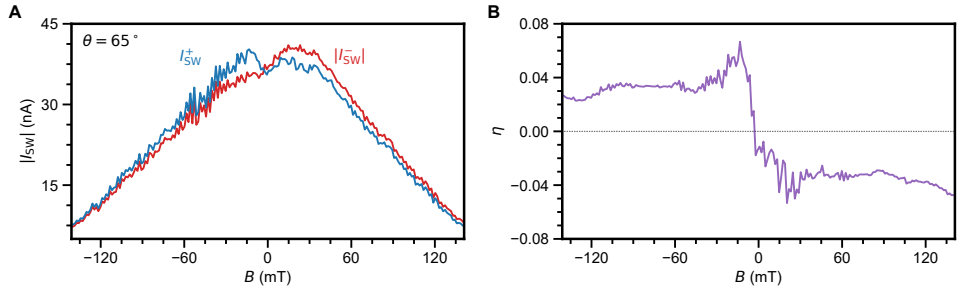

Figure 9.16: **Additional data: Persistent SDE at high field perpendicular to the nanowire axis.** **(A)** I^+_{SW} and $|I^-_{SW}|$ versus B, taken at $V_{SG} = 2.21\,V$, $V_{TG} = 3.61\,V$ and $\theta = 65^\circ$. **(B)** η versus B. The SDE persist up to a high perpendicular magnetic field $B = 140\,mT$, above which the switching current cannot be reliable detected.

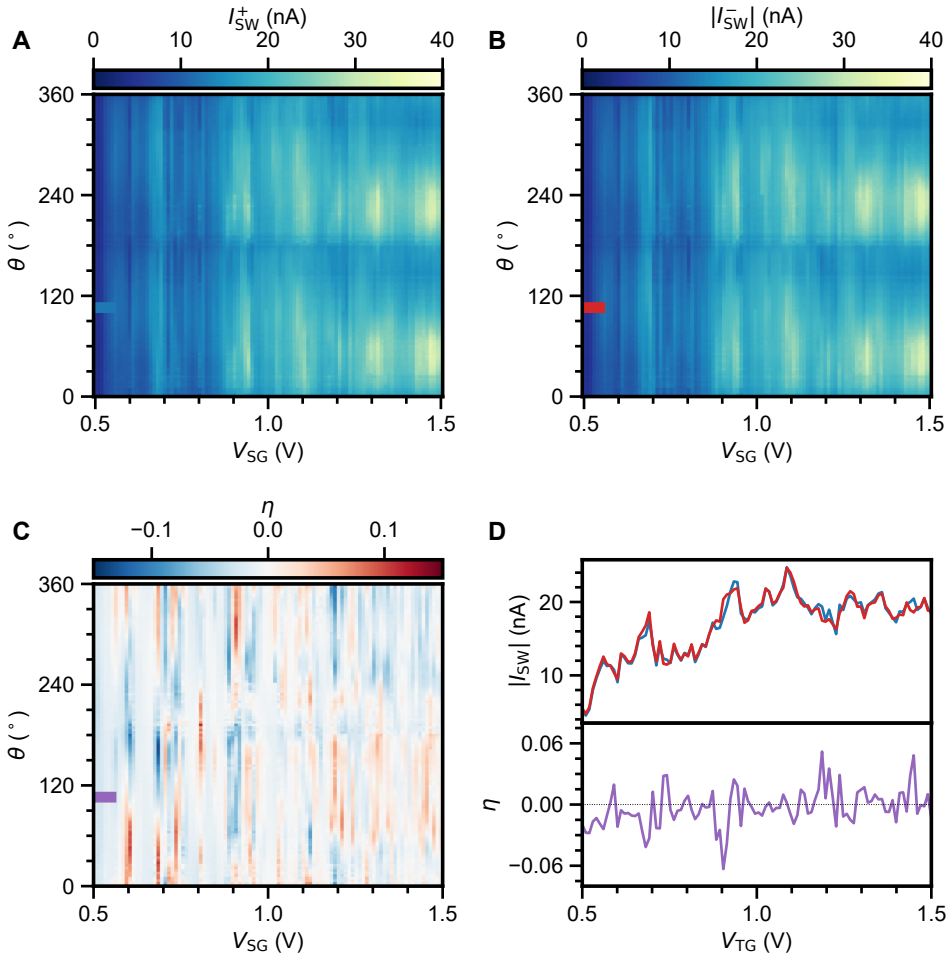

Figure 9.17: **Additional data: SDE at high field perpendicular to the nanowire axis.** **(A,B)** I^+_{SW} and $|I^-_{SW}|$ versus V_{SG} and θ, taken at $V_{TG} = 3.61\,V$ and $B = 60\,mT$. **(C)** η versus V_{SG} and θ. **(D)** I^+_{SW}, $|I^-_{SW}|$ and η taken at the maximum efficiency angle $\theta = 105^\circ$. The SDE frequently inverts sign as the super gate voltage is changed.

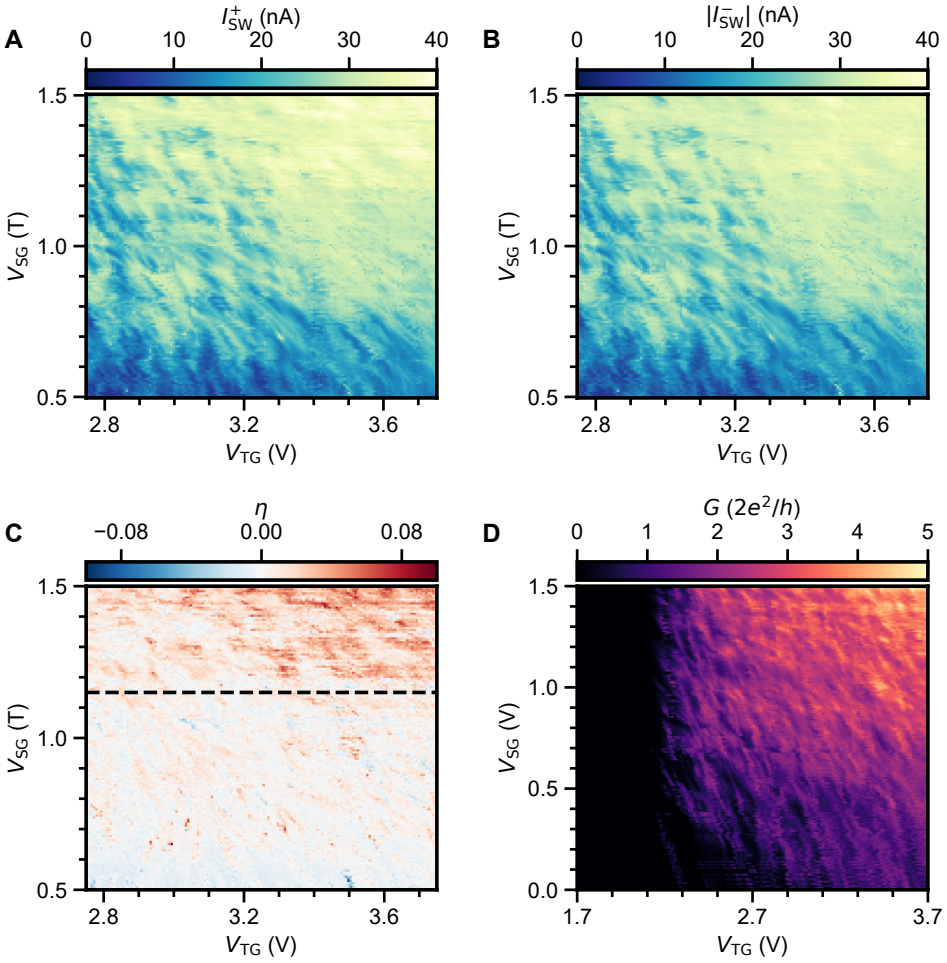

Figure 9.18: **Additional data: cross-capacitance between tunnel gate and super gates.** (**A,B**) I^{+}_{SW} and $|I^{-}_{SW}|$ versus V_{TG} and V_{TG}, taken at $B = 12\,\mathrm{mT}$ and $\theta = 105^{\circ}$. (**C**) η versus V_{TG} and V_{SG}. Below $V_{SG} < 1.15\,\mathrm{V}$ (dashed line), the SDE is strongly reduced. (**D**) Device conductance as a function of V_{TG} and V_{SG}, showing a minimal cross-capacitance between the gates. Data taken by applying a small bias voltage $V_{dc} = 1\,\mathrm{mV}$ across the device and measuring the resulting current I, such that $G = I/V_{dc}$.

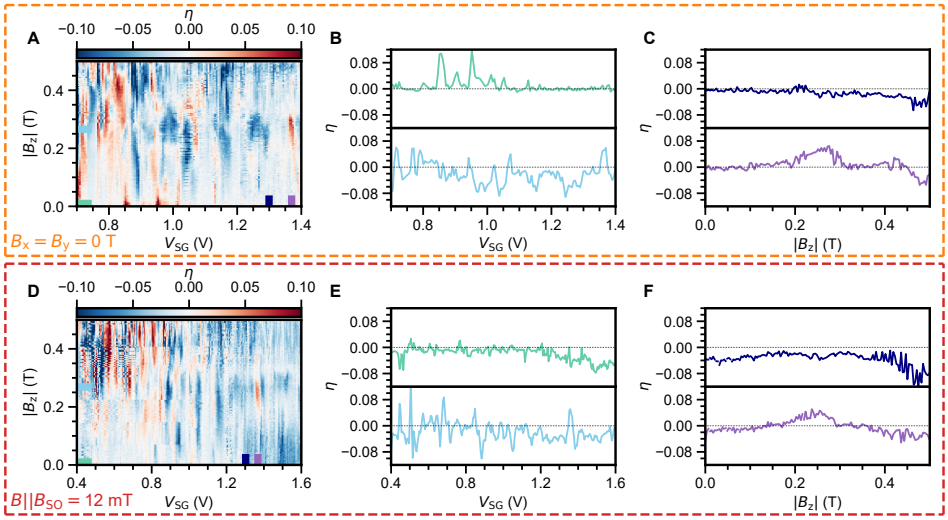

Figure 9.19: **Additional data: Evolution of the superconducting diode effect as a function of magnetic field parallel to the nanowire axis.** (**A-C**) Diode efficiency η as a function of super gate voltage V_{SG} and parallel magnetic field B_z without any magnetic field component perpendicular to the nanowire axis. (**B**) Examples of η as a function of V_{SG} taken at locations indicated by the colored bars in panel (**A**). (**C**) Examples of η as a function of B_z taken at locations indicated by the colored bars in panel (**A**). (**D-E**) Diode efficiency η as a function of super gate voltage V_{SG} and parallel magnetic field B_z with a small field applied along the maximum efficiency angle, $B = 12\,\mathrm{mT}$ and $\theta = 105^\circ$. (**E**) Examples of η as a function of V_{SG} taken at locations indicated by the colored bars in panel (**D**). (**F**) Examples of η as a function of B_z taken at locations indicated by the colored bars in panel (**D**). A perpendicular component of the magnetic field does not alter the observed SDE significantly. Thus, we do not attribute the observations to subband physics as predicted by [5].

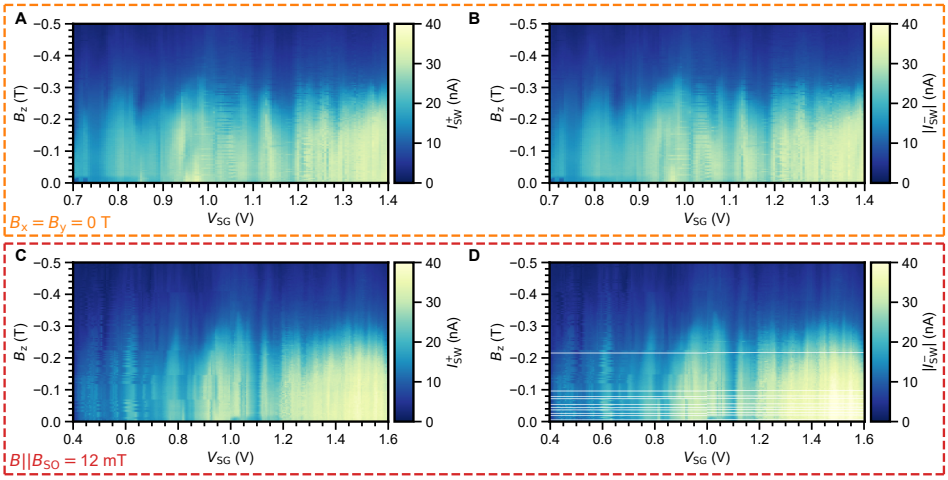

Figure 9.20: **Additional data: Switching current maps underlying Fig. 9.19.** (**A,B**) I^+_{SW} and $|I^-_{SW}|$ versus V_{SG} and B_z corresponding to Fig. 9.19A-C. (**C,D**) I^+_{SW} and $|I^-_{SW}|$ versus V_{SG} and B_z corresponding to Fig. 9.19D-F.

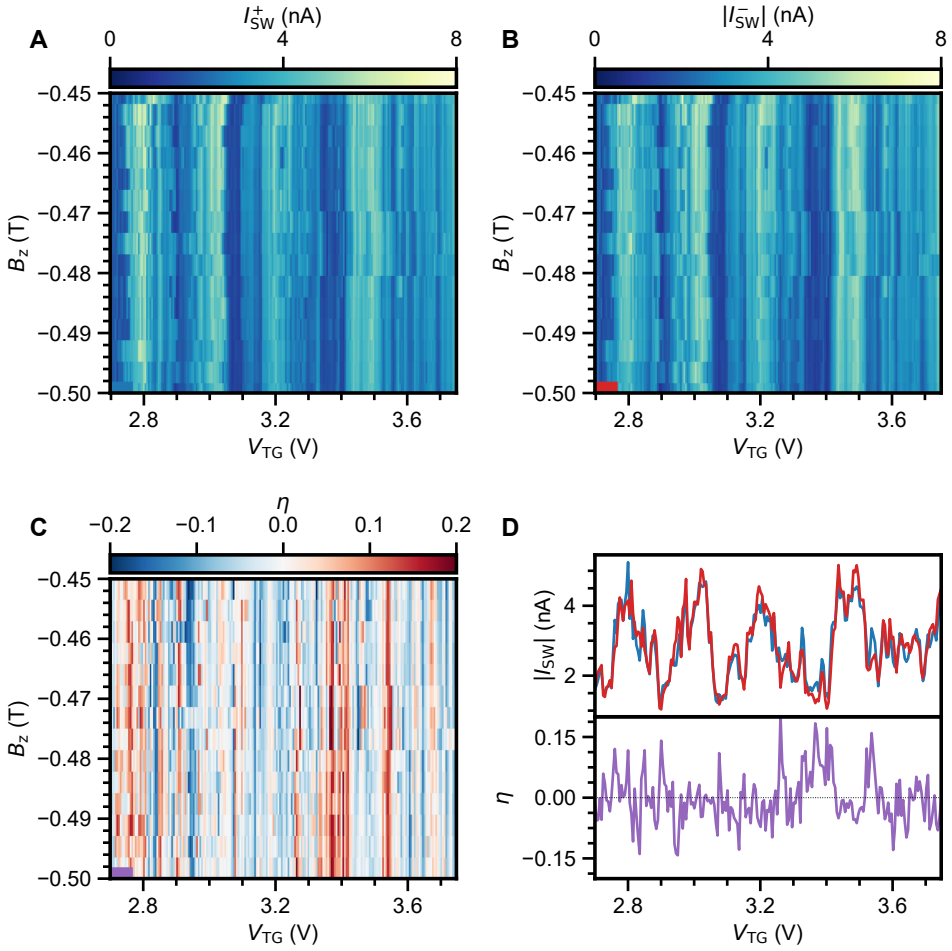

Figure 9.21: **Additional data: Rapid sign inversion under a high parallel Zeeman field.** (**A**,**B**) I^+_{SW} and $|I^-_{SW}|$ versus V_{TG} and B_z. The tunnel gate voltage sweeps across many resonances in the junction, causing a modulation in the switching current. Taken at $V_{SG} = 0.7$ V. (**C**) η versus V_{TG} and B_z. As the tunnel gate sweeps across junction resonances, the diode efficiency frequently inverts its sign and its magnitude is strongly modulated. (**D**) I^+_{SW}, $|I^-_{SW}|$ and η as a function of V_{TG} at $B_z = -0.5$ T.

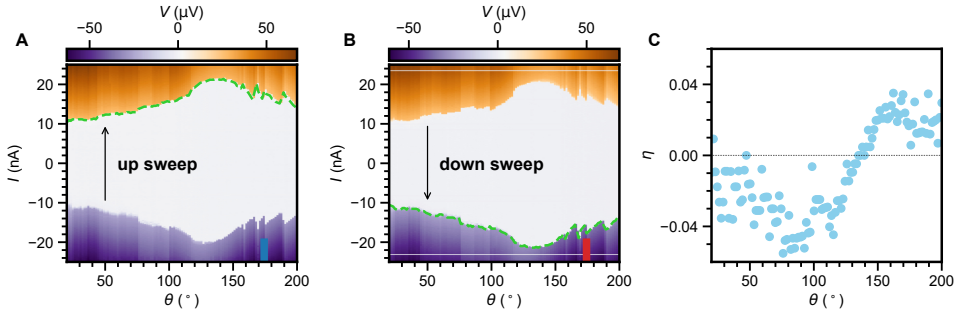

Figure 9.22: **SDE measured in a DC setup.** (**A,B**) I-V curves taken as a function of θ at V_{SG} = 3.0 V, V_{TG} = 2.0 V and B = 30 mT. Data is taken in a 2-terminal geometry and corrected for a series resistance of 5815 Ω. Dashed green lines indicate the extracted switching current values. Curves shown in main text 9.1C are taken from these maps at the locations indicated by the colored bars ($\theta = 174^{\circ}$). (**C**) Diode efficiency η taken from the DC maps in panel (**A**). The DC setup only takes a single switching current value, such that the stochastic nature of switching current results in a large spread in η as a function of θ. Moreover, the $\eta(\theta)$ appears to be non-sinusoidal, in agreement with the high-field data shown in 9.4 and Fig. 9.12.

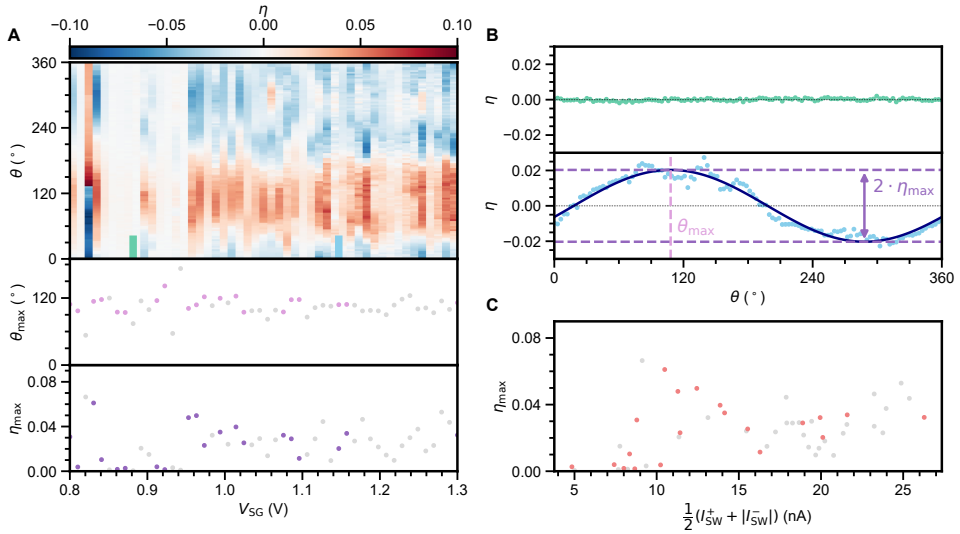

Figure 9.23: **Reproduction of the dependence of superconducting diode effect on super gate voltage on a second device.** (**A**) Top: Diode efficiency η as a function of super gate voltage V_{SG} and θ, taken with V_{TG} = 4.5 V and B = 12 mT. Middle: Estimation of the maximum efficiency angle θ_{max} underneath the hybrid. Bottom: Maximum diode efficiency η_{max} as a function of V_{SG}. The dashed black line indicates that the diode effect is suppressed below V_{SG} < 1.15 V. (**B**) Top: lack of an SDE. Bottom: Presence of an SDE. Linecuts taken from (**A**) top, at locations indicated by the colored bars. In the bottom panel, the dashed pink line specifies the maximum efficiency angle, whereas the maximum diode efficiency is depicted by the dashed purple lines. (**C**) η_{max} as a function of average switching current, taken along $\theta = 105^{\circ}$. In all panels, grey data points correspond to a poor sinusoidal fit (R^2 < 0.85) of η as a function of θ.

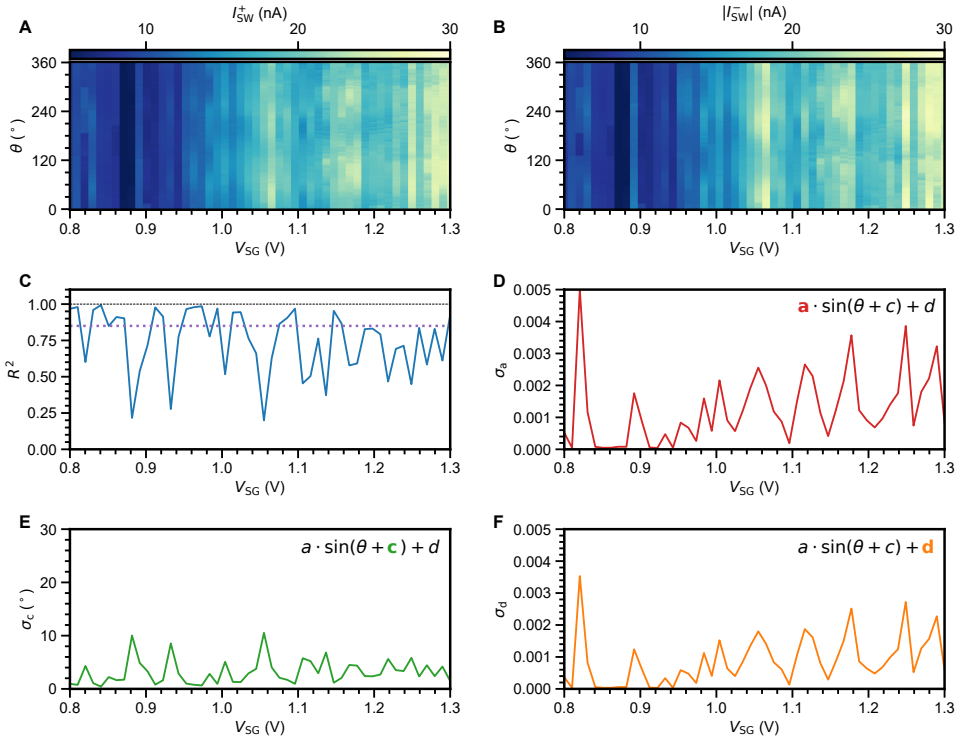

Figure 9.24: **Additional data: Switching current and analysis underlying the reproduction device, Fig. 9.23.** **(A,B)** I^+_{SW} and $|I^-_{SW}|$ versus V_{SG} and θ. **(C)** R^2 of the sinusoidal fit to the data. R^2 oscillates around $R^2 = 0.85$, indicating an SDE due to a mix of junction and lead physics. **(D)** Standard deviation σ_a of the amplitude of the sine fits. **(E)** Standard deviation σ_c of the phase of the sine fits. **(F)** Standard deviation σ_d of the offset of the sine fits.

References

[1] F. Ando, Y. Miyasaka, T. Li, J. Ishizuka, T. Arakawa, Y. Shiota, T. Moriyama, Y. Yanase, and T. Ono, *Observation of superconducting diode effect,* Nature **584**, 373 (2020).

[2] V. M. Edelstein, *The Ginzburg-Landau equation for superconductors of polar symmetry,* Journal of Physics: Condensed Matter **8**, 339 (1996).

[3] R. Wakatsuki, Y. Saito, S. Hoshino, Y. M. Itahashi, T. Ideue, M. Ezawa, Y. Iwasa, and N. Nagaosa, *Nonreciprocal charge transport in noncentrosymmetric superconductors,* Science Advances **3**, e1602390 (2017).

[4] K.-R. Jeon, J.-K. Kim, J. Yoon, J.-C. Jeon, H. Han, A. Cottet, T. Kontos, and S. S. Parkin, *Zero-field polarity-reversible Josephson supercurrent diodes enabled by a proximity-magnetized Pt barrier,* Nature Materials , 1 (2022).

[5] H. F. Legg, D. Loss, and J. Klinovaja, *Superconducting diode effect due to magnetochiral anisotropy in topological insulators and Rashba nanowires,* Phys. Rev. B **106**, 104501 (2022).

[6] N. F. Yuan and L. Fu, *Supercurrent diode effect and finite-momentum superconductors,* Proceedings of the National Academy of Sciences **119**, e2119548119 (2022).

[7] T. Yokoyama, M. Eto, and Y. V. Nazarov, *Josephson current through semiconductor nanowire with spin–orbit interaction in magnetic field,* Journal of the Physical Society of Japan **82**, 054703 (2013).

[8] T. Yokoyama, M. Eto, and Y. V. Nazarov, *Anomalous Josephson effect induced by spin-orbit interaction and Zeeman effect in semiconductor nanowires,* Physical Review B **89**, 195407 (2014).

[9] M. Davydova, S. Prembabu, and L. Fu, *Universal Josephson diode effect,* Science Advances **8**, eabo0309 (2022).

[10] Y. Hou, F. Nichele, H. Chi, A. Lodesani, Y. Wu, M. F. Ritter, D. Z. Haxell, M. Davydova, S. Ilić, F. S. Bergeret, *et al.*, *Ubiquitous superconducting diode effect in superconductor thin films,* arXiv preprint arXiv:2205.09276 (2022).

[11] H. Wu, Y. Wang, Y. Xu, P. K. Sivakumar, C. Pasco, U. Filippozzi, S. S. Parkin, Y.-J. Zeng, T. McQueen, and M. N. Ali, *The field-free Josephson diode in a van der Waals heterostructure,* Nature **604**, 653 (2022).

[12] S. Heedt, M. Quintero-Pérez, F. Borsoi, A. Fursina, N. van Loo, G. P. Mazur, M. P. Nowak, M. Ammerlaan, K. Li, S. Korneychuk, *et al.*, *Shadow-wall lithography of ballistic superconductor–semiconductor quantum devices,* Nat. Commun. **12**, 1 (2021).

[13] N. van Loo, G. Mazur, T. Dvir, G. Wang, R. Dekker, J.-Y. Wang, M. Lemang, C. Sfiligoj, A. Bordin, D. van Driel, *et al.*, *Electrostatic control of the proximity effect in the bulk of semiconductor-superconductor hybrids,* arXiv preprint arXiv:2211.06709 (2022).

[14] C. Li, J. C. de Boer, B. de Ronde, S. V. Ramankutty, E. van Heumen, Y. Huang, A. de Visser, A. A. Golubov, M. S. Golden, and A. Brinkman, *4π-periodic Andreev bound states in a Dirac semimetal,* Nature Materials **17**, 875 (2018).

[15] S. Hart, H. Ren, M. Kosowsky, G. Ben-Shach, P. Leubner, C. Brüne, H. Buhmann, L. W. Molenkamp, B. I. Halperin, and A. Yacoby, *Controlled finite momentum pairing and spatially varying order parameter in proximitized HgTe quantum wells,* Nature Physics **13**, 87 (2017).

[16] B. Pal, A. Chakraborty, P. K. Sivakumar, M. Davydova, A. K. Gopi, A. K. Pandeya, J. A. Krieger, Y. Zhang, S. Ju, N. Yuan, *et al.*, *Josephson diode effect from Cooper pair momentum in a topological semimetal,* Nature Physics , 1 (2022).

[17] J. Shabani, M. Kjaergaard, H. J. Suominen, Y. Kim, F. Nichele, K. Pakrouski, T. Stankevic, R. M. Lutchyn, P. Krogstrup, R. Feidenhans'l, S. Kraemer, C. Nayak, M. Troyer, C. M. Marcus, and C. J. Palmstrøm, *Two-dimensional epitaxial superconductor-semiconductor heterostructures: A platform for topological superconducting networks,* Phys. Rev. B **93**, 155402 (2016).

[18] C. Baumgartner, L. Fuchs, A. Costa, S. Reinhardt, S. Gronin, G. C. Gardner, T. Lindemann, M. J. Manfra, P. E. Faria Junior, D. Kochan, *et al.*, *Supercurrent rectification and magnetochiral effects in symmetric Josephson junctions,* Nature Nanotechnology **17**, 39 (2022).

[19] M. Gupta, G. V. Graziano, M. Pendharkar, J. T. Dong, C. P. Dempsey, C. Palmstrøm, and V. S. Pribiag, *Superconducting diode effect in a three-terminal Josephson device,* arXiv preprint arXiv:2206.08471 (2022).

[20] A. Sundaresh, J. I. Väyrynen, Y. Lyanda-Geller, and L. P. Rokhinson, *Supercurrent non-reciprocity and vortex formation in superconductor heterostructures,* arXiv preprint arXiv:2207.03633 (2022).

[21] B. Turini, S. Salimian, M. Carrega, A. Iorio, E. Strambini, F. Giazotto, V. Zannier, L. Sorba, and S. Heun, *Josephson diode effect in high mobility InSb nanoflags,* arXiv preprint arXiv:2207.08772 (2022).

[22] C. Leroux, A. Parra-Rodriguez, R. Shillito, A. Di Paolo, W. D. Oliver, C. M. Marcus, M. Kjaergaard, A. Gyenis, and A. Blais, *Nonreciprocal devices based on voltage-tunable junctions,* arXiv preprint arXiv:2209.06194 (2022).

[23] L. J. Splitthoff, A. Bargerbos, L. Grünhaupt, M. Pita-Vidal, J. J. Wesdorp, Y. Liu, A. Kou, C. K. Andersen, and B. van Heck, *Gate-tunable kinetic inductance in proximitized nanowires,* Phys. Rev. Applied **18**, 024074 (2022).

[24] A. Zwerver, T. Krähenmann, T. Watson, L. Lampert, H. C. George, R. Pillarisetty, S. Bojarski, P. Amin, S. Amitonov, J. Boter, *et al.*, *Qubits made by advanced semiconductor manufacturing,* Nature Electronics **5**, 184 (2022).

[25] F. Borsoi, G. P. Mazur, N. van Loo, M. P. Nowak, L. Bourdet, K. Li, S. Korneychuk, A. Fursina, J.-Y. Wang, V. Levajac, E. Memisevic, G. Badawy, S. Gazibegovic, K. van Hoogdalem, E. P. A. M. Bakkers, L. P. Kouwenhoven, S. Heedt, and M. Quintero-Pérez, *Single-shot fabrication of semiconducting–superconducting nanowire devices,* Adv. Func. Mater. , 2102388 (2021), https://onlinelibrary.wiley.com/doi/pdf/10.1002/adfm.202102388 .

[26] V. Levajac, G. P. Mazur, N. van Loo, F. Borsoi, G. Badawy, S. Gazibegovic, E. P. Bakkers, S. Heedt, L. P. Kouwenhoven, and J.-Y. Wang, *Impact of junction length on supercurrent resilience against magnetic field in InSb–Al nanowire Josephson junctions,* arXiv preprint arXiv:2211.07858 (2022).

[27] C. W. J. Beenakker and H. van Houten, *Josephson current through a superconducting quantum point contact shorter than the coherence length,* Phys. Rev. Lett. **66**, 3056 (1991).

[28] C. W. J. Beenakker, *Universal limit of critical-current fluctuations in mesoscopic josephson junctions,* Phys. Rev. Lett. **67**, 3836 (1991).

[29] M. Zgirski, M. Foltyn, A. Savin, and K. Norowski, *Flipping-coin experiment to study switching in Josephson junctions and superconducting wires,* Phys. Rev. Applied **11**, 054070 (2019).

[30] U. C. Coskun, M. Brenner, T. Hymel, V. Vakaryuk, A. Levchenko, and A. Bezryadin, *Distribution of supercurrent switching in graphene under the proximity effect,* Phys. Rev. Lett. **108**, 097003 (2012).

[31] D. Bouman, R. J. J. van Gulik, G. Steffensen, D. Pataki, P. Boross, P. Krogstrup, J. Nygård, J. Paaske, A. Pályi, and A. Geresdi, *Triplet-blockaded Josephson supercurrent in double quantum dots,* Phys. Rev. B **102**, 220505 (2020).

[32] *See supplementary information.* .

[33] J. D. S. Bommer, H. Zhang, O. Gül, B. Nijholt, M. Wimmer, F. N. Rybakov, J. Garaud, D. Rodic, E. Babaev, M. Troyer, D. Car, S. R. Plissard, E. P. A. M. Bakkers, K. Watanabe, T. Taniguchi, and L. P. Kouwenhoven, *Spin-orbit protection of induced superconductivity in Majorana nanowires,* Phys. Rev. Lett. **122**, 187702 (2019).

[34] A. E. Antipov, A. Bargerbos, G. W. Winkler, B. Bauer, E. Rossi, and R. M. Lutchyn, *Effects of gate-induced electric fields on semiconductor Majorana nanowires,* Phys. Rev. X **8**, 031041 (2018).

[35] C. Reeg, D. Loss, and J. Klinovaja, *Metallization of a Rashba wire by a superconducting layer in the strong-proximity regime,* Phys. Rev. B **97**, 165425 (2018).

[36] P. Jarillo-Herrero, J. A. Van Dam, and L. P. Kouwenhoven, *Quantum supercurrent transistors in carbon nanotubes,* Nature **439**, 953 (2006).

[37] L. Han, M. Chan, D. de Jong, C. Prosko, G. Badawy, S. Gazibegovic, E. P. Bakkers, L. P. Kouwenhoven, F. K. Malinowski, and W. Pfaff, *Variable and orbital-dependent spin-orbit field orientations in a insb double quantum dot characterized via dispersive gate sensing,* arXiv preprint arXiv:2203.06047 (2022).

[38] R. M. Lutchyn, E. P. Bakkers, L. P. Kouwenhoven, P. Krogstrup, C. M. Marcus, and Y. Oreg, *Majorana zero modes in superconductor–semiconductor heterostructures,* Nat. Rev. Mater. **3**, 52 (2018).

[39] E. Prada, P. San-Jose, M. W. de Moor, A. Geresdi, E. J. Lee, J. Klinovaja, D. Loss, J. Nygård, R. Aguado, and L. P. Kouwenhoven, *From Andreev to Majorana bound states in hybrid superconductor–semiconductor nanowires,* Nat. Rev. Phys. **2**, 575 (2020).

[40] M. W. A. de Moor, J. D. S. Bommer, D. Xu, G. W. Winkler, A. E. Antipov, A. Bargerbos, G. Wang, N. van Loo, R. L. M. O. het Veld, S. Gazibegovic, D. Car, J. A. Logan, M. Pendharkar, J. S. Lee, E. P. A. M. Bakkers, C. J. Palmstrøm, R. M. Lutchyn, L. P. Kouwenhoven, and H. Zhang, *Electric field tunable superconductor-semiconductor coupling in Majorana nanowires,* New J. Phys. **20**, 103049 (2018).

[41] J. Shen, G. W. Winkler, F. Borsoi, S. Heedt, V. Levajac, J.-Y. Wang, D. van Driel, D. Bouman, S. Gazibegovic, R. L. M. Op Het Veld, D. Car, J. A. Logan, M. Pendharkar, C. J. Palmstrøm, E. P. A. M. Bakkers, L. P. Kouwenhoven, and B. van Heck, *Full parity phase diagram of a proximitized nanowire island,* Phys. Rev. B **104**, 045422 (2021).

[42] R. S. Souto, M. Leijnse, and C. Schrade, *The Josephson diode effect in supercurrent interferometers,* arXiv preprint arXiv:2205.04469 (2022).

[43] D. Szombati, S. Nadj-Perge, D. Car, S. Plissard, E. Bakkers, and L. Kouwenhoven, *Josephson ϕ0-junction in nanowire quantum dots,* Nature Physics **12**, 568 (2016).

[44] G. P. Mazur, N. van Loo, J.-Y. Wang, T. Dvir, G. Wang, A. Khindanov, S. Korneychuk, F. Borsoi, R. C. Dekker, G. Badawy, *et al.*, *Spin-mixing enhanced proximity effect in aluminum-based superconductor–semiconductor hybrids,* Advanced Materials , 2202034 (2022).

10

Conclusion and Outlook

The bulk of this thesis investigated the properties of semiconductor-superconductor hybrid nanowires, in an attempt to create Majorana zero modes following the Lutchyn-Oreg approach. Time and effort, however, have taught us that this is not a simple task. In this chapter, we will reflect on what was learned during this endeavor. Although the approach as mentioned above turned out to not be feasible, we have demonstrated the creation of Poor Man's Majorana zero modes in an artificial Kitaev chain. While these are not topologically protected, they are predicted to possess all of the other Majorana properties - most notably the non-abelian exchange statistics. The way forward thus seems unmistakably clear: Focusing efforts on the development of quantum information based on the implementation of a Kitaev chain, rather than sticking to the continuous nanowire approach. This chapter will briefly discuss future prospects for both.

10.1 Beyond-beyond Lutchyn-Oreg

10.1.1 Resolving the Majorana paradox

In the initial stages of this Ph.D. project, the state-of-the-art semiconductor-superconductor hybrids were grown by depositing aluminum films on the InSb nanowire growth chip [1]. These nanowires had two major downsides: The superconducting shell could not be grounded, and the unstable interface between InSb and Al put constraints on the lifetime of the growth chip and the thermal budget of the device fabrication. We have thus developed shadow-wall lithography to counter these effects. On the one hand, moving the superconductor deposition to be one of the last fabrication steps allows the bulk of the device fabrication to be done as pre-fabrication without any limiting thermal budget or time constraints. This enabled low-quality fabrication steps, such as room-temperature sputtering of the gate dielectric, to be replaced with high-quality processes like atomic layer deposition of Al_2O_3 and HfO_2 at elevated temperatures. Indeed, both the quality and reproducibility of these devices improved tremendously as a result. On the other hand, the superconductor deposition at an angle while the nanowire is already placed on a substrate opens up the ability to connect the superconductor to the film on the substrate - thereby creating a ground connection. Crucially, this allowed the hybrid section of the nanowire to be probed from both sides. All in all, shadow-wall lithography has provided a major breakthrough in the fabrication of semiconductor-superconductor hybrids.

One of the main drawbacks of the relatively-thick aluminum as the superconductor is the poor field compatibility of the devices. This naturally led to the question if we could reach sufficiently high Zeeman energies in our hybrids. Moreover, the superconducting gap would have shrunk significantly in a typical magnetic field for which zero-energy states form in the hybrid. We have consequently reduced the thickness of the aluminum film in combination with spin-mixing provided by platinum adatoms. This allowed us to increase the field compatibility of the hybrid devices drastically.

Utilizing the technique of radio-frequency reflectometry, we have done extensive studies of zero-energy states in semiconductor-superconductor hybrids. We found that such states can evolve with elaborate patterns, all of which compatible with the behavior of Majorana zero modes. These include stable zero-bias peaks over large values of the parameter space, parabolic patterns in the parameter space, and oscillations with increasing amplitude as a function of the magnetic field. However, the ability to observe the other side of the hybrid showed a remarkable lack of end-to-end correlation. This implies that the observations can not be attributed to a topological phase transition of the hybrid nanowire segment.

Around the same time, we have implemented the technique of nonlocal conductance spectroscopy to investigate the bulk properties of hybrid nanowires. Even though we did observe a reopening of the induced gap in a single nanowire, it was not accompanied by the formation of zero-bias peaks. Hence, we do not believe this reopening was associated with a topological phase transition. Instead, it is more likely the result of a relatively short wire with a low carrier density, where a handful of discrete states are crossing

zero energy due to a combination of the Zeeman effect and the orbital effect of the magnetic field. Our investigation of the superconducting properties at zero magnetic field, however, turned out to be more fruitful, as we were able to show that the coupling between the semiconductor and the superconductor could reproducibility be tuned between strong-coupling and weak-coupling regimes. This turned out to be especially important because near the crossover between these regimes, there is the possibility to generate individual Andreev bound states in the hybrid segment. Indeed, this was a critical development that enabled the creation of a minimal Kitaev chain. The same effect also enables control over the superconducting diode effect in nanowire-based Josephson junctions.

Our observations demonstrate that there is a fundamental issue when the hybrids are relatively long. The absence of end-to-end correlation and the observation of discrete states, even in long nanowires, suggests that strong disorder is present in these samples. In fact, it seems that the disorder potential is large compared to the inter-subband spacing in these hybrids [2]. A pristine sample should indeed exhibit specific features as the result of subband physics, such as a discrete reduction of the induced gap [3]. While we did observe a reduction of the induced gap in the experiments of chapter 7, the stepwise features that should accompany the transition between subbands were not present. Thus, it seems that the disorder is strong enough to cause a mixing of the subbands and a resulting absence of a subband structure.

The works in this thesis have shown that through a combination of improved fabrication, improved materials, and new detection methods, the created devices exhibit a reduction of signatures of Majorana zero modes. This indeed contradicts the expectation that with better samples, one would see an improvement in the observed Majorana signatures. We can then only conclude that the observation of Majorana signatures in the past was unrelated to a topological phase transition - thereby resolving the Majorana paradox[1] introduced in chapter 1.

10.1.2 The need for better materials

The idea that disorder limits the observation of a topological phase transition was also explored in theory quite recently [4, 5]. These works put an upper limit on the density of charge impurities in the material of $\sim 10^{15}\,\mathrm{cm}^{-3}$, which corresponds to a mobility on the order of $300\,000\,\mathrm{cm}^2/\mathrm{V{\cdot}s}$. The InSb nanowires used in this work are obtained from growth chips where the nanowires have mobilities around $40\,000\,\mathrm{cm}^2/\mathrm{V{\cdot}s}$ [6]. However, the wires used for that mobility characterization have a substantially larger diameter. As the mobility is limited by scattering on the surface and hence the surface-to-volume ratio, it is more likely that the actual mobility of the nanowires used in this work is lower, maybe as low as $20\,000\,\mathrm{cm}^2/\mathrm{V{\cdot}s}$. Also note that the required mobility number is given for a *hybrid* nanowire, whereas the measured mobility is actually for the *semiconductor* nanowire

[1] The Majorana paradox: There exists an abundance of experimental work which claims to have observed Majorana zero modes. Yet, not a single lab has demonstrated a qubit or any experiment more advanced than the demonstration of zero-bias peaks.

only. This number is only expected to worsen due to the fabrication of the samples, which removes the native nanowire oxide and replaces it with a polycrystalline metal. Yet, it is not known how much worse it gets - experiments that measure the mobility can not be executed on the structures once the superconductor is deposited. It is safe to say that even order of magnitude improvement to the semiconductor mobility would be insufficient to allow topological superconductivity to arise in the hybrid structures. Other materials, like shallow 2-dimensional electron gases in InSb, InAs, or InAsSb, are likely to suffer the same fate as their mobility numbers before nanofabrication are comparable [7–9]. Thus, dramatic improvements in the base quality of the semiconductors are needed as a start.

The optimization of hybrid structures may also include a barrier material between the semiconductor and superconductor. Such a barrier would decouple the semiconductor and the superconductor, where the thickness of the barrier material provides an additional tuning knob to control the electronic density and semiconductor-superconductor coupling. The inclusion of such a layer is also expected to increase the mobility of the hybrid structure in proportion to the thickness of the barrier material. This has been well established for InAs-based hybrids [10, 11] through the use of an InGaAs barrier material. For InSb, the natural material of choice is CdTe, as it is nearly lattice matched to InSb. Developments of these heterostructures is still in an early stage, however, as field-effect transistors have not yet shown an enhanced mobility and exhibit hysteretic voltage thresholds [12]. In addition, induced superconductivity has yet to be demonstrated in InSb hybrids with a CdTe barrier. Here, too, the burden lies in improving the material stack quality.

In addition, it is currently unknown what is the electronic density at which the InSb/Al nanowires in this work operate. Under the assumption that these hybrids form a band structure that is discretized in one-dimensional subbands, this means that it is yet unknown how many of these are active for a given gate voltage. This could, in principle, be estimated through simulations [3], although this does require information on the band offset between InSb and Al (and potentially including any barrier material) - information that is currently not known. Thus, it would be beneficial to first estimate this band offset through angle-resolved photoemission experiments, as was done for the InAs/Al system [13]. This input can then be used to design hybrid structures with the optimal geometry to realize a topological phase [3]. Any such hybrids will then have to be subjected to the same three-terminal experiments presented in chapter 7 in order to investigate the properties of the induced superconductivity, which in turn provides feedback for the design of the next generation of devices. Finally, reproduction and large-scale mapping of the phase diagrams of such devices as we did in chapters 5 and 7 can provide valuable information to calibrate how much disorder is present in the hybrid devices [5].

10.2 Beyond Poor Man's Majorana zero modes

The realization that Andreev bound states in short hybrid segments can be used to mediate coherent transport between the two ends of the hybrid has proven to be quintessential. It directly enabled a different approach to the formation of Majorana zero modes, which we demonstrated with the realization of an artificial Kitaev chain. With the prospects

for the continuous nanowire approach being so inconceivably unfavorable, the artificial Kitaev chain will likely revolutionize the research into Majorana zero modes and topological superconductivity. While the Majorana zero modes demonstrated in chapter 8 are not topologically protected, this can be achieved by making the chain sufficiently long. Yet, the size of the topological gap that would emerge in a long chain is of the size of the interaction strength between the coupled quantum dots - in our case, on the order of $2\Delta \sim 25\,\mu$eV. This value is indeed relatively small and will need to be improved. Finally, we note that the Poor Man's Majorana zero modes in a chain with only two dots already possess non-abelian exchange statistics and can readily be used for the development of qubits.

10.2.1 Majorana parity readout and fusion

As we have seen in section 2.2.1, the presence of Majorana zero modes in a topological superconductor introduces a degeneracy in the ground state. The two degenerate states only differ in the occupation number of the nonlocal fermion comprised of the two Majoranas. Quantum information can be encoded in the parity of the pair of Majoranas $p_{12} = i\gamma_1\gamma_2$, using the even and odd occupation of the nonlocal fermion as the two basis states. Thus, the key challenge is to be able to read out the parity of a pair of Majoranas. Fortunately, a decade of research into Majorana zero modes

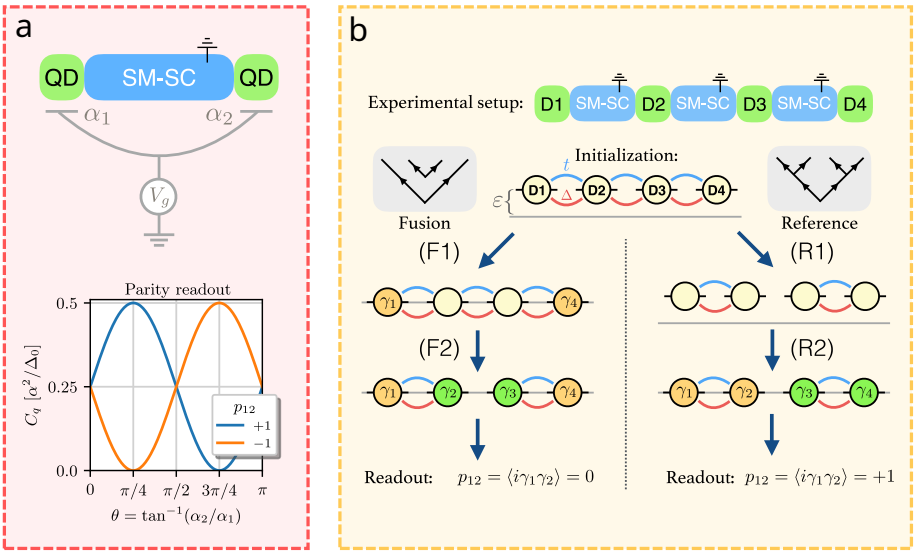

Figure 10.1: **Parity readout and Majorana fusion in the Kitaev chain. a.** Parity readout of a minimal Kitaev chain through a joint quantum capacitance measurement on both quantum dots. α_1 and α_2 represent the lever arms to the quantum dots. In particular, when either is zero, we have $\theta = 0$ or $\theta = \pi/2$, resulting in a loss of the quantum capacitance signal. **b.** Fusion protocol using a Kitaev chain with four sites. Depending on the order of various operations, in this case, the cutting of the chain and the initialization of the chain, one expects different outcomes of the parity measurement p_{12}. Adapted from [14].

has resulted in ample theoretical proposals on how to do this in the generic case of continuous wires. These proposals typically rely on coupling the pair of Majoranas to a common quantum dot [15, 16], or embed both in the arm of an interferometer [17, 18].

In general, a pair of Majoranas in a topological superconductor forms a delocalized fermionic mode. The consequence of their spatial separation is that local perturbations do not affect the system, which both protects the system and simultaneously complicates the readout of its properties - such as the parity of the Majorana pair. In the minimal Kitaev chain, this is reflected as stability against changes in the chemical potential of one of the two quantum dots. The implication is that measurements on one of the quantum dots, like a measurement of the charge, cannot distinguish between the two parity ground states of the chain [19]. Fortunately, however, the chain is not stable against variations of the chemical potential of both quantum dots. This instability can indeed be used to read out the parity of the Majorana pair. One way to do this is to simultaneously apply a perturbation of the chemical potential on both quantum dots and look at the fluctuations of the combined charge, using joint quantum capacitance measurements or shared coupling to a single-electron transistor [14, 19] as shown in figure 10.1a.

Once parity measurements have been realized, the road seems paved for the real breakthrough experiments: demonstration of the non-abelian exchange statistics. This can be pursued through fusion or braiding experiments, both of which require a setup with at least four Majorana zero modes. Many proposals for either type of experiment have been done over the last decade for continuous nanowires [15, 16, 18, 20], of which the same ideas apply to the Kitaev chain system. In particular, the Kitaev-chain adaptation of a fusion proposal, as depicted in figure 10.1b, seems the most viable in the near future. In such an experiment, one attempts to sequentially fuse different pairs of Majorana modes. Such a fusion is equivalent to a measurement of the parity of that Majorana pair: Fusing them either yields the vacuum state or a single fermion, indeed corresponding to the even and odd parity states. Like braiding, the order in which various operations are carried out influences the final result. Demonstrating such fusion rules would be an important stepping stone towards braiding experiments.

One of the things to consider is the time scale of such a fusion protocol. In order to avoid diabatic errors, the operations need to be executed sufficiently slowly [20]. The timescale $\tau = \hbar/\Delta$ for such errors is set by the induced gap of the system - that is, our value of the coupling parameter Δ. Depending on the exact experimental implementation of the protocol, different fusion outcomes could be distinguishable if the operations are on the order of $\tau = 25\hbar/\Delta \sim 1\,\text{ns}$ or slower [14]. On the other hand, the dephasing of the system puts an upper bound on the allowed time scale. Any deviations or fluctuations from the exact sweet spot in a minimal chain effectively couple the two Majorana modes, which results in fluctuations of their parity. Finally, flips in the parity can also be caused by quasiparticle poisoning. The time scale associated with this is not yet known, yet it plays a crucial role in the viability of future fusion and braiding experiments. Once parity readout has been demonstrated, the quasiparticle poisoning time can be readily obtained by executing time-resolved parity measurements.

10.2.2 Kitaev chains and Majorana qubits protected by a charging energy

The realization that quasiparticle poisoning is the main threat to the operation of Majorana-based quantum processors [21, 22] in fact inspired the latest generation of qubit designs [15, 20]. Such designs typically employ a charging energy in order to suppress quasiparticle poisoning of the qubit. Therefore, adapting the minimal Kitaev chain to use a floating superconductor [23] instead of a grounded superconductor could help incorporate a charging energy and thereby suppress quasiparticle poisoning. In addition, this would make it compatible with the many proposals for the continuous

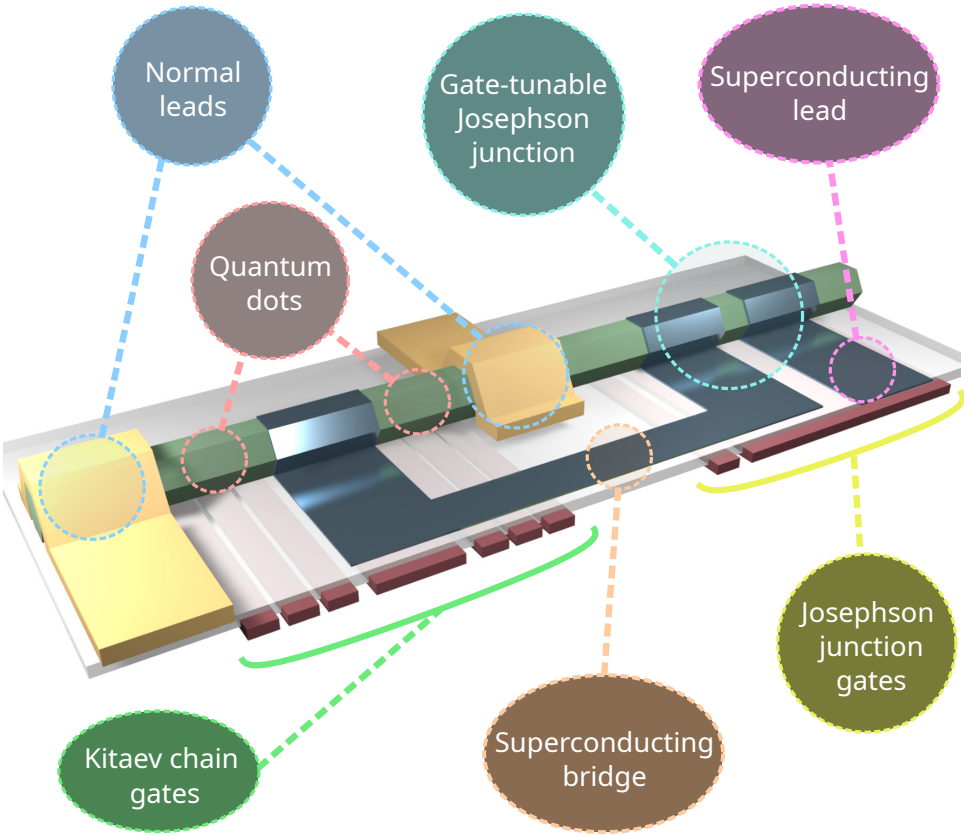

Figure 10.2: **Design for a Kitaev chain with tunable charging energy.** To study the emergence of Majorana zero modes in a floating Kitaev chain, this design can be used. The Kitaev chain is still formed out of two quantum dots separated by a narrow superconductor. The dots are formed with an array of gates underneath, and a gate for the hybrid segment can be used to tune its chemical potential. Normal leads can be used to perform spectroscopy on the two quantum dots. The superconducting segment is connected to a Josephson junction via the superconducting bridge. Gates underneath the Josephson junction can be used to tune the connection between the Kitaev chain and the grounded superconducting lead, resulting in a gate-tunable charging energy of the chain.

nanowire approach, which rely on a finite charging energy for the operations - such as the conversion of parity to charge [20, 24, 25]. Instead of simply interrupting the superconducting lead, it may be advantageous to replace it with a gate-tunable junction so that the device can be operated either with or without an charging energy [26]. An example of such a device is shown in figure 10.2. The minimal Kitaev chain is still formed using two quantum dots connected by a superconducting segment. However, the superconducting segment in this design loops around to a different part of the nanowire. There, a Josephson junction is formed with a second connecting piece of superconductor, while a narrow gate is used to deplete the part of the semiconducting

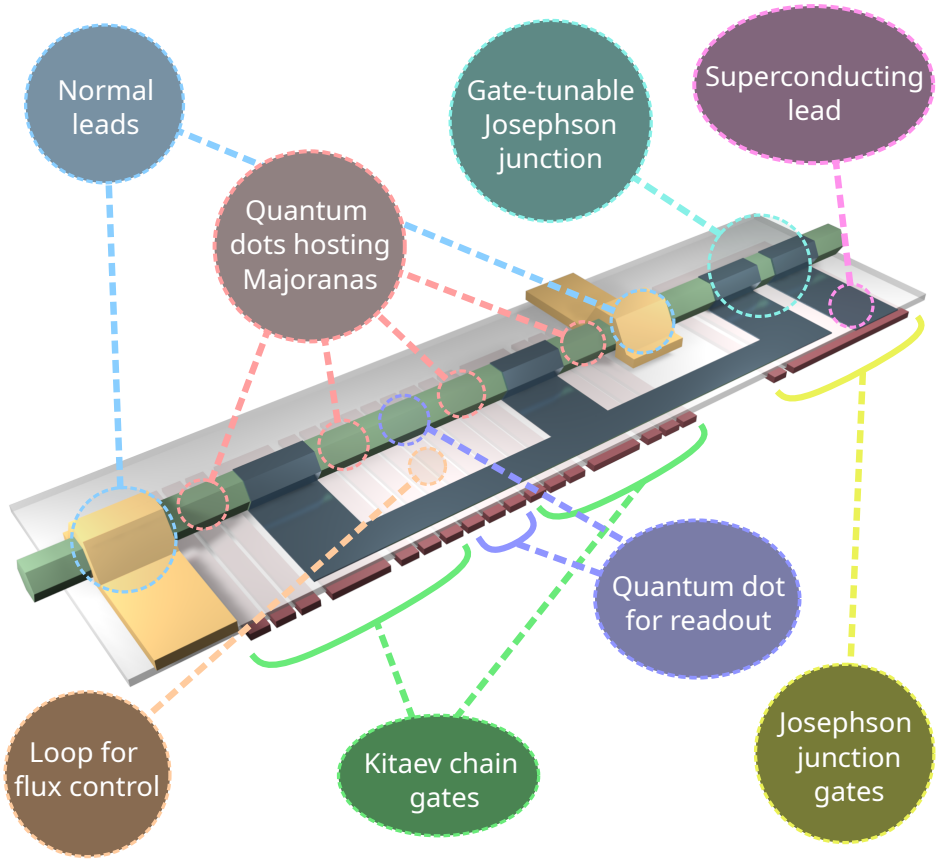

Figure 10.3: **Design for a loop qubit realized with two short Kitaev chains and a tunable charging energy.** A prototypical loop qubit requires the presence of four Majorana modes and can be realized using two minimal Kitaev chains. The gate-tunable Josephson junction can be used to adjust the charging energy of the qubit. A central dot can be used to detect the parity of the two inner Majorana modes. The two normal leads can be used to perform spectroscopy on the two outer dots in order to tune up the system. Otherwise, tuning of the quantum dots and readout of arbitrary pairs of Majoranas may be implemented via charge sensing of individual or pairs of quantum dots. In addition, the loop provides an additional knob to control the qubit via tuning of the flux with an external magnetic field.

wire which connects the Josephson junction and the right Ohmic contact. A large gate underneath the Josephson junction can be used to control its transmission, acting similar to those with a global back gate, as presented in chapter 4. If the junction is fully open, a supercurrent effectively connects the superconducting bridge to the superconducting lead without any additional resistance. On the other hand, the junction can be fully depleted, which disconnects the Kitaev chain from the electrical ground, so that it attains a finite charging energy. Combined with parity readout, the tunable junction can thus be used to determine the relation between the quasiparticle poisoning time and the charging energy.

It is straightforward to extend the design in order to form a prototypical Majorana qubit, as shown in figure 10.3. As a Majorana qubit requires at least four Majorana zero modes, this can be realized with two copies of a minimal Kitaev chain. Connecting them via a shared superconductor effectively realizes the Majorana box qubit [15, 18], which can be used to demonstrate measurement-based qubit operations. In such a qubit, parity measurements of different pairs of Majoranas act as the various qubit gates, depending on which pair is measured. This can be implemented using the joint readout of a pair of quantum dots via quantum capacitance measurements or shared coupling to a single-electron transistor.

10.2.3 Majoranas in longer Kitaev chains

As we have seen, the minimal Kitaev chain lacks stability against variations of system parameters and only hosts well-separated Majorana zero modes at a specific sweet spot. It is for this reason that the Poor Man's Majorana zero modes are said to be non-topological [19], despite exhibiting non-abelian exchange statistics. The minimal Kitaev chain does not really have a bulk excitation gap to protect it. However, this changes as more sites are added to the chain. Already for a chain with three sites, the central quantum dot should exhibit a quasiparticle gap whenever the chain is tuned near the sweet spot while the outer two dots again host the Majorana zero modes. In a nanowire geometry, however, it will be challenging to show such a bulk gap because its one-dimensional nature does not allow to fabricate an additional probe for the central quantum dot. Instead, one can look to measure the supercurrent between the two superconducting leads surrounding the dot. As an indirect measure, the absence of states near zero energy when the chain is tuned near the sweet spot should alter the supercurrent [27]. To obtain a direct observation of the bulk gap, it may be advantageous to switch to a different material platform. Two-dimensional electron gases in InAsSb have already demonstrated to possess the necessary ingredients for creating artificial Kitaev chains [28], so extending it into a three-site chain with an additional probe for the central dot should be well within reach.

Longer chains will also benefit any potential qubit designs in the future. The minimal chain does not possess any stability against variations in the ratio of Δ/t, and indeed this may be the main cause for the dephasing of any Majorana qubit. Fortunately, stability against these fluctuations is already gained for a three-site chain and only improves as the chain becomes longer. In figure 10.4, we calculated the energy spectrum of the Kitaev chain Hamiltonian 2.17. Figures 10.4a-d depict the spectrum as a function of the chemical

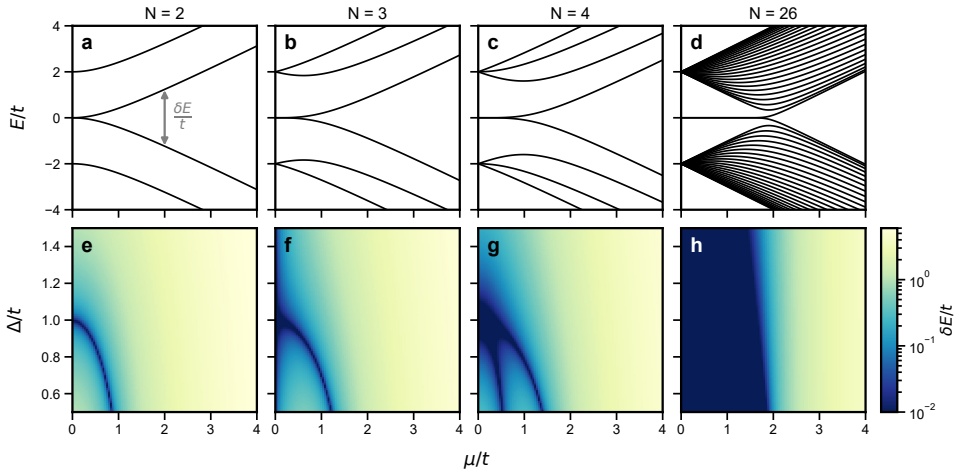

Figure 10.4: **Spectrum and zero-energy stability in longer Kitaev chains. a-d.** Energy spectrum of the Kitaev chain Hamiltonian 2.17 for $N = 2$ sites (**a**), $N = 3$ sites (**b**), $N = 4$ sites (**c**) and $N = 26$ sites (**d**). **e-h.** Energy splitting of the lowest energy state as the ratio of the couplings Δ/t, and the chemical potential, are varied. Near the sweet spot $\Delta/t = 1$ and $\mu/t = 0$, the zero energy modes are well-separated Majoranas. Their stability is visible as an increasingly large region with a small energy splitting as the length of the chain is increased. However, for small values of Δ there may also exist unstable modes near zero energy which do not represent Majoranas.

potential μ/t with $\Delta = t$, where we see that the stability of the zero-bias peak becomes enhanced with each added site - extending all the way up to $\mu = 2t$ for the long reference chain with $N = 26$ sites. In figures 10.4e-h, the energy splitting of the lowest energy state $\delta E/t$ is shown as a function of the chemical potential and coupling are changed. As the number of sites is increased, the region for which the zero-energy modes are stable grows surrounding the $\Delta/t = 1$, $\mu/t = 0$ sweet spot - signaling an enhanced dephasing time for potential qubits made with the longer chains.

One of the main critiques on the use of artificial Kitaev chains in contrast to long continuous nanowires is that it seems challenging to be able to tune up a longer chain. Each additional site comes with three additional gates for the quantum dot, one additional lead for the connecting superconductor, and an additional gate to tune that superconducting segment. Such challenges, however, are not unlike those seen in the spin qubit community, where quantum dot arrays as large as sixteen quantum dots have been successfully controlled [29]. Indeed, learning from the advances in that research field will significantly aid the development of longer Kitaev chains. Similarly, autonomous tuning based on machine learning may prove to be of paramount importance [30, 31].

10.2.4 Increased strength of the interaction between coupled quantum dots

Any attempt to do quantum information with Majorana zero modes would require the operations to be adiabatic. This means that the time of the operations should be large compared to the relevant energy scale, that is $\tau \gg \hbar/\Delta$. The values of $\Delta \sim 12\,\mu$eV obtained in

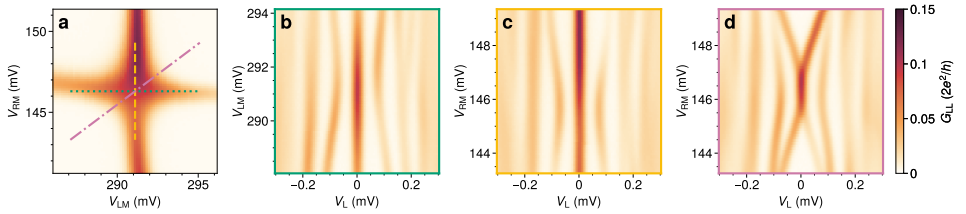

Figure 10.5: **Enhanced Majorana zero modes using proximitized quantum dots. a.** Charge stability diagram of two proximitized quantum dots near the sweet spot. **b.** Stability of the Majorana zero mode against fluctuations of the left quantum dot chemical potential. **c.** Stability of the Majorana zero mode against fluctuations of the right quantum dot chemical potential. **d.** Quadratic splitting of the zero-energy mode when both chemical potentials are varied simultaneously. Borders of panels b,c, and d indicate the variation of the chemical potential across the charge stability diagram indicated by the colored lines in a.

chapter 8 are indeed rather small, so there is a need for improvement. Since the number is determined by the coupling between the quantum dots, the most obvious way to do this is to simply lower the tunnel barriers leading to the central superconductor. However, this has the side effect of generating a superconducting pairing on the quantum dot, which effectively transforms the quantum dot levels into Andreev bound states, as described in section 2.3.2. In this form, the Kitaev chain can still be formed despite not having normal quantum dot levels [32]. Experiments are already progressing in this direction, as shown in figure 10.5. In figure 10.5a, the charge stability diagram of such a sweet spot is shown. Figures 10.5b and c show the stability against fluctuations of one of the quantum dot chemical potentials, exhibiting a dispersing excited state but a stable zero-bias peak. Variation of both chemical potentials, as shown in figure 10.5d, quadratically splits the zero-bias peak as expected. Notably, at the sweet spot, the spectrum has a quadruple increase in the energy gap, on the order of $2\Delta \sim 80\,\mu$eV. The deterministically increased coupling between the quantum dots and the superconductor automatically results in a stronger inter-dot coupling. At the same time, that increased coupling also makes it significantly easier to reproduce and tune the quantum dots to the Majorana sweet spot. With the normal dots we could only reproduce a strong-enough coupling in 2 out of 6 devices, whereas this type of chain with an enhanced coupling can be reproducibly be created in every device. Finally, the sweet spot is also significantly more stable against fluctuations of the gate voltage, being able to tolerate an order of magnitude larger voltage fluctuations.

The observable coupling in such systems is limited by the energy of the Andreev bound state mediating the coupling between the quantum dots. This energy is determined both by the coupling of the state to the superconductor and the value of the Zeeman energy. In general, larger magnetic fields result in a better polarization of the quantum dots but also reduce the ABS energy. Thus, it may be advantageous in the long term to investigate materials with a larger superconducting gap instead of aluminum, such as lead or niobium.

References

[1] S. Gazibegovic, D. Car, H. Zhang, S. C. Balk, J. A. Logan, M. W. De Moor, M. C. Cassidy, R. Schmits, D. Xu, G. Wang, *et al.*, *Retracted article: Epitaxy of advanced nanowire quantum devices,* Nature **548**, 434 (2017).

[2] B. D. Woods, S. Das Sarma, and T. D. Stanescu, *Subband occupation in semiconductor-superconductor nanowires,* Phys. Rev. B **101**, 045405 (2020).

[3] A. E. Antipov, A. Bargerbos, G. W. Winkler, B. Bauer, E. Rossi, and R. M. Lutchyn, *Effects of gate-induced electric fields on semiconductor majorana nanowires,* Phys. Rev. X **8**, 031041 (2018).

[4] B. D. Woods, S. D. Sarma, and T. D. Stanescu, *Charge-impurity effects in hybrid majorana nanowires,* Physical Review Applied **16**, 054053 (2021).

[5] S. Ahn, H. Pan, B. Woods, T. D. Stanescu, and S. D. Sarma, *Estimating disorder and its adverse effects in semiconductor majorana nanowires,* Physical Review Materials **5**, 124602 (2021).

[6] G. Badawy, S. Gazibegovic, F. Borsoi, S. Heedt, C.-A. Wang, S. Koelling, M. A. Verheijen, L. P. Kouwenhoven, and E. P. Bakkers, *High mobility stemless insb nanowires,* Nano letters **19**, 3575 (2019).

[7] Z. Lei, C. A. Lehner, E. Cheah, M. Karalic, C. Mittag, L. Alt, J. Scharnetzky, W. Wegscheider, T. Ihn, and K. Ensslin, *Quantum transport in high-quality shallow insb quantum wells,* Applied Physics Letters **115**, 012101 (2019).

[8] M. Aghaee, A. Akkala, Z. Alam, R. Ali, A. A. Ramirez, M. Andrzejczuk, A. E. Antipov, M. Astafev, B. Bauer, J. Becker, *et al.*, *Inas-al hybrid devices passing the topological gap protocol,* arXiv preprint arXiv:2207.02472 (2022).

[9] C. M. Moehle, C. T. Ke, Q. Wang, C. Thomas, D. Xiao, S. Karwal, M. Lodari, V. van de Kerkhof, R. Termaat, G. C. Gardner, *et al.*, *Insbas two-dimensional electron gases as a platform for topological superconductivity,* Nano Letters **21**, 9990 (2021).

[10] J. Shabani, M. Kjaergaard, H. J. Suominen, Y. Kim, F. Nichele, K. Pakrouski, T. Stankevic, R. M. Lutchyn, P. Krogstrup, R. Feidenhans'l, S. Kraemer, C. Nayak, M. Troyer, C. M. Marcus, and C. J. Palmstrøm, *Two-dimensional epitaxial superconductor-semiconductor heterostructures: A platform for topological superconducting networks,* Phys. Rev. B **93**, 155402 (2016).

[11] J. S. Lee, B. Shojaei, M. Pendharkar, M. Feldman, K. Mukherjee, and C. J. Palmstrøm, *Contribution of top barrier materials to high mobility in near-surface inas quantum wells grown on gasb(001),* Phys. Rev. Mater. **3**, 014603 (2019).

[12] G. Badawy, B. Zhang, T. Rauch, J. Momand, S. Koelling, J. Jung, S. Gazibegovic, O. Moutanabbir, B. J. Kooi, S. Botti, *et al.*, *Electronic structure and epitaxy of cdte shells on insb nanowires,* Advanced Science **9**, 2105722 (2022).

[13] S. Schuwalow, N. B. Schröter, J. Gukelberger, C. Thomas, V. Strocov, J. Gamble, A. Chikina, M. Caputo, J. Krieger, G. C. Gardner, *et al.*, *Band structure extraction at hybrid narrow-gap semiconductor–metal interfaces,* Advanced Science **8**, 2003087 (2021).

[14] C.-X. Liu, H. Pan, F. Setiawan, M. Wimmer, and J. D. Sau, *Fusion protocol for majorana modes in coupled quantum dots,* arXiv preprint arXiv:2212.01653 (2022).

[15] T. Karzig, C. Knapp, R. M. Lutchyn, P. Bonderson, M. B. Hastings, C. Nayak, J. Alicea, K. Flensberg, S. Plugge, Y. Oreg, C. M. Marcus, and M. H. Freedman, *Scalable designs for quasiparticle-poisoning-protected topological quantum computation with majorana zero modes,* Phys. Rev. B **95**, 235305 (2017).

[16] G. Széchenyi and A. Pályi, *Parity-to-charge conversion for readout of topological majorana qubits,* Phys. Rev. B **101**, 235441 (2020).

[17] L. Fu, *Electron teleportation via majorana bound states in a mesoscopic superconductor,* Physical review letters **104**, 056402 (2010).

[18] S. Plugge, A. Rasmussen, R. Egger, and K. Flensberg, *Majorana box qubits,* New Journal of Physics **19**, 012001 (2017).

[19] M. Leijnse and K. Flensberg, *Parity qubits and poor man's majorana bound states in double quantum dots,* Phys. Rev. B **86**, 134528 (2012).

[20] D. Aasen, M. Hell, R. V. Mishmash, A. Higginbotham, J. Danon, M. Leijnse, T. S. Jespersen, J. A. Folk, C. M. Marcus, K. Flensberg, and J. Alicea, *Milestones toward majorana-based quantum computing,* Phys. Rev. X **6**, 031016 (2016).

[21] D. Rainis and D. Loss, *Majorana qubit decoherence by quasiparticle poisoning,* Physical Review B **85**, 174533 (2012).

[22] M. Cheng, R. M. Lutchyn, and S. D. Sarma, *Topological protection of majorana qubits,* Physical Review B **85**, 165124 (2012).

[23] A. Tsintzis, R. S. Souto, and M. Leijnse, *Creating and detecting poor man's majorana bound states in interacting quantum dots,* Phys. Rev. B **106**, L201404 (2022).

[24] M. Hell, J. Danon, K. Flensberg, and M. Leijnse, *Time scales for majorana manipulation using coulomb blockade in gate-controlled superconducting nanowires,* Phys. Rev. B **94**, 035424 (2016).

[25] R. S. Souto and M. Leijnse, *Fusion rules in a majorana single-charge transistor,* SciPost Phys. **12**, 161 (2022).

[26] M. Valentini, M. Borovkov, E. Prada, S. Martí-Sánchez, M. Botifoll, A. Hofmann, J. Arbiol, R. Aguado, P. San-Jose, and G. Katsaros, *Majorana-like coulomb spectroscopy in the absence of zero-bias peaks,* Nature **612**, 442 (2022).

[27] J.-P. Cleuziou, W. Wernsdorfer, V. Bouchiat, T. Ondarçuhu, and M. Monthioux, *Carbon nanotube superconducting quantum interference device,* Nature nanotechnology **1**, 53 (2006).

[28] Q. Wang, S. L. ten Haaf, I. Kulesh, D. Xiao, C. Thomas, M. J. Manfra, and S. Goswami, *Triplet cooper pair splitting in a two-dimensional electron gas,* arXiv preprint arXiv:2211.05763 (2022).

[29] F. Borsoi, N. W. Hendrickx, V. John, S. Motz, F. van Riggelen, A. Sammak, S. L. de Snoo, G. Scappucci, and M. Veldhorst, *Shared control of a 16 semiconductor quantum dot crossbar array,* arXiv preprint arXiv:2209.06609 (2022).

[30] R. Koch, D. van Driel, A. Bordin, J. L. Lado, and E. Greplova, *Adversarial hamiltonian learning of quantum dots in a minimal kitaev chain,* arXiv preprint arXiv:2304.10852 (2023).

[31] A. Dawid, J. Arnold, B. Requena, A. Gresch, M. Płodzień, K. Donatella, K. A. Nicoli, P. Stornati, R. Koch, M. Büttner, *et al.*, *Modern applications of machine learning in quantum sciences,* arXiv preprint arXiv:2204.04198 (2022).

[32] I. C. Fulga, A. Haim, A. R. Akhmerov, and Y. Oreg, *Adaptive tuning of majorana fermions in a quantum dot chain,* New journal of physics **15**, 045020 (2013).

Acknowledgments

During my time as a master student in physics, the field of Majorana research was living its high days. For me, the promise that Majorana qubits held far beyond that of conventional qubits sparked sheer excitement - the prime reason for starting a Ph.D. in this field. As the Ph.D. journey unfolded, however, it became increasingly apparent that the path ahead was going to be much more challenging than initially anticipated. It even came to the point where the hope of creating Majorana zero modes in long nanowires was lost completely. Yet, thanks to a true intervention of serendipity, we are left with an alternative paradigm and renewed prospects for the future. And so, remarkably, we find ourselves back at the starting point: on the cusp of constructing the inaugural Majorana qubits. The journey has come full circle, a journey marked by many highs and lows, successes and failures. That roller-coaster of emotions would not have been the same without all the incredible people involved. First off, my sincere thanks to **Chris**, **Georgios**, **Jelena**, **Gary** and **Jos** for taking the time and effort to be a part of my doctoral defense committee.

Leo, it is hard to express how different this journey had been from the one I imagined, and I think few people can say they have been through a similar experience. There have been some very dark moments we had to face together in a world that is not always fair or just. Yet, these were also precious learning experiences and now, in the end, I know for certain that the sun always shines behind the clouds. I will be forever grateful for the opportunity you have given me, a ticket to a ride that let me experience wondrous science and amazing people above all. You have created an extraordinary place to learn and conduct research, and the depths of your knowledge never ceased to amaze me. Yet, perhaps the single most important thing for me to thank you for, is moving me from the SAG project to the Loop Qubit team a few months after I started my Ph.D. It is there that I found the opportunities and confidence that ultimately made this thesis possible in a way I do not think would have happened otherwise.

The first year of my Ph.D. was quite a difficult time, though. Our fabrication process did not yield great results and took a long time to optimize. It was only early in my second year that this started to work, but the tedious process left me drained of energy and ideas. It was around that time that you joined our lab **Greg**, and we both found ourselves in similar positions: uncertain what to do or work on. It was thus quite natural for us to join forces, and your out-of-the-box thinking quickly restored my enthusiasm for research. What I did not know then is how easy and fun I would find working with you. We have shared so many great memories together, from brainstorming ideas over a coffee or a beer to me taking over your March meeting talk because your daughter was being born at that very moment. Your ceaseless stream of ideas has also led us to try so many different things, though inevitably, some of them would not work out. Such moments would leave me feeling down and disappointed, but you taught me the most valuable lesson because of

that: Not everything we do is great, nor does not have to be. Working with you inspired within me the ambition to do great science, and together we have created the foundation upon which the recent successes are built. Thank you for being a fantastic colleague and friend, and thank you for saving my Ph.D.

Here is to two people who have been with me on this journey from the very start. Two people with whom I have shared some of the darkest times one can imagine in a scientific career together, and such things were only bearable because of them. But more importantly, with whom I have shared a far greater amount of good times and memories. **Guan**, you have been a fantastic physicist from the start (perhaps except blowing up my very first sample), and it has been a true honor to work with someone as talented as you. I have enjoyed many great laughs together with you over a coffee or on one of our trips, for sure memories of Miami and America the Beautiful will stay with me for life. I wish you all the best in Stanford, and know that you will be deeply missed here. **Di**, I have learned a great deal of skills in the cleanroom from you, and you made these moments so much more enjoyable. I also remember vividly our bizarre trip to Colorado. We had just arrived in Denver a few days before the March meeting, only to discover that it would be canceled a few hours after our arrival. Despite missing out on the conference, the trip led to many beautiful sights and was an amazing experience.

In a lab with many people, it makes sense for them to team up around larger projects. For the largest part of my Ph.D., that has been the Loop Qubit team - a team with the purpose of building a Majorana loop qubit. **Marina**, **Sebastian**, and **Francesco B**, the three of you formed a powerful trinity that seemed able to conquer any challenge. Your persistence, even when things looked dire, was of paramount importance for the success of the team. More importantly, you formed the foundation for developing the smart wall technology and thereby did the same for this thesis. A special thanks to Francesco. During my toughest times when I was on the brink of giving up, your encouragement and the reminder that brighter days were ahead gave me the strength to keep going. The Loop Qubit team has seen many more members over the years. I am particularly grateful to **Mark**, you have been an invaluable asset to the team thanks to your unwavering dedication to the UTS. Thanks also to **Alexandra** and **Kevin**, you provided valuable support to the team in the beginning with your cleanroom and simulation skills. **Jie**, your optimism and great sense of humor never failed to spark joy. Your ambition and dedication to your work have been truly inspiring. **Ji-Yin** and **Vukan**, the two of you formed an exceptional dream team. It is impressive to see you take on a great number of very different projects, and I have enjoyed our various scientific discussions. **Cristina**, your kindness, ever-optimistic presence and cheerfulness always greatly improved the atmosphere when you were around. **Mathilde** and **Jan Cornelis**, your support of the team by running and maintaining the UTS as well as in the cleanroom has been invaluable. By providing such support, you take a huge weight off the shoulders of students like me and directly enable us to succeed. Finally, I'd like to thank the ingenious master students **May An**, **Peter**, and **Robin** that I have had the pleasure to guide over the years.

Alas, as the hopes of finding Majoranas in proximitized nanowires faded away, so did

the dream of building a loop qubit and ending the Loop Qubit team. Yet, from the ashes arose the Kitaev team. **Tom**, you recognized the true potential of the UTS platform and shadow wall technology that we had developed. Your ideas to utilize quantum dots in hybrid nanowires have directly revived the field of Majorana research. I have learned a great many things from your seemingly-limitless knowledge. You have been a true inspiration, and it is thanks to you that the future of this lab looks bright and prosperous. It has been a pleasure and honor to work with you. **David**, it has been a joy to see you evolve from a fletching master student to the accomplished and independent researcher you are now. And keep those memes rolling, for they brighten up the daily life in the lab so much. I'll never forget the wonderful America the Beautiful trip with you and Nienke. **Alberto**, it too has been amazing to see you grow over the years. Your sheer optimism and excitement for the research can be an inspiration to us all. **Francesco Z**, your grounding presence is a welcome counterweight to the strong opinions that me, and others, can have. Even though you are only in your first year, your knowledge and skills are far beyond that. In your capable hands, the future of this lab certainly looks bright - especially with the fresh additions of **Bart** and **Sebas**. **Chun-Xiao** and **Michael W**, your swift and dedicated work has built the bridge between theorists and experimentalists that will surely allow us all to thrive. The 2DEG team of **Srijit** with **Bas**, **Ivan**, **Qing**, **Yining**, and **Rebecca**, it has been fantastic to see you pick up on the Kitaev chain experiments. Surely with our combined efforts, the promise of Majorana qubits will be within our reach. It has been a great pleasure to interact with you all, both while discussing science and drinking beers in the TPKV.

The journey would not have been the same without all the marvelous people that make QuTech, and QuRe, such a special place. **Jaap**, **Marta**, **Lukas S**, **Lukas G**, and **Arno**, in a lab devoted to Majorana physics, you managed to stand out and be hugely successful by doing something different. Though I only recently started to get a feeling for CQED, your work has left a profound impression on me. The same holds for **Filip**, **Lin**, **Christian P**, and **Michael C**. I appreciate sincerely the interaction with all those who have been part of topo, like **James**, **Willemijn**, **Daniël**, **Fokko**, **Jasper**, **Damaz**, **Matt**, **Vanessa**, **Luca**, **Ting**, **Christian M**, **Prasana**, **Senja**, **Chien-An**, **Kiefer** and many more. I have learned so much from all of you. A special thanks to **Jouri** for training and guiding me in the first steps of the cleanroom and in the lab, as well as to **Michiel** and **Hao**.

One of the things that makes QuTech an extraordinary place to do research is the supporting staff, to which I owe tremendous gratitude. **Jason**, **Olaf**, **Remco**, **Roy**, **Jelle**, **Siebe**, **Vinod** and **Erik W**, from setting up and maintaining the wirebonder, to making sure the fridges and cooling water keep running, to maintaining the UTS, and countless other responsibilities - without you, QuTech would crumble. Your hard work and technical expertise are, without a doubt, indispensable. **Jenny**, it is always a joy to meet you in the office. Thank you for dealing with all the administrative tasks, but even more so for organizing the various trips, parties, and barbecues! **Csilla**, meeting you in the office is equally joyful. Thank you especially for all the effort you put towards diversity, inclusion and social safety! **Delphine**, thanks for your efforts to professionalize our fabrication and bridging the gap between the TU and TNO. **Raymonds**, your deep

knowledge of electronics and circuits has proven vital for many of the experiments done in this work. My deepest gratitude also to the **cleanroom staff**. Your tireless work to maintain and improve the cleanroom, and teach so many people the ropes of nanofabrication, are nothing but an incredible feat. It has also been astounding to see QuRe diversify beyond Majorana research in the lab of **Christian A. Anton**, your feedback on the various projects that I've worked on over the years was very valuable and appreciated. I greatly enjoyed interactions with you and your research group in the coffee corner.

I have had the opportunity to collaborate with and learn from many others outside of QuTech. This thesis would have been impossible to complete if not for the unrivaled nanowires from **Ghada**, **Roy**, **Sasa**, and **Erik B**. I have also been fortunate to benefit from collaboration with the Microsoft lab. **Amrita** and **Elvedin**, your work in the cleanroom has been a meaningful contribution towards designing our fabrication flow. **Kongyi**, **Svetlana**, **Mariusz**, and **Emrah**, seeing our samples in your TEM cuts and analysis has been both fascinating and critical. I have also learned a great deal from discussions and interaction with **Aleksei**, **Andrey**, **Dmitry**, **Roman**, **Léo**, **Georg**, **Philippe**, **Frenk**, **Ivana** and many more.

Vaak wordt de indruk gewekt dat het leven van een promovendus voornamelijk om werk draait. Maar om al dat werk vol te kunnen houden, is niets belangrijker dan de mensen daarbuiten. Ik heb door de jaren heen ontzettend veel plezier gehad tijdens onze DnD-campagnes samen met **Victor**, **Jeroen**, **Joël**, **Hidde**, **Rory** en **Jens**. Het was geweldig om af en toe met jullie te kunnen ontsnappen aan de werkelijkheid, natuurlijk onder het genot van lekkere hapjes en drankjes. Ik wil ook iedereen van **DWH/Outsite** heel erg bedanken; dankzij jullie is de vereniging al die jaren een tweede thuis voor mij geweest. Daarbij wil ik in het bijzonder **Iris**, **Gijs**, **Kishan**, **Mike**, **Wessel**, **Andreas**, **Bouke**, **Casper**, **Daan**, **Dante**, **Govert**, **Jelle**, **Leon**, **Niv**, **Quinten** en **Wouter** bedanken voor al jullie gezelligheid en vriendschap.

Misschien wel de meeste dank ben ik verschuldigd aan mijn ouders. **Pap**, **Marjon** en **Mam**, zonder jullie steun was ik nooit zo ver gekomen. Woorden kunnen niet uitdrukken hoe dankbaar ik ben voor jullie. Mam, ik draag je altijd bij me in mijn hart. Ik kan me alleen maar voorstellen hoe trots je nu wel niet zou zijn. Ik ben ook ontzekkend dankbaar voor mijn geweldige **familie**, voor al jullie interesse en de mooie herinneringen die we samen hebben gemaakt.

Als laatste mijn diepste dank naar **Victor**. Je bent er atijd voor me geweest en hebt alle momenten, goed en slecht, van dichtbij meegemaakt. Van de teleurstelling wanneer dingen weer is niet werkten tot de vreugde als papers eindelijk gepubliceerd waren. Jouw liefde, luisterend oor en onaflatende steun ben ik je eeuwig dankbaar voor.

Curriculum Vitæ

Nick van Loo

1991/08/30	Born in Velsen the Netherlands
2003-2010	Ichthus Lyceum Driehuis the Netherlands
2010-2014	B.Sc. Applied Physics, Delft University of Technology the Netherlands
2014-2018	M.Sc. Applied Physics, Delft University of Technology the Netherlands Supervisor: Prof. dr. ir. Leo P. Kouwenhoven
2018-2023	Ph.D. research at QuTech, Delft University of Technology the Netherlands Promotor: : Prof. dr. ir. Leo P. Kouwenhoven

List of Publications

Not everything we do is great.

Grzegorz P. Mazur

Journal publications and preprints

17. *Crossed Andreev reflection and elastic co-tunneling in a three-site Kitaev chain nanowire device*
A. Bordin, X. Li, D. van Driel, J.C. Wolff, Q. Wang, S.L.D. ten Haaf, G. Wang, **N. van Loo**, L.P. Kouwenhoven and T. Dvir
arXiv:2306.07696 (2023)

16. *Realization of a minimal Kitaev chain in coupled quantum dots*
T. Dvir†, G. Wang†, **N. van Loo**†, C.-X. Liu, G.P. Mazur, A. Bordin, S.L.D. ten Haaf, J.-Y. Wang, D. van Driel, F. Zatelli, X. Li, F.K. Malinowski, S. Gazibegovic, G. Badawy, E.P.A.M. Bakkers, M. Wimmer and L.P. Kouwenhoven
Nature 614, 445–450 (2023)

15. *Spin-filtered measurements of Andreev bound states*
D. van Driel†, G. Wang†, A. Bordin, **N. van Loo**, F. Zatelli, G.P. Mazur, D. Xu, S. Gazibegovic, G. Badawi, E.P.A.M. Bakkers, L.P. Kouwenhoven and T. Dvir†
arXiv:2212.10241 (2022)

14. *Controlled crossed Andreev reflection and elastic co-tunneling mediated by Andreev bound states*
A. Bordin†, G. Wang†, C.-X. Liu†, S.L.D. ten Haaf, G.P. Mazur, **N. van Loo**, D. Xu, D. van Driel, F. Zatelli, S. Gazibegovic, G. Badawy, E.P.A.M. Bakkers, M. Wimmer, L.P. Kouwenhoven and T. Dvir
arXiv:2212.02274 (2022)

13. *The gate-tunable Josephson diode*
G.P. Mazur†, **N. van Loo**†, D. van Driel, J.-Y. Wang, G. Badawy, S. Gazibegovic, E.P.A.M. Bakkers and L.P. Kouwenhoven
arXiv:2211.14283 (2022)

12. *Singlet and triplet Cooper pair splitting in hybrid superconducting nanowires*
G. Wang†, T. Dvir†, G.P. Mazur†, C.-X. Liu, **N. van Loo**, S.L.D. ten Haaf, A. Bordin, S. Gazibegovic, G. Badawy, E.P.A.M. Bakkers, M. Wimmer and L.P. Kouwenhoven
Nature 612, 448–453 (2022)

11. *Impact of junction length on supercurrent resilience against magnetic field in InSb-Al nanowire Josephson junctions*
V. Levajac, G.P. Mazur, **N. van Loo**, F. Borsoi, G. Badawy, S. Gazibegovic, E.P.A.M. Bakkers, S. Heedt, L.P. Kouwenhoven and J.-Y. Wang
arXiv preprint arXiv:2211.07858 (2022)

10. *Electrostatic control of the proximity effect in the bulk of semiconductor-superconductor hybrids*
N. van Loo†, G.P. Mazur†, T. Dvir, G. Wang, R.C. Dekker, J.-Y. Wang, M. Lemang, C. Sfiligoj, A. Bordin, D. van Driel, G. Badawy, S. Gazibegovic, E.P.A.M. Bakkers and L.P. Kouwenhoven
arXiv:2211.06709 (2022)

9. *Parametric exploration of zero-energy modes in three-terminal InSb-Al nanowire devices*
J.-Y. Wang, **N. van Loo**, G.P. Mazur, V. Levajac, F.K. Malinowski, M. Lemang, F. Borsoi, G. Badawy, S. Gazibegovic, E.P.A.M. Bakkers, M. Quintero-Pérez, S. Heedt and L.P. Kouwenhoven
Physical Review B 106, 075306 (2022)

8. *Nonlocal measurement of quasiparticle charge and energy relaxation in proximitized semiconductor nanowires using quantum dots*
G. Wang†, T. Dvir†, **N. van Loo**, G.P. Mazur, S. Gazibegovic, G. Badawy, E.P.A.M. Bakkers, L.P. Kouwenhoven and G. de Lange
Physical Review B 106 (6), 064503

7. *Spin-mixing enhanced proximity effect in aluminum-based superconductor-semiconductor hybrids*
G.P. Mazur†, **N. van Loo**†, J.-Y. Wang, T. Dvir, G. Wang, A. Khindanov, S. Korneychuk, F. Borsoi, R.C. Dekker, G. Badawy, P. Vinke, S. Gazibegovic, E.P.A.M. Bakkers, M. Quintero-Pérez, S. Heedt and L.P. Kouwenhoven
Advanced Materials 2022, 34, 2202034

6. *Single-Shot Fabrication of Semiconducting–Superconducting Nanowire Devices*
F. Borsoi, G.P. Mazur, **N. van Loo**, M.P. Nowak, L. Bourdet, K. Li, S. Korneychuk, A. Fursina, J.-Y. Wang, V. Levajac, E. Memisevic, G. Badawy, S. Gazibegovic, K. van Hoogdalem, E.P.A.M. Bakkers, L.P. Kouwenhoven, S. Heedt and M. Quintero-Pérez
Advanced Functional Materials 31 (34), 2102388

5. *Shadow-wall lithography of ballistic superconductor-semiconductor quantum devices*
S. Heedt†, M. Quintero-Pérez†, F. Borsoi†, A. Fursina, **N. van Loo**, G.P. Mazur, M.P. Nowak, M. Ammerlaan, K. Li, S. Korneychuk, J. Shen, M.A.Y. van de Poll, G. Badawy, S. Gazibegovic, N. de Jong, P. Aseev, K. van Hoogdalem, E.P.A.M. Bakkers and L.P. Kouwenhoven
Nature Communications 12, 4914 (2021)

4. *Large zero-bias peaks in InSb-Al hybrid semiconductor-superconductor nanowire devices*
H. Zhang†, M.W.A. de Moor†, J.D.S. Bommer†, D. Xu, G. Wang, **N. van Loo**, C.-X. Liu, S. Gazibegovic, J.A. Logan, D. Car, R.L.M. op het Veld, P.J. van Veldhoven, S. Koelling, M.A. Verheijen, M. Pendharkar, D.J. Pennachio, B. Shojaei, J.S. Lee, C.J. Palmstrøm, E.P.A.M. Bakkers, S. Das Sarma and L.P. Kouwenhoven
arXiv:2101.11456 (2021)

3. *Electric field tunable superconductor-semiconductor coupling in Majorana nanowires*
M.W.A. de Moor†, J.D.S. Bommer†, D. Xu†, G.W. Winkler, A.E. Antipov, A. Bargerbos, G. Wang, **N. van Loo**, R.L.M. op het Veld, S. Gazibegovic, D. Car, J.A. Logan, M. Pendharkar, J.S. Lee, E.P.A.M. Bakkers, C.J. Palmstrøm, R.M. Lutchyn, L.P. Kouwenhoven and H. Zhang
New Journal of Physics 20 (10), 103049

2. *DNA nanopore translocation in glutamate solutions*
C. Plesa, **N. van Loo** and C. Dekker
Nanoscale 7.32 (2015): 13605-13609

1. *Velocity of DNA during translocation through a solid-state nanopore*
C. Plesa, **N. van Loo**, P. Ketterer, H. Dietz and C. Dekker
Nano letters 15 (1), 732-737

Patent applications

1. *Semiconductor-superconductor hybrid device and fabrication thereof*
G.P. Mazur, **N. van Loo** and M. Quintero-Pérez.
WO 2021/170252 World Intellectual Property Organization (02 September 2021)

† Equal contribution